

Advances in Meteorology

Data Assimilation in Numerical Weather and Climate Models

Guest Editors: Shaoqing Zhang, Guijun Han, Yuanfu Xie, and Juan Jose Ruiz





Data Assimilation in Numerical Weather and Climate Models

Advances in Meteorology

Data Assimilation in Numerical Weather and Climate Models

Guest Editors: Shaoqing Zhang, Guijun Han, Yuanfu Xie,
and Juan Jose Ruiz



Copyright © 2015 Hindawi Publishing Corporation. All rights reserved.

This is a special issue published in “Advances in Meteorology.” All articles are open access articles distributed under the Creative Commons Attribution License, which permits unrestricted use, distribution, and reproduction in any medium, provided the original work is properly cited.

Editorial Board

J. Antonio Adame, Spain
C. Azorin-Molina, Spain
G. Baigorria, USA
Marina Baldi, Italy
Abderrahim Bentamy, France
Massimo A. Bollasina, UK
Stefania Bonafoni, Italy
Isabella Bordi, Italy
Alex Cannon, Canada
Claudio Carbone, Italy
Dominique Carrer, France
Charles Chemel, UK
Annalisa Cherchi, Italy
James Cleverly, Australia
Jill S. M. Coleman, USA
Gabriele Curci, Italy
M. Ćurić, Serbia
Klaus Dethloff, Germany
P. C. S. Devara, India
Julio Diaz, Spain
Arona Diedhiou, France
Stefano Dietrich, Italy
Eugenio D.n. Vilches, Spain
Antonio Donateo, Italy
Igor Esau, Norway
Stefano Federico, Italy
Enrico Ferrero, Italy
Rossella Ferretti, Italy
Roberto Fraile, Spain
C. Franklin, Australia
Jan Friesen, Germany

M. Ángeles García, Spain
Herminia García Mozo, Spain
Eduardo García-Ortega, Spain
Luis Gimeno, Spain
Jorge E. Gonzalez, USA
Ismail Gultepe, Canada
Rafiq Hamdi, Belgium
Adel Hanna, USA
Hiroyuki Hashiguchi, Japan
Tareq Hussein, Jordan
Bradley G. Illston, USA
Ivar S A Isaksen, Norway
Yasunobu Iwasaka, Japan
Pedro Jiménez-Guerrero, Spain
Kuruvilla John, USA
Charles Jones, USA
Hann-Ming H. Juang, USA
George Kallos, Greece
Harry D. Kambezidis, Greece
Nir Y. Krakauer, USA
Simon O. Krichak, Israel
Hisayuki Kubota, Japan
Haim Kutiel, Israel
Richard Leaitch, Canada
Monique Leclerc, USA
Ilan Levy, Israel
Gwo-Fong Lin, Taiwan
Anthony R. Lupo, USA
Paolo Madonia, Italy
Andreas Matzarakis, Germany
Samantha Melani, Italy
Nicholas Meskhidze, USA

C. Messenger, France
Mario M. Miglietta, Italy
Takashi Mochizuki, Japan
Andrea Montani, Italy
Goro Mouri, Japan
Brian R. Nelson, USA
E. I. Nikolopoulos, USA
Sandip Pal, USA
Giulia Panegrossi, Italy
Giulia Pavese, Italy
Kyaw T. Paw, USA
Olivier P. Prat, USA
Sara C. Pryor, USA
Philippe Ricaud, France
Tomeu Rigo, Spain
Filomena Romano, Italy
Jose Antonio Ruiz-Arias, Spain
Haydee Salmun, USA
Pedro Salvador, Spain
A. Sanchez-Lorenzo, Spain
Andres Schmidt, USA
S. Shukla, USA
Fiona Smith, UK
F. J. Tapiador, Spain
Yoshihiro Tomikawa, Japan
Tomoo Ushio, Japan
R. Van Der Velde, The Netherlands
S. M. Vicente-Serrano, Spain
Francesco Viola, Italy
Alastair Williams, Australia
Olga Zolina, France

Contents

Data Assimilation in Numerical Weather and Climate Models, Shaoqing Zhang, Guijun Han, Yuanfu Xie, and Juan Jose Ruiz

Volume 2015, Article ID 626893, 2 pages

Initialized Decadal Predictions by LASG/IAP Climate System Model FGOALS-s2: Evaluations of Strengths and Weaknesses, Bo Wu, Xiaolong Chen, Fengfei Song, Yong Sun, and Tianjun Zhou

Volume 2015, Article ID 904826, 12 pages

Statistical Prediction of the South China Sea Surface Height Anomaly, Caixia Shao, Weimin Zhang, Chunjian Sun, Xinmin Chai, and Zhimin Wang

Volume 2015, Article ID 907313, 9 pages

An Evaluation Method of Underwater Ocean Environment Safety Situation Based on D-S Evidence Theory, Yuxin Zhao, Renfeng Jia, and Chang Liu

Volume 2015, Article ID 207656, 8 pages

A Study of Coupling Parameter Estimation Implemented by 4D-Var and EnKF with a Simple Coupled System, Guijun Han, Xinrong Wu, Shaoqing Zhang, Zhengyu Liu, Ionel Michael Navon, and Wei Li

Volume 2015, Article ID 530764, 16 pages

Diffusion Filters for Variational Data Assimilation of Sea Surface Temperature in an Intermediate Climate Model, Xuefeng Zhang, Dong Li, Peter C. Chu, Lianxin Zhang, and Wei Li

Volume 2015, Article ID 751404, 17 pages

Using Adjoint-Based Forecast Sensitivity Method to Evaluate TAMDAR Data Impacts on Regional Forecasts, Xiaoyan Zhang, Hongli Wang, Xiang-Yu Huang, Feng Gao, and Neil A. Jacobs

Volume 2015, Article ID 427616, 13 pages

Research on Cold Core Eddy Change and Phytoplankton Bloom Induced by Typhoons: Case Studies in the South China Sea, Xiao-dong Shang, Hai-bin Zhu, Gui-ying Chen, Chi Xu, and Qi Yang

Volume 2015, Article ID 340432, 19 pages

Low-Frequency Variability of the Yellow Sea Cold Water Mass Identified from the China Coastal Waters and Adjacent Seas Reanalysis, Xuewei Li, Xidong Wang, Peter C. Chu, and Dongliang Zhao

Volume 2015, Article ID 269859, 14 pages

Some Aspects of Sensitivity Analysis in Variational Data Assimilation for Coupled Dynamical Systems, Sergei Soldatenko, Peter Steinle, Chris Tingwell, and Denis Chichkine

Volume 2015, Article ID 753031, 22 pages

An Assessment of Data from the Advanced Technology Microwave Sounder at the Met Office, Amy Doherty, Nigel Atkinson, William Bell, and Andrew Smith

Volume 2015, Article ID 956920, 16 pages

Prediction of Moderate and Heavy Rainfall in New Zealand Using Data Assimilation and Ensemble, Yang Yang, Phillip Andrews, Trevor Carey-Smith, Michael Uddstrom, and Mike Revell

Volume 2015, Article ID 460243, 14 pages



Impact of Argo Observation on the Regional Ocean Reanalysis of China Coastal Waters and Adjacent Seas: A Twin-Experiment Study, Caixia Shao, Lili Xuan, Yingzhi Cao, Xiaojian Cui, and Siyu Gao
Volume 2015, Article ID 793825, 15 pages

Upper Ocean Thermal Responses to Sea Spray Mediated Turbulent Fluxes during Typhoon Passage, Lianxin Zhang, Changlong Guan, Chunjian Sun, Siyu Gao, and Shaomei Yu
Volume 2015, Article ID 752947, 15 pages

Editorial

Data Assimilation in Numerical Weather and Climate Models

Shaoqing Zhang,¹ Guijun Han,² Yuanfu Xie,³ and Juan Jose Ruiz⁴

¹*Geophysical Fluid Dynamics Laboratory, NOAA, Princeton, NJ 08542, USA*

²*National Marine Data and Information Service, State Oceanic Administration, Tianjin 300171, China*

³*Earth System Research Laboratory, NOAA, Boulder, CO 80305, USA*

⁴*University of Buenos Aires, Viamonte, 430 1053 Buenos Aires, Argentina*

Correspondence should be addressed to Shaoqing Zhang; shaoqing.zhang@noaa.gov

Received 2 June 2015; Accepted 9 June 2015

Copyright © 2015 Shaoqing Zhang et al. This is an open access article distributed under the Creative Commons Attribution License, which permits unrestricted use, distribution, and reproduction in any medium, provided the original work is properly cited.

Great efforts have been made in climate modeling in the past decades. While a coupled model can simulate the interaction of the atmosphere, ocean, ice, and land and assess the fundamental feature of climate evolution, modeling on weather phenomena has been progressively advanced. The model resolution is higher and higher and the model physics are more and more accurate. Now, seamless weather-climate models are emerging. One expects more extensive applications of weather-climate models in environment monitoring and forecasting. Assessing instantaneous variability and providing accurate initial conditions for model forecasts require scientifically incorporating instrumental data into numerical model systems. This process is data assimilation.

Data assimilation uses model dynamics and physics to extract observational information from measured data which are usually scattered in time and space. The modern data assimilation pursues balanced and coherent state analysis and estimation and has grown as an important branch field in earth sciences. Not only does a good data assimilation product provide initial conditions for weather-climate predictions, but it serves also as a basis for one to further understand the mechanisms of weather-climate development, through reconstructing the continuous time series of weather and climate variables with three-dimensional structures. Furthermore, derived from information estimation theory, data assimilation develops out an important topic—how to use observational information to optimize model parameters, called “parameter estimation.” Parameter estimation helps modelers more accurately understand the sensitivity of model parameters and more objectively determine the values of parameters. We can predict that data assimilation will become a more important field in the near future due to the

demanding of the society on the high quality of environment monitoring and forecasting.

In this special issue, we collect 13 papers that cover observing system assessment and impact (3), weather-climate analysis and prediction (5), analysis and model mechanism studies (2), recent advances in data assimilation methods (1), and parameter estimation (1), as well as ocean safety study (1). This collection includes most of the major topics in modern data assimilation. We expect that, through this special issue, more scientists recognize the importance of data assimilation in weather-climate modeling and predictions. While a high quality weather-climate forecast makes more societal significance, as the return, it helps advance the earth science.

Observing system assessment and impact is an important branch field in data assimilation. In the paper “Impact of Argo Observation on the Regional Ocean Reanalysis of China Coastal Waters and Adjacent Seas: A Twin-Experiment Study,” the authors design a twin experiment to study the Argo impact on regional ocean reanalysis, providing an insight on importance of Argo for coastal areas. Nowadays, satellite observations play more and more important roles in numerical weather prediction. Assessing data quality is crucial for the best use of them. The paper “An Assessment of Data from the Advanced Technology Microwave Sounder at the Met Office” addresses this concern for ATMS data by comparing their departure from UK Met Office forecasts to AMSU and MHS satellite. It provides a complimentary validation of the data quality to the assessment at ECMWF for improving prediction of severe weather events. Tropospheric Airborne Meteorological Data Reporting (TAMDAR) has been providing a continuous operational stream

of real-time observations for regional weather forecasts. In the paper “Using Adjoint-Based Forecast Sensitivity Method to Evaluate TAMDAR Data Impacts on Regional Forecasts,” an adjoint-based Forecast Sensitivity to Observation (FSO) method is used to evaluate the impact of TAMDAR observations on regional 24-hour forecast error reduction over the Continental United States domain. Compared to the traditional observation-denial method, often referred to as Observation System Experiments (OSEs), the FSO method is advantageous due to its efficiency on the impact estimation for a complete set of observations, or any subset of observations grouped by type of observing system, observed variable, geographic region, vertical level, or other categories.

An important issue in data assimilation is how to deal with the multiscale nature of ocean and atmospheric dynamics. In the paper “Diffusion Filters for Variational Data Assimilation of Sea Surface Temperature in an Intermediate Climate Model,” a gradient diffusion filter technique is introduced to reconstruct the multiscale variability of a scalar field from a nonuniform observation network. The approach successfully recovers large scale patterns over the entire domain and accurately reconstructs small scale features over densely observed regions. This methodology has been successfully tested with a simplified coupled general circulation model producing a positive impact upon the representation of the oceanic and atmospheric flow.

Reanalysis data sets of the ocean and the atmosphere are extremely valuable tools for the study of physical processes and the variability of the system at different spatial and time scales. In the paper entitled “Low-Frequency Variability of the Yellow Sea Cold Water Mass Identified from the China Coastal Waters and Adjacent Seas Reanalysis,” the interannual and decadal variability of the yellow sea temperature is analyzed and related to the known coupled variability modes (i.e., Artic Oscillation, El Niño/Southern Oscillation, and Pacific Decadal Oscillation) in order to advance in the understanding of the physical processes that drive the climatology of the Yellow Sea. The paper “Statistical Prediction of the South China Sea Surface Height Anomaly” combines an ocean data assimilation product and statistics to explore the forecast of South China Sea surface height, providing a method for local ocean variable forecast. The papers “Research on Cold Core Eddy Change and Phytoplankton Bloom Induced by Typhoons: Case Studies in the South China Sea” and “Upper Ocean Thermal Responses to Sea Spray Mediated Turbulent Fluxes during Typhoon Passage” investigate the influences of tropical cyclones on eddy-associated phytoplankton bloom and sea spray associated turbulent fluxes, providing us a new view angle to understand the impact of typhoon on local ocean states. One societal impact of severe weather is heavy precipitation causing flooding. The paper “Prediction of Moderate and Heavy Rainfall in New Zealand Using Data Assimilation and Ensemble” investigates the moderate and heavy rainfall events in New Zealand. The authors’ experience with these severe weather events in New Zealand could help us better predict heavy rainfall events at complex terrain with observations and by more sophisticated ensemble methods.

The impact of parameter uncertainties on the results of data assimilation can be studied using sensitivity analysis. In the paper “Some Aspects of Sensitivity Analysis in Variational Data Assimilation for Coupled Dynamical Systems,” a sensitivity analysis method, based on the theory of shadowing pseudoorbits in dynamical systems, is applied under the framework of four-dimensional variational data assimilation (4D-Var) to a low-order coupled nonlinear dynamical system composed of fast and slow versions of the Lorenz model. Results demonstrated that this proposed sensitivity analysis method is more efficient compared with the conventional method. The paper “A Study of Coupling Parameter Estimation Implemented by 4D-Var and EnKF with a Simple Coupled System” investigates the difference performance of 4D-Var and EnKF parameter estimation using cross-media observations in coupled systems. Although the study was carried out within a simple coupled system, it provides guidance for coupling parameter estimation.

The paper “Initialized Decadal Predictions by LASG/IAP Climate System Model FGOALS-s2: Evaluations of Strengths and Weaknesses” provides a thorough statistical evaluation of a decadal prediction system, which is meaningful for us to understand some aspects of decadal prediction significances. In addition, in the paper “An Evaluation Method of Underwater Ocean Environment Safety Situation Based on D-S Evidence Theory,” authors present an evaluation method for underwater environment safety situation based on the Dempster-Shafer evidence theory. In terms of ocean engineering, this study provides a new view angle for oceanographer to understand the ocean safety.

*Shaoqing Zhang
Guijun Han
Yuanfu Xie
Juan Jose Ruiz*

Research Article

Initialized Decadal Predictions by LASG/IAP Climate System Model FGOALS-s2: Evaluations of Strengths and Weaknesses

Bo Wu,¹ Xiaolong Chen,^{1,2} Fengfei Song,^{1,2} Yong Sun,¹ and Tianjun Zhou¹

¹*LASG, Institute of Atmospheric Physics, Chinese Academy of Sciences, Beijing 100029, China*

²*University of Chinese Academy of Sciences, Beijing 100049, China*

Correspondence should be addressed to Bo Wu; wubo@mail.iap.ac.cn

Received 29 September 2014; Accepted 19 January 2015

Academic Editor: Shaoqing Zhang

Copyright © 2015 Bo Wu et al. This is an open access article distributed under the Creative Commons Attribution License, which permits unrestricted use, distribution, and reproduction in any medium, provided the original work is properly cited.

Decadal prediction experiments are conducted by using the coupled global climate model FGOALS-s2, following the CMIP 5 protocol. The paper documents the initialization procedures for the decadal prediction experiments and summarizes the predictive skills of the experiments, which are assessed through indicators adopted by the IPCC AR5. The observational anomalies of surface and subsurface ocean temperature and salinity are assimilated through a modified incremental analysis update (IAU) scheme. Three sets of 10-year-long hindcast and forecast runs were started every five years in the period of 1960–2005, with the initial conditions taken from the assimilation runs. The decadal prediction experiment by FGOALS-s2 shows significant high predictive skills in the Indian Ocean, tropical western Pacific, and Atlantic, similar to the results of the CMIP5 multimodel ensemble. The predictive skills in the Indian Ocean and tropical western Pacific are primarily attributed to the model response to the external radiative forcing associated with the change of atmospheric compositions. In contrast, the high skills in the Atlantic are attributed, at least partly, to the improvements in the prediction of the Atlantic multidecadal variability coming from the initialization.

1. Instruction

In recent years, near-term climate predictions for the next 10–30 years is increasingly concerned by the community of climate modeling and policy makers for its potential values in dealing with the economic and social problems associated with the climate change (e.g., [1]). The pioneering decadal prediction studies based on climate models were published during 2007–2009 (e.g., [2–5]). Then extensive cooperative researches involving decadal predictions, the ENSEMBLES projects [6], and a coordinated decadal prediction experiment under the framework of the CMIP5 [7, 8] were launched successively. Sixteen modeling centers had submitted their decadal prediction experiment results to the CMIP5, which were used in the fifth assessment report of the Intergovernmental Panel on Climate Change (IPCC AR5 [9]).

As noted in Meehl et al. [7], decadal prediction is a combination of an initial value problem and a forced boundary condition problem, because decadal prediction encompasses

the climate system changes due to internally generated variability as well as externally forced variability. The externally forced variability is driven by external forcing factors, such as changes of atmospheric compositions associated with human activity or volcanic eruption, solar variations, and others, which can be considered as specified external forcing in climate models, as done by historical simulations or RCP projections [8].

Predictive skills of internal variability coming from initializations are primary added value of the decadal prediction experiments relative to the historical simulations and RCP projections. As an initial condition problem, the prediction of internal variability depends on the accurate estimation of initial climate states, which is also the most challenging problem of the decadal prediction. Different institutions have their own distinctive initialization schemes, which are simply introduced in Kirtman et al. [9] and Meehl et al. [1].

For the CMIP5, model initializations performed by most institutions just assimilated oceanic surface and subsurface

temperature and salinity. However, there were also some explorations that involve observational atmosphere and sea ice data in the assimilation processes (Table 11.1 in Kirtman et al. [9]).

In terms of the approaches of dealing with the model drift in the forecast, the initialization schemes can be classified into two types, full-field initialization and anomaly initialization [10]. For the full-field initialization, though model biases are largely removed during initialization, the model drifts back towards its preferred state inevitably during hindcast/forecast due to inherent model biases. Therefore, forecast results must be corrected through posterior bias adjustments [10–14]. In the anomaly initialization, the model is constrained by observational anomalies plus model mean state [15]. Therefore, the model is not far away from its preferred state after the initialization and thus minimizes the drift during hindcast/forecast. But, so far, it is not clear which approach is better for the decadal prediction [10]. In the CMIP5, about 2/3 models use the full-field initialization, while the other 1/3 use the anomaly initialization [9].

The motivation of this study is to systematically assess the predictive skills of the decadal predictions experiments by using a coupled global climate model, FGOALS-s2, which has been submitted to the CMIP5. To make horizontal comparisons with other models' results, we use the indicators proposed by Doblas-Reyes et al. [16] to measure the prediction quality, which have been adopted as key indicators by the IPCC AR5 [9].

The rest of the paper is organized as follows. The model FGOALS-s2, experiment designs, observation data, and analysis methods are introduced in Section 2. The skills of the decadal prediction experiments are assessed in Section 3. Finally, Section 4 summarizes the major content.

2. Model, Experiment Design, Observational Data, and Analysis Method

2.1. Model. FGOALS-s2 is a coupled global climate model developed in the State Key Laboratory of Numerical Modeling for Atmospheric Sciences and Geophysical Fluid Dynamics (LASG) at the Institute of Atmospheric Physics (IAP), Chinese Academy of Sciences (hereafter LASG/IAP/CAS). It has four components, atmosphere, land, ocean, and sea ice, which are coupled together by a coupler developed in the National Center for Atmospheric Research (NCAR) [17]. The atmospheric component is Spectral Atmosphere Model in IAP LASG version 2 (SAMIL2) [18], with the horizontal resolution of about 2.81° (longitude) \times 1.66° (latitude) and 26 levels in the vertical direction. The ocean component is LASG IAP Climate System Ocean Model version 2 (LICOM2), with a horizontal resolution of about $1^\circ \times 1^\circ$ in extratropical zone and $0.5^\circ \times 0.5^\circ$ in tropics and 30 levels in the vertical direction [19, 20]. The land and ice components are Community Land Model version 3 (CLM3) [21] and Community Sea Ice Model version 5 (CSIM5) [17], respectively. Detailed description of the FGOALS-s2 and its general performances can be found in Bao et al. [18].

2.2. Experiment Designs

2.2.1. Decadal Prediction Experiments. The decadal prediction experiments include the following two steps.

(a) *Initialization.* The model was initialized through assimilating observational oceanic temperature and salinity over upper 1000 m for the period of 1955–2005 (hereafter ASSIM run). The observational oceanic data was derived from EN3_v2a, which is gridded objective analysis data, with horizontal resolution of $1^\circ \times 1^\circ$ and 42 levels in the vertical direction [22]. Only the anomalies relative to the climatology during 1961–1990 were assimilated (anomaly initialization approach noted in the introduction). The assimilation was confined in the zone of 70°S – 70°N , with 60 – 70°N and 60 – 70°S being set as transitional zone.

The observational information was introduced into the model integration through a method similar to an incremental analysis update (IAU) method. The IAU technology was designed for data assimilation system for meteorology [23] and then applied to the ocean assimilation [24] and coupled model initialization [25]. Its major advantage over the nudging approach is that it can keep analysis increment constant in model's prognostic equations and thus effectively suppress short-wave noises in the assimilation processes [23].

Because the ocean objective analysis data, EN3_v2a, is monthly mean data, the analysis interval in the assimilation processes was specified as one month ($\tau = 1$ mon). In one assimilation cycle from t to $t + \tau$, the model was integrated freely firstly, which produced the first guess for the assimilation. The analysis increments ($\Delta X'$) were calculated as

$$\Delta X' = X'_F - X'_O, \quad (1)$$

in which X'_F and X'_O represent monthly mean anomalous ocean states (temperature and salinity) derived from the free integration and the observation. Then the model was restated from t again and integrated to $t + \tau$, with analysis increments being introduced through the following way:

$$\frac{DX}{Dt} = \text{MTs} + \frac{1}{\tau} \Delta X'. \quad (2)$$

The left-hand-side term is the time tendency term. The first term in the right hand side represents the forcing and dissipation terms calculated by the model. The last term is the correction term, which keeps constant in the integration interval. The modified IAU scheme has been used in the decadal prediction experiments by using FGOALS-gl [26].

(b) *Hindcast/Forecast.* The 10-year-long hindcasts/forecasts were started every five years over the period of 1960–2005. Initial conditions were obtained from the ASSIM runs. In the hindcast and forecast stages (before and after 2005), the model was driven by the time-varying radiative forcing consistent with the historical and representative concentration pathways 4.5 (RCP4.5) simulations, respectively. The second step was conducted in strict accordance with the standard experiment design of the CMIP5 [8].

To estimate the uncertainties of the prediction, we performed 3-member ASSIM runs with different initial conditions, which further offered initial conditions for three sets of hindcasts/forecasts runs.

2.2.2. Historical and RCP4.5 Simulations. For the historical simulation, the FGOALS-s2 was integrated from 1850 to 2005 under the various historical forcing agents, including the concentrations of greenhouse gases and sulfate aerosols, solar cycle variations, and major volcanic eruptions [27]. After 2005, the model was driven by projected radiative forcing under the RCP4.5 scenario, which is referred to as the RCP4.5 simulation. The historical and RCP4.5 simulations are repeated three times with different initial conditions, following the recommendation of the CMIP5 [8].

2.3. Observational Data. The following two datasets are used as observational references to assess the predictive skills of the decadal prediction experiments: (1) HadCRUT3 combined global land and ocean gridded ($5^\circ \times 5^\circ$) surface temperature datasets for the period of 1850 to present [28] and (2) Global Precipitation Climatology Centre monthly precipitation dataset ($2.5^\circ \times 2.5^\circ$) from 1901 to present (GPCC), which is gridded from global station data [29].

2.4. Analysis Method. As noted in Section 2.2, the approach of anomaly initialization was used in the study, which can inhibit model drift during hindcast/forecast effectively [10]. Thus bias correction was not conducted as done for full-field initializations [10]. However, to prevent negative effects of any possible slight model drifts during hindcast/forecast to the predictive skill evaluations, we calculated anomalies as follows [16]:

$$Y'_{jt} = Y_{jt} - \frac{1}{N} \cdot \left(\sum_{k=1}^N Y_{kt} \right), \quad (3)$$

where Y'_{jt} and Y_{jt} are anomalous and raw fields, respectively, for the hindcast/forecast j at lead time t . N denotes ensemble size. The observational anomalies were also calculated by using corresponding years. Then to filter out interannual variability, the annual values were smoothed by a 4-year running average. In the study, we analyzed the predictions averaged over the hindcast/forecast years 2–5, 3–6, 4–7, 5–8, and 6–9.

The main strategy of evaluating the skills of the decadal prediction experiments is to compare it with corresponding historical simulations. In terms of the experiment designs (Section 2.2), their only difference is that the former is started from initialized states every five years, while the latter is successive integrations. Thus the predictions by the two experiments are referred to as INIT and NoINIT predictions, respectively. The comparisons between INIT and NoINIT demonstrate the change of the decadal predictions due to the initialization.

In this study, the skills are quantified by correlation, root mean square error (RMSE), and root mean square skill score

(RMSSS), which generally follow Doblus-Reyes et al. [16]. The RMSSS is defined as

$$\text{RMSSS} = 1 - \frac{\text{RMSE}(\text{hindcast})}{\text{RMSE}(\text{climatology})}, \quad (4)$$

in which RMSE (climatology) represents no skill baseline. The climatology is equivalent to the persistent zero anomalies. Thus high positive values of RMSSS represent high skills, while negative values represent no skills. The statistical significance of the correlation is tested by one-sided Student's t -test. The significance of the ratio in RMSE between the INIT and NoINIT predictions is tested by a two-sided F test. The significance of the RMSSS is assessed by using a one-sided F test.

3. Results

We first assess the spatial distributions of the predictive skills on near-surface air temperature and land precipitation. Then we turn to the predictive skills of the global mean near-surface air temperature and two dominant modes on the interdecadal time scales, the Atlantic multidecadal variability, and the Pacific interdecadal variability.

3.1. Spatial Distributions of Predictive Skills. Figure 1 shows the global distributions of the RMSSS to quantify the skills of the ensemble mean of the INIT runs in predicting near-surface air temperature. For the prediction averaged over hindcast years 2–5, the forecast system has positive skills over much of the Atlantic and Indian Ocean and some areas in the Eurasia continent at 15% level of significance, while the system shows the low skills over the most of the Pacific, except for the tropical western Pacific. These regions with significant high skills are generally consistent with the CMIP5 multimodel ensemble (MME) mean (Figure 11.4a in Kirtman et al. [9]). The major disadvantage of the FGOALS-s2 relative to the MME mean is that the former skills in the midlatitude North Atlantic are lower than the latter.

Many previous studies have noted that the Indian Ocean and western Pacific are primarily dominated by warming trend associated with anthropogenic forcing, which can be reasonably reproduced by historical simulations [30, 31]. To estimate the added skills coming from the initialization, the ratios of the RMSEs between the ensemble mean of the INIT runs and that of the NoINIT runs are calculated. It is clear that the RMSE of the INIT is less than that of the NoINIT over the majority of the globe. However, it is only over some areas of the Atlantic and Indian Ocean that the skill improvements pass 15% significance level.

For the prediction averaged over the hindcast years 6–9, the spatial distribution of the RMSSS generally resembles that for the hindcast years 2–5. Obvious increase of the INIT skills relative to the NoINIT is just seen over the midlatitude North Atlantic and southern Indian Ocean. The ratio of the RMSEs is also less than 1 over majority of the globe. However, there is nearly no area passing the significance test. The results indicate that the prediction information due to

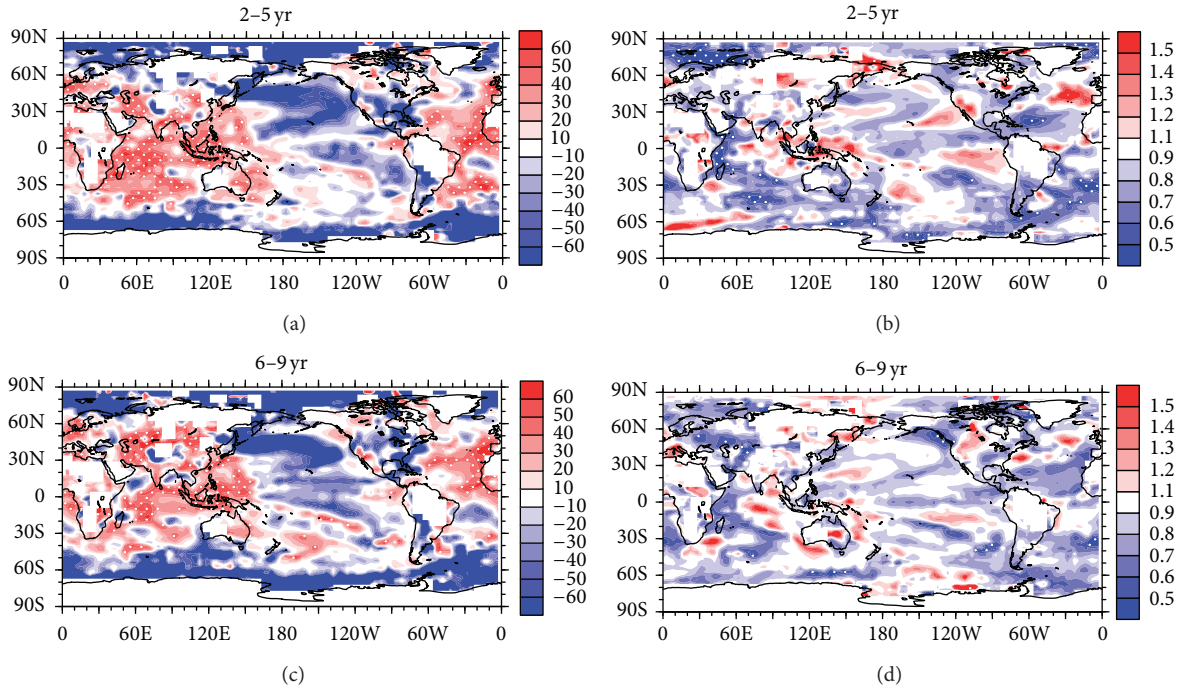


FIGURE 1: Forecast qualities of near-surface air temperature. (a) RMSSS (multiplied by 100) of the ensemble mean of the INIT runs for predictions averaged over the hindcast years 2–5. The white dots represent that the skill scores at these points are statistically significant at the 15% level based on the one-sided F test. (b) Ratio of RMSE between the ensemble mean of the INIT runs and that of the NoINIT runs for predictions averaged over the hindcast years 2–5. ((c), (d)) The same as (a) and (b) but for the years 6–9.

the initialization becomes smaller with the increase of the prediction time [1].

Compared with the near-surface air temperature, the ensemble mean of the INIT runs shows very low skills in the prediction of land precipitation for both the hindcast years 2–5 and 6–9. The global distribution of the RMSSS indicates that there are only sporadic regions with positive skills. These positive skills cannot pass 15% significance test (Figures 2(a) and 2(b)). Meanwhile, the ratio of RMSEs between the INIT and INI runs indicates that the skill improvement due to the initialization is very limited (Figures 2(c) and 2(d)). The results are consistent with the CMIP5 MME (Figure 11.5 in Kirtman et al. [9]).

3.2. Global Mean Near-Surface Temperature. Predictive skills of the area-weighted global mean near-surface air temperature (GMST) are quantified by correlation and RMSE (Figures 3(a) and 3(b)). The GMSTs simulated by all the individual members and ensemble means of the INIT and NoINIT runs for different hindcast range are highly correlated with the corresponding observational references at 5% significance level. In terms of the correlations, the skills of the INIT runs are somewhat lower than those of the NoINIT runs, especially in the early prediction time. In contrast, in terms of the RMSEs, former skills are higher than the latter. However, it is clear that the skill differences between the INIT and NoINIT become smaller with the increase in the prediction time, in terms of both the correlations

and the RMSEs. It indicates that the prediction information coming from the initialization gradually decreases with the increase of the prediction time, and the evolution of the GMST is dominated by the external forcing associated with atmospheric composition increasingly.

The temporal evolutions of the GMST for the hindcast/forecast years 6–9 and corresponding observational reference are shown (Figure 3(c)). During the latter half of the 20th century, the GMST is dominated by a significant warming trend. However, during early 21st century, a hiatus of the GMST rise is observed (e.g., [32–35]; Figure 3(c)). Both the ensemble mean of INIT runs averaged over hindcast years 6–9 and that of NoINIT runs failed to simulate the hiatus of the GMST rise; however, the former warming trend is much smaller than the latter and more close to the observation, especially after 2000 (Figure 3(c)). This feature can be seen more clearly in the hindcast years 1–4 (Figure 3(d)). The result is robust among different models (e.g., [3, 9, 36]).

It is interesting to further investigate what cause the correlation skills of the INIT runs to be lower than those of the NoINIT runs in the early prediction time. Compared with the hindcast years 6–9, the GMSTs over the hindcast years 1–4 are closer to the corresponding observation references, except for the prediction started from 1985 (Figure 3(d)). The GMST over 1986–1989 (hindcast years 1–4) is much higher than the observation. In the observation, 1986 and 1987 are dominated by a strong El Niño event, while 1988 and 1989 are dominated by a strong La Niña event (Figures 4(a)–4(d)). For the four-year average, the GMST is nearly in a neutral

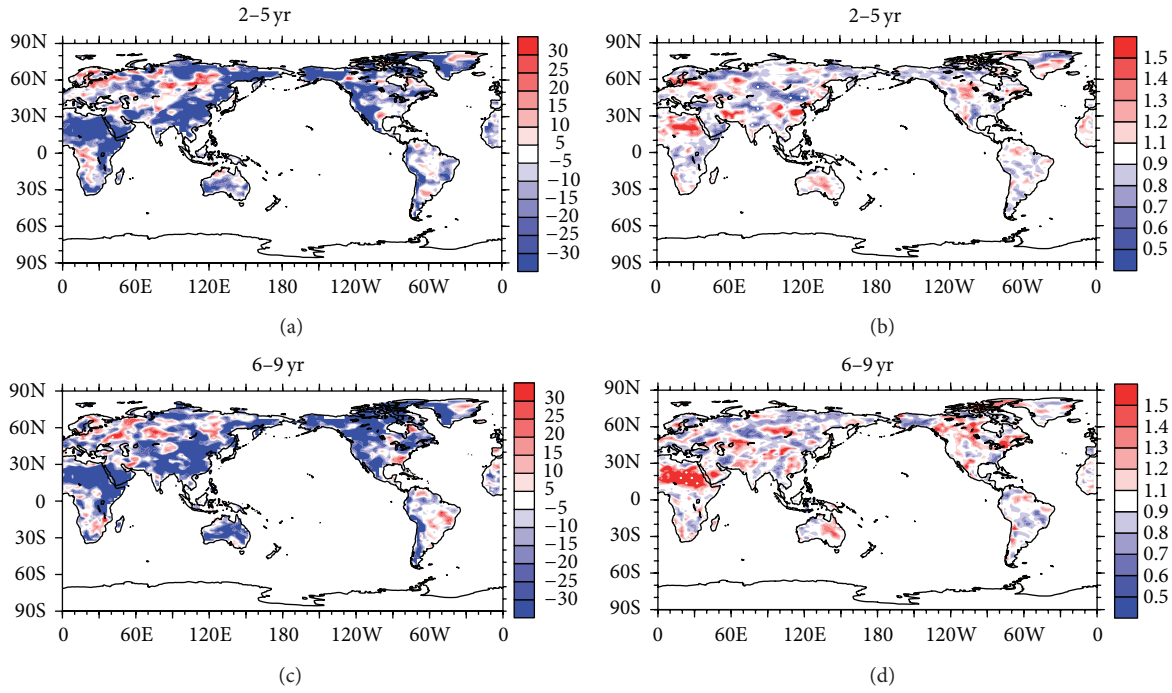


FIGURE 2: As in Figure 1, but for the land precipitation.

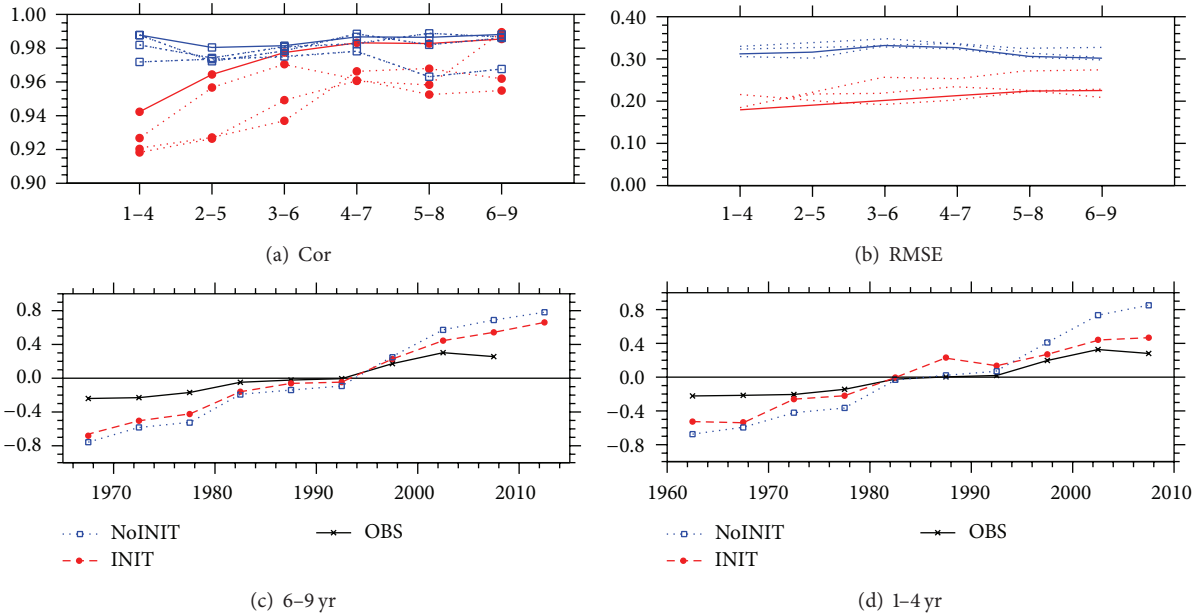


FIGURE 3: Hindcast qualities of the global mean near-surface air temperature (GMST). (a) Correlations between the model runs and the observational references along the forecast time for 4-year averages. The red (blue) lines denote INIT (NoINIT) runs. The dashed (solid) lines denote ensemble members (means). The dots represent that corresponding correlation coefficients reach the 5% significance level based on one-sided Student's t -test. (b) RMSE of the model runs along the forecast time for 4-year averages. Dots are used when RMSEs of the ensemble mean of the INIT runs are statistically significantly less than those of the ensemble mean of the NoINIT runs at 5% level, based on the one-sided F test. (c) Time series of the GMST indices predicted by the ensemble mean of the INIT (NoINIT) runs for predictions averaged over the hindcast years 6–9 and corresponding observational reference (units: K). (d) As in (c) but for hindcast years 1–4.

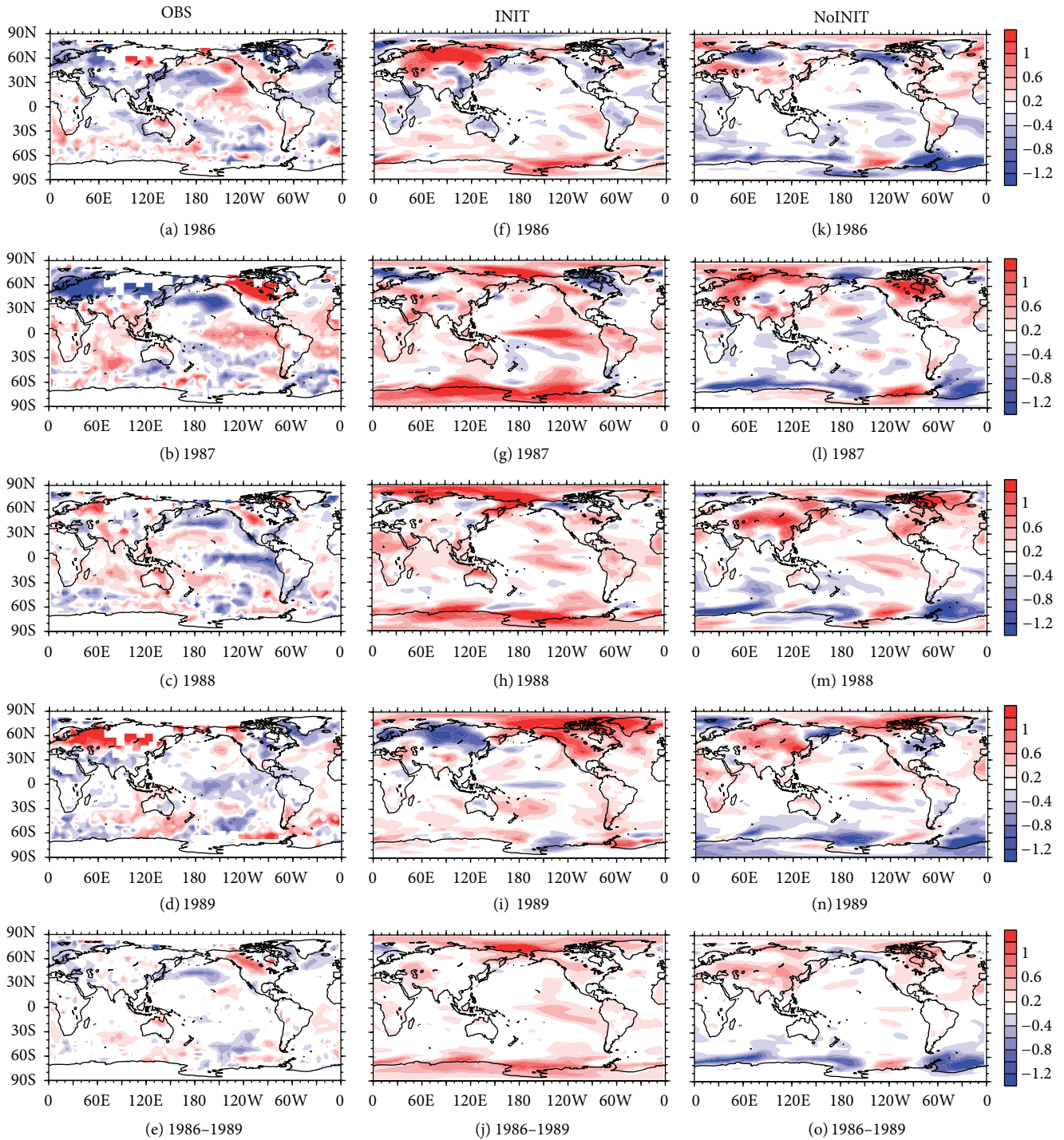


FIGURE 4: Left panel: (a)–(d) annul mean SST anomalies from 1986 to 1989 derived from the observation (units: K). (e) Average of (a)–(d). Center (right) panels: as in the left panel but from the ensemble mean of the INIT (NoINIT) runs.

state (Figure 4(e)). The hindcast started from 1985 reproduces the El Niño during 1986–1987 (Figures 4(f) and 4(g)). However, the simulated El Niño persists longer than that in the observation and evolves to a neutral state rather than a strong La Niña as in the observation (Figures 4(h) and 4(i)). Therefore, the predicted GMST averaged over the four

years is dominated by El Niño-like pattern (Figure 4(j)). For the NoINIT runs, though the ENSO evolution is completely different from that in the observation (Figures 4(k)–4(n)), the simulated GMST averaged over the four years is in the neutral state (Figure 4(o)). The results indicate that the decadal prediction is sometimes influenced by the interannual variability,

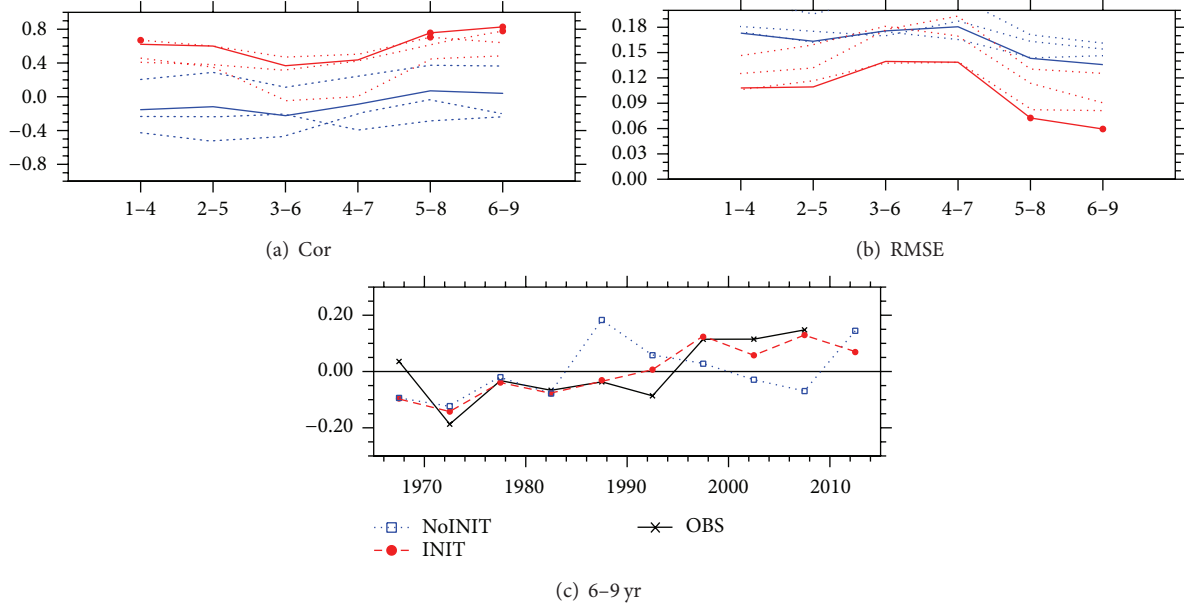


FIGURE 5: As in Figures 3(a)–3(c), but for the Atlantic multidecadal variability index.

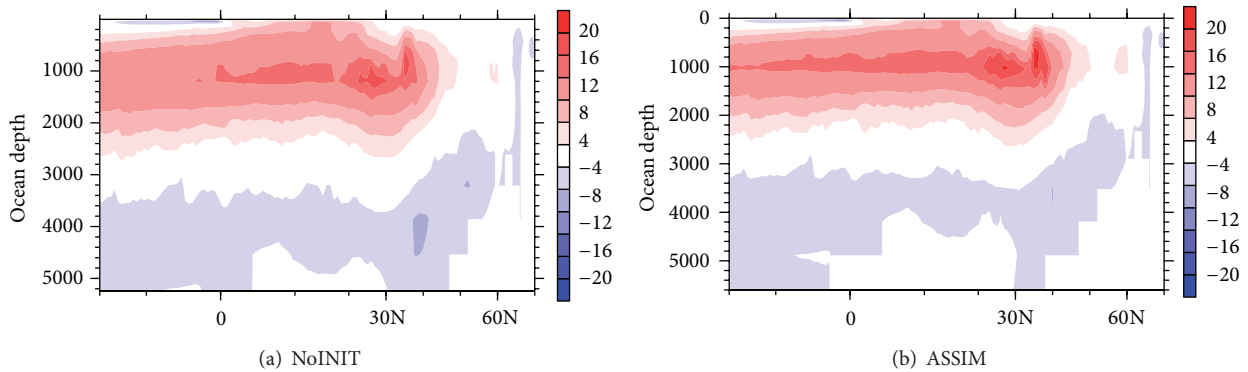


FIGURE 6: (a) Climatological Atlantic Meridional Overturning Circulation (AMOC) simulated by the ensemble mean of the NoINIT runs (units: Sv). (b) As in (a) but simulated by the ensemble mean of the ASSIM runs.

especially in the early prediction time. The negative impacts may be partly overcome through increasing the number of the hindcasts; that is, hindcasts are performed once per year instead of once every five years.

3.3. Atlantic Multidecadal Variability. The spatial distributions of the RMSSS for the near-surface temperature (Figure 1(a)) indicate that the ensemble mean of the INIT runs shows high skills in the Atlantic. In the subsection, we assess the skills of the individual members of the INIT and their ensemble mean in predicting the Atlantic multidecadal variability (AMV). The AMV is depicted by an index defined as area-averaged SST anomalies in the 0°–60°N, 80°–0°W minus the area-averaged near global SST anomalies in the 60°S–60°N [37].

The predictive skills are measured by correlation along the hindcast time for 4-year averages (Figure 5(a)). There is only one INIT member that reproduces the AMV index highly

correlated with the observation reference at 5% significance level over the hindcast years 5–8 and 6–9. The skills of the ensemble mean are higher than any individual member over the hindcast years 5–8 and 6–9. The AMV in the ensemble mean is highly correlated with the observation reference at most hindcast ranges. The highest correlation is reached in the hindcast years 6–9. In contrast, the NoINIT runs do not have any significant correlations with the observation references.

The skills of the INIT runs are further quantified by RMSE (Figure 5(b)). The skills of the ensemble mean of the INIT runs are also higher than all the members. For the ensemble mean, the smallest RMSE is reached in the forecast years 6–9. It is significantly smaller than the counterpart of the ensemble mean of the NoINIT runs, indicating that the added skill coming from the initialization is significantly in the prediction of the AMV. The high skills of the ensemble mean of the INIT runs are more clearly demonstrated by the high

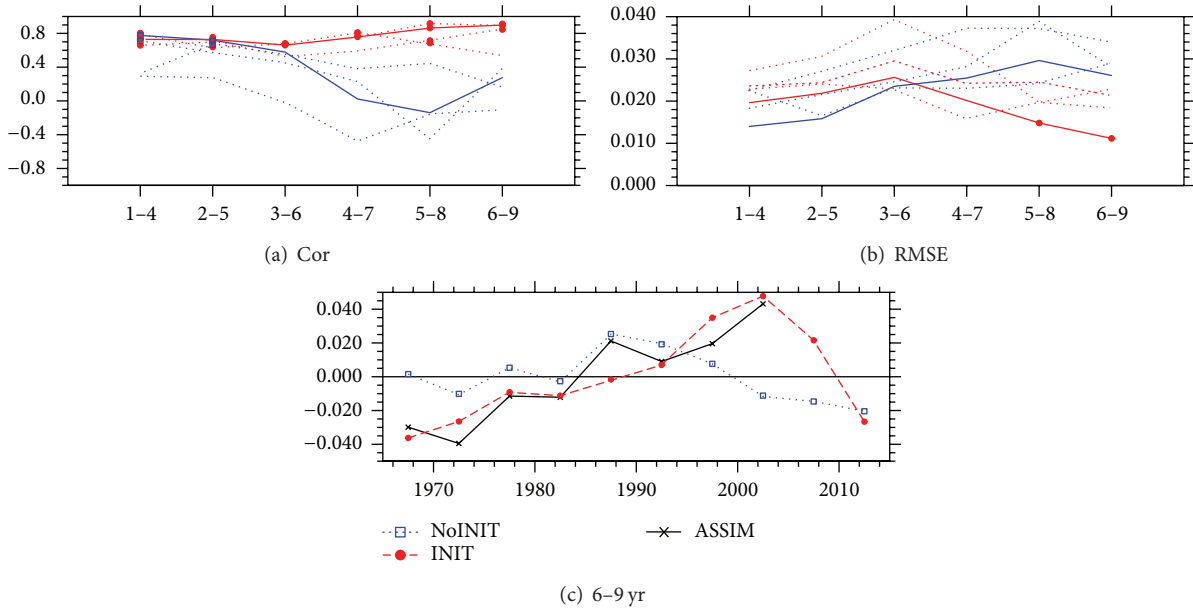


FIGURE 7: As in Figures 3(a)–3(c), but for the northward oceanic heat transport anomalies in the North Atlantic averaged over 0–40°N (units: PW). The observation references are replaced by the results from the ASSIM runs.

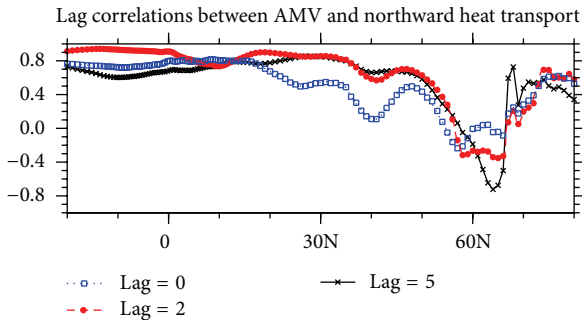


FIGURE 8: Lag correlations between the AMV index and anomalous northward oceanic heat transport (units: PW) from 20°S to 80°N for the ensemble mean of the INIT runs. The AMV index is averaged over the hindcast years 6–9 (red line in Figure 5(c)). Lag 0 represents simultaneous correlation. Lags 2 and 5 represent that the AMV index lags the heat transport anomalies by 2 and 5 years, respectively. That is, the heat transport anomalies are averaged over the hindcast years 6–9 (lag 0), 4–7 (lag 2), and 1–4 (lag 5), respectively.

consistency of the predicted time series of the AMV index for the hindcast years 6–9 and corresponding observation reference (Figure 5(c)).

The enhanced predictive skills of the AMV because of the initialization stand out in most decadal prediction experiments as the major added value relative to the historical and RCP simulations (e.g., [1, 3, 38–40] and many others). However, the performances of the FGOALS-s2 are somewhat different from previous studies. Kim et al. [41] showed that correlation skills of the AMV of seven models from the CMIP5 MME generally decrease with the prediction time far away from the initial time. In contrast, the predictive skills of

the FGOALS-s2 change little in the various hindcast ranges, and skills in the late prediction time (hindcast years 5–8 and 6–9) are even higher than the early time (Figures 5(a) and 5(b)).

Previous studies proposed that the AMV is closely associated with the low-frequency fluctuation of the Atlantic Meridional Overturning Circulation (AMOC) [42, 43]. Hence we further investigate whether the predictive skills of the AMV depend on the prediction of the AMOC variations. Figure 6 shows the climatological AMOC simulated by the ensemble mean of the NoINIT runs. The strongest overturning is about 19 Sv, which is located at about 25°–35°N, between 800 and 1200 m. The maximum value is very close to the observed value (18.5 Sv) at 26.5°N [44]. The major discrepancy of the simulated AMOC is that the northward mass flux does not reach high latitudes and the strongest downwelling is located at about 35°N. It causes the northward heat transport also not to be able to reach the high latitudes, which has some impacts on the prediction of the AMV, as we will see below.

The fluctuation of the AMOC influences the SST anomalies over the North Atlantic through modulating the northward oceanic heat transport [40, 42, 43]. Hence, we investigate the skills of the INIT runs in predicting the northward oceanic heat transport in the North Atlantic through comparing with the results from the ASSIM runs, which assimilate observational oceanic temperature and salinity and thus are taken as observational references here. Since the northward mass flux associated with the AMOC does not reach high latitudes, the northward heat transport is averaged over the 0–40°N. The ensemble mean of the INIT runs shows high skills in all the hindcast ranges. The highest skill is reached in the hindcast years 6–9 (Figures 7(a) and 7(b)). The temporal

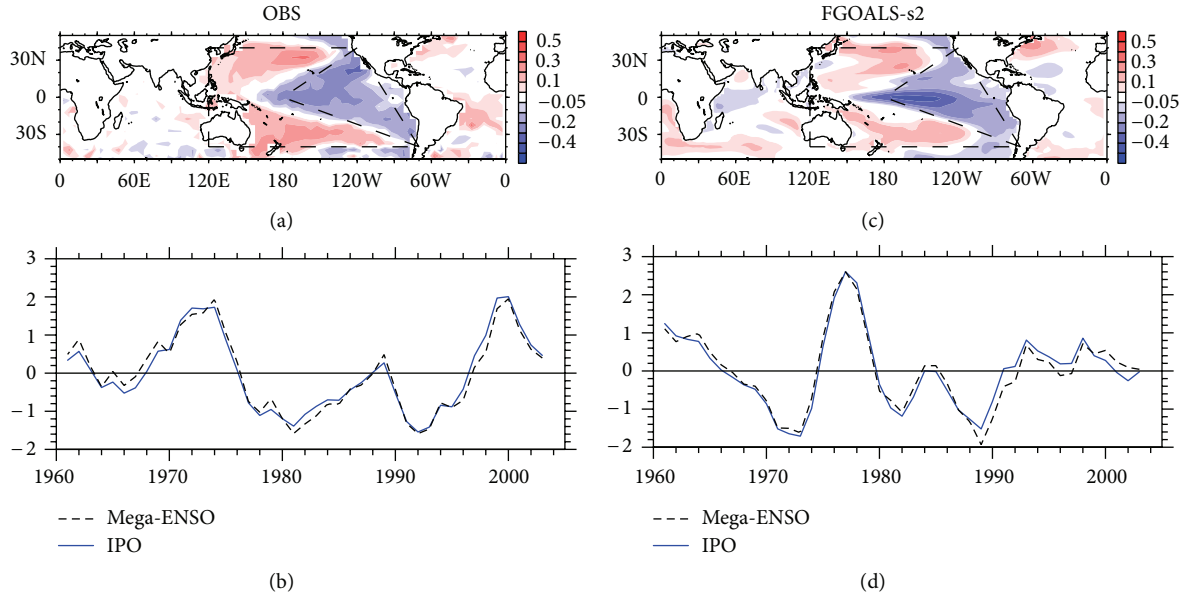


FIGURE 9: Left panel: the spatial pattern of IPO mode in the observation (a) and corresponding time series (blue line in (b)). The IPO mode is defined as the second EOF mode of 4-year running-averaged annual near global SST (50°S–50°N). The black line in (b) is Mega-ENSO index, defined as the difference in the SST anomalies between the western K-shape zone and eastern triangle zone in (a). Right panel: the same as the left panel, but for the FGOALS-s2.

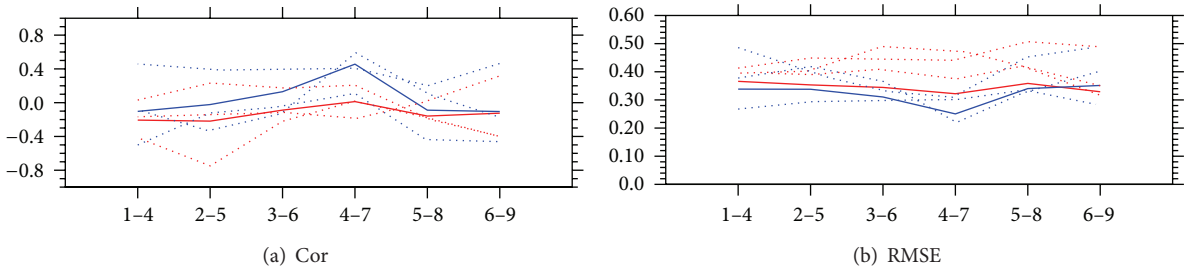


FIGURE 10: The same as Figures 3(a)-3(b), but for Mega-ENSO index. Mega-ENSO index is defined as the difference in area-averaged SST anomalies between the western K-shape zone and the eastern triangle zone in Figures 9(a) and 9(b).

evolution of the anomalous heat transport for the hindcast years 6–9 predicted by the ensemble mean of the INIT runs is very consistent with the corresponding results from the ensemble mean of the ASSIM runs (Figure 7(c)). In contrast, the skills of the heat transport simulated by the NoINIT runs are significantly lower than the counterparts of the INIT runs in the latter three hindcast ranges. For the former three hindcast ranges, the correlation skills of the ensemble mean of the NoINIT runs are close to the counterparts of the ensemble mean of the INIT runs. However, it is clear that the three NoINIT members show high spread and only one member shows similar skills with the INIT runs. It indicates that the skills of the ensemble mean of the NoINIT runs may be overestimated due to small sample sizes.

To test relationships between the AMV and preceding anomalous northward heat transport associated with the AMOC variations in the decadal predictions, we calculate the lag correlations between the AMV indices averaged over the hindcast years 6–9 with the heat transports averaged over the hindcast years 1–4, 3–7, and 6–9, respectively

(Figure 8). It is clear that the AMV is highly correlated with the preceding northward heat transport anomalies from the South Atlantic to about 45°N. The correlation coefficients decrease drastically to the north of 45°N, which is consistent with the location of the edge of the AMOC. In contrast, their simultaneous correlations are much lower in the North Atlantic (Figure 8). The results indicate that the predicted AMV is mainly induced by the northward heat transport anomalies associated with the preceding AMOC fluctuations. Correspondingly, the high predictive skills of the AMV in the hindcast years 6–9 mainly come from the accurate predictions of the preceding AMOC fluctuations and associated heat transport anomalies.

3.4. *Interdecadal Variability in the Pacific.* The interdecadal variability of the Pacific is dominated by the Pacific decadal oscillation (PDO) [45] or interdecadal Pacific oscillation (IPO) [46, 47], both of which are extracted through EOF analysis. Because the INIT runs are not successive integrations,

EOF analysis applied to the artificially linked predicted fields may yield false modes.

Wang et al. [48] defined a Mega-ENSO index to represent interdecadal variability in the Pacific. The index can be calculated easily and is highly correlated with the PDO or IPO indices. Therefore, we use the index as a substitute to assess the decadal predictive skills in the Pacific. Following Wang et al. [48], 4-year, instead of 13-year, weighted running averages are applied to the observed SST anomalies from 1960 to 2005, due to the short data length (in Wang et al. [48], 3-year running average was conducted). But the results are not sensitive to the choice of the window length. Then EOF analysis is conducted by using the 4-year running-averaged SST in the region 50°S–50°N. The spatial pattern of the second EOF mode shows typical characteristics of the IPO (Figure 9(a)). The principal component time series of the second EOF mode is defined as the IPO index. Based on the spatial pattern, Mega-ENSO index is defined as the difference in the area-averaged SST anomalies between the western K-shape zone and the eastern triangle zone in Figure 9(a). It is clear that the Mega-ENSO index is highly consistent with the IPO index, with correlation reaching 0.97 (Figure 9(b)). The same analysis processes are applied to the first NoINIT run. The spatial pattern of the IPO simulated by the FGOALS-s2 resembles that in the observation (Figure 9(c)). Thus the FGOALS-s2 shares the same definition of the Mega-ENSO index with the observation. The Mega-ENSO index in the NoINIT run is also highly correlated with the corresponding IPO index (Figure 9(d)).

The skills of INIT (NoINIT) runs in predicting the Mega-ENSO index are measured by correlation and RMSE (Figure 10). Unfortunately, in terms of both measures, none of the simulations can reproduce the temporal evolution of the Mega-ENSO significantly and the skills of the INIT runs are even lower than the NoINIT runs. The low skills are consistent with Figure 1(a), in which the ensemble mean of the INIT runs shows negative skills in the most areas of the Pacific. The results indicate that the initialization does not enhance the predictive skills of the interdecadal variability in the Pacific significantly, which is also indicated by the CMIP5 MME results [9].

4. Summary

In the paper, the procedures of the decadal prediction experiments by the coupled global climate model FGOALS-s2, which participated in the CMIP5, are introduced. Then the predictive skills of the experiments are assessed based on the indicators adopted by the IPCC AR5 [9, 16]. The main content is summarized as follows.

(1) The decadal prediction experiments involve two steps, initialization and hindcast/forecast. The initialization was performed by assimilating observational ocean temperature and salinity over upper 1000 m through a modified incremental analysis update (IAU) scheme. Based on the scheme, the analysis increment keeps constant in one assimilation cycle (1 month) and thus effectively suppresses the increase of the short-wave noises in the integration. Meanwhile, in the initialization, only observational anomalous fields are

assimilated to avoid the model drift in the hindcast and forecast runs. Started from the initial conditions derived from the initialization run, three sets of the 10-year-long hindcast/forecast runs are conducted with 5-year intervals between start dates from 1960 to 2005, following the CMIP5 protocol.

(2) The overall predictive skills of the decadal prediction in near-surface air temperature (TAS) and land precipitation are measured by the global distribution of the RMSS. For the TAS, the model shows significant high skills in the Indian Ocean, tropical western Pacific, and Atlantic. However, compared with the historical simulations, the decadal prediction experiments do not show significant skill improvements, except for the Atlantic. The results indicate that the skills of the decadal prediction experiments in the Indian Ocean and tropical western Pacific are primarily attributed to the specified external radiative forcing, while the skills in the Atlantic are attributed to the initialization. For the land precipitation, the decadal prediction experiments do not show significant skill improvements relative to the historical simulations.

(3) On the interdecadal time scales, the dominant variability modes are IPO/PDO/Mega-ENSO in the Pacific and AMV in the Atlantic, which are the major forecast objects of the decadal prediction experiments. The prediction system based on the FGOALS-s2 shows high predictive skills in the AMV but low skills in the IPO/PDO/Mega-ENSO, which is similar to the CMIP5 MME. An interesting point is that the predictive skills of AMV of the FGOALS-s2 change little with the increase of the prediction time and even reach highest level in the hindcast years 6–9, rather than decrease as many CMIP5 models [41]. Further investigations indicate that the predictive skills of the AMV in the hindcast years 6–9 mainly come from the accurate predictions of the northward heat transport anomalies associated with the preceding AMOC fluctuations.

(4) Historical and RCP simulations cannot capture the global warming hiatus during the early 2000s. With the introduction of the initialization, the rise of the globally averaged surface air temperature predicted by the decadal prediction experiments of the FGOALS-s2 significantly weakens, which is consistent with CMIP5 MME [9].

Conflict of Interests

The authors declare that there is no conflict of interests regarding the publication of this paper.

Acknowledgments

This work was supported by the CAS Strategic Priority Research Program (Grant no. XDA05110305), National Program on Key Basic Research Project (Grant no. 2012CB955202), the NSFC (Grant nos. 41023002, 41330423), and the China Meteorological Administration (Grant no. GYHY201006019).

References

- [1] G. A. Meehl, L. Goddard, G. Boer et al., “Decadal climate prediction: an update from the trenches,” *Bulletin of the American Meteorological Society*, vol. 95, no. 2, pp. 243–267, 2014.
- [2] D. M. Smith, S. Cusack, A. W. Colman, C. K. Folland, G. R. Harris, and J. M. Murphy, “Improved surface temperature prediction for the coming decade from a global climate model,” *Science*, vol. 317, no. 5839, pp. 796–799, 2007.
- [3] N. S. Keenlyside, M. Latif, J. Jungclaus, L. Kornbluh, and E. Roeckner, “Advancing decadal-scale climate prediction in the North Atlantic sector,” *Nature*, vol. 453, no. 7191, pp. 84–88, 2008.
- [4] H. Pohlmann, J. H. Jungclaus, A. Köhl, D. Stammer, and J. Marotzke, “Initializing decadal climate predictions with the GECCO oceanic synthesis: effects on the North Atlantic,” *Journal of Climate*, vol. 22, no. 14, pp. 3926–3938, 2009.
- [5] T. Mochizuki, M. Ishii, M. Kimoto et al., “Pacific decadal oscillation hindcasts relevant to near-term climate prediction,” *Proceedings of the National Academy of Sciences of the United States of America*, vol. 107, no. 5, pp. 1833–1837, 2010.
- [6] P. van der Linden and J. F. B. Mitchell, *ENSEMBLES: Climate Change and Its Impacts: Summary of Research and Results from the ENSEMBLES Project*, The Met Office Hadley Centre, Exeter, UK, 2009.
- [7] G. A. Meehl, L. Goddard, J. Murphy et al., “Decadal prediction: can it be skillful?” *Bulletin of the American Meteorological Society*, vol. 90, no. 10, pp. 1467–1485, 2009.
- [8] K. E. Taylor, R. J. Stouffer, and G. A. Meehl, “An overview of CMIP5 and the experiment design,” *Bulletin of the American Meteorological Society*, vol. 93, no. 4, pp. 485–498, 2012.
- [9] B. Kirtman and S. B. Power, “Near-term climate change: projections and predictability,” in *Climate Change 2013: The Physical Science Basis*, Contribution of Working Group I to the Fifth Assessment Report of the Intergovernmental Panel on Climate, Cambridge University Press, Cambridge, UK, 2013.
- [10] D. M. Smith, R. Eade, and H. Pohlmann, “A comparison of full-field and anomaly initialization for seasonal to decadal climate prediction,” *Climate Dynamics*, vol. 41, no. 11–12, pp. 3325–3338, 2013.
- [11] CLIVAR, *Data and Bias Correction for Decadal Climate Predictions*, CLIVAR Publication Series 150, International CLIVAR Project Office, 2011.
- [12] B. Wang, M. Liu, Y. Yu et al., “Preliminary evaluations of FGOALS-g2 for decadal predictions,” *Advances in Atmospheric Sciences*, vol. 30, no. 3, pp. 674–683, 2013.
- [13] G. A. Meehl and H. Teng, “CMIP5 multi-model hindcasts for the mid-1970s shift and early 2000s hiatus and predictions for 2016–2035,” *Geophysical Research Letters*, vol. 41, no. 5, pp. 1711–1716, 2014.
- [14] N. S. Fučkar, D. Volpi, V. Guemas, and F. J. Doblas-Reyes, “A posteriori adjustment of near-term climate predictions: accounting for the drift dependence on the initial conditions,” *Geophysical Research Letters*, vol. 41, no. 14, pp. 5200–5207, 2014.
- [15] D. W. Pierce, T. P. Barnett, R. Tokmakian et al., “The ACPI project, element 1: initializing a coupled climate model from observed conditions,” *Climatic Change*, vol. 62, no. 1–3, pp. 13–28, 2004.
- [16] F. J. Doblas-Reyes, I. Andreu-Burillo, Y. Chikamoto et al., “Initialized near-term regional climate change prediction,” *Nature Communications*, vol. 4, article 1715, 2013.
- [17] W. D. Collins, C. M. Bitz, M. L. Blackmon et al., “The community climate system model version 3 (CCSM3),” *Journal of Climate*, vol. 19, no. 11, pp. 2122–2143, 2006.
- [18] Q. Bao, P. Lin, T. Zhou et al., “The flexible global ocean-atmosphere-land system model, spectral version 2: FGOALS-s2,” *Advances in Atmospheric Sciences*, vol. 30, no. 3, pp. 561–576, 2013.
- [19] H. Liu, P. Lin, Y. Yu, and X. Zhang, “The baseline evaluation of LASG/IAP Climate system Ocean Model (LICOM) version 2,” *Journal of Meteorological Research*, vol. 26, no. 3, pp. 318–329, 2012.
- [20] P. Lin, Y. Yu, and H. Liu, “Long-term stability and oceanic mean state simulated by the coupled model FGOALS-s2,” *Advances in Atmospheric Sciences*, vol. 30, no. 1, pp. 175–192, 2013.
- [21] K. W. Oleson, Y. Dai, G. Bonan et al., “Technical description of the community land model (CLM),” NCAR Technical Note NCAR/TN-461+STR, National Center for Atmospheric Research, Boulder, Colo, USA, 2004.
- [22] S. Guinehut, C. Coatanoan, A.-L. Dhomp, P.-Y. Le Traon, and G. Larnicol, “On the use of satellite altimeter data in Argo quality control,” *Journal of Atmospheric and Oceanic Technology*, vol. 26, no. 2, pp. 395–402, 2009.
- [23] S. C. Bloom, L. L. Takacs, A. M. da Silva, and D. Ledvina, “Data assimilation using incremental analysis updates,” *Monthly Weather Review*, vol. 124, no. 6, pp. 1256–1271, 1996.
- [24] B. Huang, J. L. Kinter III, and P. S. Schopf, “Ocean data assimilation using intermittent analyses and continuous model error correction,” *Advances in Atmospheric Sciences*, vol. 19, no. 6, pp. 965–992, 2002.
- [25] H. Tatebe, M. Ishii, T. Mochizuki et al., “The initialization of the MIROC climate models with hydrographic data assimilation for decadal prediction,” *Journal of the Meteorological Society of Japan*, vol. 90, pp. 275–294, 2012.
- [26] B. Wu and T. Zhou, “Prediction of decadal variability of sea surface temperature by a coupled global climate model FGOALS-gl developed in LASG/IAP,” *Chinese Science Bulletin*, vol. 57, no. 19, pp. 2453–2459, 2012.
- [27] T. Zhou, F. Song, and X. Chen, “Historical evolution of global and regional surface air temperature simulated by FGOALS-s2 and FGOALS-g2: how reliable are the model results?” *Advances in Atmospheric Sciences*, vol. 30, no. 3, pp. 638–657, 2013.
- [28] P. Brohan, J. J. Kennedy, I. Harris, S. F. B. Tett, and P. D. Jones, “Uncertainty estimates in regional and global observed temperature changes: a new data set from 1850,” *Journal of Geophysical Research D: Atmospheres*, vol. 111, no. 12, Article ID D12106, 2006.
- [29] B. Rudolf, A. Becker, U. Schneider, A. Meyer-Christoffer, and M. Ziese, “The new ‘GPCC Full Data Reanalysis Version 5’ providing high-quality gridded monthly precipitation data for the global land-surface is public available since December 2010,” Tech. Rep., The Global Precipitation Climatology Centre (GPCC), 2010, <http://gpcc.dwd.de/>.
- [30] V. Guémas, S. Corti, J. García-Serrano, F. J. Doblas-Reyes, M. Balmaseda, and L. Magnusson, “The Indian ocean: the region of highest skill worldwide in decadal climate prediction,” *Journal of Climate*, vol. 26, no. 3, pp. 726–739, 2013.
- [31] L. Dong, T. Zhou, and B. Wu, “Indian Ocean warming during 1958–2004 simulated by a climate system model and its mechanism,” *Climate Dynamics*, vol. 42, no. 1–2, pp. 203–217, 2014.
- [32] D. R. Easterling and M. F. Wehner, “Is the climate warming or cooling?” *Geophysical Research Letters*, vol. 36, no. 8, Article ID L08706, 2009.

- [33] G. A. Meehl, J. M. Arblaster, J. T. Fasullo, A. Hu, and K. E. Trenberth, "Model-based evidence of deep-ocean heat uptake during surface-temperature hiatus periods," *Nature Climate Change*, vol. 1, no. 7, pp. 360–364, 2011.
- [34] Y. Kosaka and S.-P. Xie, "Recent global-warming hiatus tied to equatorial Pacific surface cooling," *Nature*, vol. 501, no. 7467, pp. 403–407, 2013.
- [35] J. Tollefson, "Climate change: the case of the missing heat," *Nature*, vol. 505, no. 7483, pp. 276–278, 2014.
- [36] G. A. Meehl, H. Teng, and J. M. Arblaster, "Climate model simulations of the observed early-2000s hiatus of global warming," *Nature Climate Change*, vol. 4, no. 10, pp. 898–902, 2014.
- [37] K. E. Trenberth and D. J. Shea, "Atlantic hurricanes and natural variability in 2005," *Geophysical Research Letters*, vol. 33, no. 12, Article ID L12704, 2006.
- [38] D. M. Smith, R. Eade, N. J. Dunstone et al., "Skilful multi-year predictions of Atlantic hurricane frequency," *Nature Geoscience*, vol. 3, no. 12, pp. 846–849, 2010.
- [39] G. J. van Oldenborgh, F. J. Doblas-Reyes, B. Wouters, and W. Hazeleger, "Decadal prediction skill in a multi-model ensemble," *Climate Dynamics*, vol. 38, no. 7-8, pp. 1263–1280, 2012.
- [40] X. Yang, A. Rosati, S. Zhang et al., "A predictable AMO-like pattern in the GFDL fully coupled ensemble initialization and decadal forecasting system," *Journal of Climate*, vol. 26, no. 2, pp. 650–661, 2013.
- [41] H.-M. Kim, P. J. Webster, and J. A. Curry, "Evaluation of short-term climate change prediction in multi-model CMIP5 decadal hindcasts," *Geophysical Research Letters*, vol. 39, no. 10, Article ID L10701, 2012.
- [42] J. R. Knight, R. J. Allan, C. K. Folland, M. Vellinga, and M. E. Mann, "A signature of persistent natural thermohaline circulation cycles in observed climate," *Geophysical Research Letters*, vol. 32, no. 20, Article ID L20708, 2005.
- [43] R. Msadek and C. Frankignoul, "Atlantic multidecadal oceanic variability and its influence on the atmosphere in a climate model," *Climate Dynamics*, vol. 33, no. 1, pp. 45–62, 2009.
- [44] S. A. Cunningham, T. Kanzow, D. Rayner et al., "Temporal variability of the Atlantic meridional overturning circulation at 26.5°N," *Science*, vol. 317, no. 5840, pp. 935–938, 2007.
- [45] N. J. Mantua, S. R. Hare, Y. Zhang, J. M. Wallace, and R. C. Francis, "A Pacific interdecadal climate oscillation with impacts on salmon production," *Bulletin of the American Meteorological Society*, vol. 78, no. 6, pp. 1069–1079, 1997.
- [46] S. Power, T. Casey, C. Folland, A. Colman, and V. Mehta, "Inter-decadal modulation of the impact of ENSO on Australia," *Climate Dynamics*, vol. 15, no. 5, pp. 319–324, 1999.
- [47] G. A. Meehl and A. Hu, "Megadroughts in the Indian monsoon region and southwest North America and a mechanism for associated multidecadal Pacific Sea surface temperature anomalies," *Journal of Climate*, vol. 19, no. 9, pp. 1605–1623, 2006.
- [48] B. Wang, J. Liu, H.-J. Kim, P. J. Webster, S.-Y. Yim, and B. Xiang, "Northern Hemisphere summer monsoon intensified by mega-El Niño/southern oscillation and Atlantic multidecadal oscillation," *Proceedings of the National Academy of Sciences of the United States of America*, vol. 110, no. 14, pp. 5347–5352, 2013.

Research Article

Statistical Prediction of the South China Sea Surface Height Anomaly

Caixia Shao,^{1,2} Weimin Zhang,¹ Chunjian Sun,² Xinmin Chai,² and Zhimin Wang²

¹National University of Defense Technology, Changsha, Hunan 410073, China

²Key Laboratory of Marine Environmental Information Technology, SOA, National Marine Data and Information Service, Tianjin 300171, China

Correspondence should be addressed to Caixia Shao; shaocx@163.com

Received 16 December 2014; Revised 8 February 2015; Accepted 26 February 2015

Academic Editor: Shaoqing Zhang

Copyright © 2015 Caixia Shao et al. This is an open access article distributed under the Creative Commons Attribution License, which permits unrestricted use, distribution, and reproduction in any medium, provided the original work is properly cited.

Based on the simple ocean data assimilation (SODA) data, this study analyzes and forecasts the monthly sea surface height anomaly (SSHA) averaged over South China Sea (SCS). The approach to perform the analysis is a time series decomposition method, which decomposes monthly SSHAs in SCS to the following three parts: interannual, seasonal, and residual terms. Analysis results demonstrate that the SODA SSHA time series are significantly correlated to the AVISO SSHA time series in SCS. To investigate the predictability of SCS SSHA, an exponential smoothing approach and an autoregressive integrated moving average approach are first used to fit the interannual and residual terms of SCS SSHA while keeping the seasonal part invariant. Then, an array of forecast experiments with the start time spanning from June 1977 to June 2007 is performed based on the prediction model which integrates the above two models and the time-independent seasonal term. Results indicate that the valid forecast time of SCS SSHA of the statistical model is about 7 months, and the predictability of SCS SSHA in Spring and Autumn is stronger than that in Summer and Winter. In addition, the prediction skill of SCS SSHA has remarkable decadal variability, with better phase forecast in 1997–2007.

1. Introduction

Study on the variation of the sea surface height anomaly (SSHA) is an important issue in physical oceanography and meteorological science. Changes in SSHA will influence the frequency and impact of extreme sea level events which engender lots of negative impact [1, 2]. Previous studies found that the regional SSHA variability at the interannual time scale dominated by ocean variability is much larger than the global SSHA [3–5]. As the largest marginal sea in Western Pacific, South China Sea (SCS) is a crucial link between Pacific and Indian Ocean, and it has significant impacts on human activities and the sustainable development of coastal economy and society.

Analysis and forecast are two crucial aspects of SCS SSHA. As far, most attentions have been paid to the analysis of the SSHA in SCS, like the annual variability [6, 7], interannual variability [8, 9], seasonal variability [10], the rising rate [11, 12], the forcing of the variations [13–16], and the variability associated with El Niño and Southern Oscillation

(ENSO) [8, 9, 16, 17]. For the forecast of SCS SSHA, the forecast model of SCS SSHA, mainly, includes the dynamical models and statistical methods. Now the 3D dynamical prediction system of the SCS SSHA has been improved [18, 19]. For example, Wei et al. [18] use a fine-grid dynamical model covering SCS to produce monthly and annual mean SSHA of the SCS from 1992 to 2000, and the model-produced data is in good agreement with altimeter measurements. While the dynamical approaches have been studied widely [1, 20, 21], little attentions have been paid to the statistical forecast of SSHA in SCS, which is simple and feasible in practice. The Pacific ENSO Applications Climate (PEAC) Centre at the National Oceanographic and Atmospheric Administration (NOAA) uses a statistical model to calculate site-specific seasonal sea level outlooks, and the results indicated that the statistical model is potentially useful in predicting seasonal sea level variations in the U.S.-affiliated Pacific Islands (USAPI) [22]. Imani et al. [23] used the Holt-Winters exponential smoothing technique to analyze and forecast Caspian Sea level anomalies from 15-year altimetry

data from 1993 to 2008 and found that the modeling results of a 3-year forecasting time span (2005–2008) agree well with the observed time series. As far as we know, no literature on the statistical prediction of SCS SSHA has been documented. Also it is feasible to use the statistical models to implement the forecast of the SCS SSHA compared with the complicated dynamical models. In this study, based on the long-term monthly time series of SCS SSHA derived from the Simple Ocean Data Analysis (SODA), we first use a time series decomposition method to analyze the variability of monthly SCS SSHA. Then, a statistical model is constructed to fit the monthly SCS SSHA and used to perform an array of forecast experiments. Finally, the statistical prediction skill of SCS SSHA is investigated.

The remainder of this study is organized as follows: the data, the time series decomposition method, and the statistical model construction are introduced in Section 2. Section 3 presents the analysis results of SSHA in SCS while the forecast results are shown in Section 4. Summary and discussion are given in Section 5.

2. Methodology

2.1. Data

2.1.1. SODA. An ocean reanalysis product, namely, simple ocean data assimilation (SODA), is used in this study, which is based on the Parallel Ocean Program ocean model with an average horizontal resolution of $0.5^\circ \times 0.5^\circ$ and with 40 vertical levels during January 1948 to December 2007 [24]. SODA data is downloaded from web site at http://dsrs.atmos.umd.edu/DATA/soda_2.2.4/. For our study, we first calculate the monthly mean values of SSH so as to derive the monthly SSHA. Then, we average the monthly SSHA over the South China Sea (5°N – 25°N , 105°E – 121°E) to form the basic datasets used in this study.

2.1.2. AVISO. A merged gridded product of Maps of Sea Level Anomaly produced by AVISO (Archivage Validation et Interpretation des donnees des Satellites Oceanographiques) based on TOPEN/Poseidon, Janson 1, ERS-1, and ERS-2 satellite data is used for evaluating the correctness of SODA data. This product provides SSHAs from January 1993 to December 2007, which consists of maps produced every day on a $1/8^\circ \times 1/8^\circ$ Cartesian grid. The monthly SSHA in AVISO is first computed and then used to derive the monthly SCS SSHA.

2.2. Statistical Methods for Modeling and Forecasting

2.2.1. Decomposition Method. In this section, we briefly introduce the time series decomposition method, that is, the centralized moving average scheme. This method partitions a monthly time series into the following three components: the interannual component T_t , the seasonal component S_t , and the residual component R_t as follows:

$$x_t = T_t + S_t + R_t, \quad (1)$$

where x_t represents the monthly value at time t . The computational processes of T_t , S_t , and R_t are listed as follows.

(a) *Interannual Component.* A simple centralized moving average technique with 12-month time scale is used to obtain the interannual term as

$$T_t = \frac{0.5x_{t-6} + x_{t-5} + \cdots + x_{t+5} + 0.5x_{t+6}}{12}, \quad (2)$$

$$t \in (7, N - 6),$$

where N represents the length of x_t . Apparently, with the smoothing-scale being set to 12 months, $\{T_t\}$ filters the short time scale (less than 12 months) information of $\{x_t\}$ and keeps the interannual variations. Thus, $\{T_t\}$ describes the interannual variabilities of $\{x_t\}$. Note that the valid period of $\{T_t\}$ is from July 1948 to June 2007. The following decomposition and analysis as well as the forecast experiments will be also based on $\{x_t\}$ during the same period.

(b) *Seasonal Component.* After the interannual term of $\{x_t\}$ has been computed with the above method, we first subtract T_t from $\{x_t\}$ to get the remaining term. In this study, the seasonal term (S_t) corresponds to the climatology of the remaining term. Thus, although the length of S_t is the same as T_t , the period of S_t is 12 months.

(c) *Residual Component.* With the interannual term (T_t) and the seasonal term (S_t) being determined, the residual term R_t of x_t is directly computed by

$$R_t = x_t - T_t - S_t. \quad (3)$$

According to the time scales of T_t and S_t , it is easy to derive that R_t reflects the variability of x_t whose time scale is interseasonal or smaller. As the resolution of x_t is monthly, it is expected that R_t is noise-dominant. In addition, the summation of R_t and T_t represents the anomaly of x_t . Due to the static nature of S_t , the forecasting of x_t mainly depends on the prediction of the anomaly of x_t which consists of R_t and T_t . Because of the different time scales of R_t and T_t , different statistical models are used to fit and forecast R_t and T_t .

2.2.2. Models for Fitting and Forecasting. To investigate the statistical predictability of SSHA in SCS, the statistical forecast model is first constructed in this section.

(a) *The Model for Interannual Term.* Due to the simplicity and robustness [23, 25], Holt's linear exponential smoothing technique is widely used to handle nonseasonal time series by introducing smoothing parameters [26], like the precipitation prediction [27] and the maxima and minima air temperature prediction [28]. In this study, we also use Holt's linear exponential smoothing technique to fit and forecast T_t . The fit formula of T_t is

$$\hat{T}_{t+1} = a_t + b_t, \quad (4)$$

where

$$\begin{aligned} a_t &= \alpha \widehat{T}_t + (1 - \alpha)(a_{t-1} + b_{t-1}), \\ b_t &= \beta (a_t - a_{t-1}) + (1 - \beta)b_{t-1}. \end{aligned} \quad (5)$$

Here α and β denote the smoothing parameters. The initial values of a_0 and b_0 are usually set to 0. Given preset values (i.e., first guesses) of α and β , the fitness of T_t (denoted as \widehat{T}_t , $t = 8, N - 6$) can be calculated sequentially with known \widehat{T}_{t-1} . Note that 7 is the starting index of T_t (see (2)) and $\widehat{T}_7 = T_7$. Then a cost function between T_t and \widehat{T}_t is established. Taking α and β as the control variables to be optimized, an optimization algorithm, like the L-BFGS-B algorithm [29], is used to obtain the optimum α and β . In addition, to avoid the overflow of α and β , the $[0, 1]$ bound is applied to these two parameters during the optimizing process.

For the forecast of T_t , a linear function of the lead time is constructed as follows:

$$T_{t+k} = a_t + b_t k. \quad (6)$$

Here k is the lead time in month.

(b) *The Model for Residual Term.* Due to the noise-dominant nature of R_t , we use an auto-regression integrated moving average model (denoted as ARIMA(p, d, q) [30, 31]) to construct the fit model of R_t . Here p represents the order of the autoregression model (i.e., AR(p)); d is the order of time differential of R_t ; q indicates the order of the moving average model. The model can be formulated as

$$\begin{aligned} \widehat{W}_t &= \varphi_1 \widehat{W}_{t-1} + \varphi_2 \widehat{W}_{t-2} + \dots + \varphi_p \widehat{W}_{t-p} + e_t \\ &\quad - \theta_1 e_{t-1} - \dots - \theta_q e_{t-q}, \\ W_t &= \nabla^d R_t, \end{aligned} \quad (7)$$

where W_t represents the time series of d -order time differentiate of R_t , t is the time, $\varphi_1, \varphi_2, \dots, \varphi_p$ are coefficients of the autoregressive integrated model, $\theta_1, \theta_2, \dots, \theta_q$ are coefficients of the moving average model, and e_t is a white noise time series [32].

For the fitness model, the determination process of the parameters is described as follows. First, the values of p , d , and q are automatically determined by auto.arima library in R software, according to statistic tests. The value of d is selected based on successive KPSS unit-root tests and then p and q are chosen based on the approach of Akaike's Information Criterion (AIC) [33]. Then there are a total of $p+q$ parameters to be determined. Taking $d = 1$ as an example, according to (7), given the previous fitted $\varphi_1, \varphi_2, \dots, \varphi_p, \theta_1, \theta_2, \dots, \theta_q$ can be computed accordingly. Then a cost function is established between R_t and e_t to determine the optimized parameters with an optimization algorithm.

Given that the fitness model has been determined, the \widehat{R}_t is integrated by W_t , and the same values of parameters are consistently used to perform the forecast experiment.

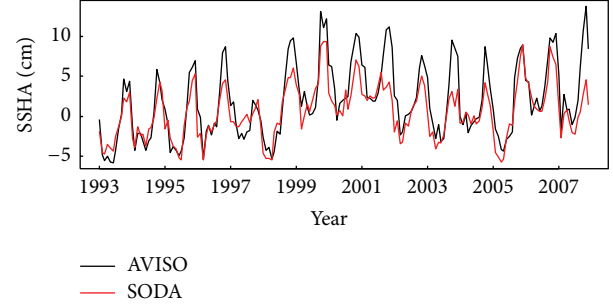


FIGURE 1: Time series of monthly SCS SSHA (cm) derived from AVISO (black) and SODA (red).

3. Modeling Construction

Affected by various factors, such as solar radiation, evaporation and precipitation, monsoon, and El Niño and Southern Oscillation (ENSO), the SCS SSHA has significant characteristics on different time scales. In this section, we roughly analyze the time variability of SCS SSHA with the time series decomposition method (Section 2.2.1) based on the SODA product.

3.1. *Verification of SODA SSHA.* Before applying the time series decomposition to the SCS SSHA derived from the SODA product, the correctness of this dataset should be first verified. Figure 1 shows the time series of the monthly SCS SSHA derived from SODA (red) and AVISO (black). It can be seen that the most prominent signal is the seasonality in both products. The correlation coefficient between two time series reaches 0.89 with the significance level above 95%. The root-mean-square error between two time series is 2.56 cm. The SODA product can well capture the temporal variability of SCS SSHA.

To detect the significant periods of these two datasets, we perform the power spectrum analysis. Figure 2 presents the power spectrum of SCS SSHA for AVISO (blue) and SODA (black), where the dashed curves represent the 95% confidence upper limits. Obviously, both time series have 1-year and half-year significant periods.

Due to the limited length of AVISO SSHA data, we cannot systematically verify the correctness of the whole time series of SCS SSHA derived from SODA data. However, based on the above analysis, it is reasonable to assume that the quality of the time series of SCS SSHA from SODA data is reliable.

3.2. *Results of Time Series Decomposition.* Given that the correctness of the SODA SSHA data has been validated by AVISO data, we apply the time series composition to the monthly SCS SSHA from SODA with a 60-year length. Figure 3 shows the time series of three decomposed terms of SSHA in SCS, where the interannual term, residual term, and seasonal term are represented by black, red, and blue curves. For the interannual term, it has significant interannual variability. During most of El Niño years, SCS SSHA is smaller than that during other years. Moreover, there are some inflexions most of which correspond to El Niño or

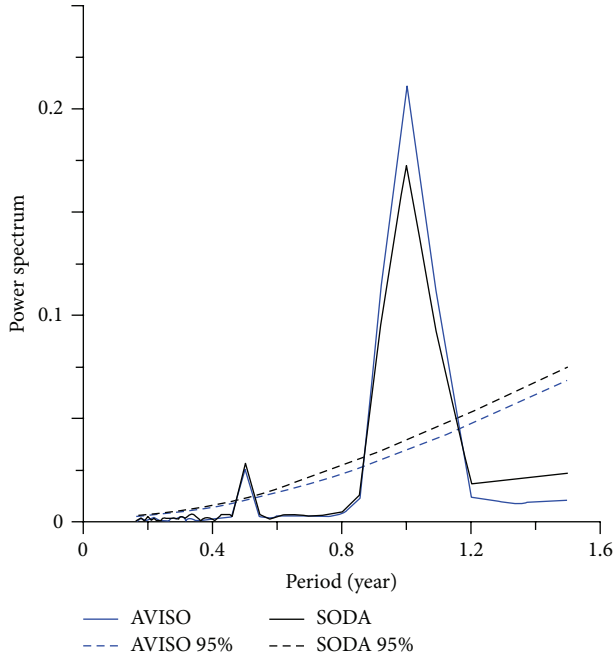


FIGURE 2: The power spectrums of SCS SSHA for the AVISO (blue) and SODA (black). The dashed curves represent the 95% confidence upper limit.

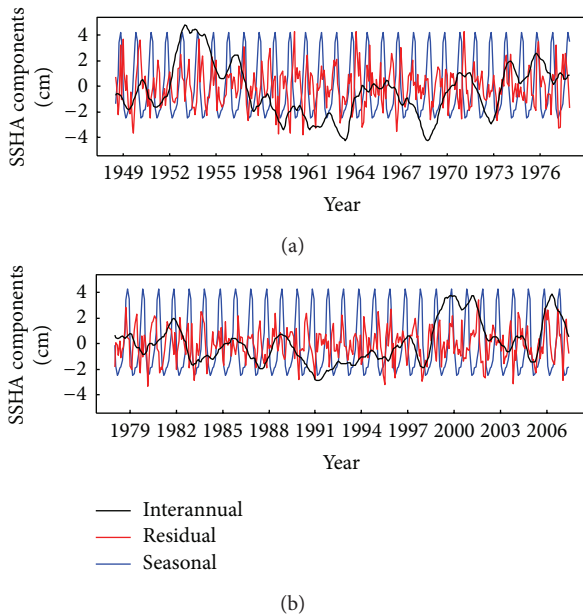


FIGURE 3: Time series (1948–1977 in (a); 1978–2007 in (b)) of three components (unit: cm) of SSHA in SCS, including the interannual term (black), the seasonal term (blue), and the residual term (red).

La Nina years, like 1997-1998 and 2005-2006 El Niños. Thus, SSHA variations in SCS are strongly modulated by ENSO. For the seasonal term, the minima (maxima) occur in Summer (Winter) which may have some connection with the SCS monsoon [10, 13]. For the residual term that oscillates around 0, its amplitude is smaller than the seasonal term and the interannual term.

3.3. Model Construction. Before performing the forecast experiments of SSHA, the forecast model of SCS SSHA should be first established. Note that the SSHAs from now on indicate the SSHA anomalies. Due to the invariant property of the seasonal term, the forecast model is divided into two parts: the Holt-Winters model for the interannual term and the ARIMA model for the residual term. Given the time series of SCS SSHA, the fitness models for the interannual term and the residual term are first, respectively, constructed and then used to forecast these two quantities. Finally the forecasted interannual term and the residual term are added together to form the forecasted anomaly of SCS SSHA. In this section, we examine the qualities of fitness for the interannual and residual terms.

Figures 4(a) and 4(b) show the fitted values (red curve) and SODA values (blue curve) of the interannual and residual terms of SSHA in SCS. Note that as the time series composition needs to remove the first and last 6 months' SSHAs, the actual fitting model uses the time series between July 1948 and June 2007. For the interannual term, the Holt-Winters model can exactly track the trajectory of the SODA data with little biases in the points of minimum and maximum. For the residual term, the ARIMA model can well simulate the phase of the SODA data, although the simulation of the amplitude is not so good, which may be attributed to the nearly white noise nature of the residual term. Figure 4(c) plots the fitted and SODA values of total SSHA in SCS. The fitted curve is strongly correlated with the SODA time series. Figure 4(d) presents the time series of the biases (computed as the difference between the fitted value and the observed value) of the fitted interannual term (black curve), residual term (blue dashed curve), and total SCS SSHA (red curve). The bias of the fitted total SCS SSHA oscillates around 0 and mainly consists of residual biases. The analysis indicates that the added statistical model is effective and flexible, and then we use the added model to do forecast experiments as follows.

4. Forecast Results

The last 30 years' analysis results are used to perform the forecast experiment which is similar to the dynamical forecast of physical processes (like ENSO [34, 35]). For each month from December 1977 to December 2007, we first decompose the time series (from January 1948 to the current month) of SSHA in SCS into three parts and then use Holt-Winters and ARIMA models to fit the interannual and residual terms, respectively. Then, both models are integrated forward up to 2 years to forecast the interannual and residual terms of SSHA in SCS. Thus, 361 forecast experiments are conducted. Note that as the time series composition needs to remove the SSHAs during the first and last 6 months, the actual initial forecast months for 361 forecast experiments correspond to June 1977 and June 2007. The forecast SSHA anomaly (interannual term plus residual term) is compared to the SODA data with seasonal cycle removed. Figure 5 gives a sketch map of the forecast experiments.

Based on the forecast results, we investigate the predictability of SCS SSHA from the following three aspects.

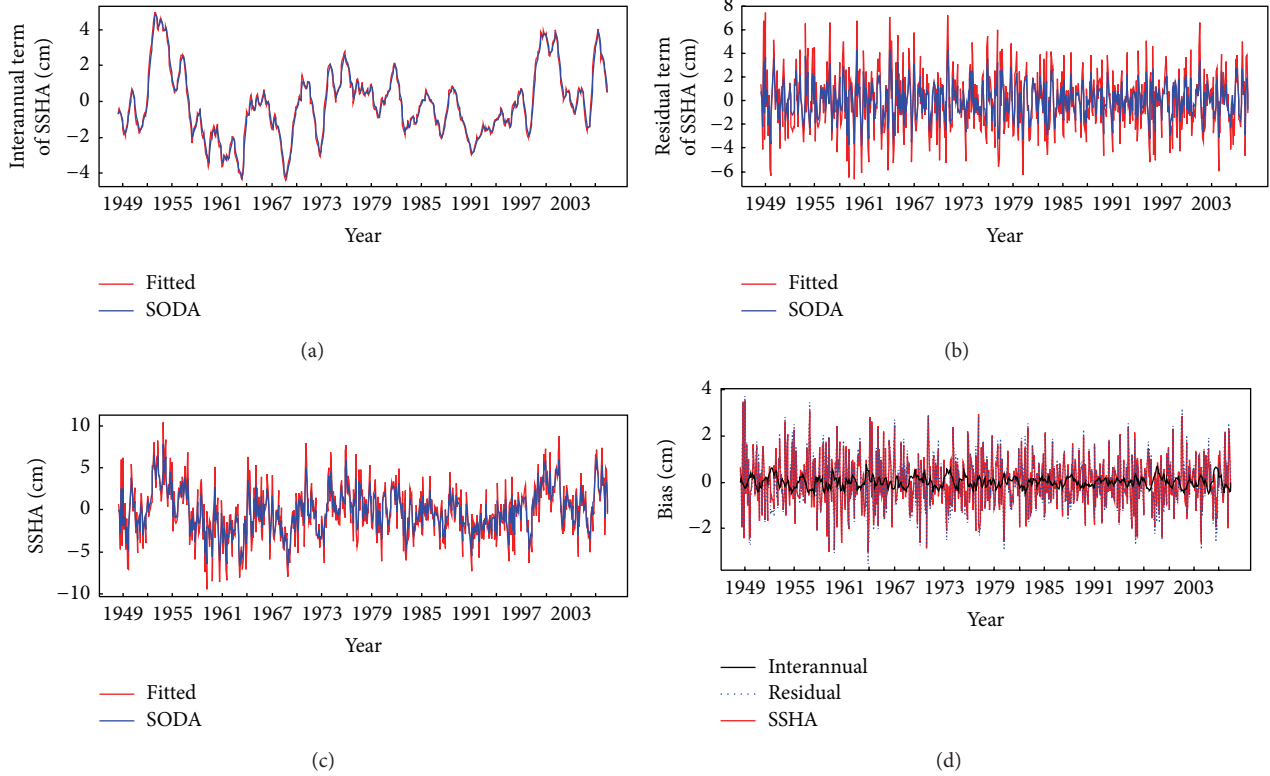


FIGURE 4: Time series of fitted (red curve) and SODA's (blue curve) interannual term (a) and residual term (b) of SSHA in South China Sea as well as the total SSHA (c). (d) presents the time series of the biases (computed as the difference between the fitted value and the observed value) of the fitted interannual term (black curve), residual term (blue dashed curve), and total SCS SSHA (red curve).

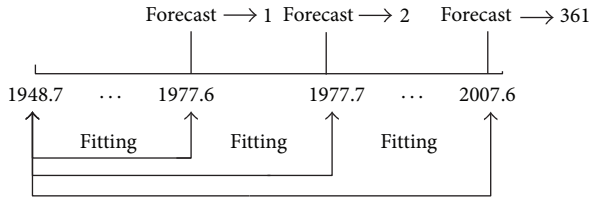


FIGURE 5: The schematic diagram of the forecast experiments.

4.1. Forecast Skill. We first totally examine the prediction skill of SSHA in SCS with the anomaly correlation coefficient (ACC) and the root-mean-square error (RMSE) relative to the SODA data. The ACC and RMSE are defined as follows:

$$\text{ACC}_s = \frac{\sum_{i=1}^{361} (x'_{i,s} - \bar{x}'_s)(x^o_{i,s} - \bar{x}^o_s)}{\sqrt{\sum_{i=1}^{361} (x'_{i,s} - \bar{x}'_s)^2} \sqrt{\sum_{i=1}^{361} (x^o_{i,s} - \bar{x}^o_s)^2}}, \quad (8)$$

$$\text{RMSE}_s = \sqrt{\frac{1}{361} \sum_{i=1}^{361} \left(\frac{x'_{i,s} - x^o_{i,s}}{\sigma_c} \right)^2},$$

where s and i index the lead time and the forecast experiment; x' and x^o represent the forecasted and SODA anomaly of SCS SSHA while \bar{x}' and \bar{x}^o denote the averages of x' and x^o over all

forecast experiments; σ_c indicates the climatological standard deviation of anomaly of SCS SSHA.

Figures 6(a) and 6(b) show the variation of RMSE (Figure 6(a)) and ACC (Figure 6(b)) of forecasted SSHA anomaly in SCS with respect to lead time (in months) and start month. The solid curves in Figures 6(a) and 6(b) indicate the 1.0-contour and 0.6-contour, respectively. According to the results of RMSE, we find that the RMSEs forecasted from Spring (like April and May) and Autumn (like October and November) are smaller than the other seasons. The minima of the RMSE happen in May and November, and the maxima occur in June. If an *ad hoc* 0.6 value of ACC is used to define the valid lead time, the valid forecast time of SCS SSHA anomaly is 9 (7) months in Spring (other seasons).

To further investigate the contributions of the interannual term and residual term to the total quantity, we separately analyze the predictabilities of the interannual term and the residual term. Figures 6(c), 6(d), 6(e), and 6(f) present the same results as Figures 6(a) and 6(b) but for the interannual term and the residual term, respectively. We can see that the valid forecast time of the interannual term is 12 (9) months in Summer (other seasons). In contrast, the prediction skill of the residual term is much worse than the total quantity, especially for the ACC and the RMSEs forecasted from Spring and Autumn. This may be caused by the white noise in the forecast model (i.e., the ARIMA model) of the residual term, which increases the uncertainty of the forecasted residual

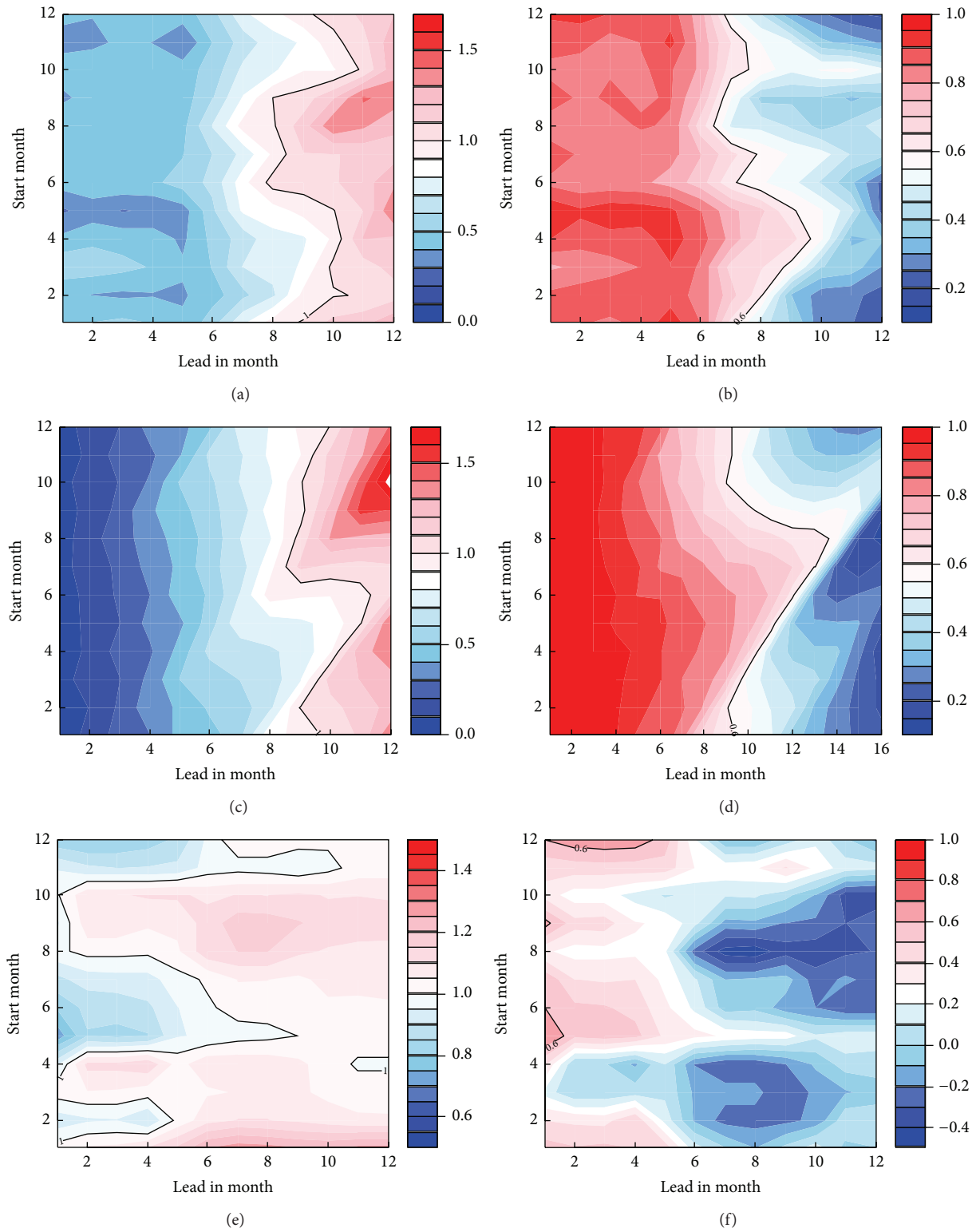


FIGURE 6: Variations of RMSE (a, c, and e) and ACC (b, d, and f) of forecasted SCS SSHA anomaly (a, b), forecasted interannual term (c, d), and forecasted residual term (e, f) with respect to lead time (in month) and start month. The solid curve in (a, c, and e) [b, d, f] is (1.0-contour) [0.6-contour]. Note that RMSEs in (a, c, and e) have been normalized by the climatological standard deviations of SCS SSHA anomaly, interannual term, and residual term, respectively.

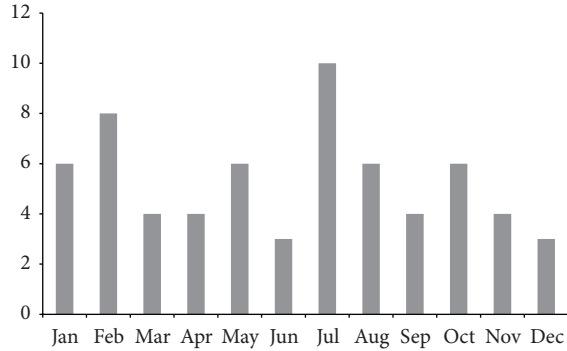


FIGURE 7: The number of extreme (including maximum and minimum) values of the interannual term (decomposed from the SODA SCS SSHA time series between July 1977 and June 2007) happens in each month.

term. Therefore, the forecast skill of the anomaly of SCS SSHA is mainly contributed by the counterpart of the interannual term and more or less reduced by the bad prediction skill of the residual term.

To figure out the possible reason causing the prediction skill of the interannual term, we calculate the number of extreme (including maximum and minimum) values of the interannual term (decomposed from the SODA SCS SSHA time series between July 1977 and June 2007) that happens in each month (Figure 7). Due to the linear property of the forecast model (i.e., the Holter-Winter model) of the interannual term, the linear trend between the maximum and the minimum can enhance the prediction skill of the interannual term. Thus, if a forecast is started from a month where the extreme value happens, the prediction skill is likely to be improved. From Figure 7, we can see that most extreme values happen in July which is consistent with the results in Figure 6(d) with an exception of the case of June.

4.2. Seasonal Forecast Skill. According to the analysis in last section, the valid forecast time of SCS SSHA is about 7 months. We now assess the seasonal forecasts in this section. Figure 8 plots the SODA data (blue) and 6-month (red in Figure 8(a)) or 9-month (red in Figure 8(b)) lead SCS SSHA anomalies. We can see that, in the seasonal forecast, the statistical model can capture the main variability of SSHA anomaly in SCS, especially for the 6-month lead. The correlation coefficient between the SODA data and the 6-month (9-month) lead SCS SSHA anomaly is 0.77 (0.45) with 95% significance level.

4.3. Decadal Variability of the Forecast Skill. To investigate the decadal variability of the prediction skill of SCS SSHA, we divide 361 forecast experiments into three arrays, corresponding to three decades. Figure 9 shows the variations of ACC and RMSE of the predicted SCS SSHA anomaly with respect to the lead time (month) for three decades (green for 1977.6–1987.5; blue for 1987.6–1997.5; red for 1997.6–2007.5) and total thirty years (black). Note that the RMSE here is not normalized by the climatological standard deviation.

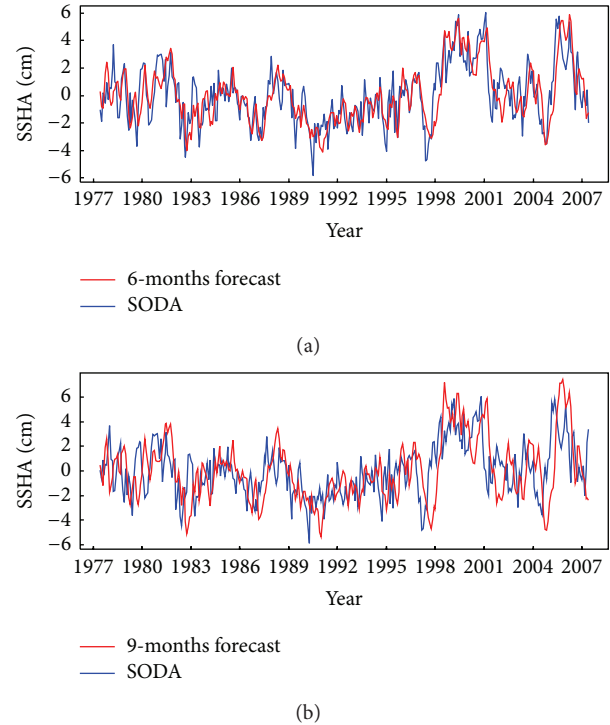


FIGURE 8: Time series of SODA data (blue curve) and forecasted (red curve) SCS SSHA anomaly with 6 (a) and 9 (b) lead months.

The SSHA in SCS can be forecasted in 6-month lead for all three decades. As the previous studies indicated, the SCS is modulated by PDO, and the SSH variability in SCS is coherent with PDO [16]. We also find that the ACCs for the last decade and the total thirty years with the 7 lead months are higher than those for other two decades, when the two decades (1977–1997) are in warm Pacific Decadal Oscillation (PDO) phase [36]. In addition, when we construct the forecast model, the SODA SSHA time series is not long enough. Thus, the forecast model may not catch both the cold and the warm phases, and the forecast in cold phase decades is better than in warm. Conversely, the RMSEs for the last decade are the worst, which may be related to the quality of SODA. From the results of the total years, the valid forecast time of SCS SSHA is about 7 months. Obviously, the prediction skill of SCS SSHA anomaly has apparent decadal variability.

5. Summary and Discussion

In this study, we first simply contrast the time series of monthly SSHAs calculated from SODA and AVISO datasets in SCS to verify the correctness of the SODA SCS SSHA which is used to construct the forecast model of SCS SSHA. Results show that SODA well correlates with AVISO data. Afterwards, we use the long-term time series from 1948 to 2007 of SODA SCS SSHA to establish the statistical forecast model. A time series decomposition method is used to decompose the monthly time series of SCS SSHA into the following three parts: interannual term, seasonal term, and

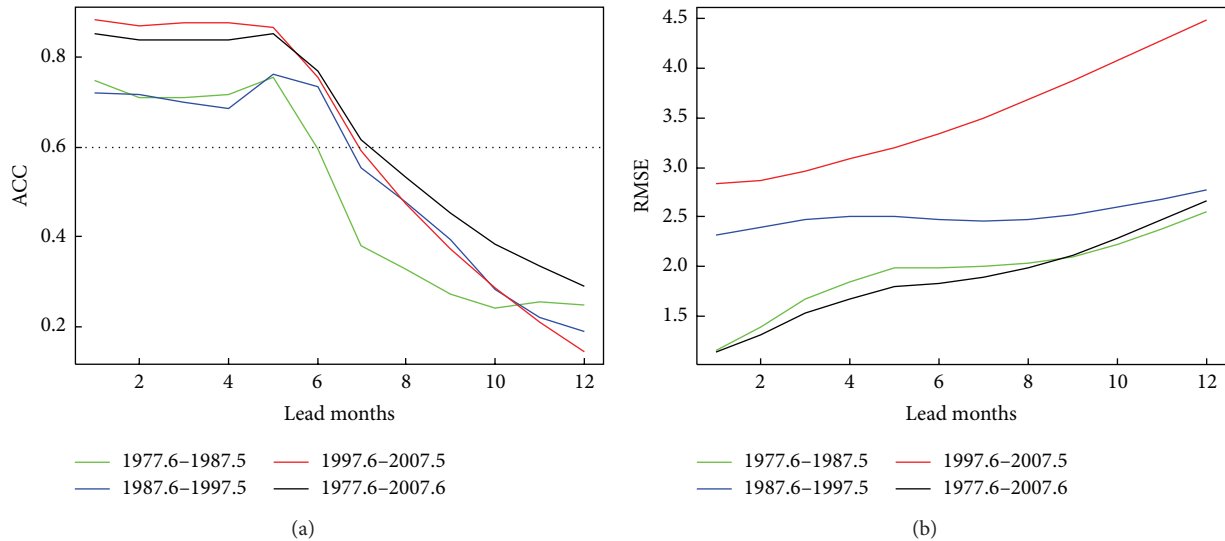


FIGURE 9: Variations of RMSE (black curve) and ACC (blue curve) of the forecasted SSHA anomaly in SCS with respect to the forecast lead time (in months). The dotted line indicates the 0.6-ACC.

residual term. Then we, respectively, use the Holt-Winters and ARIMA models to fit the interannual and residual terms of SSHA in SCS, aiming to construct the forecast models of these two parts. Results of fitting demonstrate that the Holt-Winters model can exactly track the trajectory of SODA counterpart while the ARIMA can well simulate the phase of the residual term. Finally, we perform an array of forecast experiments based on the above two models. Results show that the valid forecast time of SCS SSHA is about 7 months. The predictability of SCS SSHA in Spring and Autumn is stronger than that in Summer and Winter, and the forecast skill of the anomaly of SCS SSHA is mainly contributed by the counterpart of the interannual term and more or less reduced by the bad prediction skill of the residual term. In addition, the prediction skill of SCS SSHA has remarkable decadal variability.

In the future studies, we will focus on the following three aspects. First, the statistical method used in this study can be applied to each grid to investigate the spatial distribution of the predictability of SSHA in SCS. Second, the results produced by this statistical model should be compared to other statistical models or dynamical models. Third, the physical mechanism causing the decadal variability of the prediction skill of SCS SSHA should be further investigated.

Conflict of Interests

The authors declare that there is no conflict of interests regarding the publication of this paper.

Acknowledgments

The authors would like to express their gratitude to two reviewers for their helpful comments and suggestions, which contributed to greatly improve the original manuscript. This research was jointly supported by grants of National

Basic Research Program (2013CB430304), National Natural Science Foundation (41176003, 41206178, 41376013, 41376015, and 41306006), National High-Tech R&D Program (2013AA09A505), and Global Change and Air-Sea Interaction (GASI-01-01-12) of China.

References

- [1] E. Miles, C. Spillman, P. McIntosh, J. Church, A. Charles, and R. de Wit, "Seasonal sea-level predictions for the Western Pacific," in *Proceedings of the 20th International Congress on Modeling and Simulation*, pp. 1-6, December 2013.
- [2] R. J. Nicholls, P. P. Wong, V. R. Burkett et al., "Coastal systems and low-lying areas," in *Contribution of Working Group II to the Fourth Assessment Report of the Intergovernmental Panel on Climate Change*, pp. 315-356, Cambridge University Press, Cambridge, UK, 2007.
- [3] J. L. Chen, C. R. Wilson, D. P. Chambers, R. S. Nerem, and B. D. Tapley, "Seasonal global water mass budget and mean sea level variations," *Geophysical Research Letters*, vol. 25, no. 19, pp. 3555-3558, 1998.
- [4] C. Boening, J. K. Willis, F. W. Landerer, R. S. Nerem, and J. Fasullo, "The 2011 La Niña: so strong, the oceans fell," *Geophysical Research Letters*, vol. 39, no. 19, Article ID L19602, 2012.
- [5] M. Becker, B. Meyssignac, C. Letetrel, W. Llovel, A. Cazenave, and T. Delcroix, "Sea level variations at tropical Pacific islands since 1950," *Global and Planetary Change*, vol. 80-81, pp. 85-98, 2012.
- [6] P.-T. Shaw, S.-Y. Chao, and L.-L. Fu, "Sea surface height variations in the South China Sea from satellite altimetry," *Oceanologica Acta*, vol. 22, no. 1, pp. 1-17, 1999.
- [7] C. Y. Zhang, B. Wang, and G. Chen, "Annual sea level amplitudes in the South China Sea revealed by merged altimeter data," *Geophysical Research Letters*, vol. 33, no. 14, Article ID L14606, 2006.
- [8] G. Fang, H. Chen, Z. Wei, Y. Wang, X. Wang, and C. Li, "Trends and interannual variability of the South China Sea surface

- winds, surface height, and surface temperature in the recent decade,” *Journal of Geophysical Research C: Oceans*, vol. 111, no. 11, Article ID C11S16, 2006.
- [9] D. Peng, H. Palanisamy, A. Cazenave, and B. Meyssignac, “Interannual sea level variations in the South China Sea over 1950–2009,” *Marine Geodesy*, vol. 36, no. 2, pp. 164–182, 2013.
- [10] C.-R. Ho, Q. Zheng, Y. S. Soong, N.-J. Kuo, and J.-H. Hu, “Seasonal variability of sea surface height in the South China Sea observed with TOPEX/Poseidon altimeter data,” *Journal of Geophysical Research C: Oceans*, vol. 105, no. 6, pp. 13981–13990, 2000.
- [11] R. R. Ding, J. C. Zuo, L. Du, L. Li, and P. L. Li, *Sea level change in the South China sea and its relations to the steric height variation and wind [M.S. thesis]*, Ocean University of China, Qingdao, China, 2007, (Chinese).
- [12] H. L. Chen and P. M. Rizzoli, “Sea level rising trends in the South China Sea over 1993–2011,” in *Proceedings of the 7th International Conference on Asia and Pacific Coasts*, pp. 979–983, 2013.
- [13] Z. Liu, H. Yang, and Q. Liu, “Regional dynamics of seasonal variability in the South China Sea,” *Journal of Physical Oceanography*, vol. 31, no. 1, pp. 272–284, 2001.
- [14] Q. Y. Liu, Y. L. Jia, H. J. Yang, and Z. Y. Liu, “Seasonal variation mechanism of sea surface height in the north of the SCS,” *Acta Oceanologica Sinica*, vol. 24, supplement 1, pp. 134–141, 2002 (Chinese).
- [15] X. H. Cheng and Y. Q. Qi, “On steric and mass-induced contributions to the annual sea-level variations in the South China Sea,” *Global and Planetary Change*, vol. 72, no. 3, pp. 227–233, 2010.
- [16] J. Zhou, P. L. Li, and H. L. Yu, “Characteristics and mechanisms of sea surface height in the South China Sea,” *Global and Planetary Change*, vol. 88–89, pp. 20–31, 2012.
- [17] Z. R. Rong, Y. G. Liu, H. Zong, and Y. C. Cheng, “Interannual sea level variability in the South China Sea and its response to ENSO,” *Global and Planetary Change*, vol. 55, no. 4, pp. 257–272, 2007.
- [18] Z. X. Wei, G. H. Fang, B.-H. Choi, Y. Fang, and Y. J. He, “Sea surface height and transport stream function of the South China Sea from a variable-grid global ocean circulation model,” *Science in China, Series D: Earth Sciences*, vol. 46, no. 2, pp. 139–148, 2003.
- [19] C.-R. Wu and C.-W. J. Chang, “Interannual variability of the South China Sea in a data assimilation model,” *Geophysical Research Letters*, vol. 32, no. 17, Article ID L17611, 2005.
- [20] T. N. Stockdale, “Coupled ocean-atmosphere forecasts in the presence of climate drift,” *Monthly Weather Review*, vol. 125, no. 5, pp. 809–829, 1997.
- [21] M. Menendez, F. J. Mendez, and I. J. Losada, “Forecasting seasonal to interannual variability in extreme sea levels,” *ICES Journal of Marine Science*, vol. 66, no. 7, pp. 1490–1496, 2009.
- [22] M. R. Chowdhury, P.-S. Chu, T. Schroeder, and N. Colasacco, “Seasonal sea-level forecasts by canonical correlation analysis—an operational scheme for the U.S.-affiliated Pacific Islands,” *International Journal of Climatology*, vol. 27, no. 10, pp. 1389–1402, 2007.
- [23] M. Imani, R. J. You, and C. Y. Kuo, “Accurate Forecasting of the satellite-derived seasonal Caspian sea level anomaly using polynomial interpolation and holt-winters exponential smoothing,” *Terrestrial, Atmospheric and Oceanic Sciences*, vol. 24, no. 4, pp. 521–530, 2013.
- [24] J. A. Carton and B. S. Giese, “A reanalysis of ocean climate using Simple Ocean Data Assimilation (SODA),” *Monthly Weather Review*, vol. 136, no. 8, pp. 2999–3017, 2008.
- [25] A. Corberán-Vallet, J. D. Bermúdez, and E. Vercher, “Forecasting correlated time series with exponential smoothing models,” *International Journal of Forecasting*, vol. 27, no. 2, pp. 252–265, 2011.
- [26] E. O. Oyatoye and T. V. O. Fabson, “A comparative study of simulation and time series model in quantifying bullwhip effect in supply chain,” *Serbian Journal of Management*, vol. 6, no. 2, pp. 145–154, 2011.
- [27] M. J. I. Sofla, B. Salahi, and M. T. Masomi, “Germi county seasonal precipitation routing and analysis, using Holt-Winters method for time series with non-seasonal changes,” *Technical Journal of Engineering and Applied Sciences*, vol. 3, no. 11, pp. 950–953, 2013.
- [28] M. J. Gundalia and M. B. Dholakia, “Prediction of maximum/minimum temperatures using Holt Winters Method with Excel Spread Sheet for Junagadh Region,” *International Journal of Engineering Research & Technology*, vol. 1, no. 6, pp. 1–8, 2012.
- [29] D. C. Liu and J. Nocedal, “On the limited memory BFGS method for large scale optimization,” *Mathematical Programming*, vol. 45, no. 3, pp. 503–528, 1989.
- [30] D. M. Nickerson and B. C. Madsen, “Nonlinear regression and ARIMA models for precipitation chemistry in East Central Florida from 1978 to 1997,” *Environmental Pollution*, vol. 135, no. 3, pp. 371–379, 2005.
- [31] J. Meher and R. Jha, “Time-series analysis of monthly rainfall data for the Mahanadi River Basin,” *Sciences in Cold and Arid Regions*, vol. 5, no. 1, pp. 73–84, 2013.
- [32] J. D. Cryer and K. S. Chan, *Time Series Analysis with Applications in R*, Springer, Berlin, Germany, 2nd edition, 2010.
- [33] R. J. Hyndman and Y. Khandakar, “Automatic time series forecasting: the forecast package for R,” *Journal of Statistical Software*, vol. 27, no. 3, pp. 1–22, 2008.
- [34] D. Chen, S. E. Zebiak, A. J. Busalacchi, and M. A. Cane, “An improved procedure for El Niño forecasting: implications for predictability,” *Science*, vol. 269, no. 5231, pp. 1699–1702, 1995.
- [35] D. Chen, M. A. Cane, A. Kaplan, S. E. Zebiak, and D. Huang, “Predictability of El Niño over the past 148 years,” *Nature*, vol. 428, no. 6984, pp. 733–736, 2004.
- [36] Y. Zhang, M. W. John, and S. B. David, “ENSO-like interdecadal variability: 1900–93,” *Journal of Climate*, vol. 10, no. 5, pp. 1004–1020, 1997.

Research Article

An Evaluation Method of Underwater Ocean Environment Safety Situation Based on D-S Evidence Theory

Yuxin Zhao, Renfeng Jia, and Chang Liu

College of Automation, Harbin Engineering University, Harbin 150001, China

Correspondence should be addressed to Yuxin Zhao; zhaoyuxin@hrbeu.edu.cn

Received 15 December 2014; Accepted 29 January 2015

Academic Editor: Shaoqing Zhang

Copyright © 2015 Yuxin Zhao et al. This is an open access article distributed under the Creative Commons Attribution License, which permits unrestricted use, distribution, and reproduction in any medium, provided the original work is properly cited.

Because of complex ocean environment, underwater vehicles are facing many challenges in navigation safety and precise navigation. Aiming at the requirements of underwater navigation safety, this paper presents an evaluation method of underwater ocean environment safety situation based on Dempster-Shafer (D-S) evidence theory. Firstly, the vital ocean environment factors which affect the underwater navigation safety are taken into account, and a novel basic probability assignment (BPA) construction method of ocean environment factors is proposed according to their characteristics. Then, a new transformation method of BPA to decision-making probability is put forward to deal with the uncertainty degree. Furthermore, the super-standard weight is applied to preprocess the BPA, and D-S combination rule is used to acquire the evaluation result by fusing the preprocessed BPA. Ocean environment safety situation index is obtained by quantizing the evaluation grades. Finally, experimental results show that the method proposed has the superior practicability and reliability in actual applications.

1. Introduction

Ocean is the main resource for human survival in the future. With the increasing demand for ocean development and military applications, the underwater vehicle is a powerful tool for human to explore and utilize ocean, which has become the field to which the world technological power (the United States, Britain, Japan, etc.) gives priority to develop [1]. In order to obtain more ocean interests, a large number of autonomous underwater vehicles (AUVs) and remotely operated vehicles (ROVs) are widely applied in ocean surveys, scientific experiments, and resource explorations. Whatever the purposes of underwater vehicles are, the navigation safety is the fundamental premise to make them complete various tasks effectively. The navigation safety is affected by many ocean environment factors, and it is closely related to the basic characteristics and distribution of ocean environment factors. Ocean environment factors are often the “double-edged sword”; they not only can bring some advantages, but also can bring the challenges to underwater navigation safety. If ocean environment factors are well used, they can improve the operational effectiveness of underwater vehicles. Otherwise, they will threaten the navigation safety. Over

the long-term explorations (including ocean surveys, ocean researches, the establishments of various ocean observation instruments, etc.), humans have a certain level of knowledge and ability to control ocean. But so far, they have not solved effectively and completely the problem of navigation safety of underwater vehicles in complex ocean environment. Even if underwater navigation technology has been quite advanced, navigation safety accidents of underwater vehicles happened frequently in recent years. The problem of underwater vehicles' navigation safety has become the topic of common concern.

Evaluating ocean environment (particularly underwater environment) safety situation is very important for underwater navigation safety, which can provide objective, accurate, and quantitative evaluation result and supply the basis for underwater vehicles to take advantage of ocean environment effectively. Although domestic and foreign scholars have acquired many achievements in underwater vehicles environment modeling theory [2–7], they almost paid no attention to ocean environment safety situation. This paper puts forward a method to evaluate ocean environment safety situation and tries to seek a scientific, rational, objective, and feasible solution for improving underwater navigation safety.

Underwater navigation decision-making is a kind of intelligent behavior, which should be based on the whole situation description of ocean environment factors, rather than their accurate distribution results. In addition, ocean environment has strong randomness and uncertainty, which make it difficult to evaluate the safety situation. Therefore, evaluation method should be able to solve above problems effectively. D-S evidence theory [8, 9] has advantages and reliability in dealing with fuzzy and uncertain problems, which make it widely applied in many areas such as information fusion [10], fault diagnosis [11], and risk evaluation [12, 13]. D-S evidence theory has profound theory foundation. It can surprisingly deal with uncertainty information and take full advantage of the multisource information to obtain better fusion results. Moreover, it has been proved that D-S evidence theory could achieve fast convergence without a priori probability and conditional probability [14]. So D-S evidence theory is used to evaluate the underwater ocean environment safety situation in this paper.

There are a lot of ocean environment factors which affect the underwater navigation safety. If all ocean environment factors are taken into account in the evaluation, which not only adds the complexity of evaluation model, but also may weaken the roles of main ocean environment factors, so it is required to follow the principles such as representative, independence, and feasibility. Based on these principles, this paper mainly discusses the influence of ocean current, tide current, and pycnocline on the underwater navigation safety.

In this paper, an efficient evaluation method of underwater ocean environment safety situation based on D-S evidence theory is presented to make underwater vehicles navigate safely. The next content is composed of three sections. In Section 2, the implementation process of evaluation method is introduced. In Section 3, experiments illustrate the effectiveness of the proposed method. Finally, the conclusion of this paper is described in Section 4.

2. Materials and Methods

The establishment of evaluation model based on D-S evidence theory includes constructing the BPA, dealing with the uncertainty degree, fusing the BPA, and obtaining the safety situation index. In this section, they will be illustrated in detail.

2.1. D-S Evidence Theory. D-S evidence theory is based on a nonempty set Θ , called the frame of discernment (FOD). The elements in FOD Θ are mutually exclusive and exhaustive. A BPA is a mapping $m: 2^\Theta \rightarrow [0, 1]$, satisfying

$$\begin{aligned} \sum_{A \in \Theta} m(A) &= 1, \\ m(\emptyset) &= 0. \end{aligned} \quad (1)$$

If $m(A) > 0$, A is called a focal element.

The lower bound for a set A , represented as $\text{Bel}(A)$, is defined as follows:

$$\text{Bel}(A) = \sum_{B \subseteq A} m(B). \quad (2)$$

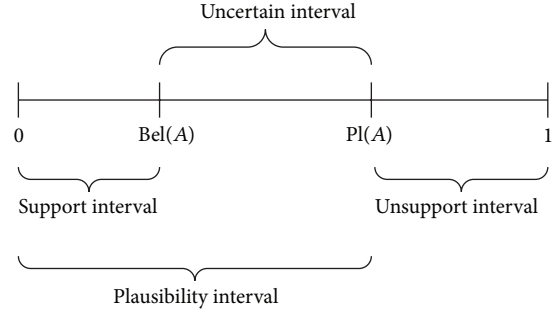


FIGURE 1: The relation between $\text{Bel}(A)$ and $\text{Pl}(A)$.

The upper bound for a set A , represented as $\text{Pl}(A)$, is defined as follows:

$$\text{Pl}(A) = \sum_{A \cap B \neq \emptyset} m(B). \quad (3)$$

The relation between $\text{Bel}(A)$ and $\text{Pl}(A)$ can be seen from Figure 1.

D-S evidence theory provides a very useful combination rule, denoted by $(m_1 \oplus m_2)$ (also called the orthogonal sum of m_1 and m_2), which is defined as follows:

$$m(A) = \frac{1}{1-k} \sum_{B \cap C = A} m_1(B) m_2(C), \quad (4)$$

where

$$k = \sum_{B \cap C = \emptyset} m_1(B) m_2(C). \quad (5)$$

k reflects the conflict between m_1 and m_2 . Its role is to avoid nonzero probability being assigned to empty set during combination. D-S combination rule is both commutative and associative.

2.2. Constructing the BPA. The effective application of D-S evidence theory depends on rational construction of the BPA. However, how to construct the BPA is still an open issue. Currently, there are some researches in this field [15–23]. But the existing methods are not suitable for ocean environment factors. Therefore, this paper proposes a construction method of the BPA according to ocean environment factors' features.

First of all, the set of evaluation grades is denoted by $\Theta = \{e_1, e_2, \dots, e_N\}$, and N is the number of grades. Here we set $N = 5$, $\{e_1, e_2, e_3, e_4, e_5\}$, representing {"Very Safe (VS)", "More Safe (MS)", "General Safe (GS)", "More Dangerous (MD)", "Very Dangerous (VD)"} respectively, and corresponding risk intervals are presented in Table 1.

Afterwards, the BPA $m_{i,n}$ of i th factor f_i on n th evaluation grade e_n is calculated separately according to the following two cases.

Case 1. If the value x_i of ocean environment factor f_i belongs to intervals VS, MS, GS, and MD, then $m_{i,n}$ is defined as

$$m_{i,n} = \frac{\lambda}{\lambda + ||x_i| - (a_n + b_n)/2|.} \quad (6)$$

TABLE 1: The risk intervals.

Factors	VS	MS	GS	MD	VD
Ocean current (m/s)	[0.0, 1.0]	(1.0, 2.0]	(2.0, 3.0]	(3.0, 4.0]	(4.0, +∞)
Tide current (m/s)	[0.0, 0.6]	(0.6, 1.0]	(1.0, 1.5]	(1.5, 2.0]	(2.0, +∞)
Pycnocline (kg/m ⁴)	[0.0, 0.2]	(0.2, 0.4]	(0.4, 0.6]	(0.6, 0.8]	(0.8, +∞)

Case 2. If the value x_i of ocean environment factor f_i belongs to interval VD, then $m_{i,n}$ is defined as

$$m_{i,n} = 1, \quad (7)$$

where a_n and b_n represent the boundaries of each interval, and $\lambda = b_n - a_n$ is the adjustment parameter, which is used to ensure $m_{i,n} \in [0, 1]$.

Due to the influence of uncertainty factors, there may be some uncertainty degree when calculating the BPA, which makes $m_{i,n}$ not necessarily equal to one. The following equation is used to represent the uncertainty degree:

$$m(\Theta) = 1 - m_{i,n}. \quad (8)$$

2.3. *Dealing with the Uncertainty Degree.* In order to obtain better evaluation result, $m(\Theta)$ need to be assigned to each evaluation grade, which requires transformation of decision-making probability. At present, there are a lot of transformation methods of decision-making probability [24–34], and these methods have certain advantages as well as some drawbacks. Based on the existing methods, for the sake of improving the shortcomings of Daniel's proportion transformation methods, this paper proposes a transformation method of decision-making probability based on the certainty degree. In accordance with the characteristics of BPA, the sum of each single proposition's BPA is regarded as the certainty degree of system, and the decision-making probability of each proposition is acquired by linear combination, which is the transformation method of decision-making probability based on proportional belief and proportional plausibility.

2.3.1. Daniel's Proportional Transformations

(1) *Proportional Belief Transformation.* Consider

$$\text{PropBelP}(A) = \sum_{A \subseteq X \in 2^\Theta} \frac{m(A)}{\sum_{B \in X} m(B)} m(X). \quad (9)$$

This method uses belief ratio between single proposition and multiple propositions to obtain the decision-making probability. The attitude of transformation is more optimistic, which is easy to increase the risk of decision-making.

(2) *Proportional Plausibility Transformation.* Consider

$$\text{PropPIP}(A) = \sum_{A \subseteq X \in 2^\Theta} \frac{\text{Pl}(A)}{\sum_{B \in X} \text{Pl}(B)} m(X). \quad (10)$$

This method uses plausibility ratio between single proposition and multiple propositions to obtain decision-making probability. The attitude of transformation is more conservative, which is not conducive to make decision.

2.3.2. *Transformation Based on the Certainty Degree.* In order to better take advantage of proportional transformation methods and overcome their deficiencies, this paper linearly combines these two approaches, which makes the attitude of transformation neither optimistic nor conservative, and draws reasonable decision-making probability.

Since single proposition's BPA reflects the precise level of system about the proposition, single proposition's BPA is larger, which indicates that the certainty degree of system about the proposition will be higher, and vice versa. Therefore, depending on the similar nature between the part and the whole, the sum of each single proposition's BPA can be regarded as the certainty degree of system and used as the weight to combine the proportional belief transformation method and proportional plausibility transformation method. When the certainty degree of system about the proposition is larger, the attitude of transformation should be relatively optimistic. On the contrary, it should be conservative.

Based on the foregoing, the transformation formula of new method is defined as follows:

$$P_{\text{new}}(A) = \beta \cdot \sum_{A \subseteq X \in 2^\Theta} \frac{m(A)}{\sum_{B \in X} m(B)} m(X) + (1 - \beta) \cdot \sum_{A \subseteq X \in 2^\Theta} \frac{\text{Pl}(A)}{\sum_{B \in X} \text{Pl}(B)} m(X), \quad (11)$$

where

$$\beta = \sum_{X \in 2^\Theta, |X|=1} m(X). \quad (12)$$

Since A is single proposition, so formula (11) can be written as follows:

$$P_{\text{new}}(A) = m(A) + \sum_{A \subseteq X \in 2^\Theta, |X|>1} \left[\beta \cdot \frac{m(A)}{\sum_{B \in X} m(B)} + (1 - \beta) \cdot \frac{\text{Pl}(A)}{\sum_{B \in X} \text{Pl}(B)} \right] m(X). \quad (13)$$

The effectiveness of new method can be illustrated by the following example.

Example 1. Suppose FOD $\Theta = \{\theta_1, \theta_2, \theta_3, \theta_4\}$; then, the BPA is given in Table 2.

The results of new method compared to the other usual methods are shown in Table 3.

TABLE 2: The BPA.

Propositions	θ_1	θ_2	θ_3	θ_4	$\theta_1 \cup \theta_2 \cup \theta_3 \cup \theta_4$
m	0.8	0	0	0	0.2

TABLE 3: The comparisons of different methods.

Methods	θ_1	θ_2	θ_3	θ_4
BetP	0.850	0.050	0.050	0.050
PFT	0.625	0.125	0.125	0.125
CuzzP	0.850	0.050	0.050	0.050
PrPl	0.925	0.025	0.025	0.025
PrBel	1.000	0.000	0.000	0.000
PrNPl	0.625	0.125	0.125	0.125
PraPl	0.925	0.025	0.025	0.025
PropBelP	1.000	0.000	0.000	0.000
PropPIP	0.925	0.025	0.025	0.025
This paper	0.985	0.005	0.005	0.005

In the methods of PFT and PrNPl, $P(\theta_1) = 0.625 < m(\theta_1) = 0.8$, which is obviously unreasonable. Because the BPA of $\theta_1 \cup \theta_2 \cup \theta_3 \cup \theta_4$ should not be assigned to θ_1 completely, the results of PrBel and PropBelP are also unreasonable. In new method, $P(\theta_1) = 0.985$ is far larger than $P(\theta_2) = P(\theta_3) = P(\theta_4) = 0.005$, which shows that new method is more reasonable and helpful to make decision than other methods.

2.4. Fusing the BPA. The navigation safety of underwater vehicles is affected by various ocean environment factors. If one factor makes underwater vehicles dangerous and others make underwater vehicles very safe, underwater vehicles should be in dangerous condition. Therefore, the BPA of each factor needs to be preprocessed before fusing to increase the weight of factor that makes underwater vehicles dangerous, which is consistent with the concept of super-standard weight. So the super-standard weight is used to deal with the BPA of each factor, and then a weighted average BPA is computed by the weight. Finally, D-S combination rule is used to obtain evaluation result through the former weighted average BPA.

The literature [35] gave a method to determine the super-standard weight according to the membership degree:

$$\omega'_i = \sum_{j=1}^N j r_{ij}, \quad (14)$$

where N is the number of evaluation grades and r_{ij} is the membership degree of i th factor on j th evaluation grade.

Definition 2. Here the BPA $m_{i,n}$ of i th factor on n th evaluation grade e_n is used to replace r_{ij} :

$$\omega''_i = \sum_{n=1}^N n m_{i,n}. \quad (15)$$

TABLE 4: Evaluation grades and quantitative intervals.

Evaluation grade	Evaluation interval (x)	Average value
VS	$0 \leq x < 20$	10
MS	$20 \leq x < 40$	30
GS	$40 \leq x < 60$	50
MD	$60 \leq x < 80$	70
VD	$80 \leq x \leq 100$	90

Definition 3. The weight ω_i of each factor can be obtained by normalizing the ω''_i :

$$\omega_i = \frac{\omega''_i}{\sum_{i=1}^k \omega''_i}, \quad (16)$$

where k is the number of factors.

Definition 4. The weighted average BPA \bar{m} is acquired by using the weighted average method to deal with the BPA of each factor.

The weight of each factor and their BPAs can be written as in matrices A and B :

$$A = [\omega_1 \ \omega_2 \ \cdots \ \omega_k]$$

$$B = \begin{bmatrix} m_1(e_1) & m_1(e_2) & \cdots & m_1(e_N) \\ m_2(e_1) & m_2(e_2) & \cdots & m_2(e_N) \\ \cdots & \cdots & \cdots & \cdots \\ m_k(e_1) & m_k(e_2) & \cdots & m_k(e_N) \end{bmatrix}. \quad (17)$$

So \bar{m} can be defined as

$$\begin{aligned} \bar{m} &= A \cdot B \\ &= [\omega_1 \ \omega_2 \ \cdots \ \omega_k] \\ &\quad \cdot \begin{bmatrix} m_1(e_1) & m_1(e_2) & \cdots & m_1(e_N) \\ m_2(e_1) & m_2(e_2) & \cdots & m_2(e_N) \\ \cdots & \cdots & \cdots & \cdots \\ m_k(e_1) & m_k(e_2) & \cdots & m_k(e_N) \end{bmatrix} \\ &= [m_1 \ m_2 \ \cdots \ m_N]. \end{aligned} \quad (18)$$

At last, the evaluation result $C = [r_1 \ r_2 \ r_3 \ r_4 \ r_5]$ can be acquired by using $k - 1$ times D-S combination rule to fuse \bar{m} .

2.5. Obtaining the Safety Situation Index. Safety situation should be a comprehensive description about each evaluation grade. Therefore, in order to make evaluation result of ocean environment safety situation more intuitive, the evaluation result needs to be disposed to obtain a rational and clear safety situation index. Here evaluation grades are quantized with different quantitative intervals, set $\{VS, MS, GS, MD, VD\} = \{0-19, 20-39, 40-59, 60-79, 80-100\}$, and take their average values: $\{10, 30, 50, 70, 90\}$. Evaluation grades and corresponding quantitative intervals are as shown in Table 4.

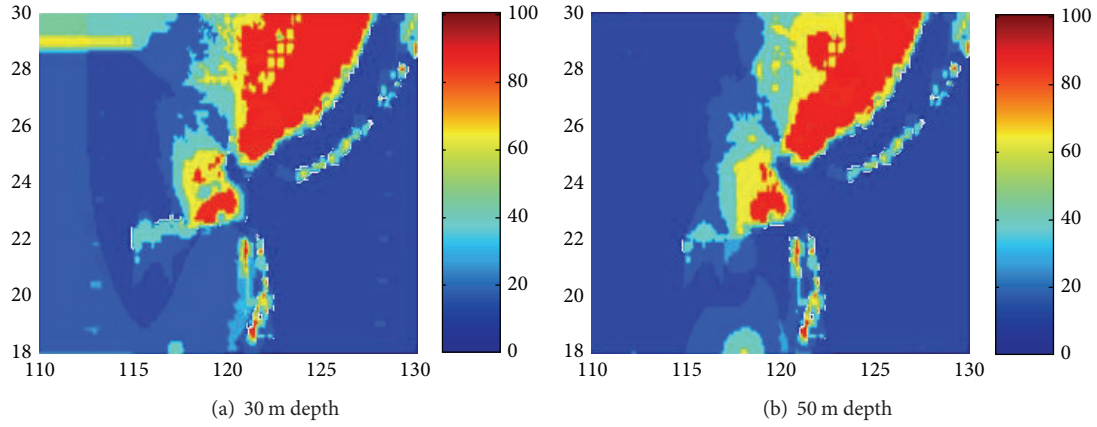


FIGURE 2: Safety situation (February).

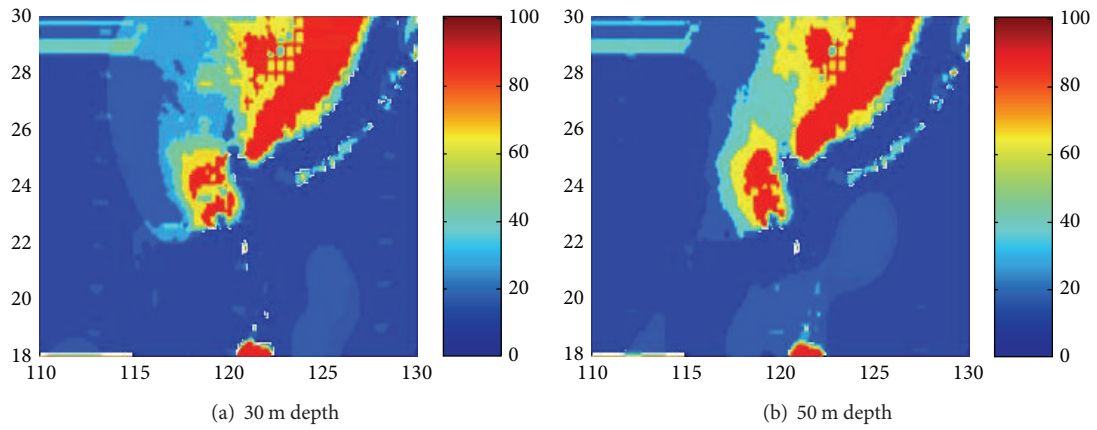


FIGURE 3: Safety situation (April).

The quantitative average values can be seen as a vector: $D = [10 \ 30 \ 50 \ 70 \ 90]^T$.

Definition 5. Safety situation index is obtained by the product between the evaluation result and the average values. If the index is higher, the evaluation grade is more dangerous.

Namely, safety situation index SSI can be defined as:

$$\begin{aligned}
 \text{SSI} &= C \cdot D \\
 &= [r_1 \ r_2 \ r_3 \ r_4 \ r_5] \cdot [10 \ 30 \ 50 \ 70 \ 90]^T.
 \end{aligned}
 \tag{19}$$

Obviously, $\text{SSI} \in [0, 100]$.

3. Results and Discussion

In this section, simulations have been carried out aiming at validating the performance of evaluation method. According to the existing data of National Marine Data and Information Service, the analyzed data of ocean current, the forecasting data of tide current, and the statistical data of pycnocline are chosen, resolution is 0.125° , depth is 30 m and 50 m, month is February, April, June, August, October, and December, longitude ranges from 110°E to 130°E , and latitude ranges

from 18°N to 30°N . Since the existing data are all too small to fully describe the safety situation, in order to better illustrate the effectiveness of the proposed method, the existing data are magnified. The results can be seen in Figures 2–7. The different colors represent the different safety situation indexes, and horizontal axis represents longitude, while vertical axis represents latitude in each figure.

From results in Figures 2–7, it is obvious that the influence of ocean environment on underwater navigation safety has regional characteristics and seasonal characteristics. Safety situation indexes of various depths are different at the same position in the same month. Safety situation index is larger in some regions, and it is smaller in other regions. With the change of seasons, safety situation index also varies. The reason is that the values of ocean environment factors are various in different seasons. That is to say, ocean environment factors have seasonal characteristics. From the BPAs of ocean environment factors, it is easy to find that tide current plays a leading role in evaluating safety situation. With the change of months, the impact is also different. As can be seen from Figures 2 and 3, most areas are very dangerous, because the values of tide current in these areas are larger in February and April. However, tide current has a little impact on safety situation in June, August, October, and December. In Figures

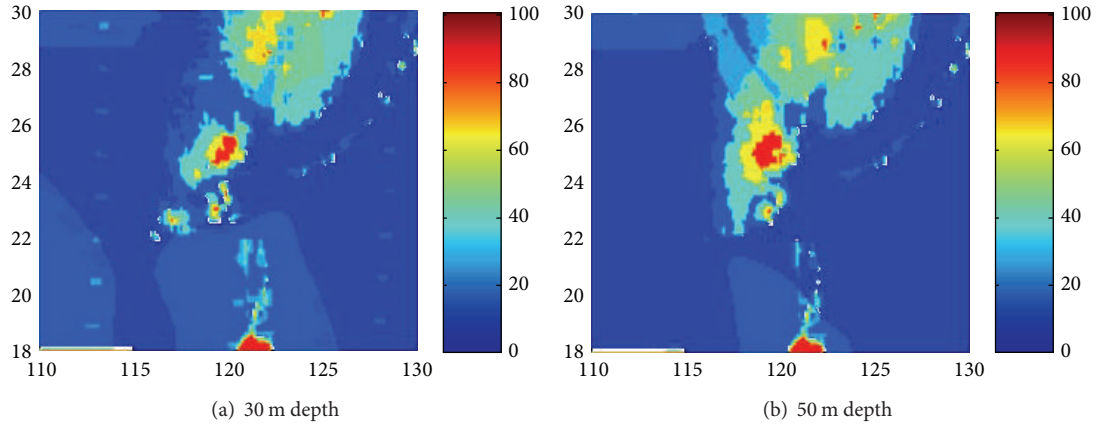


FIGURE 4: Safety situation (June).

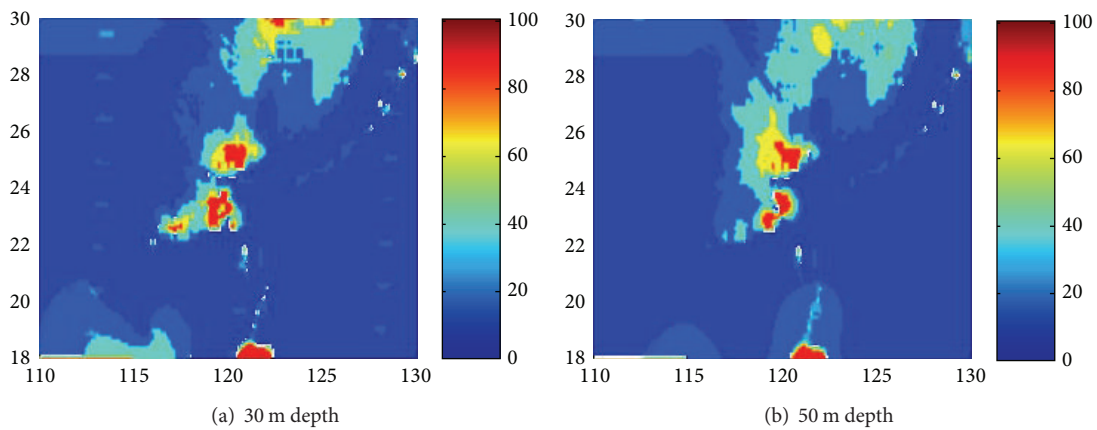


FIGURE 5: Safety situation (August).

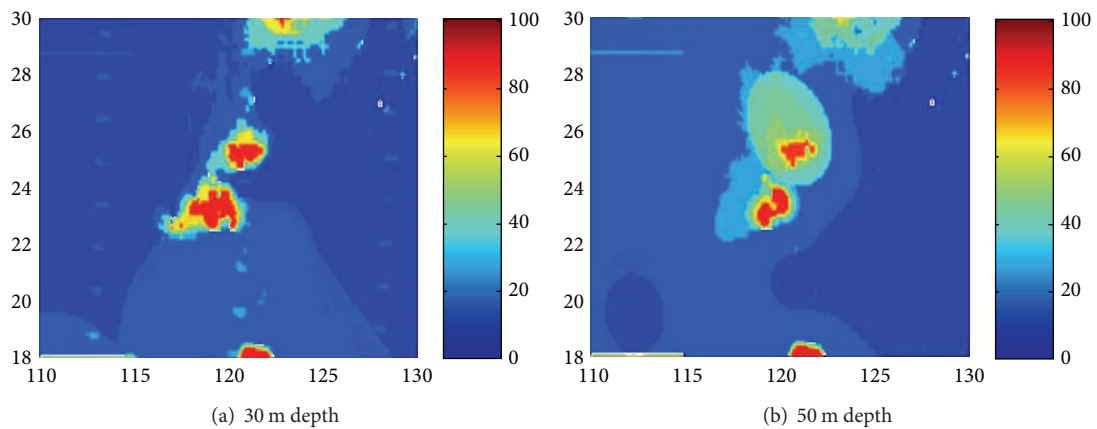


FIGURE 6: Safety situation (October).

4, 5, and 6, there are few “very dangerous” regions and “more dangerous” regions. In particular, they is almost none in Figure 7.

4. Conclusions

Ocean environment has a significant impact on underwater navigation safety. No matter how an underwater vehicle

is carrying out the task or sailing, the influence of ocean environment on navigation safety needs to be closely grasped. Due to distinguished performance of D-S evidence theory on handling uncertainty information, it is quite befitting for evaluating underwater ocean environment safety situation. This theory is used to deal with ocean environment information to acquire evaluation result of underwater ocean environment safety situation in this paper. The simulation results

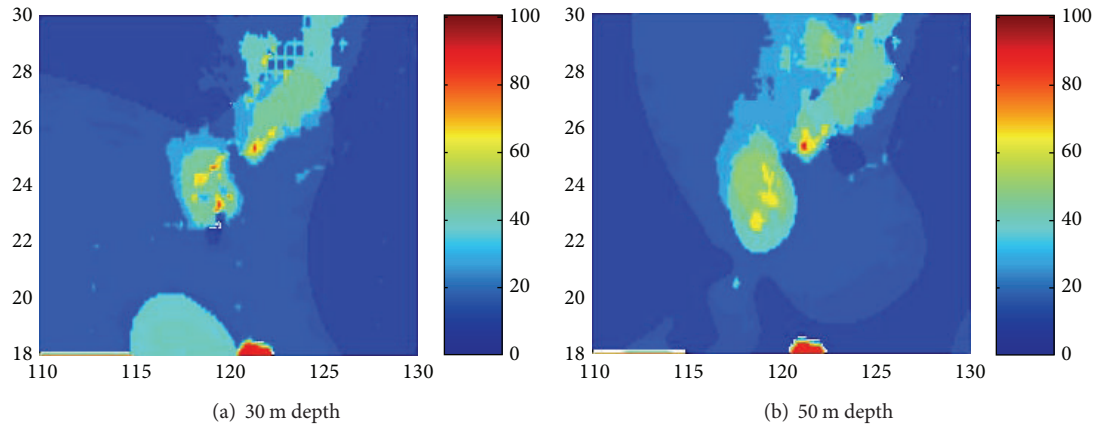


FIGURE 7: Safety situation (December).

validate that the method proposed is of great theoretical value and practical significance.

Conflict of Interests

The authors declare that there is no conflict of interests regarding the publication of this paper.

Acknowledgments

This paper is supported by the National Natural Science Foundation of China (Projects nos. 51379049 and 51109045), the Fundamental Research Funds for the Central Universities (Projects nos. HEUCFX41302 and HEUCF041410), the Scientific Research Foundation for the Returned Overseas Chinese Scholars (Heilongjiang Province, no. LC2013C21), and the Young College Academic Backbone of Heilongjiang Province (no. 1254G018).

References

- [1] Y. R. Xu and K. Xiao, "Technology development of autonomous ocean vehicle," *Acta Automatica Sinica*, vol. 33, no. 5, pp. 518–521, 2007.
- [2] Y. Gao, B. Yin, Z. Q. Wei, F. X. Gong, and X. P. Ji, "On-line real-time path planning for underwater vehicle in dynamic uncertain environment," *Periodical of Ocean University of China*, vol. 43, no. 12, pp. 106–110, 2013.
- [3] D. Q. Zhu, W. C. Li, and M. Z. Yan, "Map building for underwater vehicle based on D-S information fusion algorithm," *System Simulation Technology*, vol. 8, no. 3, pp. 181–186, 2012.
- [4] X. Li and D. Q. Zhu, "Path planning for autonomous underwater vehicle based on artificial potential field method," *Journal of Shanghai Maritime University*, vol. 31, no. 2, pp. 35–39, 2010.
- [5] N. K. Yilmaz, C. Evangelinos, P. F. J. Lermusiaux, and N. M. Patrikalakis, "Path planning of autonomous underwater vehicles for adaptive sampling using mixed integer linear programming," *IEEE Journal of Oceanic Engineering*, vol. 33, no. 4, pp. 522–537, 2008.
- [6] I. Tena Ruiz, S. de Raucourt, Y. Petillot, and D. M. Lane, "Concurrent mapping and localization using sidescan sonar," *IEEE Journal of Oceanic Engineering*, vol. 29, no. 2, pp. 442–456, 2004.
- [7] A. Alvarez, A. Caiti, and R. Onken, "Evolutionary path planning for autonomous underwater vehicles in a variable ocean," *IEEE Journal of Oceanic Engineering*, vol. 29, no. 2, pp. 418–429, 2004.
- [8] A. P. Dempster, "Upper and lower probabilities induced by a multi-valued mapping," *The Annals of Mathematical Statistics*, vol. 38, pp. 325–339, 1967.
- [9] G. Shafer, *A Mathematical Theory of Evidence*, Princeton University Press, Princeton, NJ, USA, 1976.
- [10] Y. Leung, N.-N. Ji, and J.-H. Ma, "An integrated information fusion approach based on the theory of evidence and group decision-making," *Information Fusion*, vol. 14, no. 4, pp. 410–422, 2013.
- [11] H. Luo, S. L. Yang, X. J. Hu, and X. X. Hu, "Agent oriented intelligent fault diagnosis system using evidence theory," *Expert Systems with Applications*, vol. 39, no. 3, pp. 2524–2531, 2012.
- [12] B. Li and F.-W. Pang, "An approach of vessel collision risk assessment based on the D-S evidence theory," *Ocean Engineering*, vol. 74, pp. 16–21, 2013.
- [13] J. P. Yang, H.-Z. Huang, L.-P. He, S.-P. Zhu, and D. W. Wen, "Risk evaluation in failure mode and effects analysis of aircraft turbine rotor blades using Dempster-Shafer evidence theory under uncertainty," *Engineering Failure Analysis*, vol. 18, no. 8, pp. 2084–2092, 2011.
- [14] R. P. Srivastava, T. J. Mock, and L. Gao, "The Dempster-Shafer theory: an introduction and Fraud risk assessment illustration," *Australian Accounting Review*, vol. 21, no. 3, pp. 282–291, 2011.
- [15] B. Y. Kang, Y. Li, Y. Deng, Y. J. Zhang, and X. Y. Deng, "Determination of basic probability assignment based on interval numbers and its application," *Acta Electronica Sinica*, vol. 40, no. 6, pp. 1092–1096, 2012.
- [16] J. Y. Xiao, M. M. Tong, C. J. Zhu, and X. L. Wang, "Basic probability assignment construction method based on generalized triangular fuzzy number," *Chinese Journal of Scientific Instrument*, vol. 33, no. 2, pp. 429–434, 2012.
- [17] T. Denœux and M.-H. Masson, "EVCLUS: evidential clustering of proximity data," *IEEE Transactions on Systems, Man, and Cybernetics Part B: Cybernetics*, vol. 34, no. 1, pp. 95–109, 2004.
- [18] X. Guan, Y. He, and X. Yi, "Attribute measure recognition approach and its applications to emitter recognition," *Science in China, Series F: Information Sciences*, vol. 48, no. 2, pp. 225–233, 2005.
- [19] W. Jiang, A. Zhang, and Q. Yang, "Fuzzy approach to construct basic probability assignment and its application in multi-sensor

- data fusion systems,” *Chinese Journal of Sensors and Actuators*, vol. 21, no. 10, pp. 1717–1720, 2008.
- [20] Y. Deng, W. Jiang, X. B. Xu, Q. Li, and D. Wang, “Determining BPA under uncertainty environments and its application in data fusion,” *Journal of Electronics*, vol. 26, no. 1, pp. 13–17, 2009.
- [21] F. Han, W. H. Yang, and X. G. Yuan, “Evidence theory information fusion method based on fuzzy set,” *Control and Decision*, vol. 25, no. 3, pp. 449–452, 2010.
- [22] N. Li, C.-W. Qu, D.-F. Ping, and F. Su, “Emitter identification based on distributed sensors information fusion,” *Control and Decision*, vol. 25, no. 12, pp. 1793–1798, 2010.
- [23] W. Jiang and S. Wu, “Multi-data fusion fault diagnosis method based on SVM and evidence theory,” *Chinese Journal of Scientific Instrument*, vol. 31, no. 8, pp. 1738–1743, 2010.
- [24] P. Smets and R. Kennes, “The transferable belief model,” *Artificial Intelligence*, vol. 66, no. 2, pp. 191–234, 1994.
- [25] B. R. Cobb and P. P. Shenoy, “On the plausibility transformation method for translating belief function models to probability models,” *International Journal of Approximate Reasoning*, vol. 41, no. 3, pp. 314–330, 2006.
- [26] P.-D. Xu, D.-Q. Han, and Y. Deng, “An optimal transformation of basic probability assignment to probability,” *Acta Electronica Sinica*, vol. 39, no. 3A, pp. 121–125, 2011.
- [27] L. Hu, Y. He, X. Guan, Y. Deng, and D. Han, “A new probabilistic transformation in generalized power space,” *Chinese Journal of Aeronautics*, vol. 24, no. 4, pp. 449–460, 2011.
- [28] W.-Q. Wang, Y.-J. Zhao, J. Huang, and T. Lai, “Transformation of basic probability assignment to probability based on uncertainty degree,” *Control and Decision*, vol. 28, no. 8, pp. 1214–1218, 2013.
- [29] J. J. Sudano, “Pignistic probability transforms for mixes of low- and high probability events,” in *Proceedings of the 4th International Conference on Information Fusion*, pp. 23–27, Montreal, Canada, 2001.
- [30] W. Jiang, C. C. Wu, J. Jia, and Z. J. Li, “A probabilistic transformation of basic probability assignment (BPA) in D-S evidence theory,” *Journal of Northwestern Polytechnical University*, vol. 31, no. 2, pp. 295–299, 2013.
- [31] L. F. Hu, Y. He, X. Guan, D. Q. Han, and Y. Deng, “New probabilistic transformation of imprecise belief structure,” *Journal of Systems Engineering and Electronics*, vol. 22, no. 5, pp. 721–729, 2011.
- [32] J. J. Sudano, “Yet another paradigm illustrating evidence fusion (YAPIEF),” in *Proceedings of the 9th International Conference on Information Fusion (FUSION '06)*, July 2006.
- [33] J. Dezert and F. Smarandache, “A new probabilistic transformation of belief mass assignment,” in *Proceedings of the 11th International Conference on Information Fusion*, pp. 1–8, Cologne, Germany, July 2008.
- [34] M. Daniel, “Consistency of probabilistic transformations of belief functions,” in *Proceedings of the 10th International Conference on Information Processing and Management of Uncertainty in Knowledge-Based Systems (IPMU '04)*, pp. 1135–1142, Perugia, Italy, 2004.
- [35] J. H. Shen, X. Y. Fu, and Y. X. Zhao, “Improvement of the fuzzy comprehensive evaluation model,” *Fuzzy Systems and Mathematics*, vol. 25, no. 3, pp. 127–132, 2011.

Research Article

A Study of Coupling Parameter Estimation Implemented by 4D-Var and EnKF with a Simple Coupled System

Guijun Han,¹ Xinrong Wu,¹ Shaoqing Zhang,² Zhengyu Liu,^{3,4}
Ionel Michael Navon,⁵ and Wei Li¹

¹Key Laboratory of Marine Environmental Information Technology, State Oceanic Administration, National Marine Data and Information Service, Tianjin 300171, China

²Geophysical Fluid Dynamics Laboratory, National Oceanic and Atmospheric Administration, Princeton University, Princeton, NJ 08542, USA

³Center for Climate Research and Department of Atmospheric and Oceanic Sciences, University of Wisconsin-Madison, Madison, WI 53706, USA

⁴Laboratory of Ocean-Atmosphere Studies, Peking University, Beijing 100871, China

⁵Department of Scientific Computing, Florida State University, Tallahassee, FL 32306, USA

Correspondence should be addressed to Xinrong Wu; xinrong-wu@yahoo.com

Received 24 October 2014; Revised 5 January 2015; Accepted 5 January 2015

Academic Editor: Hiroyuki Hashiguchi

Copyright © 2015 Guijun Han et al. This is an open access article distributed under the Creative Commons Attribution License, which permits unrestricted use, distribution, and reproduction in any medium, provided the original work is properly cited.

Coupling parameter estimation (CPE) that uses observations to estimate the parameters in a coupled model through error covariance between variables residing in different media may increase the consistency of estimated parameters in an air-sea coupled system. However, it is very challenging to accurately evaluate the error covariance between such variables due to the different characteristic time scales at which flows vary in different media. With a simple Lorenz-atmosphere and slab ocean coupled system that characterizes the interaction of two-timescale media in a coupled “climate” system, this study explores feasibility of the CPE with four-dimensional variational analysis and ensemble Kalman filter within a perfect observing system simulation experiment framework. It is found that both algorithms can improve the representation of air-sea coupling processes through CPE compared to state estimation only. These simple model studies provide some insights when parameter estimation is implemented with a coupled general circulation model for improving climate estimation and prediction initialization.

1. Introduction

Due to its potential to reduce initial shocks between different media in a coupled climate system, coupled data assimilation (CDA) that uses coupled model dynamics to extract observational information in one or more media is emerging as an important topic in the climate community ([1–6] the related discussion at the Sixth World Meteorological Organization Data Assimilation Symposium (<http://das6.cscamm.umd.edu/>)). Based on Bayes’ rule, two main data assimilation algorithms, four-dimensional variational analysis (4D-Var) [7–9], and ensemble Kalman filter (EnKF) [10] have been used to develop CDA systems [3, 4]. Many efforts have been made to compare the performances of 4D-Var and EnKF either under CDA or not [11–16]. It has been found that 4D-Var and EnKF

have a comparable performance when the former uses an appropriate minimization time window (MTW) and the latter adopts a suitable variance inflation scheme [17]. While 4D-Var requires a shorter spin-up time in the weather timescale (like days), EnKF can produce a better forecast skill at a long lead time [18–20] in the season timescale (like months).

To reduce model errors and improve coupled model predictability, coupled model parameter estimation (also referred to as parameter optimization in the literature) has been introduced into CDA [21–27]. However, coupling parameter estimation (CPE) that uses observations in one medium to estimate the model parameters in other media has not yet been studied in 4D-Var and EnKF. In a climate system that has multiple characteristic time scales, model parameters have remarkable impacts on all model variables. Thus, it

is expected that CPE may further enhance the consistency of estimated parameters and model states in a coupled system. Although data assimilation in a multiple space and time scale system has been explored [2, 28], the CPE in such a system has not been fully investigated. Both 4D-Var and EnKF can be used to implement CPE. It is well known that although they originated from the same information estimation theory (Bayes' rule), different numerical implementations make different performances of 4D-Var and EnKF data assimilation [17]. On one hand, by minimizing a cost function that measures the distance between observations and model states within a specific MTW, 4D-Var CPE seeks a posterior maximum likelihood solution of model parameters in different media in terms of the best fitting of modeling trajectory to observations. On the other hand, EnKF CPE uses flow-dependent coupling error covariance (i.e., error covariance between a model variable in the observational medium and a parameter in another medium) to project observational information onto the parameter being estimated, thereby implementing CPE in a sequential manner.

Since evaluating the error covariance of variables residing in different media with a finite ensemble is difficult [6] and a specific MTW is difficult to capture multiple time scales in minimization, CPE is therefore challenging in both EnKF and 4D-Var. A fundamental issue is can 4D-Var or EnKF CPE improve representation of the model air-sea coupling process? Based on a conceptual coupled model [25] which couples a chaotic atmosphere [29] with a slab ocean, we set up an observing system simulation experiment (OSSE) [30] which takes a Nature Run as the truth of model states to answer this question. Within this framework, in both 4D-Var CPE and EnKF CPE, "observations" drawn from a "truth" model that uses the default parameter values are assimilated into the assimilation model which uses erroneously set parameter values for optimizing the coupling parameters.

The paper is organized as follows. Section 2 describes the methodology, starting from introducing the simple coupled model, followed by the OSSE setup as well as implementation of the 4D-Var CPE and EnKF CPE. This section also presents the scale analysis of perturbed terms in the model equations and the sensitivity study of model parameters. Sections 3 and 4 examine the results of 4D-Var CPE and EnKF CPE, respectively. Different performances of EnKF CPE and 4D-Var CPE are investigated in Section 5. Summary and discussions are given in Section 6.

2. Methodology

2.1. The Simple Coupled Model. To study coupling parameter estimation (CPE) implemented by 4D-Var and EnKF so as to answer the question (i.e., can 4D-Var or EnKF CPE improve representation of the model air-sea coupling process?) posed in Section 1, we employ a simple "climate" model [25] which consists of a chaotic atmosphere model [29] coupled to a slab ocean model to simulate the interaction of the fast atmosphere and slow ocean:

$$\begin{aligned}\dot{x}_1 &= -\sigma x_1 + \sigma x_2, \\ \dot{x}_2 &= -x_1 x_3 + (1 + c_1 w) \kappa x_1 - x_2,\end{aligned}$$

$$\dot{x}_3 = x_1 x_2 - b x_3,$$

$$O_m \dot{w} = c_2 x_2 - O_d w + S_m + S_s \cos\left(\frac{2\pi t}{S_{pd}}\right), \quad (1)$$

where an overdot denotes time tendency; x_1 , x_2 , and x_3 (hereafter denoted by $x_{1,2,3}$ if they are presented together) are the high-frequency variables of the atmosphere and w represents the slab ocean. (O_m , O_d) define the oceanic time scale, where O_m is the ratio of heat capacity between the slab ocean and the chaotic atmosphere while O_d is the damping coefficient of the temperature w ($^{\circ}\text{C}$) of the slab ocean. O_m is a dimensionless parameter. The unit of O_d is $1/\Delta t$, where Δt represents the dimensionless time step. The "atmosphere" and the "ocean" interact with each other through the coupling coefficients c_1 and c_2 . Here, the unit of c_1 is $(^{\circ}\text{C})^{-1}$ while c_2 is a dimensionless parameter. The external solar forcing is represented by $S_m + S_s \cos(2\pi t/S_{pd})$, where S_m represents the annual mean temperature ($^{\circ}\text{C}$) of the slab ocean and S_s (in $^{\circ}\text{C}$) and S_{pd} (in Δt) represent the amplitude and period of the model seasonal cycle.

While the detailed description of the model construction can be found in [25], here, we only comment on the setting of model parameter values. The "atmospheric" parameters σ , κ , and b take their standard values of 9.95, 29, and 8/3. For maintaining the chaotic nature of the "atmosphere" and the stability of the system, the values of c_1 and c_2 are chosen as $0.1 (^{\circ}\text{C})^{-1}$ and 1. O_m and O_d are set to 10 and 1, which defines the oceanic time scale as 10 times of the atmospheric time scale. The parameters S_m and S_s are set as 10°C and 1°C , respectively. The S_{pd} is chosen as 10 Time Units (TU, 1 TU = 100 time steps = $100\Delta t$) so that the period of the forcing is comparable with the oceanic time scale, defining the time scale of the model seasonal cycle. Given the value of S_{pd} , the model calendar year is defined as 10 TUs. If we assume that one year has 360 model days, Δt is equivalent to 0.36 model days.

Using a leap-frog time stepping scheme with a Robert-Asselin time filter [31, 32] and starting from the initial conditions $(x_1, x_2, x_3, w) = (0, 1, 0, 0)$ (note that since the leap-frog time stepping scheme is applied, initial conditions at both time 0 and time 1 are set to $(0, 1, 0, 0)$), the model is first freely run for 10^4 TUs by setting the parameters (σ , κ , b , c_1 , c_2 , O_m , O_d , S_m , S_s , S_{pd} , and γ), where γ is the time filtering coefficient, to be the default values as prescribed in Table 1.

2.2. OSSE Setup. OSSE that takes a Nature Run as the "truth" is an effective way to preliminarily study the validity of data assimilation algorithm and/or assess the observing system impact [30]. In this study, we setup an OSSE to study the EnKF CPE and the 4D-Var CPE. For simplicity, we assume that the model error only comes from the errors of the parameters to be estimated (see Table 1). The coupled model with the default parameter values produces the true solution for the parameter estimation problem. The "observations" are the samples of the "truth" model states after the spin-up of 10^4 TUs. A random Gaussian noise is superimposed on the "truth" values every 5 time steps for $x_{1,2,3}$ and every 20

TABLE 1: Default values and values used in OSSE of the model parameters.

Parameter	Default value	Value used in OSSE	Unit
σ	9.95	9.95	—
κ	29	29	—
b	8/3	8/3	—
c_1	0.1	0.11	(°C) ⁻¹
c_2	1	1.1	—
O_m	10	10	—
O_d	1	1	1/ Δt
S_m	10	10	°C
S_s	1	1	°C
S_{pd}	10	10	Δt
γ	0.25	0.25	—

time steps for w , respectively, to produce the corresponding observations. Note that, to simulate the real world sampling frequency, the atmospheric observations are taken more frequently (4 times) than the oceanic observations. The standard deviations of observational errors are 2 for $x_{1,2,3}$ and 0.2 for w , respectively.

The parameters to be estimated are c_1 and c_2 that are the coupling parameters between the ocean and the atmosphere. Through examining the estimation of c_1 and c_2 , we can directly study the impact of coupling parameter estimation on the representation of coupling processes. First guess of the parameters c_1 and c_2 is 0.11 (the “truth” is 0.1) and 1.1 (the “truth” is 1.0), respectively. From the initial condition $(x_1, x_2, x_3, w) = (0, 1, 0, 0)$, the assimilation model with the first guess of c_1 and c_2 is spun up for 10^4 TUs to produce the assimilation initial conditions of $x_{1,2,3}$ and w (denote as Π). Continuous integrations from these initial values of the assimilation model serve as a control run without any observational constraint. Therefore, this is a free model run, that is, without data assimilation.

To study the 4D-Var CPE and EnKF CPE, we design four experiments for each algorithm: (1) EXP-1: the atmospheric and oceanic observations are used to estimate the states of the atmosphere and the ocean while keeping c_1 and c_2 constant; (2) EXP-2: the atmospheric and oceanic observations are used to estimate the states of the atmosphere and the ocean as well as c_2 while keeping c_1 constant; (3) EXP-3: the atmospheric and oceanic observations are used to estimate the states of the atmosphere and the ocean as well as c_1 while keeping c_2 constant; (4) EXP-4: the atmospheric and oceanic observations are used to estimate the states of the atmosphere and the ocean, c_1 and c_2 . Table 2 gives the details of assimilation schemes of these four experiments. The data assimilation period is set to be 100 TUs. Parameter estimation is activated after 10 TUs of state estimation which reaches quasi-equilibrium so that the state-parameter covariance used for parameter estimation is signal-dominated [25]. In addition, the leap-frog time stepping requires two time-level adjustments [33] (i.e., observations at time t are used to adjust the model states at time t and time $t - 1$). And also, to investigate the sensitivity of the 4D-Var CPE and the EnKF CPE with

TABLE 2: The instantaneous state and parameter estimations in four data assimilation experiments.

Experiment	Observations	Adjusted variables and parameters
EXP-1	$x_{1,2,3}^o, w^o$	$x_{1,2,3}, w$
EXP-2	$x_{1,2,3}^o, w^o$	$x_{1,2,3}, w, c_2$
EXP-3	$x_{1,2,3}^o, w^o$	$x_{1,2,3}, w, c_1$
EXP-4	$x_{1,2,3}^o, w^o$	$x_{1,2,3}, w, c_1, c_2$

respect to the observational interval, four pairs of (atmosphere and ocean) observational intervals: (0.05, 0.2), (0.1, 0.4), (0.2, 0.8), and (0.5, 2.0) TUs are examined. Finally, the results of the last 50 TUs are used for CPE evaluation. Note that, given the low-order model and the scalar nature of parameters, the absolute error of the estimated parameter or the air-sea coupling processes which refer to the truth is the main criterion of the CPE evaluation.

We see from time series of x_2 (Figure 1(a)) and w (Figure 1(b)) in the truth, model control, and “observations” that the erroneous parameters can lead the model states of the free run to depart far away from the truth and observations. According to the governing equation (Equation (1)) of the simple coupled model, the Lorenz-atmosphere is forced by the term $c_1 w$ from the slab ocean while the slab ocean couples with the atmosphere via the term $c_2 x_2$. Thus, we examine the $c_1 w$ and $c_2 x_2$ errors to study the representation of the air-sea coupling processes in this study.

2.3. Scale Analysis of the Perturbed Terms in the Model Equations. Within the OSSE framework, here, we make a scale analysis of the size of the perturbed terms in the model equations. Since the model error is assumed to arise from the uncertainties of c_2 and c_1 , in the ocean, the impact of an erroneous parameter c_2 and an erroneous atmosphere x_2 is contained in the term $c_2 x_2$. The error is $\delta(c_2 x_2) = x_2 \delta(c_2) + c_2 \delta(x_2)$. The characteristic scales of $\delta(c_2)$ and $\delta(x_2)$ are 0.1 and 10, respectively. Thus, given the default value (i.e., 1.0) of c_2 and the characteristic scale (i.e., 10) of x_2 , the scale [i.e., the term $x_2 \delta(c_2)$ which is about 1.0] of correction of the oceanic parameter c_2 would be one order smaller than the scale [i.e., the term $c_2 \delta(x_2)$ which is about 10] of correction of the atmospheric state x_2 .

Similarly, in the atmosphere, the impact of an erroneous parameter c_1 and an erroneous ocean w is contained in the term $c_1 w$. The error is $\delta(c_1 w) = w \delta(c_1) + c_1 \delta(w)$. The characteristic scales of $\delta(c_1)$ and $\delta(w)$ are 0.01 and 1.0, respectively. Thus, given the default value (i.e., 0.1) of c_1 and the characteristic scale (i.e., 10) of w , the scale [i.e., the term $w \delta(c_1)$ which is about 0.1] of correction of the atmospheric parameter c_1 would be the same as the scale [i.e., the term $c_1 \delta(w)$ which is about 0.1] of correction of the oceanic state w .

To summarize, the error of the oceanic state is one order smaller than the error of the atmospheric state. Thus, estimating the oceanic parameter c_2 will be more difficult than estimating the atmospheric parameter c_1 .

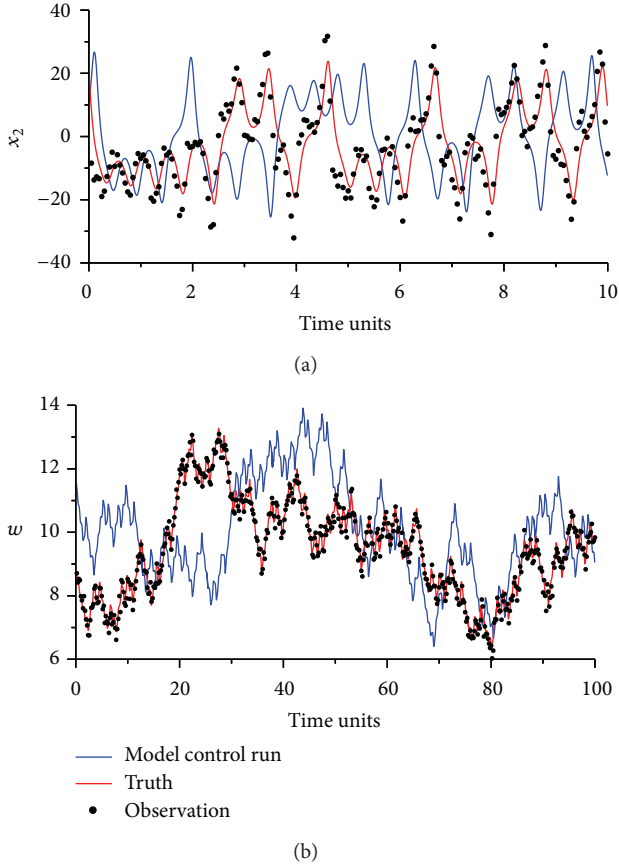


FIGURE 1: Time series of (a) x_2 for the first 10 TUs and (b) w for 100 TUs of the assimilation period derived from the truth (red), model control run (blue), and observations (black solid circle), respectively.

2.4. Model Sensitivities with respect to Parameters. We perform a sensitivity study for seven empirical parameters (σ , κ , b , O_m , O_d , c_1 , and c_2) using the same strategy as [26]. Each examined parameter is perturbed through adding a Gaussian noise to its default value (a percentage of the default value as the standard deviation of the noise) while other parameters remain unperturbed. With an ensemble size of 20, the model is freely run for 20 TUs. It is found that, as long as the perturbed parameter values can maintain the stochastic nature of the “atmosphere,” the examined ensemble spread does not have much dependence on the perturbation amplitude (i.e., the standard deviation of the above Gaussian noise) but the spin-up time is a little longer for a small perturbation. For a 5% perturbation (i.e., the standard deviation of the Gaussian noise is 5% of the default value), Figure 2 shows the time series of the ensemble spreads of x_2 (Figure 2(a)) and w (Figure 2(b)), where the black, blue, red, green, yellow, dashed-black, and pink curves, respectively, represent the results of b , c_1 , c_2 , κ , O_d , O_m , and σ . Here, the ensemble spreads of x_2 and w have been normalized by their own climatological standard deviations (14.5 for x_2 and 1.5 for w). We can see that different variables have different response times (defined as the spin-up period of ensemble spread) with regard to various parameters. For the four atmospheric parameters, the response times of x_2 and w are about 3 TUs and 6 TUs,

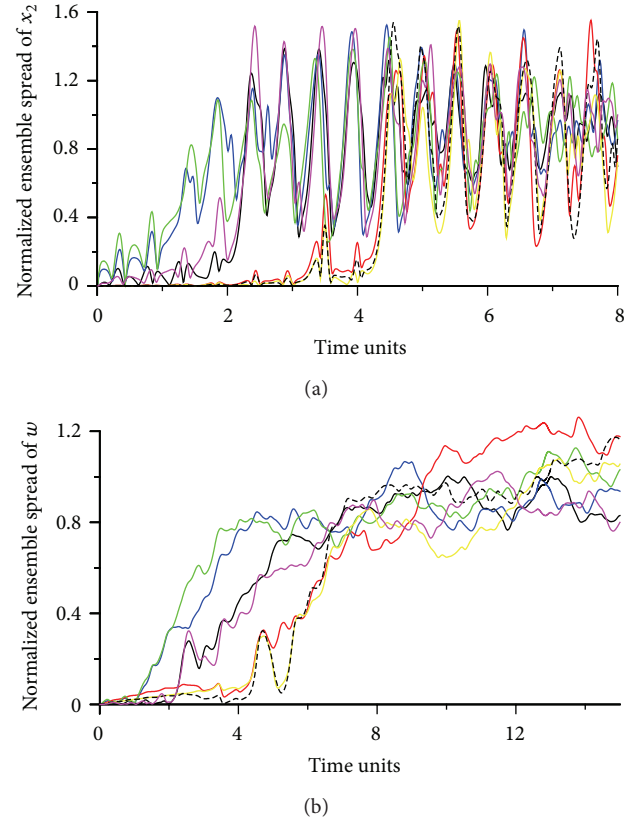


FIGURE 2: Time series of sensitivities of (a) x_2 and (b) w with respect to σ (pink), κ (green), b (black), O_m (dashed-black), O_d (yellow), c_1 (blue), and c_2 (red). Note that here the sensitivities of x_2 and w are computed as the ensemble spreads normalized by their climatological standard deviations (i.e., 14.5 and 1.5). Parameters σ , κ , b , O_m , and c_2 are dimensionless while the units of O_d and c_1 are $1/\Delta t$ and $(^\circ\text{C})^{-1}$, where Δt is the dimensionless time step.

respectively. For the three oceanic parameters, the response times of x_2 and w are about 5 TUs and 10 TUs, respectively. Therefore, if 4D-Var is used to perform CPE of the oceanic parameters, the typical lengths of MTWs for x_2 and w could, respectively, be 5 TUs and 10 TUs. For example, for x_2 , an MTW less than 5 TUs is regarded as a short window while an MTW greater than 5 TUs is regarded as a long window.

From Figure 2, we can see that, among four atmospheric parameters (σ , κ , b and c_1), both x_2 and w have the largest sensitivities with respect to κ (green) and c_1 (blue) during the spin-up period. Similarly, for the three oceanic parameters (O_d , O_m , and c_2), x_2 and w are most sensitive to the coupling parameter c_2 (red). Combining the question presented in Section 1, two coupling parameters c_1 and c_2 are chosen as the parameters to be estimated in the following CPE experiments.

2.5. Implementation of 4D-Var CPE. Consistent with Table 2, the formulas of the cost functions for four experiments are

$$\begin{aligned}
 J_{\text{EXP-1}}(\mathbf{X}) &= \frac{1}{2} [\mathbf{X}(t_0) - \mathbf{X}_b]^T \mathbf{B}^{-1} [\mathbf{X}(t_0) - \mathbf{X}_b] \\
 &+ \frac{1}{2} \sum_{i=1}^N \{ \mathbf{H}[\mathbf{X}(t_i)] - \mathbf{Y}^o(t_i) \}^T \mathbf{R}^{-1} \{ \mathbf{H}[\mathbf{X}(t_i)] - \mathbf{Y}^o(t_i) \},
 \end{aligned} \tag{2}$$

$$\begin{aligned}
J_{\text{EXP-2}}(\mathbf{X}, c_2) &= \frac{1}{2} [\mathbf{X}(t_0) - \mathbf{X}_b]^T \mathbf{B}^{-1} [\mathbf{X}(t_0) - \mathbf{X}_b] \\
&+ \frac{1}{2V_{c_2}} (c_2 - c_2^b)^2 \\
&+ \frac{1}{2} \sum_{i=1}^N \{\mathbf{H}[\mathbf{X}(t_i)] - \mathbf{Y}^o(t_i)\}^T \\
&\quad \cdot \mathbf{R}^{-1} \{\mathbf{H}[\mathbf{X}(t_i)] - \mathbf{Y}^o(t_i)\},
\end{aligned} \tag{3}$$

$$\begin{aligned}
J_{\text{EXP-3}}(\mathbf{X}, c_1) &= \frac{1}{2} [\mathbf{X}(t_0) - \mathbf{X}_b]^T \mathbf{B}^{-1} [\mathbf{X}(t_0) - \mathbf{X}_b] \\
&+ \frac{1}{2V_{c_1}} (c_1 - c_1^b)^2 \\
&+ \frac{1}{2} \sum_{i=1}^N \{\mathbf{H}[\mathbf{X}(t_i)] - \mathbf{Y}^o(t_i)\}^T \\
&\quad \cdot \mathbf{R}^{-1} \{\mathbf{H}[\mathbf{X}(t_i)] - \mathbf{Y}^o(t_i)\},
\end{aligned} \tag{4}$$

$$\begin{aligned}
J_{\text{EXP-4}}(\mathbf{X}, c_1, c_2) &= \frac{1}{2V_{c_1}} (c_1 - c_1^b)^2 + \frac{1}{2V_{c_2}} (c_2 - c_2^b)^2 \\
&+ \frac{1}{2} [\mathbf{X}(t_0) - \mathbf{X}_b]^T \mathbf{B}^{-1} [\mathbf{X}(t_0) - \mathbf{X}_b] \\
&+ \frac{1}{2} \sum_{i=1}^N \{\mathbf{H}[\mathbf{X}(t_i)] - \mathbf{Y}^o(t_i)\}^T \\
&\quad \cdot \mathbf{R}^{-1} \{\mathbf{H}[\mathbf{X}(t_i)] - \mathbf{Y}^o(t_i)\},
\end{aligned} \tag{5}$$

where $\mathbf{X} = (x_1^0, x_2^0, x_3^0, w^0, x_1^1, x_2^1, x_3^1, w^1)^T$ represents the initial $x_{1,2,3}$ and w at two time levels whose background values are denoted as \mathbf{X}_b . The superscript “ T ” denotes the transpose. The background error covariance matrix is simply set as the observational error covariance matrix $\mathbf{R} = \text{diag}\{4.0, 4.0, 4.0, 0.04, 4.0, 4.0, 4.0, 0.04\}$. t_0 is the initial time within an MTW. N represents the number of observations within the MTW. \mathbf{H} is the linearized observation operator which is $\text{diag}\{1, 1, 1, 1, 0, 0, 0, 0\}$ in this study. $\mathbf{Y}^o = (x_1^o, x_2^o, x_3^o, w^o)^T$ is the observation vector in which $x_{1,2,3}^o$ and w^o , respectively, represent the observations of $x_{1,2,3}$ and w . c_1^b and c_2^b indicate the background values of c_1 and c_2 , respectively. The background error variances of c_1 and c_2 , that is, V_{c_1} and V_{c_2} , are set to 0.0055^2 and 0.055^2 .

The gradient of the cost function with respect to the parameter can be obtained using the adjoint method [34]. Due to the nonlinearity of the Lorenz-63 model, many local minima of the cost function exist in the space of parameter values when the MTW is relatively long, which may cause the standard quasi-Newton method (e.g., L-BGFS) [35] fail to find the optimal solution. In this study, we employ a limited

memory bundle method (LMBM) [16, 36, 37] to implement the minimization of 4D-Var. Different from other methods [17, 38] for solving the multiple minima issue, LMBM is a hybrid of the variable metric bundle methods [39] and the limited memory variable metric methods [40]. This method is a solver of large-scale nonsmooth global optimization which neither needs to solve the time-consuming direction-finding issue in the standard bundle method nor needs to increase the number of stored subgradients when the dimension of the problem grows. The necessary input for LMBM algorithm includes the number of control variables, the maximum bundle dimension, the upper limit for maximum number of stored corrections, the maximum number of stored corrections, the first guess of control variables, the cost function value, the tolerance for the first or second termination criterion, and the maximum number of iterations [41]. Trial and error tests suggest that the last two inputs should be set to 10^{-5} and 200.

In addition to the observational interval, the sensitivity of the 4D-Var CPE with respect to the length of MTW is also studied. We examined five MTWs: 0.5, 1.0, 2.0, 5.0, and 10 TUs. For all four data assimilation experiments, 4D-Var optimizes the initial fields when observations are available; that is, the analysis interval is the same as the observational interval. The absolute error of the optimized initial field relative to the truth is used to assess the quality of the 4D-Var CPE.

2.6. Implementation of EnKF CPE. In this study, a derivative of deterministic EnKF which does not need to perturb observations, the ensemble adjustment Kalman filter (EAKF) [11], is employed to implement the EnKF CPE.

For an EnKF algorithm, the analysis solution includes the following two parts. One is the updated ensemble mean formulated as

$$\bar{\mathbf{X}}^a = \bar{\mathbf{X}}^b + \mathbf{K} [\mathbf{Y}^o - \mathbf{H}\bar{\mathbf{X}}^b], \tag{6}$$

where $\bar{\mathbf{X}}^a$ and $\bar{\mathbf{X}}^b$ are the analysis and background of ensemble mean ($\bar{\mathbf{X}}$) of state vector \mathbf{X} and \mathbf{K} is the Kalman-gain matrix sampled by a finite ensemble. The other is the analysis solution of ensemble perturbations, which depends on the version of EnKF.

When observation errors are assumed to be uncorrelated, EAKF can sequentially assimilate observations with the following two steps. First, the observational increment in one medium is computed as follows:

$$\begin{aligned}
\Delta y_i &= \left(\sqrt{\frac{r^2}{r^2 + (\sigma_y^p)^2}} - 1 \right) (y_i^p - \bar{y}^p) \\
&+ \frac{(\sigma_y^p)^2}{r^2 + (\sigma_y^p)^2} (y - \bar{y}^p),
\end{aligned} \tag{7}$$

where \bar{y}^p represents the prior ensemble mean (i.e., the model estimate) of observation y ; r and σ_y^p denote the standard

deviation of observational errors and the prior standard deviation of y . The i th prior ensemble of y , y_i^p , is usually obtained through applying a linear interpolation to the prior ensemble of state variable. In this study, y represents one of $(x_1^o, x_2^o, x_3^o, w^o)$.

Second step projects the observational increment onto related model variables and parameters. Realizations of this step for four EnKF CPE experiments are different. Similar to (2)–(5), here, we also give the linear regression formulas for four experiments as follows:

$$\text{EXP-1: } \Delta x_i = \frac{\text{cov}(x, y)}{(\sigma_y^p)^2} \Delta y_i, \quad (8)$$

$$\text{EXP-2: } \Delta x_i = \frac{\text{cov}(x, y)}{(\sigma_y^p)^2} \Delta y_i, \quad \Delta c_{2,i} = \frac{\text{cov}(c_2, y)}{(\sigma_y^p)^2} \Delta y_i, \quad (9)$$

$$\text{EXP-3: } \Delta x_i = \frac{\text{cov}(x, y)}{(\sigma_y^p)^2} \Delta y_i, \quad \Delta c_{1,i} = \frac{\text{cov}(c_1, y)}{(\sigma_y^p)^2} \Delta y_i, \quad (10)$$

$$\text{EXP-4: } \Delta x_i = \frac{\text{cov}(x, y)}{(\sigma_y^p)^2} \Delta y_i, \quad \Delta c_{1,i} = \frac{\text{cov}(c_1, y)}{(\sigma_y^p)^2} \Delta y_i, \\ \Delta c_{2,i} = \frac{\text{cov}(c_2, y)}{(\sigma_y^p)^2} \Delta y_i, \quad (11)$$

where Δx_i is the contribution of y to the model variable x for the i th ensemble member. In this study, x represents one of $(x_1^0, x_2^0, x_3^0, w^0, x_1^1, x_2^1, x_3^1, w^1)$ with superscripts “0” and “1” indicating time $t - 1$ and time t . $\text{cov}(x, y)$ denotes the error covariance between the prior ensemble of x and the model-estimated ensemble of y . It is worth mentioning that all experiments adopt the same observational increments and (8)–(11) are the main analysis equations of four experiments.

Coupling parameter estimation in EnKF is a process similar to multivariate adjustment in state estimation for a nonobservable variable. Without dynamical support, the model parameter ensemble is easier to suffer the filter divergence than the model state. Thus, variance inflation is necessary for parameter estimations. The parameter variance inflation scheme adopted in this study is the same as that in the previous studies [23, 24, 26, 27, 42]; that is, when the current spread of the parameter ensemble is less than one-tenth of the initial spread, it will be inflated to this amount. For the state inflation scheme, although many sophisticated adaptively multiplicative inflation schemes are available [43–46], due to the low dimension of the simple coupled model and the perfect OSSE configuration here, we apply the static-multiplicative inflation scheme [47] that inflates the perturbations of model states with a constant factor. Since the coupled system has two characteristic time scales, two independent inflation factors are, respectively, applied to the chaotic atmospheric variables $x_{1,2,3}$ and the slab oceanic variable w . Through repeating the EnKF CPE experiment in

the 2-dimensional space ($[1, 1.2] \times [1, 1.2]$) of the two inflation factors with the interval of 0.01, the inflation factors that minimize the time-averaged (last 50 TUs) absolute errors of ensemble means of model states are chosen as the best pair to perform the state inflation.

The ensemble initial conditions of model states are generated through adding a Gaussian noise to the initial field $\mathbf{\Pi}$. The initial ensembles of c_2 and c_1 are generated by adding a Gaussian noise with standard deviations of 0.055 and 0.0055 to the biased values 1.1 and 0.11. All four data assimilation experiments in the EnKF CPE start from the same ensemble initial conditions. The observations used in the EnKF CPE are the same as those used in the 4D-Var CPE. The absolute error of ensemble mean relative to the truth is used to evaluate the quality of the EnKF CPE. To investigate the dependence of the EnKF CPE on ensemble size, four ensemble sizes (10, 20, 50, and 100) are examined.

3. Results of 4D-Var CPE

In this section, we first evaluate the quality of the 4D-Var-estimated coupling parameters and then investigate the impact of the estimated-parameters on the representation of coupling processes.

3.1. Coupling Parameters. Figure 3 shows the dependence of time mean normalized absolute errors of c_2 (Figures 3(a) and 3(b)) and c_1 (Figures 3(c) and 3(d)) on the observational interval and the length of MTW for EXP-2 (Figure 3(a)), EXP-3 (Figure 3(c)), and EXP-4 (Figures 3(b) and 3(d)). Note that the absolute errors of c_2 and c_1 here are normalized by their initial errors (0.1 and 0.01). Note that we use observational interval instead of atmospheric observational interval in the following text. In EXP-4, 4D-Var can well estimate c_1 for all observational intervals and MTWs. For short MTWs (like 50 and 100 time steps), 4D-Var cannot effectively estimate c_2 with too small (like 5 and 10 time steps) or too large (like 50 time steps) observational intervals. According to the analysis in Section 2.3, it is more difficult to estimate c_2 than c_1 . For short MTWs, no sufficient signals of c_2 are implied in the cost function of 4D-Var, which may increase the possibility of the failure of parameter estimation. In EXP-2 that only estimates c_2 , we can see that 4D-Var fails in most cases except the situations with short MTWs (like 50 and 100 time steps) and a moderate observational interval (like 20 time steps). Since the model error is mainly caused by the error of c_1 , 4D-Var cannot accurately estimate c_2 without estimation of c_1 . In contrast, 4D-Var can effectively estimate c_1 in most cases in EXP-3. Once c_1 is estimated, the signal-to-noise ratio of c_2 in the cost function is correspondingly enhanced, which accordingly improves the quality of the estimated c_2 (see Figures 3(a) and 3(b)). Additionally, although contribution of c_2 to the model error is much less than c_1 , introducing the estimation of c_2 to EXP-3 still can more or less further improve the accuracy of the estimated c_1 (see Figures 3(c) and 3(d)).

From Figures 3(b) and 3(d), we can also see that the analysis accuracies of two parameters (especially for c_2) strongly depend on both MTW and observational intervals

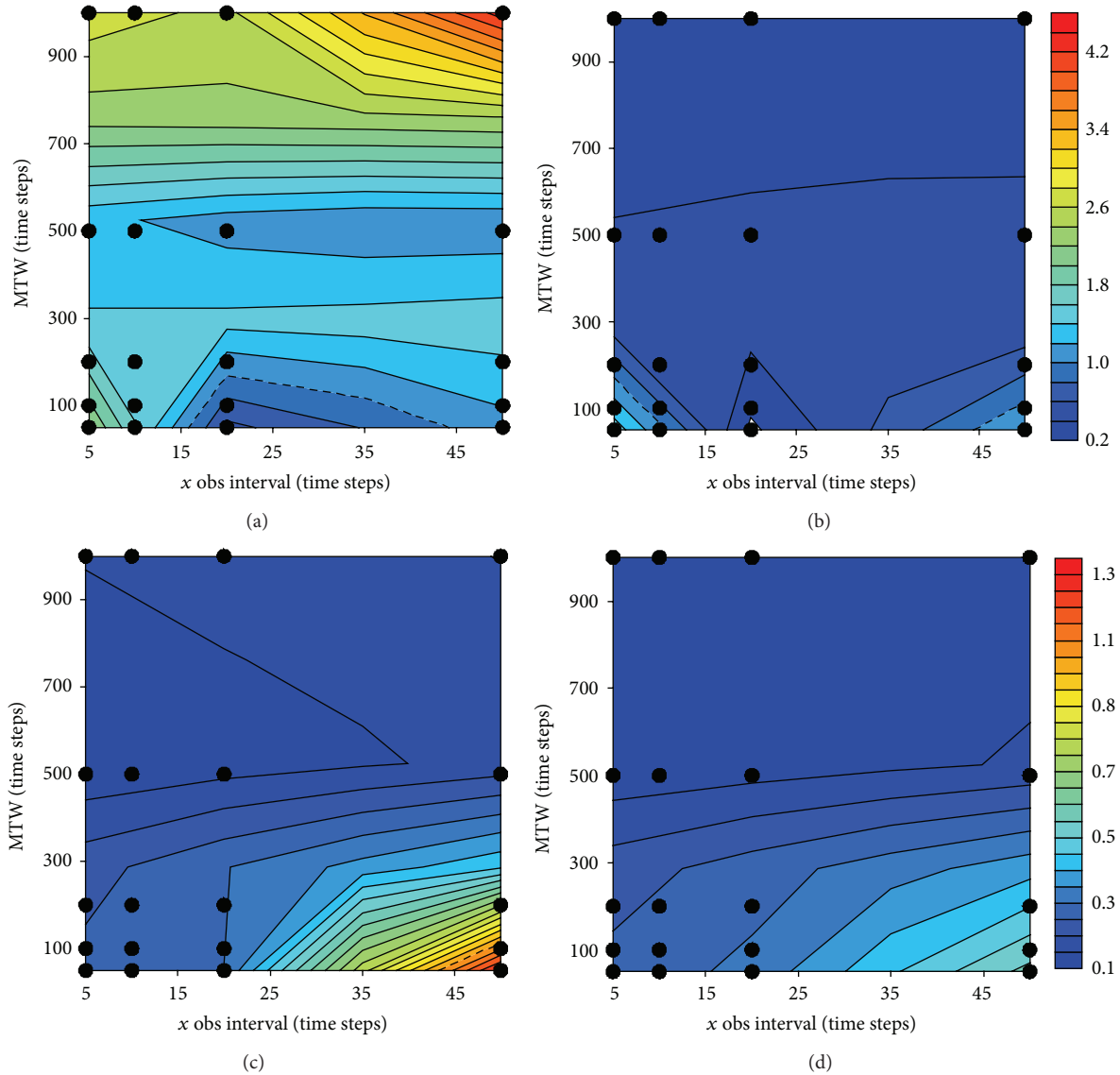


FIGURE 3: Time-averaged normalized absolute errors of (a) c_2 in EXP-2, (b) c_2 in EXP-4, (c) c_1 in EXP-3, and (d) c_1 in EXP-4 of the 4D-Var CPE. The absolute errors of c_2 and c_1 are normalized by their initial errors, that is, 0.1 and 0.01, respectively. The x -axis is the atmospheric observational interval while the y -axis denotes the minimization time window (MTW) in 4D-Var. The black solid circles stand for the scatter points used to create the contours. The dashed curve represents the 1.0 contour. Panels (a) and (b) use the upper shade scale while panels (c) and (d) use the lower shade scale. Note that 1 Time Unit = 100 time steps. EXP-1 only performs state estimation. EXP-2 instantaneously conducts state estimation and parameter estimation of c_2 . EXP-3 instantaneously conducts state estimation and parameter estimation of c_1 . EXP-4 instantaneously conducts state estimation and parameter estimations of c_1 and c_2 .

when MTW is less than 500 time steps. This means that, to obtain good analysis solutions of both c_1 and c_2 , an appropriate MTW (about 500 time steps here) should be used. Note that, due to the limited number of experiments performed in this study, for example, no experiment with MTW between 200 and 500 time steps is conducted; here, the appropriate MTW is an approximation.

3.2. Coupling Processes. Figure 4 displays the time-averaged normalized absolute errors of the sea-to-air coupling

process (represented by $c_1 w$) for EXP-1 (Figure 4(a)), EXP-2 (Figure 4(b)), EXP-3 (Figure 4(c)), and EXP4 (Figure 4(d)). Here, the absolute error is normalized by the climatological standard deviation (0.15) of $c_1 w$. Compared to EXP-1, estimating c_2 obtains nearly the same analysis of $c_1 w$ (see Figure 4(b)). However, once c_1 is estimated, the sea-to-air coupling process is significantly improved (compare Figure 4(a) with Figure 4(c)). The given parameter c_1 has been suitably corrected (see Figure 3(c)) in EXP-3, further estimating that c_2 can also partly improve the sea-to-air coupling process (compare Figure 4(c) with Figure 4(d)).

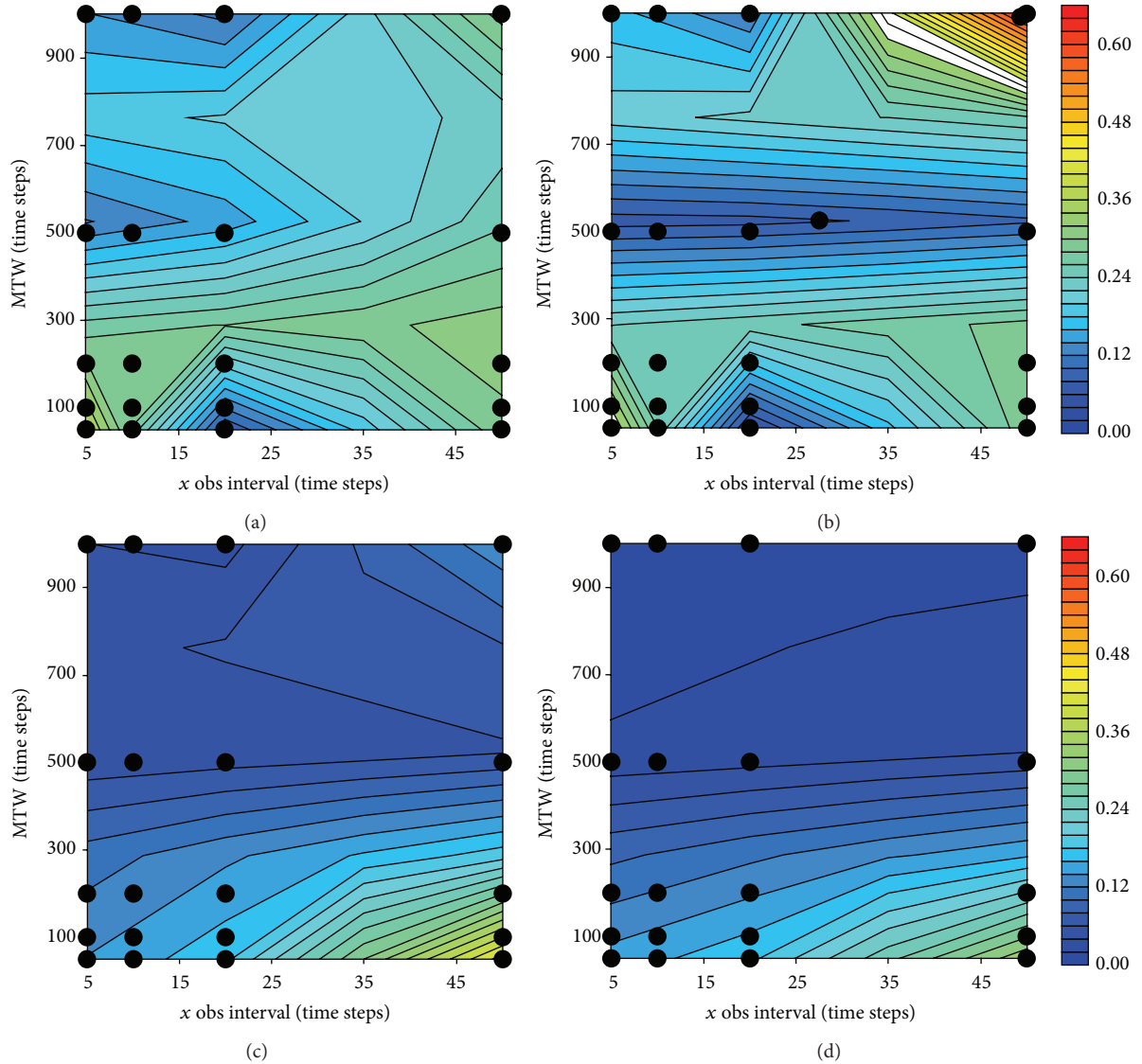


FIGURE 4: Time-averaged normalized absolute errors of $c_1 w$ in (a) EXP-1, (b) EXP-2, (c) EXP-3, and (d) EXP-4 of the 4D-Var CPE. The absolute error of $c_1 w$ is normalized by its climatological standard deviation (0.15). All panels use the same shade scale.

Figure 5 shows the same results as Figure 4 but for the air-to-sea coupling process (represented by $c_2 x_2$). Based on EXP-1, estimating c_2 cannot significantly improve the quality of $c_2 x_2$ (compare Figure 5(b) with Figure 5(a)). However, when c_1 is further estimated, the quality of the air-to-sea coupling processes is greatly enhanced, especially for long MTWs. In addition, comparison between Figure 5(c) and Figure 5(d) justifies that given c_1 has been corrected and the quality of the air-to-sea coupling processes can also be somehow enhanced by estimating c_2 . Thus, unlike the sea-to-air coupling process ($c_1 w$) which is governed by the c_1 accuracy, the air-to-sea coupling process ($c_2 x_2$) is affected by both c_1 and c_2 greatly.

To look into the detailed performance of 4D-Var CPE, we choose an appropriate MTW (i.e., 500 time steps) and a moderate observational interval (i.e., 10 time steps) to examine the time series of the absolute errors of the air-to-sea (Figure 6(b)) and the sea-to-air (Figure 6(a)) coupling processes for EXP-1 (red) and EXP-4 (blue). Relative to the state

estimation, coupling parameter estimation of c_1 and c_2 can markedly enhance the accuracy of coupling processes. According to Section 2.4, model states are more sensitive to c_1 than c_2 . Scale analysis (Section 2.3) also justifies that estimating c_2 is more difficult than estimating c_1 . Thus, the model error in this study is mainly attributed to the bias of c_1 , causing that the improvement of the air-to-sea coupling process is less than that of the sea-to-air coupling process.

Analyses above show that, compared to traditional state estimation, 4D-Var CPE can improve the representation of air-sea coupling processes through coupling parameter estimation.

4. Results of EnKF CPE

In this section, same as in the 4D-Var case, we first assess the quality of EnKF-estimated coupling parameters and then

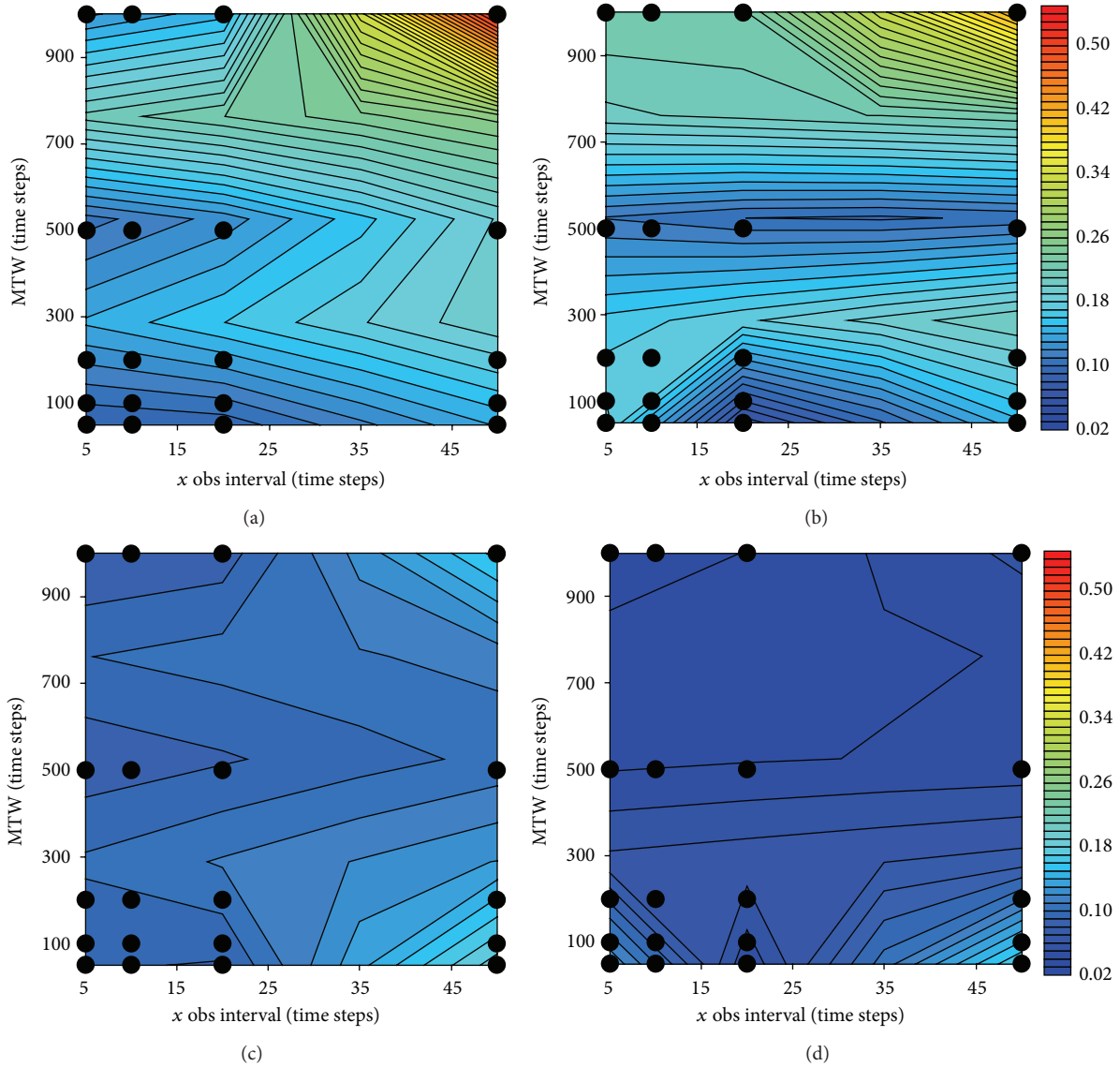


FIGURE 5: Same as Figure 4 but for c_2x_2 . The absolute error of c_2x_2 is normalized by its climatological standard deviation (14.5).

investigate the impact of the estimated-parameters on the representation of coupling processes.

4.1. Coupling Parameters. Figure 7 gives the same results as Figure 3 but for EnKF CPE. Here, the y -axis represents ensemble size. Different from 4D-Var (Figure 3(a)), EnKF can effectively estimate c_2 in EXP-2 (Figure 7(a)). Based on EXP-2, EXP-4 can further reduce the error of estimated c_2 through adjusting c_1 . Both EXP-3 and EXP-4 can do a good job for the estimation of c_1 . Thus, it is not so necessary that EnKF should firstly estimate c_1 rather than c_2 . This may be attributed to the high signal-to-noise ratios of c_2 implied in the error covariance between observations and c_2 .

4.2. Coupling Processes. Figure 8 plots the same results as Figure 4 but for EnKF CPE. From Figures 8(a) and 8(b), we

can see that estimation of c_2 cannot significantly improve the representation of the sea-to-air coupling process. This is because the term c_1w is directly controlled by c_1 and w rather than c_2 . If we compare Figure 8(c) to Figure 8(a), we can see that estimating c_1 can substantially enhance the accuracy of c_1w . When c_2 is further estimated based on EXP-3, the error of c_1w is also further reduced.

Figure 9 shows the same results as Figure 8 but for the air-to-sea coupling process. Relative to EXP-1, both EXP-2 and EXP-3 can reduce the error of c_2x_2 while simultaneously estimating c_1 and c_2 produces the best results. Additionally, due to the low-order model in this study, the dependence of the quality of estimated air-to-sea coupling process on observational interval is stronger than that on ensemble size.

To look into the detailed performance of EnKF CPE, we set observational interval as 10 time steps and ensemble size as 20 to examine the time series of absolute errors of the

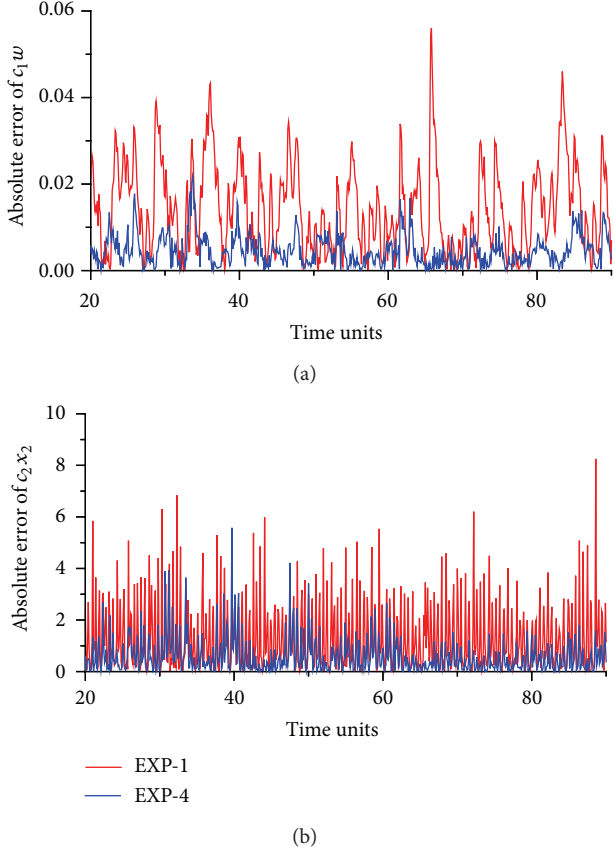


FIGURE 6: Time series (20–90 TUs) of the absolute errors of (a) $c_1 w$ and (b) $c_2 x_2$ in the 4D-Var CPE with the observational interval and the minimization time window being 10 and 500 time steps. Here, the red and blue curves represent the results in EXP-1 and EXP-4, respectively.

air-to-sea (Figure 10(b)) and the sea-to-air (Figure 10(a)) coupling processes for EXP-1 (red) and EXP-4 (blue). Compared to the air-to-sea coupling process, the improvement of the sea-to-air coupling process from EXP-1 to EXP-4 is more significant (i.e., the error of $c_1 w$ is reduced by 92%, from 0.53 to 0.04).

Analyses above show that EnKF CPE can also enhance the representation of the air-sea coupling processes through coupling parameter estimation relative to traditional state estimation.

5. Different Performances of EnKF CPE and 4D-Var CPE

Although both 4D-Var and EnKF are derived from Bayes' rule, their implementations are different. In practice, 4D-Var attempts to obtain an optimal initial condition using the observational information within a specific MTW for each analysis step. The length of MTW is usually longer than the analysis interval, leading the observations being used more than once. In contrast, EnKF does not repeatedly

use observations in this study (although it could do so in practice). From this point, it seems unfair to compare the performances of two algorithms. However, additional experiments for 4D-Var which only uses each observation for one time obtain worse results. Thus, we still can roughly compare the performances of EnKF CPE and 4D-Var CPE in this section.

5.1. Coupling Parameters. Comparison between Figure 3(a) and Figure 7(a) demonstrates that EnKF-estimated c_2 is more accurate than that estimated by 4D-Var. Without estimating c_1 , the signal implied in the error covariance between observation and c_2 is stronger than that implied in the cost function of 4D-Var. Since the model error is mainly attributed to the bias of c_1 , the signal in the cost function of 4D-Var is dominated by c_1 rather than c_2 . Under this circumstance, it is hard for 4D-Var to correctly estimate c_2 . In EXP-3, results of EnKF CPE are still better than those for 4D-Var CPE which reduces the initial error of c_1 by 74% on average. In EXP-4, to facilitate the comparison, we use the same shade scale for Figure 3(b) and Figure 7(b) and Figure 3(d) and Figure 7(d). For both parameters, the performance of EnKF CPE with a moderate ensemble size (like 50) is comparable to that of 4D-Var CPE with an appropriate MTW (like 500 time steps).

To summarize, EnKF is better than 4D-Var when a single parameter is estimated. The ensemble-evaluated error covariance is more effective than the cost function of 4D-Var.

5.2. Coupling Processes. We first attempt to compare the results of EXP-1 for 4D-Var CPE and EnKF CPE. For the sea-to-air coupling process represented by $c_1 w$, the quality of the estimated $c_1 w$ is determined by the quality of w since c_1 is not estimated. From Figures 4(a) and 8(a), it seems that $c_1 w$ produced by 4D-Var CPE is much better than that generated by EnKF CPE. Thus, we may speculate that the 4D-Var-estimated w is also better than EnKF-estimated w . However, results (not shown) demonstrate that the EnKF-produced w is much better than that produced by 4D-Var.

To understand why a good EnKF-produced w leads a bad $c_1 w$, we examine an experiment for details with the observational interval, ensemble size, and MTW being 5 time steps, 50 time steps, and 500 time steps. Figure 11 plots the time series of w (Figure 11(a)) and $c_1 w$ (Figure 11(b)) for 4D-Var CPE (black), truth (red), and EnKF CPE (blue) in EXP-1. Obviously, the EnKF-produced w is better than 4D-Var-produced w . We start from the following formulation of the absolute error of $c_1 w$ to answer the question at the beginning of this paragraph:

$$\left| c_1^{\text{est}} w^{\text{est}} - c_1^{\text{tru}} w^{\text{tru}} \right|, \quad (12)$$

where the superscripts “est” and “tru” indicate the estimation and truth of c_1 and w . As we stated in Section 2.2, the truth value of c_1 is 0.1 while the initial biased value of c_1 in 4D-Var CPE is 0.11 and ensemble means of c_1 for all ensemble sizes in EnKF CPE also approximate 0.11. Therefore, the computational process of (12) can be described as first scaling the truth

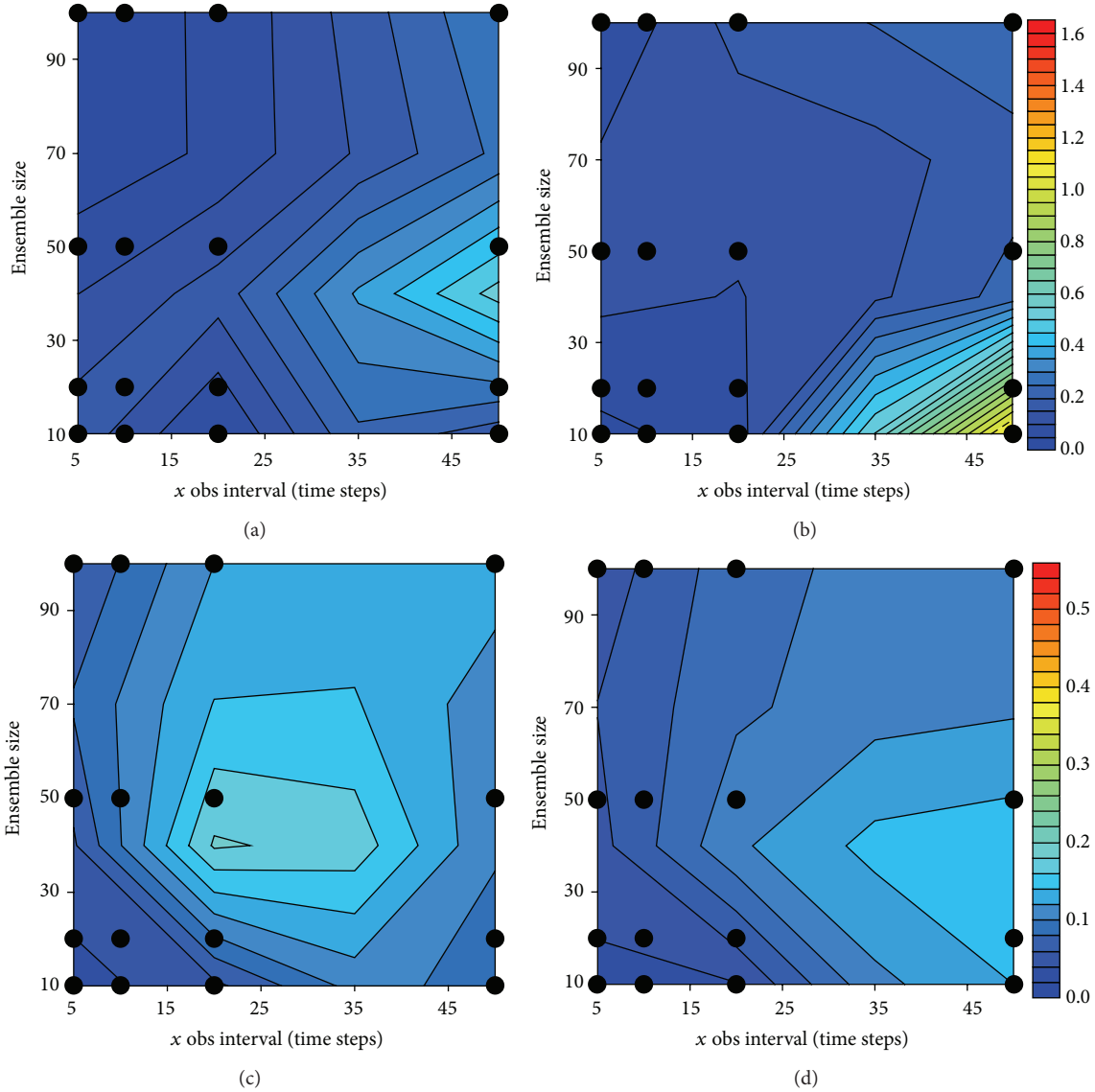


FIGURE 7: Same as Figure 3 but for the EnKF CPE. Note that panels (a) and (b) use the upper shade scale while panels (c) and (d) use the lower shade scale.

value of w by 0.1 and the values of estimated w values by 0.11, then computing the absolute value of the difference. From Figure 11, it happens that the first step converts the worse 4D-Var-produced w to the appearing better $c_1 w$. Therefore, it is difficult to determine which algorithm produces better coupling processes without parameter estimation.

To fairly compare the performances of two algorithms, we focus on the results in EXP-4. From Figures 4(d) and 8(d), we find that the representation of the sea-to-air coupling process produced by 4D-Var CPE with a MTW over 500 time steps is comparable to EnKF CPE. However, the EnKF CPE with ensemble size less than 50 improves the assimilation quality of 4D-Var CPE with a MTW shorter than 500 time steps by 59% (from 0.157 to 0.065) on average. Here, we choose an extreme case (i.e., the observational interval, ensemble size, and MTW being 50 time steps, 10 time steps, and 50 time steps) to

compare the performance of two algorithms. Figure 12 shows time series of absolute errors of $c_1 w$ for 4D-Var CPE (blue) and EnKF CPE (red) in EXP-4. The EnKF CPE is better than the 4D-Var CPE. According to Figures 3(d) and 7(d), in the above parameter setting, the EnKF-estimated c_1 is much better than the 4D-Var-estimated c_1 , since the MTW is too short to exactly retrieve c_1 for 4D-Var. In addition, we found that the 4D-Var-produced w is comparable to that produced by EnKF (not shown). Thus, the superiority of EnKF CPE over 4D-Var CPE is mainly attributed to the estimation of c_1 .

For the air-to-sea coupling process, comparison between Figure 5(d) and Figure 9(d) reveals that 4D-Var CPE outperforms EnKF CPE when MTW exceeds a critical value (here is about 500 time steps) while EnKF CPE has advantages over 4D-Var CPE with a short MTW for a small observational interval. Here, we take two extreme cases to compare the

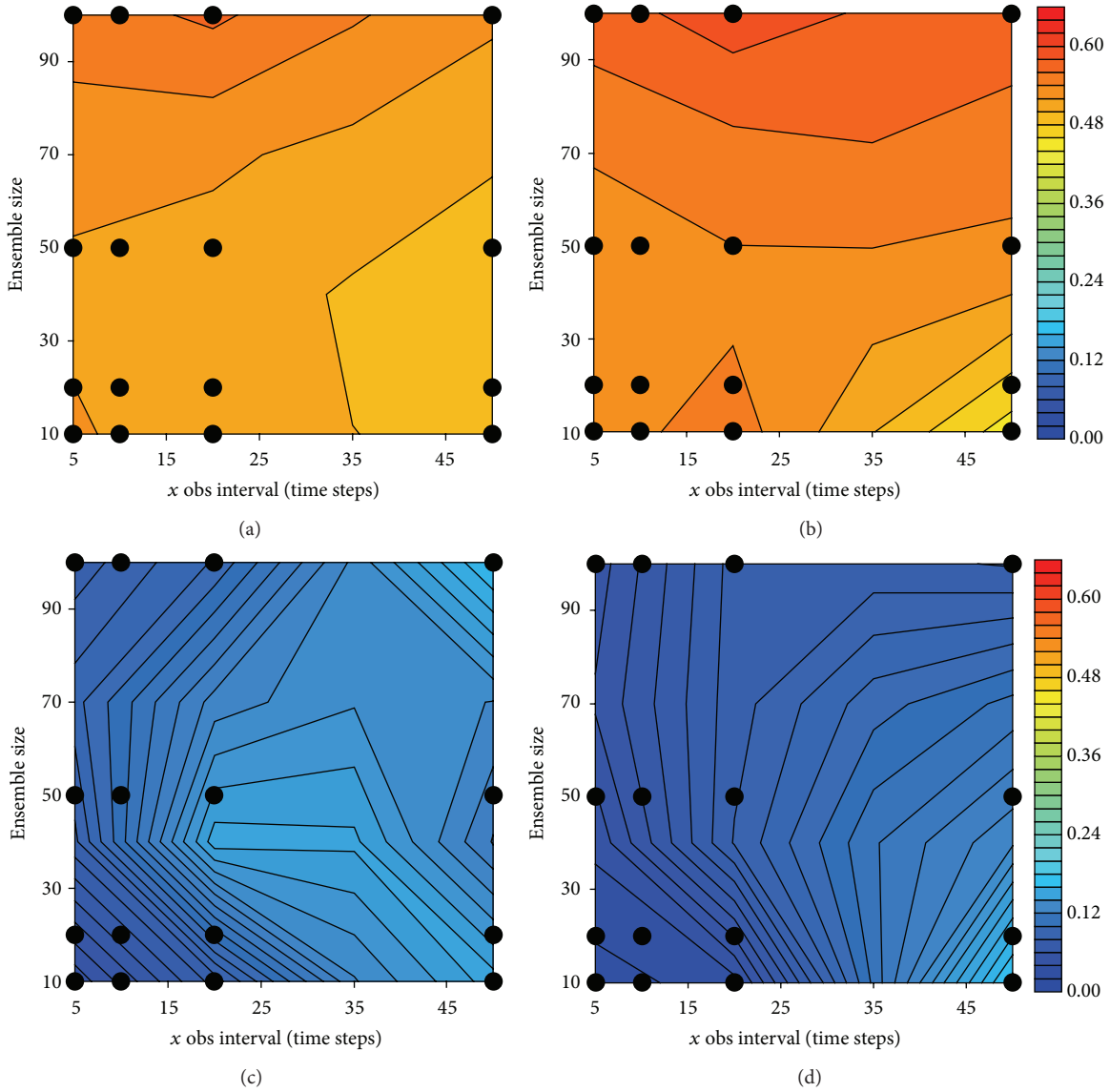


FIGURE 8: Same as Figure 4 but for the EnKF CPE.

performances of 4D-Var CPE and EnKF CPE. First, we check the results of two methods for the observational interval, ensemble size, and MTW being 50 time steps, 100 time steps, and 1000 time steps. Figure 13(a) plots time series of absolute errors of c_2x_2 for 4D-Var CPE (blue) and EnKF CPE (red) in EXP-4. After the spin-up period (about 40 TUs), the air-to-sea coupling process represented by 4D-Var CPE is better than that produced by EnKF CPE. Although the observational interval is very large and both 4D-Var CPE and EnKF CPE can effectively estimate c_2 (see Figures 3(b) and 7(b)), 4D-Var CPE can produce better x_2 than EnKF CPE (not shown). Second, we check the results (Figure 13(b)) of two methods for the observational interval, ensemble size, and MTW being 5 time steps, 10 time steps, and 50 time steps. According to Figures 3(b) and 7(b), it is difficult for 4D-Var CPE to estimate c_2 with a short MTW while EnKF CPE can well estimate c_2 with an ensemble size of 10. For x_2 , 4D-Var

CPE can produce similar results as EnKF CPE (not shown). Therefore, the EnKF CPE-produced c_2x_2 is better than that produced by 4D-Var CPE.

6. Summary and Discussions

A simple coupled model that characterizes the interaction of media with two different time scales is used to study the feasibility of the 4D-Var and EnKF coupling parameter estimation (CPE). Within a perfect OSSE framework which assumes that model errors only arise from the erroneously-set coupling parameters, the results demonstrate that, compared to traditional state estimation, both 4D-Var CPE and EnKF CPE algorithms can greatly improve the representation of air-sea coupling processes. An appropriate MTW exists in the 4D-Var CPE. Thus, if 4D-Var is used to implement CPE, the cost

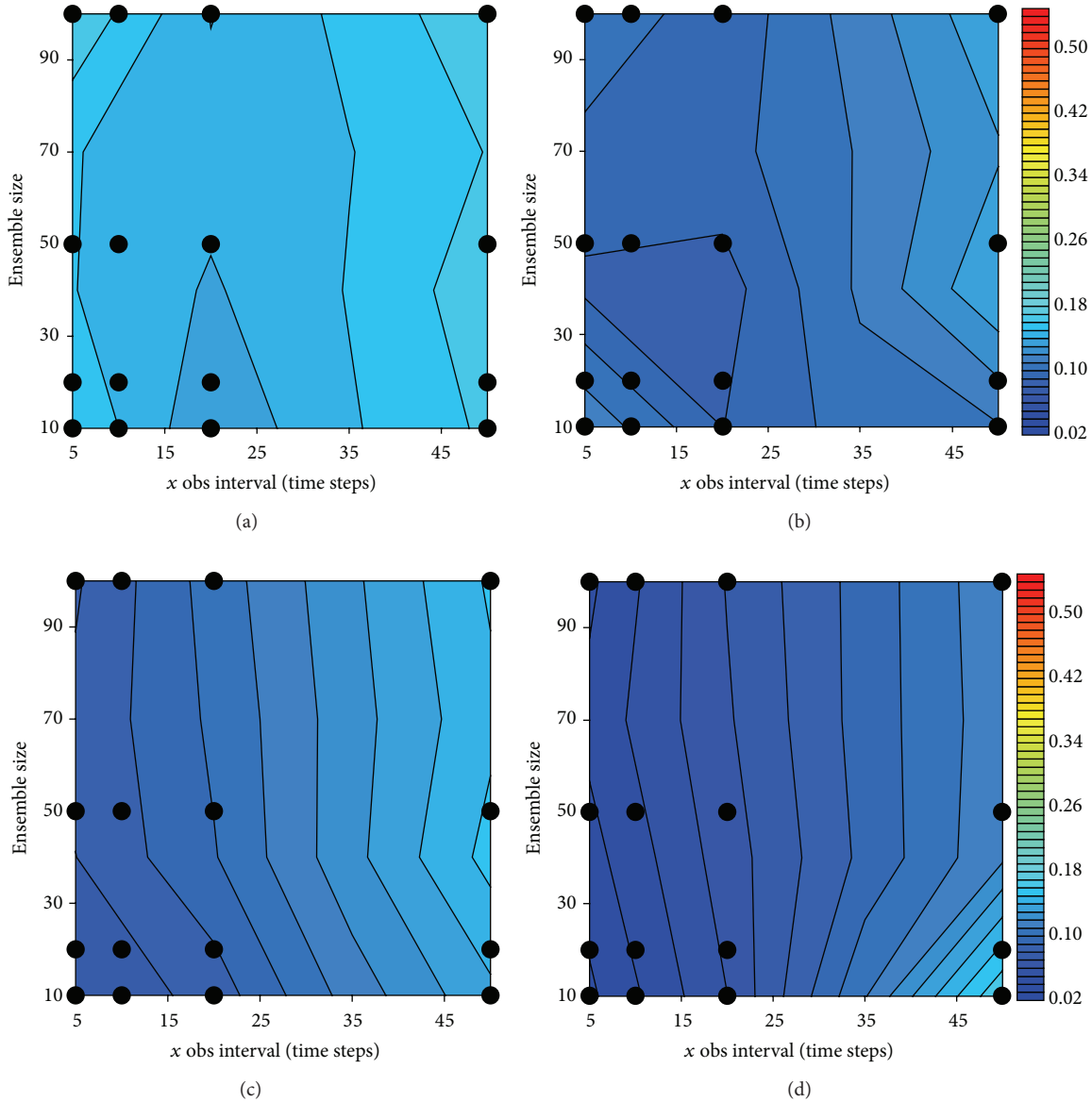


FIGURE 9: Same as Figure 5 but for the EnKF CPE.

function should include observations from both the atmosphere and ocean, and an appropriate MTW should also be chosen. A roughly comparison between two assimilation methods demonstrates that EnKF CPE outperforms 4D-Var CPE with a MTW shorter than 5 TUs (i.e., 180 model days) for the sea-to-air coupling process. For the air-to-sea coupling process, 4D-Var CPE with a MTW longer than 5 TUs is better than EnKF CPE. The EnKF CPE is better than the 4D-Var CPE with a MTW shorter than 5 TUs for short observational intervals.

Many challenges remain before CPE can be applied to a coupled general circulation model (CGCM). First, the perfect OSSE that uses the same model to setup the Truth (also called the Nature Run) and the assimilation experiments can be overoptimistic in the results. Thus, the perfect OSSE should

be first extended to a biased OSSE and then put forward to the real world. Second, some of the above conclusions depend on the sensitivities of the coupling parameters and model errors. Thus, the conclusions should be further validated under more complicated model errors in CGCMs. Third, the static-multiplicative inflation scheme in the EnKF CPE should be updated to an adaptive inflation scheme [44]. Last, the impact of the observing system on the CPE should be examined with a GCM or a CGCM through varying the temporal and spatial densities of different observation variables or types.

Conflict of Interests

The authors declare that there is no conflict of interests regarding the publication of this paper.

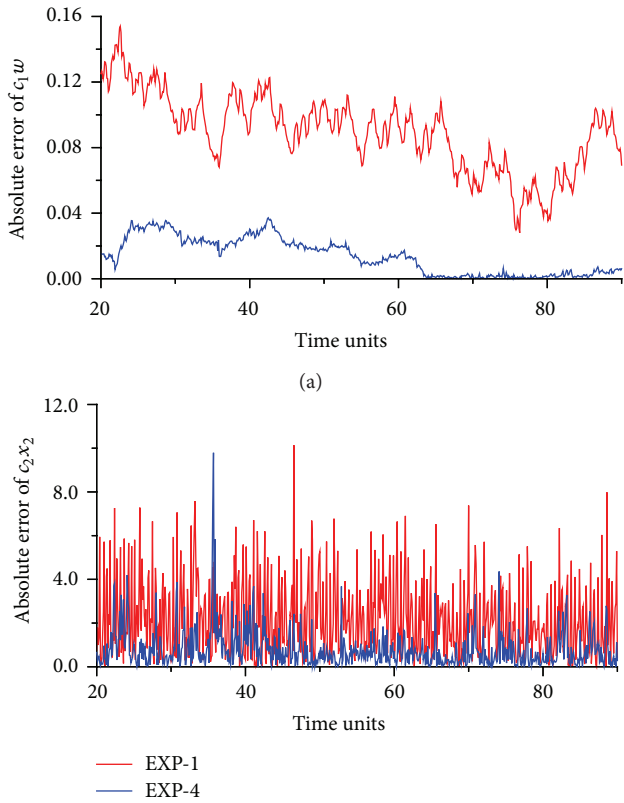


FIGURE 10: Same as Figure 6 but for the EnKF CPE with 20-ensemble size.

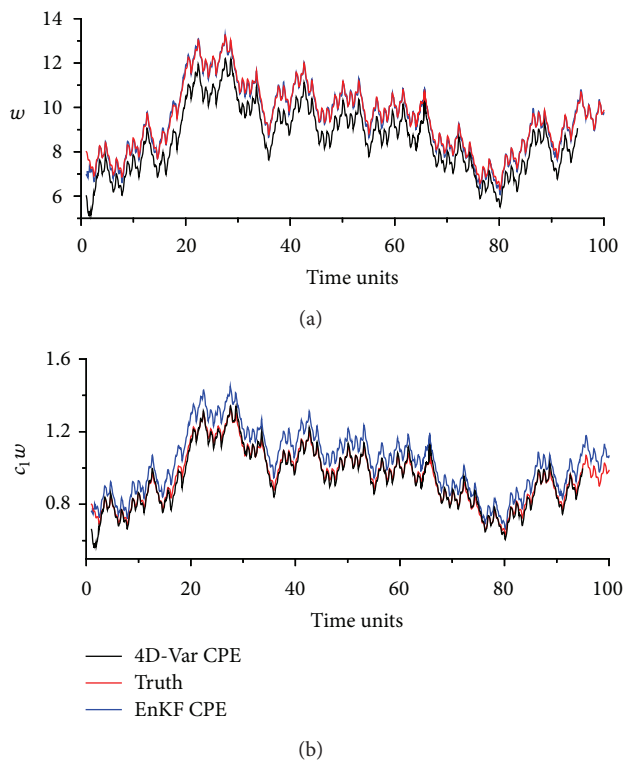


FIGURE 11: Time series of w (panel (a)) and c_1w (panel (b)) for 4D-Var CPE (black) with MTW being 500 time steps, truth (red), and EnKF CPE (blue) with ensemble size being 50 in EXP-4. Here, the observational interval is set to 5 time steps.

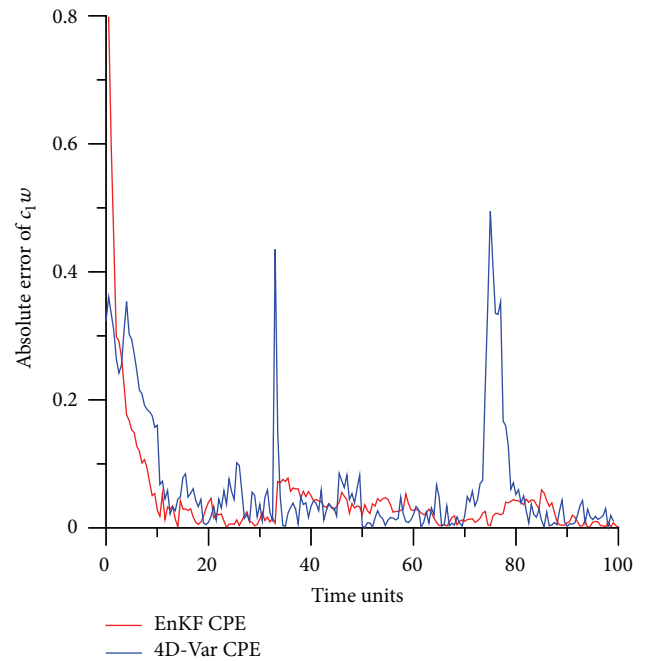


FIGURE 12: Time series of absolute errors of c_1w for 4D-Var CPE (blue) with MTW being 50 time steps and EnKF CPE (red) with 10-ensemble size in EXP-4. Here, the observational interval is 50 time steps.

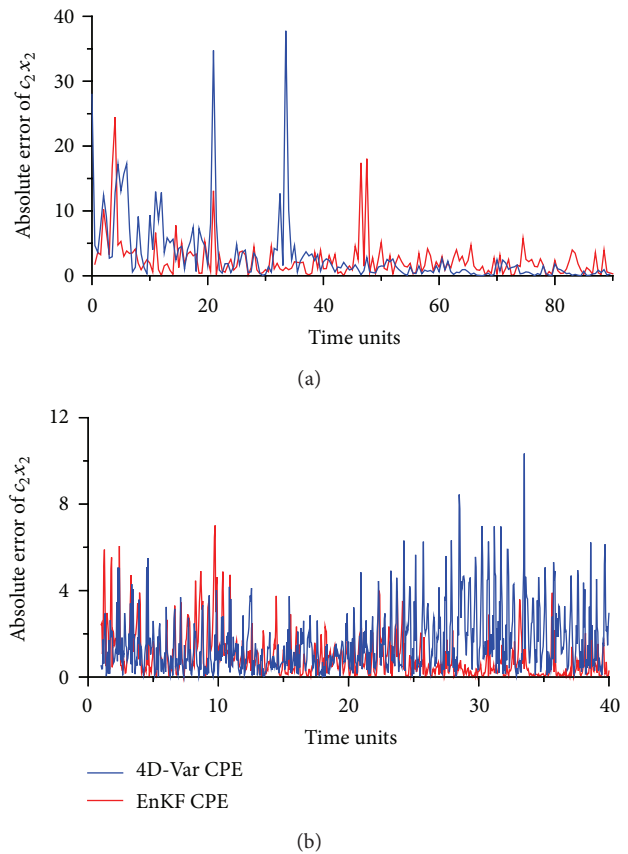


FIGURE 13: Time series of absolute errors of c_2x_2 for 4D-Var CPE (blue) and EnKF CPE (red) in EXP-4. In panel (a) (panel (b)), values of the observational interval, ensemble size, and MTW are 50 (5) time steps, 100 (10) time steps, and 1000 (50) time steps.

Acknowledgments

This research is cosponsored by grants of the National Basic Research Program (2013CB430304), National Natural Science Foundation (41306006, 41376015, 41376013, 41206178, and 41176003), and National High-Tech R&D Program (2013AA09A505), and the NSF Grant of the US (0968383).

References

- [1] D. Chen, M. A. Cane, S. E. Zebiak, R. Canizares, and A. Kaplan, "Bias correction of an ocean-atmosphere coupled model," *Geophysical Research Letters*, vol. 27, no. 16, pp. 2585–2588, 2000.
- [2] M. Peña and E. Kalnay, "Separating fast and slow modes in coupled chaotic systems," *Nonlinear Processes in Geophysics*, vol. 11, no. 3, pp. 319–327, 2004.
- [3] S. Zhang, M. J. Harrison, A. Rosati, and A. Wittenberg, "System design and evaluation of coupled ensemble data assimilation for global oceanic climate studies," *Monthly Weather Review*, vol. 135, no. 10, pp. 3541–3564, 2007.
- [4] N. Sugiura, T. Awaji, S. Masuda et al., "Development of a four-dimensional variational coupled data assimilation system for enhanced analysis and prediction of seasonal to interannual climate variations," *Journal of Geophysical Research: Oceans*, vol. 133, no. 10, Article ID C10017, 2008.
- [5] T. Singleton, *A data assimilation study using a simple coupled ocean-atmosphere system [Ph.D. thesis]*, University of Maryland, College Park, Md, USA, 2011.
- [6] G. Han, X. Wu, S. Zhang, Z. Liu, and W. Li, "Error covariance estimation for coupled data assimilation using a Lorenz atmosphere and a simple pycnocline ocean model," *Journal of Climate*, vol. 26, no. 24, pp. 10218–10231, 2013.
- [7] J. M. Lewis and J. C. Derber, "The use of adjoint equations to solve a variational adjustment problem with advective constraints," *Tellus A*, vol. 37, no. 4, pp. 309–322, 1985.
- [8] P. Courtier, J.-N. Thepaut, and A. Hollingsworth, "A strategy for operational implementation of 4D-Var, using an incremental approach," *Quarterly Journal of the Royal Meteorological Society*, vol. 120, no. 519, pp. 1367–1387, 1994.
- [9] F. Rabier, H. Järvinen, E. Klinker, J.-F. Mahfouf, and A. Simmons, "The ECMWF operational implementation of four-dimensional variational assimilation. I: experimental results with simplified physics," *Quarterly Journal of the Royal Meteorological Society*, vol. 126, no. 564, pp. 1143–1170, 2000.
- [10] G. Evensen, "Sequential data assimilation with a nonlinear quasi-geostrophic model using Monte Carlo methods to forecast error statistics," *Journal of Geophysical Research*, vol. 99, pp. 10143–10162, 1994.
- [11] J. L. Anderson, "An ensemble adjustment Kalman filter for data assimilation," *Monthly Weather Review*, vol. 129, no. 12, pp. 2884–2903, 2001.
- [12] A. C. Lorenc, "The potential of the ensemble Kalman filter for NWP—a comparison with 4D-Var," *Quarterly Journal of the Royal Meteorological Society*, vol. 129, no. 595, pp. 3183–3203, 2003.
- [13] S. C. Yang, M. Corazza, A. Carrasi, E. Kalnay, and T. Miyoshi, "Comparison of local ensemble transform Kalman filter, 3DVAR, and 4DVAR in a quasigeostrophic model," *Monthly Weather Review*, vol. 137, no. 2, pp. 693–709, 2009.
- [14] T. Miyoshi, Y. Sato, and T. Kadowaki, "Ensemble Kalman filter and 4D-Var intercomparison with the Japanese operational global analysis and prediction system," *Monthly Weather Review*, vol. 138, no. 7, pp. 2846–2866, 2010.
- [15] M. Zhang, F. Zhang, X.-Y. Huang, and X. Zhang, "Intercomparison of an ensemble Kalman filter with three- and four-dimensional variational data assimilation methods in a limited-area model over the month of June 2003," *Monthly Weather Review*, vol. 139, no. 2, pp. 566–572, 2011.
- [16] J. L. Steward, I. M. Navon, M. Zupanski, and N. Karmitsa, "Impact of non-smooth observation operators on variational and sequential data assimilation for a limited-area shallow-water equation model," *Quarterly Journal of the Royal Meteorological Society*, vol. 138, no. 663, pp. 323–339, 2012.
- [17] E. Kalnay, H. Li, T. Miyoshi, S.-C. Yang, and J. Ballabrera-Poy, "4-D-Var or ensemble Kalman filter?" *Tellus, Series A: Dynamic Meteorology and Oceanography*, vol. 59, no. 5, pp. 758–773, 2007.
- [18] A. Caya, J. Sun, and C. Snyder, "A comparison between the 4DVAR and the ensemble Kalman filter techniques for radar data assimilation," *Monthly Weather Review*, vol. 133, no. 11, pp. 3081–3094, 2005.
- [19] M. Buehner, P. L. Houtekamer, C. Charette, H. L. Mitchell, and B. He, "Intercomparison of variational data assimilation and the ensemble Kalman filter for global deterministic NWP. Part I: description and single-observation experiments," *Monthly Weather Review*, vol. 138, no. 5, pp. 1550–1566, 2010.
- [20] M. Buehner, P. L. Houtekamer, C. Charette, H. L. Mitchell, and B. He, "Intercomparison of variational data assimilation and the ensemble Kalman filter for global deterministic NWP. Part II: one-month experiments with real observations," *Monthly Weather Review*, vol. 138, no. 5, pp. 1567–1586, 2010.
- [21] J. D. Annan, J. C. Hargreaves, N. R. Edwards, and R. Marsh, "Parameter estimation in an intermediate complexity earth system model using an ensemble Kalman filter," *Ocean Modelling*, vol. 8, no. 1–2, pp. 135–154, 2004.
- [22] D. Kondrashov, C. Sun, and M. Ghil, "Data assimilation for a coupled ocean-atmosphere model. Part II: parameter estimation," *Monthly Weather Review*, vol. 136, no. 12, pp. 5062–5076, 2008.
- [23] S. Zhang, "Impact of observation-optimized model parameters on decadal predictions: simulation with a simple pycnocline prediction model," *Geophysical Research Letters*, vol. 38, no. 2, Article ID L02702, 2011.
- [24] S. Zhang, "A study of impacts of coupled model initial shocks and state—parameter optimization on climate predictions using a simple pycnocline prediction model," *Journal of Climate*, vol. 24, no. 23, pp. 6210–6226, 2011.
- [25] S. Zhang, Z. Liu, A. Rosati, and T. Delworth, "A study of enhance parameter correction with coupled data assimilation for climate estimation and prediction using a simple coupled model," *Tellus A*, vol. 64, no. 1, Article ID 10963, 2012.
- [26] X. Wu, S. Zhang, Z. Liu, A. Rosati, T. L. Delworth, and Y. Liu, "Impact of geographic-dependent parameter optimization on climate estimation and prediction: simulation with an intermediate coupled model," *Monthly Weather Review*, vol. 140, no. 12, pp. 3956–3971, 2012.
- [27] X. Wu, S. Zhang, Z. Liu, A. Rosati, and T. L. Delworth, "A study of impact of the geographic dependence of observing system on parameter estimation with an intermediate coupled model," *Climate Dynamics*, vol. 40, no. 7–8, pp. 1789–1798, 2013.
- [28] J. Ballabrera-Poy, E. Kalnay, and S. C. Yang, "Data assimilation in a system with two scales—combining two initialization techniques," *Tellus, Series A: Dynamic Meteorology and Oceanography*, vol. 61, no. 4, pp. 539–549, 2009.

- [29] E. N. Lorenz, "Deterministic non-periodic flow," *Journal of the Atmospheric Sciences*, vol. 20, pp. 130–141, 1963.
- [30] M. Masutani, J. S. Woollen, S. J. Lord et al., "Observing system simulation experiments at the National Centers for Environmental Prediction," *Journal of Geophysical Research: Atmospheres*, vol. 115, no. 7, Article ID D07101, 2010.
- [31] A. Robert, "The integration of a spectral model of the atmosphere by the implicit method," in *Proceedings of the WMO/IUGG Symposium on NWP*, pp. 19–24, Japan Meteorological Society, Tokyo, Japan, 1969.
- [32] R. Asselin, "Frequency filter for time integrations," *Monthly Weather Review*, vol. 100, no. 6, pp. 487–490, 1972.
- [33] S. Zhang, J. L. Anderson, A. Rosati, M. Harrison, S. P. Khare, and A. Wittenberg, "Multiple time level adjustment for data assimilation," *Tellus*, vol. 56, no. 1, pp. 2–15, 2004.
- [34] I. M. Navon, "Practical and theoretical aspects of adjoint parameter estimation and identifiability in meteorology and oceanography," *Dynamics of Atmospheres and Oceans*, vol. 27, no. 1–4, pp. 55–79, 1998.
- [35] D. C. Liu and J. Nocedal, "On the limited memory BFGS method for large scale optimization," *Mathematical Programming*, vol. 45, no. 3, pp. 503–528, 1989.
- [36] M. Haarala, K. Miettinen, and M. M. Mäkelä, "New limited memory bundle method for large-scale nonsmooth optimization," *Optimization Methods & Software*, vol. 19, no. 6, pp. 673–692, 2004.
- [37] N. Haarala, K. Miettinen, and M. M. Mäkelä, "Globally convergent limited memory bundle method for large-scale nonsmooth optimization," *Mathematical Programming*, vol. 109, no. 1, pp. 181–205, 2007.
- [38] C. Pires, R. Vautard, and O. Talagrand, "On extending the limits of variational assimilation in nonlinear chaotic systems," *Tellus A*, vol. 48, no. 1, pp. 96–121, 1996.
- [39] J. Vlček and L. Lukšan, "Globally convergent variable metric method for nonconvex nondifferentiable unconstrained minimization," *Journal of Optimization Theory and Applications*, vol. 111, no. 2, pp. 407–430, 2001.
- [40] R. H. Byrd, J. Nocedal, and R. B. Schnabel, "Representations of quasi-Newton matrices and their use in limited memory methods," *Mathematical Programming*, vol. 63, no. 2, pp. 129–156, 1994.
- [41] N. Karmitsa, "LMBM-FORTRAN subroutines for large-scale nonsmooth minimization: user's manual," TUCS Technical Report 856, Turku Centre for Computer Science, Turku, Finland, 2007.
- [42] A. Aksoy, F. Zhang, and J. W. Nielsen-Gammon, "Ensemble-based simultaneous state and parameter estimation with MM5," *Geophysical Research Letters*, vol. 33, no. 12, 2006.
- [43] J. L. Anderson, "An adaptive covariance inflation error correction algorithm for ensemble filters," *Tellus, Series A: Dynamic Meteorology and Oceanography*, vol. 59, no. 2, pp. 210–224, 2007.
- [44] J. L. Anderson, "Spatially and temporally varying adaptive covariance inflation for ensemble filters," *Tellus, Series A: Dynamic Meteorology and Oceanography*, vol. 61, no. 1, pp. 72–83, 2009.
- [45] H. Li, E. Kalnay, and T. Miyoshi, "Simultaneous estimation of covariance inflation and observation errors within an ensemble Kalman filter," *Quarterly Journal of the Royal Meteorological Society*, vol. 135, no. 639, pp. 523–533, 2009.
- [46] T. Miyoshi, "The gaussian approach to adaptive covariance inflation and its implementation with the local ensemble transform Kalman filter," *Monthly Weather Review*, vol. 139, no. 5, pp. 1519–1535, 2011.
- [47] J. L. Anderson and S. L. Anderson, "A Monte Carlo implementation of the nonlinear filtering problem to produce ensemble assimilations and forecasts," *Monthly Weather Review*, vol. 127, no. 12, pp. 2741–2758, 1999.

Research Article

Diffusion Filters for Variational Data Assimilation of Sea Surface Temperature in an Intermediate Climate Model

Xuefeng Zhang,^{1,2} Dong Li,² Peter C. Chu,³ Lianxin Zhang,^{2,4} and Wei Li²

¹College of Automation, Harbin Engineering University, Harbin 150001, China

²Key Laboratory of Marine Environmental Information Technology, National Marine Data and Information Service, State Oceanic Administration, Tianjin 300171, China

³Naval Ocean Analysis and Prediction Laboratory, Department of Oceanography, Naval Postgraduate School, Monterey, CA 93943, USA

⁴College of Physical and Environmental Oceanography, Ocean University of China, Qingdao 266100, China

Correspondence should be addressed to Xuefeng Zhang; xfz_nmdis@126.com

Received 6 December 2014; Accepted 7 April 2015

Academic Editor: Juan Jose Ruiz

Copyright © 2015 Xuefeng Zhang et al. This is an open access article distributed under the Creative Commons Attribution License, which permits unrestricted use, distribution, and reproduction in any medium, provided the original work is properly cited.

Sequential, adaptive, and gradient diffusion filters are implemented into spatial multiscale three-dimensional variational data assimilation (3DVAR) as alternative schemes to model background error covariance matrix for the commonly used correction scale method, recursive filter method, and sequential 3DVAR. The gradient diffusion filter (GDF) is verified by a two-dimensional sea surface temperature (SST) assimilation experiment. Compared to the existing DF, the new GDF scheme shows a superior performance in the assimilation experiment due to its success in extracting the spatial multiscale information. The GDF can retrieve successfully the longwave information over the whole analysis domain and the shortwave information over data-dense regions. After that, a perfect twin data assimilation experiment framework is designed to study the effect of the GDF on the state estimation based on an intermediate coupled model. In this framework, the assimilation model is subject to “biased” initial fields from the “truth” model. While the GDF reduces the model bias in general, it can enhance the accuracy of the state estimation in the region that the observations are removed, especially in the South Ocean. In addition, the higher forecast skill can be obtained through the better initial state fields produced by the GDF.

1. Introduction

In general, standard three-dimensional variational data assimilation (3DVAR) can be formulated as the minimization of the following cost function [1, 2]:

$$J(x) = \frac{1}{2} (x - x_b)^T B^{-1} (x - x_b) + \frac{1}{2} (Hx - y)^T R^{-1} (Hx - y) = J_b + J_o, \quad (1)$$

where x is the analysis vector, x_b is the background vector, y is the observation vector, H is an interpolation operator from model space to observation space, R is the observational error covariance matrix, $(\cdot)^T$ indicates transpose, and $(\cdot)^{-1}$ indicates inversion. B is the background error covariance matrix.

It is a challenge to determine B in any data assimilation including 3DVAR. The spatial structure and the magnitude of the correction for the state variables being estimated are determined completely by B .

Two common approaches are used to prescribe B . The first approach is the correlation scale method (CSM) [3], in which B is represented by the Gaussian function:

$$B = A(x, y) \exp\left(-\frac{r_x^2}{L_x^2} - \frac{r_y^2}{L_y^2}\right), \quad (2)$$

where A is an estimate of the magnitude of the background error, r_x and r_y are the distances between two grid points, and L_x and L_y are the characteristic length scales reflecting the extent of spatial correction of the background error in the x and y directions, respectively. A more general anisotropic

shape with an ellipsoid about the spatial covariance can also be found [4]. It is noted that B is explicitly generated statistically using the correlation scales [3, 5–7]. However, limitations of the CSM are (1) positive value for each element in B (which is not always true), (2) nonexistence of B^{-1} unless using sufficiently small correction scales, and (3) requirement of large computer memory to store B since every element in B is calculated explicitly. To avoid the inversion of B and to speed up the convergence of descent algorithms such as the steepest descent and conjugate-gradient methods, a new vector w is introduced by Lorenc [8] and Derber and Rosati [3], defined as

$$w = B^{-1}(x - x_b). \quad (3)$$

Then the cost function J can now be rewritten as

$$J(w) = \frac{1}{2}w^T B^T w + \frac{1}{2}(HBw - d)^T R^{-1}(HBw - d), \quad (4)$$

where $d = y - Hx_b$ is the ‘‘innovation’’ vector, and for simplification, hereafter, we will call it observation.

Considering $B^T = B$, (4) is equal to

$$J(w) = \frac{1}{2}w^T B w + \frac{1}{2}(HBw - d)^T R^{-1}(HBw - d). \quad (5)$$

The effect of Bw in (5) can be modeled by applying an equivalent spatial filter on w .

The second approach to prescribe B is the recursive filter method (RFM) [9],

$$\begin{aligned} Y_i &= \alpha Y_{i-1} + (1 - \alpha) X_i \quad \text{for } i = 1, \dots, n, \\ Z_i &= \alpha Z_{i+1} + (1 - \alpha) Y_i \quad \text{for } i = n, \dots, 1, \end{aligned} \quad (6)$$

where X_i is the initial value at grid point i , Y_i is the value after filtering for $i = 1$ to n , Z is the initial value after one pass of the filter in each direction, and α is the filter coefficient, which determines the extent of spreading of observational information over the analysis domain. Multipass filter can be built up by repeated application of (6). Multidimensional filter can be constructed by applying this one-dimensional filter in each direction. It can be shown [10] that such multidimensional filter, when applied with several passes, can accurately model isotropic Gaussian error correlations. The implementation using recursive filter to model B has been widely used due to its relatively computational inexpensiveness [10–13].

An outstanding issue of either CSM or RFM is its inefficiency in capturing the spatial multiscale information by observations. A difficulty in practice is how to properly choose the characteristic length scales L_x and L_y in the CSM or the filter coefficient α in the RFM. Observational studies show that (L_x, L_y) change with location, depth, and time [14–16]. If they are too large, the analysis is too smooth and shortwave information is lost. If they are too small, the analysis lacks coherent structure in data sparse regions because the longwave information cannot be properly corrected. Thus, in the past it has been thought that the characteristic length scales (L_x, L_y) in the CSM or the filter coefficient α in the RFM is responsible for the unsatisfactory analysis in the 3DVAR.

To avoid empirically or statistically setting the characteristic length scales and to correctly minimize the longwave and shortwave errors in turn, a sequential 3DVAR (S3DVAR) method was developed [17] to assimilate sea surface temperature (SST) in a global ocean model [18]. The S3DVAR method is simply composed of a series of 3DVars, each of which uses recursive filters with different filter coefficients. These 3DVars sweep through all resolvable scales by observational networks from longwaves to shortwaves. In addition, a multigrid data assimilation scheme was also introduced to extract the resolvable information from longwave to shortwave in an observational system [19]. Recently, a sequential variational approach based on the multigrid data assimilation method was proposed to accurately retrieve the multiscale information from available observation systems [20].

Since the matrix B is treated as the Gaussian type in the CSM and modeled as the diffusion process (or Gaussian filtering process) in the RFM, the spread of the information from the analysis point to the entire region is interpreted as the diffusion phenomenon [21]. The diffusion filter (DF) was developed on the base of the Gaussian diffusion process and therefore can be used directly to model B . Several spatial multiscale variational analysis schemes, based on the modification to the standard DF scheme, are proposed in this study. As a pilot study, one of the spatial multiscale variational analysis schemes, the gradient DF (GDF), is used to assimilate SST observations into an intermediate coupled model within a perfect ‘‘twin’’ experiment framework.

The paper is organized as follows. The methodology of the standard DF scheme is described in Section 2. Several spatial multiscale DF schemes are presented in Section 3. In Sections 4 and 5, simple observing/assimilation system simulation experiments and global SST simulation with an intermediate coupled atmosphere-ocean-land model are conducted to evaluate one of the new DF schemes, that is, the gradient DF (GDF), on the model estimation and forecast. The conclusions are summarized in Section 6.

2. Diffusion Filter

The DF is in fact a Gaussian filter. Given the following initial value problem for one-dimensional diffusion equation

$$\begin{aligned} \frac{\partial u}{\partial t} &= a \frac{\partial^2 u}{\partial x^2}, \\ u &= w(x), \\ t &= 0, \end{aligned} \quad (7)$$

where $a > 0$ is the diffusion coefficient, assumed to be constant. Its solution can be formulated by the convolution of $w(x)$ with a Gaussian kernel $G(x, t)$:

$$u(x, t) = w(x) * G(x, t), \quad (8)$$

where $(*)$ indicates convolution, $G(x, t) = (1/\sqrt{2\pi\sigma})e^{-x^2/2\sigma^2}$, $\sigma = \sqrt{2at}$. That is, $u(x, t)$ is equivalent to applying a Gaussian filter on initial value $w(x)$. The second moment of the filter kernel is $\sigma^2 = 2at$, which characterizes the intrinsic spatial

scale. And σ^2 is only determined by diffusion coefficient a when “time” duration t is set to be constant, which implies that the larger the value of a is, the lower the frequency information of $w(x)$ would be acquired by $u(x, t)$.

Generally, in a two-dimensional finite domain, the diffusion model can be written by

$$\begin{aligned} \frac{\partial u}{\partial t} &= a \frac{\partial^2 u}{\partial x^2} + b \frac{\partial^2 u}{\partial y^2} \quad (x, y) \in \Omega, \quad t \in (0, S], \\ u &= w(x, y) \quad (x, y) \in \bar{\Omega}, \quad t = 0, \\ \frac{\partial u}{\partial n} &= 0 \quad (x, y) \in \Gamma, \end{aligned} \quad (9)$$

where $\bar{\Omega} = [0, D] \times [0, H]$, $\Omega = \bar{\Omega} \setminus \Gamma$ is the interior domain of $\bar{\Omega}$, Γ is the boundary of $\bar{\Omega}$, n is the outer normal direction of Γ , and a and b are the diffusion coefficients in x and y directions, respectively.

If $u^S(w)$ denotes $u(w)|_{t=S}$, the cost function (5) then becomes

$$\begin{aligned} J(w) &= \frac{1}{2} w^T u^S(w) \\ &+ \frac{1}{2} (Hu^S(w) - d)^T R^{-1} (Hu^S(w) - d). \end{aligned} \quad (10)$$

Now the analysis is converted to the problem of optimizing the initial value of the diffusion equation (9). To do so, we need the gradient of the cost function, which can be derived by using adjoint methods, just as four-dimensional variational (4DVAR) data assimilation usually does.

For convenience of illustration, a continuous adjoint system is considered and J_b is omitted. It is also assumed that the observations are located at analysis points and H is the identity matrix. Then the adjoint of the tangential linear model of (9) takes the following form:

$$\begin{aligned} -\frac{\partial R}{\partial t} - a \frac{\partial^2 R}{\partial x^2} - b \frac{\partial^2 R}{\partial y^2} &= f \quad (x, z) \in \Omega, \quad 0 < t \leq S, \\ R(x, y, S) &= 0, \quad (x, z) \in \bar{\Omega}, \\ \frac{\partial R}{\partial n} &= 0 \quad (x, y) \in \Gamma, \end{aligned} \quad (11)$$

where

$$f = \begin{cases} d_{\text{res}}(w) = d - u^S(w) & t = S, \\ 0 & t < S. \end{cases} \quad (12)$$

Note that $d_{\text{res}}(w)$ is the observation residue, which characterizes the remaining observational signals after the abstracted information at current solution w , $u^S(w)$, has been removed from observations d , and $d_{\text{res}}(w)$ is set to be zero at the grid points with no observations.

The gradient of J with respect to w is $g(w) = -R^0(w)$, where $R^0(w)$ is the initial value of the adjoint variables. Once the adjoint model is available, the analysis can be performed in the following steps.

- (1) Choose an appropriate diffusion coefficient a ; give the initial guess of w ($w = 0$, for instance).
- (2) Integrate the diffusion model (9) from “time” $t = 0$ to S to obtain $u^S(w)$.
- (3) Calculate f according to (12).
- (4) Integrate the adjoint model (11) from “time” $t = S$ to 0 to obtain $R^0(w)$; then the gradient $g(w)$ of the cost function J is $-R^0(w)$.
- (5) Use descent algorithms to adjust w .
- (6) Loop from step (2) until the convergence criterion is met.

Use of DF for determining the matrix B is called the DF method (DFM), which has the same computation loads as the RFM if the ADI difference scheme (or the other operator splitting scheme; see Appendix) is applied to calculate the diffusion equation (9). The diffusion filter scheme has the same problem as the recursive filter scheme in extracting observational information. As the extent of spatial dispersion is only determined by diffusion coefficient a when “time” duration t is set to be constant, if a is large, the shortwave information will be lost. Conversely, if a is small, the longwave information will not be properly captured. Obviously, the diffusion coefficient a plays the same role as the filter coefficient α does in the recursive filter scheme.

3. Spatial Multiscale Diffusion Filters

To retrieve longwave information over the whole domain and shortwave information over data-dense regions, three spatial multiscale variational analysis schemes, based on the diffusion filter, are proposed.

3.1. Sequential Diffusion Filter (SDF). The sequential diffusion filter (SDF) scheme is similar to the S3DVar method derived by Xie et al. [17]. The SDF scheme uses a sequence of 3DVars to obtain the final estimation to retrieve information from all wavelengths from long- to shortwaves in turn. The matrix B is modeled by applying the diffusion filter sequentially in x and y direction, respectively. SDF begins its sequence with a big value of the diffusion coefficient a ; then an initial estimation is obtained through analyzing the observed data. After that, a S3DVar is solved using the diffusion filter with a smaller a than before. For the S3DVars, observations to be assimilated are produced by subtracting the previously analyzed values from the observations assimilated by the previous 3DVar until the diffusion coefficient a is small enough. The final estimation is the summation of all the previous 3DVar analyses based on the diffusion filter.

From the above description, it is noted that the SDF scheme is a simple extension of the DF, in which information is retrieved step by step from long- to shortwaves. During the process of the SDF, B is changed gradually with the different diffusion coefficient a and thus becomes flow dependent and anisotropic following the multiscale information of the observation.

3.2. *Adaptive Diffusion Filter (ADF)*. Due to the introduction of the heat diffusion equation, the gradient of the cost function with respect to the state variables can be obtained using the adjoint method with 4DVar. In general, the diffusion coefficients $a(x, y)$ and $b(x, y)$ are not constants but are space dependent. Therefore, it is possible to optimize not only the state variables but also the diffusion coefficients using 4DVar. State variables and diffusion coefficients are used together as control variables, so values of $a(x, y)$ and $b(x, y)$ will change adaptively according to the distribution of observations.

Set $\overline{I}_{h_1}, \overline{I}_{h_2}, \overline{I}_\tau$ as

$$\begin{aligned}\overline{I}_{h_1} &= \left\{ x_i = ih_1 \mid i = 0, 1, \dots, I, h_1 = \frac{D}{I} \right\}, \\ \overline{I}_{h_2} &= \left\{ y_j = jh_2 \mid j = 0, 1, \dots, J, h_2 = \frac{H}{J} \right\}, \\ \overline{I}_\tau &= \left\{ t_n = n\tau \mid n = 0, 1, \dots, N, \tau = \frac{S}{N} \right\}, \\ \overline{\Omega}_h &= \overline{I}_{h_1} \times \overline{I}_{h_2}.\end{aligned}\quad (13)$$

The cost function is transferred to the following form:

$$\begin{aligned}J(w, a, b) &= \frac{1}{2} \sum_{i=1}^{I-1} \sum_{j=1}^{J-1} w_{i,j}^2 \\ &+ \frac{1}{2} \sum_{m=1}^M \left\{ p^{(m)} \left[\sum_{i=1}^{I-1} \sum_{j=1}^{J-1} (q_{i,j}^{(m)} u_{i,j}^N) - d^{(m)} \right]^2 \right\},\end{aligned}\quad (14)$$

where M is the number of observations and $q_{i,j}^{(m)}$ is the interpolation coefficient of the grid point (i, j) with respect to the m th observation. $p^{(m)}$ is the m th element of the diagonal matrix R^{-1} . For calculating the gradients of the cost function J with respect to w, a, b in (12), the discrete adjoint models of (A.1)–(A.11) should be deduced firstly according to the Lagrange multiplier method,

$$\begin{aligned}\frac{R_{i,j}^n - R_{i,j}^{n-1/2}}{\tau/2} + \Delta_y (b_{i,j} \overline{\Delta}_y (R_{i,j}^n + R_{i,j}^{n-1/2})) &= f, \\ n \in [1, N]; i \in [1, I-1]; j \in [1, J-1], \\ \frac{R_{i,j}^{n+1/2} - R_{i,j}^n}{\tau/2} + \Delta_x (a_{i,j} \overline{\Delta}_x (R_{i,j}^{n+1/2} + R_{i,j}^n)) &= 0, \\ n \in [0, N-1]; i \in [1, I-1]; j \in [1, J-1],\end{aligned}$$

$$\begin{aligned}R_{i,j}^N &= 0, \\ i \in [0, I]; j \in [0, J], \\ \Delta_x R_{0,j}^n &= 0, \\ \overline{\Delta}_x R_{I,j}^n &= 0, \\ \Delta_y R_{i,0}^n &= 0, \\ \overline{\Delta}_y R_{i,J}^n &= 0, \\ n \in [0, N-1], \\ \Delta_x R_{0,j}^{n+1/2} &= 0, \\ \overline{\Delta}_x R_{I,j}^{n+1/2} &= 0, \\ \Delta_y R_{i,0}^{n+1/2} &= 0, \\ \overline{\Delta}_y R_{i,J}^{n+1/2} &= 0, \\ n \in [0, N-1],\end{aligned}\quad (15)$$

where

$$f = \begin{cases} 2 \sum_{m=1}^M \left\{ p^{(m)} q_{i,j}^{(m)} \left[\sum_{i=1}^{I-1} \sum_{j=1}^{J-1} (q_{i,j}^{(m)} u_{i,j}^N) - d^{(m)} \right] \right\} & n = N, \\ 0 & n < N. \end{cases}\quad (16)$$

The gradients of the cost function J with respect to w, a, b can be expressed as follows:

$$\begin{aligned}\frac{\partial J}{\partial w_{i,j}} &= w_{i,j} - \frac{R_{i,j}^0}{\tau} - \frac{1}{2} \Delta_y (b_{i,j} \overline{\Delta}_y R_{i,j}^0), \\ \frac{\partial J}{\partial a_{i,j}} &= \frac{1}{2} \sum_{n=1}^{N-1} [\overline{\Delta}_x u_{i,j}^{n+1/2} \cdot \overline{\Delta}_x (R_{i,j}^n + R_{i,j}^{n+1/2})], \\ \frac{\partial J}{\partial b_{i,j}} &= \frac{1}{2} \sum_{n=1}^{N-1} (\overline{\Delta}_y u_{i,j}^n \overline{\Delta}_y R_{i,j}^n + \overline{\Delta}_y u_{i,j}^{n+1} \overline{\Delta}_y R_{i,j}^{n+1/2}).\end{aligned}\quad (17)$$

The process for the state estimation with the 4DVar is outlined as follows. (a) Begin with the initial w, a, b . (b) Integrate the model equations (A.1)–(A.11) forward into a fixed time window and calculate the value of the cost function $J(w, a, b)$ using (14). (c) Integrate the adjoint model (15) backward in time and calculate the values of the gradient of the cost function with respect to the control variables ∇J using (17). (d) With the values of the cost function $J(w, a, b)$ and the gradient ∇J , use the Broyden-Fletcher-Goldfarb-Shanno (BFGS) quasi-Newton minimization algorithm to obtain the new values of the control variables, namely, the two diffusion coefficients a, b and the state variables w . (e) With the updated control variables from process (d), repeat processes (b), (c), and (d) until the convergence criterion for the minimization is satisfied.

3.3. *Gradient Diffusion Filter (GDF)*. The algorithm is a variant of the spatial multiscale recursive filter [22]. For small diffusion coefficients a, b , the gradient contains not only all the observational signals from longer to shorter wavelengths, but also a lot of erroneous signals in data sparse regions, which causes lack of coherent longwave structure in space. If this gradient is simply introduced into the minimization algorithm without careful considerations, the analysis departs far from reality. Thus, a prerequisite for the minimization algorithm used in 3DVAR is needed to extract the longwave information from the gradient and at the same time to preserve the valuable shortwave signals.

However, the longwave information implied in the gradient cannot be made best use of to construct a reasonable descent direction in general minimization algorithms. Take the steepest descent algorithm as an example, in which the descent direction is simply chosen as $-g(w)$. Suppose the initial guess of w (i.e., w_0) is equal to zero. Then at the i th iteration, the new solution $w_i = w_{i-1} + l_{i-1} * (-g(w_{i-1}))$ is obtained by using a line search algorithm to find an appropriate step size l_{i-1} . According to what have been indicated, the gradient $g(w_0)$ actually represents certain scales of observations d , and these scales will be extracted by the line search at the first iteration and incorporated into a new solution w_1 . However, if the diffusion coefficients a, b are small, the gradient $g(w_0)$ will lack coherent structure in data sparse regions though it actually carries all observational signals. And since the new solution w_1 is simply obtained along the descent direction, $-g(w_0)$, the same problem will also exist in w_1 , which indicates that the longwave information of observations d is not effectively extracted from the gradient $g(w_0)$ at the first iteration. Similarly, at the second iteration, the longwave information of the observation residue after the first iteration will not be extracted from the gradient $g(w_1)$ and incorporated into the new solution w_2 , and so on. As a consequence, in data sparse regions, the final analysis will also lose the longwave structure of observations. The same problem also exists for other minimization algorithms such as BFGS and the conjugate gradient method, for the same reason.

The GDF scheme is designed to effectively retrieve the longwave information over the whole domain and shortwave information over data-dense regions. Since the gradient carries all observational information, the main idea of this new scheme is to apply the diffusion filter on the gradient to extract the implied longwave signal. While the diffusion coefficient decreases continuously with iteration, the multiscale information, from long to short wavelengths, can be extracted successively. The algorithm is designed as follows:

- (1) Give an initial guess of w (i.e., w_0) which equals zero. Then select diffusion coefficients a, b as small ones and give a large enough value to an extra diffusion coefficient denoted as β .
- (2) Use the diffusion filter with coefficient a, b to calculate Bw in (5).
- (3) Calculate the difference between observations d and HBw , namely, the observation residue.

- (4) Calculate the gradient g of the cost function J with respect to w using the DF through the adjoint model.
- (5) Apply the diffusion filter with coefficient β on $-g$ to calculate the descent direction $E(-g)$, where E represents a positive definite operator.
- (6) Select $E(-g)$ as the descent direction, and use line search algorithm to find the step size, l ; then w is adjusted to $w = w + l * E(-g)$.
- (7) The value of β diminishes.
- (8) Loop from step (2) until the convergence criterion is met.

If the background term J_b is involved in the cost function J , the same procedure is performed except that g calculated in step (4) is the gradient of cost function J , which includes both J_b and J_o .

4. Observing/Assimilation System Simulation Experiments

Observing/assimilation system simulation experiments are performed to evaluate the spatial multiscale variational analysis. The “truth” field in these experiments is represented by an analytic temperature field defined over the area of 100°E – 110°E and 30°N – 40°N . The “truth” field of the temperature is plotted in Figure 1(b), whose high nonlinearity can be seen from Figure 1(a). The grid resolution is set to $1/8^\circ \times 1/8^\circ$, and the total numbers of the grid are 80×80 . The observational dataset is generated using the analytic solution. Observational error is simulated by adding a sample of white noise with a standard deviation of 0.2 to the “truth.” Three experiments are conducted in which different configurations of numbers of observations are employed.

4.1. *Experiment 1*. In this experiment, the number of observations is set to 2000 at first, and the observations are randomly and uniformly distributed in the whole domain, which can be seen from the black dots in Figure 1(b). In the experiment with DF, several values of the diffusion coefficient are used to verify the impacts on the analyzed field. In the experiment with GDF, the processes (1)–(8) described in Section 3.3 are conducted. The diffusion coefficients a, b are set to a small value, of 0.1, which suggests almost all the observational signals, from long to short wavelengths, can be retrieved. However, a large enough value, 1.0, is given to the extra diffusion coefficient β of the gradient at the first step. For the subsequent steps, β is reduced by 0.1 from the previous step. At the last step, β becomes 0.1, which is small enough for the case. The limited memory BFGS quasi-Newton minimization algorithm [23] is used during the minimizing procedure.

The major scales of the truth field are reconstructed by 2000 observations almost fully using the GDF (Figure 2(a)), but not well reconstructed using the DF with different diffusion coefficients (a, b): 1.0 (Figure 2(b)), 0.5 (Figure 2(c)), and 0.1 (Figure 2(d)). The small scale features begin to dominate the analyzed fields when the diffusion coefficients are reduced gradually, while the large scale signals are contaminated dramatically by an abundance of small scale features.

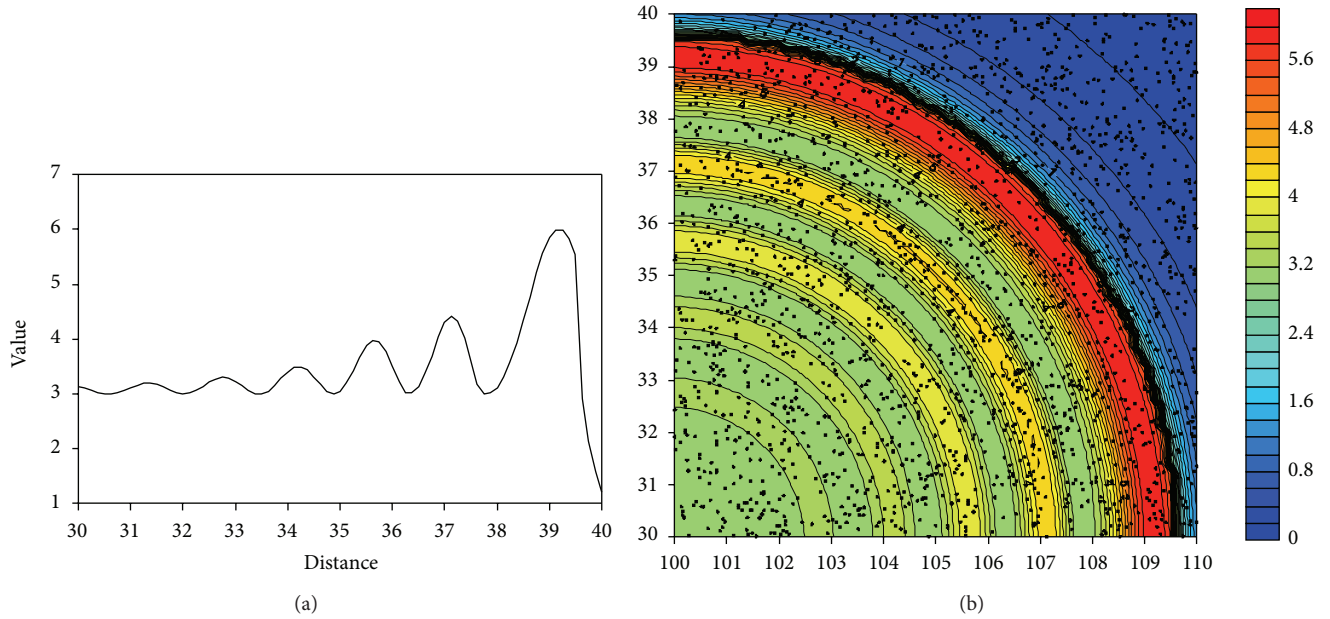


FIGURE 1: The true temperature field to be analyzed (unit: °C): (a) latitudinal variation along 100°E and (b) ichnography image. Black dots in the panel (b) show the distribution of 2000 random observations.

As He et al. [18] indicated, artificial signals can be produced during the data assimilation if the chosen diffusion coefficient cannot represent the actual scale. In contrast, the GDF can handle spatial multiscale analysis pretty well compared to the simple DF with a fixed diffusion coefficient. In addition, the GDF is easy to avoid in empirical selection of the diffusion coefficient.

Figure 3 shows the performance of GDF and DF when the number of observations decreases from 2000 to 500. The GDF (Figure 3(a)) can retrieve large scale information from observations and leave the unresolved scale as errors on top of the resolvable scales. These errors are smaller than those generated by DF with a fixed diffusion coefficient (Figure 3(b)) in the condition of the sparseness of the observations and the lack of information.

4.2. Experiment 2. The second experiment is conducted with removal of observations in the area of 103°E~107°E and 35°N~40°N (Figure 4) to further evaluate the GDF capability in retrieving the multiscale information from observations. The analyzed field of the GDF (Figure 5(a)) performs much better in the data void region than that of the DF with $(a, b) = 0.8$ (Figure 5(b)) and 0.5 (Figure 5(c)). The GDF can reconstruct the temperature field (Figure 5(a)) reasonably well despite the absence of the observations in the region as shown in Figure 4. The spatial pattern of the whole temperature field can be captured roughly according to the large scale information derived from all the observations in the whole analyzed region. However, the DF fails to reconstruct the temperature field and produces false features especially in the data void region. For example, a strong cold tongue is produced for $(a, b) = 0.8$ (Figure 5(b)), and large scale temperature field is distorted with displacement of the thermal front in the data void region for $(a, b) = 0.5$ (Figure 5(c)). Little information of

the observations can be extracted from data rich area to the data void region using DF.

Such capabilities make the GDF invaluable to get well represented values for the data void (or insufficiently covered) areas such as a typhoon-affected area during typhoon passage or the Southern Hemisphere Oceans (compared to other ocean basins). The GDF can reconstruct the analyzed field roughly according to the longwave information of the observations beyond the data void area such as typhoon-affected region or the Southern Ocean. On the other hand, both the standard DF and the traditional RF may lead to false results in the data void region, as shown in Figures 5(b)-5(c); an improper analysis is also likely to be produced, which will affect the analysis/forecast accuracy seriously.

In addition, several classical geostatistical tools, such as inverse distance to a power, triangulation with linear interpolation, and Kriging method are used to interpolate such observations (no white noise is imposed on the observations). Compared to the other two geostatistical tools, the Kriging method is able to accurately fill in the hidden information (Figures 6(a) and 6(b) versus 6(c)). However, compared with the variational method, the geostatistical tools have a limited application and cannot handle corrections between different analysis variables or physical balances and other constraints [20].

5. Global SST Assimilation Using GDF

In this section, we apply the GDF to assimilate the SST into an intermediate climate model to improve the climate representation and forecast.

5.1. Brief Description of an Intermediate Atmosphere-Ocean-Land Coupled Model. An intermediate atmosphere-ocean-land coupled model [24] is employed as the first step to

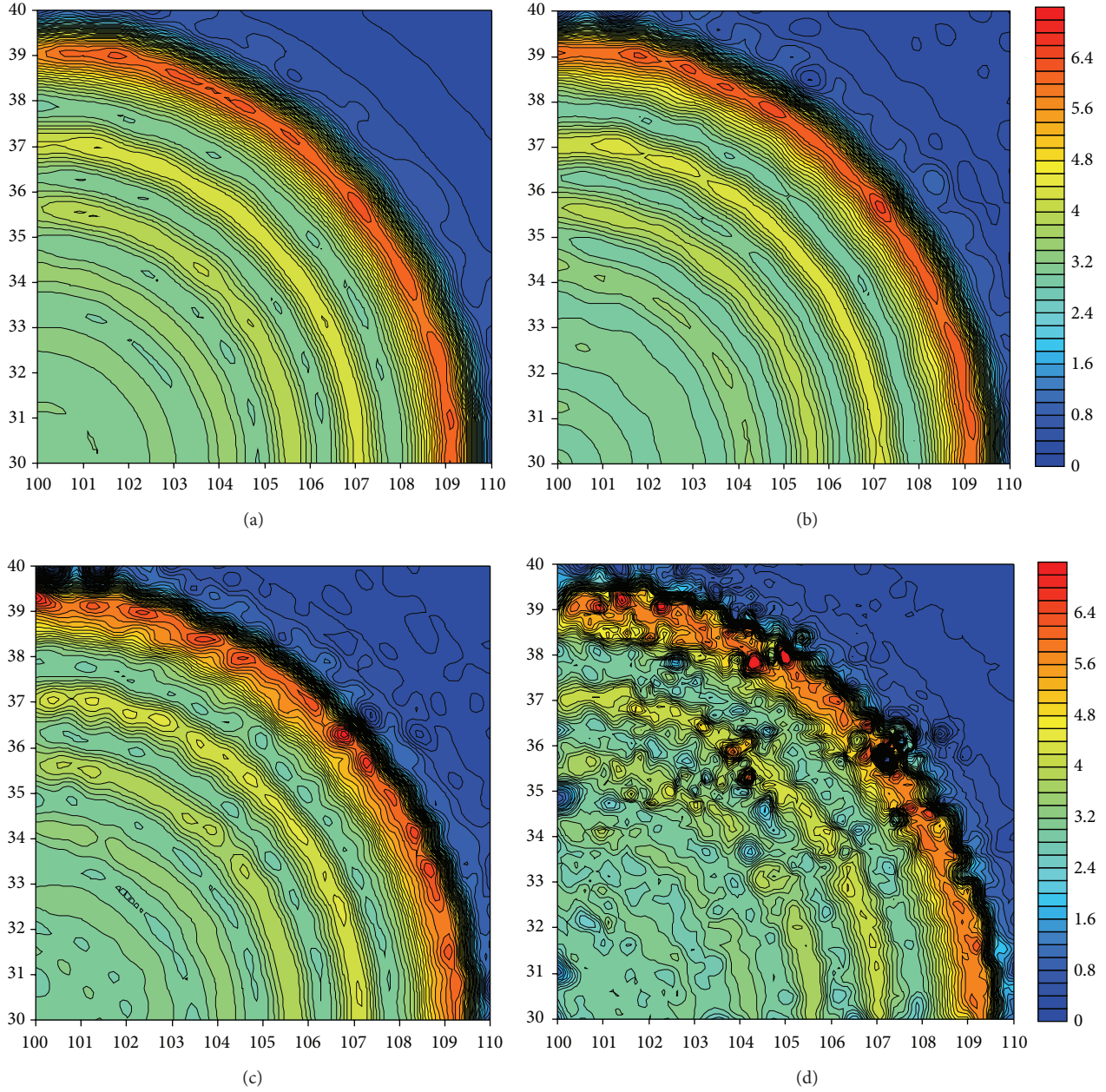


FIGURE 2: The analyzed temperature fields (unit: °C) using (a) GDF, (b) DF with $a, b = 1.0$, (c) DF with $a, b = 0.5$, and (d) DF with $a, b = 0.1$.

examine the GDF. Despite limitations in the representations of some basic physical processes such as the absence of ENSO dynamical mechanism, the model is of sufficient mathematical complexity for the purposes of this study. The intermediate coupled model has some successful applications in coupled data assimilation fields recently. For example, Wu et al. [25] investigated the impact of the geographic dependence of observing system on parameter estimation, and Zhang et al. [26] studied parameter optimization when the assimilation model contains biased physics within a biased assimilation experiment framework. The configuration of the model is presented here. The atmosphere is represented by

a global barotropic spectral model based on the potential vorticity conservation:

$$\frac{\partial q}{\partial t} + J(\psi, q) = \begin{cases} \lambda(T_o - \mu\psi) & \text{ocean \cdot surface} \\ \lambda(T_l - \mu\psi) & \text{land \cdot surface,} \end{cases} \quad (18)$$

where $q = \beta y + \nabla^2 \psi$, $\beta = df/dy$, f is the Coriolis parameter, y is the meridional distance from the equator (northward positive), and ψ is the geostrophic atmosphere stream function. μ is a scale factor which converts stream function to temperature. λ is the flux coefficient from the ocean (land) to the atmosphere. T_o and T_l denote SST

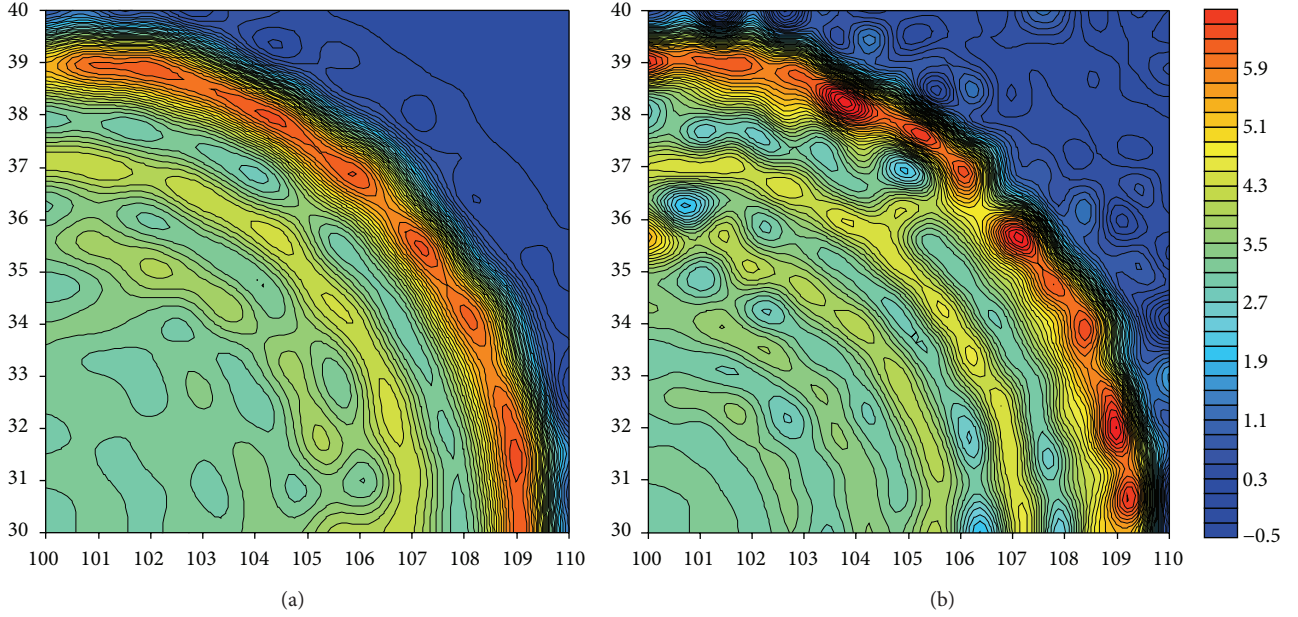


FIGURE 3: The analyzed temperature fields (unit: $^{\circ}\text{C}$) with 500 observations: analyzed fields using (a) GDF and (b) DF with $a, b = 1.0$.

and land surface temperature (LST), respectively. Wu et al. [27] used the nonlinear atmospheric model to develop a compensatory approach of the fixed localization in EnKF analysis to improve short-term weather forecasts.

The ocean is composed of a 1.5-layer baroclinic ocean with a slab mixed layer [28] as

$$\begin{aligned} \frac{\partial}{\partial t} \left(-\frac{\phi}{L_0^2} \right) + \beta \frac{\partial \phi}{\partial x} &= \gamma \nabla^2 \psi - K_q \nabla^2 \phi, \\ \frac{\partial}{\partial t} T_o + u \frac{\partial T_o}{\partial x} + v \frac{\partial T_o}{\partial y} - K_h \phi & \\ = -K_T T_o + A_T \nabla^2 T_o + s(\tau, t) + C_o (T_o - \mu \psi), & \end{aligned} \quad (19)$$

where ϕ is the oceanic stream function and $L_0^2 = g'h_0/f^2$ is the oceanic deformation radius, with g' and h_0 being the reduced gravity and mean thermocline depth. γ denotes momentum coupling coefficient between the atmosphere and ocean. K_q is the horizontal diffusive coefficient of ϕ . K_T and A_T are the damping coefficient and horizontal diffusive coefficient of T_o ; $K_h = K_T \times \kappa \times f/g'$ [29], where κ is the ratio of upwelling to damping. C_o is the flux coefficient from the atmosphere to the ocean. $s(\tau, t)$ is the solar forcing which introduces the seasonal cycle.

The evolution of land surface temperature (LST) is given by

$$m \frac{\partial}{\partial t} T_l = -K_L T_l + A_L \nabla^2 T_l + s(\tau, t) + C_l (T_l - \mu \psi), \quad (20)$$

where m represents the ratio of heat capacity between the land and the ocean mixed layer, K_L and A_L are damping and diffusive coefficients of T_l , respectively, and C_l denotes the flux coefficient from the atmosphere to the land.

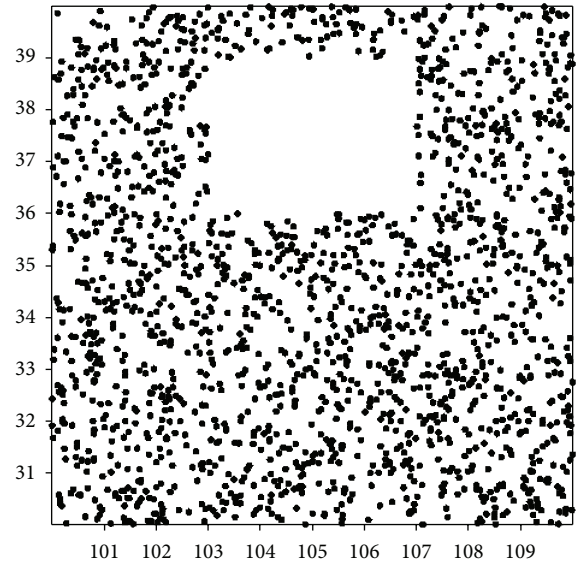


FIGURE 4: The distribution of 2000 random observations, but removal of the observations located in the range of $103^{\circ}\text{N}\sim 107^{\circ}\text{N}$ and $35^{\circ}\text{E}\sim 40^{\circ}\text{E}$.

All the three model components adopt 64×64 Gaussian grid and are forwarded by a leap frog time stepping with a half hour integration step size. There are 2287 and 1169 grid points over the ocean and land, respectively. An Asselin-Robert time filter [30, 31] is introduced to damp spurious computational modes in the leap frog time integration. Default values of all parameters are listed in Table 1 in Wu et al. [24].

Starting from initial conditions $Z0 = (\psi^0, \phi^0, T_o^0, T_l^0)$, where ψ^0, ϕ^0, T_o^0 , and T_l^0 are zonal mean values of corresponding climatological fields, the coupled model is run for 60 years

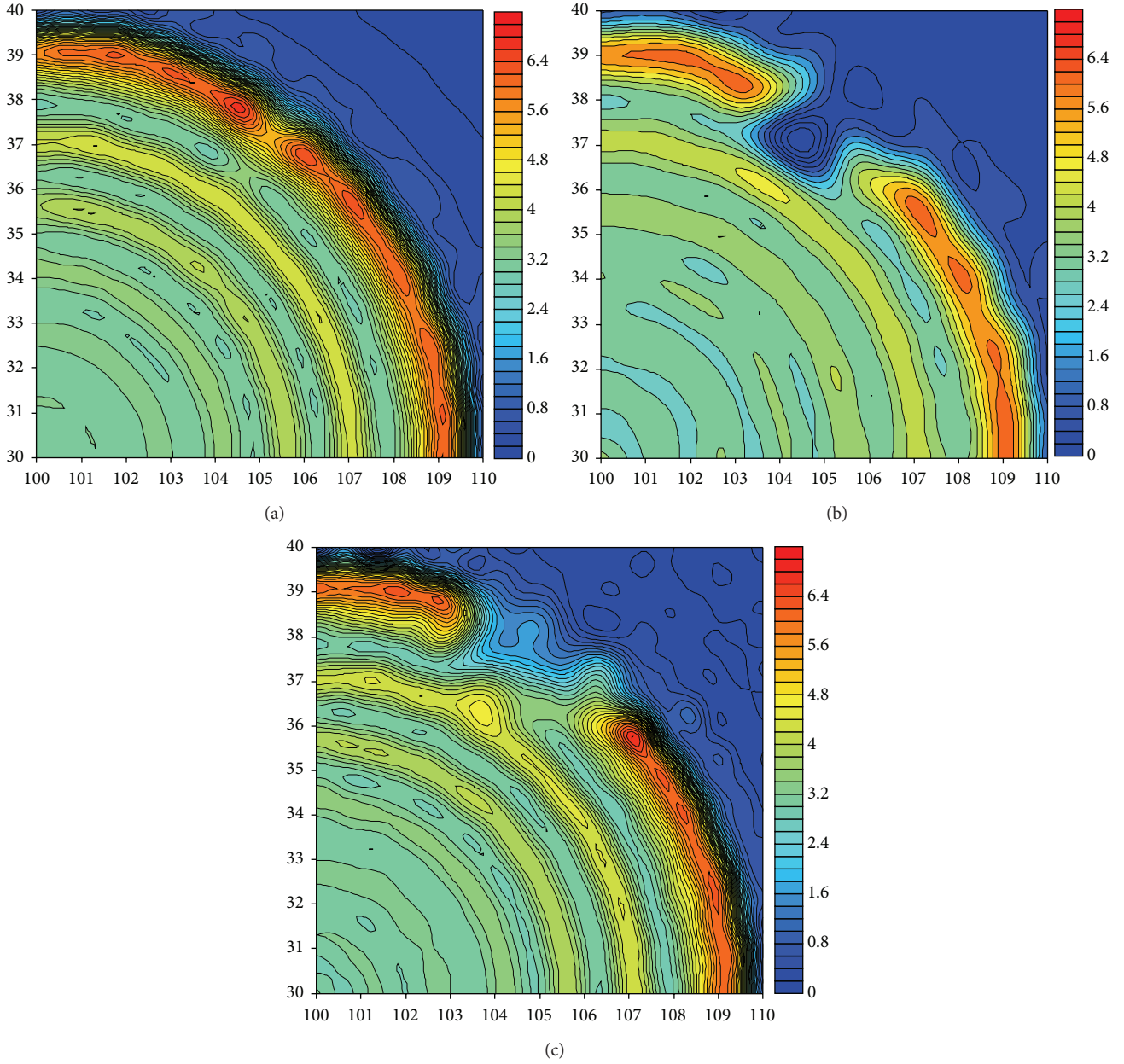


FIGURE 5: The analyzed temperature fields (unit: °C) using (a) GDF, (b) DF with $a, b = 0.8$, (c) DF with $a, b = 0.5$.

to generate the model states $Z1 = (\psi^1, \phi^1, T_o^1, T_l^1)$. The last 10 years' model states ($Z1$) are used as the "truth" fields. Figure 7 shows the annual mean of ψ (Figure 7(a)), ϕ (Figure 7(b)), T_o and T_l (Figure 7(c)), where the associated wave trains in the ψ field are observed. For ϕ , one can see the distinct pattern of the western boundary currents, gyre systems and the Antarctic Circumpolar Current (ACC). For T_o and T_l , reasonable temperature gradients are also produced. Note that the low temperature in tropical lands can be attributed to the linear damping of K_T in the solar forcing. The above model configuration is called the "truth" model, which has reasonable but rough representation for the basic climate characteristics of the atmosphere, land, and ocean.

5.2. Model "Bias" Arising from the Initial States. However, starting also from the same initial conditions $Z0$, the Gaussian random numbers are added to ψ^0 and ϕ^0 , with standard deviations of $10^7 \text{ m}^2\text{s}^{-1}$ (for ψ^0) and $10^5 \text{ m}^2\text{s}^{-1}$ (for ϕ^0), respectively. The coupled model is also run for 60 years to generate the model states $Z2 = (\psi^2, \phi^2, T_o^2, T_l^2)$. The last 10 years' model states are used for analysis. This model configuration is called the biased model.

The model "biases" induced by perturbed initial fields are examined. Figure 8 shows time series of the spatial averaged root mean square errors (RMSEs) of ψ , ϕ , T_o , and T_l for the assimilation model, which are calculated according to the difference in the assimilation model and the "truth" model.

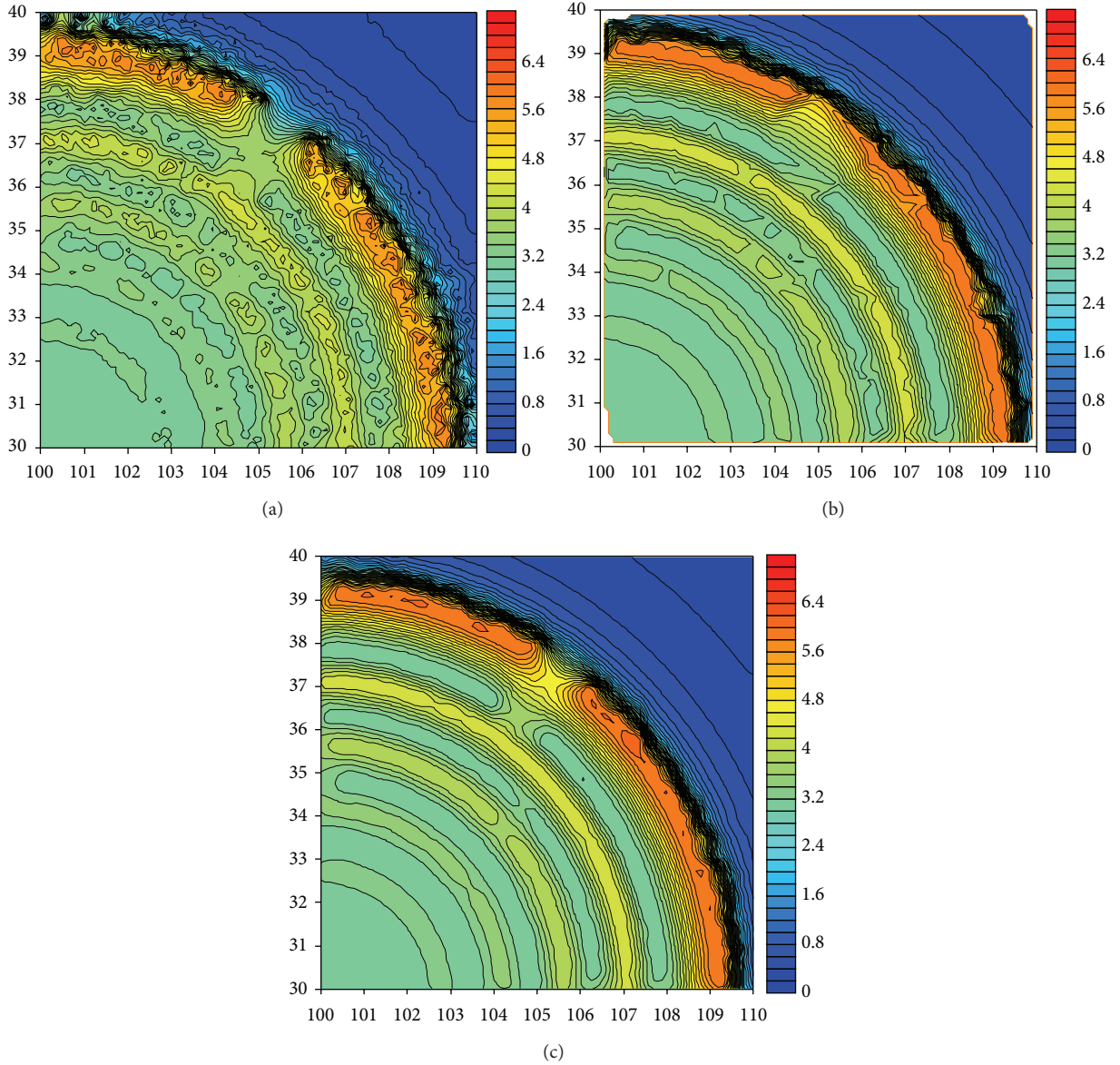


FIGURE 6: Analyzed temperature results (unit: °C) from classical geostatistical tools such as (a) inverse distance to a power, (b) triangulation with linear interpolation, and (c) Kriging method.

The obvious difference about all the four components can be seen from Figure 8. The RMSE of ψ reaches about $1.6 \times 10^7 \text{ m}^2 \text{ s}^{-1}$ with a high frequent oscillation (see Figure 8(a)). In contrast, the RMSE of ϕ performs smoothly and rapidly decreases within the first year and gradually reaches a low and stable value about $10^4 \text{ m}^2 \text{ s}^{-1}$ (see Figure 8(b)). The RMSEs of T_o (Figure 8(c)) and T_l (Figure 8(d)) increase rapidly in the first year, which are generated by the initially perturbed ψ^0 and ϕ^0 through the coupling. High frequency oscillation is noted in the time series of the RMSE of T_l , which indicates that the land surface temperature T_l is dominated by the atmospheric motion (ψ). However, time series of the RMSE of T_o is much smoother than that of T_l , indicating that T_o is modulated by the oceanic motion (ϕ).

The spatial distribution of RMSE of T_o for the biased model (Figure 9) shows a notable bias in the ACC region of the Southern Ocean with a maximum value over 15 K near the southern tip of Africa. Besides, obvious biases also exist in the west boundaries of the ocean in the subtropical regions.

5.3. Twin Experiment Design. In this section, with the intermediate model and DF/GDF data assimilation scheme described above, a perfect twin experiment framework is designed with the assumption that the errors of initial model states are the only source of assimilation model biases. Starting from the model states, Z1, described in Section 5.1, the “truth” model is run for 1 year to generate the time series of the “truth” states. Only synthetic observations of T_o

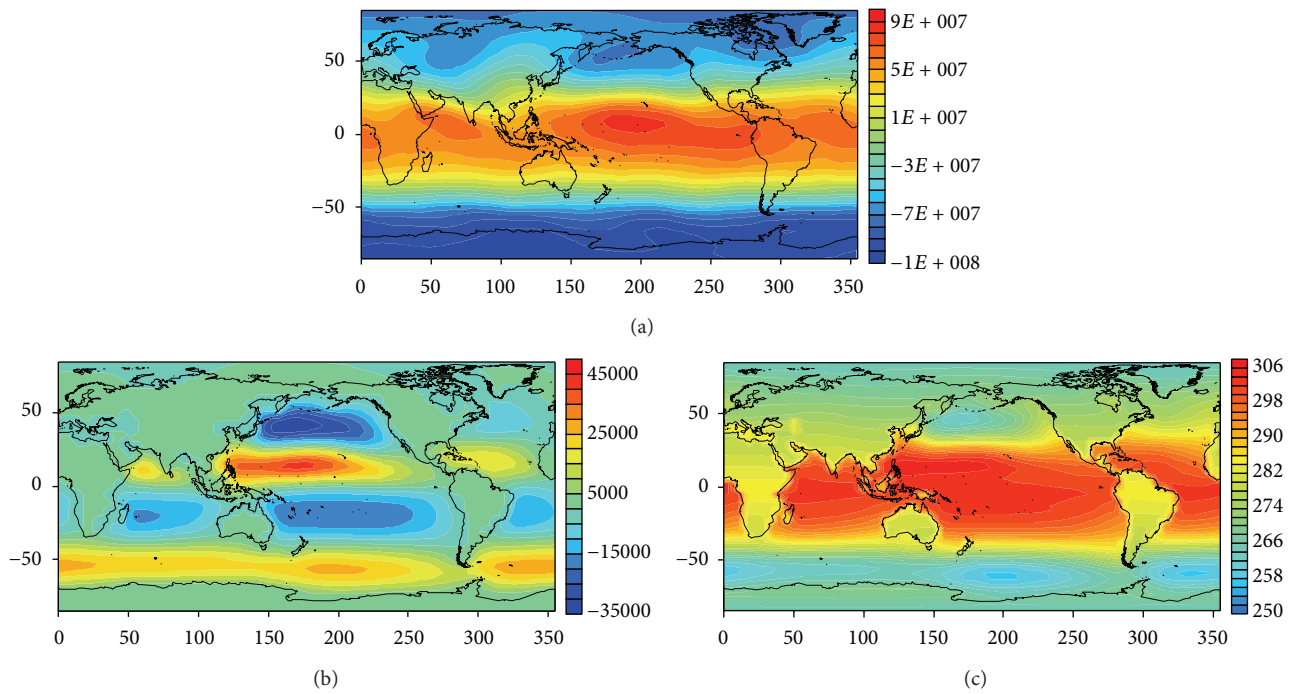


FIGURE 7: Annual mean of (a) atmospheric stream function (unit: m^2s^{-1}), (b) oceanic stream function (unit: m^2s^{-1}), and (c) sea surface temperature and land surface temperature (unit: K).

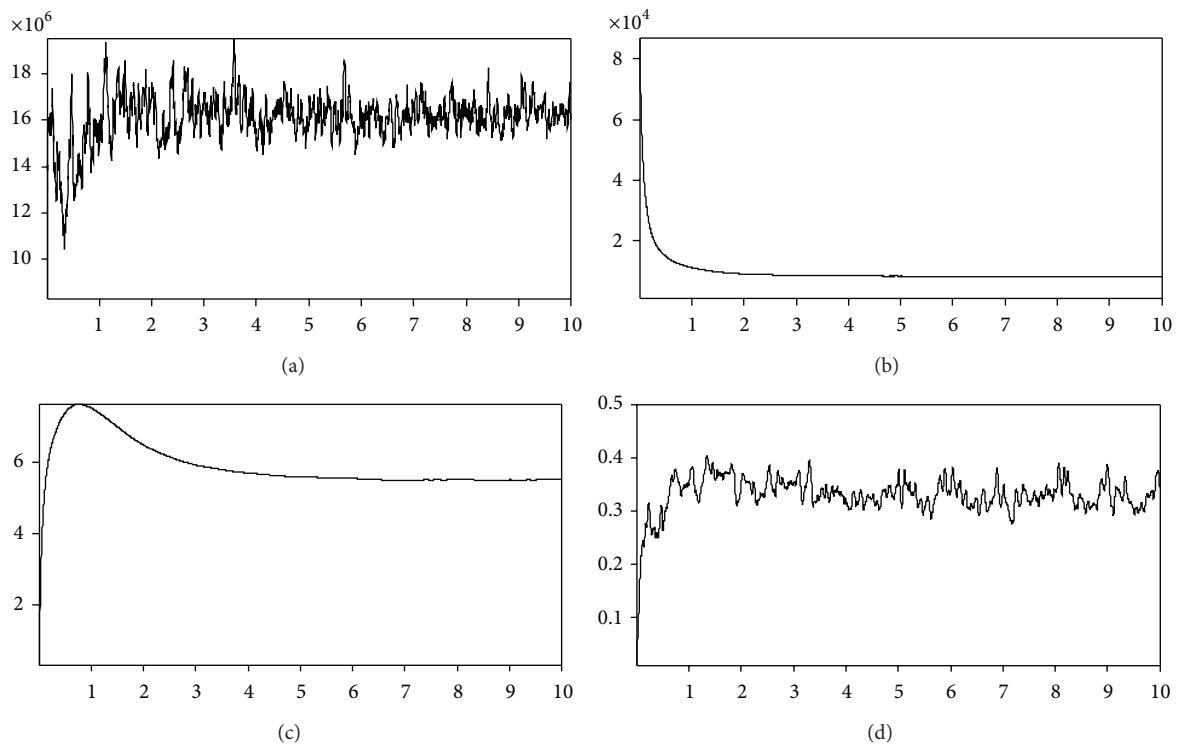


FIGURE 8: Time series of RMSEs of (a) atmospheric stream function, (b) oceanic stream function, (c) sea surface temperature, and (d) land surface temperature for the assimilation model.

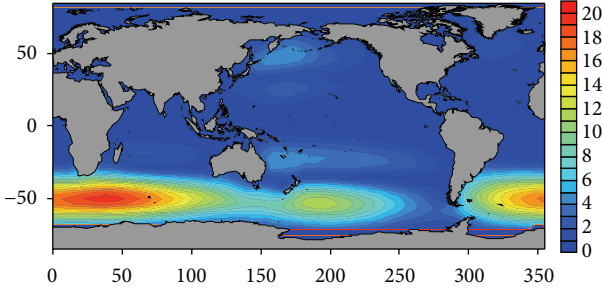


FIGURE 9: The spatial distribution of RMSE of sea surface temperature for the biased model.

are produced through sampling the “truth” states at specific observational frequencies. A Gaussian white noise is added for simulating observational errors. The standard deviations of observational errors are 0.5°C for T_o . The sampling period is 24 hours. The “observation” locations of T_o are global randomly distributed with the same density of the ocean model grid points.

The biased model uses the biased initial fields depicted in Section 5.2. Starting from the biased model states, Z2, the experiment E.GDF consists on assimilating observations into model states using the GDF scheme. In comparison, the experiment E_DF is carried out, where the standard DF scheme is used with the diffusion coefficients $a, b = 0.5$. In addition, a control run without any observational constraint, called CTRL, serves as a reference for the evaluation of assimilation experiments.

5.4. Impact of the GDF on the Estimate of the States. The performance of GDF is investigated. Figures 10(a)–10(d) show time series of RMSEs of ψ , ϕ , T_o , and T_l for the CTRL (solid line) and the GDF (dash line). Compared to the CTRL (solid line in Figure 10(c)), T_o of the GDF has significant improvement (dash line in Figure 10(c)), in which the RMSE decreases to approximately 0.5 K . Figure 11 presents the spatial distributions of RMSEs of T_o using GDF. The RMSE of T_o over ocean is obviously reduced compared with that of the CTRL (see Figure 9), especially in the Southern Ocean, the subtropical and the subpolar regions. In particular, the reduction of RMSE is much significant in the ACC region, in which the RMSE decreases from above 15 K to below 3 K .

Unlike the RMSEs of T_o , there is no direct observations constraint for ψ , ϕ , and T_l ; therefore, their RMSEs decrease gradually owing to the effect of the coupling. The RMSEs of ψ for the GDF are reduced significantly from about $1.6 \times 10^7\text{ m}^2\text{s}^{-1}$ to about $1.1 \times 10^7\text{ m}^2\text{s}^{-1}$ with a high frequent oscillation (see Figure 10(a)). The ϕ in GDF is also improved significantly comparing to CTRL (solid versus dash lines in Figure 10(b)), whose RMSE decreases gradually and smoothly, but it does not reach a stable value within the experimental period, indicating that the low frequency signal needs a much longer time to reach equilibrium compared to the high frequency signal. For T_l , the GDF reduces the error by approximately 60%. Note that T_o has no direct effect on T_l , which can be realized according to the framework

of the coupling model (see (18)–(20)). Instead, T_o affects T_l indirectly via ψ . The improved T_o by the observational constraint increases the quality of ψ over land through the dynamical constraint. Then, the improved ψ ameliorates T_l through the process of the external forcing.

5.5. Removal of Observational Data in the Southern Ocean. In the real ocean, the observations are scarce in the southern polar region. Therefore, another set of data assimilation experiment is carried out, which is the same as the experiment in Section 5.3, but in which the observations, south of 50°S and $50^{\circ}\text{E}\sim 300^{\circ}\text{E}$, are removed completely.

Figures 12(a)–12(d) show the time series of RMSEs of ψ , ϕ , T_o , and T_l with the GDF (black line) and the standard DF with $a, b = 0.5$ (red line). The RMSE of T_o for the DF increases persistently during the experimental period, while the RMSE for the GDF begins to descend after 0.2 years and converges after 0.6 years (Figure 12(c)). When the diffusion coefficients are set to different values in the DF experiment (e.g., $a, b = 0.2, 0.8, 1.0$), similar results as the ones presented in Figure 12 are obtained. Results indicate that DF cannot correct the model bias in the data void region. However, the GDF is able to mitigate the model bias to some degree through extracting the spatial multiscale information from the available observations to the data void region. Figure 13 presents the spatial distributions of RMSEs of T_o for the GDF and the standard DF with $a, b = 0.5$. Compared to the DF, the GDF produces a significant improvement within the data void region in the Southern Ocean (compare Figures 13(a) and 13(b)).

The RMSE of ψ in the GDF is not always smaller than the DF owing to the strong nonlinear nature of the high frequent atmosphere (red line versus black line in Figure 12(a)). In contrast, the evolution of T_l in the model (see (20)) is rather simple (i.e., linear); the RMSE in the GDF is almost always smaller than that for the DF (red line versus black line in Figure 12(d)). For the low frequent component ϕ (see Figure 12(b)), the RMSEs of both the GDF and the DF decrease gradually, indicating that the effect of the data void region on the low frequent signal is small in the given time scale.

5.6. Impact of the GDF on the Forecast. From a more practical point of view, the role of the GDF should be judged from the model forecast. In this section, two forecast experiments without any observational constraint are integrated for 1 year, respectively, starting from the final analyzed states of the above two assimilation experiments (the GDF and the DF).

Figures 14(a)–14(d) show the forecasted time series of RMSEs of ψ , ϕ , T_o , and T_l for the GDF (black line) and the DF with $a, b = 0.5$ (red line). The GDF performs much better than the DF in 1 year’s forecast lead time of all the state variables such as the high frequent component ψ and the low frequent component ϕ (black versus red curves in Figures 14(a) and 14(b)). It is interesting that the forecasted RMSE of ϕ still decreases inertially owing to the longer adjustment time of the low frequent signal, but whose trend becomes mildly with the increase of the forecasted lead time. For

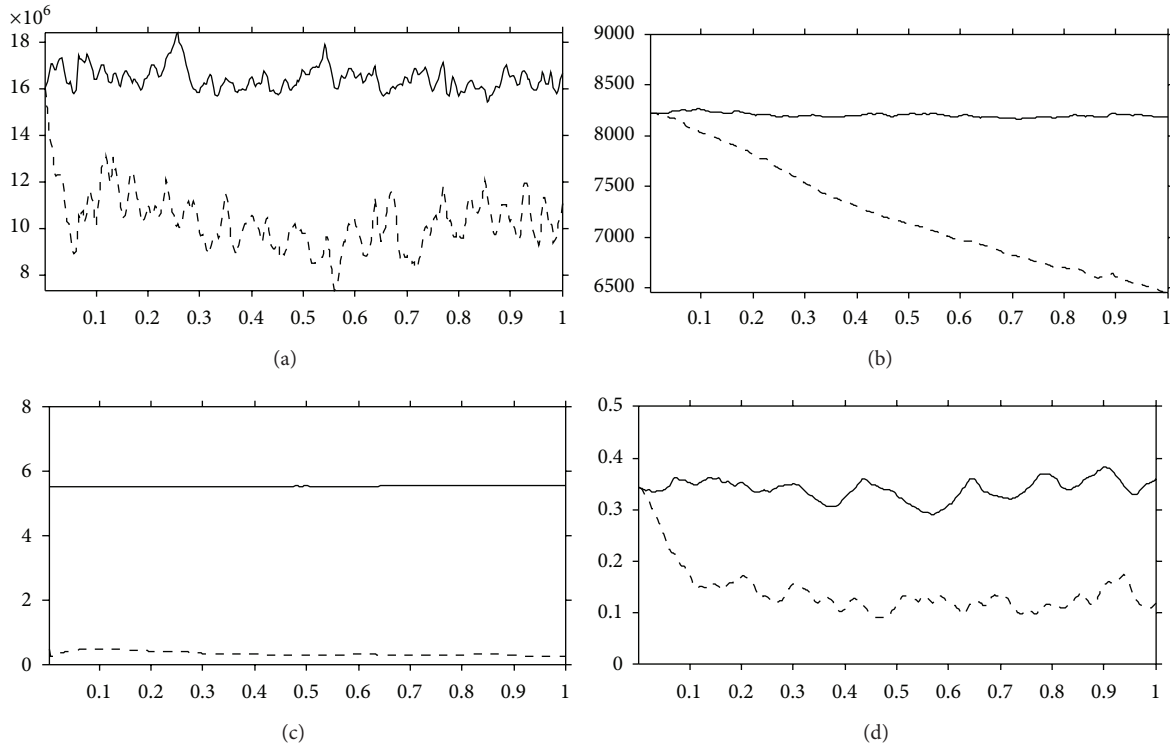


FIGURE 10: Time series of RMSEs of (a) atmospheric stream function, (b) oceanic stream function, (c) sea surface temperature, and (d) land surface temperature for CTRL (solid curve) and GDF (dashed curve).

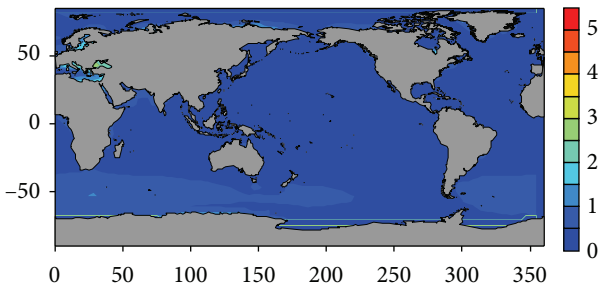


FIGURE 11: The spatial distribution of RMSE of sea surface temperature using GDF.

T_o , because of the absence of the observational constraint, the forecasted RMSE has an obvious positive trend (see Figure 14(c)), indicating that the forecasted state is gradually drifting away from the truth. Anyway, the GDF retains its superiority relative to the DF during the entire forecasted lead time. The forecasted RMSEs of T_l have similar patterns to those of T_o (see Figure 14(d)).

6. Conclusions and Discussions

In this study, the diffusion filter (DF) is introduced as a concrete implementation of the 3DVAR scheme. Similar to the recursive filter (RF), the outstanding issue of DF is its

inefficiency in capturing the spatial multiscale information resolved by observations. Therefore, several spatial multiscale variational analysis schemes based on the DF are proposed to retrieve the spatial multiscale information from longwaves to shortwaves. As one of the spatial multiscale variational analysis schemes, the gradient diffusion filter (GDF) scheme is proposed and verified through a set of observing/assimilation system simulation experiments, where the “truth” field of the sea surface temperature is represented by a high nonlinear analytic function in a given sea region, and the observations are sampled randomly and uniformly in the whole domain. Results of the assimilation experiments indicate that the GDF has noticeable advantages over the standard RF and DF schemes, especially in the data void region. The GDF can retrieve the longwave information over the whole domain and the shortwave information over data-dense regions.

After that, a perfect twin experiment framework is designed to study the effect of the GDF on the state estimation based on an intermediate atmosphere-ocean-land coupled model. In this framework, the assimilation model is subject to “biased” initial fields from the “truth” model. The RMSE of the sea surface temperature can be reduced significantly through the observational constraint via the GDF. At the same time, the RMSEs of the other model components, such as the land surface temperature and the atmospheric and oceanic stream functions can also be mitigated by the dynamical constraint and the external constraint through the ocean-atmosphere-land coupled process. For simulating the real

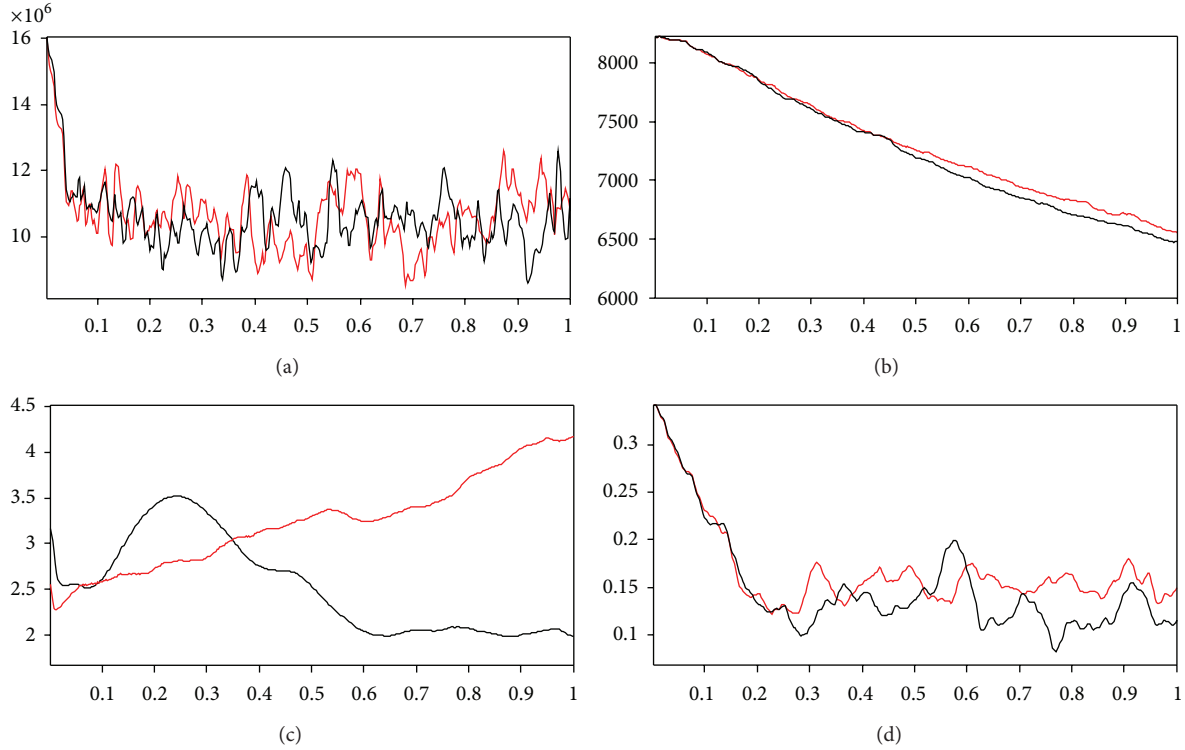


FIGURE 12: Time series of RMSEs of (a) atmospheric stream function, (b) oceanic stream function, (c) sea surface temperature, and (d) land surface temperature for GDF (black curve) and DF with $a, b = 0.5$ (red curve).

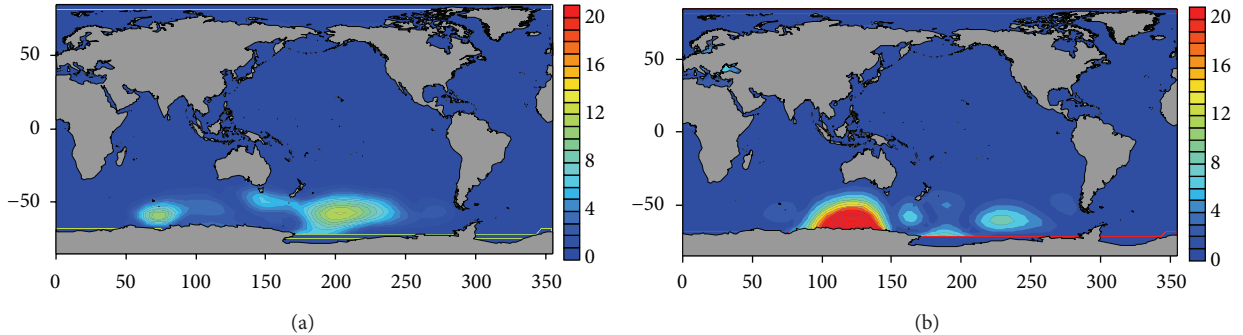


FIGURE 13: The spatial distributions of RMSEs of SST using (a) GDF and (b) DF with $a, b = 0.5$.

observational networks in the world ocean roughly, the observations locating in the Southern Ocean are removed to investigate the role of the GDF in retrieving the multiscale information from observations. While the standard DF hardly removes the model bias in the data void region, the GDF may mitigate the model bias to some degree through extracting the multiscale information from the observations beyond the data void region. In addition, the higher forecast skill can also be obtained through the better initial state fields produced by the GDF.

It should be noted that the background term J_b is omitted in the above assimilation experiments. When high-density, accurate, resolvable information is available in observational datasets, it is much essential to extract the multiscale information from the observations with deterministic data assimilation approaches, as this study does. High-quality

background fields can be obtained firstly when deterministic data assimilation approaches are carried out. Next, the statistical data assimilation approaches, such as traditional 3DVar and 4Dvar, can be used to treat observations as random variables, in which J_b will be included to extract the information that cannot be resolved by the observation networks.

In spite of the promising results produced by the GDF in the intermediate climate model, much work is needed to explore the impact of the multiscale variational analysis schemes on the state estimation and forecast in real applications using general circulation models (GCMs). In addition, other spatial multiscale variational analysis schemes based on the DF, such as the adaptive diffusion filter (ADF) scheme, should also be studied to further improve the convergence speed and accuracy.

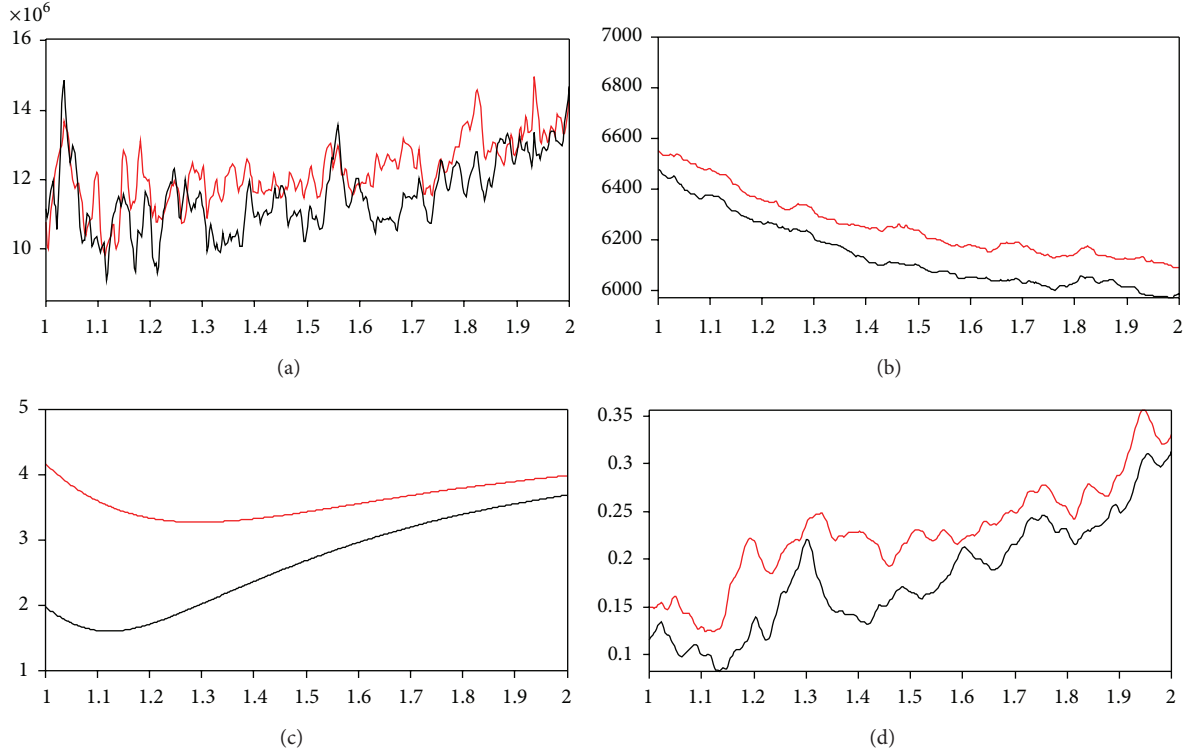


FIGURE 14: Forecasted time series of RMSEs of (a) atmospheric stream function, (b) oceanic stream function, (c) sea surface temperature, and (d) land surface temperature for GDF (black curve) and DF with $a, b = 0.5$ (red curve).

Appendix

Equivalence between the RF and DF Methods

Using ADI scheme, (9) can be discretized as follows:

$$\begin{aligned} \frac{u_{i,j}^{n+1/2} - u_{i,j}^n}{\tau/2} - \Delta_x (a_{i,j} \bar{\Delta}_x u_{i,j}^{n+1/2}) \\ - \Delta_y (b_{i,j} \bar{\Delta}_y u_{i,j}^n) = 0, \end{aligned} \quad (\text{A.1})$$

$$n \in [0, N-1]; i \in [1, I-1]; j \in [1, J-1],$$

$$\begin{aligned} \frac{u_{i,j}^{n+1} - u_{i,j}^{n+1/2}}{\tau/2} - \Delta_x (a_{i,j} \bar{\Delta}_x u_{i,j}^{n+1/2}) \\ - \Delta_y (b_{i,j} \bar{\Delta}_y u_{i,j}^{n+1}) = 0, \end{aligned} \quad (\text{A.2})$$

$$n \in [0, N-1]; i \in [1, I-1]; j \in [1, J-1],$$

$$u_{i,j}^0 = w_{i,j} \quad i \in [0, I]; j \in [0, J], \quad (\text{A.3})$$

$$\Delta_x u_{0,j}^n = 0, \quad (\text{A.4})$$

$$\bar{\Delta}_x u_{I,j}^n = 0, \quad (\text{A.5})$$

$$\Delta_y u_{i,0}^n = 0, \quad (\text{A.6})$$

$$\bar{\Delta}_y u_{i,J}^n = 0 \quad n \in [0, N], \quad (\text{A.7})$$

$$\Delta_x u_{0,j}^{n+1/2} = 0, \quad (\text{A.8})$$

$$\bar{\Delta}_x u_{I,j}^{n+1/2} = 0, \quad (\text{A.9})$$

$$\Delta_y u_{i,0}^{n+1/2} = 0, \quad (\text{A.10})$$

$$\bar{\Delta}_y u_{i,J}^{n+1/2} = 0 \quad n \in [0, N-1], \quad (\text{A.11})$$

where $\Delta_x, \Delta_y, \bar{\Delta}_x, \bar{\Delta}_y$ are forward and backward difference operator in x and y direction, respectively. τ is the time step, i, j and I, J are grid index and grid numbers in x and y direction, respectively, and n and N are the time index and the total time step numbers. The common tridiagonal matrix algorithm (TDMA) can be used to solve both (A.1) and (A.2). For example, the tridiagonal equation (A.2) in the j th row can be written as follows:

$$Au = \gamma, \quad (\text{A.12})$$

where

$$A = \begin{bmatrix} m_1 & l_1 & \cdots & 0 \\ l_1 & m_2 & l_2 & \vdots \\ & l_2 & m_3 & \\ \vdots & & \ddots & \ddots & l_{I-2} \\ 0 & \cdots & l_{I-2} & m_{I-1} \end{bmatrix},$$

$$u = \begin{bmatrix} u_{1,j}^{n+1/2} \\ u_{2,j}^{n+1/2} \\ u_{3,j}^{n+1/2} \\ \vdots \\ u_{I-1,j}^{n+1/2} \end{bmatrix},$$

$$\gamma = \begin{bmatrix} \gamma_1 \\ \gamma_2 \\ \gamma_3 \\ \vdots \\ \gamma_{I-1} \end{bmatrix},$$

$$l_i = -\frac{\tau}{2h_1^2} a_{i+1,j}, \quad i \in [1, I-2],$$

$$m_i = \begin{cases} 1 - l_{i-1} - l_i, & i \in [2, I-2] \\ 1 - l_1, & i = 1 \\ 1 - l_{I-2}, & i = I-1, \end{cases}$$

$$\gamma_i = u_{i,j}^n + \frac{\tau}{2} \Delta_y (b_{i,j} \bar{\Delta}_y u_{i,j}^n), \quad i \in [1, I-1].$$

(A.13)

It is easily testified that A is a positive definite and symmetrical matrix. Therefore, the Cholesky decomposition of A can be processed as follows:

$$\begin{aligned} A &= LL^T \\ &= \begin{bmatrix} p_1 & \cdots & 0 \\ q_1 & p_2 & \vdots \\ & q_2 & p_3 \\ \vdots & & \ddots \\ 0 & \cdots & q_{I-2} & p_{I-1} \end{bmatrix} \begin{bmatrix} p_1 & q_1 & \cdots & 0 \\ & p_2 & q_2 & \vdots \\ & & p_3 & \ddots \\ \vdots & & & \ddots \\ 0 & \cdots & & p_{I-1} \end{bmatrix} \end{aligned} \quad (\text{A.14})$$

which leads to

$$\begin{aligned} L\varphi &= \gamma, \\ L^T u &= \varphi, \end{aligned} \quad (\text{A.15})$$

where

$$\begin{aligned} \varphi_{i+1} &= -\frac{q_i}{p_{i+1}} \varphi_i + \frac{1}{p_{i+1}} \gamma_{i+1}, \quad i = 1, 2, \dots, I-2, \\ \varphi_1 &= \frac{1}{p_1} \gamma_1, \end{aligned}$$

$$\begin{aligned} u_i &= -\frac{q_i}{p_i} u_{i+1} + \frac{1}{p_i} \varphi_i, \quad i = I-2, I-1, \dots, 1, \\ u_{I-1} &= \frac{1}{p_{I-1}} \varphi_{I-1}. \end{aligned} \quad (\text{A.16})$$

Specially, if $a_{i,j}$ is a constant, which is equivalent to an isotropic filter, we know that

$$\begin{aligned} p_i &= p, \quad i \in [1, I-2], \\ q_i &= q, \quad i \in [1, I-2], \\ p + q &= 1. \end{aligned} \quad (\text{A.17})$$

Set $\alpha = -q/p$, then (18) and (19) can be formulated as

$$\begin{aligned} \varphi_{i+1} &= \alpha \varphi_i + (1 - \alpha) \gamma_{i+1}, \quad i = 1, 2, \dots, I-2, \\ u_i &= \alpha u_{i+1} + (1 - \alpha) \varphi_i, \quad i = I-2, I-1, \dots, 1. \end{aligned} \quad (\text{A.18})$$

Equation (A.18) has the same form as (6) in the RFM.

Conflict of Interests

The authors declare that there is no conflict of interests regarding the publication of this paper.

Acknowledgments

The authors would like to express their gratitude to two reviewers for their helpful comments and suggestions, which contributed to greatly improve the original paper. This work was supported by the National Basic Research Program of China (no. 2013CB430304), National High-Tech R&D Program of China (no. 2013AA09A505), and National Natural Science Foundation of China (nos. 41206178, 41376015, 41376013, and 51379049).

References

- [1] A. C. Lorenc, "Analysis methods for numerical weather prediction," *Quarterly Journal of the Royal Meteorological Society*, vol. 112, no. 474, pp. 1177–1194, 1986.
- [2] P. Courtier, "Variational methods," *Journal of the Meteorological Society of Japan*, vol. 75, no. 1, pp. 211–218, 1997.
- [3] J. Derber and A. Rosati, "A global oceanic data assimilation system," *Journal of Physical Oceanography*, vol. 19, no. 9, pp. 1333–1347, 1989.
- [4] P. Tandeo, E. Autret, B. Chapron, R. Fablet, and R. Garello, "SST spatial anisotropic covariances from METOP-AVHRR data," *Remote Sensing of Environment*, vol. 141, pp. 144–148, 2014.
- [5] D. W. Behringer, M. Ji, and A. Leetmaa, "An improved coupled model for ENSO prediction and implications for ocean initialization. Part I: the ocean data assimilation system," *Monthly Weather Review*, vol. 126, no. 4, pp. 1013–1021, 1998.
- [6] S. Masina and N. Pinardi, "A global ocean temperature and altimeter data assimilation system for studies of climate variability," *Climate Dynamics*, vol. 17, no. 9, pp. 687–700, 2001.

- [7] B. Huang, J. L. Kinter III, and P. S. Schopf, "Ocean data assimilation using intermittent analyses and continuous model error correction," *Advances in Atmospheric Sciences*, vol. 19, no. 6, pp. 965–992, 2002.
- [8] A. C. Lorenc, "Optimal nonlinear objective analysis," *Quarterly Journal—Royal Meteorological Society*, vol. 114, no. 479, pp. 205–240, 1988.
- [9] C. M. Hayden and R. J. Purser, "Recursive filter objective analysis of meteorological fields: applications to NESDIS operational processing," *Journal of Applied Meteorology*, vol. 34, no. 1, pp. 3–15, 1995.
- [10] R. J. Purser, W.-S. Wu, D. F. Parrish, and N. M. Roberts, "Numerical aspects of the application of recursive filters to variational statistical analysis. Part I: spatially homogeneous and isotropic Gaussian covariances," *Monthly Weather Review*, vol. 131, no. 8, pp. 1524–1535, 2003.
- [11] A. Lorenc, "Iterative analysis using covariance functions and filters," *Quarterly Journal of the Royal Meteorological Society*, vol. 118, no. 505, pp. 569–591, 1992.
- [12] X.-Y. Huang, "Variational analysis using spatial filters," *Monthly Weather Review*, vol. 128, no. 7, pp. 2588–2600, 2000.
- [13] J. Gao, M. Xue, K. Brewster, and K. K. Droegemeier, "A three-dimensional variational data analysis method with recursive filter for Doppler radars," *Journal of Atmospheric and Oceanic Technology*, vol. 21, no. 3, pp. 457–469, 2004.
- [14] P. C. Chu, S. K. Wells, S. D. Haeger, C. Szczechowski, and M. Carron, "Temporal and spatial scales of the Yellow Sea thermal variability," *Journal of Geophysical Research C: Oceans*, vol. 102, no. 3, pp. 5655–5667, 1997.
- [15] P. C. Chu, W. Guihua, and Y. Chen, "Japan Sea thermohaline structure and circulation. Part III: autocorrelation functions," *Journal of Physical Oceanography*, vol. 32, no. 12, pp. 3596–3615, 2002.
- [16] K.-A. Park and J. Y. Chung, "Spatial and temporal scale variations of sea surface temperature in the East Sea using NOAA/AVHRR data," *Journal of Oceanography*, vol. 55, no. 2, pp. 271–288, 1999.
- [17] Y. Xie, S. E. Koch, J. A. McGinley, S. Albers, and N. Wang, "A sequential variational analysis approach for mesoscale data assimilation," in *Proceedings of the 21st Conference on Weather Analysis and Forecasting/17th Conference on Numerical Weather Prediction*, 15B.7, American Meteorological Society, Washington, DC, USA, 2005, <http://ams.confex.com/ams/pdfpapers/93468.pdf>.
- [18] Z. He, Y. Xie, W. Li et al., "Application of the sequential three-dimensional variational method to assimilating SST in a global ocean model," *Journal of Atmospheric and Oceanic Technology*, vol. 25, no. 6, pp. 1018–1033, 2008.
- [19] W. Li, Y. Xie, Z. He et al., "Application of the multigrid data assimilation scheme to the China seas' temperature forecast," *Journal of Atmospheric and Oceanic Technology*, vol. 25, no. 11, pp. 2106–2116, 2008.
- [20] Y. Xie, S. E. Koch, J. A. McGinley et al., "A space–time multiscale analysis system: a sequential variational analysis approach," *Monthly Weather Review*, vol. 139, no. 4, pp. 1224–1240, 2011.
- [21] A. Weaver and P. Courtier, "Correlation modeling on the sphere using a generalized diffusion equation," *Quarterly Journal of the Royal Meteorological Society*, vol. 122, pp. 535–561, 2001.
- [22] D. Li, X. Zhang, H. L. Fu, L. Zhang, X. Wu, and G. Han, "A spatial multi-scale three-dimensional variational analysis based on recursive filter algorithm," *Journal of Atmospheric and Oceanic Technology*. In press.
- [23] D. C. Liu and J. Nocedal, "On the limited memory BFGS method for large scale optimization," *Mathematical Programming*, vol. 45, no. 1–3, pp. 503–528, 1989.
- [24] X. Wu, S. Zhang, Z. Liu, A. Rosati, T. L. Delworth, and Y. Liu, "Impact of geographic-dependent parameter optimization on climate estimation and prediction: simulation with an intermediate coupled model," *Monthly Weather Review*, vol. 140, no. 12, pp. 3956–3971, 2012.
- [25] X. Wu, S. Zhang, Z. Liu, A. Rosati, and T. L. Delworth, "A study of impact of the geographic dependence of observing system on parameter estimation with an intermediate coupled model," *Climate Dynamics*, vol. 40, no. 7–8, pp. 1789–1798, 2013.
- [26] X. Zhang, S. Zhang, Z. Liu, X. Wu, and G. Han, "Parameter optimization in an intermediate coupled climate model with biased physics," *Journal of Climate*, vol. 28, no. 3, pp. 1227–1247, 2015.
- [27] X. Wu, W. Li, G. Han, S. Zhang, and X. Wang, "A compensatory approach of the fixed localization in EnKF," *Monthly Weather Review*, vol. 142, no. 10, pp. 3713–3733, 2014.
- [28] Z. Liu, "Interannual positive feedbacks in a simple extratropical air-sea coupling system," *Journal of the Atmospheric Sciences*, vol. 50, pp. 3022–3028, 1993.
- [29] S. G. H. Philander, T. Yamagata, and R. C. Pacanowski, "Unstable air-sea interactions in the tropics," *Journal of the Atmospheric Sciences*, vol. 41, no. 4, pp. 604–613, 1984.
- [30] R. Asselin, "Frequency filter for time integrations," *Monthly Weather Review*, vol. 100, no. 6, pp. 487–490, 1972.
- [31] A. Robert, "The integration of a spectral model of the atmosphere by the implicit method," in *Proceedings of the WMO/IUGG Symposium on NWP*, pp. 19–24, Japan Meteorological Society, Tokyo, Japan, 1969.

Research Article

Using Adjoint-Based Forecast Sensitivity Method to Evaluate TAMDAR Data Impacts on Regional Forecasts

Xiaoyan Zhang,^{1,2} Hongli Wang,³ Xiang-Yu Huang,^{1,4} Feng Gao,¹ and Neil A. Jacobs⁵

¹National Center for Atmospheric Research, Boulder, CO 80301, USA

²Earth System Science Interdisciplinary Center (ESSIC), University of Maryland, College Park, MD 20740, USA

³Cooperative Institutes for Research in the Atmosphere (CIARA), Colorado State University, Fort Collins, CO 80523, USA

⁴Centre for Climate Research Singapore, Meteorological Service Singapore, Singapore

⁵Panasonic Avionics Corporation, Morrisville, NC 27560, USA

Correspondence should be addressed to Xiaoyan Zhang; xyzucar@gmail.com

Received 7 October 2014; Accepted 22 December 2014

Academic Editor: Guijun Han

Copyright © 2015 Xiaoyan Zhang et al. This is an open access article distributed under the Creative Commons Attribution License, which permits unrestricted use, distribution, and reproduction in any medium, provided the original work is properly cited.

This study evaluates the impact of Tropospheric Airborne Meteorological Data Reporting (TAMDAR) observations on regional 24-hour forecast error reduction over the Continental United States (CONUS) domain using adjoint-based forecast sensitivity to observation (FSO) method as the diagnostic tool. The relative impact of TAMDAR observations on reducing the forecast error was assessed by conducting the WRFDA FSO experiments for two two-week-long periods, one in January and one in June 2010. These experiments assimilated operational TAMDAR data and other conventional observations, as well as GPS refractivity (GPSREF). FSO results show that rawinsonde soundings (SOUND) and TAMDAR exhibit the largest observation impact on 24 h WRF forecast, followed by GeoAMV, aviation routine weather reports (METAR), GPSREF, and synoptic observations (SYNOP). At 0000 and 1200 UTC, TAMDAR has an equivalent impact to SOUND in reducing the 24-hour forecast error. However, at 1800 UTC, TAMDAR has a distinct advantage over SOUND, which has the sparse observation report at these times. In addition, TAMDAR humidity observations at lower levels of the atmosphere (700 and 850 hPa) have a significant impact on 24 h forecast error reductions. TAMDAR and SOUND observations present a qualitatively similar observation impact between FSO and Observation System Experiments (OSEs).

1. Introduction

Tropospheric Airborne Meteorological Data Reporting (TAMDAR), developed by AirDat (AirDat was acquired by Panasonic Avionics Corporation in 2013), has been providing a continuous operational stream of real-time observations from regional commercial airlines since December 2004. These observations include temperature, winds, water vapor, pressure, icing, and turbulence. Aircraft equipped with TAMDAR typically fly regional routes and cruise at altitudes generally below 25000 ft [1], providing coverage over North America, including Alaska and Mexico, as well as Hawaii, Caribbean, and Europe. TAMDAR was designed to fill in the spatial data voids of traditional Aircraft Meteorological Data Relay (AMDAR) flights, which tend to fly higher altitude routes into major airport hubs with only a small number

of planes collecting water vapor, as well as the spatial and temporal data voids of radiosondes, which are launched every 12 h from limited locations.

The current TAMDAR-equipped fleets make more than 1800 daily flights, providing roughly 3600 radiosonde-like profiles during the ascent and descent phase of flight at various regional and major airports across North America and Europe. The time-based horizontal resolution in cruise is 3 min, and the pressure-based vertical resolution during ascent and descent is 10 hPa. The data are transmitted via satellite to a ground-based operation center for quality control and are available for assimilation within 15 s of sampling [1]. These observations are rapidly becoming a major source of critical data utilized by various assimilation systems for the improvement of mesoscale numerical weather prediction (NWP) and the overall safety of aviation for the future [2].

The TAMDAR data have been producing promising impacts on NWP forecasts over the Continental United States (CONUS) for several years and for many different data assimilation systems (e.g., [3–6]), as well as hurricane track prediction [7]. Using the four-dimensional nudging data assimilation method, Liu et al. [4] verified that TAMDAR had a positive impact for mesoscale NWP. Moninger et al. [6] found positive impacts of TAMDAR on 3 h Rapid Update Cycle (RUC) forecasts of temperature, relative humidity, and winds.

The Weather Research and Forecasting (WRF) community variational data assimilation (WRFDA) system [8–10] developed at National Center for Atmospheric Research (NCAR) has been enhanced to assimilate TAMDAR observations and investigate TAMDAR data impact on the forecast for hurricane Ike [7]. Their study was followed by further research of observation error tuning [5] to improve the performance of TAMDAR observations in the WRFDA system. Although positive impacts of TAMDAR data on hurricane Ike and regional forecasts were reported, those two previous studies neither compared TAMDAR with other observation types, nor isolated the impact of each observed variable from TAMDAR.

In addition to the traditional observation-denial method, often referred to as Observation System Experiments (OSEs), used in the studies mentioned above, the adjoint-based forecast sensitivity to observation (FSO) method is an efficient approach to assess relative observation impact on a measured aspect of the forecast error. Unlike OSEs, which measure effects of a single observation on all forecast metrics, FSO quantifies the response of a single forecast metric to all perturbations of the observing systems [11]. It can directly assess the impact of any or all observations used by a forecasting system during data assimilation on a selected measure of short-range forecast error, as opposed to adding or withholding observations during assimilation.

The observation impacts from the FSO method can be easily aggregated by various metrics (e.g., observation variable type, data location) providing a powerful tool with potential applications within data assimilation and observing systems. The FSO method has been used in global data assimilation systems to evaluate the observation impact with respect to a scalar function representing the short-range forecast error [11–19]. Two methods of observation impact estimation (i.e., OSEs and FSO) were evaluated and compared by Gelaro and Zhu [19] and by Cardinali [11]. The authors reported qualitatively similar observation impacts on short-range forecasts using both methods.

In this study, the observation impact of TAMDAR on regional forecasts is evaluated using the adjoint-based FSO method in a limited-area model for two periods in 2010. This evaluation employs the WRF model [20], its adjoint model (WRFPLUS; [21]), and its three-dimensional variational data assimilation (3D-Var) system [10], centered on the CONUS. The adjoint-based FSO tool used in this study was developed by Auligné et al. [22] under the framework of WRFDA. The observation impact from FSO is compared to that from OSEs for TAMDAR and SOUND observations.

The updated WRFDA system with TAMDAR data assimilation capability has been in operation, providing routine

analyses and forecasts since 2010. In addition to comparing the overall impact of TAMDAR data with that of other observation types in the operational system, this study also evaluates the impact of TAMDAR on operational short-range forecasts by quantifying the contribution of observed wind (u, v), temperature (T), and moisture (q) using the adjoint-based FSO method.

TAMDAR impact can be directly compared to other observations such as SOUND at specific vertical levels or for observed variables. Use of the WRFDA FSO system allows the measurement of TAMDAR observation impact when the entire dataset is present in the data assimilation system. This provides the rank of TAMDAR observational impacts on reducing short-range forecast error with respect to the set of all assimilated observations. It also allows for the identification of problems and refinement of potential features of TAMDAR observations, which are crucial for directing further investigation.

The remainder of this paper is structured as follows. In Section 2, the methods of the forecast sensitivity to observation and the WRFDA FSO system will be described. Section 3 presents the experiment design. Detailed results and comparisons between FSO and OSEs are illustrated in Section 4, and summary and discussions are given in Section 5.

2. WRFDA FSO

The adjoint-based FSO system used in this study is WRFDA FSO, which was developed at NCAR in 2008 [22, 23], and has been verified and employed to examine observation impact in the East Asian region during tropical cyclone seasons [24]. Readers are referred to Jung et al. [24] for a detailed description of the concept of forecast sensitivity to observations and application in the WRFDA system. WRFDA FSO includes the WRF model, its adjoint (WRFPLUS), and WRFDA and its adjoint.

WRFPLUS includes a linearization and its adjoint of the dry dynamics of the WRF model, a simplified vertical diffusion scheme, and a large-scale condensation scheme. There are no other moist processes represented in WRFPLUS. WRFDA FSO is capable of calculating the impact of all available conventional and satellite radiance data on the analysis and short-range forecast. It combines higher order approximations of forecast error measurement and their characteristics in the context of the adjoint-based observation impact calculation discussed by Errico [16], Gelaro et al. [17], Tremolet [25], and Descu and Todling [26].

According to the theory of adjoint-based FSO discussed in previous studies, the calculation of observation impact is a three-step process that involves WRFDA FSO. It seeks the gradient of the forecast error cost function with respect to the vector of observations.

(i) *Forecast Sensitivity to Analysis.* The calculation of forecast sensitivity to analysis is obtained using two forecast trajectories (i.e., 24 h) by the WRF model, which is initialized with the analysis and background, respectively. The background is typically a prior model forecast (e.g., 6-hour forecast), and

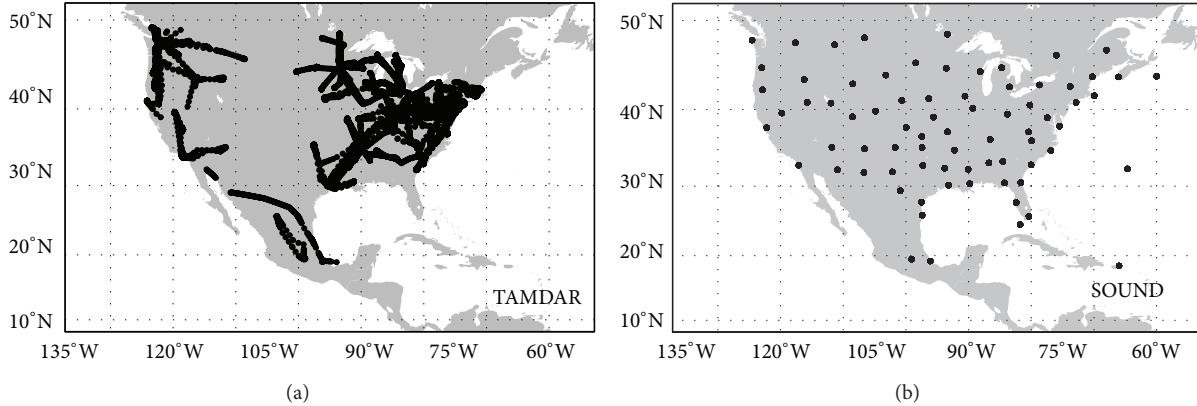


FIGURE 1: The model geographical configuration with the coverage of TAMDAR (a) and SOUND (b) observations (black dots) at 0000 UTC 2 January 2010.

the analysis is produced by optimally assimilating observations with the background into the WRFDA 3D-Var system. Therefore, the forecast trajectory of the background is starting 6 hours before the trajectory of the analysis. At the forecast time, with a selected reference atmospheric state (REFER) as the truth, the forecast error will be calculated for the forecast of analysis and background. A forecast error cost function will be defined based on the difference between those two forecast errors. Along the forecast back trajectory, the WRFPLUS adjoint model is able to calculate the forecast sensitivity to analysis with the forecast error cost function. In WRFDA FSO, the REFER could be the global analysis from other data assimilation systems or the internal analysis of WRFDA. Detailed methods of forecast sensitivity to analysis are described by ((A.1)–(A.7)) in the Appendix.

(ii) *Forecast Sensitivity to Observation.* The second step is to extend the forecast sensitivity to analysis from the grid point provided by the previous step into the observation space using the adjoint of WRFDA 3D-Var. It involves the adjoint of the observation operator, observation error covariance, and the inverse of the Hessian matrix of the cost function that can be obtained by using the iterative Lanczos method in the minimization procedure [27]. The formula is provided by ((A.8)–(A.9)) in the Appendix.

(iii) *Observation Impact.* The observation impact is therefore obtained through calculating the inner product of the forecast error sensitivity to observation and the innovation vector, which is described by (A.9) in the Appendix. This step is implemented within WRFDA and allows users to easily perform various observational impact studies. It should be noted that greater innovation corresponds to greater observation impact. The negative values of observation impact correspond to the forecast error reduction due to improved initial conditions by assimilating observations meaning that the observation has a positive impact on the forecast.

3. Experiment Design

The purpose of this study is to compare the impact of TAMDAR data with other observation types in the

operational WRFDA system and to evaluate the contribution of TAMDAR wind, temperature, and moisture observations on operational short-range forecasts. Therefore, FSO experiments are conducted over a two-week period for January of 2010 and a two-week period for June of 2010. The WRF model domain for this study has a single 134×84 grid that covers the US and surrounding oceanic regions (Figure 1) with 60 km horizontal resolution and 35 vertical levels defined in sigma coordinates with a model top of 50 hPa. Compared to the operational CONUS domain run by AirDat, this domain has a much lower resolution and smaller coverage, but it is sufficient to cover the entire North American TAMDAR distribution (Figure 1(a)). This specific configuration is designed for reducing the expensive computational cost of adjoint runs.

WRFDA 3D-Var is used to obtain the analysis by assimilating rawinsonde (SOUND), PILOT, PROFILER, surface data from SYNOP, METAR, SHIP, BUOY, aircraft data from AIREP and TAMDAR, satellite retrieved wind (GeoAMV) and GPS precipitable water (GPSPW), and GPS refractivity (GPSREF). It should be mentioned that the TAMDAR data were provided directly from the AirDat original observing network, instead of TAMDAR data used at National Centers for Environmental Prediction (NCEP), which received approximately 3% of all available operational TAMDAR observations. The other assimilated datasets come from the Global Telecommunication System (GTS). Figure 1 gives an example of assimilated TAMDAR and SOUND horizontal distribution over the model domain. It should be noted that the restricted Aircraft Communications Addressing and Reporting System (ACARS) data are not used here since they were not available to AirDat in real time.

The quality control (QC) of conventional data including TAMDAR observations in WRFDA is first done in observation preprocessing procedure (obs.proc). Details can be found in the WRFDA user guide (http://www2.mmm.ucar.edu/wrf/users/wrfda/Docs/user_guide_V3.4.1/users_guide_chap6.htm). The second QC is taken inside WRFDA before minimization, in which WRFDA does the same QC procedure for TAMDAR data, as well as other conventional data. Observations will be rejected when their innovations are

larger than 5 times of the standard error of the observation. In this study, no bias correction or thinning procedures are used for TAMDAR data since these functions are not developed in WRFDA, although, compared to SOUND measurement, TAMDAR has the bias of 1.57% for RH, -0.04 K for temperature, and 0.004 m/s for wind [5].

The observation error for temperature from TAMDAR used in this study is 1.0 K, which is the same for most observation types in this study, except for SHIP and BUOY with 2.0 K. The wind observation error is 3.6 m s^{-1} for TAMDAR and AIREP, 2.7 m s^{-1} for SOUND, BUOY, SYNOP, and METAR, 2.8 m s^{-1} for PROFILER and PILOT, and 4.5 m s^{-1} for GeoAMV. For TAMDAR relative humidity, we assume the error to be 10%, which is used for other observation types as well in this study. The observation errors are kept uniform for both January and June experiments. The background error covariance (BE) is generated with National Meteorological Center (NMC) method [28] prior to each study period using monthly statistics of differences between WRF 24 and 12 h daily forecasts over the configuration shown in Figure 1. The same BE is used for both experiments in January and June.

WRFDA 3D-Var is performed each day at 0000, 0600, 1200, and 1800 UTC with a 6 h assimilation time window from -3 h to $+3$ h. The background of every cycle is obtained from the WRF 6 h forecast initialized from NCEP global final analysis (FNL), instead of the previous WRF analyses. In order to calculate the forecast sensitivity, two 24 h WRF forecast trajectories are performed for all analysis times, which are initialized with background and analysis, respectively. It is noted here that the 24 h forecast trajectory of background is starting 6 h before analysis trajectory. The forecasts utilize the Kain-Fritsch cumulus parameterization [29], Goddard cloud microphysics scheme, and the Yonsei University (YSU) planetary boundary layer parameterization [30]. The 24 h WRFPLUS adjoint simulations are run along with the WRF trajectory, but only with physical processes of a simple vertical diffusion scheme and a large-scale condensation scheme. All WRFDA 3D-Var and the WRF forecast and WRFPLUS runs use the same model domain configuration and resolution.

For the observation impact calculation, the dry energy norm ((A.3b) in the Appendix) is used to define the forecast error, and the forecast error is calculated for the entire domain (Figure 1). To define the forecast error, the reference analysis that assimilated all observation types described previously with WRFDA 3D-Var is considered the true state in this study. The augmented form of the third-order Taylor series approximation of forecast error discussed by Gelaro et al. [17] is selected for the most accuracy as shown in the Appendix (A.10).

4. Observation Impact Results

4.1. Two-Week Time Average. The observation impact of the conventional dataset on the 24 h forecast error has been investigated at the four synoptic times (i.e., 0000, 0600, 1200, and 1800 UTC) for two selected periods in January and June, which allows for examining the seasonal variations in the observational impact on the WRF short-range

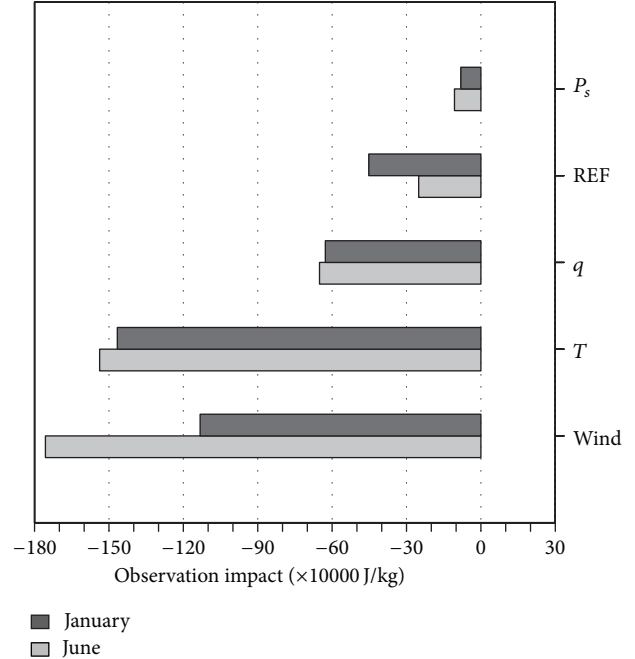


FIGURE 2: Time-average total observation impact (J kg^{-1}) of the types of variables in June (grey) and January (black) 2010. Negative values correspond to a decrease in the energy norm of forecast error. “REF” stands for the GPS refractivity (GPSREF).

forecast during the summer and winter period over the CONUS domain. The two-week time-averaged total observation impacts aggregated with the observation variables (i.e., wind, T , q , P_s , and REF) over all of the four synoptic times are organized in Figure 2. Negative values correspond to a decrease of forecast error due to assimilating a specific observation variable.

Overall, the forecast error reduction is negative for all variables in two selected periods, implying that the forecast error starting from analysis is smaller than that starting from background. This result also implies that the assimilation of observations in the WRFDA system reduces the forecast error. The observation impact in the two seasons is significantly different for wind observation being larger in June and smaller in January. For January, the largest forecast error decrease is due to temperature observations, followed by wind observations for this specific region and 24 h forecast length, whereas the largest forecast error reduction for June is due to wind observations followed by temperature observations. The possible reason is that the observation number of GeoAMV from GTS in June 2010 is much more than January for unclear reasons. The next important observation variable to reduce the forecast error is the moisture (q), the refractivity (REF) of GPS, and the surface pressure (P_s). The comparison shows that in general all observation variables except for REF reduce the forecast error by a larger amount in June than in January. The forecast error is highly affected by the synoptic situation, for example, in summer; there are more convective cases than winter. Convective forecasting is usually more challenging in NWP, while the observation amount of GPSREF in the experiment period of January is

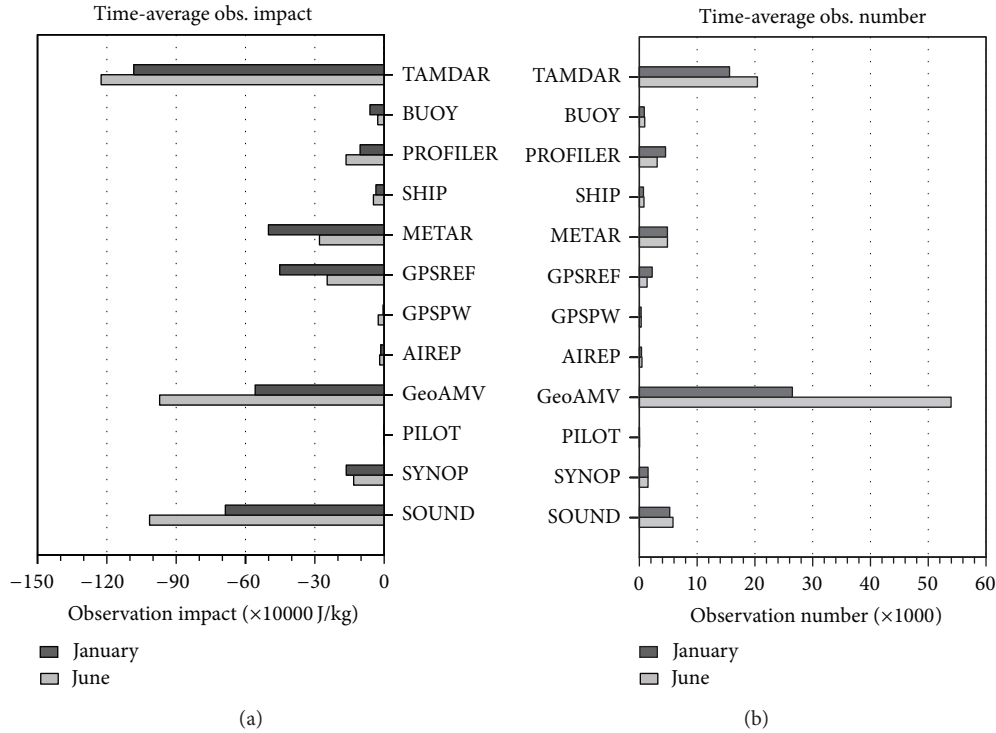


FIGURE 3: Time-average total observation impact (J kg^{-1}) (a) and the corresponding assimilated observation number (b) of the types of observing systems in June (grey) and January (black) 2010.

more than that in June, which could be the possible reason that GPSREF has larger impact in January than in June.

The time-averaged total observation impact for the various observing systems and the corresponding assimilated observation amount for June and January are grouped in Figure 3. For both June and January, on average all of the observing systems provide the most consistent improvement for 24 h forecast from season to season, although TAMDAR, SOUND, and GeoAMV drop their impact from summer to winter period. The common seasonal variation exists with smaller observation impact in the winter period and larger in the summer period for each variable (Figure 2) and observing system (Figure 3), which is consistent with the results of Zapotocny et al. [31]. Therefore, Figure 3 suggests that the WRFDA properly assimilated these observations and improved the initial conditions of the forecast. Overall, for two selected periods, the largest forecast error reduction is due to TAMDAR and SOUND, followed by GeoAMV, METAR, GPSREF, PROFILER, SYNOP, and PILOT. The total forecast error reductions from AIREP, GPSPW, BUOY, and SHIP are smaller because of their sparse coverage with limit data amount as shown in Figure 3(b). The primary reason for the small impact from AIREP is that the ACARS is a restricted dataset and not available for operational assimilation by nongovernmental agencies. Figure 3(b) shows that the assimilated AIREP observation numbers are obviously less than others. We expect that this would be a dominant observing system if ACARS data were included in this study (e.g., [32]).

From the cross-reference of Figures 3(a) and 3(b), the assimilated observation numbers of TAMDAR are much more than SOUND. This is the main reason that TAMDAR data are leading the observation impact in this system when considering that they have the same observed variables (wind, temperature, and humidity) and similar observation errors as SOUND. GeoAMV also has a large observation number; however, the impact is not as obvious as TAMDAR and SOUND because it is only located at certain levels and with only wind observations and larger observation error (Section 3). The observation number of GeoAMV from GTS in June 2010 is much more than January for unclear reasons, which certifies that the larger observation impact of GeoAMV in summer versus winter period is closely related to the number of datasets.

The surface observation types SYNOP, METAR, BUOY, and SHIP have similar trends in the summer and winter period. However, the observation impact is slightly different with an increase from summer to winter period, even with equivalent observation numbers and the same observation error. This difference appears to be a result of the WRF 24-hour forecast error for the surface, which is larger in January than in June. With the surface pressure instrument, METAR, observation impact is significantly different in winter versus summer period; however, this does not change the total P_s observation impact between the winter period and summer period in Figure 2. The reason is the P_s in Figure 2 including the surface pressure observation from SOUND and SYNOP in the WRFDA FSO procedure.

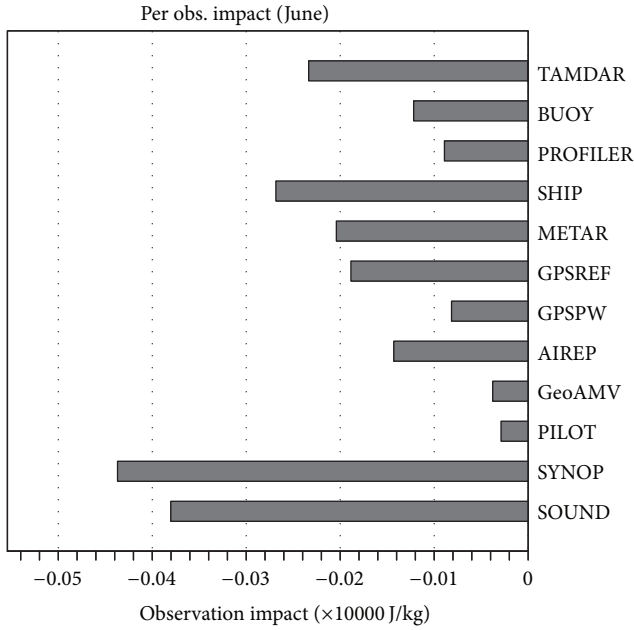


FIGURE 4: Time-average per-observation impact (J kg^{-1}) for June 2010, which is time-averaged total observation impact divided by the observation number.

In order to evaluate the normalized observation impact, the observation impact per observation numbers for all assimilated observation systems in June is calculated (Figure 4), which is the averaged observation impact (shown in Figure 3(a)) divided by the observation number (shown in Figure 3(b)). January has a similar per-observation impact, and the redundant figure is not shown here. Figure 4 indicates that SYNOP surface observations have the greatest normalized observation impact, although they have a relatively small contribution to the total observation impact as shown in Figure 3(a). It means every single SYNOP observation contains important information to reduce model surface forecast error which is usually larger and more difficult than the upper air for model forecast. The rank of other normalized observation impacts is in order of SOUND, TAMDAR, GeoAMV, METAR, and GPSREF from high to low. The TAMDAR observation, which has the greatest total impact, has a smaller normalized observation impact than SOUND. The reason is likely because TAMDAR uses a larger wind observation error (3.6 m s^{-1}) than that of SOUND (2.7 m s^{-1}). Additional comparisons between these two observing systems will be addressed in the following sections with greater detail.

4.2. Observation Impact across Four Synoptic Times. In the previous section, it was shown that the assimilation of large sets of observational data reduces the 24h WRF regional forecast error. However, the observation impact of individual observations varies widely, and the adjoint-based calculation allows us to quantify this impact for every observation at a particular analysis time. The time-averaged observation impact and dataset count for all assimilated observations

across four synoptic times are shown in Figure 5 for summer period only. Since the seasonal impact difference is understood from previous discussion of Figures 2 and 3, the redundant winter figure is omitted.

It is noted that the observation impact corresponds to the observation number when comparing Figures 5(a) and 5(b), and the observation impact of TAMDAR, SOUND, and GEOAMV varies with four synoptic times. For TAMDAR, its observation impact at 0000 UTC is the largest, 0600 UTC is the smallest, and 1200 and 1800 UTC are the closest. The observation impact of TAMDAR at 1200 UTC is slightly less than 1800 UTC, although the data amount at 1200 UTC is much less than 1800 UTC. The observation number at 1800 UTC is the greatest, followed by 0000, 1200, and 0600 UTC, which is expected based on the commercial airline flight times. The observation impact in Figure 5(a) indicates a smaller TAMDAR observation impact at 1800 UTC compared to 0000 UTC, even though the observation number (Figure 5(b)) at 1800 UTC is more than 0000 UTC. This mismatch may be because observations are more numerous but do not necessarily result in an automatically a larger impact if observation error correlations and the thinning are not properly used.

The largest observation impact of SOUND is at 1200 UTC, followed by 0000, 1800, and 0600 UTC, which is consistent with its observation number in Figure 5(b). GeoAMV observation impact was the third largest one in the system; however, it has less obvious time variation than that of TAMDAR and SOUND. GeoAMV has the same issue as TAMDAR at 1800 UTC; largest observation numbers do not bring the largest observation impact. This performance suggests that WRFDA may need more attention and effort to handle data density for assimilation. The other possible reason for the performance of GeoAMV could be that larger observation error was introduced to GeoAMV wind observation as described in Section 3. METAR and GPSREF have a comparable impact following GeoAMV at all analysis times. With smaller observation numbers, METAR, GPSREF, and PROFILER have relative large observation impacts. Based on (A.10) in the Appendix, the observation impact is depending on two elements: the departure of observation and background (d) and model forecast error. It means that the model forecast error is larger on the locations of METAR, GPSREF, and PROFILER, and these data contain important information to reduce the forecast error to a great extent. The surface observation instrument, SYNOP, produces an equally important impact for 0000, 0600, 1200, and 1800 UTC in this study, due to the equal data report amount along with those times.

The comparison between TAMDAR and SOUND shows that at 0000 UTC the observation impact from SOUND is similar to TAMDAR, and at 1200 UTC, SOUND produces more impact than TAMDAR. At 0600 and 1800 UTC, however, since SOUND has only a few records, TAMDAR has a much greater observation impact than SOUND. The amount of TAMDAR observations is significantly larger than SOUND at all assimilation times. Particularly at 1800 UTC when SOUND reports are sparse, TAMDAR observation has the thickest coverage due to the high peak of commercial flights landing and takeoff at local airport. The averaged total

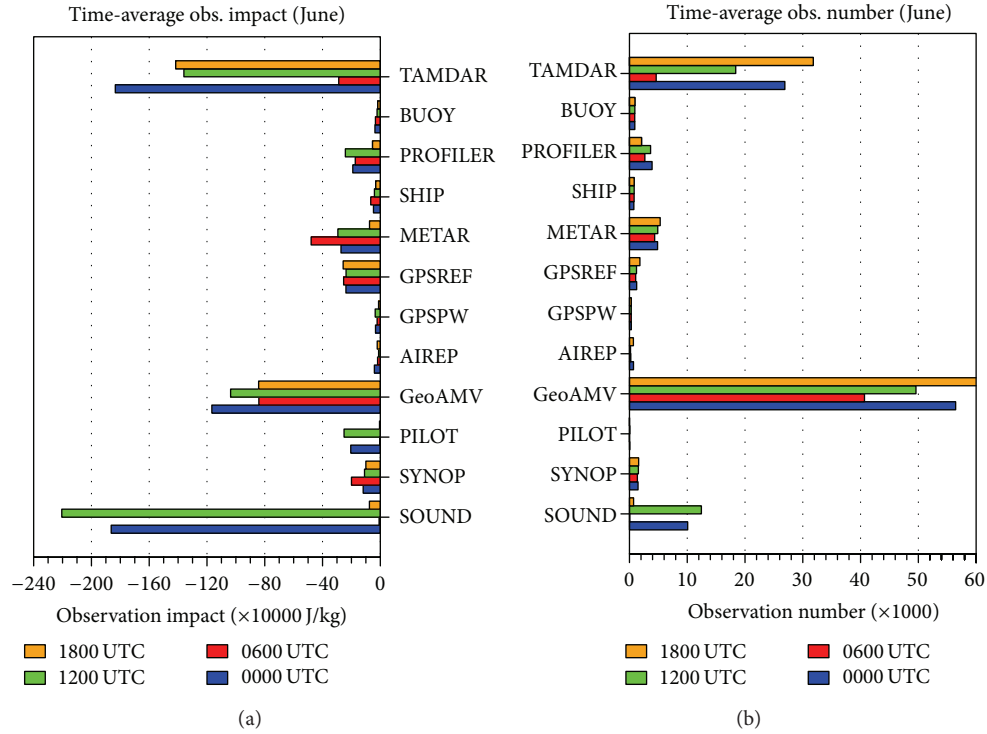


FIGURE 5: Time-average total observation impact on 24 h forecast (J kg^{-1}) (a) and the corresponding assimilate observation number (b) of the types of observing systems for 0000 (blue), 0600 (red), 1200 (green), and 1800 (orange) UTC in June 2010.

observation impact illustrates that TAMDAR has a distinct advantage at 1800 UTC in reducing the 24 h forecast error due to the dense observation record. Therefore, the larger total observation impact of TAMDAR than that of SOUND (Figure 3) mostly likely originates from the contribution of 1800 UTC observations.

4.3. Observation Impact Vertical Distribution. Since TAMDAR and SOUND have similar observation impacts discussed in Sections 4.1 and 4.2, and TAMDAR is a rawinsonde-like observation with the same observational variables, the comparison is made between TAMDAR and SOUND to investigate why the observation impact of TAMDAR is greater than SOUND at some analysis times. Figure 6 presents the vertical distribution of the time-averaged wind observation impact and observation number for TAMDAR and SOUND for the summer period at 0000 UTC. The observation impact is categorized for eight vertical levels: 1000, 850, 700, 500, 300, 200, 100, and the model top (50) hPa. From the vertical distribution, both TAMDAR and SOUND present the positive impact at all vertical pressure levels for wind. It can be seen from Figure 6(a) that TAMDAR wind observation impact resides primarily below 300 hPa corresponding to its cruise altitude below 25000 ft. At 500 hPa, TAMDAR shows a larger observation impact than SOUND corresponding with larger observation number in Figure 6(b). However, at 1000, 850, 700, and 300 hPa, TAMDAR presents smaller observation impact than SOUND although TAMDAR has more observation at these levels. It

is likely a function of the model-assigned larger observation error for TAMDAR wind observations than that of SOUND. Gao et al. [5] presented revised lower TAMDAR-specific error values, which, prior to TAMDAR, were set to the same values as AIREP.

The observation impact vertical distribution for temperature (T) and water vapor mixing ratio (q) are displayed for June in Figure 7, as well as the corresponding observation number. The q in Figure 7(c) is converted from the observed relative humidity (RH) in WRFDA. Since the adjoint model does not account for the majority of moist processes, the error of humidity impact is assumed to be ignored for the preliminary investigation in this study. Therefore, it must be declared that the humidity impact mentioned here only counts the contribution to dry energy norm. However, it is fair to make approximate comparisons of the humidity impact between TAMDAR and SOUND in the same system.

As with wind, both T and q show the positive impact to forecast at all vertical levels. In Figures 7(a) and 7(c), at 850 and 700 hPa, TAMDAR shows a larger T and q observation impact than other levels corresponding to the more observations in Figures 7(b) and 7(d); however, SOUND presents smaller observation impact at these two levels corresponding with fewer observations than TAMDAR. Therefore, the dense TAMDAR observations compensate sparse SOUND reports in the critical vertical region (lower levels) where no other moisture data is available. This analysis suggests that the humidity observation of TAMDAR has a positive impact on the WRF regional 24 h forecast, especially at lower levels (700 and 850 hPa) where convective weather originates.

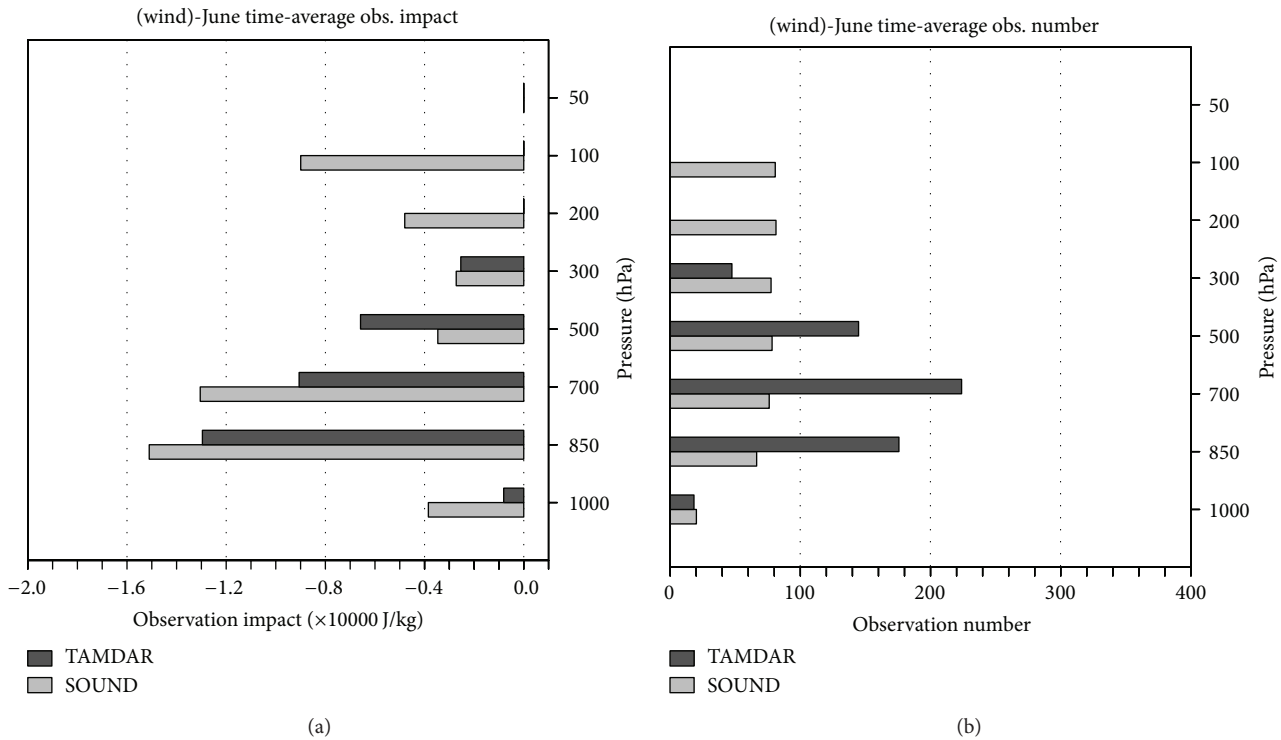


FIGURE 6: Time-average observation impact (J kg^{-1}) of TAMMDAR and SOUND wind (a) on pressure levels (hPa) from 1000 hPa above the surface up to 50 hPa at 0000 UTC in June 2010; (b) is the observation number at corresponding vertical levels.

4.4. OSEs. In previous sections, the linear estimations of observation impact are described. This section compares the impact of observations on 24 h forecast evaluated using typical OSEs with that evaluated using the adjoint-based FSO method. The REFER that assimilates all observation types (Section 3) is used as a control experiment that is referred to as OSE-ALL. Two OSEs are then conducted by performing new analysis-forecast cycles for a given period (i.e., from 1 to 15 June 2010). In the new analysis procedure, the TAMMDAR and SOUND to be evaluated are removed from the observation set in data denial experiments. The corresponding OSEs are referred to as OSE-TAMMDAR and OSE-SOUND, respectively. Through a series of OSEs, the impact of TAMMDAR and SOUND is evaluated. The configurations of the analysis and forecast system are the same as those described in Section 3 for FSO.

The observation impact of TAMMDAR from OSEs is defined as the difference of 24 h forecast error of OSE-ALL and OSE-TAMMDAR. The calculation of forecast error for OSE-ALL and OSE-TAMMDAR uses the formulation in the Appendix (A.6) with the same REFER as the true state as the FSO described in Section 3. OSE-SOUND followed the same procedure as OSE-TAMMDAR to get the observation impact of SOUND. Figure 8(a) presents the time-averaged observation impact for both OSE-TAMMDAR and OSE-SOUND in June at 0000, 0600, 1200, and 1800 UTC.

The TAMMDAR and SOUND observation impact obtained from FSO are compared in Figure 8(b). The largest

observation impact of TAMMDAR is at 1800 UTC, which is even larger than the error of removing SOUND observation and is consistent with the results of FSO (Figure 8(b)). Likewise, the observation impact of SOUND data is larger at 1200 UTC than TAMMDAR data. At 0000 UTC, the OSEs show that TAMMDAR results in slightly larger observation impact than SOUND, whereas FSO presents equal impact between TAMMDAR and SOUND. 0600 UTC is only showing the impact of TAMMDAR for both OSEs and FSO. The comparable pattern demonstrates that FSO and OSEs show similar importance at each synoptic time. The WRFDA FSO diagnostic tool is capable of highlighting the major forecast degradation due to the observations withheld compared with OSEs. However, using cross comparisons of the magnitude of observation impact between OSEs and FSO, the difference shows larger observation impact of OSEs than that of FSO. This means the linear estimate forecast error reduction from FSO method slightly underestimates that from the nonlinear method in the OSEs. This underestimation may be due to the (1) neglected moist physics in adjoint integration, (2) the validity of the tangent linear assumption, and/or (3) the validity of the tangent linear assumption of the forecast error reduction. OSEs measure the effects of either SOUND or TAMMDAR on all forecast metrics; FSO quantified the response of a single metric to all observations including TAMMDAR and SOUND. Overall, the comparable results still demonstrate that the FSO and OSEs show similar qualitative improvements due to TAMMDAR and SOUND observations.

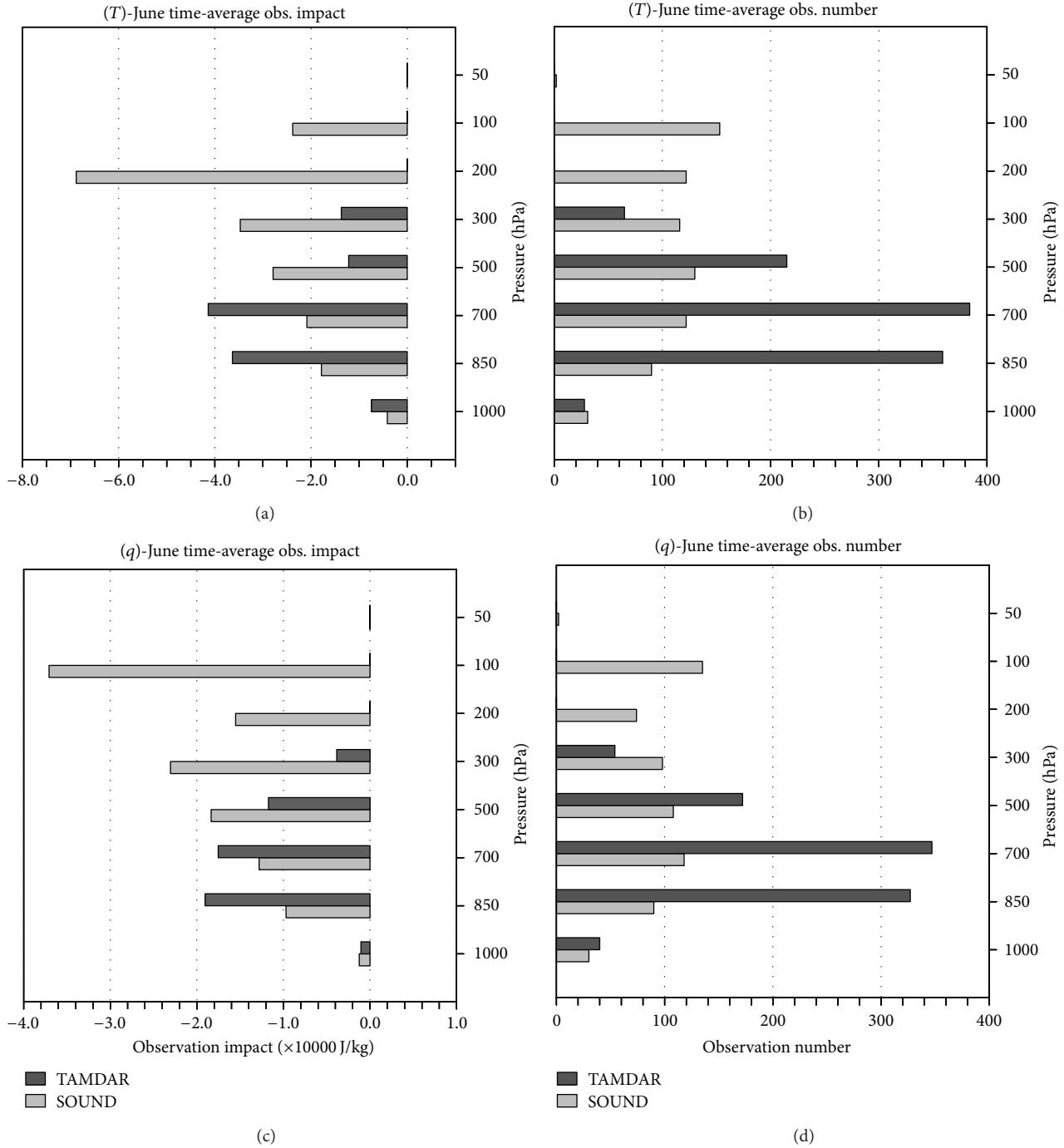


FIGURE 7: Time-average observation impact (J kg^{-1}) of (a) temperature (T) and (c) specific humidity (q) from TAMDAR and SOUND on pressure level (hPa) from 1000 hPa above the surface up to 50 hPa at 0000 UTC in June 2010; (b) and (d) are the observation number of T and q , respectively, at the corresponding vertical level.

5. Summary and Discussions

This paper presents an application of the WRFDA FSO system for estimating the impact of observations on regional forecasts and investigates influence of TAMDAR data on short-range (24 h) forecast error reduction. A significant advantage of the FSO method is that observation impact can

be efficiently estimated for a complete set of observations, or any subset of observations grouped by type of observing system, observed variable, geographic region, vertical level, or other categories. The assessment of the value of TAMDAR and SOUND observations impact through the OSEs is also performed, which demonstrates that the FSO experiments and OSEs provide similar qualitative diagnostic results. The

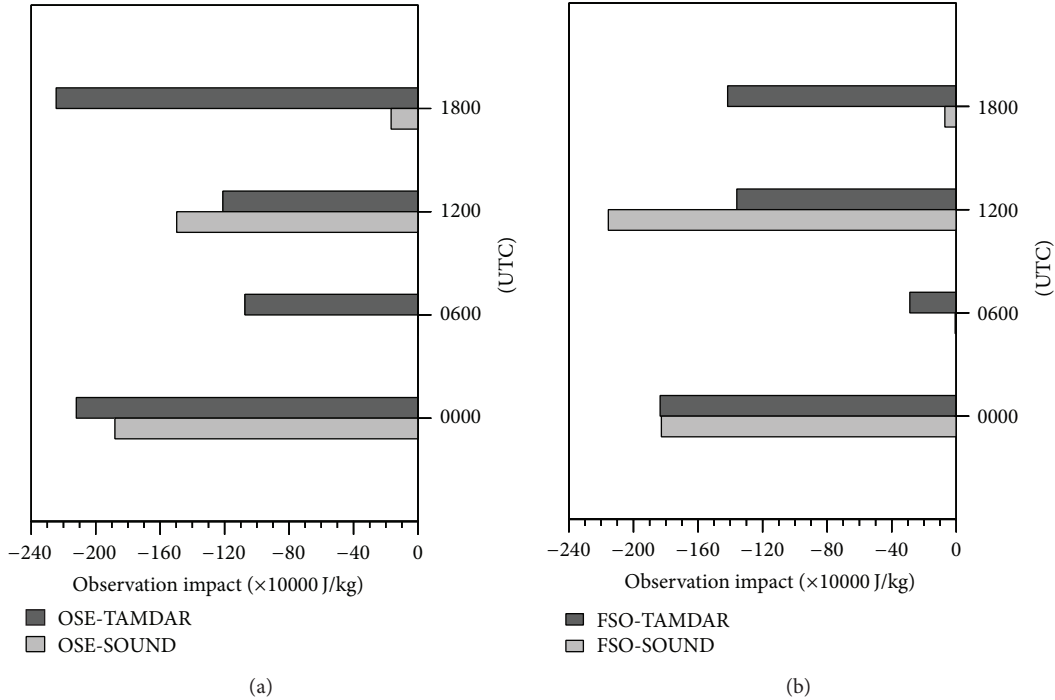


FIGURE 8: Two-week averaged observation impact (J kg^{-1}) of OSEs (a) for removing TAMDAR (OSE-TAMDAR) and SOUND (OSE-SOUND), respectively, and the observation impact of TAMDAR (FSO-TAMDAR) and SOUND (FSO-SOUND) from FSO (b) in June 2010.

FSO method also requires fewer computational resources than OSEs and can monitor the observation impact in an operational framework.

FSO results suggest that on average all the observing systems play a positive role in reducing the 24 h forecast error. The wind and temperature in the observation system make key contributions to reduce the 24 h forecast error, although the largest observation impact for June is wind, whereas it is, for January, temperature. The largest observation impact is produced by SOUND and TAMDAR and followed by GeoAMV, METAR, GPSREF, and SYNOP. However, most instruments have the seasonal variation with the larger impact in summer period than winter period. The wind, temperature, and relative humidity observations of TAMDAR have significant contributions in the operational WRFDA system, particularly at 1800 UTC.

FSO observation impact was compared to the observation impact deduced from OSEs that were performed as data denial experiments for TAMDAR and SOUND. Consistent with FSO impact results, the total observation impact of TAMDAR from OSEs is larger than SOUND at 0600 and 1800 UTC, and impact at 0000 UTC is similar to SOUND, and impact at 1200 UTC is less than SOUND. Whilst OSEs are more indicated for evaluating the longer term forecast impact of data, FSO is still a good choice to investigate the short-range forecast error reduction due to the observations. FSO is able to evaluate the impact of observations when the entire observation dataset is present in the assimilation system with one experiment, while OSEs have to perform more than one experiment to evaluate the contribution from different datasets [11].

The advantages of TAMDAR data in the operational WRFDA system are reinforced through this study using the FSO approach and include the following.

- (i) The total observation impact of TAMDAR is obvious at 0000, 1200, and 1800 UTC cycle consistently. TAMDAR at 1800 and 0600 UTC is able to complement SOUND observations to reduce forecast error.
- (ii) TAMDAR relative humidity and temperature observation are a very important supplement to SOUND data at lower levels, especially at 850 and 700 hPa.

Additionally, a few issues have been noticed with the adjoint-based observation impact estimate. First, the calculation of the sensitivity used in the WRF adjoint is limited by simple physical schemes. Secondly, the definition of the forecast error norm does not include moisture. A greater impact from moisture observation might be expected when more moist physics schemes are included in the WRF adjoint model and a total moist energy norm is used.

In this study, no bias correction or thinning procedures are used for TAMDAR data since these functions are not developed in WRFDA. As discussed in Section 2, the observation innovation and observation number directly affect the forecast error reduction. The bias correction is clearly related to the innovation, and the thinning procedure decides how many data will be assimilated. Therefore, additional work is needed to address the bias correction and thinning procedure to improve the accuracy of observation impact of TAMDAR in FSO system. Inclusion of moisture in total energy and investigation of the influence of TAMDAR data

thinning and bias correction strategy on short-term forecast error reduction should be part of future development. The new observation error for TAMDAR has been estimated and added in WRFDA [5]. It would be also interesting to study the forecast sensitivity to TAMDAR observation errors with FSO.

Appendix

Basic Concept of Observation Impact

The nonlinear forecast model can be expressed as

$$\mathbf{x}^f = M(\mathbf{x}^0), \quad (\text{A.1})$$

where M is the nonlinear propagator of the model for the time period $0 \leq t \leq f$ and \mathbf{x}^f is the forecast model state vector at time $t = f$ with initial condition vector \mathbf{x}^0 . Given a perturbation $\delta\mathbf{x}^0$ at the initial time, the linear evolution $\delta\mathbf{x}^f$ at time $t = f$ is

$$\delta\mathbf{x}^f = \mathbf{M}\delta\mathbf{x}^0, \quad (\text{A.2})$$

where \mathbf{M} is the tangent-linear propagator of M along the forecast trajectory initiated from \mathbf{x}^0 . To study the observation impact on forecasts, the forecast error, which is measured with respect to the true atmospheric state \mathbf{x}_t^f at time $t = f$, is defined as

$$e = \langle \mathbf{x}^f - \mathbf{x}_t^f, \mathbf{C}(\mathbf{x}^f - \mathbf{x}_t^f) \rangle, \quad (\text{A.3a})$$

where $\langle \cdot, \cdot \rangle$ denotes the Euclidean inner product of two vectors and \mathbf{C} is a diagonal matrix that has the weighting coefficients of the forecast error components. Usually, the dry total energy norm is used for \mathbf{C} [33–35] as

$$e = \sum_{i,j,k} \left[u'^2 + v'^2 + \left(\frac{g}{N\theta} \right)^2 \theta'^2 + \left(\frac{1}{\rho c_s} \right)^2 p'^2 \right]. \quad (\text{A.3b})$$

Using (A.2), the sensitivity (gradient) of e to initial conditions is expressed as

$$\frac{\partial e}{\partial \mathbf{x}^0} = 2\mathbf{M}^T \mathbf{C}(\mathbf{x}^f - \mathbf{x}_t^f). \quad (\text{A.4})$$

Given two forecasts \mathbf{x}_b^f and \mathbf{x}_a^f with the background (\mathbf{x}_b^0) initial condition and analysis (\mathbf{x}_a^0), respectively, the forecast error is

$$\begin{aligned} e_b &= \langle \mathbf{x}_b^f - \mathbf{x}_t^f, \mathbf{C}(\mathbf{x}_b^f - \mathbf{x}_t^f) \rangle, \\ e_a &= \langle \mathbf{x}_a^f - \mathbf{x}_t^f, \mathbf{C}(\mathbf{x}_a^f - \mathbf{x}_t^f) \rangle. \end{aligned} \quad (\text{A.5})$$

To measure the observation impact on forecast error reduction, a scalar function is defined as the difference between e_a and e_b :

$$J_e = \frac{1}{2}(e_a - e_b). \quad (\text{A.6})$$

The linear approximation of forecast error reduction J_e caused by analysis increment $\mathbf{x}_a^0 - \mathbf{x}_b^0$ can be expressed as

$$\delta e = \langle \mathbf{x}_a^0 - \mathbf{x}_b^0, \mathbf{s} \rangle, \quad (\text{A.7})$$

where \mathbf{s} is a properly defined vector that is expressed in terms of the forecast sensitivity to initial conditions [17, 36]. For example, $\mathbf{s} = (1/2)((\partial e_a / \partial \mathbf{x}_a^0) + (\partial e_b / \partial \mathbf{x}_b^0))$ is introduced by Langland and Baker [12] in their observation impact methodology.

In a data assimilation system, the analysis increments $\mathbf{x}_a^0 - \mathbf{x}_b^0$ are represented by a best linear unbiased estimation equation

$$\mathbf{x}_a^0 - \mathbf{x}_b^0 = \mathbf{K}\mathbf{d}, \quad (\text{A.8})$$

where $\mathbf{K} = \mathbf{A}\mathbf{H}^T\mathbf{R}^{-1}$ is the Kalman gain matrix, \mathbf{A} represents the matrix of analysis error covariance and corresponds (at convergence) to the inverse of the Hessian matrix of the cost function [37, 38], \mathbf{H}^T is the adjoint of the observation operator, \mathbf{R}^{-1} is the reverse of observation error covariance; \mathbf{d} is the innovation vector $\mathbf{d} = \mathbf{y} - H(\mathbf{x}_b^0)$, \mathbf{y} represents observations, and H is the nonlinear observation operator. Using (A.8) and the adjoint relationship, the forecast error reduction estimation (A.7) can be expressed as

$$\delta e = \langle \mathbf{K}\mathbf{d}, \mathbf{s} \rangle = \langle \mathbf{d}, \mathbf{K}^T \mathbf{s} \rangle, \quad (\text{A.9})$$

where $\mathbf{K}^T \mathbf{s}$ is the forecast sensitivity to observations. The quantity δe , as defined in (A.9), provides the information that is required to assess observation impact using only observation space quantities. In the case $\mathbf{d} = 0$ or $\mathbf{K}^T \mathbf{s} = 0$, there is no observation impact. Typically, e_a is smaller than e_b , so that the negative observation impact value in (A.9) is corresponding to the reduction of the forecast error due to improved initial conditions. Using (A.9), the total observation impact can be partitioned into contributions made by any individual observation or grouping of observations assimilated over the entire domain. Combining (A.4) with (A.9), the linear approximation of (A.6) can be introduced as

$$\delta e = \langle \mathbf{d}, \mathbf{K}^T [\mathbf{M}_{,b}^T \mathbf{C}(\mathbf{x}_b^f - \mathbf{x}_t^f) + \mathbf{M}_a^T \mathbf{C}(\mathbf{x}_a^f - \mathbf{x}_t^f)] \rangle. \quad (\text{A.10})$$

Disclaimer

Any opinions, findings, and conclusions or recommendations expressed in this paper are those of the authors and do not necessarily reflect the views of the National Science Foundation.

Conflict of Interests

The authors declare that there is no conflict of interests regarding the publication of this paper.

Acknowledgment

The National Center for Atmospheric Research is sponsored by the National Science Foundation.

References

- [1] T. S. Daniels, W. R. Moninger, and R. D. Mamrosh, "Tropospheric airborne meteorological data reporting (TAMDAR) overview," in *Proceedings of the 10th Symposium on Integrated Observing and Assimilation Systems for Atmosphere, Oceans, and Land Surface (IOAS-AOLS '06)*, American Meteorological Society, Atlanta, Ga, USA, January 2006.
- [2] A. Fischer, "The use of TAMDAR as a convective forecasting supplement in the northern plains and upper midwest," in *Proceedings of the 10th Symposium on Integrated Observing and Assimilation Systems for Atmosphere, Oceans, and Land Surface (IOAS-AOLS '06)*, American Meteorological Society, Atlanta, Ga, USA, January 2006.
- [3] N. Jacobs, Y. Liu, and C. Druse, "Evaluation of temporal and spatial distribution of TAMDAR data in short-range mesoscale forecasts," in *Proceedings of the 10th Symposium on Integrated Observing and Assimilation Systems for the Atmosphere, Oceans, and Land Surface (IOAS-AOLS '06)*, Amer. Meteor. Soc., Atlanta, Ga, USA, January 2006.
- [4] Y. Liu, N. A. Jacobs, W. Yu et al., "An OSSE study of TAMDAR data impact on mesoscale data assimilation and prediction," in *Proceedings of the 11th Symposium on Integrated Observing and Assimilation Systems for the Atmosphere, Oceans, and Land Surface (IOAS-AOLS '07)*, American Meteorological Society, San Antonio, Tex, USA, January 2007.
- [5] F. Gao, X. Zhang, N. A. Jacobs, X.-Y. Huang, and P. P. Childs, "Estimation of TAMDAR observational error and assimilation experiments," *Weather and Forecasting*, vol. 27, no. 4, pp. 856–877, 2012.
- [6] W. R. Moninger, S. G. Benjamin, B. D. Jamison, T. W. Schlatter, T. L. Smith, and E. J. Szoke, "Evaluation of regional aircraft observations using TAMDAR," *Weather and Forecasting*, vol. 25, no. 2, pp. 627–645, 2010.
- [7] H. Wang and X.-Y. Huang, "TAMDAR observation assimilation in WRF 3D-Var and its impact on hurricane Ike (2008) forecast," *Atmospheric and Oceanic Science Letters*, vol. 5, no. 3, p. 206, 2012.
- [8] D. M. Barker, W. Huang, Y.-R. Guo, A. J. Bourgeois, and Q. N. Xiao, "A three dimensional variational data assimilation system for MM5: implementation and initial results," *Monthly Weather Review*, vol. 132, no. 4, pp. 897–914, 2004.
- [9] X. Y. Huang, Q. Xiao, D. M. Barker et al., "Four-dimensional variational data assimilation for WRF: formulation and preliminary results," *Monthly Weather Review*, vol. 137, no. 1, pp. 299–314, 2009.
- [10] D. Barker, X.-Y. Huang, Z. Liu et al., "The weather research and forecasting model's community variational/ensemble data assimilation system: WRFDA," *Bulletin of the American Meteorological Society*, vol. 93, no. 6, pp. 831–843, 2012.
- [11] C. Cardinali, "Monitoring the observation impact on the short-range forecast," *Quarterly Journal of the Royal Meteorological Society*, vol. 135, no. 638, pp. 239–250, 2009.
- [12] R. H. Langland and N. L. Baker, "Estimation of observation impact using the NRL atmospheric variational data assimilation adjoint system," *Tellus Series A*, vol. 56, no. 3, pp. 189–201, 2004.
- [13] N. L. Baker and R. Daley, "Observation and background adjoint sensitivity in the adaptive observation-targeting problem," *Quarterly Journal of the Royal Meteorological Society*, vol. 126, no. 565, pp. 1431–1454, 2000.
- [14] J. Morneau, S. Pellerin, S. Laroche, and M. Tanguay, "Estimation of adjoint sensitivity gradients in observation space using the dual (PSAS) formulation of the Environment Canada operational 4DVar," in *Proceedings of the 2nd THORPEX International Science Symposium*, WMO/TD no. 1355, WRP/THORPEX no. 7, pp. 162–163, Landshut, Germany, December 2006.
- [15] L. Xu, R. Langland, N. Baker, and T. Rosmond, "Development and testing of the adjoint of NAVDAS-AR," in *Proceedings of the 7th International Workshop on Adjoint Applications in Dynamic Meteorology*, Obergurgl, Austria, October 2006.
- [16] R. M. Errico, "Interpretations of an adjoint-derived observational impact measure," *Tellus*, vol. 59, no. 2, pp. 273–276, 2007.
- [17] R. Gelaro, Y. Zhu, and R. M. Errico, "Examination of various-order adjoint-based approximations of observation impact," *Meteorologische Zeitschrift*, vol. 16, no. 6, pp. 685–692, 2007.
- [18] Y. Zhu and R. Gelaro, "Observation sensitivity calculations using the adjoint of the Gridpoint Statistical Interpolation (GSI) analysis system," *Monthly Weather Review*, vol. 136, no. 1, pp. 335–351, 2008.
- [19] R. Gelaro and Y. Zhu, "Examination of observation impacts derived from observing system experiments (OSEs) and adjoint models," *Tellus Series A*, vol. 61, no. 2, pp. 179–193, 2009.
- [20] W. C. Skamarock, J. B. Klemp, J. Dudhia et al., "A description of the advanced research WRF version 3," NCAR Technical Note NCAR/TN-475+STR, 2008.
- [21] X. Zhang, X.-Y. Huang, and N. Pan, "Development of the upgraded tangent linear and adjoint of the weather research and forecasting (WRF) model," *Journal of Atmospheric and Oceanic Technology*, vol. 30, no. 6, pp. 1180–1188, 2013.
- [22] T. Auligné, X.-Y. Huang, H.-C. Lin et al., "Forecast Sensitivity to Observations (FSO)—WRF/WRFPLUS/WRFDA v3.3 User's Guide," http://www2.mmm.ucar.edu/wrf/users/wrfda/Tutorials/2012_July/docs/README.FSO_v3.3.pdf.
- [23] T. Auligné, *Forecast Sensitivity to Observations & Observation Impact*, Lecture at WRFDA Tutorial, National Center for Atmospheric Research, Boulder, Colo, USA, 2010, http://www2.mmm.ucar.edu/wrf/users/wrfda/Tutorials/2010_Aug/docs/WRFDA_sensitivity.pdf.
- [24] B.-J. Jung, H. M. Kim, T. Auligné, X. Zhang, X. Zhang, and X.-Y. Huang, "Adjoint-derived observation impact using WRF in the western North Pacific," *Monthly Weather Review*, vol. 141, pp. 4080–4097, 2012.
- [25] Y. Tremolet, "First-order and higher-order approximations of observation impact," *Meteorologische Zeitschrift*, vol. 16, no. 6, pp. 693–694, 2007.
- [26] D. N. Daescu and R. Todling, "Adjoint estimation of the variation in model functional output due to the assimilation of data," *Monthly Weather Review*, vol. 137, no. 5, pp. 1705–1716, 2009.
- [27] G. H. Golub and C. F. Van Loan, *Matrix Computations*, Johns Hopkins University Press, 3rd edition, 1996.
- [28] D. F. Parrish and J. C. Derber, "The National Meteorological Center's spectral statistical-interpolation analysis system," *Monthly Weather Review*, vol. 120, no. 8, pp. 1747–1763, 1992.
- [29] J. S. Kain, "The Kain-Fritsch convective parameterization: an update," *Journal of Applied Meteorology*, vol. 43, no. 1, pp. 170–181, 2004.
- [30] S.-Y. Hong, Y. Noh, and J. Dudhia, "A new vertical diffusion package with an explicit treatment of entrainment processes," *Monthly Weather Review*, vol. 134, no. 9, pp. 2318–2341, 2006.
- [31] T. H. Zapotocny, W. P. Menzel, J. P. Nelson III, and J. A. Jung, "An impact study of five remotely sensed and five in situ data types in the Eta Data Assimilation System," *Weather and Forecasting*, vol. 17, no. 2, pp. 263–285, 2002.

- [32] S. G. Benjamin, B. D. Jamison, W. R. Moninger, S. R. Sahn, B. E. Schwartz, and T. W. Schlatter, "Relative short-range forecast impact from aircraft, profiler, radiosonde, VAD, GPS-PW, METAR, and mesonet observations via the RUC hourly assimilation cycle," *Monthly Weather Review*, vol. 138, no. 4, pp. 1319–1343, 2010.
- [33] F. Rabier, E. Klinker, P. Courtier, and A. Hollingsworth, "Sensitivity of forecast errors to initial conditions," *Quarterly Journal of the Royal Meteorological Society*, vol. 122, no. 529, pp. 121–150, 1996.
- [34] T. N. Palmer, R. Gelaro, J. Barkmeijer, and R. Buizza, "Singular vectors, metrics, and adaptive observations," *Journal of the Atmospheric Sciences*, vol. 55, no. 4, pp. 633–653, 1998.
- [35] X. Zou, F. Vandenberghe, M. Pondecà, and Y.-H. Kuo, "Introduction to adjoint techniques and the MM5 adjoint modeling system," NCAR Technical Note NCAR/TN-435+STR, 1997.
- [36] D. N. Daescu and R. Todling, "Adjoint sensitivity of the model forecast to data assimilation system error covariance parameters," *Quarterly Journal of the Royal Meteorological Society*, vol. 136, no. 653, pp. 2000–2012, 2010.
- [37] A. C. Lorenc, "Analysis methods for numerical weather prediction," *Quarterly Journal of The Royal Meteorological Society*, vol. 112, no. 474, pp. 1177–1194, 1986.
- [38] E. Kalnay, *Atmospheric Modeling, Data Assimilation and Predictability*, Cambridge University Press, Cambridge, UK, 2003.

Research Article

Research on Cold Core Eddy Change and Phytoplankton Bloom Induced by Typhoons: Case Studies in the South China Sea

Xiao-dong Shang,¹ Hai-bin Zhu,² Gui-ying Chen,¹ Chi Xu,¹ and Qi Yang³

¹State Key Laboratory of Tropical Oceanography, South China Sea Institute of Oceanology, Chinese Academy of Sciences, Guangzhou 510301, China

²Ningxia Meteorological Observatory, Yinchuan 750002, China

³Shanghai Marine Observatory, Shanghai 201300, China

Correspondence should be addressed to Hai-bin Zhu; zhuhb04@126.com and Gui-ying Chen; gychen@scsio.ac.cn

Received 18 December 2014; Revised 13 February 2015; Accepted 28 February 2015

Academic Editor: Shaoqing Zhang

Copyright © 2015 Xiao-dong Shang et al. This is an open access article distributed under the Creative Commons Attribution License, which permits unrestricted use, distribution, and reproduction in any medium, provided the original work is properly cited.

The effects of 8 typhoons which passed by coldcore eddy (CCE) areas in the South China Sea (SCS) from 1997 to 2009 were observed and evaluated. The changes in the preexisting CCE acted upon by typhoons were described by eddy kinetic energy (EKE) and eddy available gravitational potential energy (EAGPE). The mechanical energy of CCE was estimated from a two-layer reduced gravity model. Comparing with the scenario that typhoon passes by the region without CCEs, the preexisting CCE area plays an important role in the increase of chlorophyll-a (chl-a) concentration in the CCEs impacted by the typhoons. The preexisting chl-a in CCE is about 25%~45% (8%~25%) of postexisting chl-a in CCE for higher (slower) transit speed typhoons. If the EAGPE of CCE increases greatly after typhoon passing by with slow transit speed, so does the chl-a in the CCE area. The EKE (EAGPE) changes of the preexisting CCE are in the order of $O(10^{14} \sim 10^{15} \text{ J})$. EKE and EAGPE of CCE are dominantly enhanced by typhoon with slow transit speed ($< 3 \text{ m/s}$) and the posttyphoon EAGPE is always larger than posttyphoon EKE for 8 cases. The maximum EAGPE change of the preexisting CCE reaches $5.11 \times 10^{15} \text{ J}$, which was induced by typhoon Hagibis.

1. Introduction

Ocean responses to typhoons have been investigated during the past several decades through theoretical [1], observational [2–4], and numerical methods [5–7]. Typhoons trigger phytoplankton blooms of high chl-a concentration in the ocean. This phenomenon has been previously reported [8–10]. With the development of satellites, more tropical storm-induced phytoplankton blooms in the open oceans [11, 12] and in the marginal seas [13], especially in the SCS [14–16], have been studied. The mechanism of phytoplankton blooms is generally supposed to be that typhoon-induced upwelling and vertical mixing bring cold and nutrient or chlorophyll-rich water up to the euphotic layer and thus stimulate the biological bloom [10, 11, 14]. Recently, many investigations focus on that phytoplankton blooms are enhanced in a cold core

eddy (CCE) when a typhoon passes by [15, 17]. The preexisting CCE plays a critical role in the development of typhoon-induced phytoplankton blooms, and it significantly strengthens the upper ocean dynamics and nutrient responses, which are mainly dependent on two factors [13, 18]. One is that the cyclonic eddy lifts up the isotherms prior to the arrival of the typhoons, thus leading to lower water temperature and more nutrients than in the case of no eddy at the same depth. The other factor is that typhoons have slow transit speed. Entrainment and upwelling induced by typhoons and upwelling induced by preexisting CCE can inject nutrient water to the euphotic layer and significantly promote biological bloom [19–21].

There has been also considerable research on the sea surface temperature (SST) cooling associated with preexisting mesoscale eddy in response to the passing by of typhoon. For

example, Zheng et al. [17] investigated that intensive cooling response to typhoon Hai-tang at sea surface is under pre-existing cyclonic eddy condition with uplifted thermocline induced by cyclonic flow. By two numerical experiments, Zheng et al. [22] revealed that an accurate representation of the upper dynamic conditions is required to accurately estimate the sea surface cooling by a typhoon. Prasad and Hogan [23] investigated that the variation of regions of extreme cooling depended on the simulated location of the warm core eddy (WCE) by hurricane Ivan. These studies all suggest that preexisting mesoscale eddies play an important role in SST cooling in response to typhoon. The cooling SST with low sea surface height indicates that more cooling water is uplifted by mixing and upwelling induced by cyclonic eddy. When the cooling water brings nutrient water to the upper layer, phytoplankton blooms will occur.

For the preexisting CCE, the SST cooling, sea surface height anomaly (SSHA) changes, and marine phytoplankton blooms impacted by typhoon were investigated (e.g., [13, 17, 22]). However, these rare basic physical parameters, such as SST and SSHA in the sea surface, available by satellite data, can only roughly present some characteristics of CCE. Nowadays, based on SSHA and geostrophic velocities or standard Reynolds averaging procedure [24], the sea surface kinetic energy can be easily estimated. In absence of *in situ* data, most of the relative studies about eddy kinetic energy (EKE) of CCE focused on sea surface kinetic energy [25, 26], which ignore the volume effect of CCE. Meantime, seldom work reported the variations of eddy available gravitational potential energy (EAGPE). Xu et al. [27] postulated a new method to estimate the EKE and EAGPE by a two-layer model including the contribution of an eddy's volume. When typhoons act on CCEs, studying the energy change of preexisting CCEs with volume effect has important implication with the energy transfer between the atmospheric force and the ocean response. Estimating the change of EKE and EAGPE associated with the preexisting CCEs can investigate quantitatively the energy translation from a typhoon to a mesoscale cold eddy and further tell which parameter of a typhoon plays a key role in the change of preexisting CCE's energy. What is the relationship between EAGPE of CCEs and change of chl-a? What plays a key role in the change of chl-a in the CCE area? The answers to these questions can offer observational information for the further study of the interaction between typhoons and CCEs in the physical and biophysical models.

The South China Sea (SCS) is one of the largest marginal seas in the Western Pacific (see Figure 1), and commonly its seasonal thermocline is shallow (~ 10 m) in spring and deep (~ 80 m) in winter. Meanwhile, the SCS is also a region with frequent typhoons [28] and abundant activity of mesoscale eddies observed all year around [29]. Besides, oligotrophy is a significant characteristic in upper water column of the northern SCS ($>20^\circ\text{N}$). In winter, due to the fact that the nutrient is relatively rich (the average surface phosphate concentration is 34.6 nmol/L [30]), the average chl-a concentration of the northern SCS from August 1997 to December 2009 can reach 0.47 mg/m³, while the average chl-a concentration

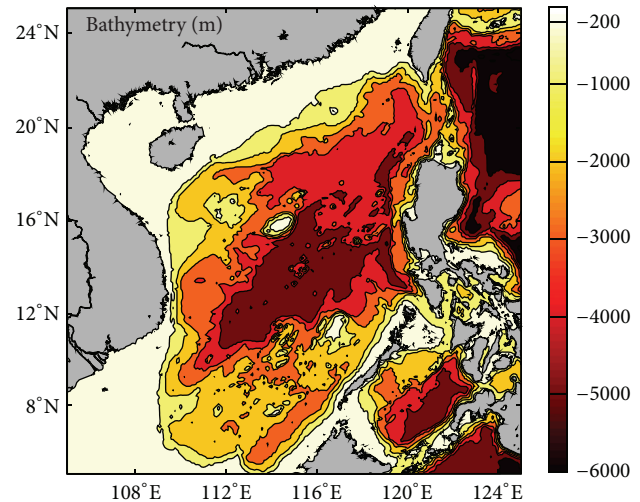


FIGURE 1: Topographical map of the South China Sea.

of the southern SCS is about 0.17 mg/m³ (see Figure 2). In summer, the average chl-a in the SCS is about 0.1192 mg/m³ because the nutrient is relative oligotrophy (the average surface phosphate concentration in summer is 17.6 nmol/L [30]). In spring, the average chl-a in the SCS is about 0.1163 mg/m³; therein, the average chl-a in the northern SCS is higher (about 0.22 mg/m³). In autumn, the average chl-a in the SCS is about 0.1492 mg/m³. Both in summer and in autumn, there is a water jet induced by monsoons [31] near the eastern Vietnam coast, where the average chl-a is very high ($0.44\sim 0.47$ mg/m³) in autumn and it is relatively weak ($0.22\sim 0.44$ mg/m³) in summer. In this paper, we proposed a method to more effectively estimate physical parameters, especially EKE and EAGPE of CCE to reveal the response of the preexisting eddy acted upon by typhoons by using satellite data and a two-layer reduced gravity model. These two parameters are important physical parameters that have a close relation to chl-a change. To avoid regional differences, eight typhoons passed by the preexisting CCE area in the SCS were used to investigate the chl-a change in the CCE area. In addition, when the wind stress of typhoons produced an effect on CCE, the changes in the EKE and EAGPE of CCE before and after the typhoons were calculated to illustrate the energy translation of CCE both on and below the sea surface.

2. Data and Methods

2.1. Selection of Cases. The chl-a data were obtained from the Sea-viewing Wide Field-of-view Sensor (SeaWiFS). The level-3 chl-a concentration values taken from the website of National Aeronautics and Space Administration (NASA, <http://oceancolor.gsfc.nasa.gov/>) were used. These data with 9 km spatial resolution and 8 -day composite were derived from an algorithm called the ocean chlorophyll 4 algorithm (OC4) [32]. Typhoon information, including center location, central pressure, and maximum sustained winds recorded once every six hours, was obtained from the Joint Typhoon Warning Center (JTWC). The average typhoon transit speed

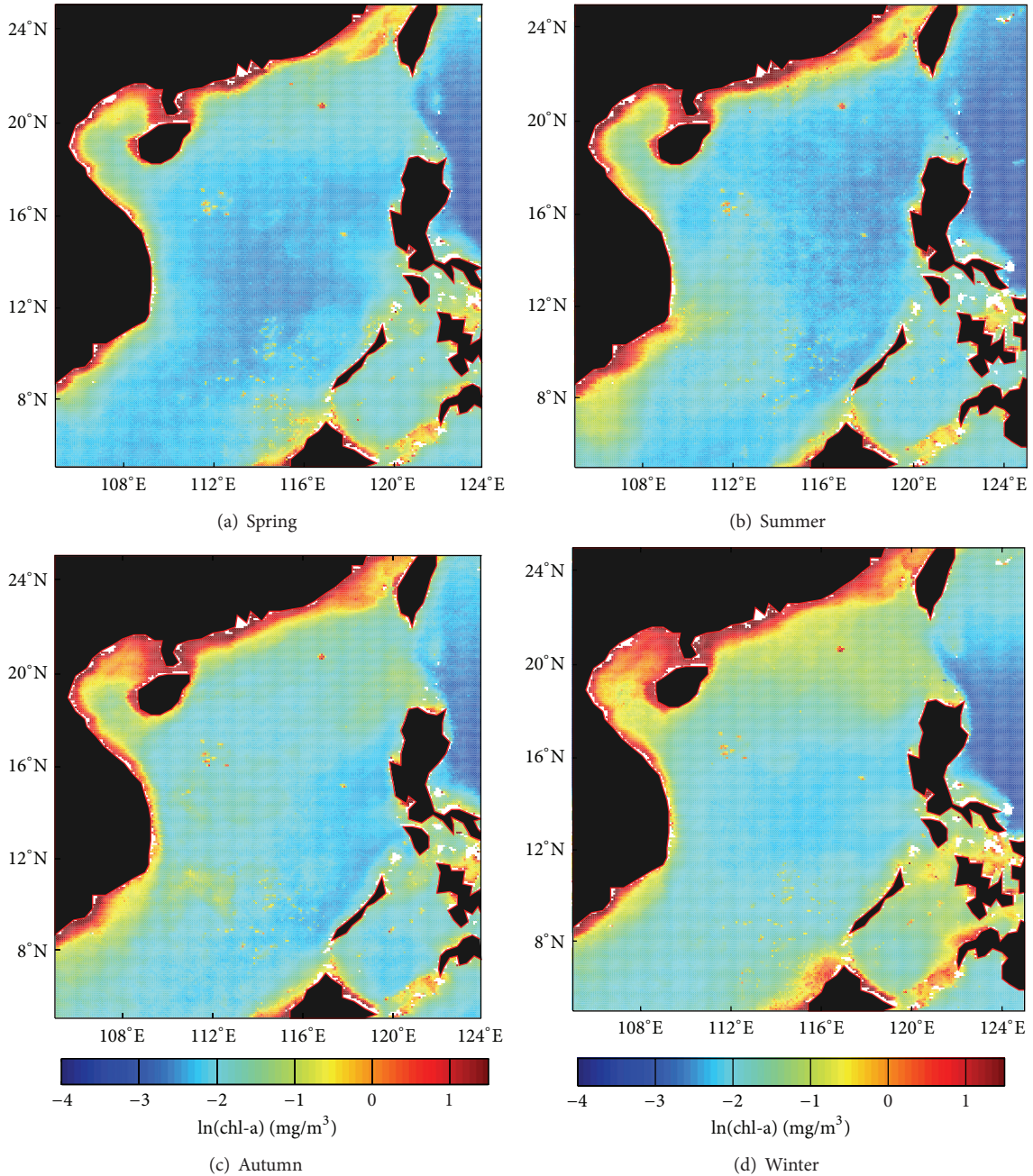


FIGURE 2: Seasonal average chl-a concentration from August 1997 to December 2009 in the South China Sea.

and average wind speed when the typhoon center was located within 100 km of the CCE were estimated. The altimeter data were merged from multisensors including TOPEX and ERS. Data were produced by AVSIO (Archiving, Validation, and Interpretation of Satellite Oceanographic data) with average spatial resolution of 0.3° and time resolution of 7 days. The daily SST data are from the Remote Sensing Systems TMI (the Tropical Rain Measuring Mission’s microwave imager).

To investigate the biological response in the eddy area under the influence of a typhoon, the eligible cases were selected by following these steps. First, the typhoon track records were used to search for the typhoons entering into

the SCS. Next the SSHA data were used to check whether the typhoons on the SCS passed by the mesoscale eddy area. Finally, chl-a concentration was calculated in the eddy area where typhoon passed by.

Because 1997 was the first year that the SeaWiFS data were available, this year was chosen as a starting point in our study. The chl-a enhanced by typhoon is mostly attributed to not only the upwelling that brings nutrient water from deep sea to upper layer, but also new phytoplankton growing in the euphotic zone [11]. Thus, the phytoplankton growth to peak concentration needs a delay of several days (~ 5 days) under the influence of a hurricane [13, 33]. In fact, the exact number

of days for chl-a to rise to its peak is still unknown, but it is not the crux of problem. Based on the above considerations, 8-day, 9 km, and level-3 composite SeaWiFS data were used to satisfy the basic study requirements. Moreover, before and after each typhoon, the SeaWiFS data without a large quantity of cloud cover were used [33], since typhoons are always accompanied by large and intensive cloud, making upper ocean chl-a invisible to the SeaWiFS sensor. In several selected cases, the disturbances of cloud were not able to be precluded. However, compared with the chl-a distribution after typhoon in mesoscale size around the CCE area farthest from the coast, the horizontal gradient of chl-a concentration before typhoon is much smaller. Hence, the data from chl-a partially covered by cloud can still be used to present chl-a distribution before typhoon. But for chl-a data after typhoon, the chl-a growth rate varies in different regions and its horizontal gradient is large. If the calculated chl-a excluded some other areas covered by cloud, it is a significant error. Therefore, those cases of cloud-free chl-a data in the CCE area were chosen so that the CCE circumscription could be accurately determined.

To identify and track the mesoscale eddy, 3 criteria were followed: (1) there were closed SSHa contours on the SSHa images, and the outermost closed contour of SSHa is the boundary of identified mesoscale eddy; (2) the water depth of the eddy center was deeper than 1000 m [34]; (3) the difference of SSHa values between center maximum and outermost contour, M , was more than 6 cm. The accuracy of altimeter data was low near the coast, whereas when the eddy area was located in open ocean, interference with chl-a pixel values from coastal or ocean bottom areas can be avoided. Thus, the second criterion is important. Because the measurement error of the SSHa was around 2 cm, the third criterion was applied.

A mesoscale eddy usually spans several hundred kilometers. A tropical storm with slow transit speed only spends about one day passing through an eddy. According to this, using daily SSHa data to determine the area covered by the eddy is needed, as the weekly SSHa data were not available to distinguish the day that a tropical storm passed through an eddy. The SSHa data of a particular day were obtained by the linear time-interpolation using the two consecutive days of available SSHa data, which were, respectively, before and after this day. The validation of linear time-interpolation was tested by comparing the SSHa data obtained by linear time-interpolation with AVISO daily SSHa product.

To investigate chl-a variation caused by typhoon, average chl-a concentration in two continuous 8-day periods were calculated (except Utor and Hagibis). The first 8-day data were defined as the “pretyphoon” period which represents the chl-a distribution before typhoon; the second 8-day data were defined as the “posttyphoon” period which represents the chl-a distribution after typhoon. When the two sets of 8-day data were used, the date of the typhoon passing by the eddy area was chosen to occur at the end of the first 8-day period or at the beginning of the second 8-day period. Because chl-a bloom needs several days after the typhoon passed, the bloom is always present in the second 8-day period. Then the SSHa grid was spatially linearly interpolated into 9×9 km, which

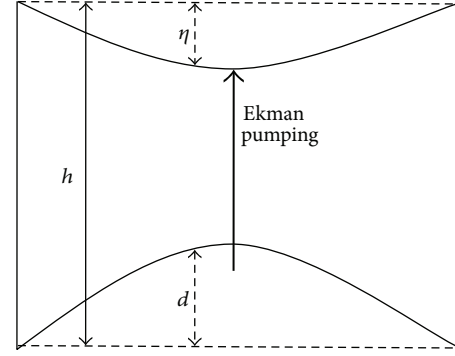


FIGURE 3: The two-layer reduced gravity model.

has the same resolution as the grid of 8-day chl-a data. The chl-a pixel values accumulated when the chl-a pixels were located on the grid points covered by the CCE influenced by typhoon. The average chl-a concentration was derived from the sum of chl-a pixel values divided by the total number of available chl-a pixels on the CCE.

2.2. CCE's Kinetic Energy and Available Gravitational Potential Energy's Calculation Methods. The EKE and EAGPE of CCE were calculated by following simplification and assumption. Because we do not have information about eddy's vertical structure and it was reasonable to treat the SSH variability as the vertical displacement signature of the first baroclinic mode [35], a two-layer model (Figure 3) was used to simulate the baroclinic structure of eddies. To specify the depth of interface and the density difference between two layers, a common approach that sets the main pycnocline (thermocline) as the interface of a two-layer model was used. Thus the internal displacement can be linked to the free surface elevation anomaly observed from satellite data to incorporate the vertical structure of eddies. By forming such a first-mode-baroclinic eddy and defining the reference state as the state when there is no surface elevation caused by eddy, both EKE and EAGPE for each eddy can be derived. Here EAGPE means the difference in gravitational potential energy between the reference state and the state where there was an eddy. The two dates of weekly SSHa used to calculate energy were the days before and after the typhoon passed by the eddy area.

In a simple reduced gravity model (Figure 3), the relationship between sea surface height anomaly η and displacement of thermocline d is

$$d = \frac{g\eta}{g'}, \quad (1)$$

where g is gravitational acceleration and g' is reduced gravitational acceleration. g' is treated as a constant, that is, 0.03 m/s^2 . In the calculation, it is assumed that water density does not change with pressure and the density difference $\Delta\rho$ exists between upper and lower layer. $\Delta\rho$ is obtained from $\Delta\rho = \rho(g'/g)$. Hence upper layer density is $\rho - \Delta\rho$ and lower layer density is ρ (a nominal value of 1020 kg/m^3 used), and h is the upper layer thickness in reduced gravity model.

TABLE 1: Typhoon information and the spatial average chl-a concentration before and after typhoon overlaid on CCE.

Typhoon's name	Transit speed (m/s)	Average wind speed (m/s)	Minimum sea level pressure (mb)	Prestorm chl-a (mg/m ³)	Poststorm chl-a (mg/m ³)
Leo	2.8864	49.901	—	0.1089	0.7174
Lingling	3.6846	55.487	927	0.1218	0.4750
Nanmadol	6.4741	40.127	967	0.1483	0.4323
Kai-tak	2.1016	29.581	963	0.1661	0.8212
Chanchu	2.7270	59.676	927	0.0847	0.3335
Durian	3.7176	44.156	954	0.1141	0.2664
Utor	4.8184	41.156	954	0.1141	0.2454
Hagibis	1.9072	31.438	982	0.1145	1.4338

The current velocities are deduced from weekly SSHA data by using the geostrophic approximation. Meridional and zonal geostrophic velocities are u_g and v_g , respectively:

$$u_g = -\left(\frac{g}{f}\right)\frac{\partial\eta}{\partial y}, \quad (2)$$

$$v_g = \left(\frac{g}{f}\right)\frac{\partial\eta}{\partial x}, \quad (3)$$

where f is the Coriolis parameter. The central difference method was used to calculate horizontal gradient of SSHA, and the number of the grids surrounded by closed outermost contour is n in the eddy area. Average kinetic energy per unit mass is given by

$$\langle \text{EKE} \rangle_m = \sum_1^n \frac{[(u_{g,i}^2 + v_{g,i}^2)/2]}{n}. \quad (4)$$

If the area of each grid is A_i , the kinetic energy of a CCE, including the contribution from the layer thickness and the eddy volume, can be expressed as

$$\text{EKE} = \sum_1^n \left[\frac{(u_{g,i}^2 + v_{g,i}^2)}{2} \right] (\rho - \Delta\rho) A_i (h_i - d), \quad (5)$$

where the only parameter that is not known is h_i . The monthly mean ocean temperature of World Ocean Atlas 2005 (WOA05) provided by National Oceanographic Data Center (NODC) was used to estimate the upper layer thickness. Horizontal resolution of the data is one degree, and temperature values are indicated on 24 layers from 0 to 1500 meters. This dataset is suitable to describe the sea water stratification before the influence of typhoon because the annual and seasonal cycles dominate the variability of the SCS, and the monthly mean climatology is useful to eliminate the effects of upper-layer deepening caused by the typhoon in the calculations of eddy energy. Wind stress energy input to the surface ageostrophic current will be much more significant than that under the circumstance without typhoon so that the upper layer depth will change significantly from pre- to posttyphoons [36], but such an effect is not part of mesoscale eddy-typhoon interaction. Besides, *in situ* measurements in

TABLE 2: EKE and EAGPE of CCE before and after typhoons.

Typhoon's name	Prestorm EKE (J)	Poststorm EKE (J)	Prestorm EAGPE (J)	Poststorm EAGPE (J)
Leo	1.70E + 14	3.70E + 14	1.13E + 15	3.43E + 15
Lingling	1.42E + 15	2.42E + 15	2.34E + 15	5.65E + 15
Nanmadol	1.45E + 14	1.93E + 14	2.89E + 15	4.53E + 15
Kai-tak	2.78E + 14	1.39E + 15	6.50E + 14	2.46E + 15
Durian	7.02E + 14	6.85E + 14	1.11E + 15	1.51E + 15
Utor	6.85E + 14	1.30E + 15	1.51E + 15	5.17E + 15
Hagibis	1.18E + 15	4.06E + 15	6.49E + 14	5.76E + 15

the South China Sea show that 16°C isotherm-depth is appropriate for the upper layer thickness [37]. Thus the depth of 16°C isotherm was adopted as the upper-layer thickness h_i in present study.

For simplicity, the original position of the sea surface in which there is no perturbation is selected as the reference level. As the definition from Huang [38] and the Appendix A in Xu et al. [27] indicated, the EAGPE of each eddy is calculated as

$$\text{EAGPE} = \frac{\sum_1^n g^2 \rho \eta_i^2 A_i}{g'}. \quad (6)$$

3. Observation and Results

Table 1 shows the mean wind speed, moving (or transit) speed, and central pressure of eight typhoons selected in the SCS. It also represents the eight typhoons passing through the corresponding preexisting CCE and remote sensing results of chl-a before and after the typhoon overlaid the CCE area. Table 2 gives the EKE and EAGPE changes of CCEs influenced by 8 typhoons. For Chanchu, the corresponding CCE below did not satisfy the 3rd criteria of eddy detection, so the EKE and EAGPE of that CCE were not included in Table 2. Here 2 typhoons, Leo and Hagibis, were addressed to show the chl-a response to typhoon in the CCE area and the change of CCE's EKE and EAGPE.

3.1. Typical Case: Typhoon Leo. Leo was the first typhoon assaulting the China mainland in 1999. After generating in the

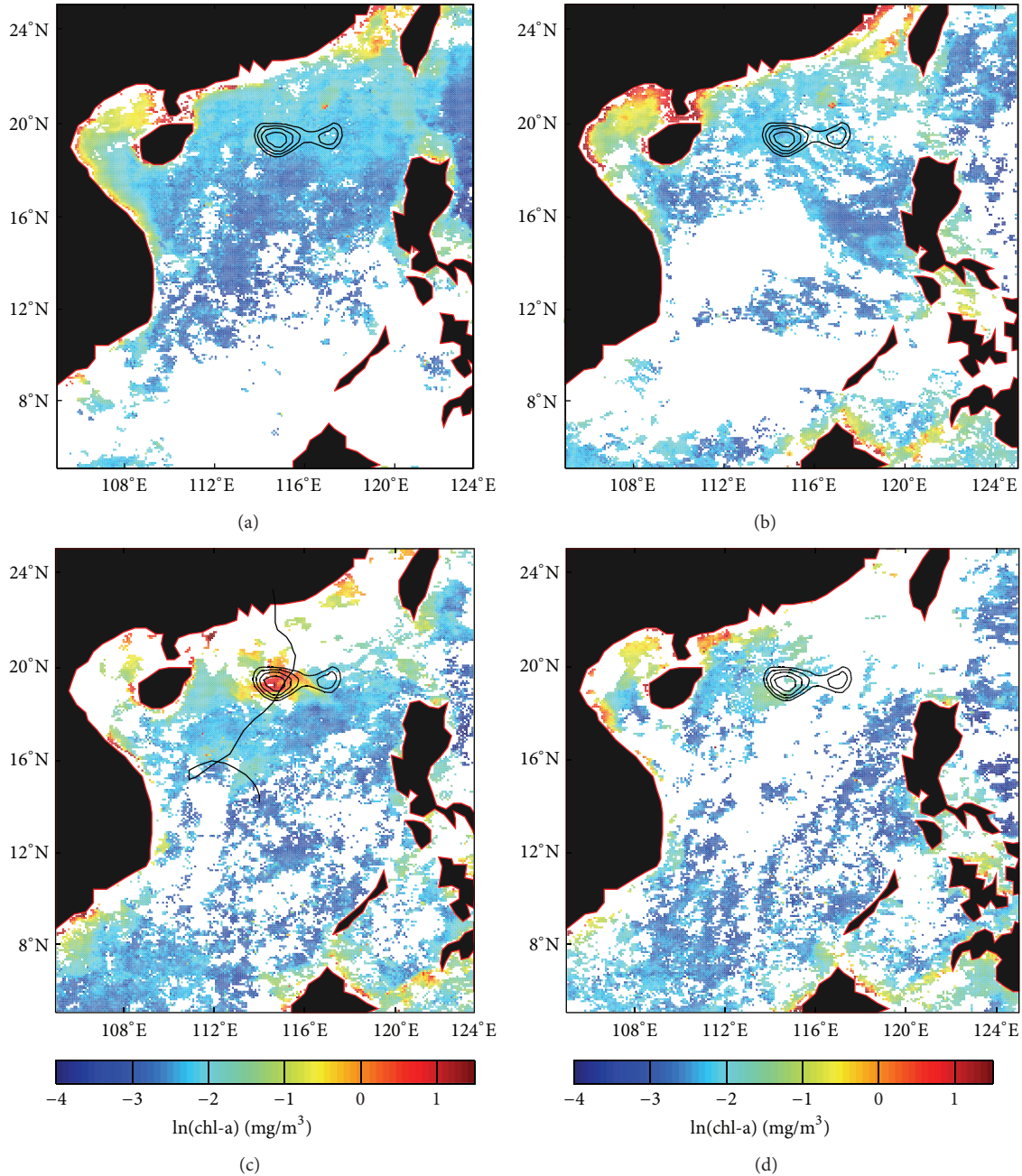


FIGURE 4: The chl-a concentration change under the influence of typhoon Leo in the CCE area. Colorbar is the natural logarithm value of chl-a concentration. (a), (b), (c), and (d) are the 8-day mean chlorophyll concentration derived from SeaWiFS in the SCS. (a) 15 April–22 April, 1999. (b) The prestorm chl-a distribution from 23 April to 30 April, 1999. (c) The poststorm chl-a distribution from 1 May to 8 May, 1999. The black solid line is the track of Leo. (d) 9 May–16 May, 1999. The contour indicates the CCE influenced by Leo. In (a), (b), (c), and (d), the CCE is the same one as on 30 April when CCE passed by Leo.

central part of the SCS on April 25, it moved northwestward as a tropical depression. By April 27, Leo began to shift northward and then completed a full circle with average maximum sustained winds of 17 m/s around east of the Vietnam coast. During April 29, Leo moved to the northeast and intensified rapidly. By April 30, its maximum sustained winds were strengthened from 42 m/s to 56 m/s. Its center passed through an ocean preexisting CCE (Figure 4(c)) with average

moving speed 2.9 m/s in the same day (April 30). The CCE had two centers. Its outermost contour value was -8 cm, and the minimum value was -17.5 cm in the western center. Although typhoon Leo had affected the cold core eddy before April 30, as tropical cyclones' wind radius (class 7 wind speed 15 m/s) spanned 150 km, the most important impact was exerted when Leo closed in on the eddy area. Thus, the typhoon average moving speed and average wind speed when the typhoon closed in

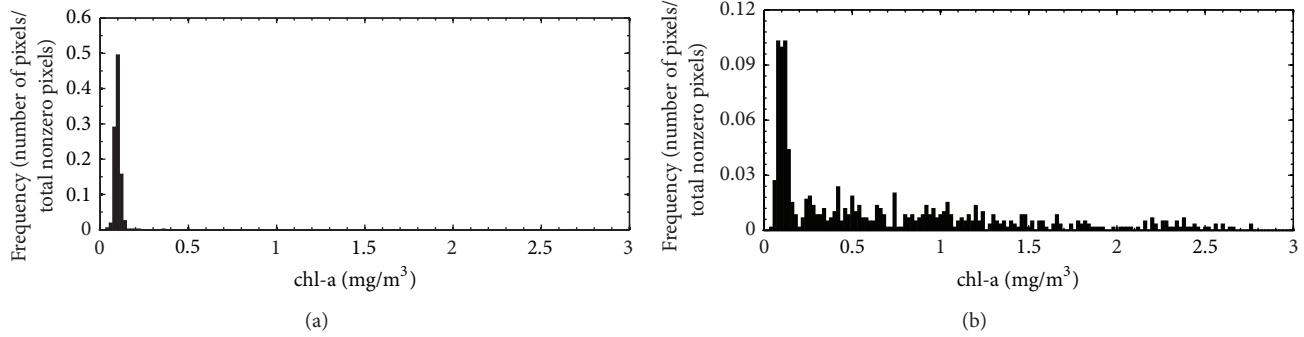


FIGURE 5: Frequency distribution of available chl-a pixel values in the CCE area derived from prestorm and poststorm images. (a) The prestorm chl-a distribution. (b) The poststorm chl-a distribution.

on the eddy area were calculated. Leo left the eddy area on May 1 and began to weaken and finally disappeared over the mainland.

Leo is a precise example to explain how to determine the prestorm and poststorm average chl-a concentration values in the eddy area. Three 8-day, 9 km, and level 3 SeaWiFS chl-a data were used according to the period when Leo persisted. Leo occurred between April 25 and May 3. The chl-a data are shown in Figures 4(b) and 4(c), and time scales are shown separately from April 23 to April 30 and from May 1 to May 8. In fact, Leo began to influence the marked eddy area before April 30; however, due to the fact that high chl-a which is a response to a typhoon usually delayed several days (e.g., 3-4 days, Walker et al. [13]), phytoplankton bloom did not exist in prestorm conditions from April 23 to April 30 (Figures 4(a) and 4(b)), and the obvious increase of chl-a is present in Figure 4(c) in CCE region. The first 8-day data (from April 23 to April 30) was set as “prestorm,” and the second 8-day data (from May 1 to May 8) as “post-storm.”

The general characteristic of chl-a spatial distribution is that chl-a concentration is higher in coastal waters and is lower in offshore waters (Figures 4(a) and 4(b)) [39]. The CCE was located in the northern continental slope of SCS where the chl-a was higher than the central ocean region. Before the effects of typhoon Leo, the average chl-a calculated in the eddy area from April 15~22 and from April 23~30 was, respectively, 0.1111 mg/m^3 and 0.1113 mg/m^3 (Figures 4(a) and 4(b)). The difference is only 0.0002 mg/m^3 . Although it is hard to determine whether the variation 0.0002 mg/m^3 was caused by Leo, the variation can be neglected when compared with the increase of chl-a in CCE after typhoon (Figure 4(c)). Figure 4(c) shows that the typhoon track has passed the CCE area, and the chl-a obviously increased in the CCE area (Figure 4(c)). It is noted that higher chl-a values were mainly present on the western center of CCE area, which is closer to the typhoon center (Figure 4(c)), rather than on the right side of the storm track. The poststorm average chl-a was up to 0.7174 mg/m^3 , more than 6 times greater than that before typhoon. An area of more than $14,400 \text{ km}^2$ had chl-a higher than 1 mg/m^3 . The region surrounded by -14 cm contour around the western center covered roughly $12,000 \text{ km}^2$, where average chl-a concentration was as high as 1.7371 mg/m^3 . But

before Leo, it was about 0.1069 mg/m^3 in the same region. The high chl-a did not last for long, as it rapidly decreased to 0.1605 mg/m^3 from May 9 to May 16 (Figure 4(d)) which was very close to the level before typhoon Leo.

Figure 5 is the frequency distribution of pretyphoon and posttyphoon chl-a in the CCE area. Before Leo, 76% chl-a concentration values mainly concentrated within a small range from 0.08 to 0.12 mg/m^3 ; after Leo, these values became dispersive. About 19% of pixel values fell within the range of 0.08 to 0.12 mg/m^3 ; 28% of pixel values were more than 1 mg/m^3 . It indicates that chl-a concentration values are relatively uniform before typhoon; after typhoon passage, chl-a values obviously increased in various amplitudes in different regions in the CCE area.

Figure 6 shows the area of associated CCE before and after typhoon Leo. The CCE was generated in local position and intensified by cyclonic wind stress of the typhoon. On the SSHA images in Figure 4(b), eddies presented a series of closed contours. The horizontal distance and height difference between the amplitude and the outermost contour of eddy separately implies eddy's area and intensity of cyclonic circulation. The intensification of CCE diagnosed from SSHA data is represented by expansion of the CCE's area and the deepening of SSHA. On April 28 before Leo, the CCE's outermost contour value was shown to be -7 cm and minimum amplitude at center was -15 cm (Figure 6(a)). The CCE covered approximately $66,700 \text{ km}^2$. By May 5 after Leo passed, the outermost contour of CCE became -11 cm ; minimum amplitude at center deepened to -25 cm ; its area expanded to $75,500 \text{ km}^2$ (Figure 6(b)). It is easy to see that CCE was intensified by Leo from the change of the SSHA. However, the description above is not clear enough and ignores the volume effects of CCE. Thus, the intensification was further described by EKE and EAGPE. The SSHA data on April 28 were used to calculate prestorm energy. EKE and EAGPE, respectively, were $1.70 \times 10^{14} \text{ J}$ and $1.13 \times 10^{15} \text{ J}$. The poststorm energy was calculated based on the SSHA at the region of CCE on May 5, which is 4 days after typhoon. (Hereafter, the same method is used to calculate EKE and EAGPE for other typhoons.) Poststorm EKE and EAGPE grew significantly, and they were 1.8 and 4.6 times, respectively, larger than those on April 28 (see Table 2). In this case,

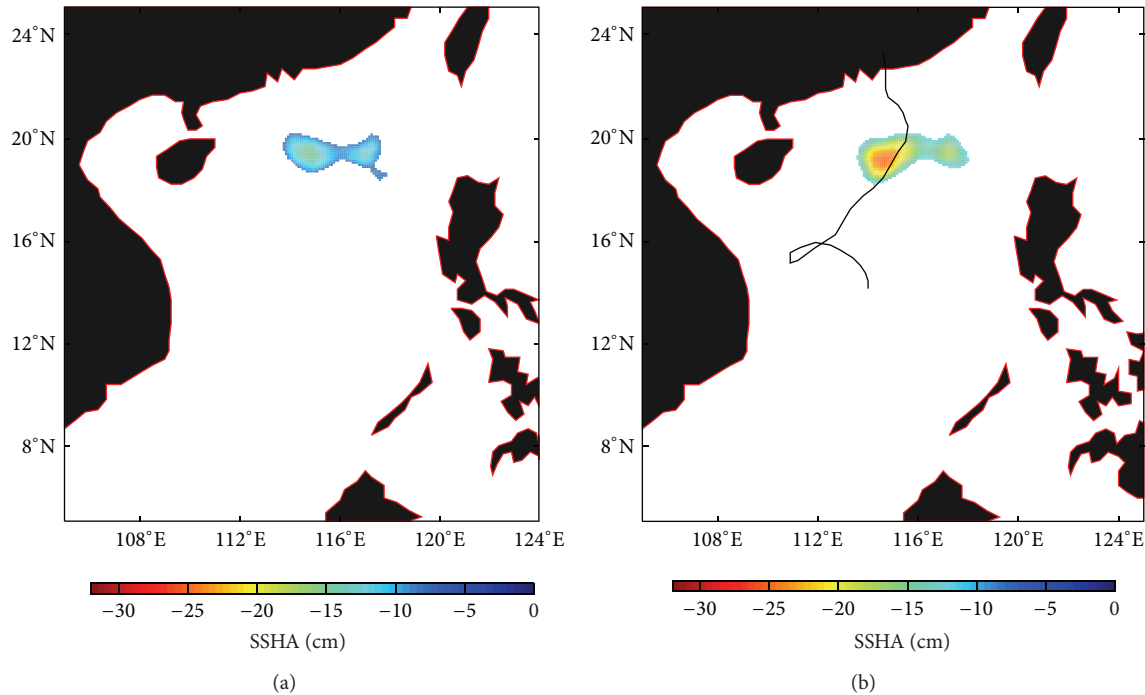


FIGURE 6: The SSHA images show the CCE which was passed by typhoon Leo. (a) SSHA on 28 April, 1999. (b) SSHA on 5 May, 1999. The black solid line is the track of Leo.

the CCE enhanced by Leo can be quantitatively calculated; the CCE extracted much more EAGPE energy than EKE.

3.2. Typical Case: Typhoon Hagibis. Typhoon Hagibis showed a special track (Figure 7(b)). Hagibis was generated over the east Pacific Ocean on November 18, 2007, near 8.6°N, 128°E. After crossing the Philippines as a tropical depression, Hagibis entered into SCS and upgraded to a tropical storm soon after. The tropical storm meandered northwest across the northern part of SCS and continued to intensify. On November 21, the storm strengthened into typhoon status and then gradually approached a CCE region to the southeast of the coast of Vietnam. Hagibis did not keep moving northwest but wobbled off the coast of Vietnam on November 22 and gradually weakened in the eastward track. By November 23, the storm turned back eastward in the SCS towards the Philippines once again. It weakened to a depression and disappeared in the east of the Philippines on November 27. Hagibis's center entered a CCE area on November 22, with a radius of 320 km and class 7 wind speed of 15 m/s. It stopped its eastward movement over the CCE area. The typhoon center left the CCE area on November 25 (Figure 7(b)). The SSHA data on November 24, when Hagibis began to turn back, were used to fix the CCE location. The outermost edge of this CCE was surrounded by 0 m contour; its minimum SSHA is -20 cm, and the eddy covered approximately 143,200 km².

From November 17~24, the CCE area was covered by cloud so extensively that seldom chl-a information was able to be obtained from this area. The previous data from November 9~16 were chosen to represent the prestorm stage. The average chl-a concentration of prestorm was shown as 0.1145 mg/m³

(Figure 7(a)), which is consistent with the general range 0.1~0.2 mg/m³. Compared with Sun et al.'s result [40] which is 0.14 mg/m³ diagnosing by the MODIS data (the area Sun et al. [40] used to calculate average chl-a concentration is larger than ours), the value of prestorm concentration is rational. From November 25 to December 2, the chl-a in the CCE area increased greatly, and the average chl-a was up to 1.4338 mg/m³. The area of chl-a whose values were higher than 1 mg/m³ was larger than 64,370 km². The high chl-a was mainly located on the eddy center (Figure 7(b)). The chl-a value was still very high until the next 8-day period from December 3~10. The average chl-a concentration became 0.9464 mg/m³ and the area of that concentration more than 1 mg/m³ exceeded 34,500 km².

The CCE changes on the SSHA image were shown in Figures 7(c) and 7(d). The prestorm SSHA data on December 21 showed a CCE whose outermost contour value was 0 m and the minimum SSHA value was -14 cm and an area covered by cyclonic circulation (Figure 7(c)). On December 28 after Hagibis, the two cyclonic circulations merged into a new larger CCE (Figure 7(d)). Its minimum SSHA value deepened from -14 to -29 cm, while the area that CCE covered was two times as large as the area before typhoon. It is noted that, first, the speed of typhoon Hagibis was slowest, and second Hagibis' special track (Figure 7(d)) made the typhoon center stay over the region of CCE for a much longer time than typhoon Leo. These two factors make Hagibis overlay over the CCE for the longest forcing time, greatly enhancing CCE. The poststorm EKE was 3.4 times larger than the prestorm EKE, while the poststorm EAGPE was about 8.8 times larger than

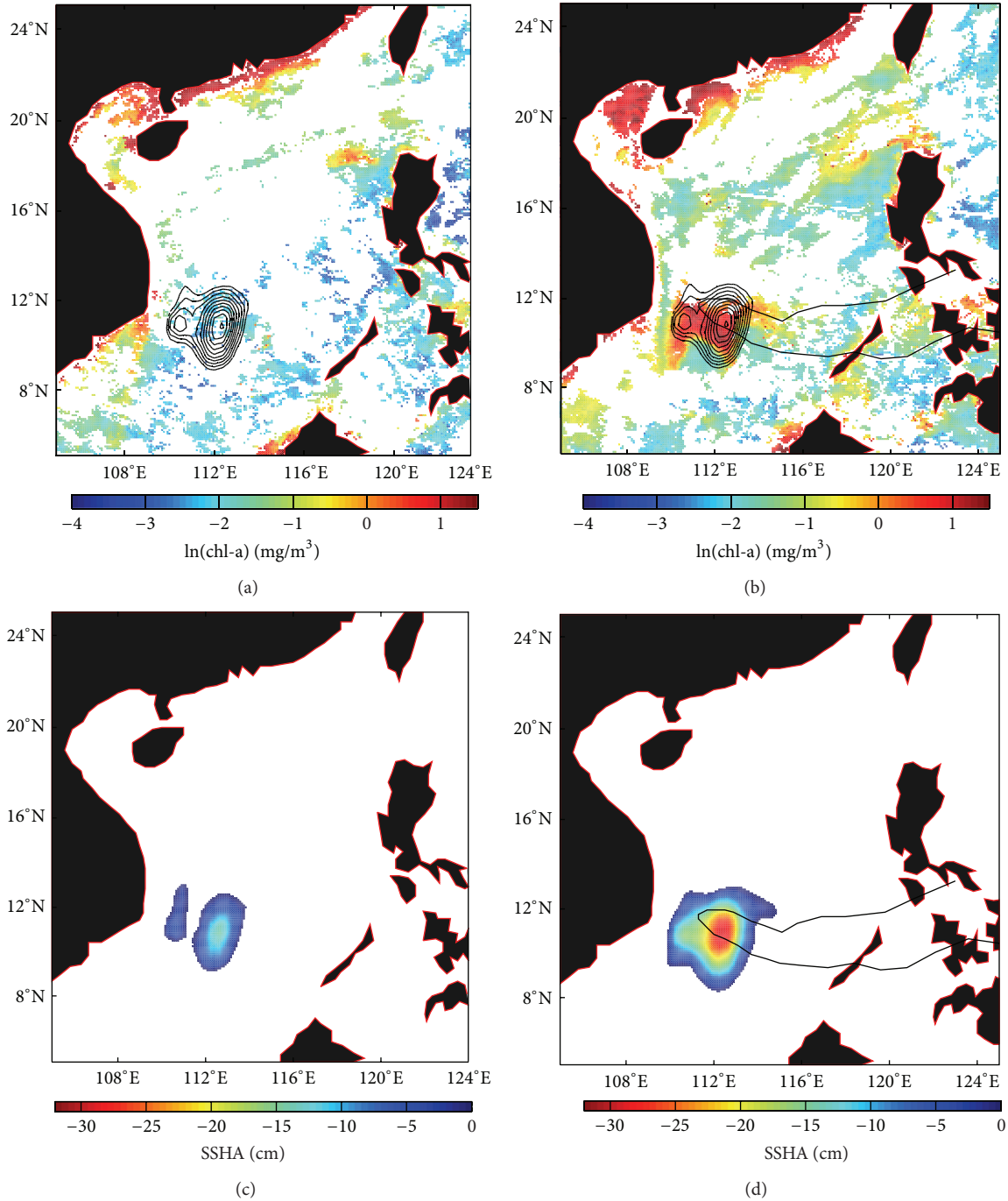


FIGURE 7: (a)-(b) The change of chl-a concentration under the influence of typhoon Hagibis in the CCE area. Colorbar is the natural logarithm value of chl-a concentration. The closed contour indicates the CCE area on 24 November. (a) Prestorm chl-a distribution from 9 November to 16 November, 2007. (b) The poststorm chl-a distribution from 25 November to 2 December, 2007. (c)-(d) The change of CCE under the influence of typhoon Hagibis. (c) The SSHA image shows the CCE on 21 November before typhoon Hagibis. (d) The SSHA image shows the CCE on 28 November after typhoon Hagibis. The thick black solid line in figures (b) and (d) is the track of Hagibis.

the prestorm one. The large baroclinic EKE and EAGPE of poststorm CCE extracted from Hagibis indicate that typhoon Hagibis intensified the energy of the associated CCEs and made the two prestorm CCEs unstable and finally combined them into one CCE. Compared with typhoon Leo, EKE and EAGPE of the associated CCE were greatly enhanced

by Hagibis, especially the EAGPE of CCE was dominantly enhanced.

3.3. *Other Typhoons.* Similar methods were used to calculate the change of chl-a and CCEs' energy under the influence of other six typhoons. According to the JTWC, Nanmadol,

TABLE 3: The prestorm and poststorm dates corresponding to Figure 11 for SST differences.

Typhoon's name	Prestorm day/month/year	Pass by CCE time day/month/year	Poststorm day/month/year
Leo	24/04/99	30/04/99	01/05/99
Lingling	04/11/01	10/11/01	11/11/01
Nanmadol	29/11/04	03/12/04	06/12/04
Kai-tak	26/10/05	30/10/05	01/11/05
Chanchu	06/05/06	16/05/06	17/05/06
Durian	23/11/06	03/12/06	04/12/06
Utor	05/12/06	12/12/06	18/12/06
Hagibis	18/11/07	24/11/07	26/11/07

Kai-tak, Chanchu, Durian, Utor, and Lingling were selected typhoons before they overlaid eddies. The associated CCEs which were overlaid by typhoons mentioned above and prestorm chl-a are shown in Figure 8 while Figure 9 shows chl-a concentration after typhoon exerted its influence on sea and corresponding typhoon tracks. Nanmadol is the only case in which the typhoon center did not pass through the CCE. Durian and Utor passed through the same CCE successively. The detailed typhoon information during the period that they overlaid corresponding CCEs is shown in Table 1 while Table 3 shows the prestorm and poststorm dates corresponding to each typhoon. Table 3 also shows the time when typhoons passed through their corresponding CCEs.

According to Table 1, four typhoons kept a slow transit speed of less than 3 m/s. Especially for Hagibis and Kai-tak, the transit speeds were less than 2.2 m/s. Six typhoons had a strong maximum mean wind speed of more than 40 m/s when they passed through the CCE areas. Nanmadol had the fastest transit speed of 6.4741 m/s and it was the only one whose center did not directly pass through the corresponding CCE. Chanchu was the strongest typhoon with maximum wind speed of 59.676 m/s when it was over the CCE.

Before typhoons overlaid the CCEs, the chl-a in the CCE region corresponding to Chanchu (see Figure 8) had the lowest value, which matches the average value in spring. In this season, the center basin of the SCS is oligotrophic. On the contrary, the chl-a in the CCE region corresponding to Kai-tak (see Figure 8) had a higher prestorm value, since the CCE was located to the eastern Vietnam coast where the high prestorm chl-a was induced by monsoons. The chl-a in the CCE region corresponding to Nanmadol was also higher, since the chl-a concentration in the northern SCS is higher in winter. It is noted that the chl-a was obviously high to the north of the CCE region, where upwelling effects were induced by the northeasterly monsoons around the Philippine Island. For Lingling, Durian, and Utor, the corresponding CCEs were in the center basin of the SCS like the scenario of Chanchu, but the chl-a in those CCEs were higher than those of Chanchu. It is because the chl-a concentration in winter is higher than that in spring.

Table 1 shows that, in general, the chl-a average in preexisting CCE was between 0.08 and 0.20 mg/m³ before typhoons' influence. After typhoons, the chl-a average was

different (see Figure 9), changing from 0.2454 to 1.4338 mg/m³ (see Table 1). It is emphasized that typhoon Durian first passed through the region of a CCE during December 3~10, 2006, and then Utor passed through the same CCE region from December 11~18, 2006. Due to typhoons continuously passing through the same region of CCE, the prestorm EKE and EAGPE of the CCE before typhoon Utor were strong. However, the chl-a increases induced by Durian and Utor were in different regions of CCE, which did not interfere with each other. These results were also shown both in SeaWiFS and MODIS chl-a data. To eliminate the interference of Durian on the data of prestorm chl-a of Utor, the chl-a data from 25 November to 2 December as the prestorm chl-a of Utor was used, same as Durian's, instead of the data from December 3~10.

Because cyclonic circulation before the influence of typhoon Chanchu on May 10, 2006, did not meet the criteria of eddy detection, the prestorm EKE and EAGPE of CCE were not able to be calculated. Table 2 shows that the order of CCE's EKE and EAGPE was 10¹⁴~10¹⁵ J. By comparing the prestorm and poststorm CCE energy, almost all eddies were enhanced by the influence of typhoons (Table 2). The exception of a reduced EKE was the scenario of typhoon Durian, when EKE was calculated from November 29 to December 6. The CCE had two cores separately located in the north and south of the CCE area. Durian passed through the CCE on December 3. By December 6, the northern core disappeared. The southern core of CCE was closer to the typhoon track as it was intensified. The new eddy with lower spin velocity had decreased EKE, while its EAGPE still increased. In other cases, the poststorm EAGPE was always more enhanced than the poststorm EKE. The minimum energy increases occurred in Nanmadol, whose center did not directly pass through the CCE and whose transit speed was rapidest. The maximum EAGPE increases occurred in Hagibis, which had slower transit speed with the longest effect on CCE.

3.4. Analysis of EKE, EAGPE, and chl-a in CCE. The scenarios of typhoon over CCE are so few that the effects of transit speed of typhoons are only examined here. In the CCE, a typhoon with slower transit speed induces greater chl-a change. Figure 10 shows that the lower transit speeds of Hagibis, Kai-tak, and Leo are corresponding to the higher ratios of poststorm chl-a/prestorm chl-a with value of 12.5, 4.9, and 6.6, poststorm EKE/prestorm EKE with value of 3.4, 5.0, and 2.2, and poststorm EAGPE/prestorm EAGPE with value of 8.9, 3.8, and 3.1. It is obvious that the ratio of poststorm EAGPE/prestorm EAGPE and the ratio of poststorm chl-a/prestorm chl-a decrease monotonously. It is clear the chl-a, EKE, and EAGPE in CCE regions are able to be enhanced by the typhoon with slow transit speed. Especially when the typhoon Hagibis interacted on CCE for a long time, the EAGPE and chl-a were greatly enhanced. However, though Lingling is a strong typhoon, the ratio of poststorm EKE/prestorm EKE is not as large as those of typhoon with slow transit speeds. Nanmadol, Utor, Durian, and Lingling with higher transit speeds are corresponding to the lower ratios of poststorm chl-a/prestorm chl-a with value of 2.9, 2.2, 2.3, and 3.9, poststorm EKE/prestorm EKE with value of 1.3,

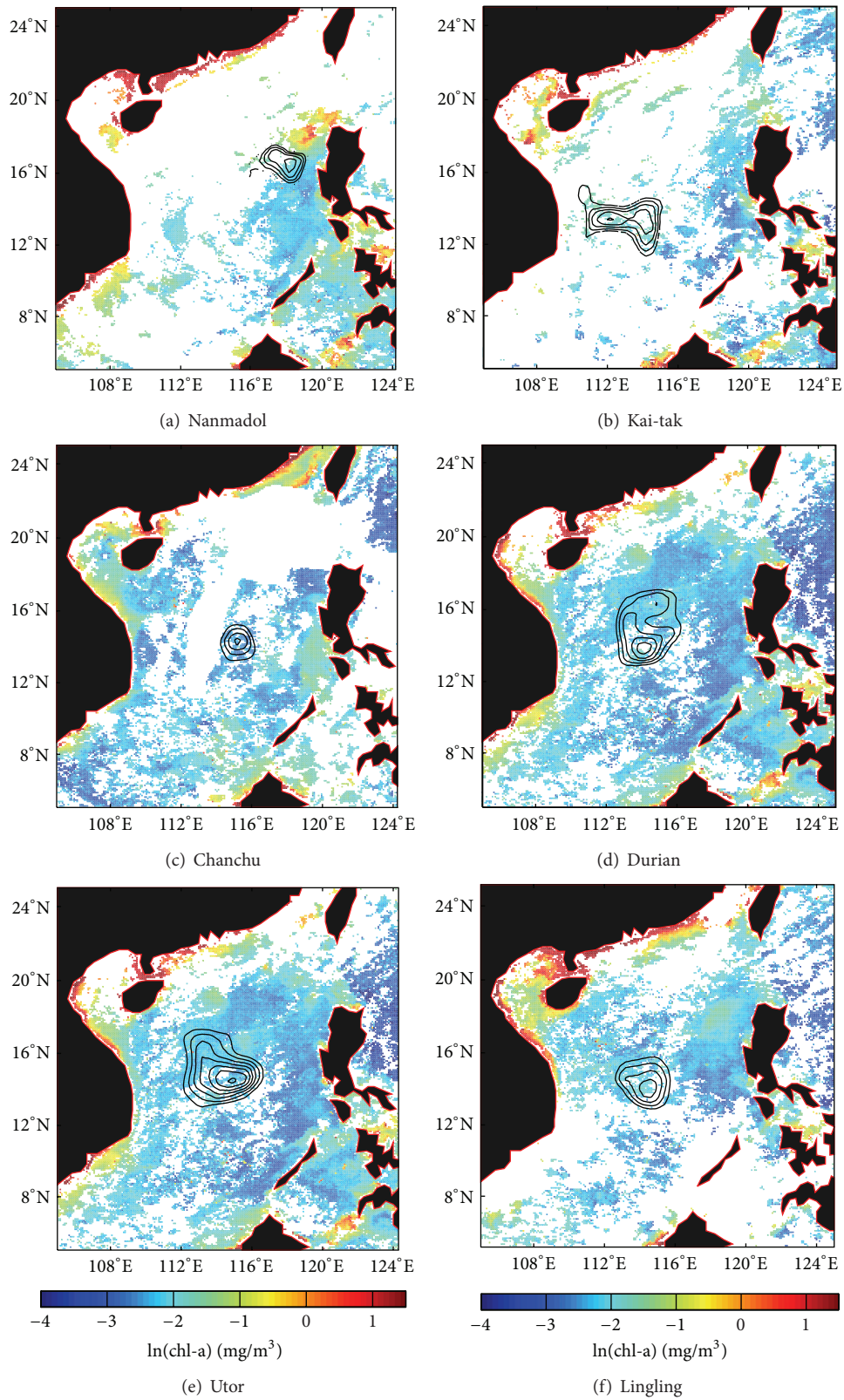


FIGURE 8: The chl-a concentration in preexisting CCEs before typhoons. Colorbar is the natural logarithm value of chl-a concentration.

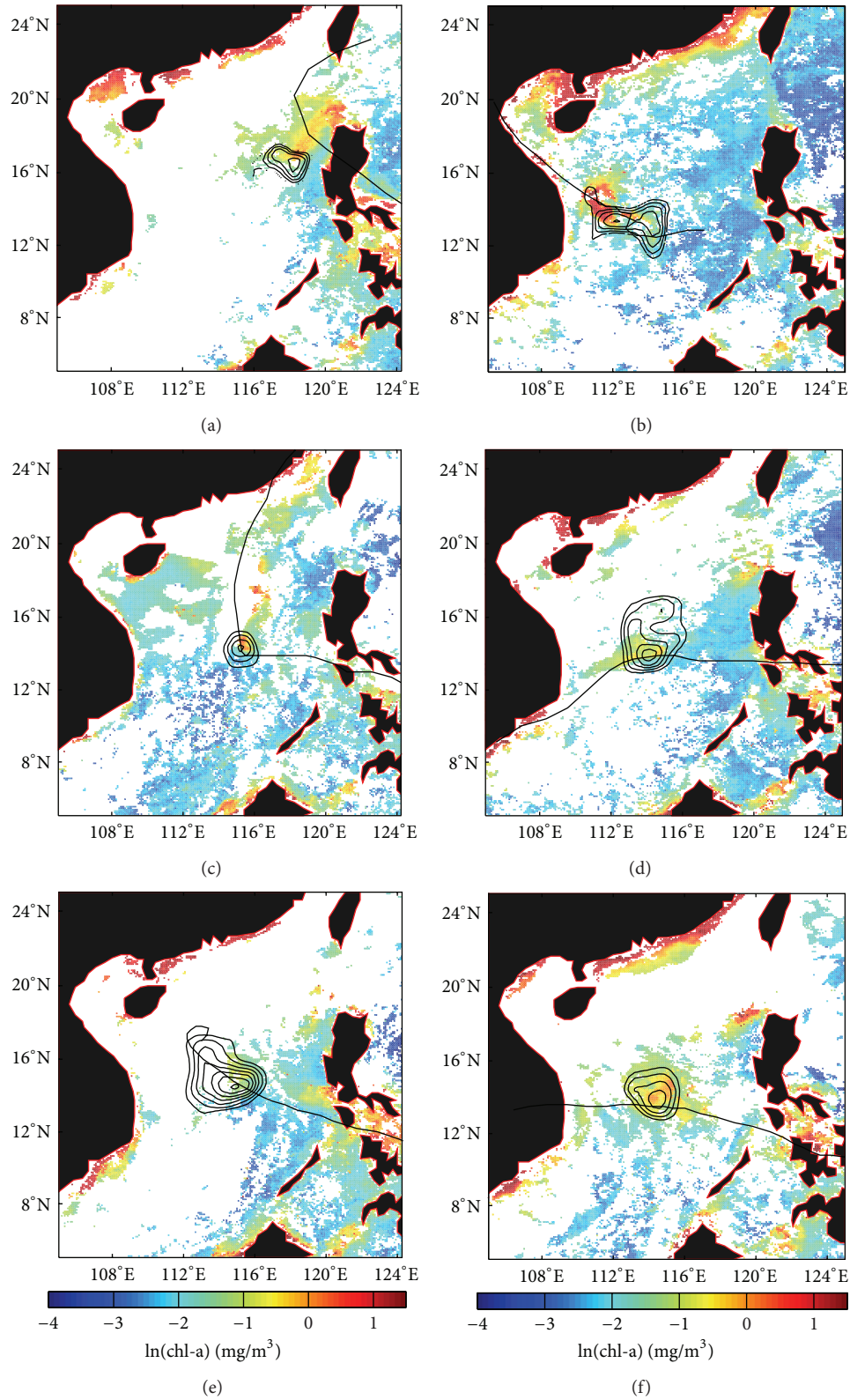


FIGURE 9: The chl-a blooms under the influence of typhoons in the CCE area. Colorbar is the natural logarithm value of chl-a concentration. The thick black solid lines in figures are typhoon tracks. The closed contours are the CCEs influenced by typhoons. (a) Typhoon Nanmadol in December 2004. chl-a concentration is from 2 December to 9 December. (b) Typhoon Kai-tak in November 2005, and chl-a concentration is from 1 November to 8 November. (c) Typhoon Chanchu in May 2006, and chl-a concentration is from 17 May to 24 May. (d) Typhoon Durian in December 2006, and chl-a concentration is from 3 December to 10 December. (e) Typhoon Utor in 2006, and chl-a concentration is from 11 December to 18 December. (f) Typhoon Lingling in 2001, and chl-a concentration is from November 9 to November 16.

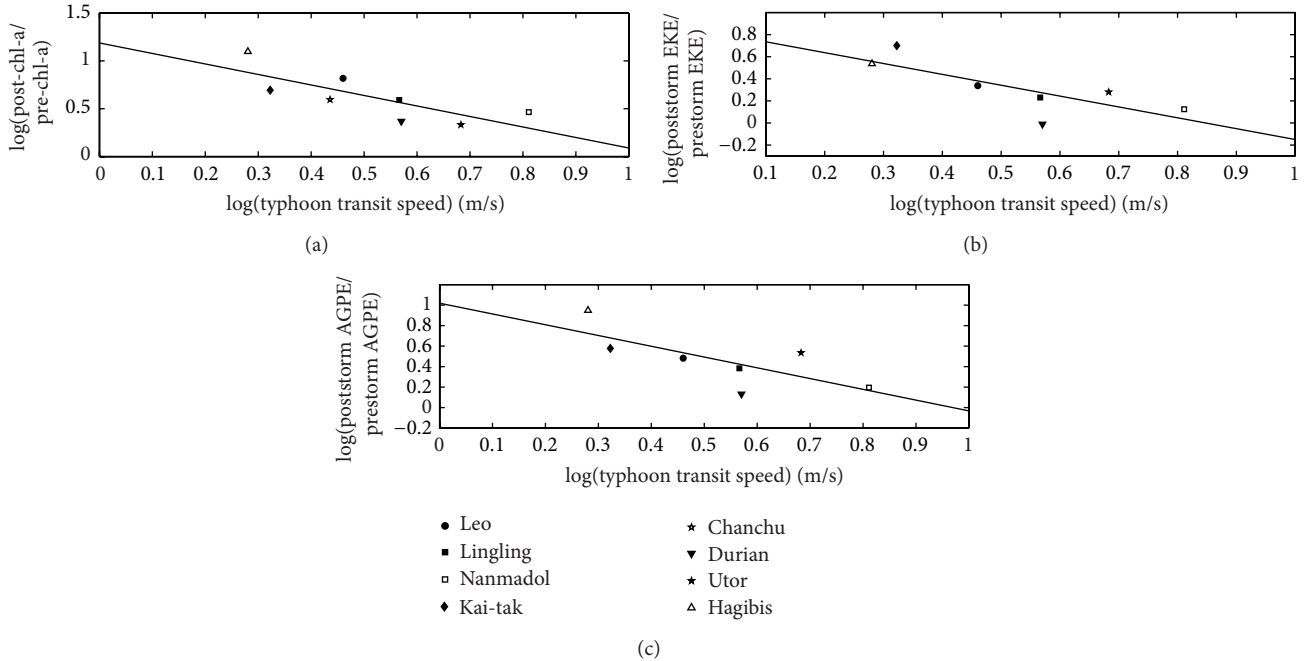


FIGURE 10: The ratio of poststorm (a) chl-a, (b) EKE, and (c) EAGPE to prestorm chl-a, EKE, and EAGPE, respectively, versus typhoon transit speed in logarithm coordinate.

1.9, 1.3, and 1.7, and poststorm EAGPE/prestorm EAGPE with value of 1.6, 3.4, 1.6, and 2.4.

Comparing EAGPE with EKE, EAGPE is much higher than EKE regardless of both prestorm or poststorm (see Table 2). EAGPE is considered as a dominant physical parameter to describe the changes of CCEs' response to typhoons. Why the poststorm EAGPE is enhanced is able to be attributed to many reasons. First, the wind stress curl of typhoon has the same polarity as the vorticity of cold eddies. Second, the wind stress vector turns clockwise as typhoon passes by on the right side of its track in the Northern Hemisphere. Hence the divergence of horizontal circulation will be enhanced, which may induce a significant horizontal pressure gradient towards the center of cold eddy. It implies that the amplitude of the SSHA in the core of cold eddy will increase, meaning the EAGPE is increased significantly. Meantime, the upper-layer deepening is able to be induced by intensified turbulent mixing under the circumstance of typhoon [36] but note that this effect is not involved in the calculation of EAGPE.

In fact, SST is a key physical factor to indicate the chl-a increase. The more the EAGPE changes, the higher the isotherms/isopycnals rise in the core of cyclonic eddy, which produces an easier condition for SST cooling. Thus, strengthened EAGPE may have lower SST in the center of the CCE and larger chl-a concentration. Figure 11 shows the SST change under the influence of typhoon in the CCE area. The maximum SST cooling, which can reach 3~9°C, always occurred 1~2 days after typhoons passed by the CCE. In the other regions along the typhoon tracks, the SST cooling was usually less than 3°C. Except Kai-tak, chl-a bloom corresponded well with the SST cooling position for the other

seven typhoons. Especially in the cases of Durian and Utor, the largest SST cooling mainly occurred on the right side of the typhoon track in the CCE area and in different regions of the same CCE area, which is consistent with the chl-a bloom in the positions separately caused by Durian and Utor. For Kai-tak, the distribution of the cooling SST in the CCE does not superpose the area of larger chl-a concentration, and thus a reasonable explanation cannot be found for this result (see Figure 11(d)).

Figures 11(b), 11(d), 11(e), and 11(h) show that variations of SST were able to reach 6~9°C. The SST in the center of CCE was cooled down to ~7.9°C by typhoon Hagibis. The EAGPE was greatly enhanced and the poststorm EAGPE had larger value of 5.76×10^{15} J, and the difference in EAGPE (poststorm EAGPE – prestorm EAGPE) was 5.11×10^{15} J. The SSTs in the center of the CCE were also cooled down to ~8°C by typhoons Lingling and Kaitak, and the enhanced EAGPE of CCE had a larger value of 2.46×10^{15} J and 5.65×10^{15} J, and the corresponding difference in EAGPE of CCE was 1.81×10^{15} J and 3.31×10^{15} J, respectively. Though typhoon Utor had a small SST cooling at the center of the CCE, the Durian and Utor typhoons continuously forced on the same CCE; thus, both Durian and Utor cooled down SST to roughly ~7°C and enhanced the EAGPE from 1.11×10^{15} to 5.17×10^{15} J, which generated the EAGPE difference of 4.06×10^{15} J in the CCE. Leo cooled down the center SST of the CCE to 4~5°C, and the ratio of poststorm EAGPE/prestorm EAGPE was 3. The difference in EAGPE of the CCE was 2.3×10^{15} J. Nanmadol's track did not pass through the center of the CCE, and the SST of the CCE was cooled down to only 3°C. The difference in EAGPE of the CCE was 1.64×10^{15} J. Hence, qualitatively,

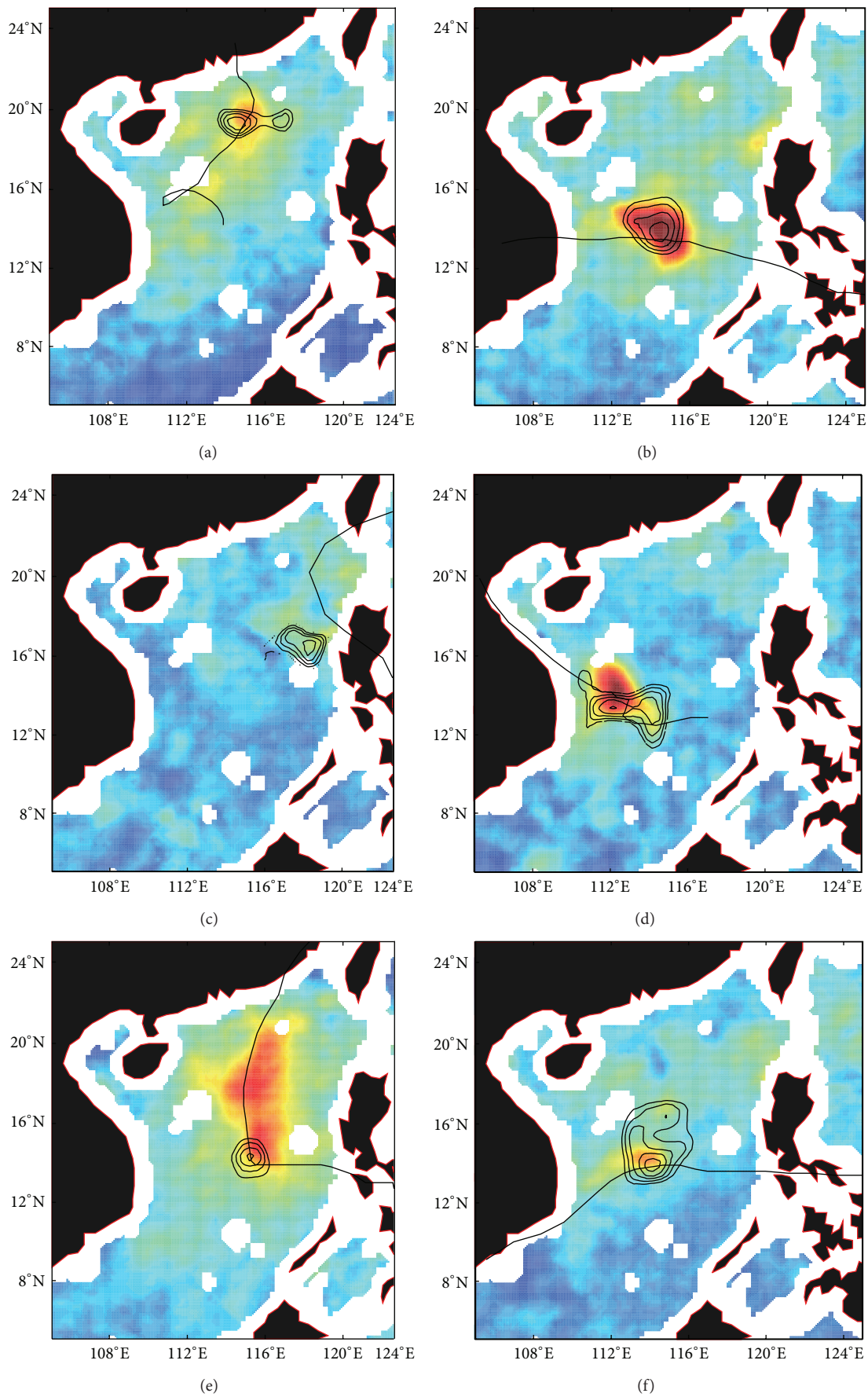


FIGURE II: Continued.

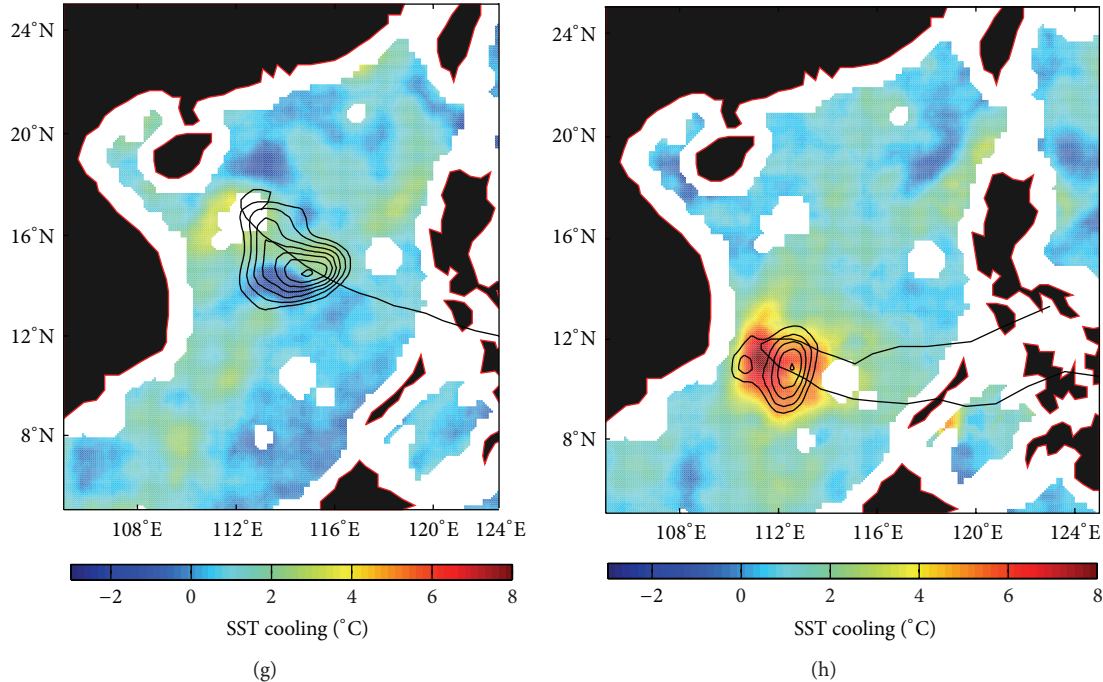


FIGURE 11: The SST cooling under the influence of typhoons in the CCE area. The thick black solid lines in figures are typhoon tracks. The closed contours are the CCEs influenced by typhoons. The colorbar is the temperature difference before storm and after storm; the exact prestorm and poststorm day are from Table 3. (a) Typhoon Leo, (b) Lingling, (c) Nanmadol, (d) Kai-tak, (e) Chanchu, (f) Durian, (g) Utor, and (h) Hagibis. The date of the CCEs is on the day that typhoon passed the CCE.

the more changes in SST at the center of the CCE caused by typhoons, the larger changes in EAGPE of the CCE. However, SST is controlled by many factors, such as turbulent mixing, surface radiative forcing, and evaporation. The relationship between SST changes and EAGPE variations cannot be so easily addressed and this is why their relationship cannot be described by a simple formula in this analysis.

4. Discussion

It is noted that the chl-a average in CCE areas is averaged from all the chl-a pixel values in the CCE. Thus, the poststorm peak pixel values are always much larger than the average ones. For example, in Leo's case, average concentration was 0.7174 mg/m^3 , while there were about 8% pixel with values higher than 2 mg/m^3 .

The increase of chl-a is related to ocean conditions such as where preexisting CCE located, over the continent slope or deep sea regions, which may influence the horizontal and vertical distribution of chl-a in preexisting CCE regions. Moreover, local nutrients, water temperature, and ocean currents also impact the condition of phytoplankton bloom. Storm factors such as maximum wind speed and transit speed of storms are also influential. Leo and Chanchu occurred in spring, and the corresponding preexisting CCEs were over the regional continent slope of the northern SCS and in the center of the SCS, respectively. The prestorm chl-a concentration was lower in the center of the SCS than that

over continent slope. Though the transit speed of Chanchu was lower than Leo's, the poststorm chl-a for Leo was higher than that for Chanchu. It is proposed that the sea water over continent slope of the northern SCS has more nutrient than that in the center of the SCS. Here, at the end of April, the monsoon with southeastern direction cannot induce the upwelling and did not influence the chl-a concentration of preexisting CCE for Leo. The preexisting CCE for Chanchu is in the center of SCS and far from the coast. The monsoon also did not influence the chl-a in the CCE; therefore the chl-a in the CCE was dominantly influenced by both the preexisting CCE and Chanchu's effect.

The other typhoons occurred in autumn and winter; the prestorm chl-a in preexisting CCEs was higher than those of Leo and Chanchu due to different seasons. Therein, the prestorm chl-a of preexisting CCE for Kai-tak was somewhat higher than others, which may be explained by upwelling induced by monsoon (see Figures 2 and 8(b)). For Nanmadol, based on Figures 2 and 8(a), it is found that the highest chl-a concentration induced by monsoon was out of the region in a preexisting CCE, and the preexisting CCE for Nanmadol was in the deep sea region ($>3000 \text{ m}$); therefore, monsoon effect can be ignored. However, in December, the southwestward wind may bring a small quality of chl-a from the Luzon Strait to the preexisting CCE; thus, the prestorm chl-a of the preexisting CCE for Nanmadol was also somewhat higher than others. In posttyphoon chl-a distribution, the chl-a pixel values had a larger gradient in the CCE area, which indicates that

the chl-a response was not uniform. There are three types of posttyphoon chl-a distributions in CCE areas.

- (1) The enhanced chl-a is around the maximum negative SSHA. For the cases of Leo, Lingling, and Hagibis, the higher chl-a values concentrated in the closed contours around the maximum negative SSHA, and there was not an obvious right-biased feature.
- (2) The enhanced chl-a concentration in CCE presents a right-biased feature such as in the cases of Chanchu, Durian, and Utor, where the chl-a increase occurs mainly on the right of each typhoon's tracks in the CCEs.
- (3) The enhanced chl-a concentration is not in the center of the CCE. For the cases of Kai-tak and Nanmadol, the distribution of higher chl-a had deviated from closed contours in the center. For Nanmadol, its track was relatively far from the CCE where the pattern of chl-a bloom was outside of the CCE. That is, higher chl-a had deviated from the CCE center and was on the right side of the track. It is noted that the region of chl-a bloom with highest concentration was near the Philippines coast, where rich nutrients from the land are washed down by rain. Based on Figures 2, 8(a), 9(a), and 11(c), it is clear that Nanmadol induced the lower SST in the CCE region; thus, the posttyphoon chl-a in the CCE was mainly induced by typhoon, though a small part of phytoplankton may be from the Luzon Strait to the CCE by horizontal advection. It is also found that between the CCE and the Philippines coast there was significantly lower chl-a, which suggests that there was no upwelling in the coast located in the eastern CCE. For slow transit typhoon Kai-tak, which overlaid a large CCE covering poor and rich nutrients regions of sea, the concentration of chl-a was highest in the region toward the coast rather than in the center of the CCE. It is noted that the chl-a concentration was not continuous and lower between the Vietnam coast and the CCE, which indicates that monsoon effects can be ignored. Based on Figures 2, 8(b), 9(b), and 11(d), the lowest SST may be induced by typhoon entrainment and mixing while the enhanced CCE interacted with the topography. Thereby, the distribution of lowest SST may be influenced by topography and was not in the center of CCE, so did the distribution of chl-a.

When typhoon overlays the region where no CCE persists, the potential upwelling velocity caused by typhoon wind stress is expressed by using the Ekman pumping velocity (EPV) formula [41],

$$EPV = \text{curl} \left(\frac{\vec{\tau}}{\rho f} \right), \quad (7)$$

where ρ is the density of sea water, f is the Coriolis parameter, and $\vec{\tau}$ is the wind stress. The EPV is a decisive factor for cooling down the sea surface temperature and transforming the nutrient water from deep layer to euphotic layer. However,

Sun et al. [40] argued that the forcing time of typhoons must exceed geostrophic adjustment time if upwelling velocity reaches EPV in (7); otherwise, the upwelling will be less. So when the forcing time reaches geostrophic adjustment time, the upwelling velocity reaches its maximum.

When a typhoon acts on the region with CCE, upwelling velocity should include two parts:

$$EPV_2 = EPV' + EPV_1, \quad (8)$$

where EPV_1 is upwelling velocity attributed to preexisting cyclonic eddy and EPV' is upwelling velocity attributed to typhoon without preexisting CCE.

When a typhoon acts on the region with CCE, the vertical mixing induced by turbulence dominates cooling (75%–90%) in the mixed layer [2], and upwelling only enhances entrainment under slowing transit typhoons and further lifts up the isotherms of CCE [18]. Both vertical mixing and upwelling all cool down the SST, indicating transformation of the nutrients from deeper to shallower.

Since upwelling can lift up the isotherms of CCE, which changes the depth of thermocline, EPV_2 should be a key parameter to transform the nutrient saltiness from the deeper layer (deeper than mixed layer) to the depth where phytoplankton blooms. Thus the amount of transporting nutrient saltiness can be estimated by this EPV_2 . Hence, in (8), supposing EPV_1 is a constant, EPV' is still a dominant factor to enhance the chl-a in a CCE region when the typhoon overlays the CCE. In the observation, the largest EPV' was for Hagibis, which corresponds to the largest chl-a increase: 1.4338 mg/m^3 in a CCE located in the poor nutrient region. The chl-a increases induced by other typhoons were much lower than the value corresponding to Hagibis, because their forcing time was less than geostrophic adjustment time.

In eight typhoon cases, those typhoons with very slow moving velocity, such as typhoon Leo, Kai-tak, and Hagibis, above their corresponding CCEs had much higher poststorm chl-a concentration than that when typhoons had no CCEs in their way (see Figures 4, 7, 9, and 10). Thus, for the slow moving typhoon, the preexisting CCE plays an important role in enhancing the chl-a concentration. Also, the prestorm chl-a concentration in a CCE influenced by monsoon can be ignored for typhoon Leo, Kai-tak, and Hagibis. For typhoons with transit speeds greater than 3 m/s like Nanmadol and Utor, the ratio of poststorm chl-a/prestorm chl-a was less than 3.9. It reveals that the chl-a contribution from preexisting CCE cannot be ignored. In short, preexisting CCE conditions are important for nutrient transport from deep to upper layers.

The CCEs studied here were generated locally, and in the observation, they did not entangle the coastal phytoplankton in their center. All in all, for the poststorm chl-a concentration, though many factors may affect an ocean response to storm, the preexisting CCE and typhoon transit speed are still the main dynamic factors to influence chl-a concentration. This result is in agreement with the previous study [18].

For chl-a concentration, the data we employed are from NASA (level-3); the arithmetic and solution are accredited. The preexisting CCEs are at least 100 km far from the Vietnam

and Philippine coasts and more than 300 km far from rivers. Therefore, the influence to our observation results by the suspended sediments and CDOM (colored or chromophoric dissolved organic matter) can also be ignored.

It is needed to point out that, except for kinetic energy and gravitational potential energy, typhoons input more energy into the surface waves (1.62 TW) [42], which may enhance vertical mixing. The amount of energy increasement of CCEs just partly demonstrates the energy that typhoons input into the ocean, which reflects the upper ocean responding to typhoons in one way. In addition to the influence of typhoons, other factors may induce the change of CCEs, such as topography and background current. According to the purposes of this study, we only concentrated on the influence of typhoons. The inertial waves induced by typhoon also can enhance the vertical mixing, which can cover the depth from mixed layer to thermocline; however, most energy of inertial waves is out of the CCE center [1, 7, 43]. In the study, the effect on CCEs by inertial waves is ignored.

From the observations, the CCEs are always intensified after typhoons, and CCEs' centers tend to move toward typhoon tracks. When typhoon influences the overlaid CCE, the preexisting CCE is transferred or merges with the cyclonic eddy that triggered by the impending typhoon. To avoid this complex process, we calculated the EKE and EAGPE from the satellite data 4 days after a typhoon passed by a CCE. At the same time, because phytoplankton blooms are 3~5 days after typhoons pass, it is more reasonable to examine the CCEs' area by SSHA data 4 days after typhoon, to describe the relation between chl-a and energy of the CCE.

The estimated value of EKE and EAGPE for CCE are based on SSHA and WOA05. Unfortunately, some idealized assumptions in definition of eddy boundaries and eddy vertical structure and the practical difficulty of observing the CCEs' change during the typhoon occurrences both limit the accuracy of eddy energy estimations. However, in order to not only qualitatively discuss the changes of CCEs' shapes influenced by the typhoons but also explore the energy flow between the atmospheric forcing and the oceanic response, a method was used to calculate the baroclinic energy of preexisting CCE response to typhoons and derive significant results. Errors exist and are hard to estimate, but we believe our results are not strongly affected by them. Moreover, the results are in agreement with the numerical results of Zheng et al. [17] and satellite data-based evaluation of Sun et al. [44] (please note that Sun et al.'s study focused on the typhoons in the Western North Pacific Ocean).

5. Conclusions

In this study, with the absence of *in situ* data, we proposed an effective method to estimate CCE areas with the influence of typhoons, examining the EKE and EAGPE changes and their ecological factors. We investigated chl-a change in CCE areas and described the CCEs' change by EKE and EAGPE using a reduced gravity model before and after eight typhoon cases in SCS. The changes of preexisting baroclinic eddies induced by typhoons are presented by the changes of EKE and EAGPE, and the increments of EKE are generally less

than these of EAGPE. The maximum ratio of poststorm EKE/prestorm EKE reaches 5.0 times, while the maximum ratio of poststorm EAGPE/prestorm EAGPE reaches about 8.9 times; thereby, typhoons significantly change the EAGPE of preexisting CCEs, though most of CCEs' EKE and EAGPE increase simultaneously by the influence of typhoons.

In eight typhoon cases, for typhoon with transit speeds greater than 3 m/s (Nanmadol, Utor), the preexisting CCE plays an important role in enhancing the chl-a, and it is not ignored comparing to poststorm CCE. The chl-a concentration in preexisting CCE is 25% to 45% of those of poststorm CCE, while for typhoon with transit speeds less than 3 m/s, the chl-a concentration in preexisting CCE is about 8% to 25% of those of poststorm CCE. In the CCE area, when the ratio of posttyphoon EAGPE to pretyphoon EAGPE is large, the corresponding ratio of posttyphoon chl-a to pretyphoon chl-a is large too. In addition, we quantitatively calculate the EAGPE (EKE) enhanced from 1.8×10^{15} (0.2×10^{15}) to 5.1×10^{15} (2.9×10^{15}) J by typhoon with transit speeds less than 3 m/s and from 0.4×10^{15} (-0.17×10^{15}) to 3.7×10^{15} (1×10^{15}) J by Typhoon with transit speeds greater than 3 m/s. The enhanced EAGPE (EKE) of CCEs offers evidence for further study on enhanced mixing and deep sea currents by poststorm CCE.

Conflict of Interests

The authors declare that there is no conflict of interests regarding the publication of this paper.

Acknowledgments

This study is supported by Grant XDA11010202, Projects U1033002, 41376022, 41276021, and 41306016 of the Natural Science Foundation of China, and Project 2013CB430303 of the National Basic Research Program. Comments from two referees are highly appreciated.

References

- [1] A. E. Gill, "On the behavior of internal waves in the wake of storms," *Journal of Physical Oceanography*, vol. 14, no. 7, pp. 1129–1151, 1984.
- [2] S. D. Jacob, L. K. Shay, A. J. Mariano, and P. G. Black, "The 3D oceanic mixed layer response to Hurricane Gilbert," *Journal of Physical Oceanography*, vol. 30, no. 6, pp. 1407–1429, 2000.
- [3] T. B. Sanford, P. G. Black, J. R. Haustein, J. W. Feeney, G. Z. Forristall, and J. F. Price, "Ocean response to a hurricane: I. Observations," *Journal of Physical Oceanography*, vol. 17, no. 11, pp. 2065–2083, 1987.
- [4] T. Dickey, D. Frye, J. McNeil et al., "Upper-ocean temperature response to hurricane Felix as measured by the Bermuda testbed mooring," *Monthly Weather Review*, vol. 126, no. 5, pp. 1195–1201, 1998.
- [5] T. D. Dickey and J. J. Simpson, "The sensitivity of upper ocean structure to time varying wind direction," *Geophysical Research Letters*, vol. 10, no. 2, pp. 133–136, 1983.
- [6] J. F. Price, "Upper ocean response to a hurricane," *Journal of Physical Oceanography*, vol. 11, no. 2, pp. 153–175, 1981.

- [7] X. P. Jiang, Z. Zhong, and J. Jiang, "Upper ocean response of the South China Sea to Typhoon Krovanh (2003)," *Dynamics of Atmospheres and Oceans*, vol. 47, no. 1–3, pp. 165–175, 2009.
- [8] M. J. Furnas, "Cyclonic disturbance and a phytoplankton bloom in a tropical shelf ecosystem," in *Red Tides: Biology, Environmental Science and Toxicology: Proceedings of the 1st International Symposium on Red Tides held November 10–14, 1987*, T. Okaichi, D. M. Anderson, and T. Nemoto, Eds., pp. 273–276, Elsevier Science Publishing, Takamatsu, Japan, 1989.
- [9] B. Delesalle, M. Pichon, M. Frankignoulle, and J. P. Gattuso, "Effects of a cyclone on coral reef phytoplankton biomass, primary production and composition (Moorea Island, French Polynesia)," *Journal of Plankton Research*, vol. 15, no. 12, pp. 1413–1423, 1993.
- [10] J. Chang, C.-C. Chung, and G.-C. Gong, "Influences of cyclones on chlorophyll a concentration and *Synechococcus* abundance in a subtropical western Pacific coastal ecosystem," *Marine Ecology Progress Series*, vol. 140, no. 1–3, pp. 199–205, 1996.
- [11] S. M. Babin, J. A. Carton, T. D. Dickey, and J. D. Wiggert, "Satellite evidence of hurricane-induced 9 phytoplankton blooms in an oceanic desert," *Journal of Geophysical Research*, vol. 109, Article ID C03043, 2004.
- [12] M. N. Hanshaw, M. S. Lozier, and J. B. Palter, "Integrated impact of tropical cyclones on sea surface chlorophyll in the North Atlantic," *Geophysical Research Letters*, vol. 35, no. 1, Article ID L01601, 2008.
- [13] N. D. Walker, R. R. Leben, and S. Balasubramanian, "Hurricane-forced upwelling and chlorophyll a enhancement within cold-core cyclones in the Gulf of Mexico," *Geophysical Research Letters*, vol. 32, no. 18, Article ID L18610, pp. 1–5, 2005.
- [14] I. Lin, W. T. Liu, C.-C. Wu et al., "New evidence for enhanced ocean primary production triggered by tropical cyclone," *Geophysical Research Letters*, vol. 30, no. 13, article 1718, 2003.
- [15] S. Shang, L. Li, F. Q. Sun et al., "Changes of temperature and bio-optical properties in the South China Sea in response to Typhoon Lingling, 2001," *Geophysical Research Letters*, vol. 35, no. 10, Article ID L10602, 2008.
- [16] Y. Chen and D. Tang, "Eddy-feature phytoplankton bloom induced by a tropical cyclone in the South China Sea," *International Journal of Remote Sensing*, vol. 33, no. 23, pp. 7444–7457, 2012.
- [17] Z.-W. Zheng, C.-R. Ho, and N.-J. Kuo, "Importance of pre-existing oceanic conditions to upper ocean response induced by Super Typhoon Hai-Tang," *Geophysical Research Letters*, vol. 35, no. 20, Article ID L20603, 2008.
- [18] X. M. Liu, M. H. Wang, and W. Shi, "A study of a Hurricane Katrina-induced phytoplankton bloom using satellite observations and model simulations," *Journal of Geophysical Research C: Oceans*, vol. 114, no. 3, Article ID C03023, 2009.
- [19] P. G. Falkowski, D. Ziemann, Z. Kolber, and P. K. Bienfang, "Role of eddy pumping in enhancing primary production in the ocean," *Nature*, vol. 352, no. 6330, pp. 55–58, 1991.
- [20] E. N. Sweeney, D. J. McGillicuddy Jr., and K. O. Buesseler, "Biogeochemical impacts due to mesoscale eddy activity in the Sargasso Sea as measured at the Bermuda Atlantic Time-series Study (BATS)," *Deep-Sea Research Part II: Topical Studies in Oceanography*, vol. 50, no. 22–26, pp. 3017–3039, 2003.
- [21] F. Nencioli, V. S. Kuwahara, T. D. Dickey, Y. M. Rii, and R. R. Bidigare, "Physical dynamics and biological implications of a mesoscale eddy in the lee of Hawai'i: cyclone Opal observations during E-Flux III," *Deep-Sea Research Part II: Topical Studies in Oceanography*, vol. 55, no. 10–13, pp. 1252–1274, 2008.
- [22] Z. W. Zheng, C. R. Ho, Q. Zheng, Y. T. Lo, N. J. Kuo, and G. Gopalakrishnan, "Effects of preexisting cyclonic eddies on upper ocean responses to Category 5 typhoons in the western North Pacific," *Journal of Geophysical Research C: Oceans*, vol. 115, no. 9, Article ID C09013, 2010.
- [23] T. G. Prasad and P. J. Hogan, "Upper-ocean response to Hurricane Ivan in a 1/25° nested Gulf of Mexico HYCOM," *Journal of Geophysical Research C: Oceans*, vol. 112, no. 4, Article ID C04013, 2007.
- [24] C. Eden and H. Dietze, "Effects of mesoscale eddy/wind interactions on biological new production and eddy kinetic energy," *Journal of Geophysical Research C: Oceans*, vol. 114, no. 5, Article ID C05023, 2009.
- [25] F. Jia, L. Wu, and B. Qiu, "Seasonal modulation of eddy kinetic energy and its formation mechanism in the southeast Indian Ocean," *Journal of Physical Oceanography*, vol. 41, no. 4, pp. 657–665, 2011.
- [26] S. M. Chen and B. Qiu, "Mesoscale eddies northeast of the Hawaiian archipelago from satellite altimeter observations," *Journal of Geophysical Research C: Oceans*, vol. 115, no. 3, Article ID C03016, 2010.
- [27] C. Xu, X.-D. Shang, and R. X. Huang, "Estimate of eddy energy generation/dissipation rate in the world ocean from altimetry data," *Ocean Dynamics*, vol. 61, no. 4, pp. 525–541, 2011.
- [28] G. Wang, J. Su, Y. Ding, and D. Chen, "Tropical cyclone genesis over the south China sea," *Journal of Marine Systems*, vol. 68, no. 3–4, pp. 318–326, 2007.
- [29] G. Wang, J. Su, and C. Chu, "Mesoscale eddies in the South China Sea observed with altimeter data," *Geophysical Research Letter*, vol. 30, article 2121, 2003.
- [30] L. Y. Yuang, *Distribution and characteristics of nutrients in the Northern South China Sea [M.S. thesis]*, Xiamen University, 2005.
- [31] S.-P. Xie, Q. Xie, D. Wang, and W. T. Liu, "Summer upwelling in the South China Sea and its role in regional climate variations," *Journal of Geophysical Research C: Oceans*, vol. 108, no. C8, article 3261, 2003.
- [32] J. E. O'Reilly, S. Maritorena, B. G. Mitchell et al., "Ocean color chlorophyll algorithms for SeaWiFS," *Journal of Geophysical Research C: Oceans*, vol. 103, no. 11, pp. 937–953, 1998.
- [33] A. Davis and X.-H. Yan, "Hurricane forcing on chlorophyll—a concentration off the northeast coast of the U.S.," *Geophysical Research Letters*, vol. 31, no. 17, Article ID L17304, 2004.
- [34] D. Roemmich and J. Gilson, "Eddy transport of heat and thermocline waters in the North Pacific: a key to interannual/decadal climate variability?" *Journal of Physical Oceanography*, vol. 31, no. 3, pp. 675–687, 2001.
- [35] G. Forget and C. Wunsch, "Estimated global hydrographic variability," *Journal of Physical Oceanography*, vol. 37, no. 8, pp. 1997–2008, 2007.
- [36] J. Y. Pan and Y. Sun, "Estimate of ocean mixed layer deepening after a typhoon passage over the south china sea by using satellite data," *Journal of Physical Oceanography*, vol. 43, no. 3, pp. 498–506, 2013.
- [37] C.-Y. Lin, C.-R. Ho, Z.-W. Zheng, and N.-J. Kuo, "Validation and variation of upper layer thickness in South China sea from satellite altimeter data," *Sensors*, vol. 8, no. 6, pp. 3802–3818, 2008.
- [38] R. X. Huang, *Ocean Circulation, Wind-Driven and Thermohaline Processes*, Cambridge University Press, Cambridge, UK, 2010.

- [39] C. Chen, P. Shi, and Q. Mao, "Satellite remotely-sensed analysis of distribution characters of chlorophyll concentration in South China Sea," *Journal of Tropical Oceanography*, vol. 20, pp. 66–70, 2001.
- [40] L. Sun, Y.-J. Yang, T. Xian, Z.-M. Lu, and Y.-F. Fu, "Strong enhancement of chlorophyll a concentration by a weak typhoon," *Marine Ecology Progress Series*, vol. 404, pp. 39–50, 2010.
- [41] J. F. Price, T. B. Sanford, and G. Z. Forristall, "Forced stage response to a moving hurricane," *Journal of Physical Oceanography*, vol. 24, no. 2, pp. 233–260, 1994.
- [42] L. L. Liu, W. Wang, and R. X. Huang, "The mechanical energy input to the ocean induced by tropical cyclones," *Journal of Physical Oceanography*, vol. 38, no. 6, pp. 1253–1266, 2008.
- [43] J. F. Price, "Internal wave wake of a moving storm. Part I: scales, energy budget and observations," *Journal of Physical Oceanography*, vol. 13, no. 6, pp. 949–965, 1983.
- [44] L. Sun, Y.-X. Li, Y.-J. Yang et al., "Effects of super typhoons on cyclonic ocean eddies in the western North Pacific: a satellite data-based evaluation between 2000 and 2008," *Journal of Geophysical Research*, vol. 119, no. 9, pp. 5585–5598, 2014.

Research Article

Low-Frequency Variability of the Yellow Sea Cold Water Mass Identified from the China Coastal Waters and Adjacent Seas Reanalysis

Xuewei Li,¹ Xidong Wang,² Peter C. Chu,³ and Dongliang Zhao¹

¹Physical Oceanography Laboratory, Ocean University of China, 238 Songling Road, Qingdao 266100, China

²Key Laboratory of Marine Environment Information Technology, SOA, National Marine Data and Information Service, Tianjin 300171, China

³Naval Ocean Analysis and Prediction Laboratory, Department of Oceanography, Naval Postgraduate School, Monterey, CA 93943, USA

Correspondence should be addressed to Xidong Wang; xidong.wang@yahoo.com

Received 19 December 2014; Revised 26 March 2015; Accepted 17 April 2015

Academic Editor: Juan Jose Ruiz

Copyright © 2015 Xuewei Li et al. This is an open access article distributed under the Creative Commons Attribution License, which permits unrestricted use, distribution, and reproduction in any medium, provided the original work is properly cited.

This study uses the China Coastal Waters and Adjacent Seas Reanalysis (CORA) data to investigate the interannual and decadal variability of the Yellow Sea cold water mass (YSCWM) and its relationship to climate indices including the Arctic Oscillation (AO), El Niño/Southern Oscillation (ENSO), and Pacific Decadal Oscillation (PDO). On the interannual timescale, the strong correlation between winter PDO and the YSCWM may indicate the dominant effect of winter PDO on the YSCWM through the modulation of local heat flux and wind stress. It is also found that the local wind stress and heat flux in summer have little impact on the interannual variability of the YSCWM. On the decadal time scale, the YSCWM is associated with winter AO and winter PDO. Winter AO mainly controls local heat flux, modulating the decadal variability of the YSCWM. In contrast, winter PDO is strongly connected with winter heat flux and wind stress to modulate the decadal variability of the YSCWM. In summer, for three climate factors, ENSO is the dominant factor controlling the decadal variability of the YSCWM.

1. Introduction

The Yellow Sea is a semienclosed marginal sea of the Pacific Ocean, bordered by the Chinese mainland to the west, the Korean Peninsula to the east, and the Bohai Bay to the north. Several rivers drain into the Yellow Sea and provide a lot of nutrients. The Yellow Sea covers an area of roughly 400,000 km² and it is mostly shallower than 80 m (Figure 1). The central trough extends from southeast to north with an average depth of 44 m [1].

The seasonal variation is evident in the circulation and hydrographical characteristics of the Yellow Sea. In winter, strong vertical mixing due to strong winds and surface heat fluxes produce a uniform and cold vertical temperature profile. In summer, the solar radiation increases and rapidly warms the upper layer of the Yellow Sea. Therefore, the seasonal thermocline rapidly forms and locates at 10–30 m

depth. Due to the combined topographic, dynamic, and thermodynamic effects, there is a remnant of cold water (<10°C) under the seasonal thermocline in the central trough of the Yellow Sea which is referred as Yellow Sea Cold Water Mass (YSCWM) and is present throughout the whole summer season occupying almost 30% of the Yellow Sea area, thus becoming one of the most important characteristics of the Yellow Sea. The YSCWM has an important effect on the hydrographic features and the phytoplankton biomass and production in the Yellow Sea [2–5].

He et al. [6] first studied the formation and properties of the YSCWM and identified that the water mass locally formed during the previous winter by the sea surface cooling and strong vertical mixing. Su [7] found that the bottom cold water in northern Yellow Sea is influenced by coastal water and then moves southward in winter, mixing with high-salinity water from the open ocean. The bottom cold water in

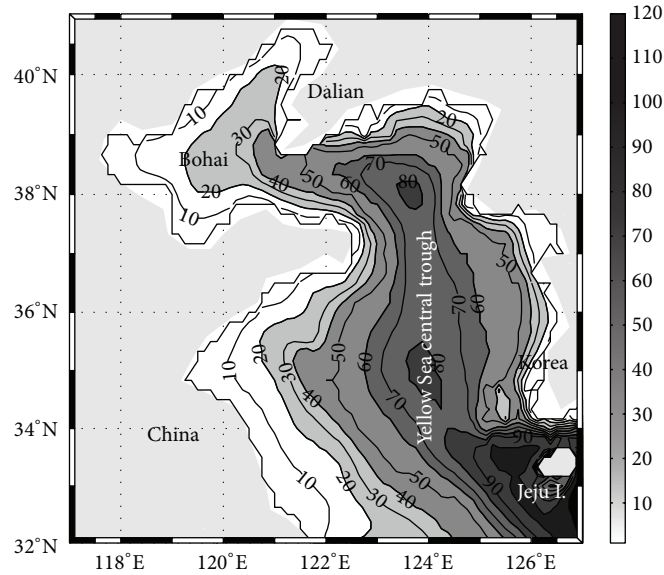


FIGURE 1: Bottom topography of the Yellow Sea (m).

northern Yellow Sea remains at the bottom in summer, and it is influenced by the Yellow Sea Coastal Water [8]. Since 1990, numerical models are used to investigate the mechanism of the YSCWM formation and its associated circulation [9–13]. Su and Huang [9], using qualitative analysis and numerical simulations, obtained that the vertical circulation is characterized by a double cell structure. Miu et al. [10, 11] used a model to explain the formation of the YSCWM and basic characteristics of density circulation based on the fluid dynamics and the thermodynamics. Recently, several studies were conducted to investigate the characteristics of the YSCWM using temperature and salinity observation. Jiang et al. [14] studied its thermohaline characteristics based on the temperature and salinity data observed by the State Oceanic Administration People’s Republic of China from 1976 to 1999. Hu and Wang [15] used empirical orthogonal function to investigate the interannual variability with temperature data collected in August from 1975 to 2003. Although previous studies investigated the interannual variability of the YSCWM through some frequently measured temperature sections, due to the lack of a long and regional observational record they could not describe the interannual and decadal variability at a regional scale. However, ocean reanalysis data has a better space-time coverage, which allows us to investigate the whole features of the YSCWM and its response to climate variability. Because the YSCWM is the most conservative among water masses in the Yellow Sea, it may contain clearer climate signals than any other water masses in the Yellow Sea. These long-term signals are important to understand the climatological evolution of the Yellow Sea [16].

Therefore, this study aims to characterize the low-frequency variability of the YSCWM and its possible relationship with three climate indices: the Arctic Oscillation (AO), El Niño/Southern Oscillation (ENSO), and the Pacific Decadal Oscillation (PDO) using the China Coastal Waters

and Adjacent Seas Reanalysis (CORA) data. CORA assimilated the *in situ* observed temperature and salinity profiles collected by the National Marine Data and Information Service People’s Republic of China, World Ocean Data 2005 (WOD05), Global Temperature and Salinity Profile Project (GTSP), and Array for Real-Time Geostrophic Oceanography (Argo) floats. It is worthy to emphasize that the dataset from the National Marine Data and Information Service People’s Republic of China integrates almost all the available historical observed temperature-salinity profiles in the Yellow Sea, which contributes to the high quality of CORA in the Yellow Sea. CORA has been validated using independent observations in previous studies. The results showed that CORA can better simulate temperature-salinity structure, mesoscale, and large-scale circulation in the western north Pacific including the Yellow Sea [17]. For further details about CORA and the assimilated observations the reader is referred to [17].

The rest of the paper is organized as follows. In Section 2, we describe the data used in this study. In Section 3, we explore the seasonal evolution and formation of the YSCWM. In Section 4, we investigate the interannual and decadal variability of the YSCWM and discuss the relationship between the YSCWM and the three climate indices (AO, ENSO, and PDO) considered in this study. Section 5 gives a brief summary and discussion.

2. Data and Methods

The CORA covers a period of 51 years from January 1958 to December 2008. The domain ranges from 99°E to 150°E and from 10°S to 52°N, including the Bohai Sea, the Yellow Sea, the East China Sea, the South China Sea, and adjacent seas. The datasets consist of monthly mean fields with horizontal resolution of 0.25° and 35 vertical depth levels.

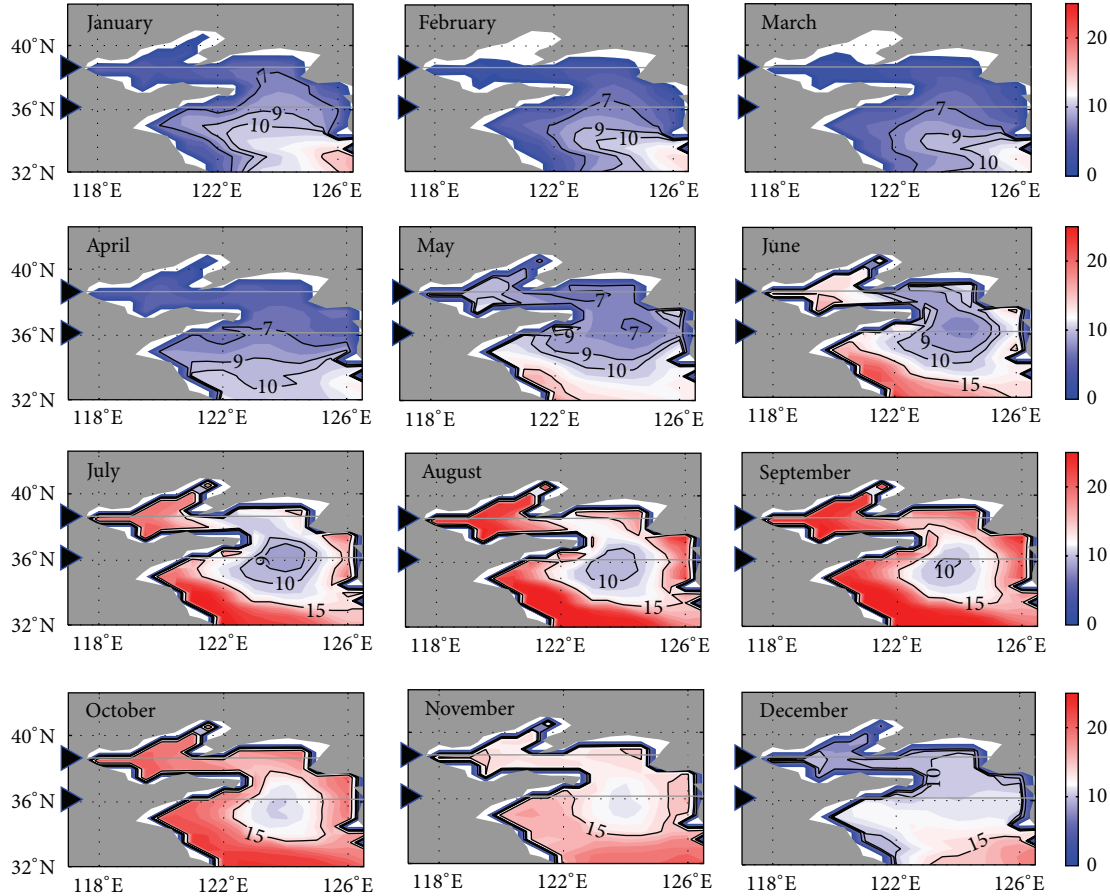


FIGURE 2: Monthly mean climatology of bottom water temperature ($^{\circ}\text{C}$) in the Yellow Sea. The triangles indicate the location where the cross sections are performed.

To examine what climate factors are associated with the YSCWM variability, three climate indices are selected: AO index [18], Multivariable ENSO index (MEI) [19, 20], and PDO index [21, 22]. AO is the dominant pattern of nonseasonal sea level pressure variability north of 20°N . It is characterized by sea level pressure anomalies with opposite signs in the Arctic and $37\text{--}45^{\circ}\text{N}$ [18]. MEI is an average of the main ENSO features contained in six observed variables over the tropical Pacific. A positive (negative) value of the MEI indicates the warm (cold) ENSO phase [19, 20]. The PDO index is defined as the leading principal component of monthly sea surface temperature variability north of 20°N in the North Pacific, and it is a long-lived El Niño-like pattern of the Pacific climate variability [21, 22].

The monthly mean wind stress and net heat flux are computed averaging the daily values obtained from the NCEP-NCAR reanalysis with the resolution of 2.5° [23]. The period of 51 years ranging from January 1958 to December 2008 is used to investigate the mechanisms of the YSCWM variability associated with AO, ENSO, and PDO. To examine the interannual and decadal variability of the YSCWM, all-time series used in this study are separated into two components including interannual and decadal variability. The decadal component is obtained by applying a 7-year Gaussian filter to the original time series. The interannual

component is obtained by subtracting the decadal component from the original time series. To extract the dominant mode of heat flux and wind stress in the Yellow Sea's region, an empirical orthogonal (EOF) analysis is performed upon the interannual and decadal time series.

3. Seasonal Evolution and Formation of the YSCWM

The YSCWM can be clearly distinguished in the bottom of the Yellow Sea. The Yellow Sea bottom water is the most stable level of the YSCWM [6]. YSCWM is traditionally defined as the cold water lower than 10°C in the bottom of the Yellow Sea in summer [6]. Thus, climatological monthly averaged temperature of the Yellow Sea bottom water during 1958–2008 is used to examine the formation and evolution of the YSCWM (Figure 2).

In winter (December–February), the temperature is gradually reduced in the Yellow Sea. The cold water area (with temperatures below 10°C) is gradually increased. In January, there is a tongue of warmer water (with temperatures warmer than 10°C) whose tip moves from (35°N , 122.5°E) to (34°N , 123°E) from January to February and further moves south-eastward in spring (Figure 2). The temperature in the central trough is higher than that of the surrounding water in winter.

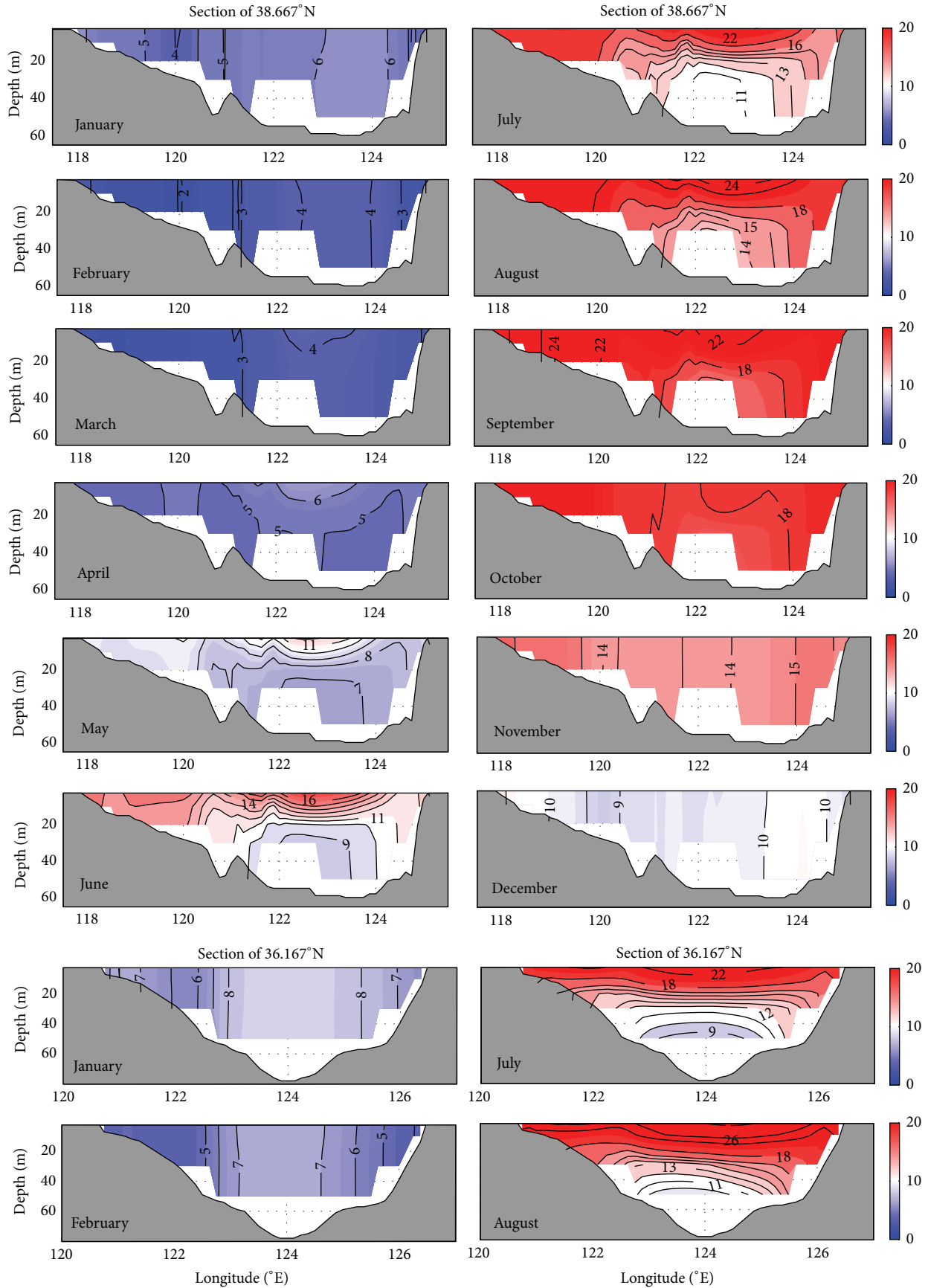


FIGURE 3: Continued.

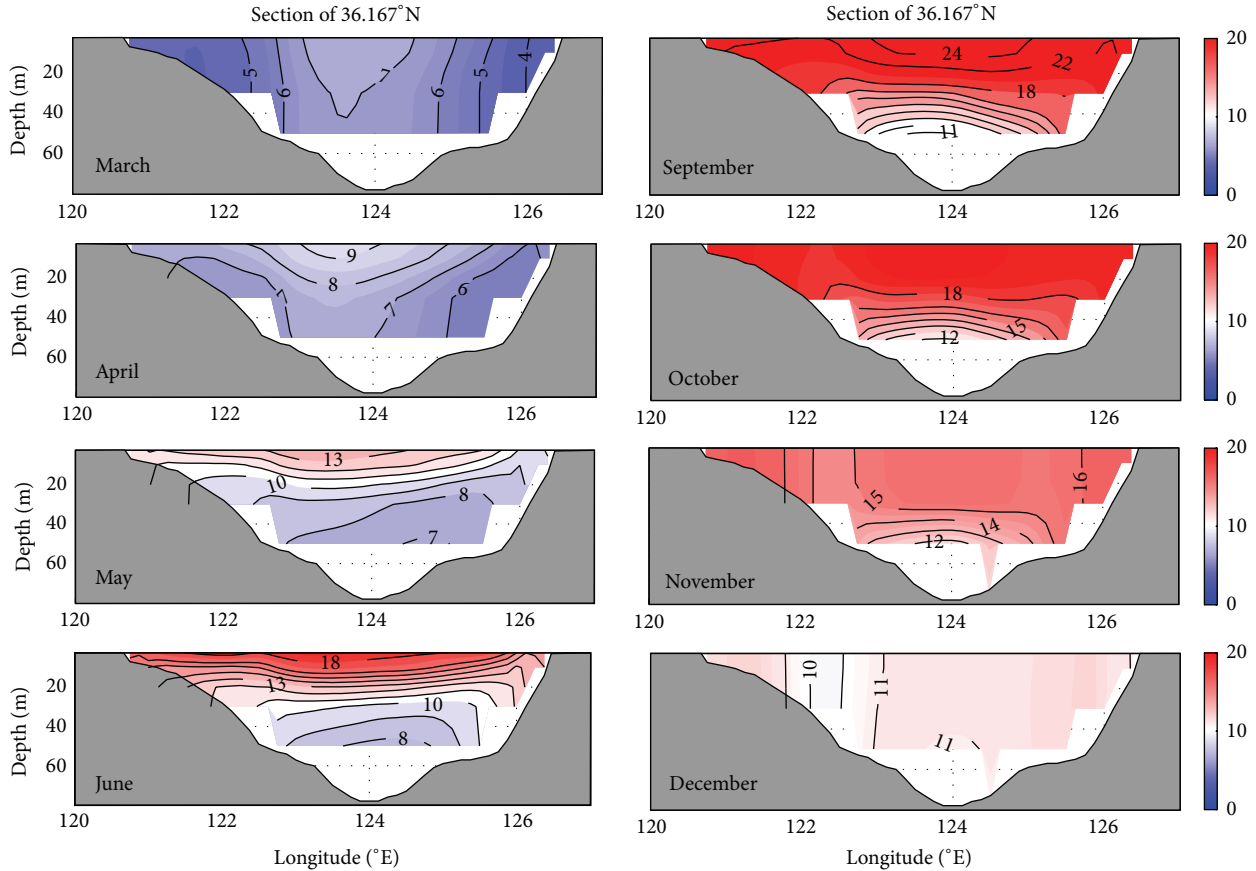


FIGURE 3: Vertical cross sections of monthly mean temperature ($^{\circ}\text{C}$) along 36.17°N and 38.667°N for the locations indicated in Figure 2.

In spring (March–May), the Yellow Sea water is warming further, and its frontal structure is changing. In March, the temperature structure is similar to that in February. The warm water trough still exists and then gradually disappears in April. However, in May, there are three cold water patches with temperatures below 7°C form around $36^{\circ} 25'\text{N}$, 122.5°E , $35^{\circ} 50'\text{N}$, 123.5°E , and $36^{\circ} 25'\text{N}$, 125°E (Figure 2). This suggests that the YSCWM has started to form in the Yellow Sea.

In summer (June–August), the cold center gradually enhances. In June, the cold center located at $36^{\circ} 25'\text{N}$, 122.5°E starts to move eastward, while the other two cold water centers merge into one during June, suggesting that the main body of the YSCWM begins to form over southern Yellow Sea. The cold water mass in the bottom of the central trough has a shape that resembles a saddle. In July, the cold water that has a temperature lower than 10°C covers a third of the Yellow Sea's total area. Compared with that in the late spring, the isotherm of 10°C expands southward from 36°N to 35.25°N (Figure 2). This indicates that the YSCWM has reached its maximum extension.

In autumn (September–November), the temperature of the coastal water drops, especially in northern Yellow Sea. Although the YSCWM is still visible until November, the lowest temperature at its center is around 12°C , and its area has also reduced. In December, the YSCWM has completely disappeared.

We have analyzed the formation and evolution of the YSCWM through the horizontal distribution of temperature at the Yellow Sea bottom. Next, we choose two vertical temperature sections of the YSCWM across southern and northern Yellow Sea, respectively. The location of the two sections is indicated with triangles in Figure 2. We will further explore the formation and the evolution mechanism of the YSCWM by analyzing the vertical structure of temperature in different seasons.

Over northern Yellow Sea, the cross section is performed at 38.66°N through the center of the YSCWM. As shown in Figure 3, in winter, the water column is completely uniform. In April, the enhanced solar radiation, the weaker convection, and mixing destroy the vertical uniform distribution of temperature, and a thermocline is formed due to water stratification. But this thermocline is weak with a maximum gradient of $\sim 0.2^{\circ}\text{C}/\text{m}$ at approximately 10 m depth. In May, the thermocline develops rapidly, and its intensity is greater than $0.3^{\circ}\text{C}/\text{m}$ at approximately 15 m depth. At the same time, an area with temperatures under 8°C forms underneath 20 m with minimum temperatures under 7°C near 38.667°N , 123°E . This cold center is also visible in Figure 2. The YSCWM has started to form at the bottom in May.

In early summer, the stratification at depths between 10 and 20 m became evident, and the thermocline becomes stable. The temperature profile presents a three-layer structure:

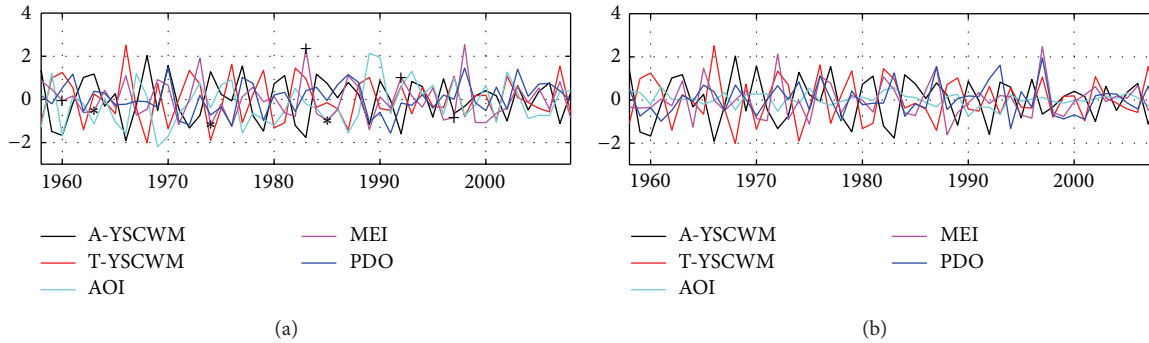


FIGURE 4: Interannual time series of (a) winter AO, MEI, and PDO indices, and A-YSCWM and T-YSCWM in August (b) summer AO, ENSO, PDO, and the A-YSCWM and T-YSCWM in August. Time series of the A-YSCWM and T-YSCWM are standardized. The A-YSCWM and T-YSCWM represent the area and averaged temperature of the YSCWM, respectively. The “+” represents the El Niño events, and the “*” represents the La Niña events.

the upper mixed layer contains warm water; the thermocline has sharp temperature gradient ($0.2\text{--}0.5^\circ\text{C}/\text{m}$); and the lower layer contains cold water which is nearly uniform. In mid-summer, the sea surface temperature rises rapidly, and the strength of thermocline reaches its maximum, which is as high as $1.0^\circ\text{C}/\text{m}$. At the same time, the bottom water still has temperatures below 10°C . In autumn, the temperature of the cold center rises from 8°C to 11°C (Figure 2). This indicates that the YSCWM is gradually decaying. In November, the thermocline disappears completely, and the YSCWM is also gone.

We choose the section at 36.167°N to examine evolution of the YSCWM in southern Yellow Sea (Figure 3). The evolution process of the thermocline in the southern Yellow Sea is similar to the northern Yellow Sea, but due to the different geographical position, topography, and tidal mixing intensity, their vertical structures are different. In spring, as the temperature increases near the coast, the thermocline weakens on both coasts of the southern Yellow Sea, and the area of the cold water increases. In May, with the increasing temperature and enhancing thermocline, three-layer structure occurs. The westward moving of the east cold center makes cold water only exists in the central trough. In June–August, the temperature of the bottom water in the central trough is less than 10°C . In October, the thermocline only exists at the central deeper water area than 30 m. The intensity of thermocline also reduces significantly. By December, the thermocline completely disappears, and the YSCWM is also gone.

There are two cold centers below the thermocline located at 122.5°E and 124.5°E in the southern Yellow Sea in April, which are different at the northern Yellow Sea (Figure 3). This difference is due to the influence of the Yellow Sea warm current. In winter, a warm tongue from west of the Jeju Island stretches northward along the central trough (Figure 2), which causes the temperature over the central part to be higher than that over the two coasts of the Yellow Sea. For example, in the cross section performed at 36.167°N , the temperature in the central part of the southern Yellow Sea is 7°C in February. However, the temperature on both coasts is $4\text{--}6^\circ\text{C}$. In April, the temperature over the central region is greater than 8°C , but the temperature on both coasts is $6\text{--}7^\circ\text{C}$

(Figure 3). The bottom temperature in the southern Yellow Sea has two cold centers on both flanks of central trough from January to April (Figure 3).

4. Interannual and Decadal Variability of the YSCWM

The YSCWM is a large water mass covering a third of the bottom layer at its largest extension. It has relatively stable properties with low temperature and high salinity. However, due to the influence of external forcings such as wind stress and heat fluxes, the thermohaline structure within the water mass may change. The YSCWM is traditionally defined as the cold water lower than 10°C in the bottom of the Yellow Sea in summer [6]. To investigate the interannual and decadal variability of the YSCWM, we define the YSCWM as the bottom water colder than 10°C . To examine the effects of the different seasonal climate forcings on the interannual and decadal variability of the YSCWM, winter (summer) climate indices averaged from December to February (July to September) are used.

4.1. Interannual Variability

4.1.1. Relationship to the Climate Forcings in Winter. On the interannual time scale, both winter AO and ENSO indices are negatively (positively) correlated with the area and averaged temperature of the YSCWM (hereafter referred to as A-YSCWM and T-YSCWM, resp.). Although the correlation coefficients are low, it is clearly shown that El Niño events (e.g., 1960, 1983, 1992, and 1997) correspond to smaller A-YSCWM and higher T-YSCWM, while La Niña (1963, 1974, 1985) events correspond to larger A-YSCWM and lower T-YSCWM (Figure 4(a) and Table 1). The correlation between the winter PDO index and A-YSCWM (T-YSCWM) is positive (negative) and statistically significant at the confidence level of 95%. The correlation between the winter PDO index and the YSCWM is the strongest among all of the three climatic indices, which may indicate that the effect of winter PDO on the YSCWM is the dominant climate forcings (Figure 4(a) and Table 1).

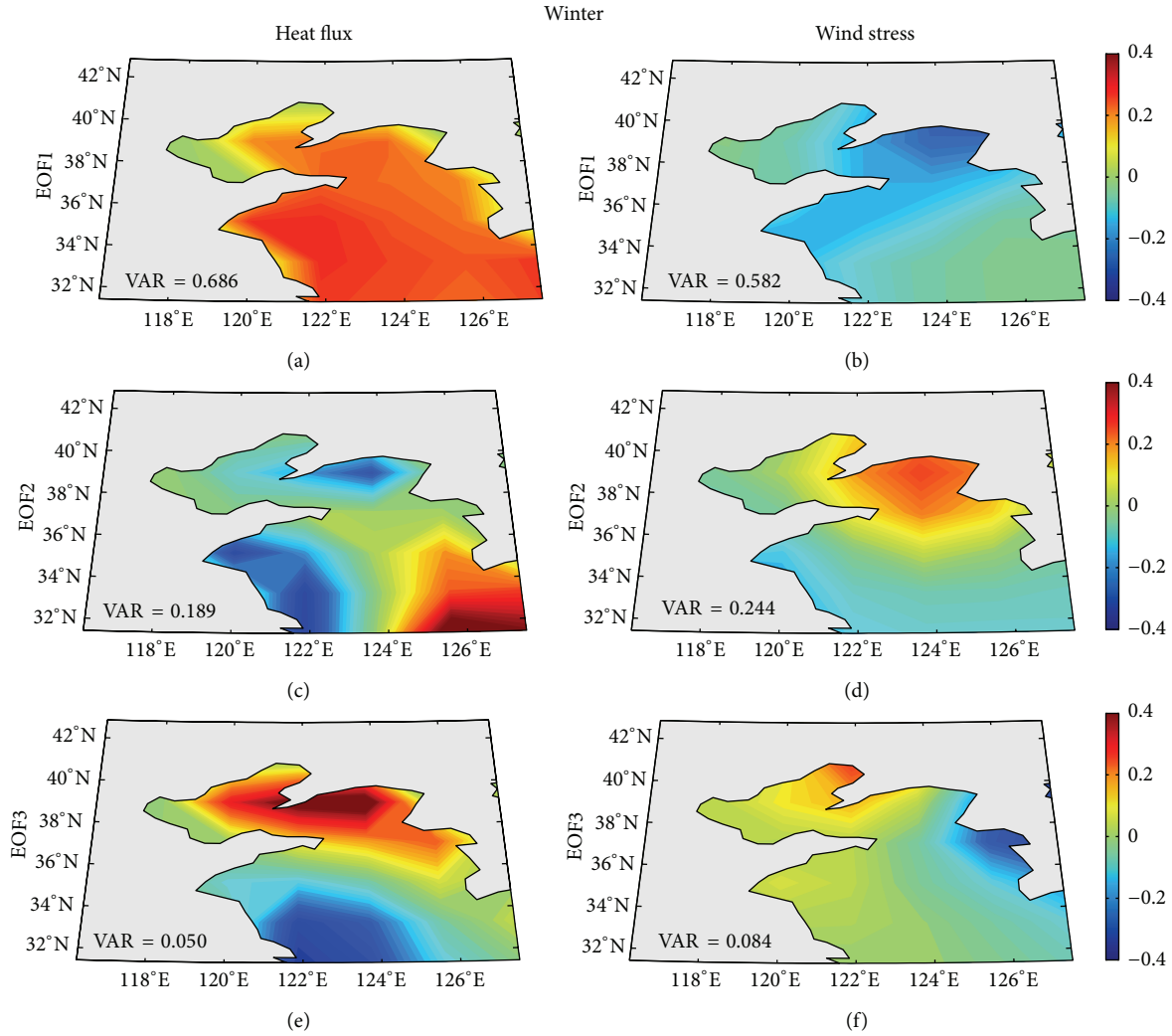


FIGURE 5: EOF1, EOF2, and EOF3 of interannual component for winter heat flux ((a), (c), and (e)) and winter wind stress ((b), (d), and (f)). Positive values indicate that heat is transferred from the ocean to the atmosphere.

To explore how the local thermal and wind forcing affect the interannual variability of the YSCWM, the interannual components of winter heat flux and wind stress are decomposed using EOFs (Figure 5). EOF1 of winter heat flux shows a positive loading over the total Yellow Sea, which explains 68.6% of the total variance (Figure 5(a)). The EOF2 of winter heat flux represents an east-west dipole structure, with positive loading in the east and negative loading in the west (Figure 5(c)). The EOF3 has a south-north dipole structure with positive loading in the northern Yellow Sea and negative loading in the southern Yellow Sea (Figure 5(e)). EOF1 of winter wind stress is characterized by negative values over almost the whole Yellow Sea, which account for 58.2% of the total variance (Figure 5(b)). The EOF2 of winter wind stress reveals a south-north dipole pattern with positive values in the northern Yellow Sea and negative values in the southern Yellow Sea (Figure 5(d)). The EOF3 exhibits a meridional alternate pattern with positive loading in the

Chinese coast and negative loading in the Korean coast (Figure 5(f)).

The EOF1 of winter heat flux is negatively (positive) correlated with the A-YSCWM (T-YSCWM) (Figure 6(a) and Table 2). This suggests that strong winter heat loss from ocean to atmosphere in the Yellow Sea can induce large A-YSCWM and low T-YSCWM. EOF1 and EOF3 of winter wind stress evidently affect the features of the YSCWM (Figure 6(c) and Table 3). It is shown that both EOF1 and EOF3 of winter wind stress are negatively (positively) correlated with A-YSCWM (T-YSCWM). This indicates that enhanced winter winds over the Yellow Sea tend to make A-YSCWM (T-YSCWM) increase (decrease) (Figure 5(a)).

Figures 7(a) and 7(c) show the interannual time series of winter AO, MEI, and PDO indices, as well as the EOF1, EOF2, and EOF3 of heat flux and wind stress. Only the winter AO index is positively correlated with the EOF3 of winter heat flux (Table 4). The variations of local winter heat flux

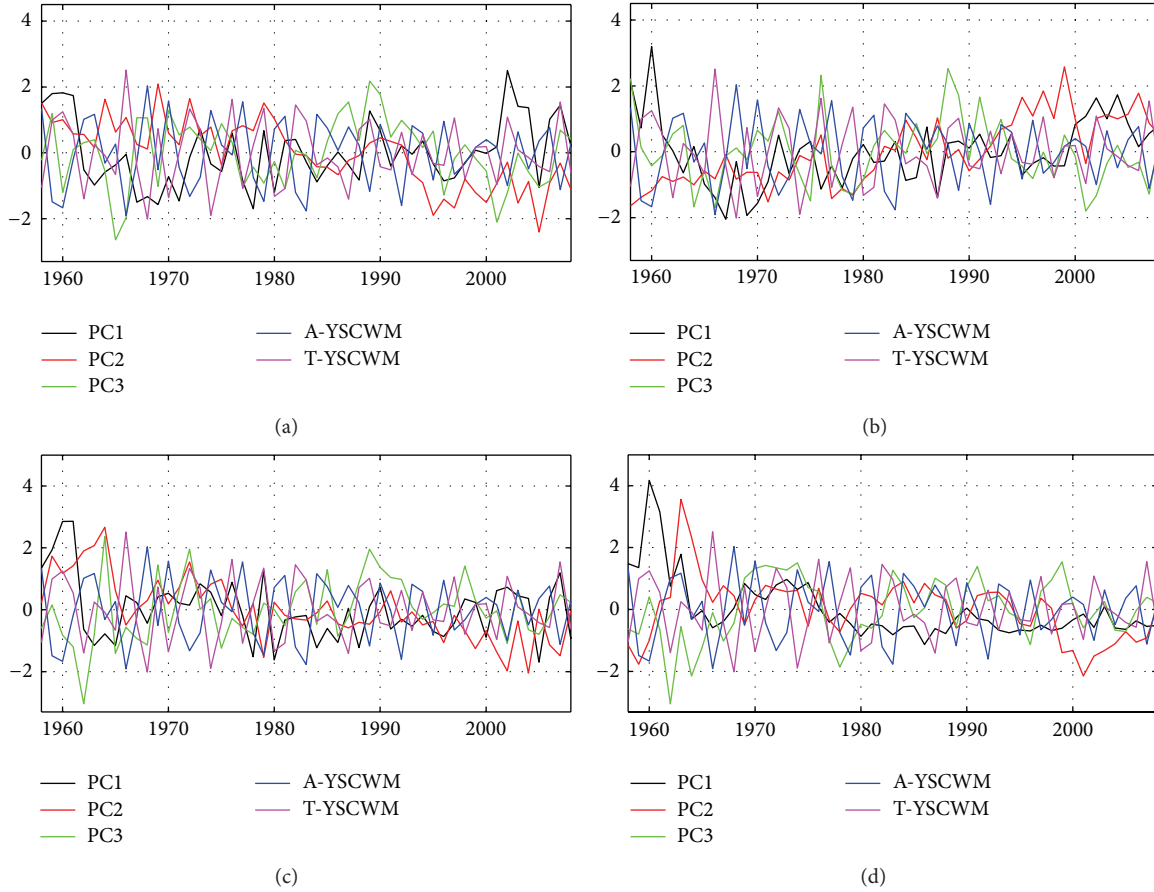


FIGURE 6: Interannual time series of (a) EOF1, EOF2, and EOF3 of winter heat flux, and the A-YSCWM and T-YSCWM in August (b) EOF1, EOF2, and EOF3 of summer heat flux, and the A-YSCWM and T-YSCWM in August (c) EOF1, EOF2, and EOF3 of winter wind stress, and the A-YSCWM and T-YSCWM in August (d) EOF1, EOF2, and EOF3 of summer wind stress, and the A-YSCWM and T-YSCWM in August. All time series are standardized. The A-YSCWM and T-YSCWM represent the area and averaged temperature of the YSCWM, respectively.

TABLE 1: Correlation coefficients between the AO, MEI, PDO, and the YSCWM area and temperature in August, including the interannual and decadal components in both summer and winter. Values in bold are statistically significant at the 95% confidence level.

	Area	Average temperature
Interannual variability		
Winter AO	-0.23	0.25
Winter MEI	-0.27	0.10
Winter PDO	0.31	-0.32
Summer AO	-0.27	0.30
Summer MEI	-0.08	0.14
Summer PDO	-0.15	0.12
Decadal variability		
Winter AO	-0.49	-0.05
Winter MEI	-0.41	0.32
Winter PDO	-0.43	0.31
Summer AO	-0.29	-0.16
Summer MEI	-0.61	0.38
Summer PDO	-0.26	0.04

and wind stress are less related to the winter MEI and PDO (Table 4). In other words, the winter MEI and PDO have less influence on the YSCWM through the modulation of the winter heat flux and wind stress.

4.1.2. Relationship to the Climate Forcings in Summer. A positive correlation exists between the summer AO index and T-YSCWM, with a correlation coefficient of 0.30 that is statistically significant at the confidence level of 95%. The correlations between MEI, PDO and A-YSCWM, T-YSCWM are low and not statistically significant (Figure 4(b) and Table 1). This suggests that ENSO and PDO may not be the main factors controlling the interannual variability of the YSCWM in summer.

The interannual variability of summer heat flux and wind stress is analyzed using EOFs. Figures 6(b) and 6(d) show the interannual time series of summer AO, MEI, and PDO indices, as well as the EOF1, EOF2, and EOF3 of heat flux and wind stress. The local heat flux and wind stress in summer have little impact on the variability of the YSCWM (Tables 2 and 3). Actually, none of the three climate indices are correlated with the local heat flux and wind stress (Figures

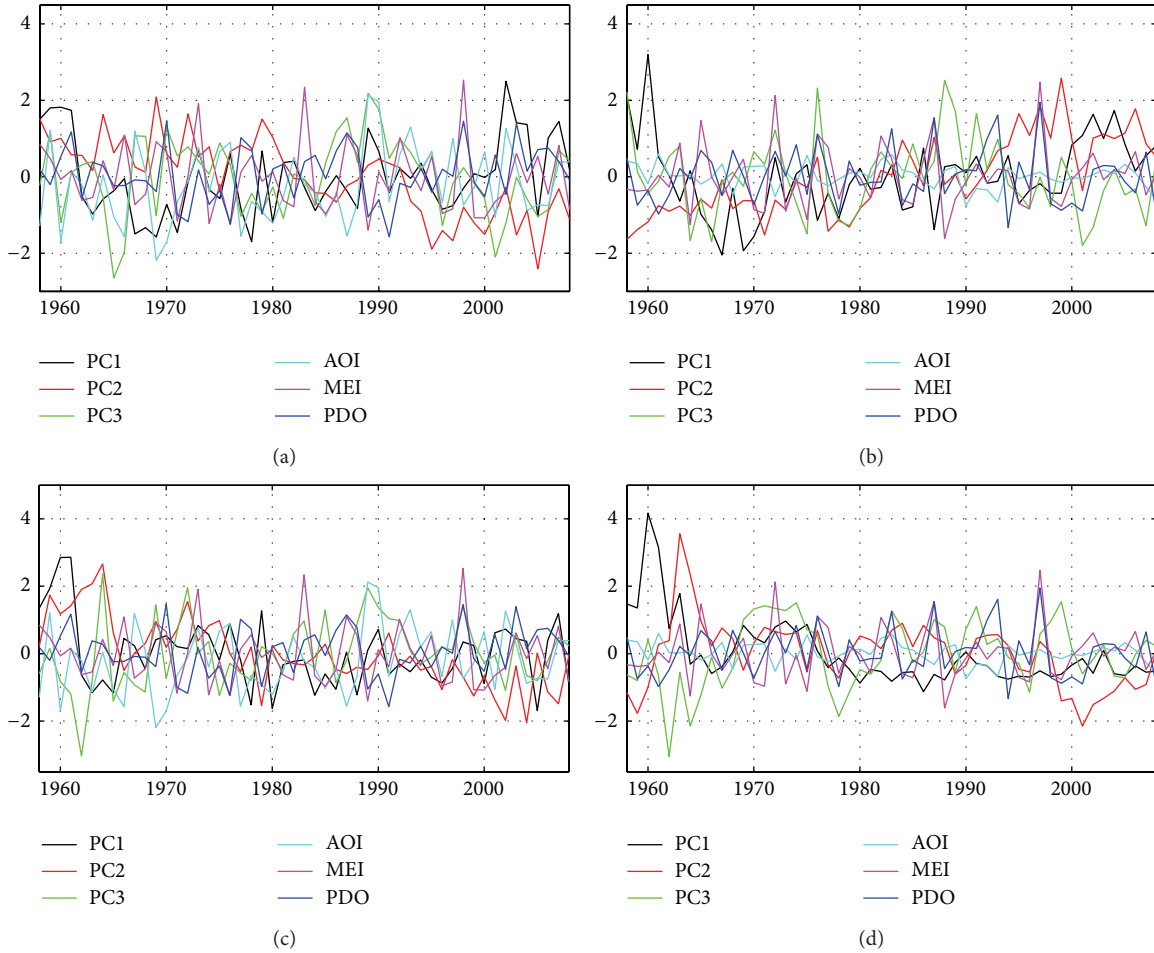


FIGURE 7: Interannual time series of (a) winter AO, MEI, PDO, EOF1, EOF2, and EOF3 of winter heat flux; (b) summer AO, MEI, PDO, EOF1, EOF2, and EOF3 of summer heat flux; (c) winter AO, ENSO, PDO, EOF1, EOF2, and EOF3 of winter wind stress; (d) summer AO, MEI, and PDO, and EOF1, EOF2, and EOF3 of summer wind stress. EOF1, EOF2, and EOF3 of heat flux and wind stress are standardized.

7(b), 7(d) and Table 5). This means that summer AO, ENSO, and PDO do not affect the YSCWM through modulating the local heat flux and wind stress.

4.2. Decadal Variability

4.2.1. Relationship with the Climate Forcings in Winter. The decadal variability of the A-YSCWM has a high correlation with the winter AO index. The negative correlation between the winter AO and the area of the YSCWM on the decadal time scale is about -0.49 (Figure 8(a) and Table 1). When the winter AO index is in its negative phase during 1958–1988, A-YSCWM usually has positive anomaly. After 1988, the AO index is continuously positive, and A-YSCWM shows a persistent negative anomaly. When the AO index is in its positive phase, the heat flux loading associated with EOF1 is negative, indicating a net heat flux from the atmosphere and into the ocean. A-YSCWM also reduces accordingly (Figures 9, 11(a) and Table 4).

The PDO index is correlated with A-YSCWM and T-YSCWM, with the correlation coefficient of -0.43 and 0.31 , respectively (Figure 8(a) and Table 1), and maintains positive

or negative values prevailing for 20–30 year periods [21, 22]. The decadal cycle of the YSCWM also shows a similar feature (Figure 8(a)). In winter, the PDO index has strong links with the Aleutian low. Negative phase of the PDO represents warm anomalies in the extratropical North Pacific [20]. The spatial pattern of the PDO is strongly associated with the EOF1 of heat flux (Figure 10(a)). When the PDO is in its positive phase, the heat flux from atmosphere to ocean is increased in the Yellow Sea, which reduces the A-YSCWM (Figures 9, 11(a) and Table 4). The reverse is true during the negative PDO phase. The PDO also has a connection with EOF2 and EOF3 of the wind stress (Figure 10(c)). Positive phase of the PDO induces positive wind stress anomaly in the Yellow Sea (Figures 9, 10(c) and Table 4). Due to the shallow depth of the Yellow Sea, a stronger wind stress can strengthen mixing, which produces a smaller A-YSCWM (Figure 11(c) and Table 3).

The correlations between MEI and A-YSCWM and T-YSCWM are -0.41 and 0.32 , respectively (Figure 8(a) and Table 1). From 1976 to 2006, the MEI represents the warm ENSO phase. The corresponding T-YSCWM (A-YSCWM) is a positive (negative) anomaly. However, the correlations

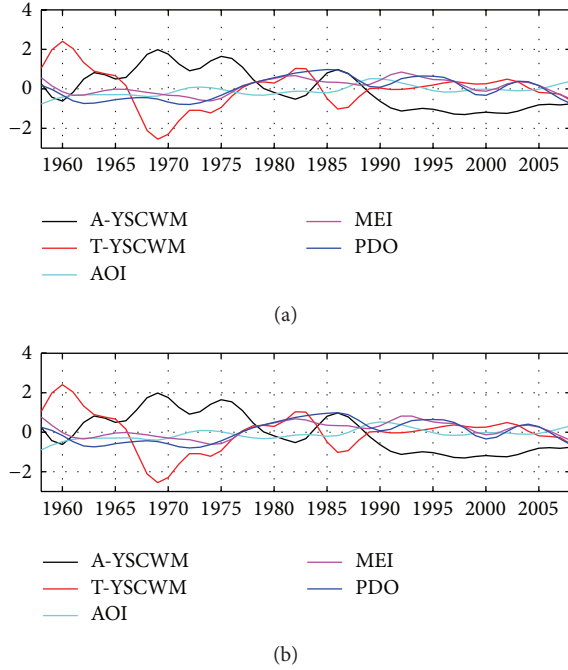


FIGURE 8: Decadal time series of (a) winter AO, MEI, and PDO index, and the A-YSCWM and T-YSCWM in August (b) summer AO, MEI, and PDO index, and the A-YSCWM and T-YSCWM in August. Time series of the A-YSCWM and T-YSCWM are standardized. The A-YSCWM and T-YSCWM represent the area and averaged temperature of the YSCWM, respectively.

TABLE 2: Correlation coefficients between EOF1, EOF2, and EOF3 of heat flux and A-YSCWM, T-YSCWM in August, including the interannual and decadal components in both summer and winter. Bold texts indicate that the correlations are statistically significant at the 95% confidence level.

	A-YSCWM	T-YSCWM
Interannual variability		
EOF1 of winter heat flux	-0.32	0.37
EOF2 of winter heat flux	-0.16	0.14
EOF3 of winter heat flux	0.04	-0.08
EOF1 of summer heat flux	-0.13	0.07
EOF2 of summer heat flux	0.04	0.03
EOF3 of summer heat flux	0.17	0.01
Decadal variability		
EOF1 of winter heat flux	0.74	-0.08
EOF2 of winter heat flux	0.02	-0.33
EOF3 of winter heat flux	0.02	-0.39
EOF1 of summer heat flux	0.59	-0.64
EOF2 of summer heat flux	-0.56	-0.11
EOF3 of summer heat flux	0.22	-0.12

between MEI and local wind stress and heat flux are low (Figures 10(a), 10(c) and Table 4). The results indicate that the winter ENSO event is strongly linked to the decadal variability of the YSCWM, but not through changes in wind stress and heat fluxes.

TABLE 3: Correlation coefficients between EOF1, EOF2, and EOF3 of wind stress and A-YSCWM, T-YSCWM in August, including the interannual and decadal components in both summer and winter. Bold texts indicate that the correlations are statistically significant at the 95% confidence level.

	A-YSCWM	T-YSCWM
Interannual variability		
EOF1 of winter wind stress	-0.33	0.33
EOF2 of winter wind stress	0.08	-0.09
EOF3 of winter wind stress	-0.31	0.27
EOF1 of summer wind stress	-0.07	0.11
EOF2 of summer wind stress	0.15	-0.07
EOF3 of summer wind stress	-0.08	0.12
Decadal variability		
EOF1 of winter wind stress	-0.13	-0.23
EOF2 of winter wind stress	-0.56	0.75
EOF3 of winter wind stress	0.31	0.08
EOF1 of summer wind stress	0.19	0.56
EOF2 of summer wind stress	-0.19	0.14
EOF3 of summer wind stress	-0.39	0.48

4.2.2. *Relationship to Climate Forcings in Summer.* On the decadal time scale, the A-YSCWM is negatively correlated with the summer AO index, with a correlation coefficient of -0.30 (Figure 8(b) and Table 1). The A-YSCWM and the summer MEI are negatively correlated with a coefficient of -0.60 (Figure 8(b) and Table 1). The correlation between T-YSCWM and summer MEI is positive with the correlation coefficient of 0.38 (Figure 8(b) and Table 1). On a decadal time scale, the summer MEI during 1966–1978 is in its negative phase while the anomaly in A-YSCWM (T-YSCWM) is positive (negative). After 1978, the summer MEI is in its positive phase (Figure 8(b)). Correspondingly, the A-YSCWM (T-YSCWM) anomaly is negative (positive). However, when PDO turns to a weak signal in summer, the correlation between the PDO and the YSCWM becomes not significant (Figure 8(b) and Table 1).

The summer AO and MEI may affect both EOF2 and EOF3 of the summer heat flux and EOF1 of summer wind stress, modulating the decadal variability of the YSCWM (Figures 10(b), 10(d) and Table 5). However, because of the low correlation between the EOF2 of the summer heat flux and the decadal variability of the YSCWM, AO and MEI may not affect the decadal variability of the YSCWM through changes in the EOF2 of the summer heat flux (Table 3). The summer AO and ENSO indices are negatively correlated with EOF3 of summer heat flux and EOF1 of summer wind stress (Table 5). When the summer AO and ENSO are in their positive phases, the heat flux from the atmosphere into the ocean is enhanced (Figures 9, 10 and Table 5). Therefore, the A-YSCWM decreases, and the T-YSCWM increases (Figure 11 and Table 3).

5. Summary

We use the CORA reanalysis data to investigate the low-frequency variability of the YSCWM. First, we examine the

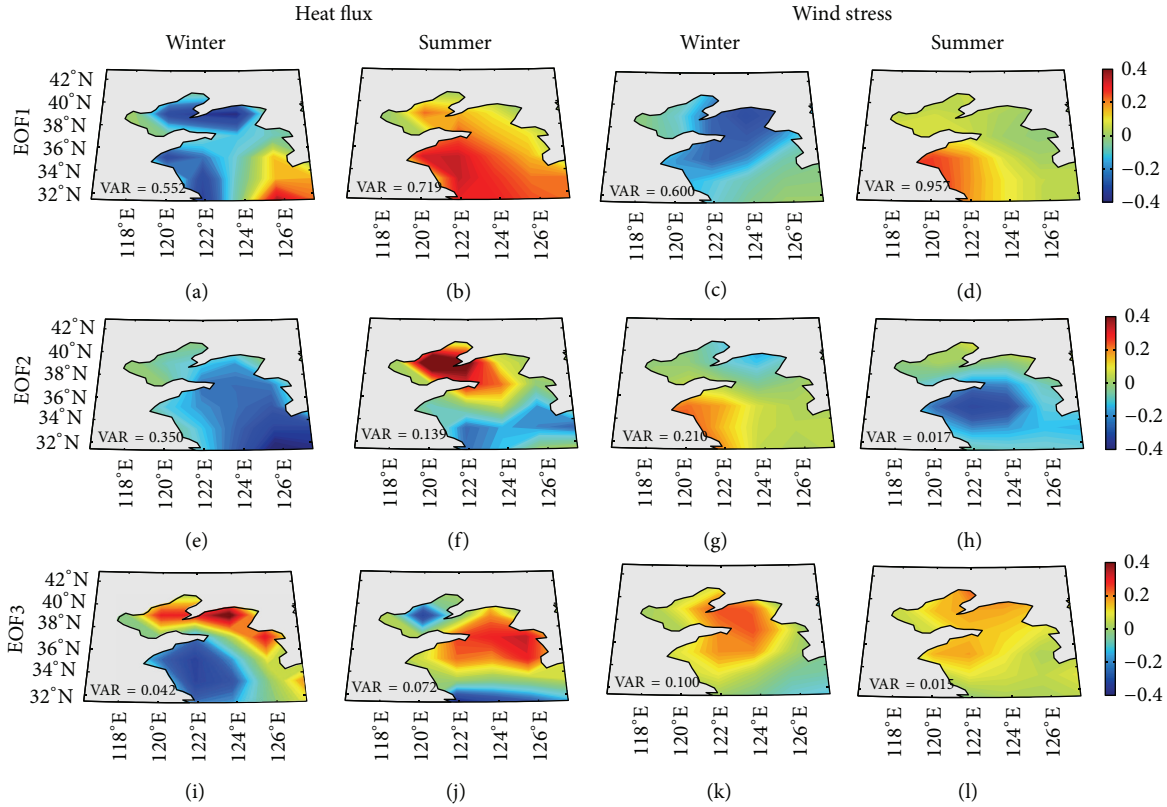


FIGURE 9: EOF1, EOF2, and EOF3 of decadal components for winter heat flux ((a), (e), and (i)) and summer heat flux ((b), (f), and (g)), winter wind stress ((c), (g), and (k)), and summer wind stress ((d), (h), and (l)). Positive values indicate that heat is transferred from the ocean to the atmosphere.

TABLE 4: Correlation coefficients between EOF1, EOF2, and EOF3 of winter heat flux, wind stress, and winter AO, ENSO, and PDO, including the interannual and decadal components. Bold texts indicate that the correlations are statistically significant at the 95% confidence level.

		Winter AO	Winter MEI	Winter PDO
Interannual variability	EOF1 of winter heat flux	0.26	0.02	-0.11
	EOF2 of winter heat flux	-0.08	0.10	-0.11
	EOF3 of winter heat flux	0.47	0	-0.03
	EOF1 of winter wind stress	0.09	0.09	-0.01
	EOF2 of winter wind stress	0.10	-0.05	-0.04
	EOF3 of winter wind stress	0.04	0.17	-0.11
Decadal variability	EOF1 of winter heat flux	-0.59	-0.12	-0.47
	EOF2 of winter heat flux	-0.09	-0.06	0.13
	EOF3 of winter heat flux	0.57	0.08	-0.31
	EOF1 of winter wind stress	0.17	-0.04	-0.10
	EOF2 of winter wind stress	-0.21	0.25	0.33
	EOF3 of winter wind stress	-0.14	-0.12	-0.77

formation and evolution of the YSCWM on the seasonal scale. The YSCWM forms in spring and reaches its maximum extension in summer. Since the early fall, the area occupied by the YSCWM starts to decrease. In December, the YSCWM disappears. The evolution process of the YSCWM derived from CORA is consistent with the evolution showed by the observations as described in previous studies [24].

Next, we examine the interannual and decadal variability of the YSCWM and its association with the climate forcing including AO, ENSO, and PDO. The climate forcing plays an important role in modulating the YSCWM variability. For the interannual variability of the YSCWM, the correlation between the winter PDO and the YSCWM is the strongest among the three climate indices, which indicates that the

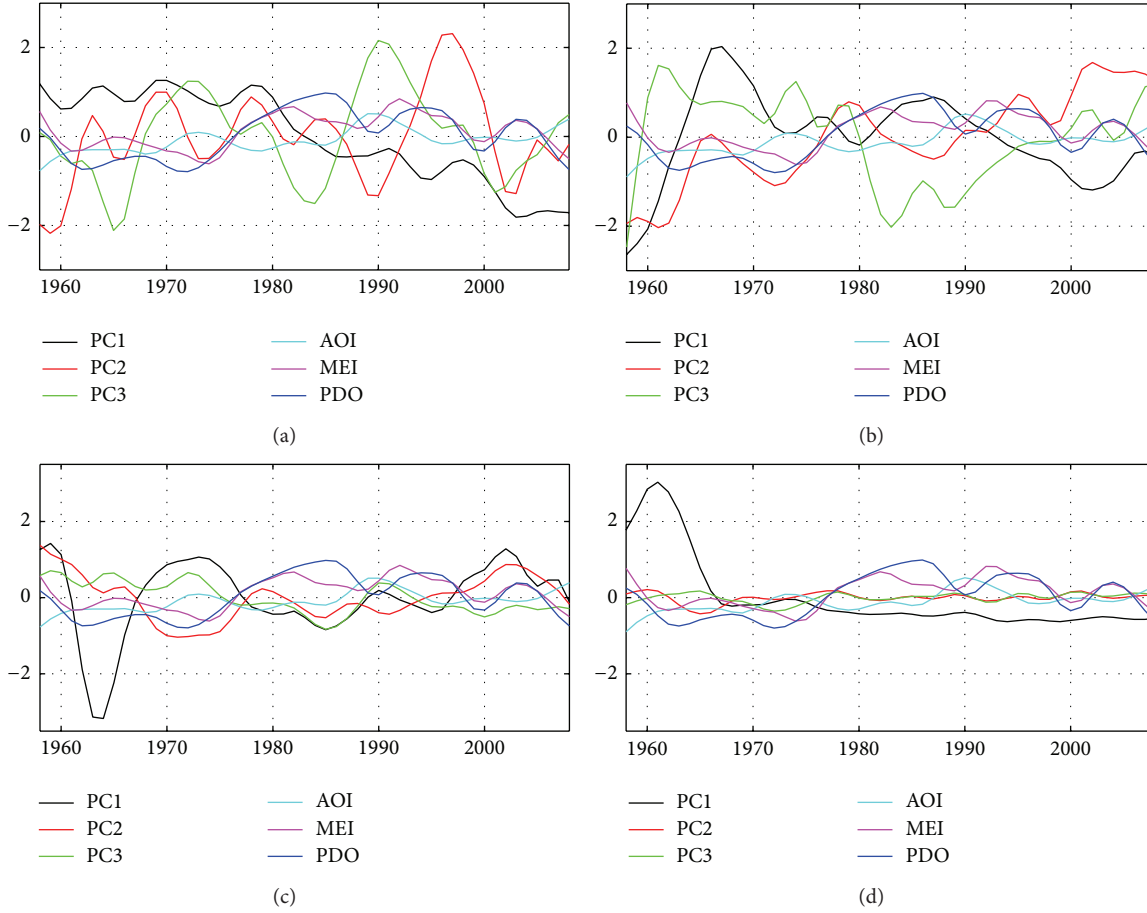


FIGURE 10: Decadal time series of (a) winter AO, MEI, PDO, EOF1, EOF2, and EOF3 of winter heat flux; (b) summer AO, MEI, PDO, EOF1, EOF2, and EOF3 of heat flux; (c) winter AO, MEI, PDO, and EOF1, EOF2, and EOF3 of winter wind stress; (d) summer AO, MEI, PDO, and EOF1, and EOF2 and EOF3 of summer wind stress. EOF1, EOF2, and EOF3 of heat flux and wind stress are standardized.

TABLE 5: Correlation coefficients between EOF1, EOF2, and EOF3 of summer heat flux, wind stress, and winter AO, ENSO, and PDO, including the interannual and decadal components. Bold texts indicate that the correlations are statistically significant at the 95% confidence level.

	Summer AO	Summer MEI	Summer PDO	
Interannual variability	EOF1 of summer heat flux	-0.07	0.01	0.01
	EOF2 of summer heat flux	0.04	0.09	0.13
	EOF3 of summer heat flux	-0.01	0.17	0.12
	EOF1 of summer wind stress	0.01	0.01	-0.05
	EOF2 of summer wind stress	-0.04	0.11	0.12
	EOF3 of summer wind stress	-0.01	0.11	0.15
Decadal variability	EOF1 of summer heat flux	0.08	-0.13	0.14
	EOF2 of summer heat flux	0.41	0.47	0.26
	EOF3 of summer heat flux	-0.40	-0.61	-0.79
	EOF1 of summer wind stress	-0.57	-0.36	-0.48
	EOF2 of summer wind stress	0.15	-0.07	-0.03
	EOF3 of summer wind stress	-0.02	0.31	0.04

effect of the winter PDO on the YSCWM is dominant. In this study, we do not investigate how PDO modulate the Yellow Sea circulation to influence the YSCWM. Previous studies suggested that the signal of PDO can be transferred into the Yellow Sea through Kuroshio and therefore affect the

circulation of the Yellow Sea [16, 25]. It was also suggested that Yellow Sea warm current can influence the variability of the YSCMW [26]. It is necessary to further investigate in a future study how PDO influences the Yellow Sea circulation and modulates the YSCWM. It is also found that the local

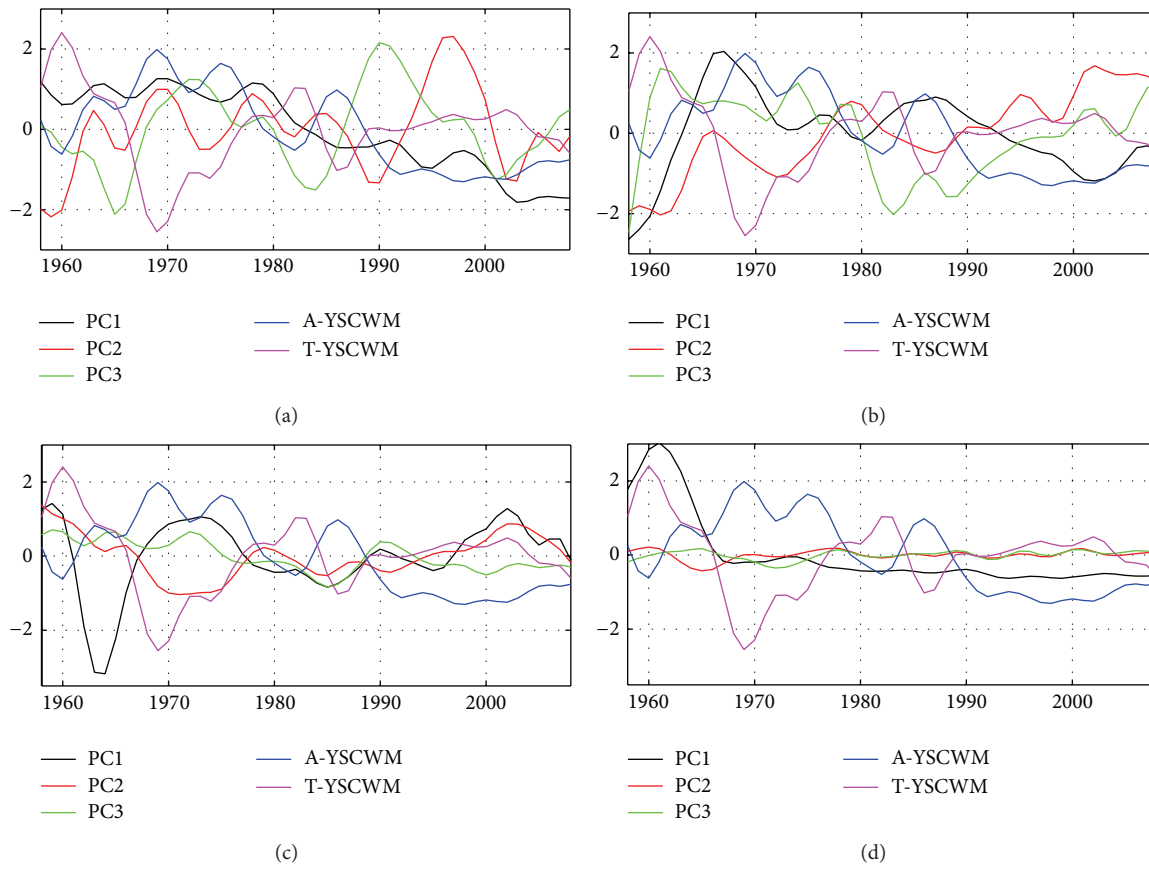


FIGURE 11: Decadal time series of (a) EOF1, EOF2, and EOF3 of winter heat flux, and the A-YSCWM and T-YSCWM in August (b) EOF1, EOF2, and EOF3 of summer heat flux, and the A-YSCWM and T-YSCWM in August (c) EOF1, EOF2, and EOF3 of winter wind stress, and the A-YSCWM and T-YSCWM in August (d) EOF1, EOF2, and EOF3 of summer wind stress, and the A-YSCWM and T-YSCWM in August. All of the time series are standardized. The A-YSCWM and T-YSCWM represent the area and averaged temperature of the YSCWM, respectively.

wind stress and heat flux in summer have little influence on the variability of the YSCWM. In summer, no correlation is found between the climate indices and the local heat flux and wind stress. This suggests that the AO, ENSO, and PDO may not affect the interannual variability of the YSCWM through modulating the local heat flux and wind stress in summer.

For the decadal variability of the YSCWM, the negative correlations between the winter AO, PDO, and the area of the YSCWM are significant. The winter AO mainly controls the first mode of heat flux to modulate the decadal variability of the YSCWM. When the winter AO is in its positive phase, the heat flux from atmosphere to ocean in the northwestern Yellow Sea is abnormally high. The average temperature of the YSCWM also increases accordingly. The winter PDO is strongly connected to the first mode of winter heat flux. When the winter PDO is in its positive phase, the increase of heat flux from atmosphere to ocean in the Yellow Sea can reduce the area of the YSCWM. At the same time, the winter PDO has positive correlation with the sea surface pressure. Along with the PDO enhanced, the enhancement of sea surface pressure is in conformity with wind speed. The positive PDO can induce positive wind stress anomaly in the Yellow Sea through the modulation of the EOF2 and EOF3. Due to the

shallow depth of the Yellow Sea, the strong wind stress and the enhanced sea surface pressure can strengthen mixing, reducing the area of the YSCWM. The correlation between winter MEI and the YSCWM is significant, suggesting a link with decadal variability of the YSCWM. However, this relationship cannot be explained by changes in the wind stress and heat fluxes. In summer, ENSO has the strongest influence on the YSCWM variability. ENSO may exert influence on the third mode of summer heat flux and the first mode of summer wind stress to modulate the decadal variability of the YSCWM.

Conflict of Interests

The authors declare that there is no conflict of interests regarding the publication of this paper.

Acknowledgments

This study is supported by the National Basic Research Program of China (2013CB430304), National Natural Science Foundation of China (41106005, 41176003, 41206178, 41376015, 41376013, 41306006, and 41276015), National High-Tech R&D Program (2013AA09A505) of China, and Global

Change and Air-Sea Interaction (GASI-01-01-12). Peter C. Chu is supported by the Naval Oceanographic Office. The Arctic Oscillation, Multivariate ENSO, and Pacific Decadal Oscillation indices are downloaded from the websites: <http://www.cpc.ncep.noaa.gov/>, <http://www.cdc.noaa.gov/>, and <http://jisao.washington.edu/pdo>, respectively.

References

- [1] Q. Tang, X. Jin, J. Wang, Z. Zhuang, Y. Cui, and T. Meng, "Decadal-scale variations of ecosystem productivity and control mechanisms in the Bohai Sea," *Fisheries Oceanography*, vol. 12, no. 4-5, pp. 223-233, 2003.
- [2] C. Yongli, H. Dunxin, and W. Fan, "Long-term variabilities of thermodynamic structure of the East China Sea Cold Eddy in summer," *Chinese Journal of Oceanology and Limnology*, vol. 22, no. 3, pp. 224-230, 2004.
- [3] S. W. Zhang, C. S. Xia, and Y. L. Yuan, "A physical-biochemical coupling model of Yellow Sea cold water mass," *Progress in Natural Science*, vol. 12, pp. 315-320, 2002.
- [4] H.-J. Lie, C.-H. Cho, J.-H. Lee, S. Lee, Y. Tang, and E. Zou, "Does the yellow sea warm current really exist as a persistent mean flow?" *Journal of Geophysical Research C: Oceans*, vol. 106, no. 10, pp. 22199-22210, 2001.
- [5] H. B. Hur, G. A. Jacobs, and W. J. Teague, "Monthly water mass analyses in the Yellow and East China Seas," *Journal of Oceanography*, vol. 55, pp. 171-184, 1999.
- [6] C. B. He, Y. X. Wang, Z. Y. Lei, and S. Xu, "A preliminary study of the formation and its properties of the Yellow Sea Cold Water Mass," *Oceanologia et Limnologia Sinica*, vol. 2, pp. 11-15, 1959.
- [7] Y. S. Su, "A survey of geographical environment, circulation systems and the central fishing grounds in the Huanghai Sea and East China Sea," *Journal of Shandong College of Oceanology*, vol. 16, no. 1, pp. 12-27, 1986.
- [8] S.-L. Wang and C.-T. A. Chen, "Bottom water at the center of the north east china sea in summer: remnant winter water," *Continental Shelf Research*, vol. 18, no. 13, pp. 1573-1580, 1998.
- [9] J. L. Su and D. J. Huang, "On the current field associated with the Yellow Sea cold water mass," *Oceanologia et Limnologia Sinica Supplement*, vol. 26, no. 5, pp. 1-7, 1995.
- [10] J. B. Miu and X. Q. Liu, "The preliminary discussion about the formation mechanism of the north Yellow Sea cold water mass-I.model solution," *Scientia Sinica Series B*, vol. 1, pp. 1311-1321, 1990.
- [11] J. B. Miu and X. Q. Liu, "The preliminary discussion about the formation mechanism of the north Yellow Sea cold water mass-II. Discussion of the model solution," *Scientia Sinica, Series B*, vol. 2, pp. 74-81, 1991.
- [12] H. Q. Li and Y. L. Yuan, "Theoretical study on the thermal structure and circulation pattern related to cold water mass of Yellow Sea," *Oceanologia et Limnologia Sinica*, vol. 23, no. 1, pp. 7-13, 1992.
- [13] H. J. Ren and J. M. Zhan, "A numerical study on the seasonal variability of the Yellow Sea cold water mass and the related dynamics," *Journal of Hydrodynamics A*, vol. 20, supplement, pp. 887-896, 2005.
- [14] B. J. Jiang, X. W. Bao, D. X. Wu, and J. P. Xu, "Interannual variation of temperature and salinity of northern Huanghai Sea Cold Water Mass and its probable cause," *Acta Oceanologica Sinica*, vol. 29, no. 4, pp. 1-10, 2007.
- [15] D. X. Hu and Q. Y. Wang, "Interannual variability of the southern Yellow Sea Cold Water Mass," *Chinese Journal of Oceanology and Limnology*, vol. 22, no. 3, pp. 231-236, 2004.
- [16] S. Park, P. C. Chu, and J.-H. Lee, "Interannual-to-interdecadal variability of the Yellow Sea Cold Water Mass in 1967-2008: characteristics and seasonal forcings," *Journal of Marine Systems*, vol. 87, no. 3-4, pp. 177-193, 2011.
- [17] G. Han, W. Li, X. Zhang et al., "A regional ocean reanalysis system for coastal waters of China and adjacent seas," *Advances in Atmospheric Sciences*, vol. 28, no. 3, pp. 682-690, 2011.
- [18] D. W. J. Thompson and J. M. Wallace, "The Arctic oscillation signature in the wintertime geopotential height and temperature fields," *Geophysical Research Letters*, vol. 25, no. 9, pp. 1297-1300, 1998.
- [19] K. Wolter and M. S. Timlin, "Monitoring ENSO in COADS with a seasonally adjusted principal component index," in *Proceedings of the 17th Climate Diagnostics Workshop*, pp. 52-57, Climate Analysis Center, National Oceanic and Atmospheric Administration (NOAA), Norman, Okla, USA, 1993.
- [20] K. Wolter and M. S. Timlin, "Measuring the strength of ENSO events: how does 1997/98 rank?" *Weather*, vol. 53, no. 9, pp. 315-324, 1998.
- [21] Y. Zhang, J. M. Wallace, and D. S. Battisti, "ENSO-like interdecadal variability: 1900-93," *Journal of Climate*, vol. 10, no. 5, pp. 1004-1020, 1997.
- [22] N. J. Mantua, S. R. Hare, Y. Zhang, J. M. Wallace, and R. C. Francis, "A Pacific Interdecadal Climate Oscillation with Impacts on Salmon Production," *Bulletin of the American Meteorological Society*, vol. 78, no. 6, pp. 1069-1079, 1997.
- [23] E. Kalnay, M. Kanamitsu, R. Kistler et al., "The NCEP/NCAR 40-year reanalysis project," *Bulletin of the American Meteorological Society*, vol. 77, no. 3, pp. 437-471, 1996.
- [24] S. W. Zhang, Q. Y. Wang, Y. Lü, H. Cui, and Y. L. Yuan, "Observation of the seasonal evolution of the Yellow Sea Cold Water Mass in 1996-1998," *Continental Shelf Research*, vol. 28, no. 3, pp. 442-457, 2008.
- [25] A. L. Gordon and C. F. Giulivi, "Pacific decadal oscillation and sea level in the Japan/East sea," *Deep Sea Research Part I: Oceanographic Research Papers*, vol. 51, no. 5, pp. 653-663, 2004.
- [26] H.-J. Lie, C.-H. Cho, J.-H. Lee, S. Lee, Y. Tang, and E. Zou, "Does the Yellow Sea Warm Current really exist as a persistent mean flow?" *Journal of Geophysical Research C: Oceans*, vol. 106, no. 10, pp. 22199-22210, 2001.

Research Article

Some Aspects of Sensitivity Analysis in Variational Data Assimilation for Coupled Dynamical Systems

Sergei Soldatenko,¹ Peter Steinle,¹ Chris Tingwell,¹ and Denis Chichkine²

¹Centre for Australian Climate and Weather Research, 700 Collins Street, Melbourne, VIC 3008, Australia

²University of Waterloo, 200 University Avenue West, Waterloo, ON, Canada N2L 3G1

Correspondence should be addressed to Sergei Soldatenko; s.soldatenko@bom.gov.au

Received 18 December 2014; Revised 24 February 2015; Accepted 11 March 2015

Academic Editor: Guijun Han

Copyright © 2015 Sergei Soldatenko et al. This is an open access article distributed under the Creative Commons Attribution License, which permits unrestricted use, distribution, and reproduction in any medium, provided the original work is properly cited.

Variational data assimilation (VDA) remains one of the key issues arising in many fields of geosciences including the numerical weather prediction. While the theory of VDA is well established, there are a number of issues with practical implementation that require additional consideration and study. However, the exploration of VDA requires considerable computational resources. For simple enough low-order models, the computational cost is minor and therefore models of this class are used as simple test instruments to emulate more complex systems. In this paper, the sensitivity with respect to variations in the parameters of one of the main components of VDA, the nonlinear forecasting model, is considered. For chaotic atmospheric dynamics, conventional methods of sensitivity analysis provide uninformative results since the envelopes of sensitivity functions grow with time and sensitivity functions themselves demonstrate the oscillating behaviour. The use of sensitivity analysis method, developed on the basis of the theory of shadowing pseudoorbits in dynamical systems, allows us to calculate sensitivity functions correctly. Sensitivity estimates for a simple coupled dynamical system are calculated and presented in the paper. To estimate the influence of model parameter uncertainties on the forecast, the relative error in the energy norm is applied.

1. Introduction

The earth system consists of several interactive dynamical subsystems and each of them covers a broad temporal and spatial spectrum of motions and physical processes. The components of the earth system have many differences in their physical properties, structure, and behavior but are linked together by fluxes of momentum and mass as well as sensible and latent heat. All of these subsystems interact with each other in different ways and can be strongly or weakly coupled. Prediction of future state of the earth system and its components is one of the most important problems of modern science. The most significant progress has been achieved in the forecasting of the atmosphere via numerical models, which describe the dynamical and physical processes in the earth's gaseous envelope. It is clear that further improvement of forecasts can be pursued via the development of coupled modeling systems that primarily combine the atmosphere

and the ocean and describe the interactions between these two systems. Since numerical weather prediction systems calculate a future state of the atmosphere and ocean by integrating a set of partial differential equations that describe the fluid dynamics and thermodynamics, initial conditions that accurately represent the state of the atmosphere and ocean at a certain initial time must be formulated. Numerical weather prediction systems use data assimilation procedures to estimate initial conditions for forecasting models from observations. Data assimilation remains one of the key issues not only in the numerical weather prediction (NWP) but also in other geophysical sciences.

One of the most advanced and effective data assimilation techniques is four-dimensional variational data assimilation (4D-Var). In particular, the weather forecasts produced by the ACCESS (Australian Community Climate and Earth System Simulator) at the Bureau of Meteorology use 4D-Var in the incremental formulation developed at the Met Office [1, 2].

A comprehensive historical review and current status of 4D-Var are presented, for example, in [3–7]. In our view point, some papers and books, such as [8–17], have contributed significantly to the development of mathematical foundation, theory, and practice of 4D-Var.

In general, the main objective of 4D-Var is to define, as perfectly as possible, the state of a dynamical system by combining, in statistically optimal manner, the observations of state variables of a real physical system together with certain prior information. In NWP this prior information is usually referred to as the background. Mathematically, 4D-Var procedures are formulated as an optimization problem, in which the initial condition plays the role of control vector and model equations are considered as constraints. While the theory of variational data assimilation is well established, there are a number of issues with practical implementation that require additional consideration and study. The performance of 4D-Var schemes depends on their key information components, such as the available observations, estimates of the observation, and background error covariances that are quantified by the corresponding matrices, as well as the background state. All of those information components strongly impact the accuracy of calculated initial conditions, thus influencing the forecast quality. Thus, it is important to estimate the sensitivity of a certain forecast aspect with respect to variations in the observational data, background information, and error statistics. This problem is usually formulated within the framework of the adjoint-based sensitivity analysis (e.g., [18–29]).

However, an adjoint model used to calculate sensitivity functions is derived from a linearized forward propagation model and contains numerous input parameters. Consequently, linearization of strongly nonlinear NWP models and also uncertainties in their numerous parameters generate errors in the initial conditions obtained by data assimilation systems. The influence of linearization and parameter uncertainties on the results of data assimilation can be studied, ideally for each particular NWP model, using sensitivity analysis [30, 31]. Even more problems arise when considering coupled 4D-Var data assimilation schemes since the atmosphere and ocean have very different physical properties and time-space spectrum of motions generating initialization shock. Several coupling strategies are being developed for use in NWP systems; however, all of them introduce issues that require additional detailed consideration. For example, the influence of coupling strength on the initial conditions obtained by 4D-Var procedures is one such issue that is important to study and analyze.

Good practice in the development of NWP models and data assimilation systems requires evaluating the confidence in the model. In this context, it is important to estimate the influence of parameter variations on system dynamics and to find those parameters that have the largest impact on system behaviour. Sensitivity analysis, which is an essential element of model building and quality assurance, addresses this very important issue.

The exploration of coupled 4D-Var systems, parameter estimation, and sensitivity analysis require considerable computational resources. For simple enough low-order coupled

models, the computational cost is minor and, for that reason, models of this class are widely used as simple test instruments to emulate more complex systems. In this paper, we describe a coupled nonlinear dynamical system, which is composed of fast (the “atmosphere”) and slow (the “ocean”) versions of the well-known Lorenz [32] model. This low-order coupled system allows us to mimic the atmosphere-ocean system and therefore serves as a key element of a theoretical and computational framework for the study of various aspects of coupled 4D-Var procedures [33, 34]. Under certain conditions the Lorenz model exhibits a chaotic behaviour and using conventional methods of sensitivity analysis can be questionable in terms of interpretation of the obtained results [35–37]. The “shadowing” method [36, 37] for estimating the system sensitivity to variations in its parameters allows us to calculate the average along the trajectory sensitivities and therefore to make a clear conclusion with respect to the system sensitivity to its parameters. This method is based on the pseudo-orbit shadowing in dynamical systems [38, 39]. Calculated sensitivity coefficients obtained via conventional methods and the “shadowing” approach are presented in the paper.

We also succinctly consider commonly used techniques for sensitivity analysis and parameter estimations of dynamical systems and study the influence of coupling strength parameter on the dynamical behaviour of the coupled system using Lyapunov characteristic exponent analysis. It was found that the coupling strength parameter strongly affects the system dynamics both quantitatively and qualitatively. This fact should be taken into consideration when choosing the coupling strategy in data assimilation systems.

2. Low-Order Coupled Dynamical System

In this section we consider a low-order coupled nonlinear dynamical system obtained by coupling of two versions of the original Lorenz model (L63) [32] with distinct time scales, which differ by a factor ε (e.g., [33, 34]):

$$\begin{aligned}\dot{x} &= \sigma(y - x) - c(aX + k), \\ \dot{y} &= rx - y - xz + c(aY + k), \\ \dot{z} &= xy - bz + c_z Z,\end{aligned}\tag{1a}$$

$$\begin{aligned}\dot{X} &= \varepsilon\sigma(Y - X) - c(x + k), \\ \dot{Y} &= \varepsilon(rX - Y - aXZ) + c(y + k), \\ \dot{Z} &= \varepsilon(aXY - bZ) - c_z z,\end{aligned}\tag{1b}$$

where lower case letters represent the fast subsystem and capital letters the slow subsystem, σ , r , and b are the parameters of L63 model, c is a coupling strength parameter for the x and y variables, c_z is a coupling strength parameter for z , k is an “uncentering” parameter, and a is a parameter representing the amplitude scale factor. The value $a = 1$ indicates that two systems have the same amplitude scale. Thus, the state vector of the coupled model (1a) and (1b) is $\mathbf{x} = (x, y, z, X, Y, Z)^T$ and the model parameter vector is

the ACF of the slow variable X is less than that of the fast variable x . The ACF envelopes for variables z and Z also decay almost exponentially from the maximum to zero. For coupling strength parameter on the interval $0.4 < c < 0.6$ the ACF of the fast variable x becomes smooth and converges to zero. At the same time, the envelopes of the ACFs of variables X , z , and Z demonstrate a fairly rapid fall, indicating the chaotic behaviour. As the parameter c increases, the ACFs become periodic and their envelopes decay slowly with time, indicating transition to regularity. For $c > 0.8$ calculated ACFs show periodic signal components.

3. The Basics of Four-Dimensional Variational Data Assimilation

Atmospheric models used for operational NWP are mainly deterministic and derived from a set of multidimensional nonlinear differential equations in partial derivatives, which are the equations of fluid dynamics and thermodynamics that describe atmospheric processes and atmosphere-underlying surface interactions. A generic atmospheric model can be represented by the following continuous autonomous dynamical system:

$$\frac{d\mathbf{x}(t)}{dt} = f(\mathbf{x}(t), \boldsymbol{\alpha}(t)), \quad t \in [0, \tau] = \mathcal{T}, \quad \mathbf{x}(0) = \mathbf{x}_0. \quad (7)$$

Here $\mathbf{x}(t)$ is the state vector belonging to a Hilbert space \mathcal{X} , $\boldsymbol{\alpha} \in \mathcal{P}$ is a parameter vector, where \mathcal{P} is a Hilbert space (the space of the model parameters), f is a nonlinear vector-valued function, such that $f : \mathcal{X} \times \mathcal{P} \times \mathcal{T} \rightarrow \mathcal{X}$, and \mathbf{x}_0 is a given vector function. This infinite-dimensional model has to be truncated by some means to finite-dimensional approximate model, for which a solution can be sought numerically. Applying either a projection onto a finite set of basic functions or a discretization in time and space, one can derive the discrete atmospheric model which can be represented as s discrete nonlinear dynamical system given by the equation

$$\mathbf{x}_{i+1} = \mathcal{M}_{i,i+1}(\mathbf{x}_i) + \boldsymbol{\varepsilon}_i^m, \quad (8)$$

where $\mathbf{x}_i \in \mathbb{R}^n$ is the n -dimensional state vector representing the complete set of the model variables that determine the internal state of the atmospheric model at time t_i , $\mathcal{M}_{i,i+1}$ is the nonlinear operator that indirectly contains model parameters and propagates the state vector from time t_i to time t_{i+1} for $i = 0, \dots, N-1$, and $\boldsymbol{\varepsilon}_i^m$ is the model errors. It is usually assumed that model (8) is “perfect” ($\boldsymbol{\varepsilon}_i^m = 0$), that is the forecast has no errors if the initial condition is perfect. In this case, given the model operator and the initial condition \mathbf{x}_0 , (8) uniquely specifies the orbit of the dynamical system. Let $\mathbf{y}_i^0 \in \mathbb{R}^m$ be the m -dimensional vector of observations measured at a discrete time t_i , $i = 0, \dots, N$ that are linked to the system state via the following equation:

$$\mathbf{y}_i^0 = \mathcal{H}_i(\mathbf{x}_i) + \boldsymbol{\varepsilon}_i^0, \quad (9)$$

where $\mathcal{H}_i : \mathbb{R}^n \rightarrow \mathbb{R}^m$ is the nonlinear observation operator that maps the state vector to observation space. It is

usually assumed that the observation errors $\boldsymbol{\varepsilon}_i^0$ are unbiased, serially uncorrelated, and normally distributed with known covariance matrices $\mathbf{R}_i \in \mathbb{R}^{m \times m}$.

Suppose that at the initial time the prior (background) model state \mathbf{x}_0^b is known and represents the “best” estimate of the “true” state \mathbf{x}_0^t before any observations are taken. This background state is provided by a previous forecast. It is assumed that \mathbf{x}_0^b has unbiased and normally distributed errors $\boldsymbol{\varepsilon}^b$ with known covariance matrix $\mathbf{B}_0 \in \mathbb{R}^{n \times n}$:

$$\mathbf{x}_0^b = \mathbf{x}_0^t + \boldsymbol{\varepsilon}^b. \quad (10)$$

Given the observations \mathbf{y}_i^0 at time t_i , the corresponding observation error covariance matrices \mathbf{R}_i ($i = 0, \dots, N$), the background initial state \mathbf{x}_0^b , and the error covariance matrix \mathbf{B}_0 , the 4D-Var data assimilation seeks to minimize, with respect to \mathbf{x}_0 , a certain cost function $J(\mathbf{x})$ expressing the “distance” between observations and corresponding model state using the model equations as constraints:

$$\mathbf{x}_0^a = \arg \min J(\mathbf{x}) \quad (11)$$

subject to \mathbf{x} satisfying the set of the “ideal” ($\boldsymbol{\varepsilon}_i^m = 0$) model equations with initial state \mathbf{x}_0 :

$$\mathbf{x}_{i+1} = \mathcal{M}_{0,i+1}(\mathbf{x}_0), \quad i = 1, \dots, N. \quad (12)$$

The 4D-Var cost function is usually written as (e.g., [17, 18]):

$$J(\mathbf{x}_0) = \frac{1}{2} (\mathbf{x}_0 - \mathbf{x}_0^b)^T \mathbf{B}_0^{-1} (\mathbf{x}_0 - \mathbf{x}_0^b) + \frac{1}{2} \sum_{i=0}^N (\mathcal{H}_i(\mathbf{x}_i) - \mathbf{y}_i^0)^T \mathbf{R}_i^{-1} (\mathcal{H}_i(\mathbf{x}_i) - \mathbf{y}_i^0). \quad (13)$$

The optimization problem (11) is nonlinear with strong constraints and an iterative minimization algorithm (e.g., gradient-based technique) is required to obtain the solution. The gradient of the cost function (13) is as follows:

$$\nabla_{\mathbf{x}_0} J(\mathbf{x}_0) = \mathbf{B}_0^{-1} (\mathbf{x}_0 - \mathbf{x}_0^b) + \sum_{i=0}^N \mathbf{M}_{0,i}^T \mathbf{H}_i^T \mathbf{R}_i^{-1} (\mathcal{H}_i(\mathbf{x}_i) - \mathbf{y}_i^0), \quad (14)$$

where $\mathbf{M}_{0,i}^T$ is the adjoint of the linearized model operator $\mathbf{M}_{0,i} = \mathcal{M}'_{0,i}(\mathbf{x}_i)$ and \mathbf{H}_i^T is the adjoint of the linearized observation operator $\mathbf{H}_i = \mathcal{H}'_i(\mathbf{x}_i)$. If the model is not “perfect” then we need to take into account the model errors $\boldsymbol{\varepsilon}^m$, which are sometimes taken as Gaussian noise:

$$\boldsymbol{\varepsilon}^m \in \mathcal{N}(0, \mathbf{Q}), \quad (15)$$

where \mathbf{Q} is a model error covariance matrix. Thus, we obtain the weakly constrained 4D-Var data assimilation and the following term

$$J_m = \frac{1}{2} \sum_{i=1}^N (\mathbf{x}_i - \mathcal{M}_{i-1,i}(\mathbf{x}_{i-1}))^T \mathbf{Q}_i^{-1} (\mathbf{x}_i - \mathcal{M}_{i-1,i}(\mathbf{x}_{i-1})) \quad (16)$$

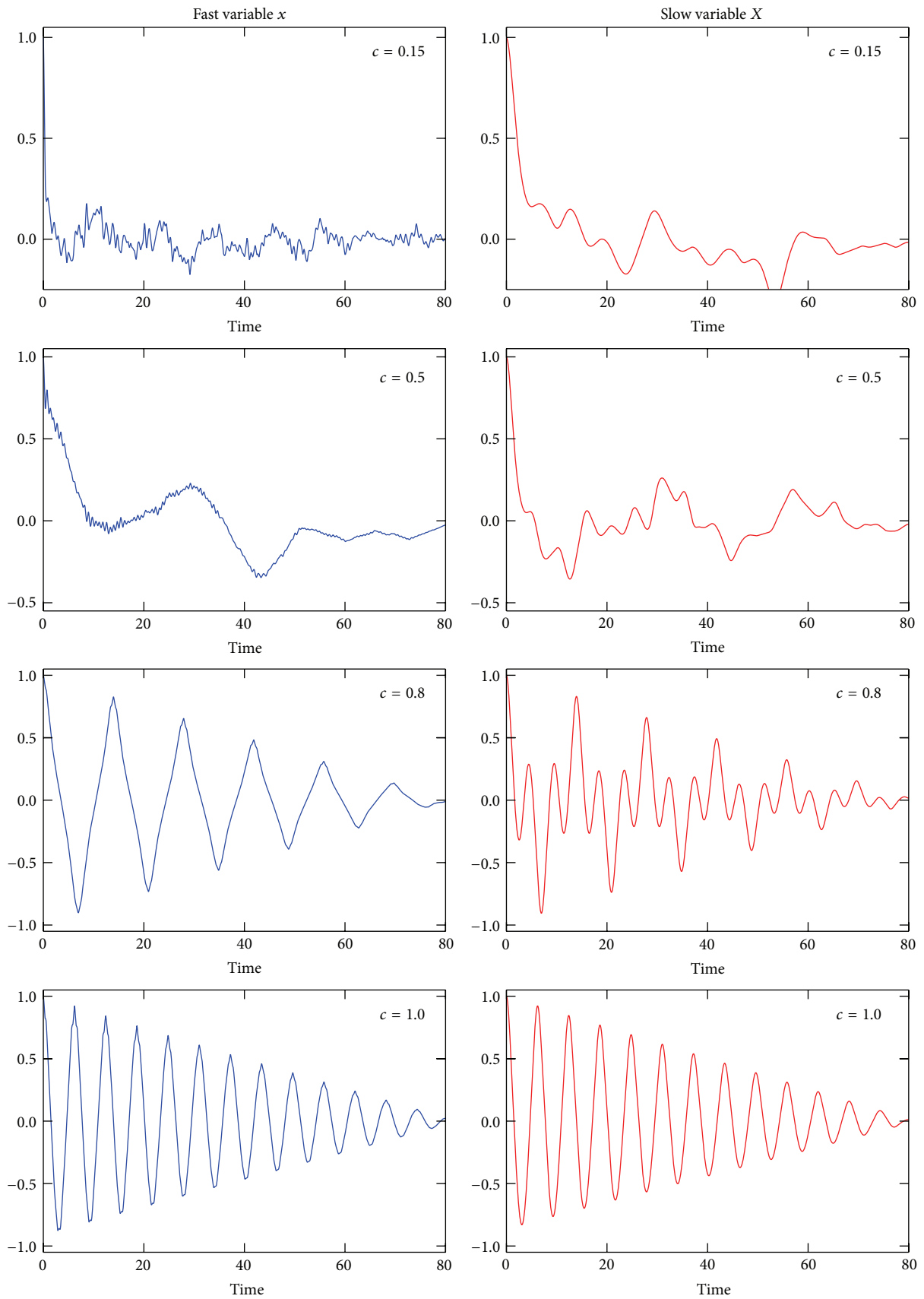


FIGURE 2: Autocorrelation functions for dynamic variables x and X for different parameter c .

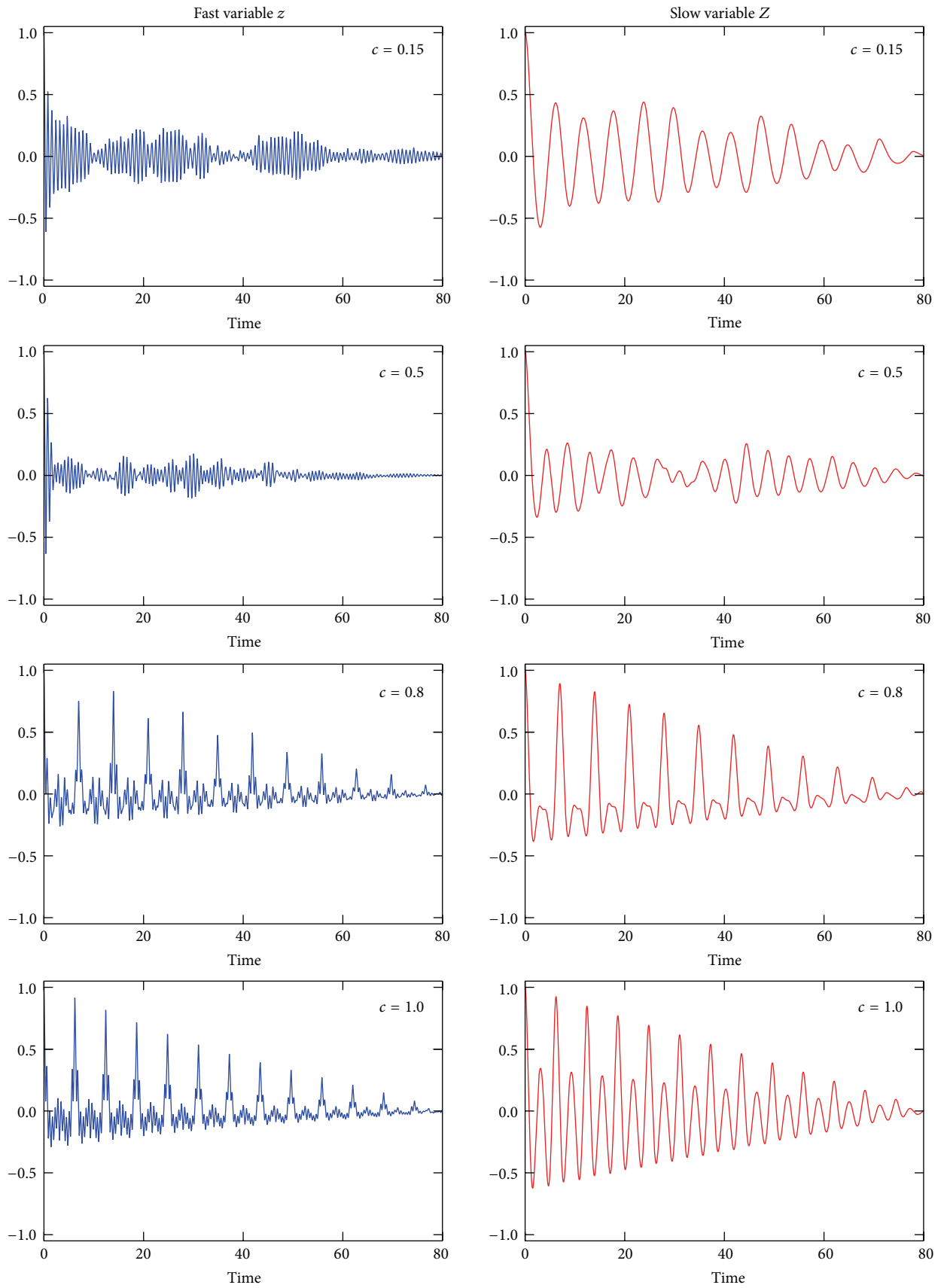


FIGURE 3: Autocorrelation functions for dynamic variables z and Z for different parameter c .

should be added to the right-hand side of the cost function (13) [6, 19].

It is important to make the following comments. While NWP has significantly improved over the last several decades, weather forecasts are still intrinsically uncertain. This is because mathematical models used in NWP have several sources of uncertainty and therefore a number of sources of errors. The first one is an intrinsic uncertainty due to chaotic nature of the system. The second one is a structural uncertainty, which is how the model itself represents the physical processes incorporated into it. It is important to underline that our knowledge of the earth system is always imperfect and, therefore, we can only theoretically design the “ideal” model. However, improving model physics demonstrated that even theoretically well-posed models failed to accurately simulate and predict the dynamics of real atmospheric processes. This is because numerical models have a parametric uncertainty (how accurate model parameters are) initial and boundary uncertainty (are initial and boundary conditions known precisely) and, in addition, numerical errors. All of those uncertainties (errors) impair the weather forecast accuracy and limit the time horizon of accurate NWP. Current time horizon of synoptic-scale NWP is several days.

The climate study has significantly longer time horizon: several decades. The sensitivity analysis of the climate system is associated with stability of characteristics of climatic model attractors with respect to perturbations in model parameters. *A priori* estimation of the behaviour of state vector, when the perturbations in the climate model parameters tend to zero, is generally an unresolved problem since it is not known whether or not the invariant measure of climate modeling system is continuous with respect to the small perturbations in the differential matrix operator of the numerical model. Indeed, at certain model parameter values, different bifurcation can occur in the system phase space. Therefore, dynamics on the attractor generated by the model may change considerably even for small parameter perturbations.

4. Sensitivity Analysis: Essentials of Conventional Approaches

One of the commonly used measures for estimating the influence of model parameter variations on the state variables is the sensitivity coefficient, which is the derivative of a certain component of a model state vector x_i with respect to some model parameter α_j [30, 31, 44]:

$$S_{ij} \equiv \left. \frac{\partial x_i}{\partial \alpha_j} \right|_{\alpha_j = \alpha_j^0} = \lim_{\delta \alpha_j \rightarrow 0} \left[\frac{x_i(\alpha_j^0 + \delta \alpha_j) - x_i(\alpha_j^0)}{\delta \alpha_j} \right], \quad (17)$$

where $\delta \alpha_j$ is the infinitesimal perturbation of parameter α_j around some fixed point α_j^0 . Differentiating (8) with respect to α , we obtain the set of nonhomogeneous ODEs, the so-called sensitivity equations, which can be written as

$$\frac{dS_j}{dt} = \mathbf{M} \cdot S_j + \mathbf{D}_j \quad j = 1, \dots, m, \quad (18)$$

where $S_j = (\partial \mathbf{x} / \partial \alpha_j) = (S_{1,j}, S_{2,j}, \dots, S_{n,j})^T$ is the sensitivity vector with respect to parameter α_j , $\mathbf{D}_j = (\partial f_1 / \partial \alpha_j, \partial f_2 / \partial \alpha_j, \dots, \partial f_n / \partial \alpha_j)^T$, and \mathbf{M} is a Jacobian matrix. Thus, to analyze the sensitivity of system (7) with respect to parameter α_j one can solve the following set of differential equations with given initial conditions:

$$\begin{aligned} \frac{d\mathbf{x}}{dt} &= f(\mathbf{x}, \alpha), \quad \mathbf{x}(0) = \mathbf{x}_0, \\ \frac{dS_j}{dt} &= \mathbf{M} \cdot S_j + \mathbf{D}_j, \quad S_j(0) = S_{j0}. \end{aligned} \quad (19)$$

Sensitivity equations describe the evolution of sensitivity coefficients along a given trajectory and therefore allow tracing the sensitivity dynamics in time. The procedure for computing sensitivity coefficients includes the following steps.

- (1) Obtain initial conditions on the system attractor at time $t = t_0$ by integrating the nonlinear model equations (7) for a long enough time range $[t_0, \tau]$, starting from random initial conditions.
- (2) Solve the nonlinear model equations (7) to calculate a trajectory $\mathbf{x}(t)$, $t \in [t_0, \tau]$.
- (3) Calculate a model Jacobian matrix and a parametric Jacobian matrix.
- (4) Solve the sensitivity equations (18) with given initial conditions to obtain the desired sensitivity coefficients.

Sensitivity analysis allows us also to explore the sensitivity of a generic objective function (performance measure), which characterizes the dynamical system (7):

$$\mathcal{F}(\mathbf{x}, \alpha) = \int_0^\tau \Phi(t; \mathbf{x}, \alpha) dt, \quad (20)$$

where Φ is a nonlinear function of the state variables \mathbf{x} and model parameters α . The gradient of the functional \mathcal{F} with respect to the parameters α around the unperturbed state vector \mathbf{x}^0

$$\nabla_{\alpha} \mathcal{F}(\mathbf{x}^0, \alpha^0) = \left(\left. \frac{d\mathcal{F}}{d\alpha_1}, \dots, \frac{d\mathcal{F}}{d\alpha_m} \right) \right|_{\mathbf{x}^0, \alpha^0} \quad (21)$$

quantifies the influence of parameters on the model output results. In particular, the effect of the j th parameter can be estimated as follows:

$$\begin{aligned} \left. \frac{d\mathcal{F}}{d\alpha_j} \right|_{\alpha_j^0} &\approx \frac{\mathcal{F}(\mathbf{x}^0 + \delta \mathbf{x}^0; \alpha_1^0, \dots, \alpha_j^0 + \delta \alpha_j, \dots, \alpha_m^0) - \mathcal{F}(\mathbf{x}^0, \alpha^0)}{\delta \alpha_j}, \end{aligned} \quad (22)$$

where $\delta \alpha_i$ is the variation in parameter α_i^0 . Note that

$$\frac{d\mathcal{F}}{d\alpha_j} = \sum_{i=1}^n \frac{\partial \mathcal{F}}{\partial x_i} \frac{\partial x_i}{\partial \alpha_j} + \frac{\partial \mathcal{F}}{\partial \alpha_j} = \sum_{i=1}^n S_{ij} \frac{\partial \mathcal{F}}{\partial x_i} + \frac{\partial \mathcal{F}}{\partial \alpha_j}. \quad (23)$$

This approach is acceptable for low-order models. However, the accuracy of sensitivity estimates strongly depends on choice of the perturbation $\delta\alpha_i$. By introducing the Gâteaux differential, the sensitivity analysis problem can be considered in the differential formulation eliminating the need to set the value of $\delta\alpha_i$ [30, 31]. The Gâteaux differential for the objective function (20) has the following form:

$$\delta\mathcal{F}(\mathbf{x}^0, \boldsymbol{\alpha}^0; \delta\mathbf{x}, \delta\boldsymbol{\alpha}) = \int_0^\tau \left(\left. \frac{\partial\Phi}{\partial\mathbf{x}} \right|_{\mathbf{x}^0, \boldsymbol{\alpha}^0} \cdot \delta\mathbf{x} + \left. \frac{\partial\Phi}{\partial\boldsymbol{\alpha}} \right|_{\mathbf{x}^0, \boldsymbol{\alpha}^0} \cdot \delta\boldsymbol{\alpha} \right) dt. \quad (24)$$

Here $\delta\mathbf{x}$ is the state vector variation due to the variation in the parameter vector in the direction $\delta\boldsymbol{\alpha}$. Linearizing the nonlinear model (7) around an unperturbed trajectory $\mathbf{x}^0(t)$, we obtain the following system of variational equations, the so-called tangent linear model, for calculating $\delta\mathbf{x}$:

$$\frac{\partial\delta\mathbf{x}}{\partial t} = \left. \frac{\partial f}{\partial\mathbf{x}} \right|_{\mathbf{x}^0, \boldsymbol{\alpha}^0} \cdot \delta\mathbf{x} + \left. \frac{\partial f}{\partial\boldsymbol{\alpha}} \right|_{\mathbf{x}^0, \boldsymbol{\alpha}^0} \cdot \delta\boldsymbol{\alpha}, \quad (25)$$

$$t \in [0, \tau], \quad \delta\mathbf{x}(0) = \delta\mathbf{x}_0.$$

Then using (24) we can calculate the variation $\delta\mathcal{F}$. Since $\delta\mathcal{F}(\mathbf{x}^0, \boldsymbol{\alpha}^0; \delta\mathbf{x}, \delta\boldsymbol{\alpha}) = \langle \nabla_{\boldsymbol{\alpha}}\mathcal{F}, \delta\boldsymbol{\alpha} \rangle$, where $\langle \cdot, \cdot \rangle$ is a scalar product, the model sensitivity with respect to parameter variations can be estimated by calculating the components of the gradient $\nabla_{\boldsymbol{\alpha}}\mathcal{F}$. However, this method is computationally ineffective if the number of model parameters m is large. The use of adjoint equations allows obtaining the required sensitivity estimates within a single computational experiment (e.g., [6, 30, 31]) since the gradient $\nabla_{\boldsymbol{\alpha}}\mathcal{F}$ can be calculated by the following equation:

$$\nabla_{\boldsymbol{\alpha}}\mathcal{F}(\mathbf{x}^0, \boldsymbol{\alpha}^0) = \int_0^\tau \left[\left. \frac{\partial\Phi}{\partial\boldsymbol{\alpha}} \right|_{\mathbf{x}^0, \boldsymbol{\alpha}^0} - \left(\left. \frac{\partial f}{\partial\boldsymbol{\alpha}} \right|_{\mathbf{x}^0, \boldsymbol{\alpha}^0} \right)^T \cdot \mathbf{x}^* \right] dt, \quad (26)$$

where the vector function \mathbf{x}^* is the solution of adjoint model

$$-\frac{\partial\mathbf{x}^*}{\partial t} - \left(\left. \frac{\partial f}{\partial\mathbf{x}} \right|_{\mathbf{x}^0, \boldsymbol{\alpha}^0} \right)^T \mathbf{x}^* = - \left. \frac{\partial\Phi}{\partial\mathbf{x}} \right|_{\mathbf{x}^0, \boldsymbol{\alpha}^0}, \quad (27)$$

$$t \in [0, \tau], \quad \mathbf{x}^*(\tau) = 0.$$

This equation is numerically integrated in the inverse time direction. Thus, the algorithm for computing sensitivity functions is as follows.

- (1) Obtain initial conditions on the system attractor at time t_0 by integrating the nonlinear model equations (7) for a long enough time range $[t_0, \tau]$, starting from random initial conditions.
- (2) Solve the nonlinear model equations (7) to calculate a trajectory $\mathbf{x}(t)$, $t \in [t_0, \tau]$.
- (3) Calculate the right-hand side of (27) and then integrate numerically this equation in the inverse time direction with the initial conditions $\mathbf{x}^*(\tau) = 0$.
- (4) Calculate the gradient (26).

5. Testing the Variational Data Assimilation

We will consider the dynamics of system (2) on its attractor. In order to obtain the model attractor, the numerical integration of (2) is started at $t_D = -20$ with the initial conditions

$$\mathbf{x}(t_D) = (0.01, 0.01, 0.01, 0.02, 0.02, 0.02)^T \quad (28)$$

and finished at $t_0 = 0$ to guarantee that the calculated model state vector $\mathbf{x}_0 = \mathbf{x}(0)$ is on the model attractor. The forecast, obtained by NWP models, is substantially determined by initial conditions, which calculated via 4D-Var. The accuracy of initial conditions strongly depends on numerous parameters of 4D-Var systems. Some of these parameters are uncertain. To estimate the influence of parameter variations on the forecast obtained by model (2), the “true” and “forecast” trajectories were calculated. The “true” trajectory $\mathbf{x}^t(t_i)$ and the “true” state $\mathbf{x}^t(t_f)$ at the verification time t_f are obtained by integrating the model equations over the time interval $[t_0, t_f]$ with unperturbed parameter vector $\boldsymbol{\alpha}^0$ and initial conditions \mathbf{x}_0 . Then, the forecast trajectory $\mathbf{x}^f(t_k)$ and the forecast state $\mathbf{x}^f(t_f)$ at t_f are obtained by integration of the “forecast” model (2) with initial conditions \mathbf{x}_0 and a certain perturbed model parameter. Thus, the “forecast” model has the same set of equations as the “true” model; however, some model parameter is slightly changed (i.e., this parameter is known with uncertainty). In order to measure forecast errors the relative error in energy norm is used:

$$e(\mathbf{x}^f) = \left[\frac{(\mathbf{x}^f - \mathbf{x}^t)^T (\mathbf{x}^f - \mathbf{x}^t)}{(\mathbf{x}^t)^T \mathbf{x}^t} \right]^{1/2}. \quad (29)$$

As an example, variations in parameters r and c are considered and forecast is made for two time periods t_f : 2.5 and 5.0 of nondimensional time units. The forecast error (29) is estimated at time t_f . Table 1 shows the results of forecast verifications. It is obvious that the less the forecast error measure $e(\mathbf{x}^f)$, the higher the forecast skill. Qualitatively, calculated results are consistent with real numerical weather forecasts obtained with complex state-of-the-art NWP models: longer t_f leads to lower forecast accuracy and smaller parameter variations (difference between the “true” parameter value and the value used in the “real” model) lead to better forecast accuracy. It can also be observed that parameter r influences the forecast accuracy almost twice as much as parameter c .

Synthetic data assimilation requires the “true” state $\mathbf{x}^t(t_i)$, the background (first guess) state $\mathbf{x}^b(t_i)$, and observations $\mathbf{y}^0(t_i)$ inside the assimilation window $[t_0, t_N]$ as well as error covariance matrices of the prior guess \mathbf{B}_0 and observations \mathbf{R}_i . The length of data assimilation window should be defined as well. The “true” and background trajectories on the data assimilation interval $[t_0, t_N]$ represent some portions of $\mathbf{x}^t(t_i)$ and $\mathbf{x}^b(t_i)$, respectively. Observations should be provided every 5–10 time steps inside the assimilation window and can be generated by adding the Gaussian random noise (with zero mean and variance $\sigma_0^2 = 0.2$) to the “true” state. Since observation grid and model grid are the same, observation

TABLE 1: Relative errors in energy norm (subscript at parameters denotes the nondimensional time unit).

	Parameter variations in percent of unperturbed value					
	1%	-1%	5%	-5%	10%	-10%
$r_{2.5}$	0.1273	0.1266	0.2871	0.2796	0.4081	0.3890
$c_{2.5}$	0.0584	0.0583	0.1312	0.1300	0.1866	0.1833
$r_{5.0}$	0.1663	0.1689	0.3617	0.3202	0.5004	0.5742
$c_{5.0}$	0.0705	0.0704	0.1583	0.1569	0.2250	0.2210

operator \mathcal{H} is simply an identity mapping. To take into consideration the background covariances, for simplicity, the assumption $\mathbf{B}_0 = \sigma_b^2 \mathbf{I}$ can be used, where $\sigma_b^2 = 0.2$ is the variance of background error and \mathbf{I} is the identity matrix. Under assumption that the observation quality is the same for all variables, the observation covariance matrix can be defined as $\mathbf{R}_i = \mathbf{R} = \sigma_0^2 \mathbf{I}$.

Testing the TL model and its adjoint is required to ensure the convergence of the minimization algorithm in data assimilation procedures. If $\zeta \delta \mathbf{x}$ is a small perturbation of the model state, then

$$\mathcal{M}(\mathbf{x} + \zeta \delta \mathbf{x}) - \mathcal{M}(\mathbf{x}) \approx \mathbf{M}(\mathbf{x}) \zeta \delta \mathbf{x}. \quad (30)$$

To verify the applicability of the TL model on the time interval $[t_0, t_N]$, the relative error

$$e_R = \frac{\mathcal{M}(\mathbf{x} + \zeta \delta \mathbf{x}) - \mathcal{M}(\mathbf{x})}{\mathbf{M}(\mathbf{x}) \zeta \delta \mathbf{x}} \quad (31)$$

should be calculated. The TL model is valid if $e_R \rightarrow 0$ when $\zeta \rightarrow 0$. The results of numerical experiments showed that the TL model passed this test with e_R tending towards zero (Table 2). The TL adjoint correctness can be tested by verification of the inner product identity

$$\langle \mathbf{M} \delta \mathbf{x}, \mathbf{M} \delta \mathbf{x} \rangle = \langle \delta \mathbf{x}, \mathbf{M}^T \mathbf{M} \delta \mathbf{x} \rangle. \quad (32)$$

It was found that this equality is essentially correct: the difference was observed only in the 7th digit, which is consistent with a round-off error. The second test to verify the adjoint model is the so-called gradient test [45], which aims to compare a finite difference representation of the gradient of 4D-Var cost function (13) with the gradient obtained via adjoint model $\nabla J(\mathbf{x}_0)$. A linear Taylor approximation of the cost function can be written as

$$J(\mathbf{x}_0 + \zeta \delta \mathbf{x}) \approx J(\mathbf{x}_0) + \zeta (\delta \mathbf{x})^T \nabla J(\mathbf{x}_0). \quad (33)$$

Let us introduce the following function:

$$\Psi(\zeta) = \frac{J(\mathbf{x}_0 + \zeta \delta \mathbf{x}) - J(\mathbf{x}_0)}{\zeta (\delta \mathbf{x})^T \nabla J(\mathbf{x}_0)}. \quad (34)$$

If the gradient is estimated correctly then the function $\Psi(\zeta) \rightarrow 1$ as $\zeta \rightarrow 0$. The perturbation vector $\delta \mathbf{x}$ is taken to be [45]

$$\delta \mathbf{x} = \frac{\nabla J(\mathbf{x}_0)}{\|\nabla J(\mathbf{x}_0)\|}, \quad (35)$$

TABLE 2: Results of verification of tangent linear model for $c = 0.8$ and $\delta \mathbf{x} = 10^{-2} \times \mathbf{x}_0$.

ζ	e_R
1	0.9182066027544249
10^{-1}	0.9997279965782743
10^{-2}	0.9999925468155463
10^{-3}	0.9999991929611531
10^{-4}	0.9999999534965012
10^{-5}	0.9999999911217883
10^{-6}	0.9999999914427087
10^{-7}	0.9999997435447022

TABLE 3: Results of verification of 4D-Var cost function gradient for $c = 0.8$ and $\delta \mathbf{x} = 10^{-2} \times \mathbf{x}_0$.

ζ	$\Psi(\zeta)$	$\log_{10}(\Psi(\zeta) - 1)$
10^{-4}	0.8727731981461396	-0.8954213897009056
10^{-5}	0.9975483775420343	-2.6105464089686840
10^{-6}	0.9998765512756632	-3.9085133935113787
10^{-7}	0.9999884562844123	-4.9376543818657845
10^{-8}	0.9999979865432855	-5.6960577024708600
10^{-9}	0.9999998912431426	-6.9635433500893210
10^{-10}	0.9999999244103234	-7.1215375125562080

where $\|\cdot\|$ is the L_2 norm. Table 3 manifests the success of the gradient test.

6. Sensitivity of the System with respect to Parameters

According to the sensitivity theory [44], general solutions of sensitivity equations for oscillatory nonlinear dynamical systems grow unbounded as time tends to infinity; therefore, sensitivity functions calculated by conventional approaches have a high degree of uncertainty. The reason is that nonlinear dynamical systems that exhibit chaotic behavior are very sensitive to its initial conditions. Thus, the solutions to the linearized Cauchy problem (7) grow exponentially as $\|\delta \mathbf{x}(t)\| \approx \|\delta \mathbf{x}(0)\| e^{\lambda t}$, where $\lambda > 0$ is the leading Lyapunov exponent. As a result, calculated sensitivity coefficients contain a fairly large error [35–37]. To illustrate this point, let us explore the sensitivity of model output to changes in the coupling

strength parameter. Let us introduce the following sensitivity coefficients:

$$\begin{aligned} S_{1c} &= \frac{\partial x}{\partial c}, & S_{2c} &= \frac{\partial y}{\partial c}, & S_{3c} &= \frac{\partial z}{\partial c}, \\ S_{4c} &= \frac{\partial X}{\partial c}, & S_{5c} &= \frac{\partial Y}{\partial c}, & S_{6c} &= \frac{\partial Z}{\partial c}. \end{aligned} \quad (36)$$

The corresponding sensitivity equations can be written as

$$\begin{aligned} \dot{S}_{1c} &= \sigma (S_{2c} - S_{1c}) - cS_{4c} - X, \\ \dot{S}_{2c} &= rS_{1c} - S_{2c} - xS_{3c} - zS_{1c} + cS_{5c} + Y, \\ \dot{S}_{3c} &= xS_{2c} + yS_{1c} - bS_{3c} + cS_{6c} + Z, \\ \dot{S}_{4c} &= \varepsilon \sigma (S_{5c} - S_{4c}) - cS_{1c} - x, \\ \dot{S}_{5c} &= \varepsilon (rS_{4c} - S_{5c} - XS_{6c} - ZS_{4c}) + cS_{2c} + y, \\ \dot{S}_{6c} &= \varepsilon (XS_{5c} + YS_{4c} - bS_{6c}) - cS_{3c} - z. \end{aligned} \quad (37)$$

Sensitivity coefficients can be introduced for any particular model parameter. Since the parameter vector α consists of five components ($\sigma, r, b, c,$ and ε), five sets of sensitivity equations can be derived from the model equations (2). The dynamics of sensitivity coefficients (36) can be traced by solving the sensitivity equations (37) along with the nonlinear model (2).

Sensitivity coefficients (36), calculated on the time interval $[0, 20]$, are shown in Figure 4. Envelopes of these coefficients grow over time while sensitivity coefficients themselves exhibit oscillating behavior. Figure 5 provides more detailed information on the evolution of sensitivity coefficients (36) calculated on the time interval $[0, 5]$. It is known that sensitivity coefficient is a measure of the change in state variable due to the variation of the estimated parameter. Unfortunately, obtained sensitivity coefficients are inherently uninformative and misleading. We cannot make a clear conclusion from them about system sensitivity to variations in the parameter c . In this regard, the average values of sensitivity functions $\nabla_{\alpha} \langle \mathcal{F}(\alpha) \rangle$ over a certain period of time can be considered as one of the most important measures of sensitivity, where \mathcal{F} is a generic objective function (20). However, the gradient $\nabla_{\alpha} \langle \mathcal{F}(\alpha) \rangle$ cannot be correctly estimated within the framework of conventional methods of sensitivity analysis since for chaotic systems it is observed that [35, 36]

$$\nabla_{\alpha} \langle \mathcal{F}(\alpha) \rangle \neq \langle \nabla_{\alpha} \mathcal{F}(\alpha) \rangle. \quad (38)$$

This is because the integral

$$\mathcal{F} = \lim_{T \rightarrow \infty} \int_0^T \lim_{\delta \alpha \rightarrow 0} \left[\frac{\mathcal{F}(\alpha + \delta \alpha) - \mathcal{F}(\alpha)}{\delta \alpha} \right] dt \quad (39)$$

does not possess uniform convergence and two limits ($T \rightarrow \infty$ и $\delta \alpha \rightarrow 0$) would not commute.

Similar results were obtained when we considered the influence of variations in the parameter r on the system dynamics. This parameter plays an important role in the formation of system's dynamical structure and transition to chaotic behavior [32]. Figure 6 shows the differences between

components of state vector $\mathbf{x}(r^0)$ obtained with $r = r^0 = 28$ and $\mathbf{x}(r^0 + \delta r)$ obtained with $r = r^0 + \delta r$, where $\delta r = 0.01r^0 = 0.28$. Even a small perturbation in the parameter r generates a tangible difference between corresponding state variables. Let us define the following sensitivity coefficients:

$$\begin{aligned} S_{1r} &= \frac{\partial x}{\partial r}, & S_{2r} &= \frac{\partial y}{\partial r}, & S_{3r} &= \frac{\partial z}{\partial r}, \\ S_{4r} &= \frac{\partial X}{\partial r}, & S_{5r} &= \frac{\partial Y}{\partial r}, & S_{6r} &= \frac{\partial Z}{\partial r}. \end{aligned} \quad (40)$$

The associated system of sensitivity equations can be written as

$$\begin{aligned} \dot{S}_{1r} &= \sigma (S_{2r} - S_{1r}) - cS_{4r}, \\ \dot{S}_{2r} &= x + rS_{1r} - S_{2r} - (xS_{3r} + zS_{1r}) + cS_{5r}, \\ \dot{S}_{3r} &= (xS_{2r} + yS_{1r}) - bS_{3r} + cS_{6r}, \\ \dot{S}_{4r} &= \varepsilon \sigma (S_{5r} - S_{4r}) - cS_{1r}, \\ \dot{S}_{5r} &= \varepsilon [X + rS_{4r} - S_{5r} - (XS_{6r} + ZS_{4r})] + cS_{2r}, \\ \dot{S}_{6r} &= \varepsilon [(XS_{5r} + YS_{4r}) - bS_{6r}] - cS_{3r}. \end{aligned} \quad (41)$$

Envelopes of calculated sensitivity coefficients (40) grow over time and sensitivity coefficients demonstrate the oscillating behavior (Figures 7 and 8). Obtained sensitivity coefficients are also uninformative and inconclusive. The ‘‘shadowing’’ approach for estimating the system sensitivity to variations in its parameters [36, 37] allows us to calculate the average sensitivities $\langle \nabla_{\alpha} J(\alpha) \rangle$ and therefore to make a clear conclusion with respect to the system sensitivity to its parameters. A detailed description of two variants of the ‘‘shadowing’’ approach is provided in an appendix, and some results of numerical experiments are presented below.

The main problem arising in the ‘‘shadowing’’ method is to calculate the pseudotrajectory. We consider two sets of numerical experiments: weak coupling ($c = 0.01$) and strong coupling ($c = 0.8$) between fast and slow systems. Fast and slow variables that correspond to the original and pseudoorbits are shown in Figures 9 and 10 when the coupling strength parameter $c = 0.01$. The Least Square Shadowing variant of the ‘‘shadowing’’ approach was used to calculate pseudotrajectories. The differences between state variables corresponding to the original and pseudotrajectories of the fast and slow systems are plotted in Figure 11. These figures show that the calculated pseudoorbits are close to corresponding true trajectories over a specified time interval, demonstrating the shadowability. The strong coupling does not introduce significant qualitative and quantitative changes in the behavior of pseudotrajectories with respect to the true orbits. The original and pseudo fast and slow variables for $c = 0.8$ are shown in Figures 12 and 13, and the differences between these state variables are presented in Figure 14. Sensitivity estimates with respect to the parameter r calculated over the time interval $[0, 20]$ for different values of coupling strength parameter are shown in Table 4. The most sensitive variables are z and Z . The sensitivity of variables $x,$

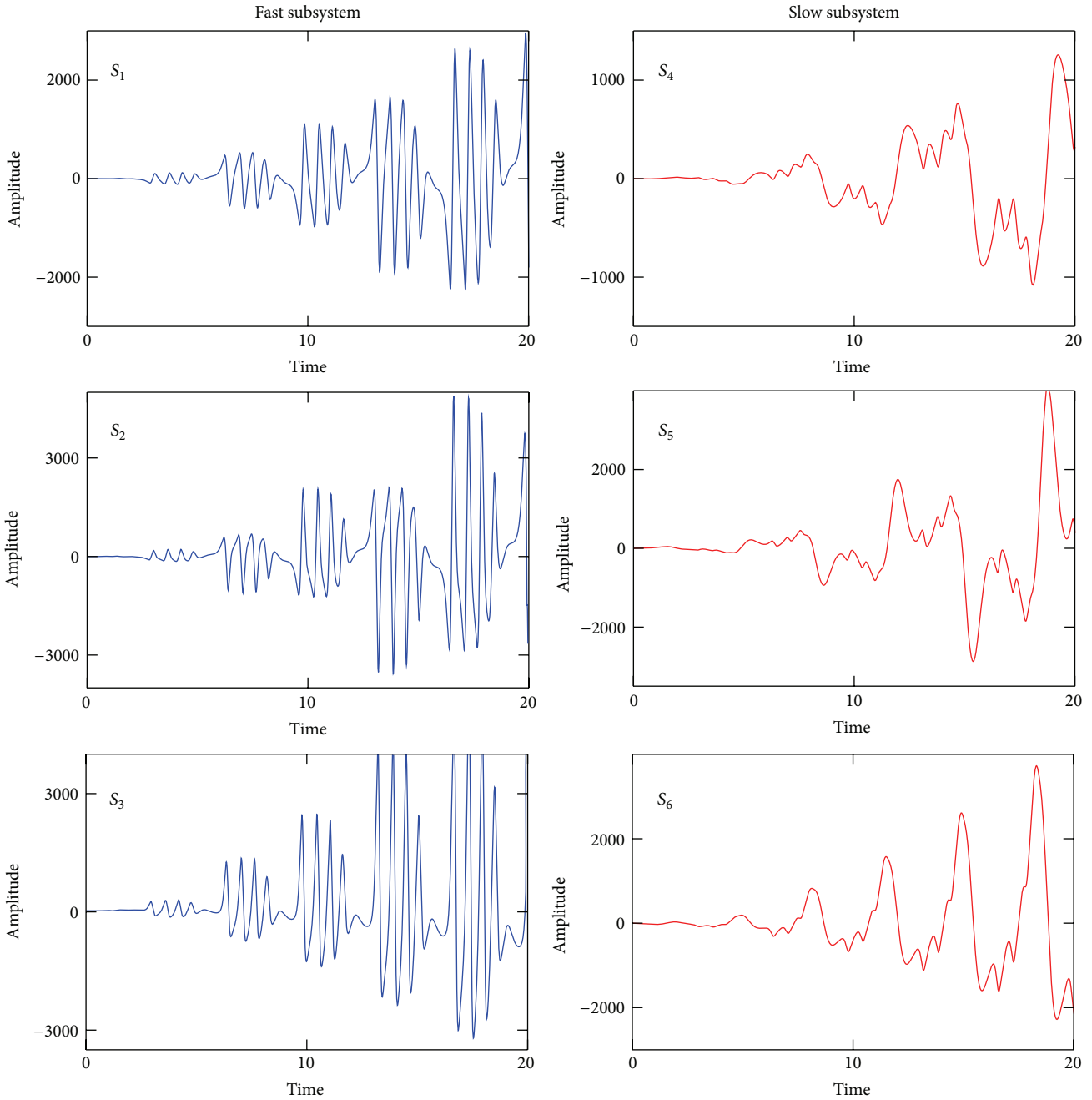


FIGURE 4: Time dynamics of sensitivity functions with respect to parameter c on the time interval $[0, 20]$ for $c^0 = 0.9$.

y , X , and Y with respect to r is significantly less than variables z and Z .

7. Concluding Remarks

We considered a coupled nonlinear dynamical system, which is composed of fast (the “atmosphere”) and slow (the “ocean”) versions of the well-known Lorenz model. This low-order mathematical tool allows us to mimic the atmosphere-ocean system and therefore serves as a key part of a theoretical and computational framework for the study of various aspects

of coupled 4D-Var procedures. Numerical models used to predict the weather are highly nonlinear but tangent linear approximations and their adjoints are used in VDA algorithms. Linear approximation of strongly nonlinear NWP models and also uncertainties in their numerous parameters generate errors in the initial conditions obtained via data assimilation systems. The influence of parameter uncertainties on the results of data assimilation can be studied using sensitivity analysis.

We discussed conventional methods of sensitivity analysis and their inefficiency with respect to calculating sensitivity

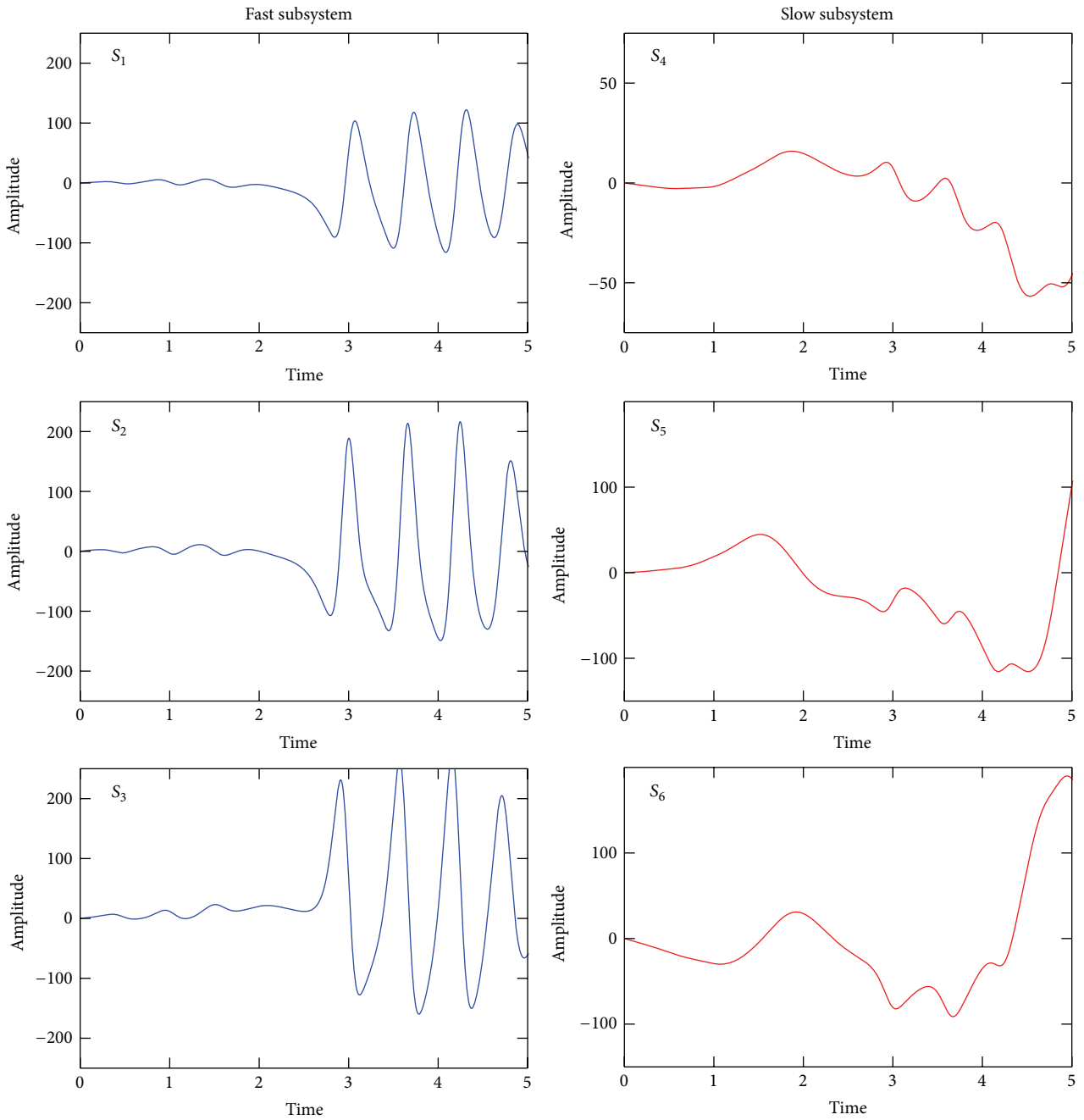


FIGURE 5: Time dynamics of sensitivity functions with respect to parameter c on the time interval $[0, 5]$ for $c^0 = 0.9$.

TABLE 4: Sensitivity estimates of fast and slow variables with respect to parameter r .

c	$\partial Z/\partial r$	$\partial Y/\partial r$	$\partial X/\partial r$	$\partial z/\partial r$	$\partial y/\partial r$	$\partial x/\partial r$
1.0	1.10	0.05	0.01	1.08	0.04	0.03
0.8	0.69	0.08	0.03	1.02	0.07	0.07
0.4	0.95	0.03	-0.01	1.03	0.09	0.09
0.15	0.91	-0.08	-0.09	1.01	-0.01	-0.01
10^{-4}	1.04	-0.02	-0.03	1.02	-0.01	-0.01

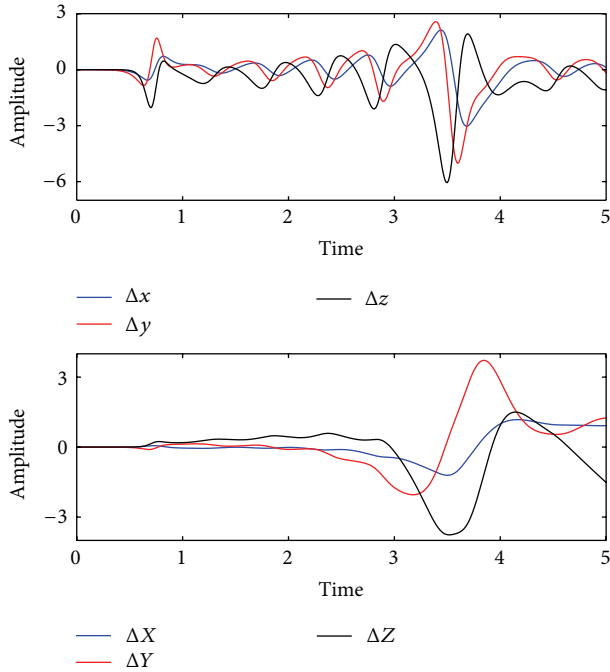


FIGURE 6: Difference between $\mathbf{x}(r^0)$ and $\mathbf{x}(r^0 + 0.01r^0)$ for fast and slow subsystems.

coefficients for chaotic dynamics. To calculate sensitivity coefficients with acceptable accuracy, the sensitivity analysis method [36, 37], developed on the basis of theory of shadowing of pseudoorbits in dynamical systems [38, 39], was applied. Previously, this method was used to analyze the sensitivity of the periodic van der Pol oscillator, the original Lorenz system, and simplified aeroelastic model that exhibit both periodic and chaotic regimes.

Calculated sensitivity coefficients obtained via conventional methods and the “shadowing” approach are presented and discussed. It was shown that envelopes of sensitivity coefficients obtained by conventional methods grow over time and the coefficients themselves exhibit the oscillating behaviour. Using the “shadowing” method allows us to calculate the average sensitivity functions (coefficients) that can be easily interpreted.

In conclusion, two comments should be highlighted.

(1) The shadowing property of dynamical systems is a fundamental feature of hyperbolic systems that was first discovered by Anosov [46] and Bowen [47]. However, most physical systems are nonhyperbolic. Despite the fact that much of shadowing theory has been developed for hyperbolic systems, there is evidence that nonhyperbolic attractors also have the shadowing property (e.g., [48–51]). In theory this property should be verified for each particular dynamical system, but this is more easily said than done.

(2) The applicability of the shadowing method for sensitivity analysis of modern atmospheric and climate models is a rather complicated problem since these models are quite complex and they contain numerous input parameters. Thus, further research and computational experiments are required. However, we are confident that, by using the basic ideas of the shadowing method, it is possible to better

understand the sensitivity analysis of atmospheric models of various levels of complexity.

Appendix

The novel sensitivity analysis method for chaotic dynamical systems developed in [36, 37] is based on the theory of pseudorbit shadowing in dynamical systems [38, 39], which is one of the most rapidly developing components of the global theory of dynamical systems and classical theory of structural stability [52]. Naturally, pseudo- (or approximate-) trajectories arise due to the presence of round-off errors, method errors, and other errors in computer simulation of dynamical systems. Consequently, we will not get an exact trajectory of a system, but we can come very close to an exact solution and the resulting approximate solution will be a pseudotrajectory. The shadowing property (or pseudorbit tracing property) means that, near an approximate trajectory, there exists the exact trajectory of the system considered, such that it lies uniformly close to a pseudotrajectory. The shadowing theory is well developed for the hyperbolic dynamics, which is characterized by the presence of expanding and contracting directions for derivatives. The study of shadowing problem was originated by Anosov [46] and Bowen [47].

Let (M, dist) be a compact metric space and let $f : M \rightarrow M$ be a homeomorphism (a discrete dynamical system on M). A set of points $X = \{x_k : k \in \mathbb{Z}\}$ is a d -pseudotrajectory ($d > 0$) of f if

$$\text{dist}(x_{k+1}, f(x_k)) < d, \quad k \in \mathbb{Z}. \quad (\text{A.1})$$

Here the notation $\text{dist}(\cdot, \cdot)$ denotes the distance in the phase space between two geometric objects within the brackets.

We say that f has the shadowing property if given $\varepsilon > 0$ there is $d > 0$ such that for any d -pseudotrajectory $X = \{x_k : k \in \mathbb{Z}\}$ there exists a corresponding trajectory $Y = \{y_k : k \in \mathbb{Z}\}$, which ε -traces X ; that is

$$\text{dist}(x_k, y_k) < \varepsilon, \quad k \in \mathbb{Z}. \quad (\text{A.2})$$

The shadowing lemma for discrete dynamical systems [53] states that, for each $\varepsilon > 0$, there exists $d > 0$ such that each d -pseudotrajectory can be ε -shadowed.

The definition of pseudotrajectory and shadowing lemma for flows (continuous dynamical systems) [38] are more complicated than for discrete dynamical systems. Let $\Phi^t : \mathbb{R} \times M \rightarrow M$ be a flow of a vector field X on M . A function $g : \mathbb{R} \rightarrow M$ is a d -pseudotrajectory of the dynamical system Φ^t if the inequalities

$$\text{dist}(\Phi^t(t, g(\tau)), g(\tau + t)) < d \quad (\text{A.3})$$

hold for any $t \in [-1, 1]$ and $\tau \in \mathbb{R}$. The “continuous” shadowing lemma ensures that, for the vector field X generating the flow Φ^t , the shadowing property holds in a small neighborhood of a compact hyperbolic set for dynamical system Φ^t .

It is very important to note that the shadowing problem for continuous dynamical systems requires reparameterization of shadowing trajectories. This is the case because for

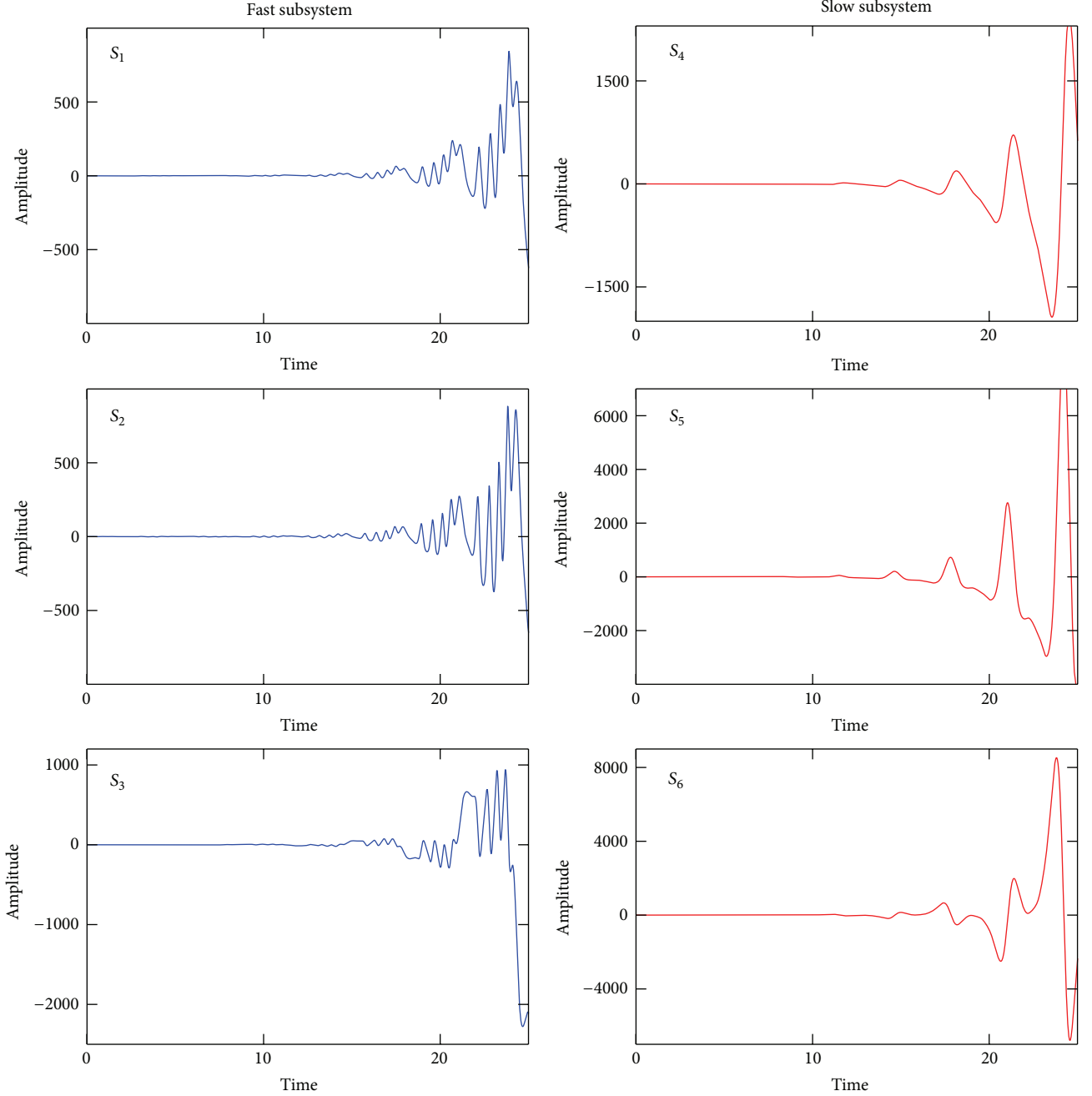


FIGURE 7: Time dynamics of sensitivity functions with respect to parameter r on the interval $[0, 25]$ for $c^0 = 0.9$.

continuous dynamical systems close points of pseudotrajectory and true trajectory do not correspond to the same moments of time. A monotonically increasing homeomorphism $h : \mathbb{R} \rightarrow \mathbb{R}$ such that $h(0) = 0$ is called a reparameterization and denoted by Rep . For $\varepsilon > 0$, $\text{Rep}(\varepsilon)$ is defined as follows [38]:

$$\text{Rep}(\varepsilon) = \left\{ h \in \text{Rep} : \left| \frac{h(t_1) - h(t_2)}{t_1 - t_2} - 1 \right| \leq \varepsilon \right\} \quad (\text{A.4})$$

for any different $t_1, t_2 \in \mathbb{R}$.

For simplicity, we will consider a generic autonomous dynamical system with one parameter α :

$$\frac{dx}{dt} = f(x, \alpha), \quad x \in \mathbb{R}^n. \quad (\text{A.5})$$

The new sensitivity analysis method [36, 37] is based on the “continuous” shadowing lemma and the following two basic assumptions.

- (a) Model state variables are considered over long time interval $t \in [0, T]$, where $T \rightarrow \infty$, and an averaged

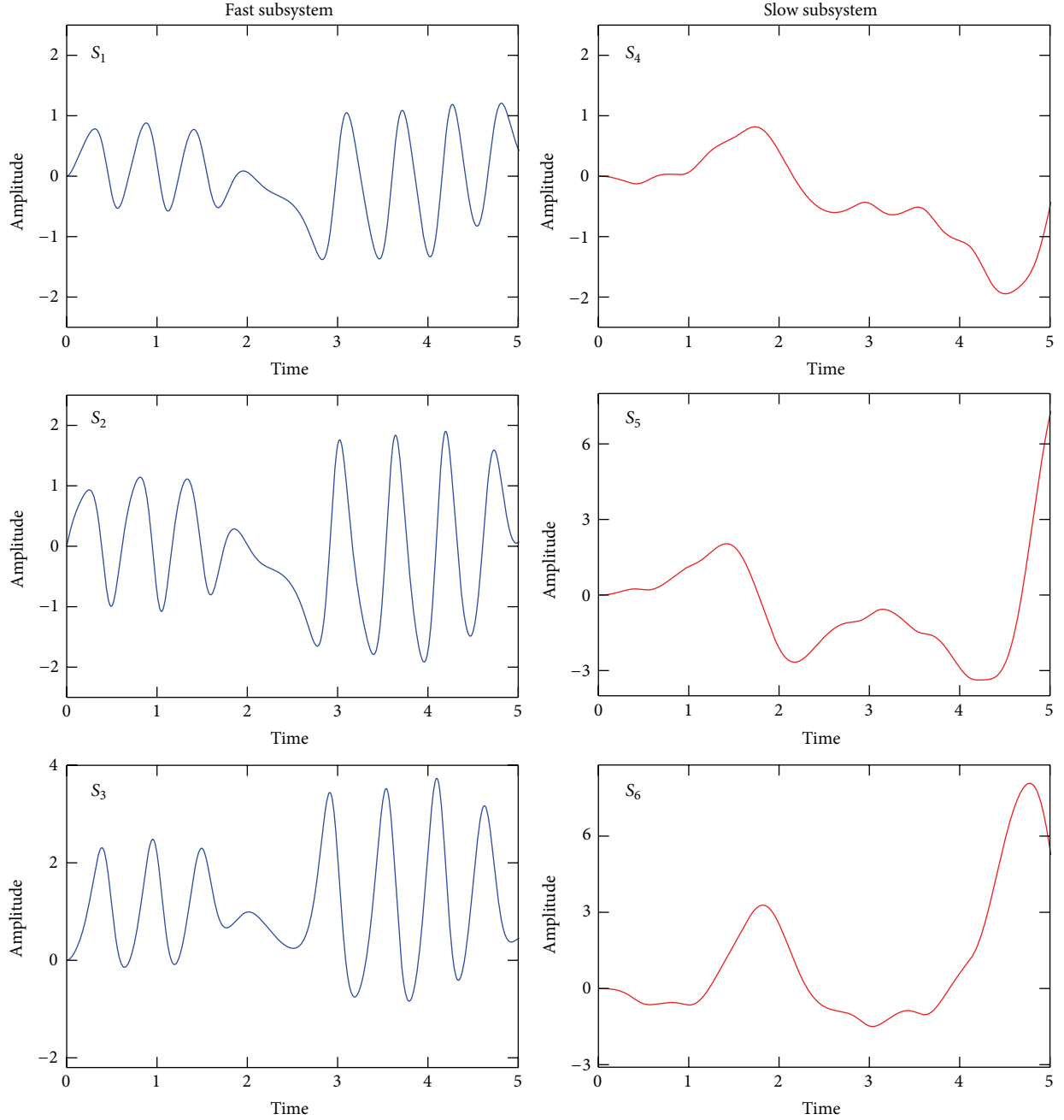


FIGURE 8: Time dynamics of sensitivity functions with respect to parameter r on the time interval $[0, 5]$ for $c^0 = 0.9$.

performance measure $\langle J(\alpha) \rangle$ is of the most interest for us:

$$\langle J(\alpha) \rangle = \lim_{T \rightarrow \infty} \frac{1}{T} \int_0^T J(x(t, \alpha), \alpha) dt. \quad (\text{A.6})$$

(b) The dynamical system under consideration is ergodic.

With these assumptions, we can use the arbitrarily chosen trajectory of the system to trace the state variables along the orbit and calculate the performance measure $J(\alpha)$. For example, the arbitrary trajectory $x(t)$ can be chosen as a

solution of the model equation, such that it is located nearby a certain reference trajectory $x_r(t)$. Taking into account the shadowing lemma, the closest orbit $x(t)$ to $x_r(t)$ satisfies the following constrained minimization problem [37]:

$$\min_{x, \tau} \frac{1}{T} \int_0^T \left[\|x(\tau(t)) - x_r(t)\|^2 + \eta^2 \left(\frac{d\tau}{dt} - 1 \right)^2 \right] dt,$$

such that $\frac{dx}{dt} = f(x, \alpha),$

(A.7)

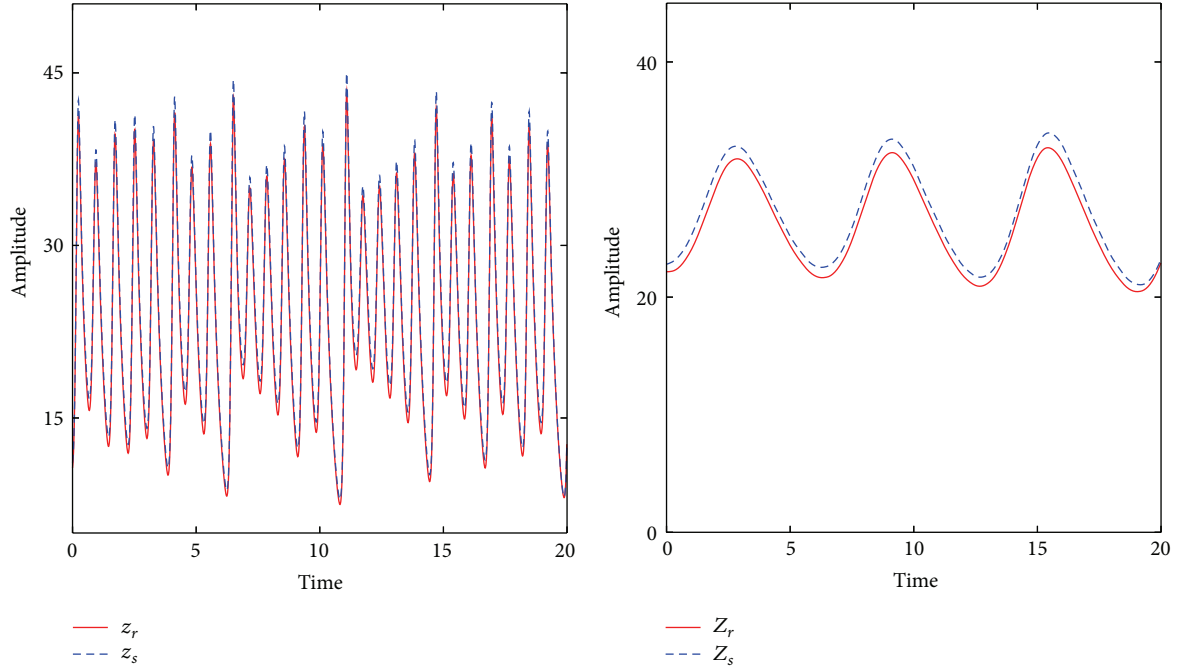


FIGURE 9: Original trajectory (in red) and pseudoorbit (in blue) for the fast z and slow Z variables for $c^0 = 0.01$.

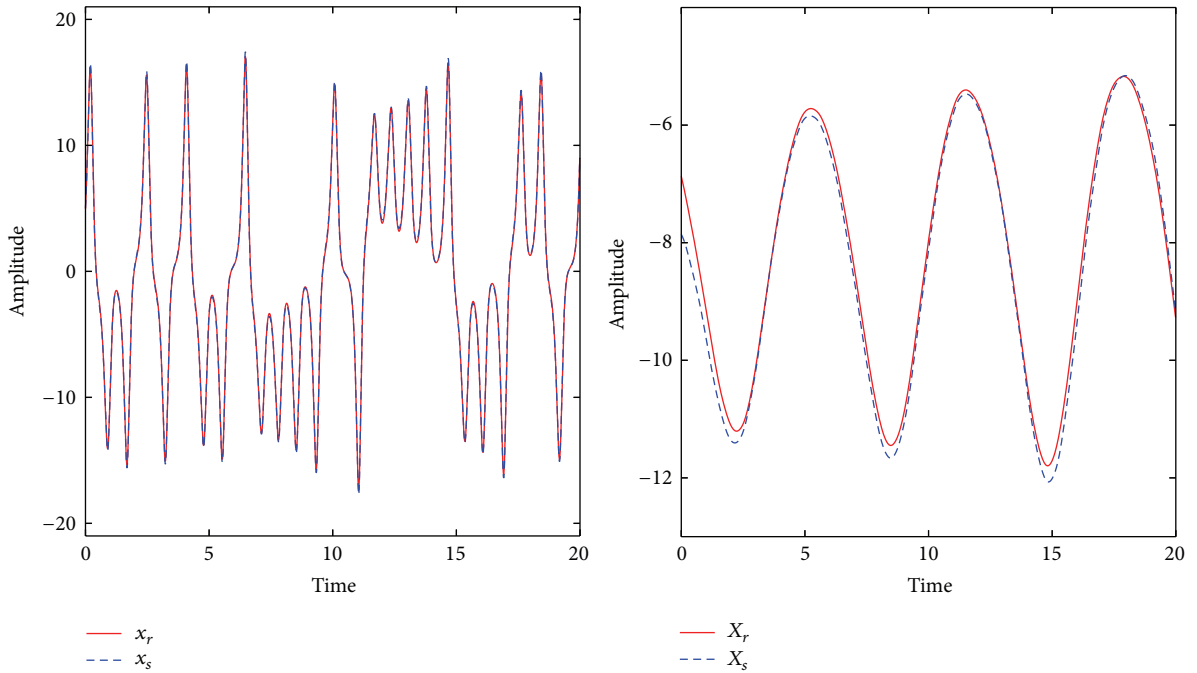


FIGURE 10: Original trajectory (in red) and pseudoorbit (in blue) for fast x and slow X variables for $c^0 = 0.01$.

where η is the parameter that provides the same order of magnitude of the two terms in the integrand and $\tau(t)$ is a time transformation. The second term in the integrand describes reparameterization. Problem (A.7) is called the nonlinear Least Square Shadowing (LSS) problem, and its solution, denoted by $x_s^{(T)}(t, \alpha)$ and $\tau_s^{(T)}(t, \alpha)$, is a solution of the model equation and time transformation that provides

the trajectory $x_s^{(T)}(t, \alpha)$ to be close to $x_r(t)$. The performance measure (A.6) averaged over the time interval $t \in [0, T]$ can be then approximated as

$$\langle J(\alpha) \rangle \approx \langle J_s^{(T)}(\alpha) \rangle = \frac{1}{\tau(T) - \tau(0)} \int_{\tau(0)}^{\tau(T)} J(x_s^{(T)}(t, \alpha), \alpha), \quad (\text{A.8})$$

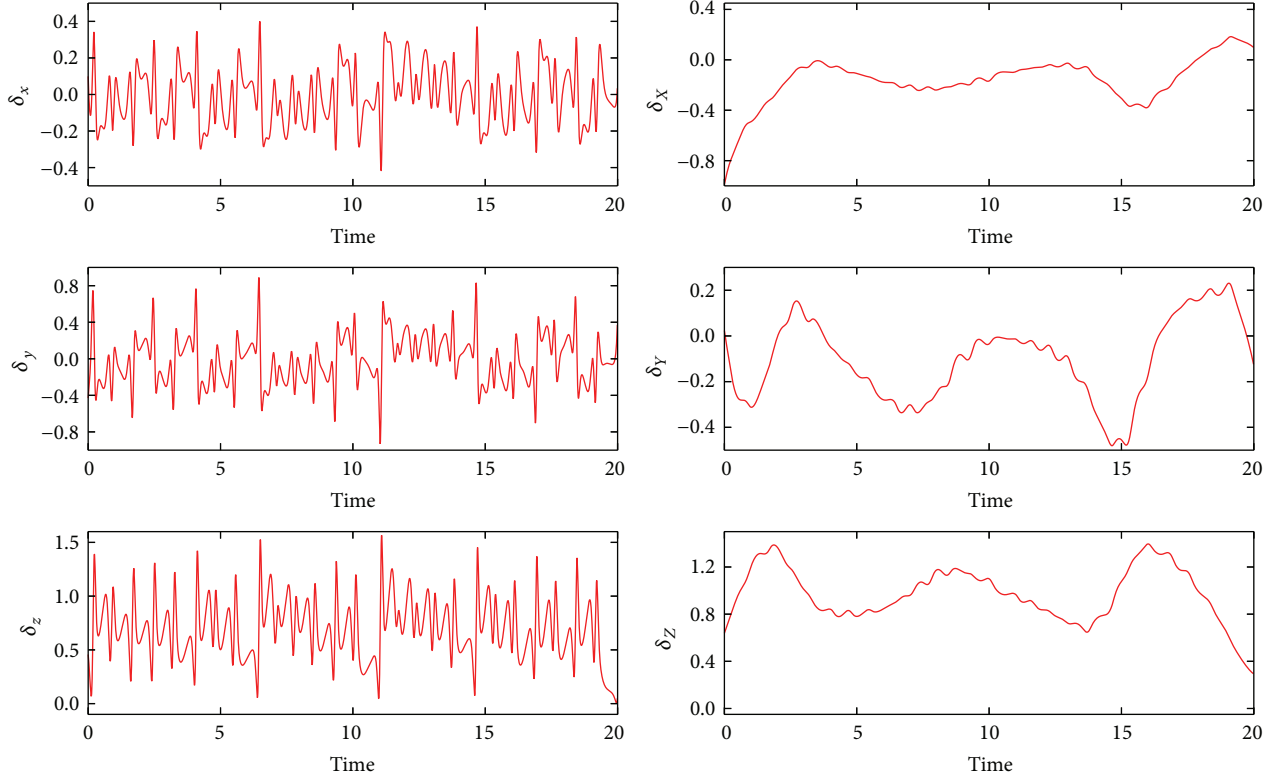


FIGURE 11: Difference between variables that correspond to the original trajectory and pseudorbit for $c^0 = 0.01$.

is based on inverting the so-called “shadowing operator” that requires calculating the Lyapunov characteristic (covariant) vectors. However, the computational cost needed for the Lyapunov eigenvector decomposition is high when the dynamical system has many positive Lyapunov exponents. To illustrate this approach, suppose that the sensitivity analysis of system (A.5) aims to estimate the following sensitivity coefficient: $S_\alpha = \partial x / \partial \alpha$. Let us introduce the following transform: $x'(x) = x + \delta x(x)$, where x and x' are true trajectory and pseudorbit, respectively. The orbit x' is generated due to the variation in parameter α . It can be shown [36] that $\delta f(x) = A \delta x(x)$, where

$$A = \left[-\left(\frac{\partial f}{\partial x} \right) + \left(\frac{d}{dt} \right) \right] \quad (\text{A.14})$$

is a “shadow” operator. Thus, to find a pseudotrajectory, we need to solve the equation $\delta x = A^{-1} \delta f$; that is, we must numerically invert the operator A for a given δf . To solve this problem, functions δx and δf are decomposed into their constituent Lyapunov covariant vectors $v_1(x), \dots, v_n(x)$:

$$\delta x(x) = \sum_{i=1}^n \psi_i(x) v_i(x), \quad (\text{A.15a})$$

$$\delta f(x) = \sum_{i=1}^n \varphi_i(x) v_i(x). \quad (\text{A.15b})$$

Note that each $v_i(x)$ satisfies the following equation:

$$\frac{dv_i(x(t))}{dt} = \frac{\partial f}{\partial x} v_i(x(t)) - \lambda_i v_i(x(t)), \quad (\text{A.16})$$

where $\lambda_1, \dots, \lambda_n$ are the Lyapunov exponents. From (A.14) one can obtain

$$A(\psi_i v_i) = \left[-\psi_i(x) \frac{\partial f}{\partial x} + \frac{d\psi_i(x)}{dt} \right] v_i(x) + \psi_i(x) \frac{dv_i(x)}{dt}. \quad (\text{A.17})$$

Substitution of (A.16) into the last term of (A.17) gives

$$A(\psi_i v_i) = \left[\frac{d\psi_i(x)}{dt} - \lambda_i \psi_i(x) \right] v_i(x). \quad (\text{A.18})$$

From (A.15a) and (A.15b) and (A.18) and the relation $\delta f(x) = A \delta x(x)$, we get

$$\delta f(x) = \sum_{i=1}^n A(\psi_i v_i) = \sum_{i=1}^n \underbrace{\left(\frac{d\psi_i}{dt} - \lambda_i \psi_i \right)}_{\varphi_i} v_i. \quad (\text{A.19})$$

Equation (A.19) gives the following relationship between $\psi_i(x)$ and $\varphi_i(x)$ along the orbit:

$$\frac{d\psi_i(x)}{dt} = \varphi_i(x) + \lambda_i \psi_i(x). \quad (\text{A.20})$$

Thus, we can calculate $\psi_i(x)$ using (A.20) by first decomposing δf as a sum (A.15b), and then the desired δx can be obtained from (A.15a). However, if dynamical system has a zero Lyapunov exponent, $\lambda_i^0 = 0$, then the algorithm described above fails to compute δx [36]. The problem can

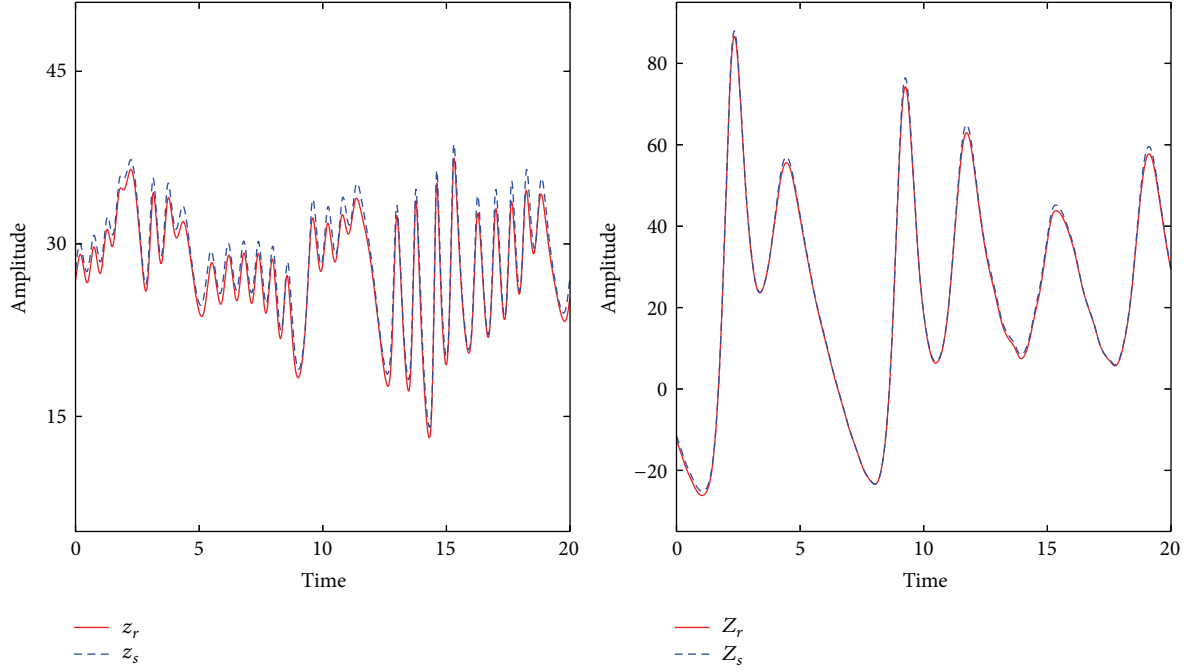


FIGURE 12: Original trajectory (in red) and pseudoorbit (in blue) for the fast z and slow Z variables for $c^0 = 0.8$.

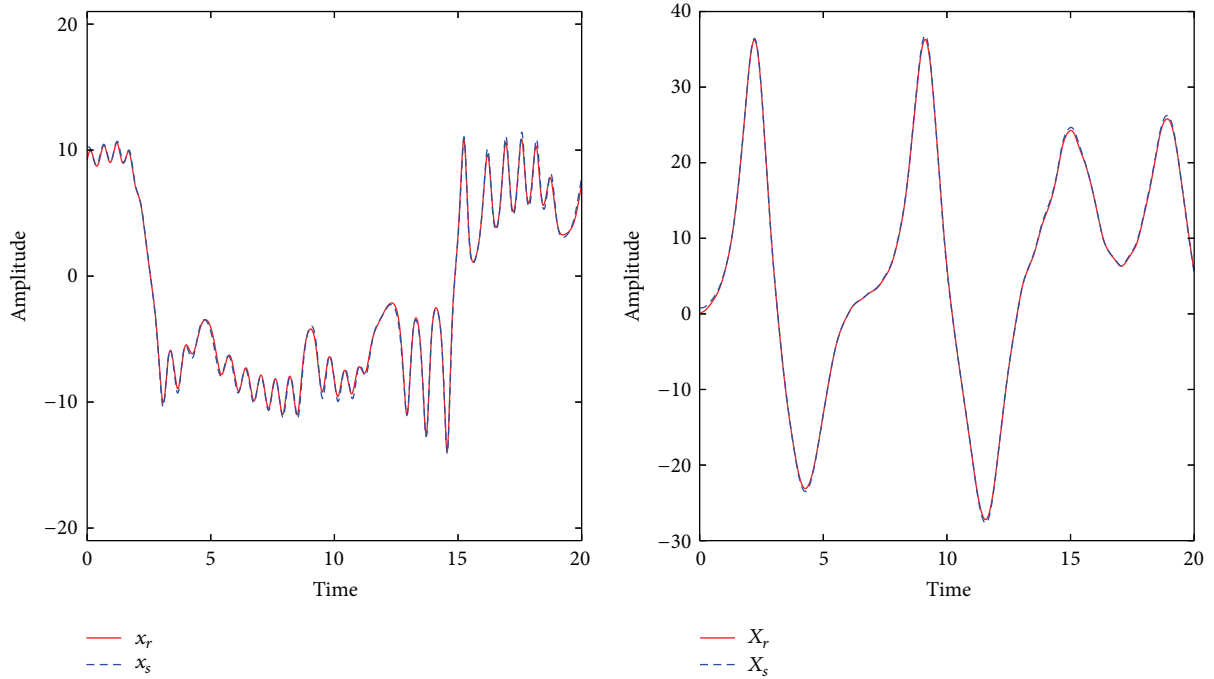


FIGURE 13: Original trajectory (in red) and pseudoorbit (in blue) for fast x and slow X variables for $c^0 = 0.8$.

be resolved by introducing a time-dilation variable μ that satisfies the following equation:

$$\mu + \langle \varphi_i^0 \rangle = 0, \quad (\text{A.21})$$

where

$$\langle \varphi_i^0 \rangle = \lim_{T \rightarrow \infty} \frac{1}{T} [\psi_i^0(x(T)) - \psi_i^0(x(0))]. \quad (\text{A.22})$$

In the presence of the variable μ , the expression for calculating δx takes the following form: $\delta x = A^{-1}(\delta f + \mu f)$. The supplement μf affects (A.20) only for $\lambda_i^0 = 0$:

$$\frac{d\psi_i^0(x)}{dt} = \varphi_i^0(x) + \mu. \quad (\text{A.23})$$

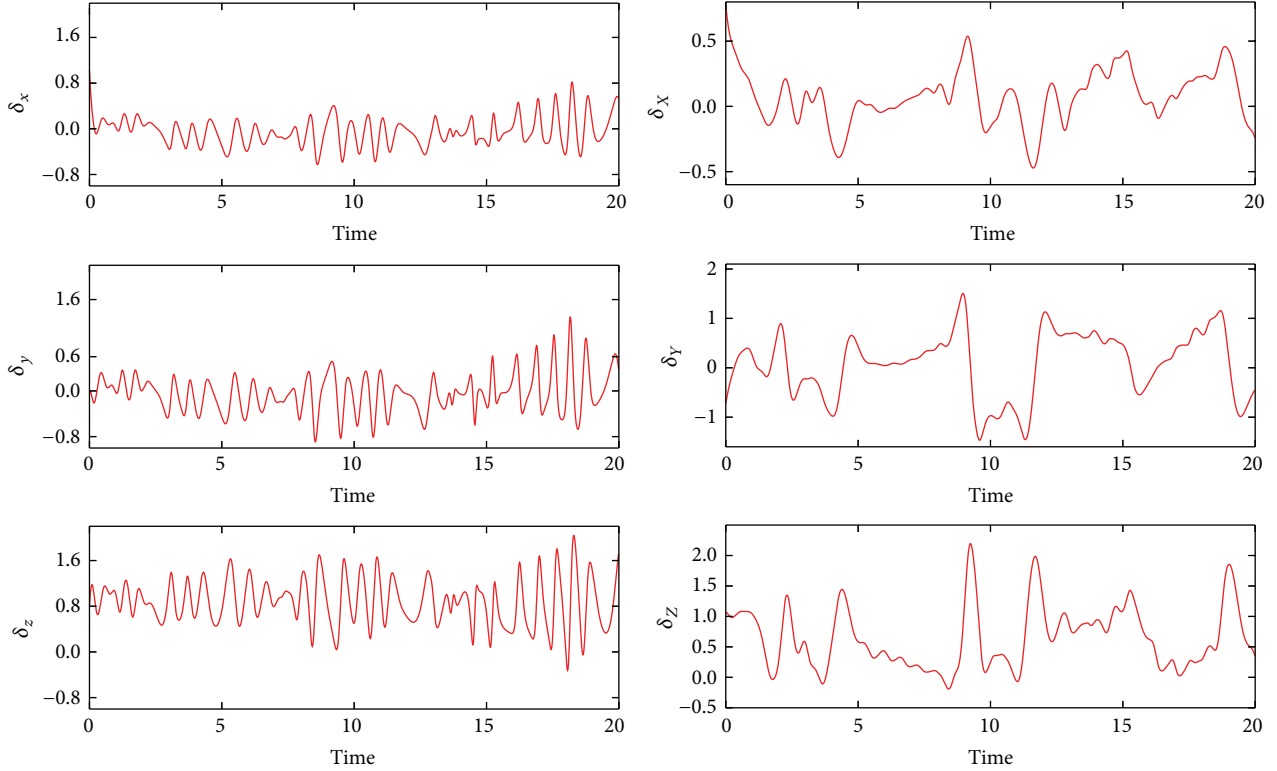


FIGURE 14: Difference between variables that correspond to the original trajectory and pseudoorbit for $c^0 = 0.8$.

In general, the procedure for solving a sensitivity analysis problem represents the following set of steps.

- (1) Obtain initial conditions of the system attractor by integrating the model equations (A.5) from $t_D = -20$ to $t_0 = 0$, starting from random initial conditions.
- (2) Solve (A.5) to obtain a trajectory $x(t)$, $t \in [0, 20]$, on the attractor.
- (3) Compute the Lyapunov exponents λ_i and the Lyapunov covariant vectors $v_i(x(t))$, $i = 1, \dots, n$.
- (4) Define $\delta f = (\partial f / \partial \alpha) \delta \alpha$ and execute the Lyapunov spectrum decomposition of δf along the trajectory $x(t)$ to obtain $\varphi_i(x)$, $i = 1, \dots, n$.
- (5) Calculate the time-dilation variable μ using (A.21).
- (6) Compute δx along the trajectory $x(t)$.
- (7) Estimate the sensitivity $S_\alpha = \partial x / \partial \alpha$ by averaging over the time interval $t \in [0, 20]$.

Conflict of Interests

The authors declare that there is no conflict of interests regarding the publication of this paper.

References

- [1] F. Rawlins, S. P. Ballard, K. J. Bovis et al., “The met office global four-dimensional variational data assimilation scheme,” *Quarterly Journal of the Royal Meteorological Society*, vol. 133, no. 623, pp. 347–362, 2007.
- [2] K. Puri, G. Dietachmayer, P. Steinle et al., “Implementation of the initial ACCESS numerical weather prediction system,” *Australian Meteorological and Oceanographic Journal*, vol. 63, no. 2, pp. 265–284, 2013.
- [3] R. Daley, *Atmospheric Data Analysis*, Cambridge University Press, New York, NY, USA, 1991.
- [4] E. Kalnay, *Atmospheric Modeling, Data Assimilation and Predictability*, Cambridge University Press, New York, NY, USA, 2003.
- [5] F. Rabier, “Overview of global data assimilation developments in numerical weather-prediction centres,” *Quarterly Journal of the Royal Meteorological Society*, vol. 131, no. 613, pp. 3215–3233, 2005.
- [6] I. M. Navon, “Data assimilation for numerical weather prediction: a review,” in *Data Assimilation for Atmospheric, Oceanic and Hydrologic Applications*, S. K. Park and L. Xu, Eds., Springer, New York, NY, USA, 2009.
- [7] D. G. Cacuci, I. M. Navon, and M. Ionescu-Bujor, *Computational Methods for Data Evaluation and Assimilation*, CRC Press, Boca Raton, Fla, USA, 2013.
- [8] I. Sasaki, “An objective analysis based on variational method,” *Journal of the Meteorological Society of Japan*, vol. 36, no. 3, pp. 29–30, 1958.
- [9] J. L. Lions, *Optimal Control of Systems Governed by Partial Differential Equations*, Springer, Berlin, Germany, 1971.
- [10] V. V. Penenko and N. N. Obraztsov, “Variational method for assimilation of meteorological fields,” *Meteorology and Hydrology*, no. 11, pp. 3–16, 1976.

- [11] F.-X. Le Dimet, "Une application des méthodes de contrôle optimal à l'analyse variationnelle," Rapport Scientifique LAMP 63170, Université Blaise Pascal, Clermont-Ferrand, France, 1981.
- [12] O. Talagrand, "A study of the dynamics of four-dimensional data assimilation," *Tellus*, vol. 33, no. 1, pp. 43–60, 1981.
- [13] D. G. Cacuci, "Sensitivity theory for nonlinear systems. I. Nonlinear functional analysis approach," *Journal of Mathematical Physics*, vol. 22, no. 12, pp. 2794–2802, 1981.
- [14] D. G. Cacuci, "Sensitivity theory for nonlinear systems. II. Extensions to additional classes of responses," *Journal of Mathematical Physics*, vol. 22, no. 12, pp. 2803–2812, 1981.
- [15] J. M. Lewis and J. C. Derber, "The use of adjoint equations to solve a variational adjustment problem with advective constraints," *Tellus A*, vol. 37, no. 4, pp. 309–322, 1985.
- [16] F.-X. Le Dimet and O. Talagrand, "Variational algorithms for analysis and assimilation of meteorological observations: theoretical aspects," *Tellus Series A*, vol. 38, no. 2, pp. 97–110, 1986.
- [17] O. Talagrand and P. Courtier, "Variational assimilation of meteorological observations with the adjoint vorticity equation. Part I. Theory," *Quarterly Journal of the Royal Meteorological Society*, vol. 113, pp. 1311–1328, 1987.
- [18] P. Courtier and O. Talagrand, "Variational assimilation of meteorological observations with the adjoint vorticity equation. II: numerical results," *Quarterly Journal of the Royal Meteorological Society*, vol. 113, no. 478, pp. 1329–1347, 1987.
- [19] F.-X. le Dimet, H.-E. Ngodock, B. Luong, and J. Verron, "Sensitivity analysis in variational data assimilation," *Journal of the Meteorological Society of Japan*, vol. 75, no. 1, pp. 245–255, 1997.
- [20] N. L. Baker and R. Daley, "Observation and background adjoint sensitivity in the adaptive observation-targeting problem," *Quarterly Journal of the Royal Meteorological Society*, vol. 126, no. 565, pp. 1431–1454, 2000.
- [21] G. Hello and F. Bouttier, "Using adjoint sensitivity as a local structure function in variational data assimilation," *Nonlinear Processes in Geophysics*, vol. 8, no. 6, pp. 347–355, 2001.
- [22] R. H. Langland and N. L. Baker, "Estimation of observation impact using the NRL atmospheric variational data assimilation adjoint system," *Tellus Series A*, vol. 56, no. 3, pp. 189–203, 2004.
- [23] R. M. Errico, "Interpretations of an adjoint-derived observational impact measure," *Tellus, Series A: Dynamic Meteorology and Oceanography*, vol. 59, no. 2, pp. 273–276, 2007.
- [24] R. Gelaro, Y. Zhu, and R. M. Errico, "Examination of various-order adjoint-based approximations of observation impact," *Meteorologische Zeitschrift*, vol. 16, no. 6, pp. 685–692, 2007.
- [25] D. N. Daescu, "On the sensitivity equations of four-dimensional variational (4D-Var) data assimilation," *Monthly Weather Review*, vol. 136, no. 8, pp. 3050–3065, 2008.
- [26] Y. Trémolet, "Computation of observation sensitivity and observation impact in incremental variational data assimilation," *Tellus, Series A: Dynamic Meteorology and Oceanography*, vol. 60, no. 5, pp. 964–978, 2008.
- [27] D. N. Daescu and R. Todling, "Adjoint estimation of the variation in model functional output due to the assimilation of data," *Monthly Weather Review*, vol. 137, no. 5, pp. 1705–1716, 2009.
- [28] R. Gelaro and Y. Zhu, "Examination of observation impacts derived from observing system experiments (OSEs) and adjoint models," *Tellus, Series A: Dynamic Meteorology and Oceanography*, vol. 61, no. 2, pp. 179–193, 2009.
- [29] D. N. Daescu and I. M. Navon, "Sensitivity analysis in nonlinear data assimilation: theoretical aspects and applications," in *Advances Numerical Methods for Complex Environmental Models: Needs and Availability*, I. Farago and Z. Zlatev, Eds., pp. 276–300, Benham Science Publishers, 2013.
- [30] D. G. Cacuci, *Sensitivity and Uncertainty Analysis, Volume I: Theory*, CRC, Boca Raton, Fla, USA, 2003.
- [31] D. G. Cacuci, M. Ionescu-Bujor, and I. M. Navon, *Sensitivity and Uncertainty Analysis*, CRC, Boca Raton, Fla, USA, 2005.
- [32] E. N. Lorenz, "Deterministic nonperiodic flow," *Journal of the Atmospheric Sciences*, vol. 20, no. 2, pp. 130–141, 1963.
- [33] M. Peña and E. Kalnay, "Separating fast and slow modes in coupled chaotic systems," *Nonlinear Processes in Geophysics*, vol. 11, no. 3, pp. 319–327, 2004.
- [34] L. Siqueira and B. Kirtman, "Predictability of a low-order interactive ensemble," *Nonlinear Processes in Geophysics*, vol. 19, no. 2, pp. 273–282, 2012.
- [35] D. J. Lea, M. R. Allen, and T. W. N. Haine, "Sensitivity analysis of the climate of a chaotic system," *Tellus*, vol. 52, no. 5, pp. 523–532, 2000.
- [36] Q. Wang, "Forward and adjoint sensitivity computation of chaotic dynamical systems," *Journal of Computational Physics*, vol. 235, no. 15, pp. 1–13, 2013.
- [37] Q. Wang, R. Hu, and P. Blonigan, "Least squares shadowing sensitivity analysis of chaotic limit cycle oscillations," *Journal of Computational Physics*, vol. 267, pp. 210–224, 2014.
- [38] S. Y. Pilyugin, *Shadowing in Dynamical Systems*, vol. 1706 of *Lecture Notes in Mathematics*, Springer, Berlin, Germany, 1999.
- [39] K. J. Palmer, *Shadowing in Dynamical Systems. Theory and Applications*, Kluwer Academic, Dordrecht, The Netherlands, 2000.
- [40] M. G. Rosenblum, A. S. Pikovsky, and J. Kurths, "Phase synchronization of chaotic oscillators," *Physical Review Letters*, vol. 76, no. 11, pp. 1804–1807, 1996.
- [41] F. Christiansen, G. Paladin, and H. H. Rugh, "Determination of correlation spectra in chaotic systems," *Physical Review Letters*, vol. 65, no. 17, pp. 2087–2090, 1990.
- [42] C. Liverani, "Decay of correlations," *Annals of Mathematics*, vol. 142, no. 2, pp. 239–301, 1995.
- [43] S. Panchev and T. Spassova, "Simple general atmospheric circulation and climate models with memory," *Advances in Atmospheric Sciences*, vol. 22, no. 5, pp. 765–769, 2005.
- [44] E. Rosenwasser and R. Yusupov, *Sensitivity of Automatic Control Systems*, CRC Press, Boca Raton, Fla, USA, 2000.
- [45] I. M. Navon, X. Zou, J. Derber, and J. Sela, "Variational data assimilation with an adiabatic version of the NMC spectral model," *Monthly Weather Review*, vol. 120, no. 7, pp. 1433–1446, 1992.
- [46] D. V. Anosov, "On class of invariant sets of smooth dynamical systems," in *Proceedings of the 5th International Conference on Nonlinear Oscillations*, vol. 2, pp. 39–45, Kiev, Ukraine, 1975.
- [47] R. Bowen, *Equilibrium States and the Ergodic Theory of Anosov Diffeomorphisms*, vol. 470 of *Lecture Notes in Mathematics*, Springer, Berlin, Germany, 1975.
- [48] A. Koropecki and E. R. Pujals, "Some consequences of the shadowing property in low dimensions," *Ergodic Theory and Dynamical Systems*, vol. 34, no. 4, pp. 1273–1309, 2014.
- [49] D. Richeson and J. Wiseman, "Symbolic dynamics for nonhyperbolic systems," *Proceedings of the American Mathematical Society*, vol. 138, no. 12, pp. 4373–4385, 2010.

- [50] A. A. Petrov and S. Y. Pilyugin, “Shadowing near nonhyperbolic fixed points,” *Discrete and Continuous Dynamical Systems*, vol. 34, no. 9, pp. 3761–3772, 2013.
- [51] S. Y. Pilyugin, *Spaces of Dynamical Systems*, De Gruyter, Berlin, Germany, 2012.
- [52] A. Katok and B. Hasselblatt, *Introduction to the Modern Theory of Dynamical Systems*, vol. 54 of *Encyclopedia of Mathematics and its Applications*, Cambridge University Press, New York, NY, USA, 1995.
- [53] D. V. Anosov, *Geodesic Flows on Closed Riemann Manifolds with Negative Curvature*, vol. 90 of *Proceedings of the Steklov Institute of Mathematics*, 1967.
- [54] S. P. Boyd and L. Vandenberghe, *Convex Optimization*, Cambridge University Press, Cambridge, UK, 2004.
- [55] Q. Wang, “Convergence of the least squares shadowing method for computing derivative of ergodic averages,” *SIAM Journal on Numerical Analysis*, vol. 52, no. 1, pp. 156–170, 2014.

Research Article

An Assessment of Data from the Advanced Technology Microwave Sounder at the Met Office

Amy Doherty, Nigel Atkinson, William Bell, and Andrew Smith

Met Office, Fitzroy Road, Exeter EX1 3PB, UK

Correspondence should be addressed to Amy Doherty; amy.doherty@metoffice.gov.uk

Received 19 December 2014; Revised 4 February 2015; Accepted 18 February 2015

Academic Editor: Yuanfu Xie

Copyright © 2015 Amy Doherty et al. This is an open access article distributed under the Creative Commons Attribution License, which permits unrestricted use, distribution, and reproduction in any medium, provided the original work is properly cited.

An appraisal of the Advanced Technology Microwave Sounder (ATMS) for use in numerical weather prediction (NWP) is presented, including an assessment of the data quality, the impact on Met Office global forecasts in preoperational trials, and a summary of performance over a period of 17 months operational use. After remapping, the noise performance (NE Δ T) of the tropospheric temperature sounding channels is evaluated to be approximately 0.1 K, comparing favourably with AMSU-A. However, the noise is not random, differences between observations and simulations based on short-range forecast fields show a spurious striping effect, due to 1/f noise in the receiver. The amplitude of this signal is several tenths of a Kelvin, potentially a concern for NWP applications. In preoperational tests, adding ATMS data to a full Met Office system already exploiting data from four microwave sounders improves southern hemisphere mean sea level pressure forecasts in the 2- to 5-day range by 1-2%. In operational use, where data from five other microwave sounders is assimilated, forecast impact is typically between -0.05 and -0.1 J/kg (3.4% of total mean impact per day over the period 1 April to 31 July 2013). This suggests benefits beyond redundancy, associated with reducing already small analysis errors.

1. Introduction

The Polar Operational Environmental Satellite (POES) series of satellites has provided key data for Numerical Weather Prediction (NWP) and climate studies since 1978. Over the next decade, continuity of these important observations will be provided by instruments of the US Joint Polar Satellite System (JPSS) [1]. The first satellite in the series was launched on 28 October 2011 and is now known as the Suomi National Polar-orbiting Partnership (Suomi-NPP).

Microwave temperature sounding data for NWP and climate applications was originally provided by the Microwave Sounding Unit (MSU) carried onboard satellites launched during the period 1978–1994 and more recently by the Advanced Microwave Sounding Unit (AMSU) carried onboard satellites launched between 1998 and 2012 [2]. One further AMSU-A instrument will be launched as part of EUMETSAT's Metop series (Metop-C, currently scheduled for 2018), with humidity sounding data provided by the Microwave Humidity Sounder (MHS). JPSS uses a new microwave sounding instrument, the Advanced Technology

Microwave Sounder (ATMS) [3], a cross-track scanning microwave radiometer similar to AMSU-A and MHS combined.

Before operational assimilation of new data by NWP centres it is standard practice to assess data quality with respect to NWP model fields and other similar instruments and to evaluate the data through data assimilation experiments. Recent studies have shown the value of using NWP fields to assess data quality from microwave sounding instruments ([4, 5]) and a detailed assessment of ATMS relative to the ECMWF NWP model has been produced by [6]. This paper presents a similar analysis with respect to the Met Office NWP model. Also reported here are an in depth investigation of the spurious striping signal seen in the innovation maps, the preoperational trial results, and a summary of the operational performance of ATMS in the Met Office system from April 2013 to November 2014.

Section 2 of this report introduces the ATMS instrument and key aspects of the Met Office data assimilation scheme. Section 3 describes findings from a comparison of ATMS data with similar AMSU/MHS data and with NWP model fields

and also presents the findings of a study into the characteristics of the striping signal. Section 4 summarises the results of two assimilation experiments in which ATMS data are added to a full Met Office assimilation and forecasting system. Section 5 provides further evidence of the efficacy of ATMS in the Met Office system when it is assimilated operationally over a period of 17 months. Section 6 presents a summary and conclusions.

2. Data and Assimilation System

2.1. Instrument Characteristics. ATMS is a cross-track scanning microwave radiometer similar to the AMSU/MHS instruments flown on the National Oceanic and Atmospheric Administration's NOAA-15 to -19 satellites and European Meteorological Satellite Agency's (EUMETSAT) Metop-A and -B satellites. ATMS has 22 channels: 5 sensitive to the surface in clear conditions, or to water vapour, rain, and cloud when conditions are not clear (at 23, 31, 50, 51, and 89 GHz, channels 1, 2, 3, 4, and 16, resp.), 11 temperature sounding channels around the 50–60 GHz oxygen band (channels 5–15), and 6 moisture sounding channels around the 183 GHz water vapour band (channels 17–22) [3].

Channels 3–15 all share the same feedhorn, local oscillator, and receiver front end, unlike AMSU-A, which has a separate LO/mixer for each of channels 3–8 with a shared LO/mixer for channels 9–14.

ATMS has 96 footprints per scan line, each separated by 1.11° . The footprint size varies with channel, the 23 and 31 GHz channels have a 5.2° -beam width, the temperature sounding channels (50–60 GHz) have a 2.2° -beam width, and the moisture sounding channels (~183 GHz) have a 1.1° -beam width. The lower frequency channels (below 100 GHz) are, therefore, highly oversampled.

The oversampling of the 50–60 GHz temperature sounding channels is accompanied by shorter integration times per footprint and results in high radiometric noise values, relative to equivalent AMSU channels. In current operational data assimilation systems, errors in the short range forecast fields, expressed as observation equivalent brightness temperatures, are typically in the range 0.05–0.10 K for mid-tropospheric temperature sounding channels. This places very demanding requirements on the performance of microwave sounding instruments, in terms of radiometric performance [7] and systematic biases in the data. Preprocessing of the ATMS data is, therefore, required to reduce the noise to acceptable levels for use in NWP.

2.2. The Met Office Data Assimilation Scheme

2.2.1. Preprocessing. The near-real-time global data stream for ATMS is generated by NOAA's Interface Data Processing Segment (IDPS), and the data are distributed to European users by EUMETSAT. The data used in this work are the antenna temperatures, which are derived from the Temperature Data Record (TDR) product.

Using the ATOVS and AVHRR Preprocessing Package (AAPP), the ATMS data are remapped and spatially averaged

to improve the noise performance and replicate the AMSU footprint size [8]. The data assessed here have been manipulated to a beam width of 3.3° (4.8° for 23 and 31 GHz, channels 1 and 2) using Fourier techniques. They are resampled to give one field of view in three (i.e., 32 fields of view) across the scan and are also resampled at a rate of 1 in 3 in the along-track direction. All the data used in this study have been remapped in this manner.

Although satellite radiances are assimilated directly at the Met Office, a one-dimensional variational analysis (1D-Var) is performed first to act as a quality control filter and to allow the derivation of additional parameters which are used subsequently [9]. The 1D-Var performs a variational retrieval of atmospheric state (T, q) and surface variables (T_{skin}) at the location of the observation with background (prior) information from the previous T + 6 hour forecast interpolated to the location of the observation. Background errors used in 1D-Var are represented by an error covariance matrix consistent with the full 4D-Var B-matrix and observation errors are more aggressive, with values typically ~75% of those used in 4D-Var.

Quality control is applied using the following:

- (1) a gross error check on the brightness temperatures;
- (2) a convergence check in 1D-Var;
- (3) a check on the background profile;
- (4) O minus B check on channels used for assimilation;
- (5) RTTOV error checking on the profile during minimisation;
- (6) O minus R check on channels used for assimilation;
- (7) cloud and rain flagging;
- (8) rejection of surface sensitive channels over land.

2.2.2. Assimilation System. The Met Office variational data assimilation system is based on incremental 4D-Var [10, 11]. The nonlinear forecast model currently has a 25 km resolution in midlatitudes; for the data assimilation experiments described here a reduced resolution of 40 km was used. The model has 70 levels from the surface to 80 km.

The operational analysis makes use of data from a range of conventional observations, including surface, sonde, and aircraft observations as well as data from satellite instruments including five ATOVS instruments (from NOAA-15, NOAA-18, NOAA-19, Metop-A, and Metop-B), advanced infrared sounder data from the Atmospheric Infrared Sounder (AIRS) and the Infrared Atmospheric Sounding Interferometer (IASI), global positioning system (GPS) radio occultation (GPSRO) data, ground based GPS, atmospheric motion vectors, geostationary radiances, and scatterometer data. The data assimilation experiments make use of a slightly earlier operational system and do not include ATOVS data from Metop-B.

NWP model fields are mapped to brightness temperatures using radiative transfer modelling; these are routinely compared with the radiance measurements. Generally, differences will be nonzero and will comprise large-scale, slowly-varying, systematic biases, small scale day-to-day features

resulting from local errors in the forecast model fields, and a random component from the instrument noise. In NWP assimilation systems it is crucial that the stationary or quasi-stationary biases (which may originate from forecast model, the radiative transfer model, or the measurement) are eliminated prior to assimilation, leaving only the errors in the model fields to be corrected. This process is termed bias correction and can be performed within the assimilation process itself (variational bias correction [12]) or can be a static correction which is updated when required.

The Met Office currently uses a static bias correction scheme based on [13] which corrects for cross-track and air mass related biases as well as instrument calibration errors, represented by global offsets.

As mentioned in the introduction, a detailed assessment of ATMS data has been carried out independently relative to the ECMWF assimilation system [6]. There are some key differences between the Met Office system and that at ECMWF.

- (1) The Met Office uses AAPP to remap the data to lower resolution during the preprocessing stage.
- (2) Vertical resolution: the work carried out in this paper used a forecast model on 70 vertical levels, while the work of Bormann et al. [6] used a model with 91 levels.
- (3) RTTOV version 9 was used in the Met Office work and version 10 in the ECMWF work.
- (4) Static bias correction is currently used at the Met Office and variational bias correction is used at ECMWF.

3. Data Quality

3.1. Comparison with the NWP Model. During the data assimilation process, model equivalents of the observed brightness temperatures are computed using a fast radiative transfer (RT) model (RTTOV version 9, [14]). Model fields from short range forecasts are interpolated in space and time to the location of the observations using forecast fields at $T + 3$, $+6$, and $+9$ hours launched from a previous analysis. Simulated or background brightness temperatures are then generated using the RT model. Differences between observations and simulations, also known as innovations or first guess departures, can then be used to diagnose errors in the observations.

For the ATMS temperature sounding channels (50–60 GHz, channels 5–15), the innovations are generally a few tenths of a Kelvin. For the humidity sounding channels (~183 GHz, channels 18–22) the innovations are usually larger, at 1–2 K (1σ). Window channel innovations are larger still at several Kelvin.

Figure 1 shows uncorrected and corrected innovation plots (O-B and C-B) for the key ATMS tropospheric temperature sounding channels 7–10 on 7 November 2013 at QU00. Large amplitude latitudinal and cross-track biases are clearly visible in the fields before bias correction (left hand column) and largely absent in those after bias correction

(right hand column) indicating that the bias correction scheme is effective. The residual biases in the corrected data are less than 0.1 K over much of the globe. Also clearly visible in the corrected fields, however, is an unphysical horizontal striping pattern, which is large enough (up to 0.2 K) to potentially degrade the influence of ATMS data on analyses and forecasts. The regular pattern of white lines (missing data) is a consequence of the fact that the spatial filtering is performed on blocks of duration 320 s, and the edge scans are discarded. A latitudinal dependence of the cross-track biases due to the nonzero emissivity of the reflector is not corrected for in the current bias correction scheme; plans to address this in the future may improve the bias correction further.

3.2. Striping. An investigation of the striping was carried out to quantify the variability associated with the signal.

The calibrated antenna temperatures were obtained from the TDRs using the AAPP for a case study over the UK on 13 August 2012 01:43 to 01:54. Coverage is shown in Figure 2. The data were received by direct broadcast.

The atmospheric signal was removed from the case study data by taking the difference between the raw measured brightness temperatures and those obtained through spatial filtering to remove the fine structure. To generate the spatially filtered scene, a fast Fourier transform method described in [8] was used to remap all channels to the beam width of channels 1 and 2. A beam width of 5.2° corresponds to a distance of ~80 km on the ground; over this distance there should be little or no striping signal as the largest correlations occur on a timescale of less than one scan (~17 km; see Figure 6), while the calibration process will remove any striping that occurs on longer timescales than 7 scans (~120 km). A difference between latitudinal and longitudinal scene variations is not expected over an 80 km distance. The three fields of view (FOV) at the edge of each scan are discarded as these may be contaminated by edge effects, leaving 90 FOVs across each scan. For channels 7–15, which are not sensitive to the surface, the resulting signal is dominated by instrument noise.

The along-scan and along-track variabilities were compared by looking at the difference scene over a 90×90 FOV region. The along-scan variability was obtained by averaging the 90 along-track spots and vice versa. These quantities are shown in Figure 3 for channels 7–11 and Figure 4 for channels 12–15. They show that for channels 7–13 the along-track variabilities (left hand plots) are a factor 2–3 larger than the cross-track variabilities (right hand plots). Some interchannel correlations are apparent, for example, the positive spike at scan 36 in channels 7–9 and the negative spike at line 81 for all channels.

Interchannel correlations were also investigated. Figure 5 shows the correlation coefficient between pairs of brightness temperature difference fields for channels 7–15.

There are significant correlations between the temperature sounding channels, which is consistent with a study using the Desroziers diagnostic [15] and also with [16]. It may be possible to extend this analysis to other channels by choosing a suitable clear-sky sea region.

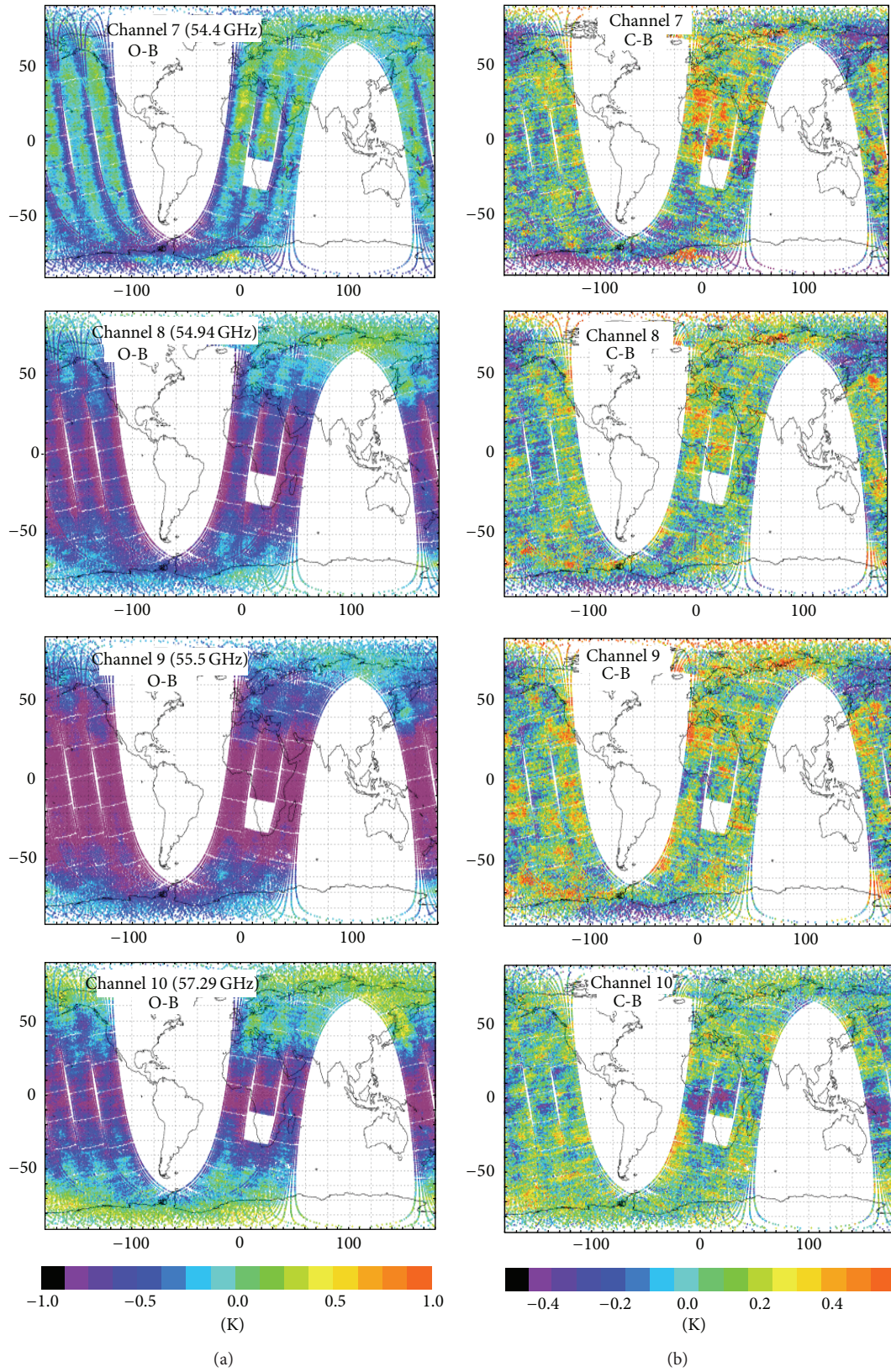


FIGURE 1: ATMS channels 7–10, difference between observations, and model background in the Met Office system at 0Z on 7 November 2013. LHS: uncorrected and RHS: corrected.

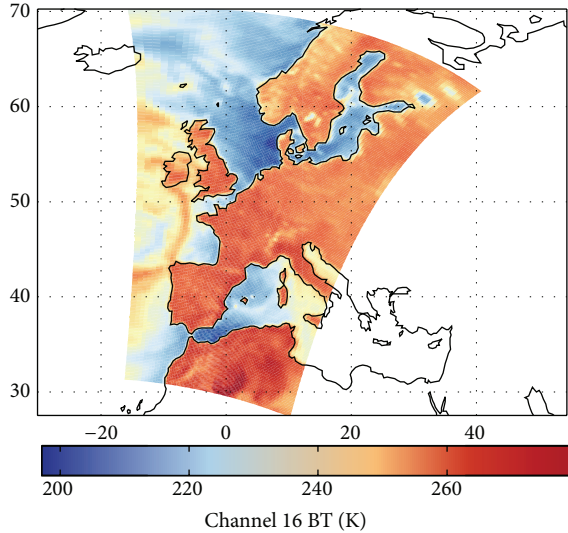


FIGURE 2: ATMS channel 16, 20120813 01:43 to 01:54.

To examine the correlations between the striping signal and calibration counts the earth scan was divided into groups of 4 pixels and each group was averaged to create a time series; the cold space counts and warm counts were also averaged. Each group was then selected in turn and the correlation coefficient between it and (i) all groups in the earth scan, (ii) space counts, (iii) warm counts, and (iv) all groups in the next earth scan were computed. The results for the four central groups for channel 7 are shown in Figure 6. This plot (and those for other channels not shown) suggests that for the lower atmospheric sounding channels there are correlations between neighbouring earth views and the calibration views, but the correlations are only significant over a time period smaller than one scan. The moisture and window channels do not show clear correlations, perhaps because these channels are inherently noisier.

This striping study found that

- (1) both calibrated antenna temperatures and earth counts showed the striping signal;
- (2) there is evidence for interchannel correlations in the signal;
- (3) the striping is not calibration noise and cannot be eliminated by changing the calibration view averaging scheme;
- (4) striping introduces spatial and spectral correlations which could be significant for NWP;
- (5) the characteristic timescale of the striping signal is less than one scan period.

The impact of striping on the overall noise is discussed in Section 3.3.

These results are based on a limited sample of data and robustness could be increased by further studies with a larger dataset. The results are borne out, however, by the subsequent discovery that the instrument manufacturers

were aware of a $1/f$ or flicker noise [17] caused by a low noise amplifier present within the ATMS instrument configuration.

The effect of the striping is allowed for within the assimilation by inflating the observation error for the affected ATMS channels.

3.3. NEAT Monitoring for ATMS. The noise equivalent delta temperature (NEAT) is an important quantity for any radiometer and is commonly monitored using the calibration counts for the black body and the cold space view readings (e.g., [18]).

The ATMS Sensor Data Records (SDRs) contain an internal estimate of NEAT: one warm NEAT and one cold NEAT per scan line. This is defined as the standard deviation of the four cold/warm calibration view readings divided by the gain (to convert from counts to K). However, this estimate of NEAT does not account for any noise sources that have a time scale longer than four times the integration time. As shown in the previous section, long-period fluctuations significantly affect the performance of the instrument; therefore, in this section a modified method is described that is suitable for routine monitoring of the NEAT.

For each scan line, i , we compute the difference between the four warm view counts for that line and a reference count consisting of the mean of the warm view counts from the lines $i-3, i-2, i-1, i+1, i+2$, and $i+3$ (note that line i is omitted). Then the NEAT is the standard deviation of these differences, divided by the channel gain. This method ensures that both random noise and longer period fluctuations ($1/f$ noise) are properly accounted for, in a similar way to the operational calibration procedure.

We can also compute an effective NEAT for a 3×3 averaged brightness temperature field; in this case we use lines $i-4, i-3, i-2, i+2, i+3$, and $i+4$ to derive the reference count, to avoid unwanted correlations between the lines under test and the lines used as reference. After subtracting the reference counts for each line, 3×3 averaging of the resulting differences is performed before computing the final standard deviation. The 3×3 NEAT is a useful diagnostic because the spatially filtered brightness temperature field used in the NWP analysis is expected to have similar noise properties to a 3×3 averaged field; both have beamwidths comparable to AMSU-A (except for channels 1-2, for which the AAPP manipulation produces a smaller beamwidth than the 3×3 average and hence a larger NEAT).

The warm-view NEATs are shown in Figure 7, together with the warm-view NEAT from the global SDR files. The effective 3×3 NEAT for the key lower atmospheric temperature sounding channels (50–60 GHz, channels 6–10) is in the range 110–160 mK. This compares favourably with the NEATs for AMSU-A on Metop-A and NOAA-19, which are the range 130–180 mK. The total noise, computed using the method described in this section, is larger than the SDR noise, due to the effect of striping: typically 20% larger for the temperature sounding channels 3–10, but as much as 50% larger for channel 16.

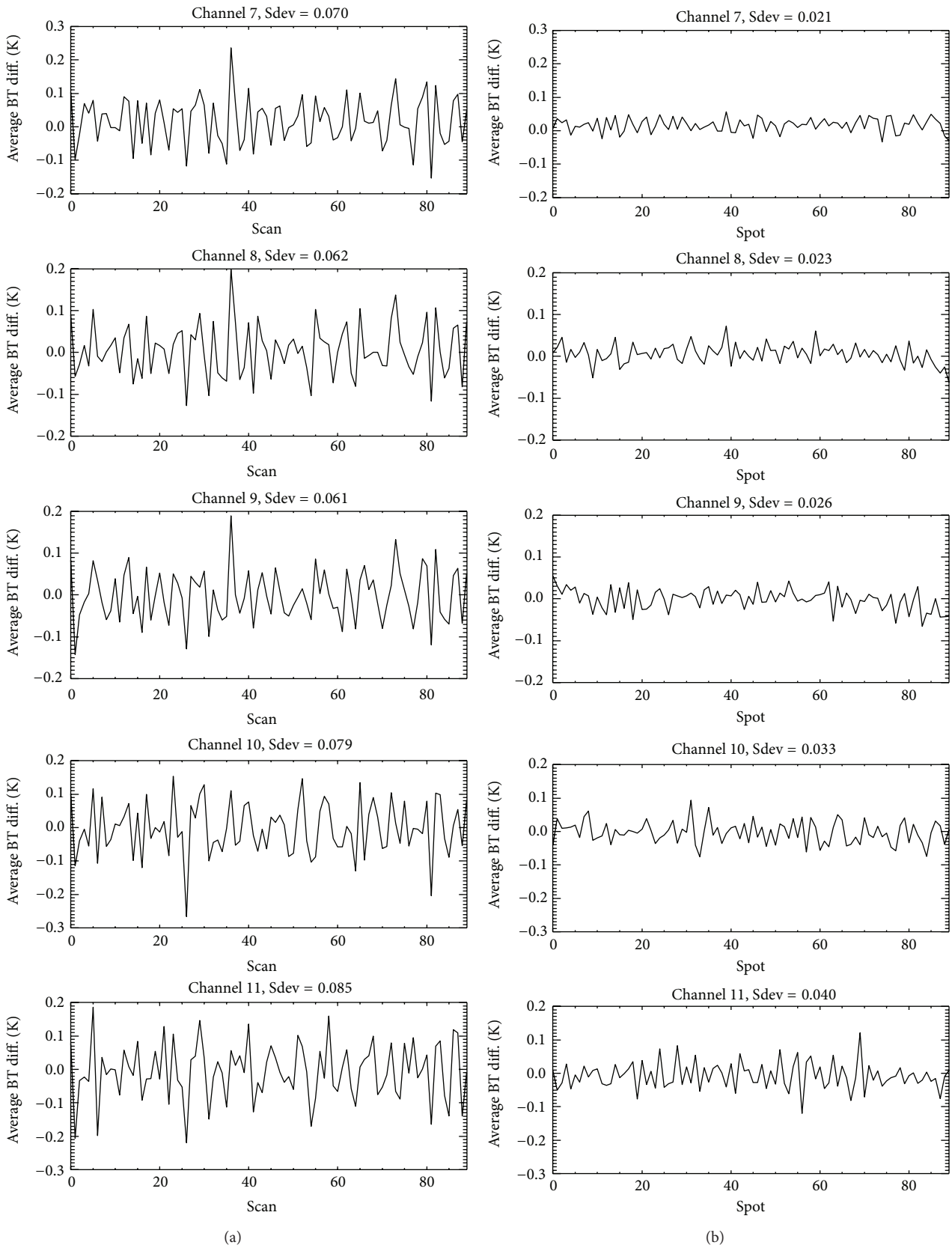


FIGURE 3: Along-track (a) and cross-track (b) variabilities due to instrument noise for channels 7–11.

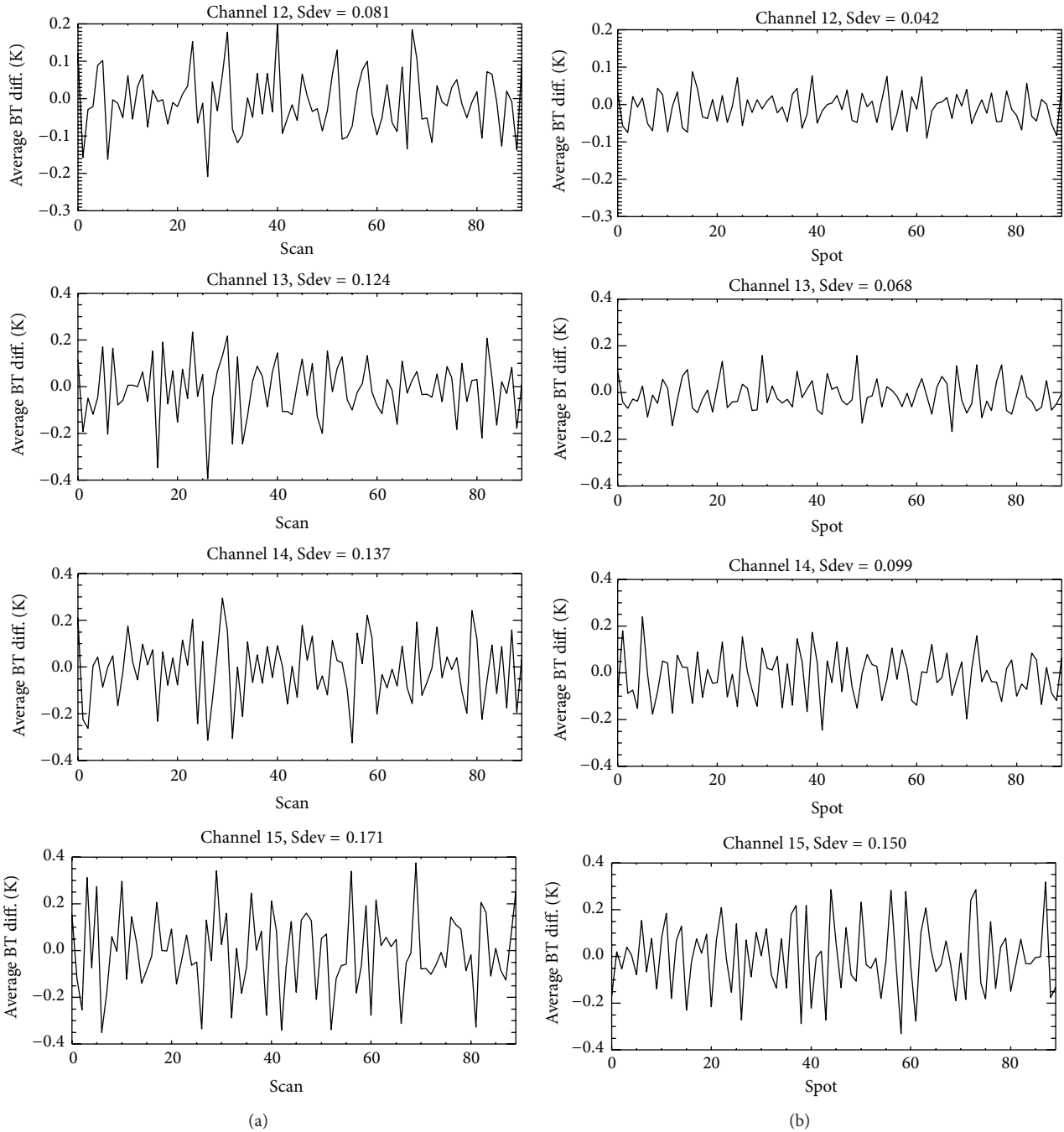


FIGURE 4: Along-track (a) and cross-track (b) variabilities for channels 12–15.

We can also see that the ratio between the single-sample NE Δ T and 3×3 NE Δ T varies between approximately 3 (the value that would be expected if the noise is random) and 2 (for the channels that are most affected by $1/f$ noise). In other words, the presence of striping degrades the ability to reduce noise through spatial averaging.

3.4. Comparison with AMSU/MHS. To assess the data quality from ATMS, it is worthwhile to compare first-guess

departures with those from equivalent sensors, in this case from AMSU/MHS, both before and after bias correction. Comparison of uncorrected data provides information on the raw data quality, whilst for the corrected data it shows the relative magnitude of residual biases in the data to be assimilated.

Comparison of ATMS and AMSU uncorrected and corrected innovations is shown in Figure 8 for data from January-February 2012. Figure 8(a) shows the mean and

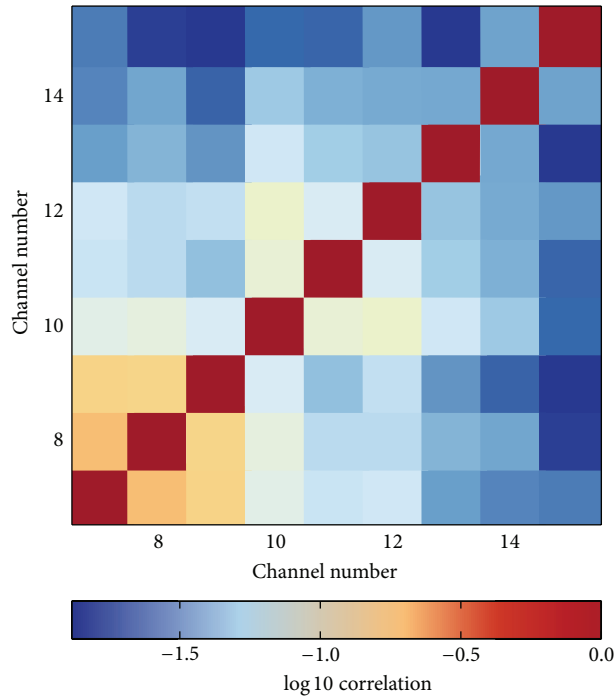


FIGURE 5: ATMS interchannel correlations. Note that all correlation coefficients are positive, so they can be displayed on a logarithmic scale.

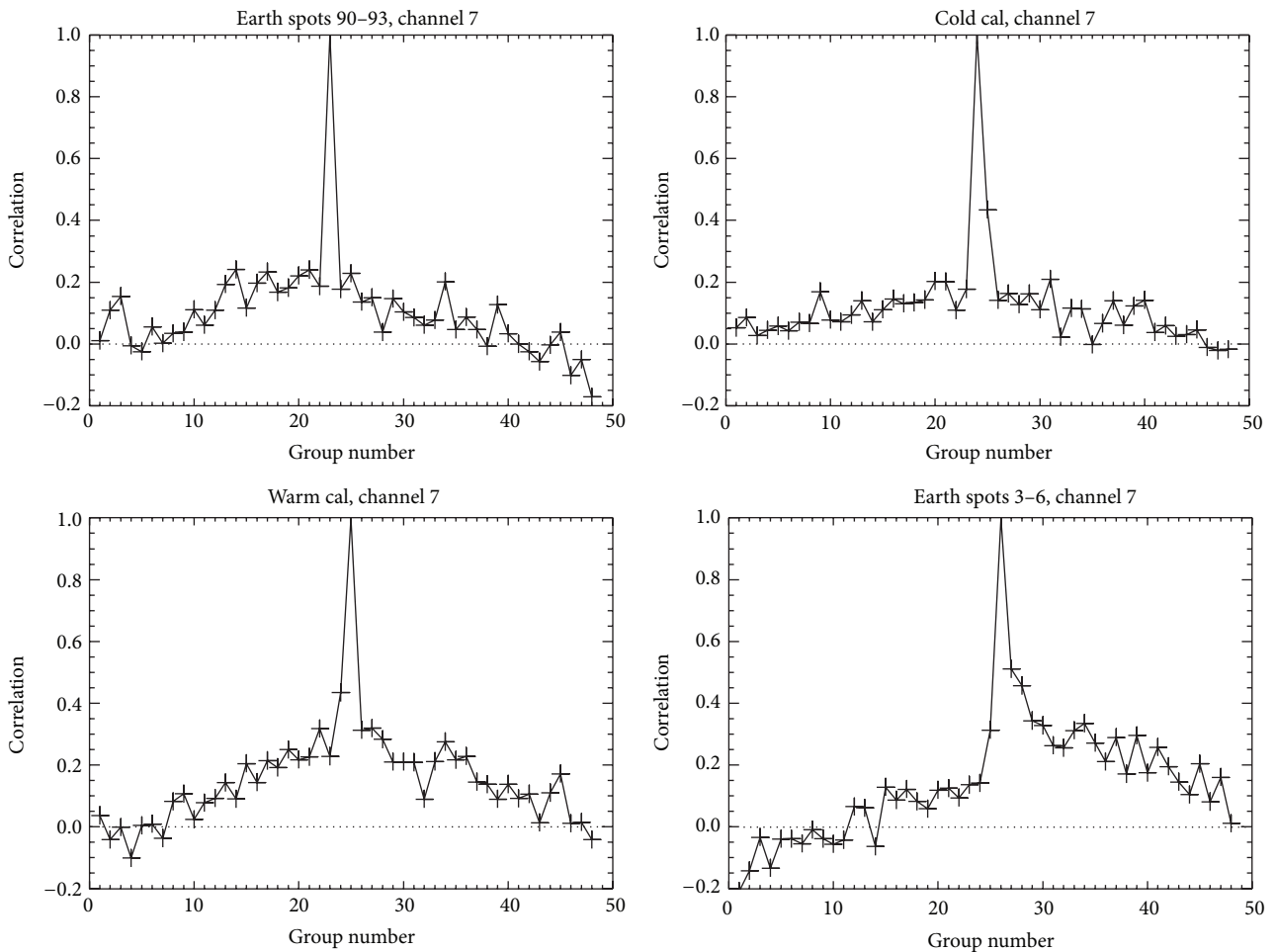


FIGURE 6: Correlations between groups of 4 pixels for ATMS channel 7. Groups 1–23 are earth views, 24 is cold cal, 25 is warm cal, and 26–48 are earth views of the next scan.

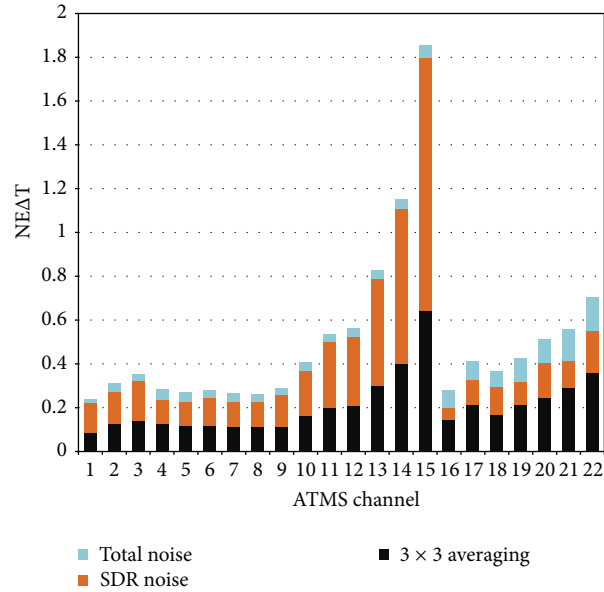


FIGURE 7: NEAT for ATMS, derived from warm view counts. Light blue: total noise for individual samples, using the method described in Section 3.3; orange: noise estimates from global SDR files; black: for 3×3 sample averaging (i.e., field of view for channels 3–15 comparable with AMSU-A). The values for total noise and 3×3 noise were derived from one month of direct broadcast data received at Exeter (November 2014).

standard deviation of the uncorrected brightness temperature difference for the temperature sounding channels and Figure 8(b) the same for the corrected values. Before bias correction the ATMS values for the sounding channels are lower than or of the same order as the AMSU values, but after bias correction the standard deviations for ATMS are consistently slightly higher than for AMSU, despite the good radiometric performance. The reason is probably that in the Met Office system AMSU observations are remapped to the HIRS grid by AAPP, which results in a spreading of the AMSU footprint and a reduction of the NEAT by a factor of 0.68. The ATMS observations are not remapped in this way.

For the humidity sounding channels (Figures 8(c) and 8(d)) the mean and standard deviations of the brightness temperature differences are broadly similar for ATMS and AMSU. The effect of instrument noise is masked by the larger signal from errors in the background humidity field at these frequencies (standard deviation of the first guess departures for MHS/AMSU-B channels is a factor of 10 larger than those of temperature sounding channels from AMSU-A).

4. Assimilation Experiments

The impact of the ATMS data on global analyses and forecasts was tested by adding the ATMS data to a full Met Office observing system. Results from a summer season are presented here for the period 28 June–28 August 2012. The low resolution version of the operational configuration

described in Section 2.2.2 was used for experiments and the corresponding controls.

The ATMS observation errors, expressed in the observation error covariance matrices, \mathbf{R} [19], were derived from those for NOAA-19 AMSU channels. For channels with frequencies below 183 GHz, the NOAA-19 values were scaled by the ratio of NEAT for equivalent channels on the two instruments, using the ATMS prelaunch specification. For channel 4 (51 GHz), which has no counterpart on AMSU, the error was estimated by interpolating between the values for channels 3 and 5. To account for the impact of striping \mathbf{R} values were then inflated to a minimum of 0.35 K. An error of 4 K was used for the 183 GHz channels. The errors for all channels are assumed to be uncorrelated. In practice, it is known that the striping noise introduces interchannel correlations (Section 3.2), but these are ignored.

ATMS temperature and moisture sounding channels (6–15 and 18–22) were used in the trial. Channels 8–15 were used over all surfaces, 18–22 over sea only, 6 over sea and sea ice, and 7 over all surfaces except high land.

Quality control tests screen out observations in the presence of deep cloud and precipitation [20–22] following the treatment of AMSU data, the data being sufficiently similar after remapping. The tests applied are an O-B threshold test, a liquid water test from the AAPP [22] to screen out ATMS channel 18 and 6, a cirrus cost test to screen out channels 18–20 [21], and the Bennartz rain test [20] which screens out channels 7–9, 21, and 22.

Observations are thinned prior to assimilation to reduce data volume and avoid spatial correlations. The operational

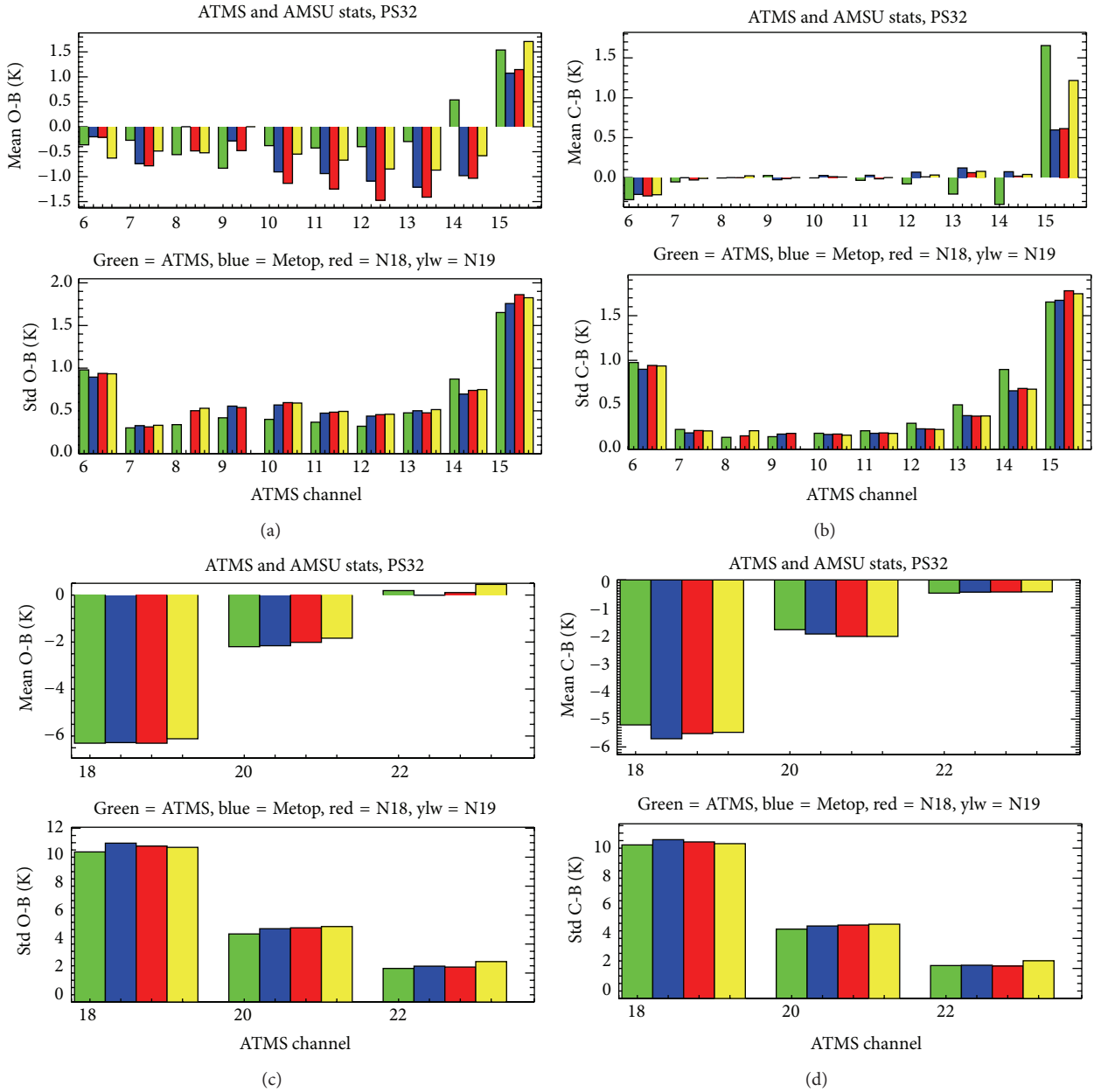


FIGURE 8: Mean and standard deviation of uncorrected (O-B) and corrected (C-B) innovations for ATMS and AMSU 50–60 GHz temperature sounding channels ((a) and (b)) and 183 GHz humidity sounding channels ((c) and (d)) January to February 2012.

treatment of AMSU was followed, with observations thinned to one per 154 km in the tropics and 1 per 125 km in the extratropics and a temporal thinning time of 3 hours. Bias correction was calculated using two weeks of data from June 2012. An additional assimilation experiment was also carried out with reduced thinning distance of 80 km and a time window of 1 hour.

4.1. Impact on Forecast Skill. Figure 9 shows the percentage change in forecast RMS errors. The impact of assimilating ATMS is positive overall for both experiments, with

the biggest impact seen in the Southern Hemisphere. The reduced thinning experiment performs slightly better for nearly all parameters.

4.2. Impact on Background Fits for AMSU. Figure 10 shows the impact of assimilating ATMS on the background fits to NOAA-18 AMSU temperature sounding channels normalised to the standard deviation of the control during the period 28 June–28 August 2012. Results are shown for operational thinning (red line) and reduced thinning (blue line) for the southern hemisphere, tropics, and northern

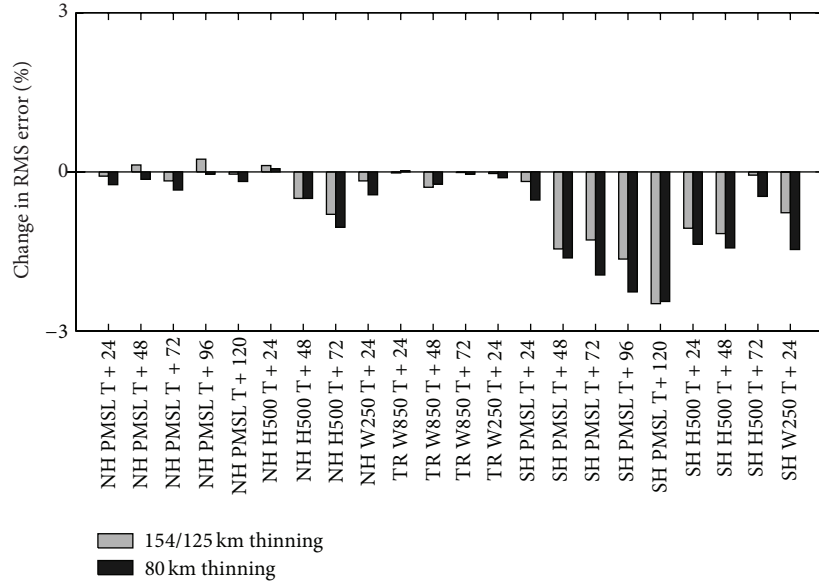


FIGURE 9: Changes in root mean square (RMS) errors in mean sea level pressure (PMSL), 500 hPa geopotential height (H500) winds at 850 hPa (W850) and 250 hPa (W250) for the northern hemisphere (NH), tropics (TR), and southern hemisphere (SH) at forecast ranges from T + 24 hours to T + 120 hours for experiments in which ATMS data is added with spatial thinning set to 125/154 km and 80 km. Verification is relative to observations during the period 28 June–28 August 2012. Changes are relative to a control experiment which is similar in configuration to the Met Office operational configuration as at January 2013.

hemisphere. Adding ATMS with operational thinning generally improves the background fit for AMSU. Results are more variable for reduced thinning. NOAA-19 and Metop-A AMSU temperature sounding channels showed similar results (not shown).

4.3. Impact on Background Fits for IASI and AIRS. Figure 11 shows the impact of ATMS on the fits to IASI and AIRS channels; the blue line is the reduced thinning trial and the red line is the operational thinning. Numbers are normalised to the standard deviation of the control (black line). Introducing ATMS data in general improves the fit of IASI to background, with the reduced thinning (blue line) performing marginally better than the operational thinning (red line). The exception to this is for the window and ozone channels with wave numbers ~820–1140 where reduced thinning shows a marked positive impact and operational thinning shows a marked degradation. The reason for this behaviour is not immediately apparent and warrants some further investigation.

For AIRS, operational thinning performs better for the channels which peak in the stratosphere (wave numbers up to about 650 cm⁻¹) and reduced thinning performs better for wave numbers 2385 cm⁻¹ and higher (water vapour and short wave channels). In between, the picture is mixed with reduced thinning generally giving more positive impact.

5. Operational Performance of ATMS

ATMS has been used operationally at the Met Office since April 2013. Its performance is stable and it contributes to the performance of the model, complimenting the other

instruments. Forecast Sensitivity to Observations analysis [23] is carried out routinely at the Met Office. A time series of the impact from ATMS within the full system as calculated by this technique is shown in Figure 12 for November 2014. The sensitivity to ATMS of the system is about 1/5 of that seen from all the AMSU-A instruments combined, as shown in Figure 13 for January 2014.

Impact on the forecast examined on a channel by channel basis shows that as expected the temperature sounding channels (53–55 GHz, channels 6–9) give the greatest impact followed by the moisture sounding channels around the 183 GHz water vapour line (channels 18–22). Figure 14 shows this for January 2014 in the operational Met Office system.

A corresponding plot for ATOVS is shown in Figure 15; a similar pattern is seen for these instruments with the tropospheric sounding channels exerting the most influence and the 183 GHz water vapour channels giving a smaller but still significant impact. For each channel, the impact from ATOVS is of the order of 4 times that of ATMS. The volume of ATOVS data (with 5 instruments currently assimilated at the Met Office) is partly responsible for the difference in impact between two nominally identical channels; also contributing will be the additional noise from the striping signal in the ATMS data (compared to the very good noise in the remapped ATOVS data; see Section 3.3) and the less finely tuned quality control for the newer instrument.

The reliability of the ATMS data can be seen in the two-year time series monitoring plot in Figure 16. In Figure 16(a) the mean of the corrected innovations (blue line) shows seasonal variability but (apart from a blip in May 2014) stays close to zero; the RMS of the corrected innovations

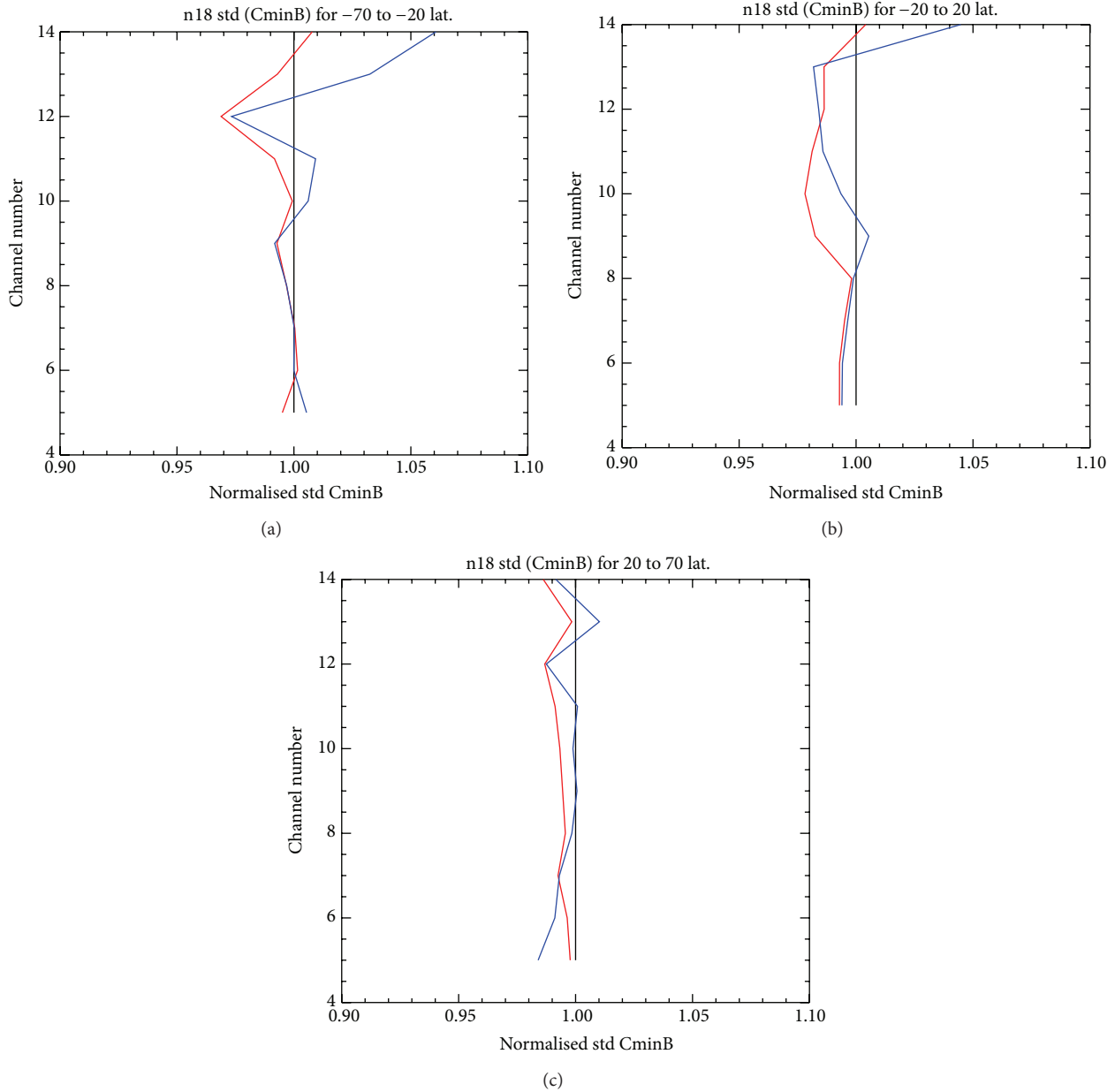


FIGURE 10: Standard deviation of corrected brightness temperature difference for NOAA-18 AMSU temperature sounding channels, normalised with respect to the control experiment (black). Southern Hemisphere (a), tropics (b), and Northern Hemisphere (c). Red line is operational thinning; blue line shows reduced thinning (28 June–28 August 2012).

(red line) is less variable. Figure 16(b) shows the observation count over the same period. Data dropouts are more frequent than for AMSU-A on all but the NOAA-15 platform; this is partly due to S-NPP data transfer issues between NOAA and EUMETSAT. Typically 6000 ATMS obs are assimilated every cycle.

6. Summary and Conclusions

An initial assessment of ATMS data has been carried out using four methods: (1) inspection of observations and of

differences between model and observation, (2) comparisons with AMSU and MHS data, (3) preoperational assimilation experiments, and (4) monitoring of operational performance in the Met Office NWP system.

Despite the radiometric performance advantage over AMSU the standard deviations of bias corrected differences from the model for most of the temperature sounding channels (6–15) are slightly worse than for AMSU-A equivalents. This can be explained by differences in the treatment of the observations within the Met Office processing system (AMSU being mapped to the HIRS grid).

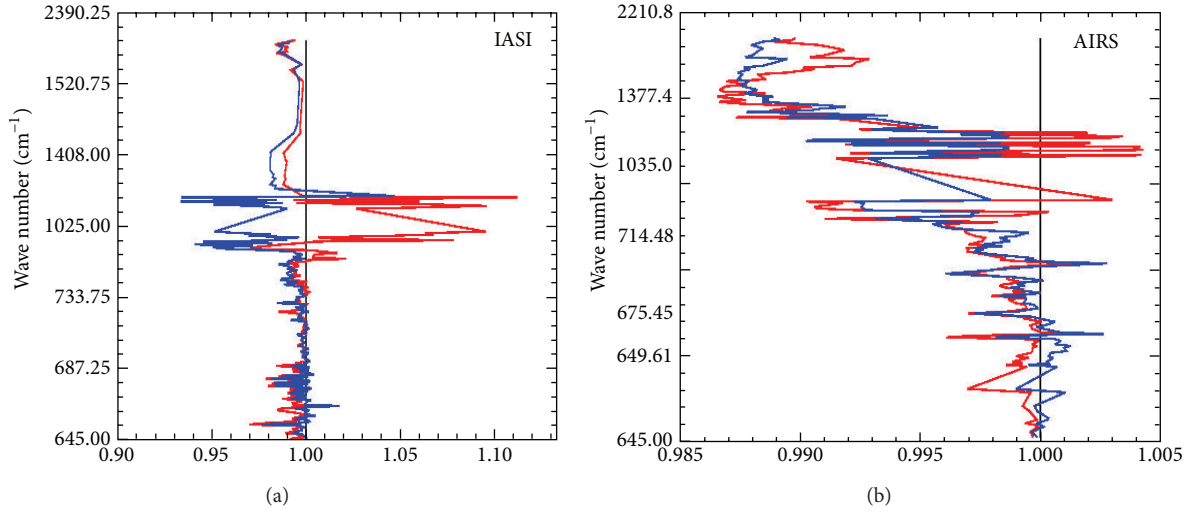


FIGURE 11: Standard deviation of corrected brightness temperature difference for IASI (a) and AIRS ((b) not a linear scale on the y-axis), normalised with respect to the control experiment (black). Red line shows the results for operational thinning; blue line shows the results for reduced thinning (28 June–28 August 2012).

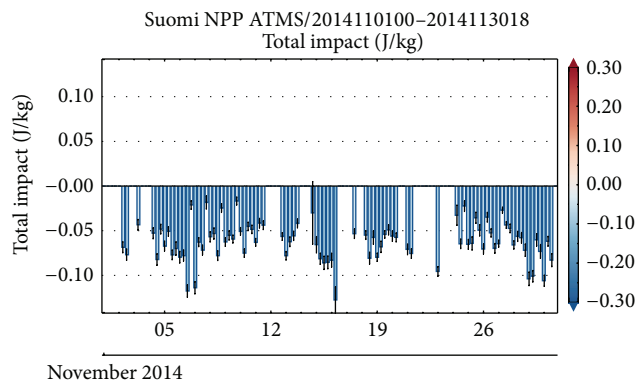


FIGURE 12: Time series of the FSO statistics for ATMS in the Met Office operational system for November 2014.

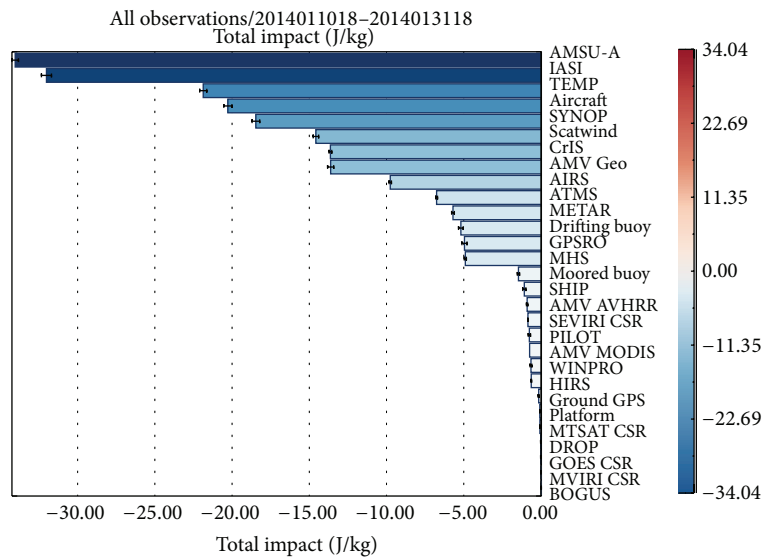


FIGURE 13: Total impact of all assimilated obs. in the Met Office DA system. Magnitude of ATMS contribution is about a fifth of that from 5 AMSU-A instruments (January 2014).

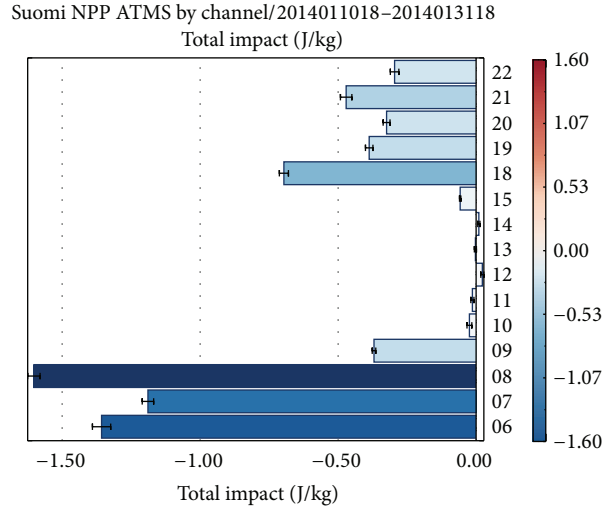


FIGURE 14: FSO statistics separated out by ATMS channel (January 2014).

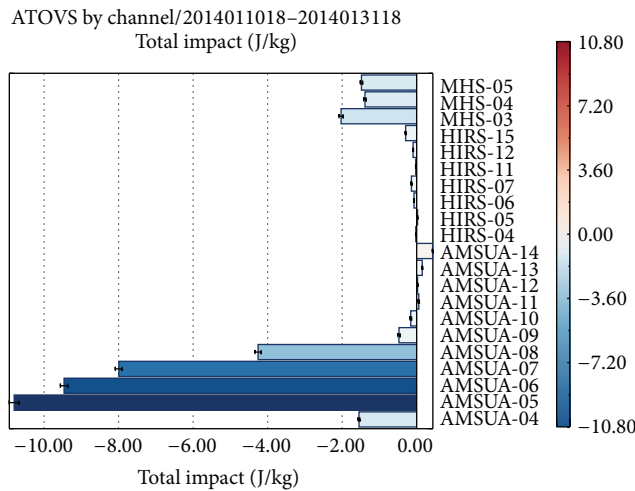


FIGURE 15: ATOVS FSO statistics by channel (January 2014).

A striping effect from the noise introduced by the low noise amplifier in the ATMS instrument is noticeable in the corrected innovations, and an inflated observation error was used to compensate for possible interchannel correlations.

For the humidity sounding channels examined (183 ± 1 , ± 3 , ± 7 GHz, channels 18, 20, and 22) the performance of ATMS is very close to that of AMSU-B/MHS. For the surface viewing channels (1–3, 5, 16, and 17) the ATMS data shows slightly larger bias and standard deviation (not shown).

Two assimilation experiments were conducted in which ATMS was added to a full Met Office system for a summer season. For the experiments using a thinning distance of 154 km in the tropics and 125 km in the extratropics, a small positive impact on RMS errors for a number of parameters was seen. For the experiment using reduced thinning (80 km), impact was more strongly positive, although closer inspection of the fit to background of other instrument types

when ATMS was added to the system showed a more mixed response which requires further study.

Assimilation of ATMS data, with the processing configuration as described in the forecast impact experiments without reduced thinning, was made operational in the Met Office global model on 30 April 2013. Routine monitoring of the data has shown that ATMS data have had a significant impact on forecast quality over the period to November 2014, despite the fact that 5 other microwave sounders (ATOVS instruments on NOAA-15, NOAA-18, NOAA-19, Metop-A, and Metop-B) are already assimilated.

Conflict of Interests

The authors declare that there is no conflict of interests regarding the publication of this paper.

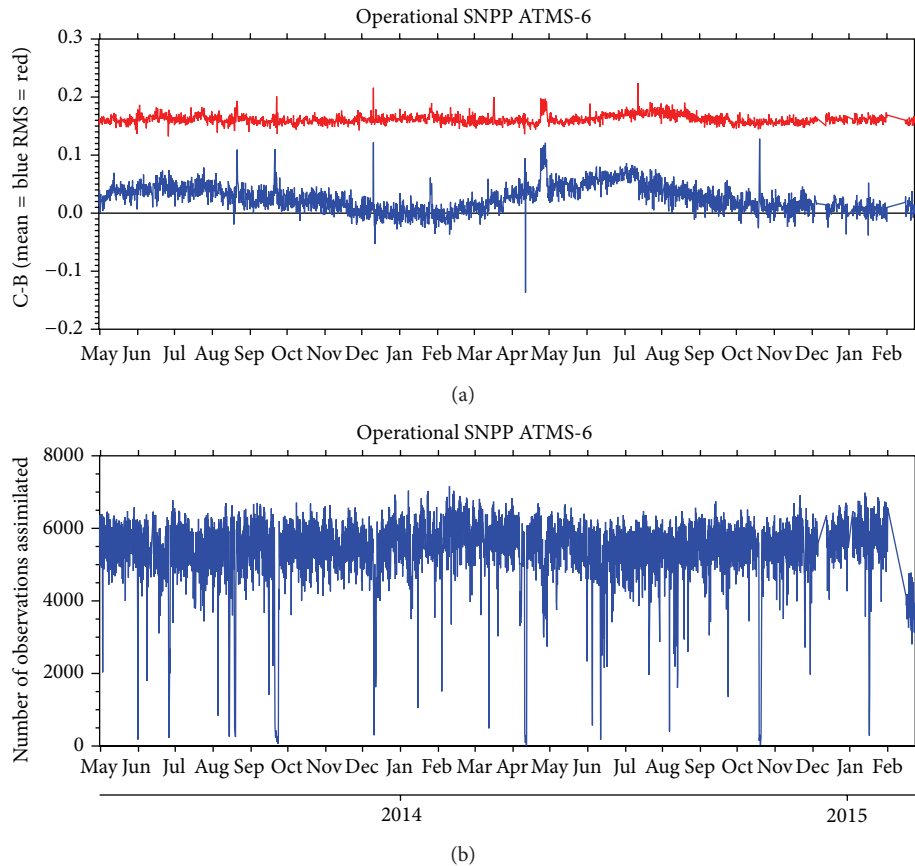


FIGURE 16: Time series for ATMS channel 6. (a) The mean (blue) and RMS (red) of the corrected innovations and (b) the assimilated observation count over a two-year period, May 2013–February 2015.

Acknowledgment

Thanks to James Cotton for the FSO plots.

References

- [1] J. H. Marburger, "Restructuring the national polar-orbiting operational environmental satellite system," White House Office of Science and Technology Policy Fact Sheet 2011, R&D Budget Submission, 2010.
- [2] G. Goodrum, K. B. Kidwell, and W. Winston, Eds., *NOAA KLM User's Guide*, NOAA, NOAA-NESDIS/NCDC, Suitland, Md, USA, 1999, <http://www.ncdc.noaa.gov/oa/pod-guide/ncdc/docs/klm/index.htm>.
- [3] C. Muth, P. S. Lee, J. C. Shiue, and W. A. Webb, "Advanced technology microwave sounder on NPOESS and NPP," in *Proceedings of the IEEE International Geoscience and Remote Sensing Symposium (IGARSS '04)*, pp. 2454–2458, September 2004.
- [4] W. Bell, S. J. English, B. Candy et al., "The assimilation of SSMIS radiances in numerical weather prediction models," *IEEE Transactions on Geoscience and Remote Sensing*, vol. 46, no. 4, pp. 884–900, 2008.
- [5] Q. Lu, W. Bell, P. Bauer, N. Bormann, and C. Peubey, "Characterizing the FY-3A microwave temperature sounder using the ECMWF model," *Journal of Atmospheric and Oceanic Technology*, vol. 28, no. 11, pp. 1373–1389, 2011.
- [6] N. Bormann, A. Fouilloux, and W. Bell, "Evaluation and assimilation of ATMS data in the ECMWF system," *Journal of Geophysical Research D: Atmospheres*, vol. 118, no. 23, pp. 12970–12980, 2013.
- [7] W. Bell, S. Di Michele, P. Bauer et al., "The radiometric sensitivity requirements for satellite microwave temperature sounding instruments for numerical weather prediction," *Journal of Atmospheric and Oceanic Technology*, vol. 27, no. 3, pp. 443–456, 2010.
- [8] NWP SAF, "Annex to AAPP scientific documentation: pre-processing of ATMS and CrIS," Document NWPSAF-MO-UD-027, 2011, http://nwpsaf.eu/deliverables/aapp/NWPSAF-MO-UD-027_ATMS-CrIS.pdf.
- [9] J. R. Eyre, "Inversion of cloudy satellite sounding radiances by nonlinear optimal estimation. II: application to TOVS data," *Quarterly Journal—Royal Meteorological Society*, vol. 115, no. 489, pp. 1027–1037, 1989.
- [10] P. Courtier, J.-N. Thepaut, and A. Hollingsworth, "A strategy for operational implementation of 4D-Var, using an incremental approach," *Quarterly Journal of the Royal Meteorological Society*, vol. 120, no. 519, pp. 1367–1387, 1994.
- [11] F. Rawlins, S. P. Ballard, K. J. Bovis et al., "The met office global four-dimensional variational data assimilation scheme," *Quarterly Journal of the Royal Meteorological Society*, vol. 133, no. 623, pp. 347–362, 2007.
- [12] T. Auligné, A. P. McNally, and D. P. Dee, "Adaptive bias correction for satellite data in a numerical weather prediction

- system,” *Quarterly Journal of the Royal Meteorological Society*, vol. 133, no. 624, pp. 631–642, 2007.
- [13] B. A. Harris and G. Kelly, “A satellite radiance-bias correction scheme for data assimilation,” *Quarterly Journal of the Royal Meteorological Society*, vol. 127, no. 574, pp. 1453–1468, 2001.
- [14] R. Saunders, M. Matricardi, A. Geer, P. Rayer, O. Embury, and C. Merchant, “RTTOV9 science and validation plan,” RTTOV-9 Science and Validation Report NWPSAF-MO-TV-020, 2010.
- [15] N. Bormann, W. Bell, A. Fouilloux, I. Mallas, N. Atkinson, and S. Swadley, “Initial results from using ATMS data at ECMWF,” in *Proceedings of the 18th International TOVS Study Conference*, Toulouse, France, March 2012.
- [16] Z. Qin, X. Zou, and F. Weng, “Analysis of ATMS striping noise from its Earth scene observations,” *Journal of Geophysical Research D: Atmospheres*, vol. 118, no. 23, pp. 13214–13229, 2013.
- [17] R. F. Voss, “1/f (flicker) noise : a brief review,” in *Proceedings of the 33rd Annual Symposium on Frequency Control*, pp. 40–46, June 1979.
- [18] N. C. Atkinson and S. McLellan, “Initial evaluation of AMSU-B in-orbit data,” in *Microwave Remote Sensing of the Atmosphere and Environment*, vol. 3503 of *Proceedings of SPIE*, pp. 276–287, Beijing, China, August 1998.
- [19] A. C. Lorenc, “Analysis methods for numerical weather prediction,” *Quarterly Journal of the Royal Meteorological Society*, vol. 112, pp. 1177–1194, 1986.
- [20] R. Bennartz, A. Thoss, A. Dybbroe, and D. B. Michelson, “Precipitation analysis using the advanced microwave sounding unit in support of nowcasting applications,” *Meteorological Applications*, vol. 9, no. 2, pp. 177–189, 2002.
- [21] S. J. English, J. R. Eyre, and J. A. Smith, “A cloud-detection scheme for use with satellite sounding radiances in the context of data assimilation for numerical weather prediction,” *Quarterly Journal of the Royal Meteorological Society*, vol. 125, no. 559, pp. 2359–2378, 1999.
- [22] T. Labrot, L. Lavanant, K. Whyte, N. Atkinson, and P. Brunel, “AAPP documentation, scientific description,” NWP SAF Document NWPSAF-MF-UD-001, Satellite Application Facility on Numerical Weather Prediction, 2006.
- [23] A. C. Lorenc and R. T. Marriott, “Forecast sensitivity to observations in the Met Office Global numerical weather prediction system,” *Quarterly Journal of the Royal Meteorological Society*, vol. 140, no. 678, pp. 209–224, 2014.

Research Article

Prediction of Moderate and Heavy Rainfall in New Zealand Using Data Assimilation and Ensemble

Yang Yang, Phillip Andrews, Trevor Carey-Smith, Michael Uddstrom, and Mike Revell

National Institute of Water and Atmospheric Research (NIWA), Private Bag 14901, Wellington 6021, New Zealand

Correspondence should be addressed to Yang Yang; y.yang@niwa.co.nz

Received 7 December 2014; Accepted 5 February 2015

Academic Editor: Yuanfu Xie

Copyright © 2015 Yang Yang et al. This is an open access article distributed under the Creative Commons Attribution License, which permits unrestricted use, distribution, and reproduction in any medium, provided the original work is properly cited.

This numerical weather prediction study investigates the effects of data assimilation and ensemble prediction on the forecast accuracy of moderate and heavy rainfall over New Zealand. In order to ascertain the optimal implementation of state-of-the-art 3Dvar and 4Dvar data assimilation techniques, 12 different experiments have been conducted for the period from 13 September to 18 October 2010 using the New Zealand limited area model. Verification has shown that an ensemble based on these experiments outperforms all of the individual members using a variety of metrics. In addition, the rainfall occurrence probability derived from the ensemble is a good predictor of heavy rainfall. Mountains significantly affect the performance of this ensemble which provides better forecasts of heavy rainfall over the South Island than over the North Island. Analysis suggests that underestimation of orographic lifting due to the relatively low resolution of the model (~12 km) is a factor leading to this variability in heavy rainfall forecast skill. This study indicates that regional ensemble prediction with a suitably fine model resolution (≤ 5 km) would be a useful tool for forecasting heavy rainfall over New Zealand.

1. Introduction

The initial conditions of a numerical weather prediction (NWP) forecast are usually generated by data assimilation, a procedure statistically combining observations and a model forecast and utilising their respective error information to create an optimum estimate of the true atmospheric state compatible with the forecast model in use. Uncertainty and errors are unavoidable in the initial conditions of an NWP due to meteorological equipment errors, sampling errors, and data assimilation errors, and so forth. Ensemble forecasts have been used for some 20 years at major meteorological prediction centres to explore the impact of these uncertainties in the atmospheric initial conditions (and other boundary conditions) on NWP. Several methodologies have been used to establish the global ensemble systems (GES) including those based on the leading singular vectors of the operator [1, 2], bred vectors [3, 4], the Monte Carlo method [5], and the Monte Carlo based ensemble Kalman filter [6].

The spatial resolution of currently operational GES is low (e.g., ~32 km for the current operational ECMWF ensemble system). Many small scale processes in the atmosphere

and the underlying surface and small scale mountains that significantly affect the evolution and development of severe weather are not resolved by GES. Regional ensemble systems (RES) were thus established. The resolution of RES differs. Some have very high resolutions so that supercell storms and convections can be resolved (e.g., [7–9]). The way to initialize a RES also differs. Some RESs are initialized from a GES. Some RESs randomly sample the climatological uncertainties of the initial state [10]. Others derive random perturbations from the background error statistics of an existing 3D/4Dvar system (e.g., [11–13]). Some RESs use different model physics and different global deterministic model outputs to generate members (e.g., [14, 15]). Some use different regional model outputs called multimodel ensemble [16]. For heavy rainfall forecasts, RES has shown higher forecasting skills than GES (e.g., [14, 17, 18]).

New Zealand lies in the midlatitude southwest Pacific, surrounded by ocean. The two main islands are North Island and South Island. North Island (Figure 1(a)) has a “spine” of mountain ranges extending from the middle, with gentle rolling farmland on both sides. The South Island is dominated by mountain ranges running its entire length. The main

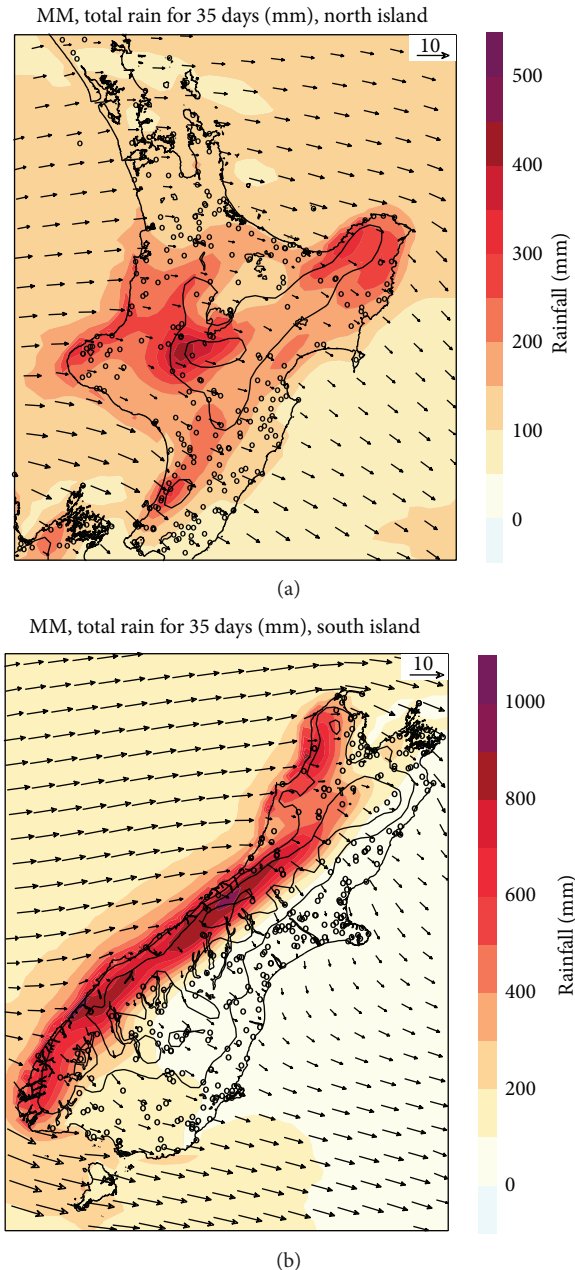


FIGURE 1: Total rainfall amount (mm) and mean surface wind vectors (m s^{-1}) of 35 days from 13 Sept to 18 Oct 2010 for the ensemble mean. The 630 sites with daily rainfall observations used in this study are denoted with open dots. Thin solid lines denote the model terrain contours of 500 m interval. Note the different scales for the two rainfall labels.

mountain range with a southwest to northeast orientation is known as the Southern Alps (Figure 1(b)). Under the prevailing midlatitude westerly winds, the western region of New Zealand is generally the windward side and the eastern region is the lee side.

Rainfall amount is much higher over land areas than over the nearby sea because of orographic lifting (Figure 1). Overall, much more rainfall occurs in the western area of the South Island than on other areas of the country, because

of orographic lifting of more consistent westerly airflows and more uniform mountains. Heavy rainfall often leads to severe flooding and landslides in New Zealand. Thus, a reliable heavy rainfall prediction is of great importance but still a big challenge, largely due to the open seas surrounding the small island country with sparse ground-based/surface observations and rawinsondes. To overcome the problem of lack of meteorological observations for New Zealand, satellite data have been widely used in a regional 3Dvar system based on the New Zealand limited area model (NZLAM, [19, 20]) for a 48-hour NWP in New Zealand. This has shown improvements [21].

4Dvar has been implemented at some major meteorological centres (e.g., Met Office and ECMWF) to replace 3Dvar. Their verification statistics show an overall higher forecasting skill for 4Dvar (e.g., [22]). Recently an experimental regional 4Dvar for NZLAM has been set up from the UK Met Office VAR codes. To compare the impact on the forecasts of the 3Dvar and 4Dvar data assimilation methods, to tune the 4Dvar for the best possible result, and to test the impact of new observation types (e.g., surface marine observations) on both analysis methods, 12 numerical experiments based on NZLAM were conducted over the period of 35 days from 13 September to 18 October 2010 (Table 1). Each experiment differs in either the analysis system, or system configuration, or the surface and satellite data assimilated.

In this study, a temporary RES was created by combining 12 experiments originally intended to compare the impact of the 3Dvar and 4Dvar techniques on the skill of NZLAM forecasts. Although the principal behind this ensemble is similar to ensemble systems which use different model physics or/and different regional/global deterministic model outputs [14–16], members of this ensemble system employed the state-of-the-art 3Dvar and 4Dvar techniques in assimilating satellite data [22]. To our knowledge, this is the first attempt at predicting heavy rainfall in New Zealand using a RES.

The objective of this study is to investigate the effect of data assimilation and ensemble method on moderate and heavy rainfall prediction over New Zealand. Of particular interest is how mountains affect the performance of a RES in prediction of moderate and heavy rainfall and therefore the suitable model resolution for a RES over New Zealand. Following the introduction, the modelling system and methodology are described in Section 2. Two heavy rainfall cases forecasted by this RES are described in Section 3. Statistical analysis regarding the performance of this RES is presented in Section 4. The effect of mountains on this RES is discussed in Section 5. Finally a short conclusion is given in the last section.

2. Description of the Modelling System and Methodology

All the simulations in this study were made by using the NZLAM, a regional configuration of the Met Office's Unified Model (UM, [23]). The UM has a nonhydrostatic, fully compressible formulation of the Navier-Stokes equations using a terrain following, height-based vertical coordinate.

TABLE 1: Description of the 12 ensemble members used in this study.

Member names	Description
3Dvar	3D analysis of surface (including buoys; land synops; ship synops and scatterometer winds), aircraft and radiosondes, AMSU-A, and AMSU-B from the NOAA-15 and NOAA-16 satellites. Half resolution of the model for the analysis grid (0.22 degrees).
3Dcli	As 3Dvar but also analyse additional surface observations at climate stations in New Zealand.
3Dclim	As 3Dcli but also analyse surface marine observations.
3DclimB	As 3Dclim but uses satellite radiance bias corrections calculated from the 3dclim run.
3DclimC	As 3DclimB but with increased satellite-derived atmospheric motion vectors (AMV) usage through modified thinning.
4Dvar11	As 3Dvar but for 4Dvar with analysis grid resolution the same as the model (0.11 degrees).
4D11a	As 4dvar11 but exclude scales <50 km during analysis.
4D11b	As 4dvar11 but exclude scales <100 km during analysis.
4Dcli	As 4D11a but also analyse additional surface observations at climate stations in New Zealand.
4Dclim	As 4Dcli but also analyse surface marine observations.
4DclimB	As 4Dclim but uses satellite radiance bias corrections calculated from the 4dclim run.
4DclimC	As 4DclimB but with increased AMV usage through modified thinning.

It employs a horizontally staggered Arakawa C-grid and a vertically staggered Charney-Phillips grid; semi-Lagrangian advection for all prognostic variables, except density, with conservative and monotone treatment of tracers; predictor-corrector implementation of a two-time-level, semi-implicit time integration scheme; and three-dimensional iterative solution of a variable-coefficient elliptic equation for the pressure increment at each time step (see [23, 24] for detailed descriptions). The NZLAM has 324 by 324 horizontal grid points with a horizontal grid spacing of 0.11° (about 12 km, [19, 20]) and 70 levels in the vertical, with the model top at about 39 km. The highest vertical resolution is near the ground such that 20 levels span the lowest 2 km of the atmosphere. A global run provided the same lateral boundary conditions for all the ensemble simulations.

All the experiments were classified as two groups with initializations based on 3Dvar (five members) and 4Dvar (seven members), respectively (Table 1). The former uses an incremental 3Dvar FGAT (first guess at appropriate time) analysis scheme [25]. The latter is based on the former with many aspects kept in common and is provided by the introduction of a linear perturbation forecast model and its adjoint [22]. In both schemes, a transform (including a parameter transform, a vertical transform, and a horizontal transform) is implemented to provide an implicit representation of the background error covariance and a practical and easy method of preconditioning the analysis minimisation problem. For the five 3Dvar-based members, the analysis resolution used (0.22 degrees) is half the model resolution, whilst, for the seven 4Dvar-based members, the resolution is the same as the model resolution (Other experiments, not presented here, have shown that using full or half resolution analysis increments for 3Dvar makes very little difference to the verification scores against observations for forecasts out to T+48; however, using lower resolution analysis increments for 4dvar significantly reduces forecast skill.) (Table 1).

The vertical transform uses zonal and seasonal average statistics to produce two-dimensional empirical modes. The horizontal transform can also be used as a filter, to remove small scale modes from each horizontal field. Following the ideas of Cullen [26] we used this to exclude scales smaller than 50 km for 4D11a and smaller than 100 km for 4D11b, 4Dcli, 4Dclim, 4DclimB, and 4DclimC. Both 3D and 4Dvar performed a 6 hourly data assimilation cycle throughout the study period. After 0000 UT on 13 September 2010 (the initial time for each experiment), the background used for the analysis for each experiment differed to some extent. 48-hour forecasts were made following the 0000, 0600, 1200, and 1800 UT analyses for each experiment each day and simulated fields were saved hourly.

The ensemble mean was calculated with an equal weight for each member. In addition to root mean square errors (RMSE) and mean errors (ME), categorical forecasts at the two thresholds were examined using the performance diagram [27] and relative operating characteristic (ROC) diagram. The performance diagram plots the hit rate (H) against the success ratio ($1 - FAR$, the false alarm ratio) and allows the bias and critical success index (CSI) to be read directly. The ROC diagram plots the hit rate against the false alarm rate (F) from which it is easier to deduce base rate independent performance metrics such as the Peirce skill score (PSS) or symmetric extreme dependence index (SEDI). The latter measure is useful for rare events as it is nondegenerate [28]. Definitions for these categorical metrics are given in Table 2.

In the following calculation and analysis, all four forecasts on each day for each member during the 35 days were used. For each forecast, the forecast rainfall was chosen to match the observations in time. The rainfall forecast at the four grid points surrounding an observation site was linearly interpolated onto that site using distance as the weighting factor.

TABLE 2: Categorical measures used in this study along with their definitions based on a binary truth table, where a is the number of events which were forecast correctly, c the number of observed events not forecast, b the number of nonevents incorrectly forecast, and d the number of nonevents correctly forecast.

Metric	Formula	Range
Frequency bias	$\text{Bias} = \frac{a+b}{a+c}$	0 to ∞ (perfect: 1)
Hit rate	$H = \frac{a}{a+c}$	0 to 1 (perfect: 1)
False alarm rate	$F = \frac{b}{b+d}$	0 to 1 (perfect: 0)
False alarm ratio	$\text{FAR} = \frac{b}{a+b}$	0 to 1 (perfect: 0)
Critical success index	$\text{CSI} = \frac{a}{a+b+c}$	0 to 1 (perfect: 1)
Peirce skill score	$\text{PSS} = \frac{ad-bc}{(b+d)(a+c)}$	-1 to 1 (perfect: 1)
Symmetric extremal dependence index	$\text{SEDI} = \frac{\ln F - \ln H + \ln(1-H) - \ln(1-F)}{\ln F + \ln H + \ln(1-H) + \ln(1-F)}$	-1 to 1 (perfect: 1)

3. Two Heavy Rainfall Cases

Daily rainfall analysis with 0.05-degree resolution over New Zealand land surface is available at the National Institute of Water and Atmosphere Research (NIWA) derived using the second order derivative trivariate thin plate smoothing spline spatial interpolation model (<http://www.maths.anu.edu.au/research/projects/thin-plate-splines>). These data may have some errors and uncertainties in mountainous areas with sparse observations, but they are the best high resolution grid point rainfall data over New Zealand. These data are compared with forecasted rainfall by the ensemble for two heavy rainfall cases.

For Case 1, a subtropical cyclone with a tropical origin moved southeastward and approached the nearby sea to the northeast of the North Island in the early morning of 13 October 2010 (Figure 2(a)). A warm front (denoted by “WARM F”) associated with the cyclone moved southwestward in the northeasterly winds of the cyclone. Ahead of the warm front were southeasterly winds. The warm front reached the southeast coastal region of the North Island on the morning of 13 October. Orographic lifting of the strong southeasterly winds ($10\text{--}15\text{ m s}^{-1}$ surface winds at a coastal station) ahead of the warm front enhanced vertical motion in the frontal rainband. This led to very heavy rainfall in a broad area of the southeast North Island (Figure 3(a)). The rainfall analysis showed a rainband with four rainfall maximum centers from northeast to southwest. At some locations, the observed 24-hour rainfall at 0900 NZST on the 14 October was about 190 mm. Figure 3(c) shows the 24-hour rainfall forecast by the ensemble mean using equal weight. Most of the heavy rainfall areas were captured by the ensemble mean. However, the ensemble missed two of the four rainfall maximum centers: the southernmost one and the one in the middle of the rainband. For the two rainfall maximum centers captured by the ensemble, the maximum was 25–50 mm lower than observations. The terrain data in Figure 3(a) with a resolution of roughly 5 km, much higher than the model terrain (Figure 3(c), roughly 12 km

resolution), can describe smaller mountains. For example, a small mountain is shown in Figure 3(a) associated with the southernmost rainfall maximum center, but not shown by the model terrain (Figure 3(c)). The mountain corresponding to the rainfall maximum center in the middle of the rainband (Figure 3(a)) is more pronounced and higher than that in the model terrain (Figure 3(c)). For this heavy rainfall case, the convective available potential energy (CAPE) was very small ($<100\text{ J kg}^{-1}$), implying a very weak contribution from convective rainfall and a correspondingly stronger orographic component. It appears that the underestimation of the heavy rainfall by the ensemble is partly due to the relatively low resolution of the model, which underestimates the orographic lifting. This will be further analysed in Sections 4.2 and 5.

The forecast occurrence of daily rainfall greater than 50 mm with probability higher than 0.6 (Figure 4(c)) captured most of the areas with observed daily rainfall greater than 50 mm (Figure 4(a)). Most of the areas in the southeast of the North Island had a daily rainfall greater than 100 mm for this heavy rainfall case (Figure 4(b)). However, less than half of these areas were forecast to get greater than 100 mm with occurrence probability higher than 0.6 (Figure 4(d)) by the ensemble. This is due to the underestimation of rainfall by the model.

For Case 2, on 28 September 2010, an eastward moving midlatitude cyclone was over the sea to the southwest of the South Island (Figure 2(b)). The westerly winds associated with the cyclone advected the cold front (denoted by “COLD F”) eastward. Ahead of the cold front were northwesterly winds. When the cold front reached the South Island, orographic lifting and island blocking of the strong northwesterly and westerly winds around the front enhanced the vertical motion in the associated rainband, leading to heavy rainfall on the windward (western) areas of the South Island on that day (Figure 3(b)). The ensemble mean generally forecast well the heavy rainfall amount and distribution, except that it missed the heavy rainfall at the southern end of the rainband (Figure 3(d)). The ensemble based forecast occurrence of daily rainfall greater than 50 mm with probability higher

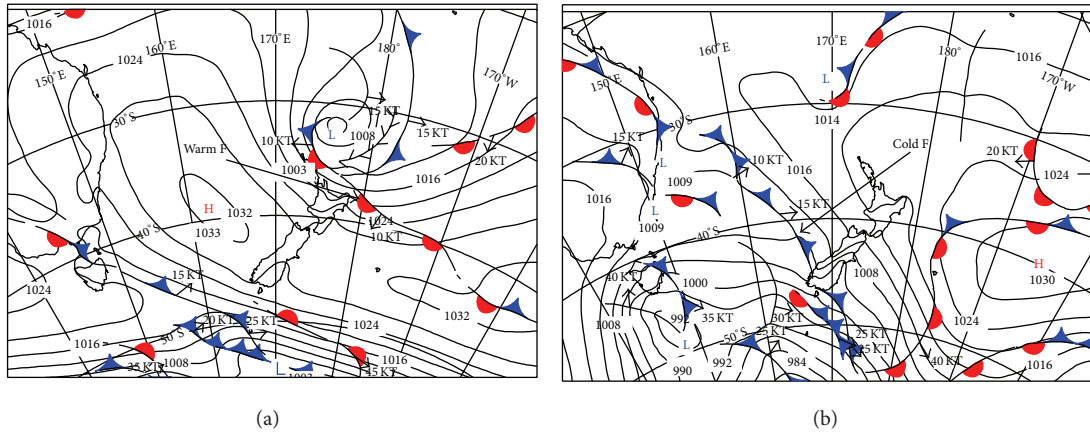


FIGURE 2: Surface analysis by MetService New Zealand at (a) 0000 NZST 13 October 2010 and (b) 1800 NZST 28 September. “WARM F” in (a) points to the warm front and “COLD F” in (b) points to the cold front. New Zealand lies in the middle of each diagram. Courtesy to MetService New Zealand.

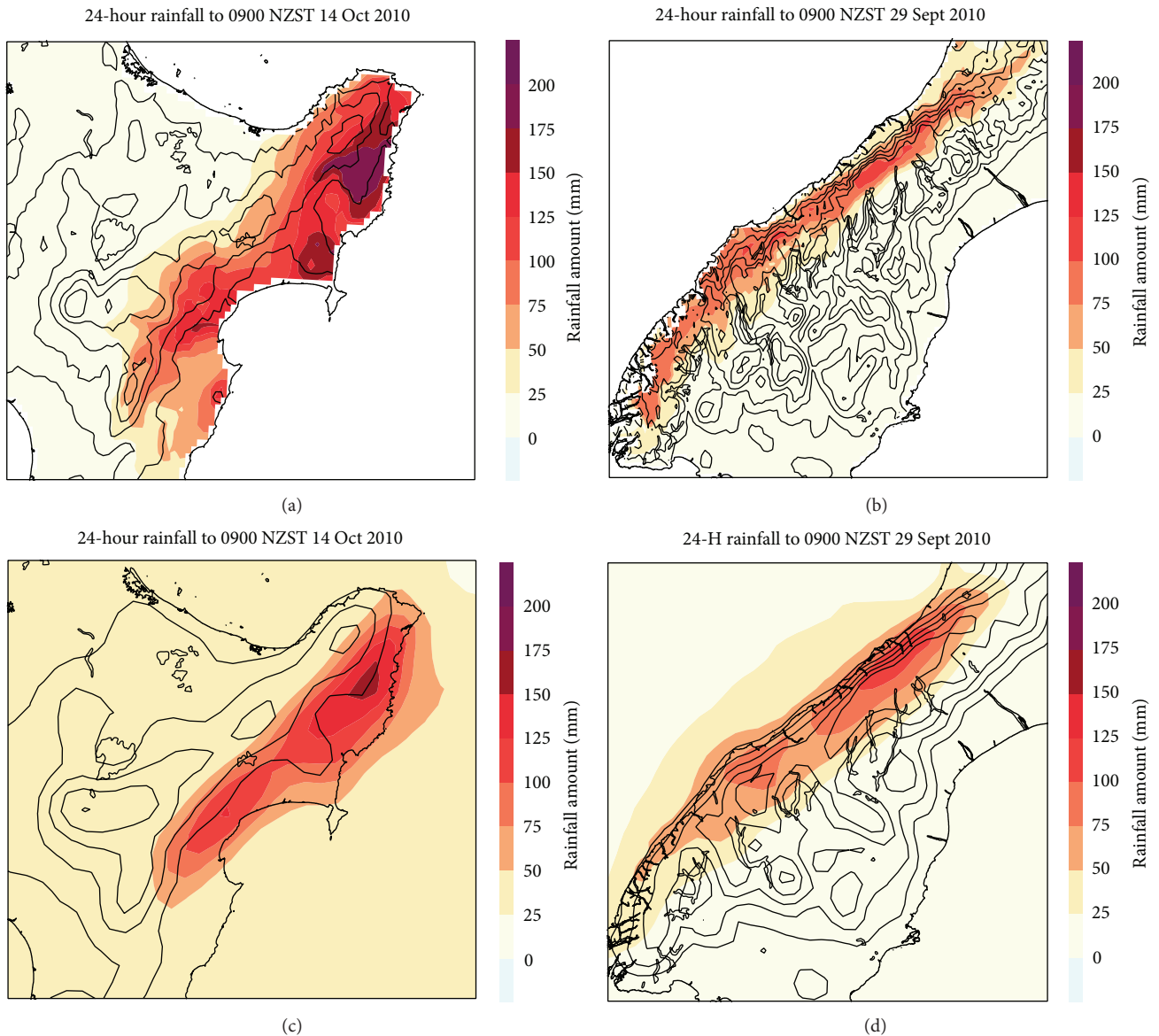


FIGURE 3: 24-hour rainfall amount (mm) valid at (a) 0900 NZST 14 October 2010 and (b) 0900 NZST 29 September from NIWA 0.05-degree grid point rainfall analysis. Simulated 24-hour rainfall amount valid at (c) 0900 NZST 14 October 2010 and (d) 0900 NZST 29 September from the ensemble mean (MM) forecasts with analysis at 0006 NZST. Thin solid lines denote terrain contours with a 250-meter interval.

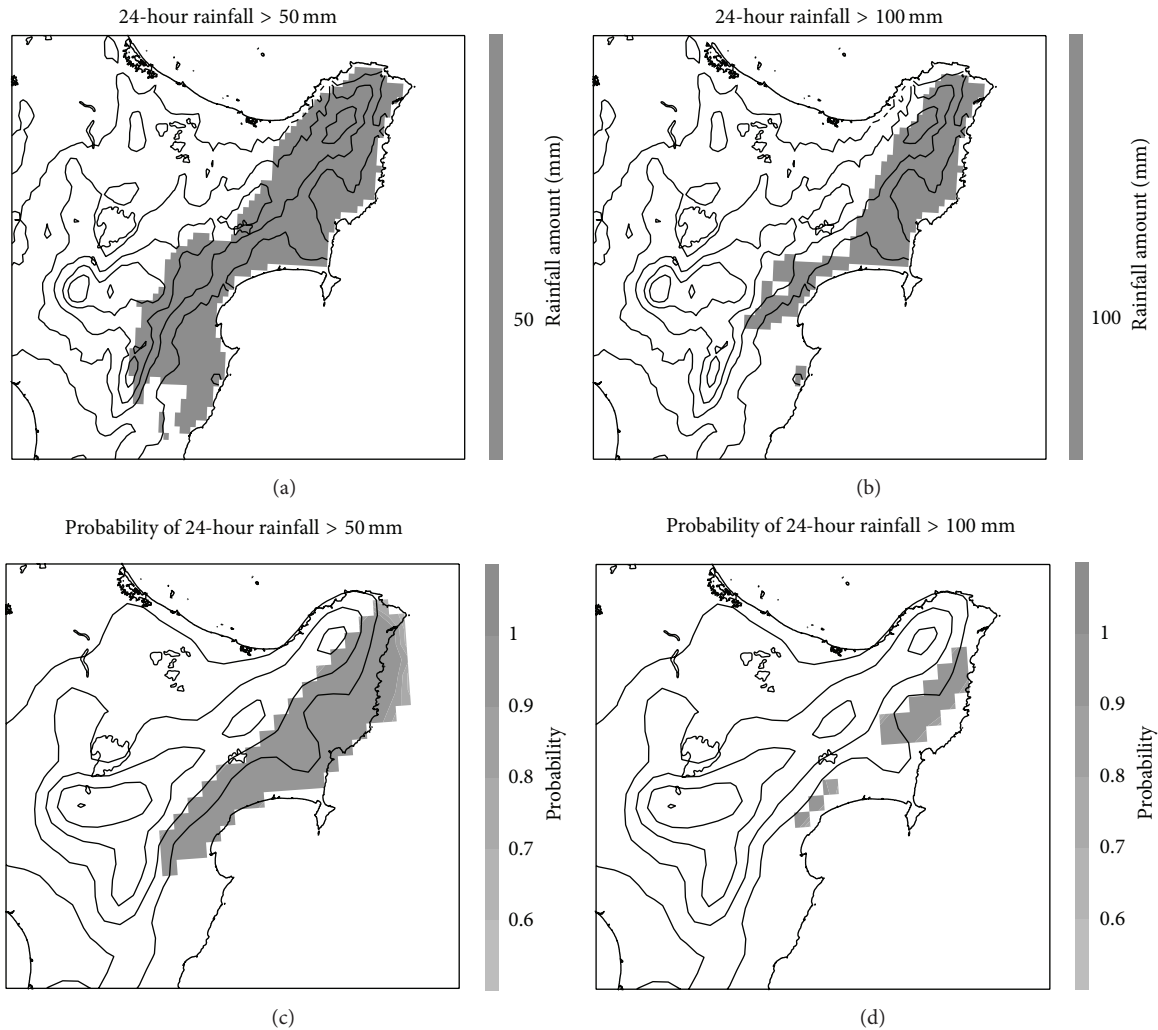


FIGURE 4: 24-hour rainfall amount (mm) valid at 0900 NZST 14 October 2010 greater than 50 mm (a) and 100 mm (b) from NIWA 0.05-degree grid point rainfall analysis. Occurrence probability higher than 0.6 for the corresponding forecasted 24-hour rainfall greater than 50 mm (c) and 100 mm (d) with analysis at 0600 NZST. Thin solid lines denote terrain contours with a 250-meter interval.

than 0.6, a large area on the windward side of the South Island (Figure 5(c)), corresponded well to most of the areas with observed daily rainfall greater than 50 mm (Figure 5(a)). Observed daily rainfall greater than 100 mm occurred only over a small area on the windward side (Figure 5(b), the small shading area in the circle). The ensemble based forecast of daily rainfall amount greater than 100 mm with probability equal to 0.6 also showed a small area (Figure 5(d), the shading area in the circle) close to that in Figure 5(b).

These analyses suggest that probability of greater than 0.6 of occurrence of rainfall greater than some threshold from the ensemble is a good predictor for heavy rainfall in New Zealand. Compared with Case 1, the ensemble performed better for Case 2, especially for daily rainfall greater than 100 mm. In fact, using the 0.05-degree grid point rainfall analysis, the RMSE of the ensemble mean for daily rainfall greater than 50 mm was 78 mm and 111 mm for Case 2 and for Case 1, respectively. The reason for the better performance

of the heavy rainfall forecast over the South Island by the ensemble will be further analysed in Sections 4.2 and 5.

4. Statistical Analysis

In this section, the ensemble RMSE, ME, and categorical skill scores for two rainfall categories are presented. The first category includes events in which either simulated or observed daily rainfall is equal to or higher than 50 mm (also called heavy rainfall). Because there were only 35 days for each experiment, a second threshold of 20 mm/day (mod-heavy rainfall) was chosen to ensure a sample size sufficient for statistically robust results. Daily rainfall observations (valid at 0900 NZST) at 630 sites over New Zealand during the 35 days were used.

4.1. The Whole Country. The ability of the different ensemble members (and ensemble means) to correctly predict rainfall

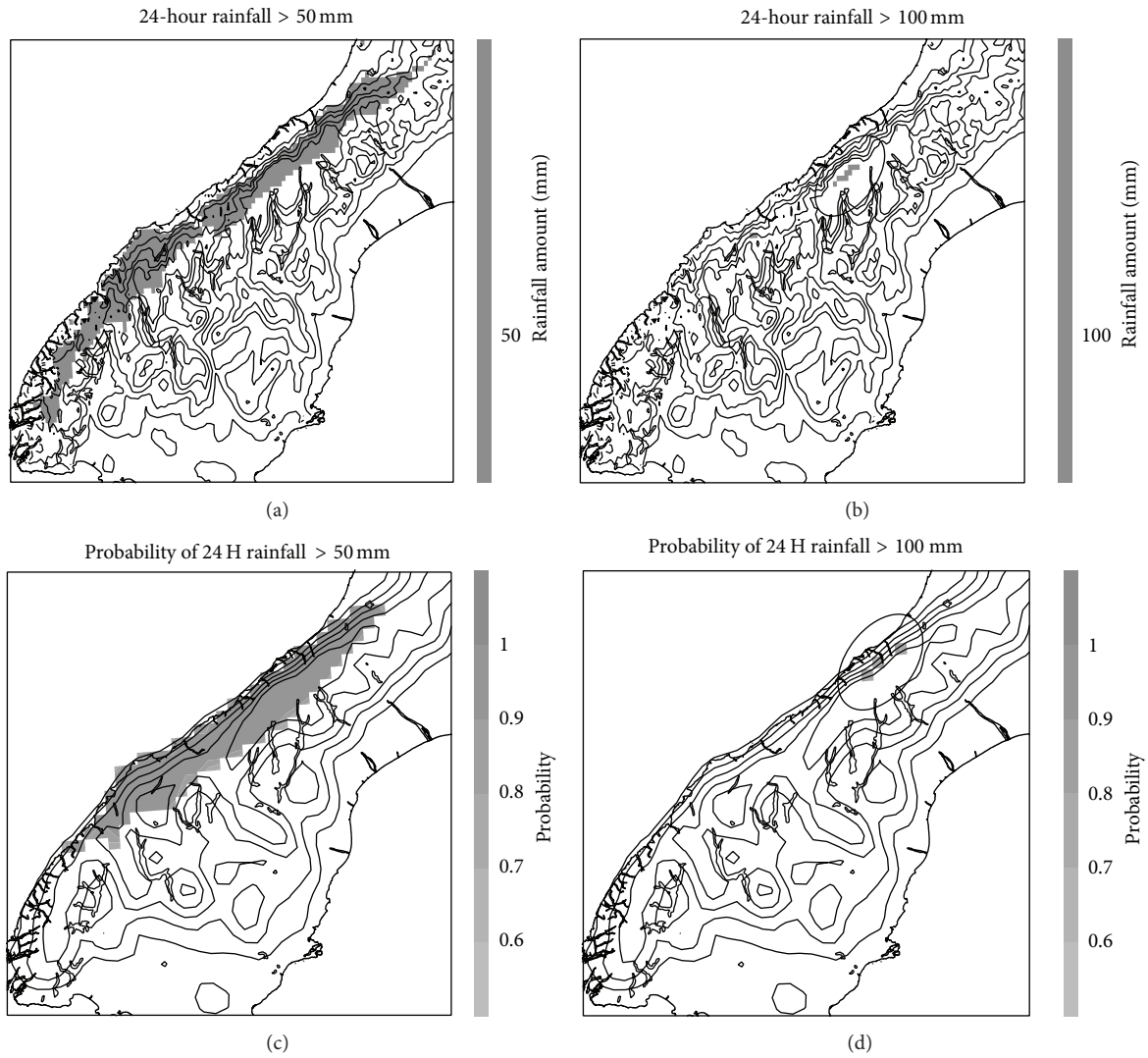


FIGURE 5: Same as Figure 3 but for 24-hour rainfall valid at 0900 NZST 29 September. Some shading areas in the circle of (b) had 24-hour rainfall greater than 100 mm and in the circle of (d) had occurrence probability higher than 0.6 for 24-hour rainfall greater than 100 mm.

TABLE 3: Contingency table for the ensemble mean (MM) for daily rainfall thresholds of 20 mm and 50 mm for the whole country (NZ), the North Island (NI), and the South Island (SI).

Observed		Forecast					
		NZ		NI		SI	
		Yes	No	Yes	No	Yes	No
Yes	20 mm	2965	2063	1193	849	1772	1214
No		2219	81565	1127	34295	1092	47270
Yes	50 mm	446	389	237	110	209	279
No		510	87467	223	36894	287	50573

events for the two different thresholds was investigated by converting the forecasts and observations into binary events. Contingency tables for the ensemble mean (MM) at these two thresholds are shown in Table 3. Figure 6 shows the categorical performance diagram for mod-heavy and heavy rainfall over all of New Zealand. MM has the highest critical

success index and the lowest false alarm ratio as compared with each member for both thresholds.

However, from Figure 6, it can be seen that the MM frequency bias for heavy rainfall is worse than for almost all of the individual members. That is, the improvement in FAR has not been matched by an improvement in hit rate, resulting in

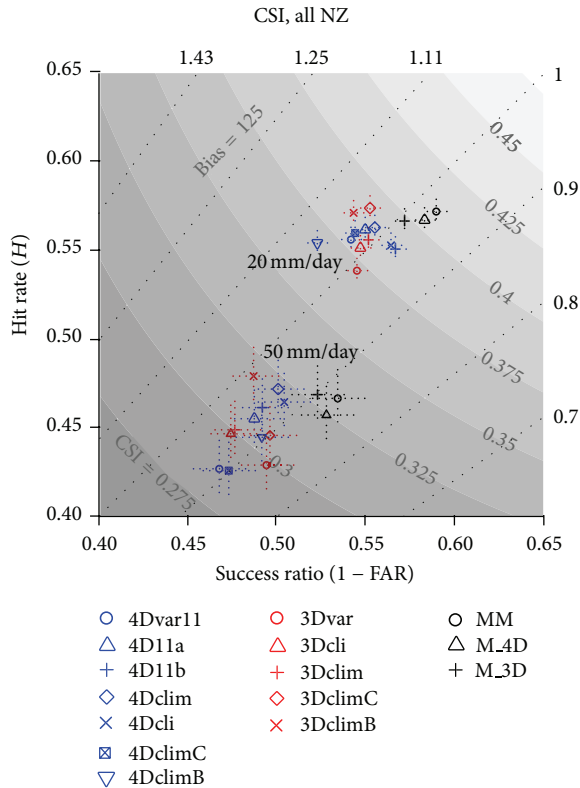


FIGURE 6: Performance diagram comparing mod-heavy and heavy rainfall for all of NZ. CSI is shown by the shaded contours and bias by the grey dotted lines. The dotted uncertainty bars show the one standard deviation error in hit rate and success ratio.

a greater tendency for MM to underpredict the occurrence of heavy rainfall events. The ability to improve the CSI by hedging, that is, by reducing the frequency of forecasted events as outlined above, is one of the undesirable properties of the CSI. The Peirce skill score (PSS) is a categorical metric which does not have this property and is also base rate independent (insensitive to the sample climatology).

Peirce skill scores are shown in the ROC diagrams in Figures 7(a) and 7(c) which contain the mod-heavy and heavy rainfall results, respectively, for all of New Zealand. In contrast to CSI, PSS does not show the ensemble mean MM as being significantly better than any of the individual members. For the mod-heavy threshold, MM has the highest score, but it is the same as 3DclimC within uncertainties. For heavy rainfall, MM does not have the best PSS, but, within uncertainties, it is not worse than any of the individual members.

While it has many desirable properties, PSS is not always appropriate as it tends to meaningless values for vanishingly rare events (known as degeneracy). Ferro and Stephenson [28] developed the symmetric extremal dependence index (SEDI), in turn based on the extreme dependency score proposed by Stephenson et al. Both of these metrics are nondegenerate, but the SEDI has the advantage as it is base rate independent and difficult to hedge. Figures 7(b) and 7(d)

contain the same data as Figures 7(a) and 7(c) except that the shading represents the SEDI instead of the PSS. From these diagrams it can be seen that, in contrast to the CSI and PSS, the magnitude of the SEDI is similar for both mod-heavy and heavy rainfall. In addition, the SEDI implies that for mod-heavy rainfall MM shows a larger improvement over the individual ensemble members and for heavy rainfall it is similar to the best performing members.

Figure 8 shows the RMSE over the whole country for all ensemble members. For mod-heavy rainfall, the RMSE of the ensemble mean (MM) was smaller than that of each member; the largest was ~ 26.0 mm for 4dvar11, about 1.8 mm higher than MM. The difference in the RMSE between each member and MM was statistically significant at the 95% level using the t -test.

For heavy rainfall, the RMSE of the MM (~ 43 mm) was smaller than that for all members except for 3Dcli (~ 43.0 mm). The largest RMSE was 46.5 mm for 4dvar11, about 3.5 mm higher than the MM. Except for 3Dcli and 4DclimB, the difference in the RMSE between each member (except for 3Dcli) and MM was statistically significant at 95% level using a t -test.

These results indicate that the ensemble mean is better than any of the individual ensemble members for forecasting mod-heavy rainfall over New Zealand. For heavy rainfall, the performance of the ensemble mean is better or similar to the best performing members. The small difference in the performance of the ensemble system between mod-heavy rainfall and heavy rainfall may be due to the smaller observation number for the latter (Table 3).

For the two daily rainfall categories, the mean errors (ME, forecast-observations) showed consistent negative values for each member (Figure 8(b)), especially for heavy rainfall, indicating that parts of the heavy rainfall forecast errors come from the negative bias. In addition to model physics, the relatively low model resolution (~ 12 km) is most likely another reason for the underestimation of rainfall. This will be further analysed in the following section and Section 5.

A possible reason for this improvement seen in the simple ensemble mean may be that it is simply due to the smoothing effect of calculating the mean of the 12 members. In other words, taking any member of the system and doing spatial smoothing, the improvement achieved might be as much as that from the ensemble mean. To investigate this possibility a 9-point smoother was applied three times to the rainfall forecast for each ensemble member and compared with the unsmoothed (Figure 9) via their RMSE. For mod-heavy rainfall, the 9-point smoother decreased the RMSE (Figure 9(a)) by 0.1–0.5 mm for each member. For MM, the smoother increased the RMSE by ~ 0.2 mm. The improvement of MM over each member was 0.5–1.6 mm for RMSE, much larger than that of each member achieved by the 9-point smoother. In contrast, for heavy rainfall the smoother significantly increased the RMSE for each member and MM by 0.8–2.0 mm. These facts indicate that the improvement of the simple ensemble mean in mod-heavy rainfall and heavy rainfall was mainly achieved from the simple ensemble system, not by the smoothing effect.

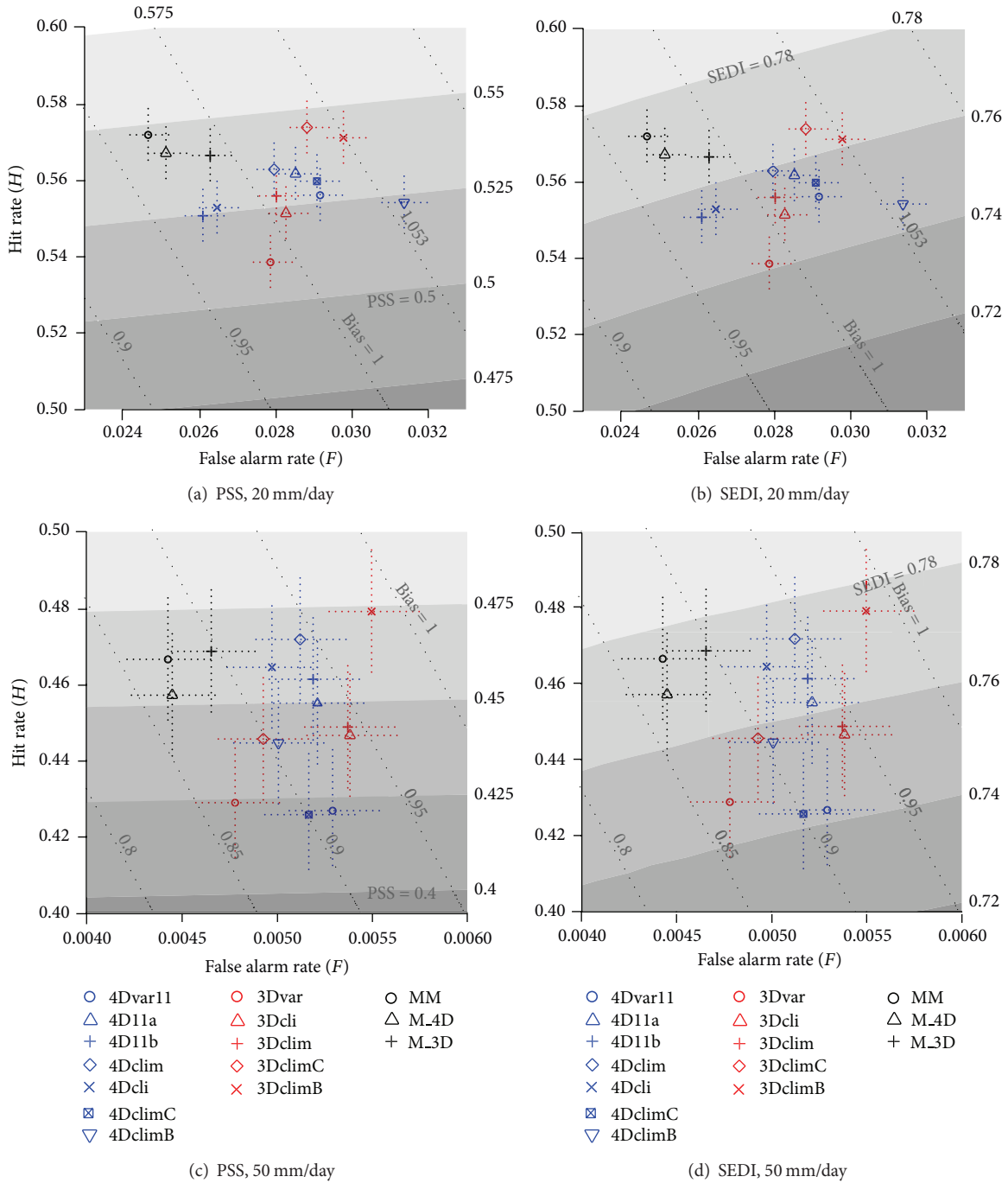


FIGURE 7: Relative operating characteristic (ROC) diagrams including all of New Zealand for the mod-heavy (a and b) and heavy (b and c) rainfall thresholds. Bias is shown by the grey dotted lines and two different measures of forecast skill, PSS (a and c) and SEDI (b and d), are shown with shading.

4.2. *Different Regions.* The results for the North and South Island ensemble mean (MM) compared to the individual members are consistent with those found for the full country. That is the forecast skill of the MM, by various measures, and is similar to or better than any individual member and the frequency bias has been reduced compared to the majority of members (not shown).

The RMSE and ME of the North and South Island results for the subset of events that were forecast correctly

or observed are shown in Figure 10 for mod-heavy rainfall and Figure 11 for heavy rainfall. For the North Island at both rainfall thresholds, MM has the lowest RMSE and for the South Island only 3Dcli has a lower RMSE than MM.

Here, a question needs to be answered is in which island (the North Island versus the South Island) the performance of the ensemble is better? The total number of rainfall observation sites and heavy rainfall observations were different between the two islands. It is not appropriate to use

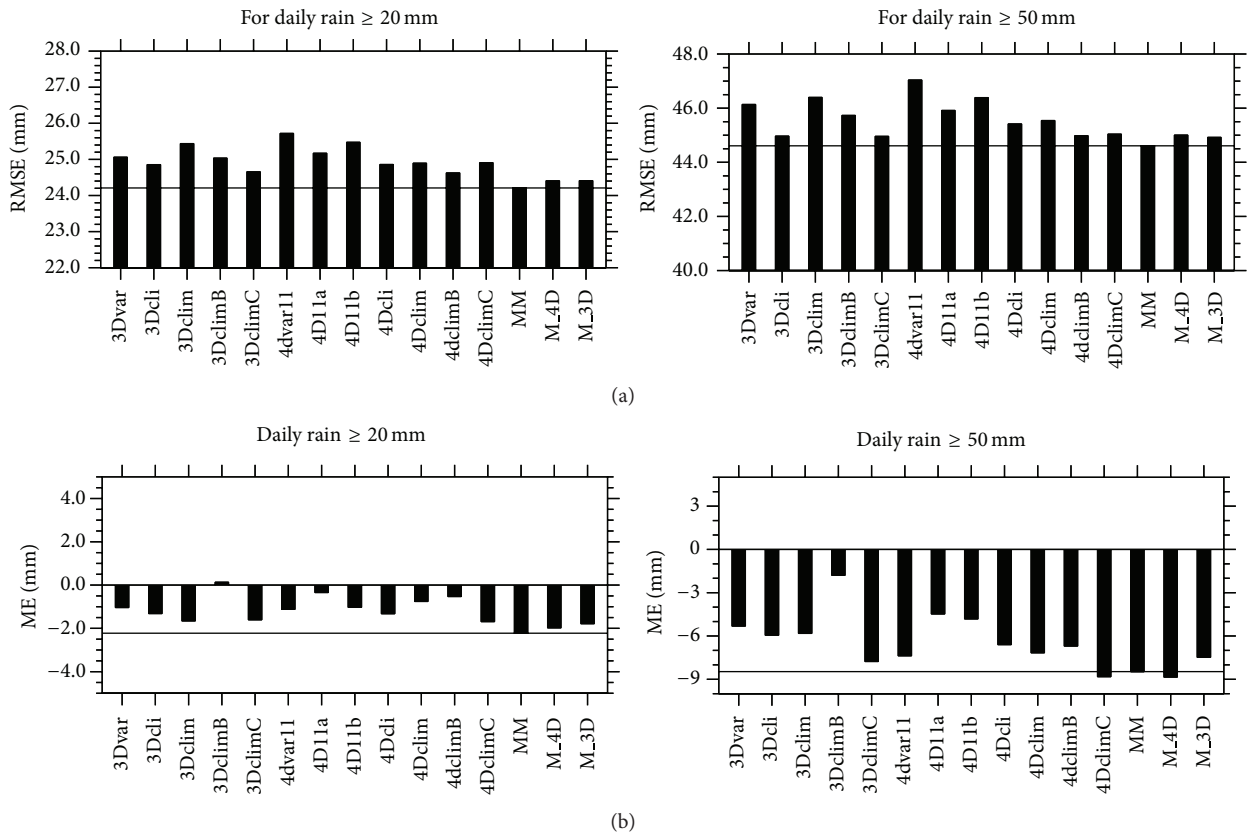


FIGURE 8: Root mean square errors (RMSE, (a)) and mean errors (ME, (b)) of daily rainfall at 630 stations for all simulations. Refer to Table 1 for the meaning of each member. MM denotes the ensemble mean of the 12 members. M_4D and M_3D denote the ensemble mean of the seven 4Dvar members and the five 3Dvar members, respectively. The solid line denotes the value of MM, the same hereafter.

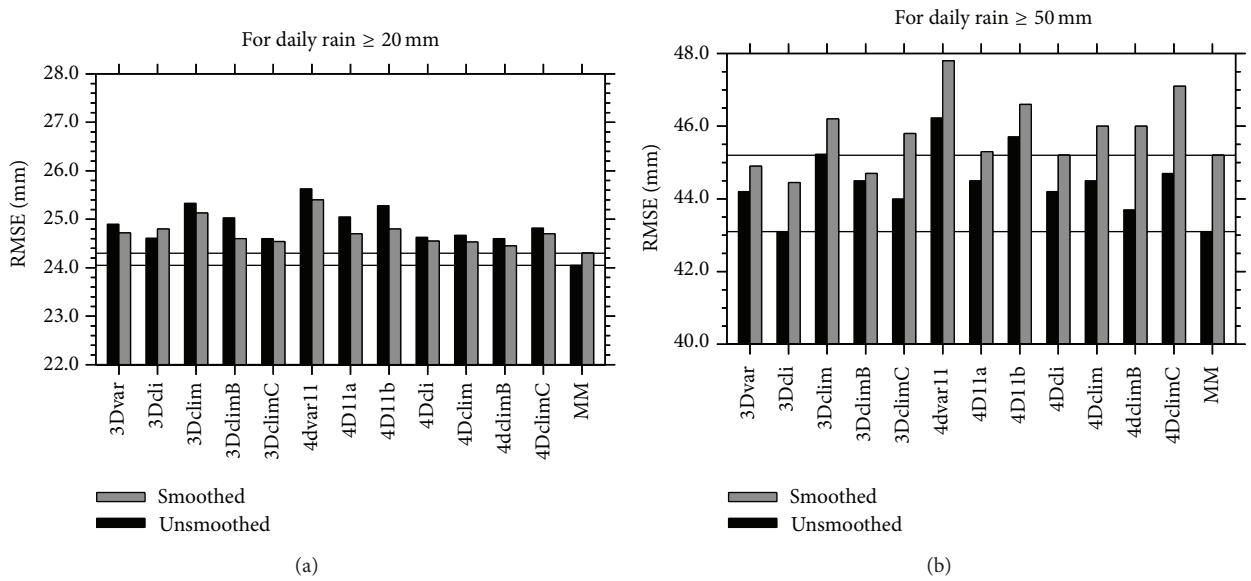


FIGURE 9: The RMSE of simulated (a) mod-heavy rainfall and (b) heavy rainfall for the whole country for smoothed forecasted rainfall (grey bars) using 9-point smooth three times and unsmoothed forecasted rainfall (dark bars).

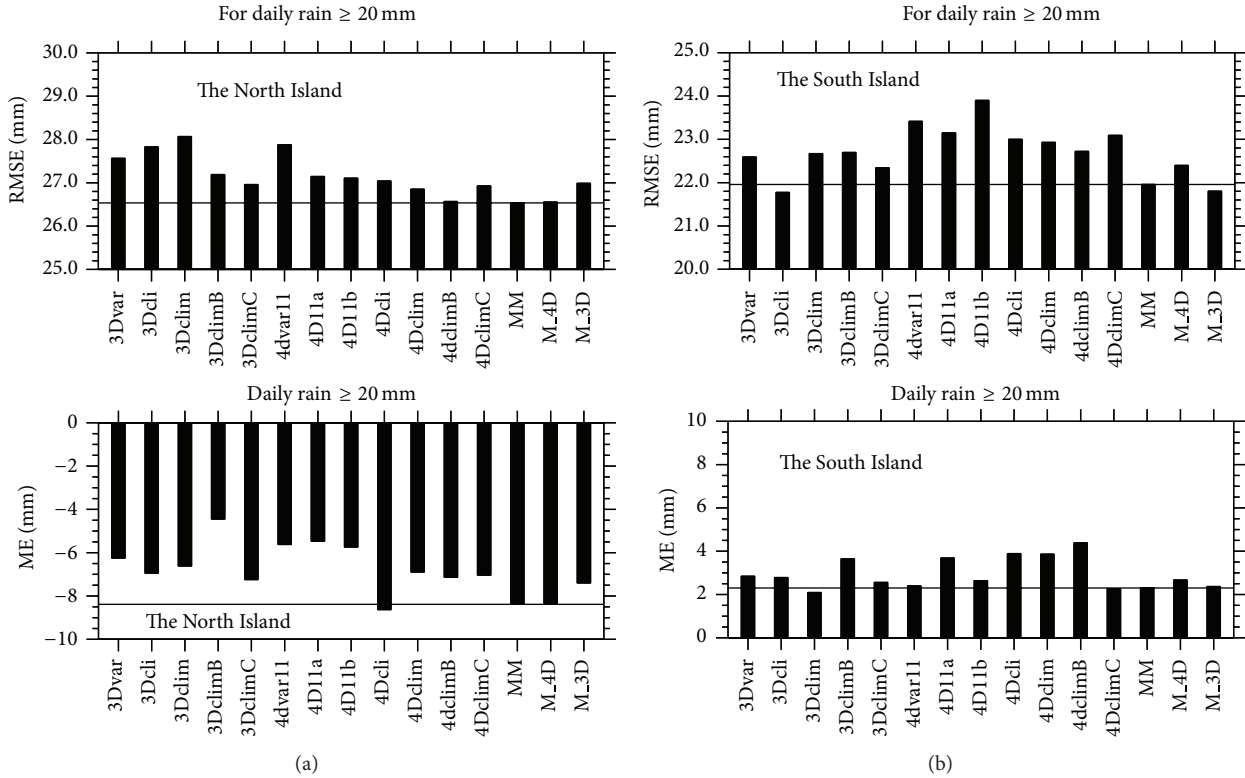


FIGURE 10: As in Figure 8 but for mod-heavy rainfall over the North Island (a) and over the South Island (b).

the forecasting skill analysis with only two rainfall categories to do the evaluation. Instead, RMSE and ME that can quantitatively show the real magnitude of rainfall forecasted errors are used.

For mod-heavy rainfall, the North Island had an RMSE of 26.5 mm for MM (Figure 10), whilst it was only 21.9 mm for South Island (Figure 10). For each member, the RMSE of rainfall was larger than 26.9 mm over the North Island; however, it was smaller than 23.5 mm for each member over the South Island. For mod-heavy rainfall, the ME of MM was 2.2 mm over the South Island, a positive bias much smaller than the negative bias (−8.2 mm) over the North Island. The magnitude of ME was almost the same for each member and the MM. For mod-heavy rainfall, ME accounted for more than 20% of the RMSE over the North Island, but only about 10% of the RMSE over the South Island.

For heavy rainfall (Figure 11), the RMSE of the MM was 50.0 mm over the North Island, whilst it was only ~36.9 mm for the South Island. The RMSE for each member was more than 50.5 mm over the North Island, whilst it was smaller than 40.5 mm over the South Island. ME was 2.5 mm over the South Island, a bias much smaller than that (−24 mm) over the North Island. The ME of each member and the MM accounted only about 10% of the RMSE over the South Island, but about 40% of the RMSE over the North Island.

In terms of RMSE and ME, the ensemble system performed better over the South Island than over the North Island for both mod-heavy and heavy rainfall. Over the North Island, the pronounced negative bias of the simulated rainfall

is a major factor leading to the worse performance of the ensemble. As described earlier, a major difference between the North Island and the South Island is the shape, height, and horizontal scale of mountains. These results indicate that mountains can significantly affect the performance of the ensemble system in moderate to heavy rainfall prediction and will be further discussed in the following section.

5. Discussion

The shape (horizontal aspect ratio and mountain height) of mountains affects the patterns and regimes of airflow past mountains [29–32] and significantly affects rainfall amount and rainfall distribution (e.g., [33–36]). As described earlier, the South Island has a relatively uniform mountain range (the Southern Alps), running some 600 km down the length of South Island and covering more than half its width, which the prevailing westerly airflow has to cross (Figure 1(b)). In contrast, the North Island has multiple ranges of hills and mountains giving it fewer clear-cut windward or lee side regions (Figure 1(a)). The spatial scales of the mountains of the North Island are smaller than those of the Southern Alps; as a result, a better description of mountain dynamic forcing (e.g., orographic lifting) exists for the latter in NZLAM (12 km resolution) than for the former. In addition, circulations associated with airflow past a larger mountain tend to have larger spatial scale. This leads to better description of the air flow patterns forced by the Southern Alps than those forced by the mountains of the North Island, in NZLAM. Thus,

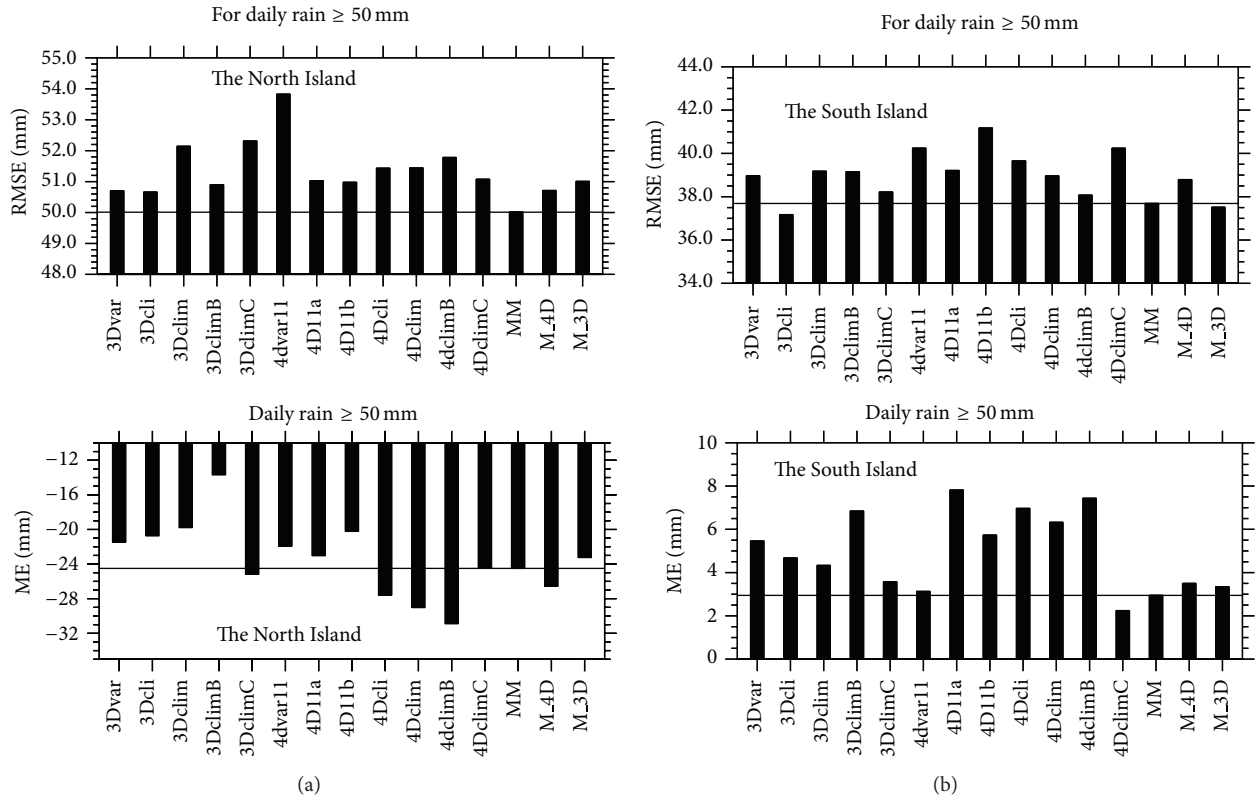


FIGURE 11: As in Figure 8 but for heavy rainfall over the North Island (a) and over the South Island (b).

the Southern Alps having uniform shape and larger spatial scales compared to the mountains of the North Island is most likely the reason for the better performance of the ensemble for the South Island.

In New Zealand, orographic lifting plays an important role in heavy rainfall occurrence. As described earlier, large negative biases of simulated moderate to heavy rainfall were found over the North Island and accounted for 20–40% of the errors. This suggests that, for the current resolution (~ 12 km) of NZLAM, the orographic lifting was underestimated for the North Island. In fact, even for the South Island, relatively large RMSE and ME were found for mod-heavy and heavy rainfall as described earlier. Part of the rainfall prediction errors was due to the rainfall prediction bias, especially for heavy rainfall. Revell et al. [37] indicated that a resolution of 5 km or higher would be needed to adequately describe the vertical motion forcing of the mountains. Therefore, a higher model resolution (preferably ≤ 5 km) than 12 km is needed for a New Zealand operational RES system for heavy rainfall prediction.

6. Conclusion

In this study, 12 experiments using the state of the art 3Dvar and 4Dvar techniques were combined as a temporary regional ensemble system. This is the first attempt at conducting ensemble prediction of rainfall directly from a regional weather modelling system in New Zealand. The objective is

to investigate the effect of data assimilation and ensemble method on moderate and heavy rainfall forecasts and the effect of mountains on the performance of a RES in New Zealand.

The RMSE, ME, and several categorical verification metrics for daily rainfall were analysed based on two thresholds, 20 mm (mod-heavy rainfall) and 50 mm (heavy rainfall). In total 630 sites in New Zealand with daily rainfall observations were used. These analyses showed that, at the same model resolution, the simple ensemble performs better than any of the 12 experiments for mod-heavy rainfall prediction. The overall better performance of the ensemble was also found for heavy rainfall. Two heavy rainfall cases showed that, in most areas with heavy rainfall, the ensemble showed a high probability of occurrence (≥ 0.6), due to the significant effect of mountains on heavy rainfall occurrence in New Zealand. This suggested that ensemble prediction of heavy rainfall using ensemble mean and occurrence probability would be a useful tool in New Zealand.

Under the prevailing westerly airflow for most time of a year, much rainfall occurs on the west side of the country, especially for the South Island with a steep west mountain slope that has a southwest-northeast orientation. Our analyses indicated that mountains can significantly affect the performance of this ensemble system with smaller errors (or RMSE) and bias (or ME) of forecasted mod-heavy rainfall and heavy rainfall over the South Island than over the North Island. This result is nothing new, but it indicates that a 12 km

model resolution of the current temporary ensemble system is not high enough to well predict heavy rainfall in New Zealand. A ~5 km or higher model resolution is required for a better performance of an operational RES system in New Zealand for heavy rainfall prediction.

This work implies that for regional ensemble prediction of heavy rainfall in complicated mountainous areas, in addition to the initial conditions, model resolution also needs to be properly treated according to the mountain scales. For future research, a similar RES with higher model resolution (~5 km or finer) will be conducted to search for the optimum resolution over New Zealand. Beyond accounting for the uncertainties in initial conditions using data assimilation, the RES will also account for uncertainties in the lower boundary conditions (including SST, soil moisture, and vegetation cover) and the lateral boundary conditions.

Conflict of Interests

The authors declare that there is no conflict of interests regarding the publication of this paper.

Acknowledgments

This research was carried out under research collaboration SC0128 with the UK Met Office and funded by the New Zealand Foundation for Research, Science and Technology under Contract C01X081. The authors thank the anonymous reviewers for comments that have helped them improve the quality of this paper.

References

- [1] F. Molteni, R. Buizza, T. N. Palmer, and T. Petroliagis, "The ECMWF ensemble prediction system: methodology and validation," *Quarterly Journal of the Royal Meteorological Society*, vol. 122, no. 529, pp. 73–119, 1996.
- [2] M. Leutbecher and T. N. Palmer, "Ensemble forecasting," *Journal of Computational Physics*, vol. 227, no. 7, pp. 3515–3539, 2008.
- [3] Z. Toth and E. Kalnay, "Ensemble forecasting at NMC: the generation of perturbations," *Bulletin of the American Meteorological Society*, vol. 74, no. 12, pp. 2317–2330, 1994.
- [4] Z. Toth and E. Kalnay, "Ensemble forecasting at NCEP and the breeding method," *Monthly Weather Review*, vol. 125, no. 12, pp. 3297–3319, 1997.
- [5] S. L. Mullen and D. P. Baumhefner, "Monte Carlo simulations of explosive cyclogenesis," *Monthly Weather Review*, vol. 122, no. 7, pp. 1548–1567, 1994.
- [6] P. L. Houtekamer and H. L. Mitchell, "Data assimilation using an ensemble Kalman filter technique," *Monthly Weather Review*, vol. 126, no. 3, pp. 796–811, 1998.
- [7] A. Aksoy, F. Zhang, and J. W. Nielsen-Gammon, "Ensemble-based simultaneous state and parameter estimation with MM5," *Geophysical Research Letters*, vol. 33, no. 12, Article ID L12801, 2006.
- [8] F. Zhang, Y. Weng, Y.-H. Kuo, J. S. Whitaker, and B. Xie, "Predicting typhoon morakot's catastrophic rainfall with a convection-permitting mesoscale ensemble system," *Weather and Forecasting*, vol. 25, no. 6, pp. 1816–1825, 2010.
- [9] Y. Jung, M. Xue, G. Zhang, and J. M. Straka, "Assimilation of simulated polarimetric radar data for a convective storm using the ensemble Kalman filter. Part II: impact of polarimetric data on storm analysis," *Monthly Weather Review*, vol. 136, no. 6, pp. 2246–2260, 2008.
- [10] A. Aksoy, D. C. Dowell, and C. Snyder, "A multicase comparative assessment of the ensemble Kalman filter for assimilation of radar observations. Part I: storm-scale analyses," *Monthly Weather Review*, vol. 137, no. 6, pp. 1805–1824, 2009.
- [11] D. M. Barker, "Southern high-latitude ensemble data assimilation in the Antarctic Mesoscale Prediction System," *Monthly Weather Review*, vol. 133, no. 12, pp. 3431–3449, 2005.
- [12] Z. Meng and F. Zhang, "Tests of an ensemble Kalman filter for mesoscale and regional-scale data assimilation. Part III. Comparison with 3DVAR in a real-data case study," *Monthly Weather Review*, vol. 136, no. 2, pp. 522–540, 2008.
- [13] R. D. Torn and G. J. Hakim, "Performance characteristics of a pseudo-operational ensemble Kalman filter," *Monthly Weather Review*, vol. 136, no. 10, pp. 3947–3963, 2008.
- [14] K. Sattler and H. Feddersen, "Limited-area short-range ensemble predictions targeted for heavy rain in Europe," *Hydrology and Earth System Sciences*, vol. 9, no. 4, pp. 300–312, 2005.
- [15] F.-C. Chien, Y.-C. Liu, and B. J.-D. Jou, "MM5 ensemble mean forecasts in the Taiwan area for the 2003 Mei-Yu season," *Weather and Forecasting*, vol. 21, no. 6, pp. 1006–1023, 2006.
- [16] T. N. Krishnamurti, M. K. Biswas, B. P. Mackey, R. G. Ellingson, and P. H. Ruscher, "Hurricane forecasts using a suite of large-scale models," *Tellus Series A: Dynamic Meteorology and Oceanography*, vol. 63, no. 4, pp. 727–745, 2011.
- [17] P. A. Chessa, G. Ficca, M. Marrocu, and R. Buizza, "Application of a limited-area short-range ensemble forecast system to a case of heavy rainfall in the mediterranean region," *Weather and Forecasting*, vol. 19, no. 3, pp. 566–581, 2004.
- [18] M. Vich and R. Romero, "Multiphysics superensemble forecast applied to Mediterranean heavy precipitation situations," *Natural Hazards and Earth System Science*, vol. 10, no. 11, pp. 2371–2377, 2010.
- [19] Y. Yang, M. Uddstrom, M. Revell et al., "Numerical simulations of effects of soil moisture and modification by mountains over New Zealand in summer," *Monthly Weather Review*, vol. 139, no. 2, pp. 494–510, 2011.
- [20] S. Webster, M. Uddstrom, H. Oliver, and S. Vosper, "A high-resolution modelling case study of a severe weather event over New Zealand," *Atmospheric Science Letters*, vol. 9, no. 3, pp. 119–128, 2008.
- [21] Y. Yang, M. Uddstrom, M. Revell, P. Andrews, and R. Turner, "Amplification of the impact of assimilating ATOVS radiances on simulated surface air temperatures over canterbury by the Southern Alps, New Zealand," *Monthly Weather Review*, vol. 140, no. 4, pp. 1367–1384, 2012.
- [22] F. Rawlins, S. P. Ballard, K. J. Bovis et al., "The met office global four-dimensional variational data assimilation scheme," *Quarterly Journal of the Royal Meteorological Society*, vol. 133, no. 623, pp. 347–362, 2007.
- [23] S. Webster, A. R. Brown, D. R. Cameron, and C. P. Jones, "Improvements to the representation of orography in the Met Office Unified Model," *Quarterly Journal of the Royal Meteorological Society*, vol. 129, no. 591, pp. 1989–2010, 2003.
- [24] T. Davies, M. J. P. Cullen, A. J. Malcolm et al., "A new dynamical core of the Met Office's global and regional modelling of the atmosphere," *Quarterly Journal of the Royal Meteorological Society*, vol. 131, no. 608, pp. 1759–1782, 2005.

- [25] A. C. Lorenc, S. P. Ballard, R. S. Bell et al., "The Met. Office global three-dimensional variational data assimilation scheme," *Quarterly Journal of the Royal Meteorological Society*, vol. 126, no. 570, pp. 2991–3012, 2000.
- [26] M. J. P. Cullen, "A demonstration of cycled 4D-Var in the presence of model error," *Quarterly Journal of the Royal Meteorological Society*, vol. 136, no. 651, pp. 1379–1395, 2010.
- [27] P. J. Roebber, "Visualizing multiple measures of forecast quality," *Weather and Forecasting*, vol. 24, no. 2, pp. 601–608, 2009.
- [28] C. A. T. Ferro and D. B. Stephenson, "Extremal dependence indices: improved verification measures for deterministic forecasts of rare binary events," *Weather and Forecasting*, vol. 26, no. 5, pp. 699–713, 2011.
- [29] R. B. Smith, "Hydrostatic airflow over mountains," *Advances in Geophysics*, vol. 31, pp. 1–41, 1989.
- [30] P. K. Smolarkiewicz and R. Rotunno, "Low Froude number flow past three-dimensional obstacles. Part II: upwind flow reversal zone," *Journal of the Atmospheric Sciences*, vol. 47, no. 12, pp. 1498–1511, 1990.
- [31] H. Ólafsson and P. Bougeault, "Nonlinear flow past an elliptic mountain ridge," *Journal of the Atmospheric Sciences*, vol. 53, no. 17, pp. 2465–2489, 1996.
- [32] M. H. Bauer, G. J. Mayr, I. Vergeiner, and H. Pichler, "Strongly nonlinear flow over and around a three-dimensional mountain as a function of the horizontal aspect ratio," *Journal of the Atmospheric Sciences*, vol. 57, no. 24, pp. 3971–3991, 2000.
- [33] Y. Yang and Y.-L. Chen, "Effects of terrain heights and sizes on island-scale circulations and rainfall for the island of Hawaii during HaRP," *Monthly Weather Review*, vol. 136, no. 1, pp. 120–146, 2008.
- [34] S.-H. Chen and Y.-L. Lin, "Orographic effects on a conditionally unstable flow over an idealized three-dimensional mesoscale mountain," *Meteorology and Atmospheric Physics*, vol. 88, no. 1–2, pp. 1–21, 2005.
- [35] B. A. Colle, "Sensitivity of orographic precipitation to changing ambient conditions and terrain geometries: an idealized modeling perspective," *Journal of the Atmospheric Sciences*, vol. 61, no. 5, pp. 588–606, 2004.
- [36] J. Stein, "Exploration of some convective regimes over the Alpine orography," *Quarterly Journal of the Royal Meteorological Society*, vol. 130, no. 597, pp. 481–502, 2004.
- [37] M. J. Revell, J. H. Copeland, H. R. Larsen, and D. S. Wratt, "Barrier jets around the Southern Alps of New Zealand and their potential to enhance alpine rainfall," *Atmospheric Research*, vol. 61, no. 4, pp. 277–298, 2002.

Research Article

Impact of Argo Observation on the Regional Ocean Reanalysis of China Coastal Waters and Adjacent Seas: A Twin-Experiment Study

Caixia Shao,^{1,2} Lili Xuan,² Yingzhi Cao,² Xiaojian Cui,² and Siyu Gao²

¹National University of Defense Technology, Hunan, Changsha 410073, China

²Key Laboratory of Marine Environmental Information Technology, SOA, National Marine Data and Information Service, Tianjin 300171, China

Correspondence should be addressed to Caixia Shao; shaocx@163.com

Received 18 December 2014; Revised 10 February 2015; Accepted 10 March 2015

Academic Editor: Shaoqing Zhang

Copyright © 2015 Caixia Shao et al. This is an open access article distributed under the Creative Commons Attribution License, which permits unrestricted use, distribution, and reproduction in any medium, provided the original work is properly cited.

A regional ocean reanalysis system of China coastal waters and adjacent seas, called CORA (China ocean reanalysis), has been recently developed at the National Marine Data and Information Service (NMDIS). In this study, based on CORA, the impact of Argo profiles on the regional reanalysis is evaluated using a twin-experiment approach. It is found that, by assimilating Argo observations, the reanalysis quality is much improved: the root mean square (RMS) error of temperature and salinity can be further reduced by about 10% and the RMS error of current can be further reduced by 18%, compared to the case only assimilating conventional in situ temperature and salinity observations. Consistent with the unique feature of Argo observations, the temperature is improved in all levels and the largest improvement of salinity happens in the deep ocean. Argo profile data have a significant impact on the regional ocean reanalysis through improvements of both hydrographic and dynamic fields.

1. Introduction

With the gradual increasing of global ocean Argo (Array for Real-Time Geostrophic Oceanography) profile [1], a lot of researches on Argo application have been carried out by scientists and many useful results have been achieved. Argo data especially have been widely used in operational oceanography, such as ocean data assimilation, forecast, and reanalysis [2–5].

Therefore, it is also necessary to evaluate the impact of Argo on ocean data assimilation. Many research works have addressed this issue. Studies related to this topic can be roughly divided into two classes. The first class is known as Observing System Experiments (OSEs). In these experiments, an ocean analysis, in which all available data are assimilated, serves as a reference. And permutations of combinations of the available observation systems are used in an analysis, in which one observational system is excluded from the analysis, so providing an estimate of the impact of the omitted observational system by comparing the analysis

with the reference. In this field lots of works have been done to evaluate the Argo impact. For example, Vidard et al. [6] assessed the relative importance of the tropical in situ mooring arrays (TAO, TRITON, and PIRATA), XBTs, and the developing Argo float network on global ocean analysis and seasonal forecasts, showing a major role for the moorings and in some ways a smaller contribution from Argo than might have been expected. Balmaseda et al. [7] assessed the impact of Argo on ECMWF operational ocean analyses and evaluated the information content of Argo temperature and salinity data, gauged in terms of influence on the ocean state and the skill of seasonal forecasts. Oke and Schiller [8] assessed the relative importance of Argo temperature and salinity profiles, sea-surface temperature, and altimetric sea-level anomalies for constraining upper-ocean T and S properties and mesoscale variability of sea-level anomalies in an eddy resolving ocean reanalysis in the Australian region. Yan et al. [9] assessed the impacts of XBT, TAO, altimetry, and Argo observations on the tropical Pacific ocean data assimilation. Huang et al. [10] investigated the impact

of Argo salinity profiles on the NCEP Global Ocean Data Assimilation System (GODAS) in the tropical Indian Ocean.

The second class is known as Observing System Simulation Experiments (OSSEs). The OSSE approach was first adopted by the meteorological community not only to assess the impact of observations but also to optimize the design of observing systems and observing networks in order to improve numerical weather predictions. Oceanographic applications to Argo impact assessment and Argo profile sampling strategy optimization have been reported by several literatures. For example, Schiller et al. [11] performed OSSE using OGCM output to assess sampling strategies for the Argo array in the Indian Ocean. Griffa et al. [12] and Raicich [13] quantitatively investigated the impact of assimilating temperature and salinity profiles from Argo floats in the Mediterranean Sea using the OSSE approach. Zhang et al. [14] show the potential of Argo profiles to initialize the Atlantic meridional overturning circulation (MOC) which is an important source of multidecadal climate variability and trends. Dunstone and Smith [15] investigated the impact of assimilating different amounts of atmosphere and ocean data, including Argo profile, on decadal climate prediction skill through a set of idealized model experiments and found that the upper 2000 m temperature and salinity observations currently provided by the Argo array of floats are potentially well suited to initializing decadal climate predictions.

However, most of the above literatures concentrate on the impact of Argo profiles on data assimilation for global ocean rather than for the marginal seas, such as the coastal waters of China and adjacent seas.

A regional ocean reanalysis experiment which is focused on the coastal waters of China and adjacent seas has already been started a few years ago by National Marine Data and Information Service (NMDIS). The present ocean reanalysis system (China ocean reanalysis, CORA) for this area is achieved, and a dataset package of sea surface height (SSH), three-dimensional (3D) temperature, salinity, and currents in this area (<http://www.cmoc-china.cn/>) is developed [5, 16].

In this paper, based on the CORA system, data assimilation identical twin-experiment approach used in OSSE technique is employed to evaluate the impact of Argo data on temperature, salinity, and current reanalysis results of China coastal waters and adjacent seas. The data assimilation identical twin-experiment approach is one of the useful methods to evaluate the impact of the ocean observation system [14, 17]. But here we do not touch Argo observing systems optimal design which will be our future goal. Ocean dynamic model, ocean data assimilation scheme used in CORA, and twin-experiment configuration are described in the following section. Section 3 mainly discusses the impact of Argo on the ocean reanalysis of this area and conclusions are given in Section 4.

2. Twin Experiment of Reanalysis

The OSSE technique consists of identical twin experiments [13], in which data extracted from a reference model run is assimilated into other runs of the same model with different initial conditions. The convergence of the other runs towards

the first one is measured to quantify the data assimilation effectiveness in driving the model with “wrong” initial conditions towards the reference, and the comparison between analyses with and without Argo profiles data assimilated can provide an estimate of impact of Argo profiles. All runs are driven by the same external forcing.

2.1. Ocean Dynamic Model. The NMDIS-developed parallel version of Princeton Ocean Model with generalized coordinate system (POMgcs) [18, 19] serves as the ocean dynamical model in CORA. The original version of POMgcs, known as POM (Princeton Ocean Model), has been widely used [20, 21]. Following [22, 23], the wave breaking parameterization of Mellor and Blumberg [24] is introduced into POMgcs to deepen the mixed temperature surface layer. The tidal generating potential and tidal open boundary condition of eight major tidal constituents ($M_2, S_2, N_2, K_2, K_1, O_1, P_1,$ and Q_1) are added to this model to simulate tidal effect.

The study area extends from 10°S to 52°N in latitude and from 99°E to 150°E in longitude. The model grid spacing is varied from $1/2^\circ$ to $1/8^\circ$ and the area with the highest horizontal resolution $1/8^\circ$ extends from 19°N to 33°N in latitude and from 117°E to 130°E in longitude. Due to the huge range and the complicated bathymetry of the study area, the hybrid coordinate of POMgcs is in use, in conformity with the study of Mellor et al. [18]. The σ -level vertical grid is used in the area with local depth less than 200 m, that is, the continental shelf, to form a terrain-following vertical grid. While in the area with local depth greater than 200 m, that is, slope area and deep sea area, in order to simulate satisfactorily the upper mixed layer and thermocline, most of the vertical levels at the upper and middle ocean are set to z -level, and at the level depth greater than 0.9 proportion of the local depth only a few vertical levels near seafloor are set to terrain-following σ -level to represent the seafloor preferably to avoid the stair-step effect. Coarse vertical level near seafloor can make the hydrostatic consistency criteria satisfied. There are 33 vertical levels with a maximum depth of 4500 m. The vertical z -level grid is listed in Table 1.

The twin experiment of reanalysis spanned four years from January 2005 to December 2008. SODA (Simple Ocean Data Assimilation) monthly-mean product of each year serves as the open boundary condition for sea surface height (SSH), temperature, salinity, and current. Wind field uses Quick Scatterometer (QuikSCAT) wind field of daily Level 3 data with the horizontal resolution being $1/4^\circ$. And heat flux field comes from the National Centers of Environment Prediction (NCEP) reanalysis version 1 product.

2.2. Ocean Data Assimilation Scheme. The ocean data assimilation scheme used in CORA is a sequential three-dimensional variational (3D-Var) analysis scheme designed to assimilate temperature and salinity using a multigrid framework [5, 16]. This sequential 3D-Var analysis scheme can extract long and short wavelength information in turn quickly from observations system and provide objective and accurate analysis. The basic idea of this data assimilation scheme can be referred to in [25–30]. In this study, 9 level grids are applied from $2 \times 2 \times 2$ (only one big cell containing

TABLE 1: The vertical z -level grid list.

Level	Depth (m)								
1	2.5	8	125	15	450	22	1100	29	2500
2	10	9	150	16	500	23	1200	30	3000
3	20	10	200	17	600	24	1300	31	3500
4	30	11	250	18	700	25	1400	32	4000
5	50	12	300	19	800	26	1500	33	4500
6	75	13	350	20	900	27	1750		
7	100	14	400	21	1000	28	2000		

the whole study domain) to $257 \times 257 \times 33$ (the horizontal interval is about $0.2^\circ \times 0.24^\circ$, and the vertical resolution is the same as that of the model). The smooth penalty parameter, weighing how strong the smoothing term will be, is set to 0.005. Square of the simulated observational error, which will be discussed in the next section, is used to specify the diagonal element of observational error covariance matrix, while the off-diagonal element is set to zero. Fifty iterations are employed to every level grid’s optimization.

The basic idea proposed by Troccoli et al. [31] is employed to make salinity adjustment during temperature assimilation. In this scheme, the T - S relation is basically conserved during the temperature data assimilation; and salinity measurements are assimilated to adjust the T - S relation only if such measurements are available. Following Troccoli et al. [31], a latitudinal filter has been applied to the salinity increments so that the whole salinity increment is applied only within 30° of the equator. Outside this region, the weight given to the salinity adjustment diminishes linearly to zero at latitudes poleward of north edge of model domain. This is done to avoid implementing the salinity correction scheme in areas where the stratification is weak and $S(z)$ persistence is more appropriate.

The assimilation is performed every day and a seven-day time window is used to incorporate as many observations as possible.

2.3. True Fields and “Observation” Construction. With the open boundary conditions and meteorological driving force described above and with CORA reanalysis of January 1, 2005 serving as the initial field, 4-year integration is carried out from January 2005 to December 2008 by using the NMDIS-developed parallel version of POMgcs. Then the 4-year simulation results serve as the true fields for comparing the following twin-experiment reanalysis results to evaluate the impact of Argo on this regional reanalysis.

Following the method in [14], “observations” needed in reanalysis twin-experiment are constructed by interpolating the above true fields to the temporal and spatial information of real temperature or salinity observation networks, including Nansen bottle, conductivity-temperature-depth (CTD), and various bathythermograph (BT) and Argo profiles. It should be noted that CTD and Argo profiles may have both temperature and salinity observations, while the others profiles may only have temperature observations. And compared to CTD profiles, Argo profiles may be distributed relatively homogeneously. A Gaussian white noise with the mean and

standard deviation being 0.0°C (0.0 psu) and 1.0°C (0.2 psu), respectively, is added to temperature (salinity) “observation” as random error simulation. The imposed white noise attempts to account for random measurement errors of the observing system. For simplicity, “observations” which have the temporal and spatial information of Nansen bottle, CTD, and variety of BT are called “conventional observations,” and those with Argo temporal and spatial information are called “Argo observations.” Distributions of “observations” used in reanalysis twin experiment from January 2005 to December 2008 are shown in Figure 1. It is found that dense “observations” in this study domain are mainly distributed around Japan, including Japan Sea and Kuroshio to the south of Japan. In other areas, except for some moored profiles which have many data, “observations” are scarcely distributed. In China coastal waters especially, including Bohai Sea (BS), Yellow Sea (YS), East China Sea (ECS), and South China Sea (SCS), most areas are measured only once per year. “Argo observations” are homogeneously distributed in the Pacific Ocean to the east of Ryukyu Island. Along with current, several Argos drifted to the west of Ryukyu Island and in 2008 several Argos drifted in the northern SCS.

2.4. Twin-Experiment Configuration. Three twin experiments are carried out to study the impact of Argo on temperature, salinity, and current reanalysis results of the China coastal waters and adjacent seas. They all use the setup ocean model described in Section 2.1 and data assimilation scheme described in Section 2.2 and are subject to the same meteorological driving force and open boundary condition as those used in construction of true field and all run for the period from January 2005 to December 2008. However, the initial condition is different from that of true field. Observational climatology of temperature and salinity field in August serves as the initial condition for the three twin experiments and the initial sea surface height and current field are obtained by one-year diagnostic spin-up using the same model. No “observation” is assimilated in Experiment 1; that is, Experiment 1 is a free run, while Experiment 2 only assimilates “conventional observations” and Experiment 3 assimilates all the “observations” including “conventional observations” and “Argo observations.” The impact of satellite SST and SSHA on reanalysis is beyond the scope of this study, so no experiment assimilates satellite observations.

By comparing the twin-experiment daily results with the true fields, root mean square error (RMSE) for 4-year

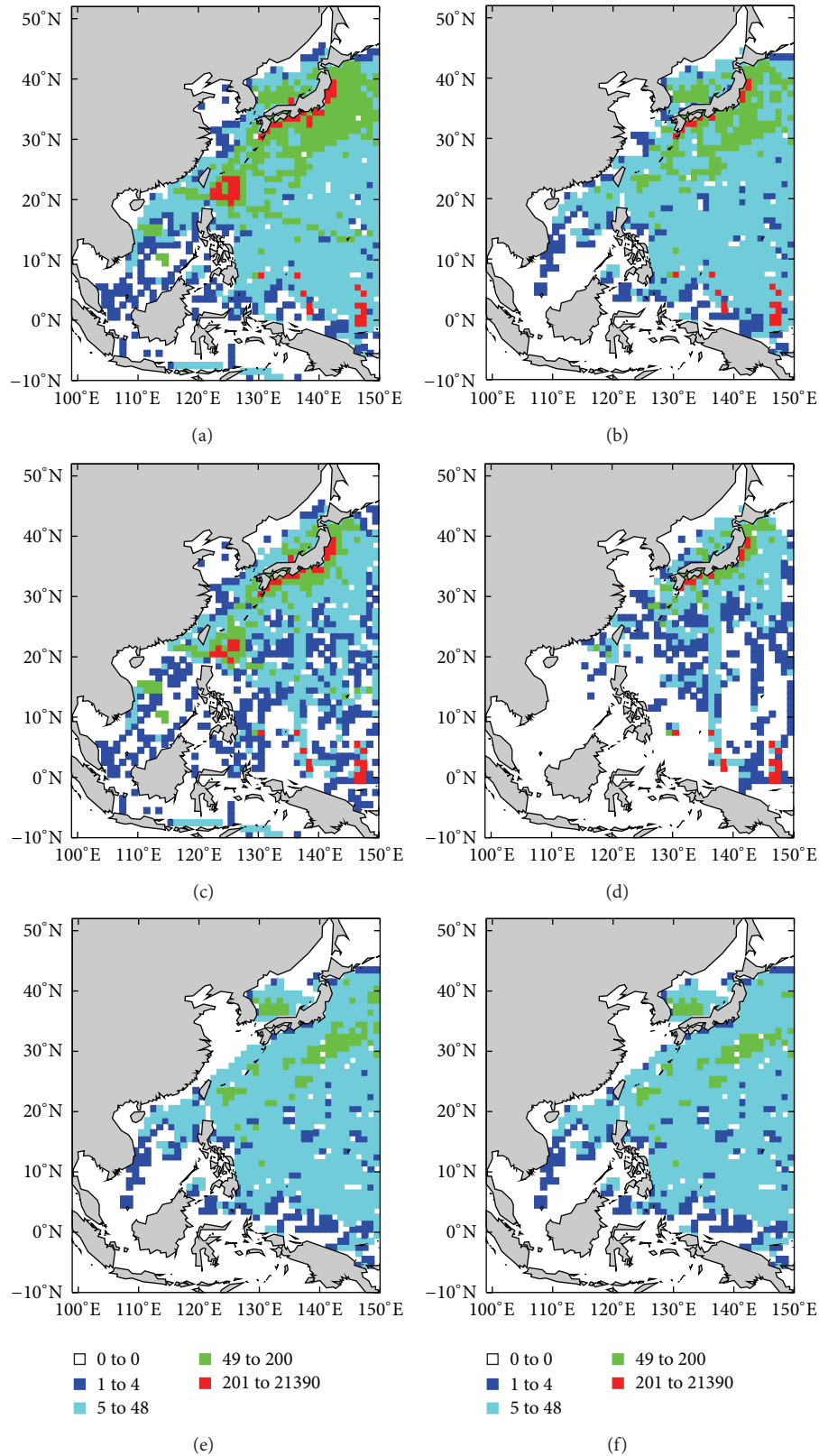


FIGURE 1: Distributions of “observations” used in reanalysis twin experiments from January 2005 to December 2008: (a), (c), and (e) are temperature “observations”; (b), (d), and (f) are salinity “observations.” (a) and (b) are for all “observations”; (c) and (d) “conventional observations”; (e) and (f) “Argo observations.” Color square represents the number of profiles.

average over the whole domain RMSE_{whole}, horizontal distribution of RMSE RMSE_H, and vertical distribution

of RMSE RMSE_V can be calculated using the following equations, and the impact of Argo on reanalysis of this study domain can be evaluated:

$$\text{RMSE}_{\text{whole}}(F) = \sqrt{\frac{\sum_{n=1}^{NM} \sum_{k=1}^{KM} \sum_{j=1}^{JM} \sum_{i=1}^{IM} \left[\left(F_{i,j,k,n}^{\text{Exp}} - F_{i,j,k,n}^{\text{True}} \right)^2 \cdot \Delta x_{i,j,k} \cdot \Delta y_{i,j,k} \cdot \Delta z_{i,j,k} \cdot M_{i,j,k} \right]}{\sum_{n=1}^{NM} \sum_{k=1}^{KM} \sum_{j=1}^{JM} \sum_{i=1}^{IM} \left(\Delta x_{i,j,k} \cdot \Delta y_{i,j,k} \cdot \Delta z_{i,j,k} \cdot M_{i,j,k} \right)}}, \quad (1)$$

$$\text{RMSE}_H(F)_{i,j} = \sqrt{\frac{\sum_{n=1}^{NM} \sum_{k=1}^{KM} \left[\left(F_{i,j,k,n}^{\text{Exp}} - F_{i,j,k,n}^{\text{True}} \right)^2 \cdot \Delta x_{i,j,k} \cdot \Delta y_{i,j,k} \cdot \Delta z_{i,j,k} \cdot M_{i,j,k} \right]}{\sum_{n=1}^{NM} \sum_{k=1}^{KM} \left(\Delta x_{i,j,k} \cdot \Delta y_{i,j,k} \cdot \Delta z_{i,j,k} \cdot M_{i,j,k} \right)}}, \quad (2)$$

$$\text{RMSE}_V(F)_k = \sqrt{\frac{\sum_{n=1}^{NM} \sum_{j=1}^{JM} \sum_{i=1}^{IM} \left[\left(F_{i,j,k,n}^{\text{Exp}} - F_{i,j,k,n}^{\text{True}} \right)^2 \cdot \Delta x_{i,j,k} \cdot \Delta y_{i,j,k} \cdot \Delta z_{i,j,k} \cdot M_{i,j,k} \right]}{\sum_{n=1}^{NM} \sum_{j=1}^{JM} \sum_{i=1}^{IM} \left(\Delta x_{i,j,k} \cdot \Delta y_{i,j,k} \cdot \Delta z_{i,j,k} \cdot M_{i,j,k} \right)}}, \quad (3)$$

where F stands for temperature, salinity, U component, or V component of current; superscript Exp represents the result of different experiments and True the true field; IM , JM , KM , and NM are the numbers of grid points of zonal, meridional, vertical directions and the number of reanalysis days, respectively; subscripts i , j , k , and n are the grid indices of zonal, meridional, vertical, and temporal directions, respectively; Δx , Δy , and Δz are the length of zonal, meridional, and vertical directions for one grid cell, and M is a mask value with 1 representing wet grid and 0 representing dry grid.

3. Impact of Argo on Ocean Reanalysis

3.1. Impact of Argo on Temperature Reanalysis. Figures 2(a), 2(b), and 2(c) show the horizontal distribution of vertical averaged temperature RMSEs of the three twin experiments, respectively, using (2). Since no “observation” is assimilated in Experiment 1 and the initial field (climatological temperature in August) has big difference compared with the true field (CORA temperature of January 2005), the mean RMSE of temperature over whole domain is about 3.676°C using (1). The largest RMSEs appear in China coastal water, Thailand Bay, and Karimata Strait where few “observations” can support the analysis. Luzon Strait, area to the east of Taiwan, Japan Sea, and Equator area also have large RMSEs. By assimilating “conventional observations,” temperature RMSE of Experiment 2 is obviously lower than that of Experiment 1 by about 40%. By further assimilating “Argo observations,” the temperature RMSE of Experiment 3 is lower than that of Experiment 2 by about 10%; that is, the temperature RMS error of Experiment 3 is lowest among all three twin experiments. Figure 2(d) shows the difference of temperature RMSEs between Experiments 1 and 2, and Figure 2(e) shows that between Experiments 1 and 3. Therefore Figures 2(d) and 2(e) represent the improvement of Experiments 2 and 3 relative to 1, respectively. Figure 2(f) shows the difference of temperature RMSEs between Experiments 2 and 3, which represents the improvement of Experiment 3 relative to 2.

Positive value means RMSE decreasing and reanalysis improving, and, on the contrary, negative value means reanalysis degenerating. It is found that the improved area of Experiment 2 compared to 1 includes Japan Sea, Kuroshio area, area to the east of Taiwan, north part of SCS, and Equator area where many “conventional observations” can support the analysis. In addition to the above improved area, the improved area of Experiment 3 compared to 1 is further enlarged, even to eastern boundary of this study domain (Figures 2(e) and 2(f)). Figure 3(a) gives the vertical structure of temperature RMS error of these three twin experiments using (3). Figures 3(b) and 3(c) represent the improvement of Experiments 2 and 3 relative to 1, respectively, and Figure 3(d) represents the improvement of Experiment 3 relative to 2. The main improvement of Experiment 2 with only “conventional observations” assimilated concentrates in the upper level, and there is somewhat degeneration beneath 2500 m level. Considering that there is big difference between “observations” and model background, data assimilation within the upper ocean may destroy the stratification in the ocean, and abnormal mixing may be generated in the ocean, which may result in the above degeneration beneath 2500 m level in Experiment 2 with only “conventional observations.” However, the deep observations of Argo may compromise this problem. Therefore, with “Argo observation” assimilated, temperatures in all levels are improved (Figures 3(c) and 3(d)) although Argo only provides upper 2000 m observations.

3.2. Impact of Argo on Salinity Reanalysis. Since no “observations” are assimilated in Experiment 1 and the initial field (climatological August salinity) has big difference with the true field (CORA salinity of January 2005), the mean RMSE of salinity over whole domain is about 0.485 psu. Similar to that of temperature analysis, the largest RMSEs of salinity appear in China coastal water, Thailand Bay, and Karimata Strait where few “observations” can support the analysis. Luzon Strait, area to the east of Taiwan, Japan Sea, and Equator area also have large RMSEs (Figure 4(a)). By assimilating

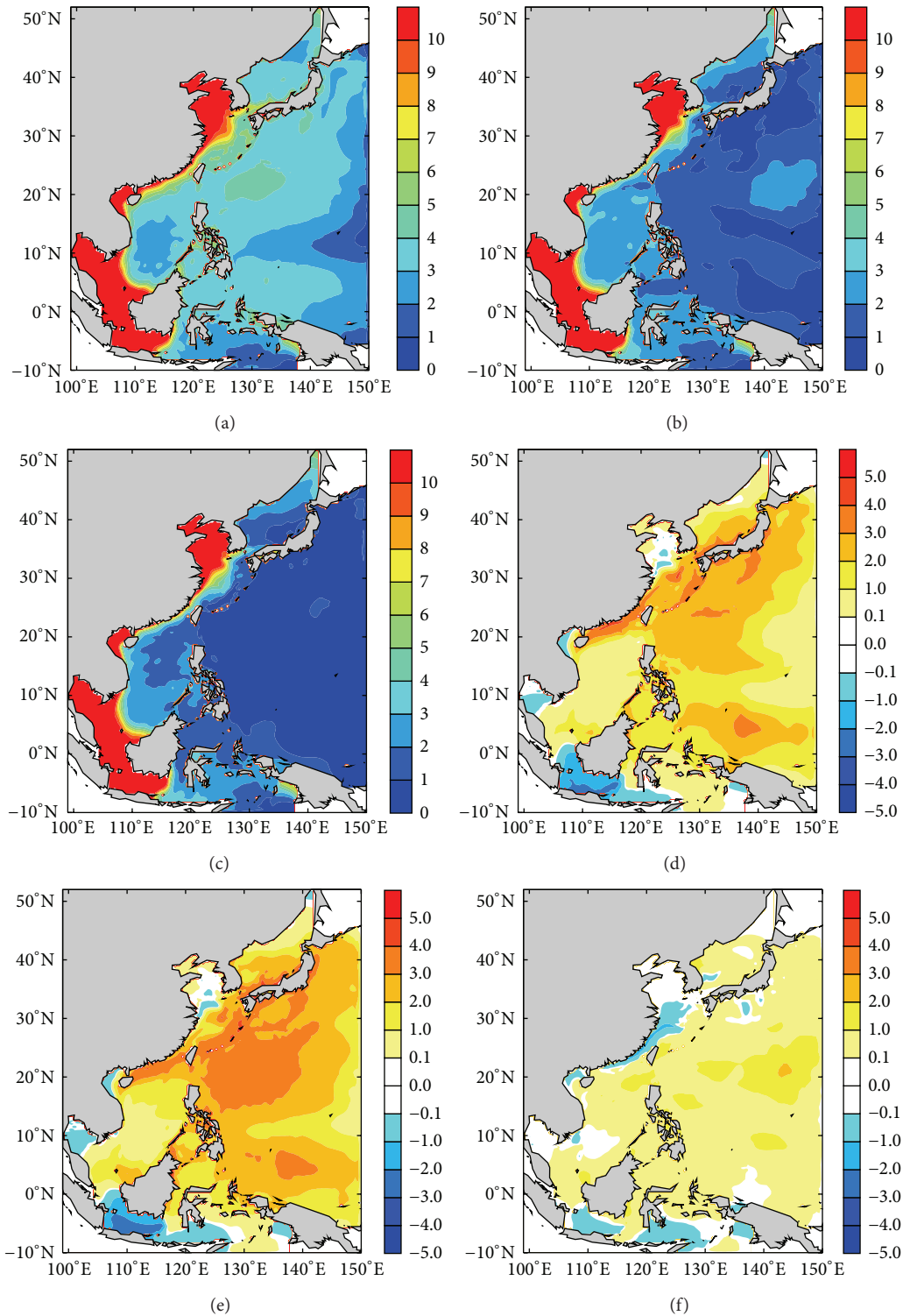


FIGURE 2: (a), (b), and (c) show the horizontal distribution of vertical averaged temperature RMSEs of three twin-experiments, respectively, using (2); (d) shows the difference of temperature RMSEs between Experiments 2 and 1, that is, Experiment 1 minus Experiment 2, and (e) is for Experiment 1 minus Experiment 3; (f) is for Experiment 2 minus Experiment 3. Unit: °C. Experiment 1 is a free run where no data is assimilated, while Experiment 2 only assimilates “conventional observations” and Experiment 3 assimilates all the “observations” including “conventional observations” and “Argo observations.”

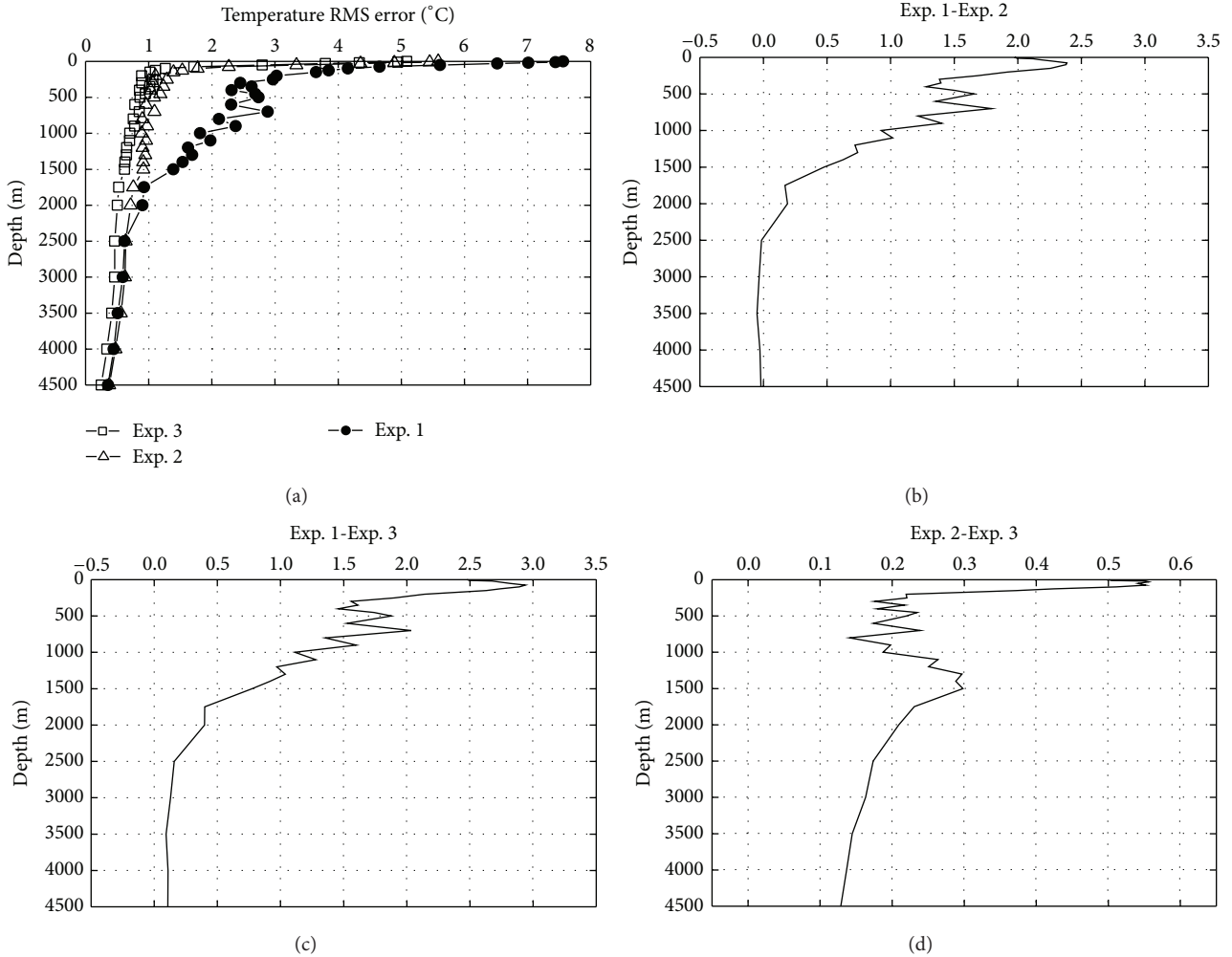


FIGURE 3: (a) The vertical structure of temperature RMSE of Experiments 1 (solid line with solid circle), 2 (solid line with hollow up-triangle), and 3 (solid line with hollow square) using (3); (b) the temperature RMSE of Experiment 1 minus that of Experiment 2; (c) is for Experiment 1 minus Experiment 3; (d) is for Experiment 2 minus Experiment 3. Unit: °C.

“conventional observations,” salinity RMSE of Experiment 2 is obviously lower than that of Experiment 1 by about 25%. By further assimilating “Argo observations,” the salinity RMSE of Experiment 3 is lower than that of Experiment 2 by about 10%; that is, the salinity RMSE of Experiment 3 is lowest among all the three twin experiments. It is found that the improved area of Experiment 2 compared to 1 includes Japan Sea, Kuroshio to the south of Japan, and area to the east of Taiwan where many “observations” can support the analysis (Figure 4(d)). Besides the above improved area, the improved area of Experiment 3 compared to 1 is further enlarged (Figure 4(e)). It can be seen from Figure 4(f), as a necessary kind of supplement to “conventional observations,” salinity data assimilation of “Argo observation” can significantly improve the salinity analysis to the east of Luzon Strait and the western part of Japan Sea. From the vertical structure of salinity RMS error of these three twin experiments (Figure 5(a)) and for the similar reason as that for temperature, the maximum RMSE is at surface, but another obvious extreme exists between 500 m and 1000 m in Experiment 1. Different from that of

temperature, although salinities in all levels are improved not only in Experiment 3 (Figure 5(c)) but also in Experiment 2 (Figure 5(b)), the maximum improvement concentrates in the middle level between 500 m and 1000 m (Figure 5(d)). Large RMSE in upper 300 m ocean mainly comes from the continental shelf (Figure 4(a)), where almost no salinity observation exists. Therefore, only a little improvement is found in the upper 300 m ocean in both Experiments 2 and 3, and Argo does not provide additional useful information to improve the salinity reanalysis on continental shelf. However, in the interior ocean, especially in the area with depth deeper than 1000 m, Argo can provide additional useful salinity observations, which can improve salinity reanalysis significantly.

3.3. *Impact of Argo on Current Reanalysis.* Since this study assimilates temperature and salinity “observations” rather than velocity “observations,” true velocity field can be added in the verification of reanalysis as an independent element (Figure 6). For both U component and V component,

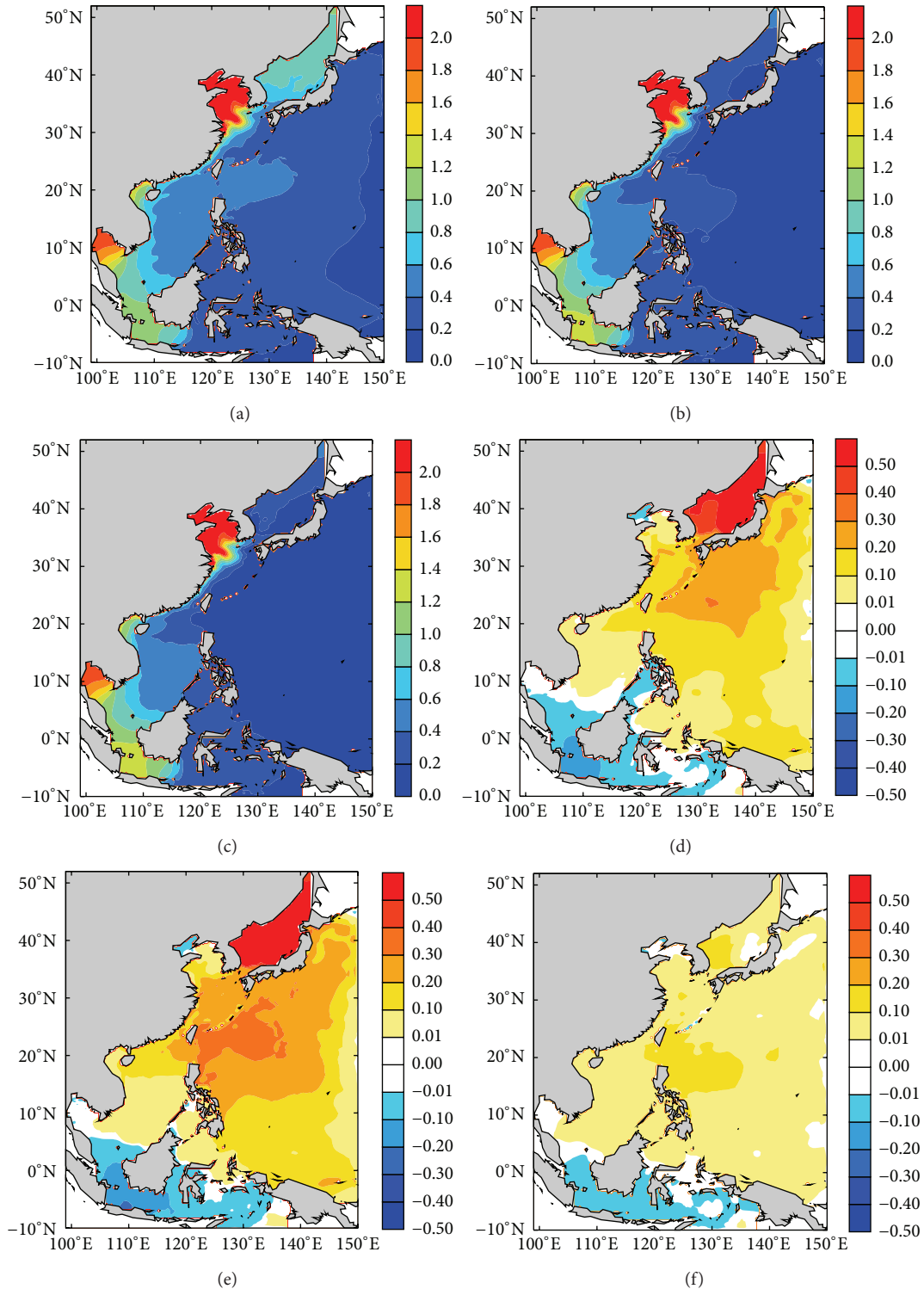


FIGURE 4: Similar to Figure 3 but for salinity. Unit: psu.

the RMSE of Experiment 1 is the biggest among these three twin experiments and that of Experiment 3 is the smallest. For U component, the RMSEs of these three twin experiments are 0.112 m/s, 0.089 m/s, and 0.069 m/s, respectively. By assimilating “conventional observations,” U component RMSE of

Experiment 2 is obviously lower than that of Experiment 1 by about 20%. By further assimilating “Argo observations,” the U component RMSE of Experiment 3 is lower than that of Experiment 2 by about 18%. For V component, the RMSEs of these three twin experiments are 0.094 m/s, 0.083 m/s,

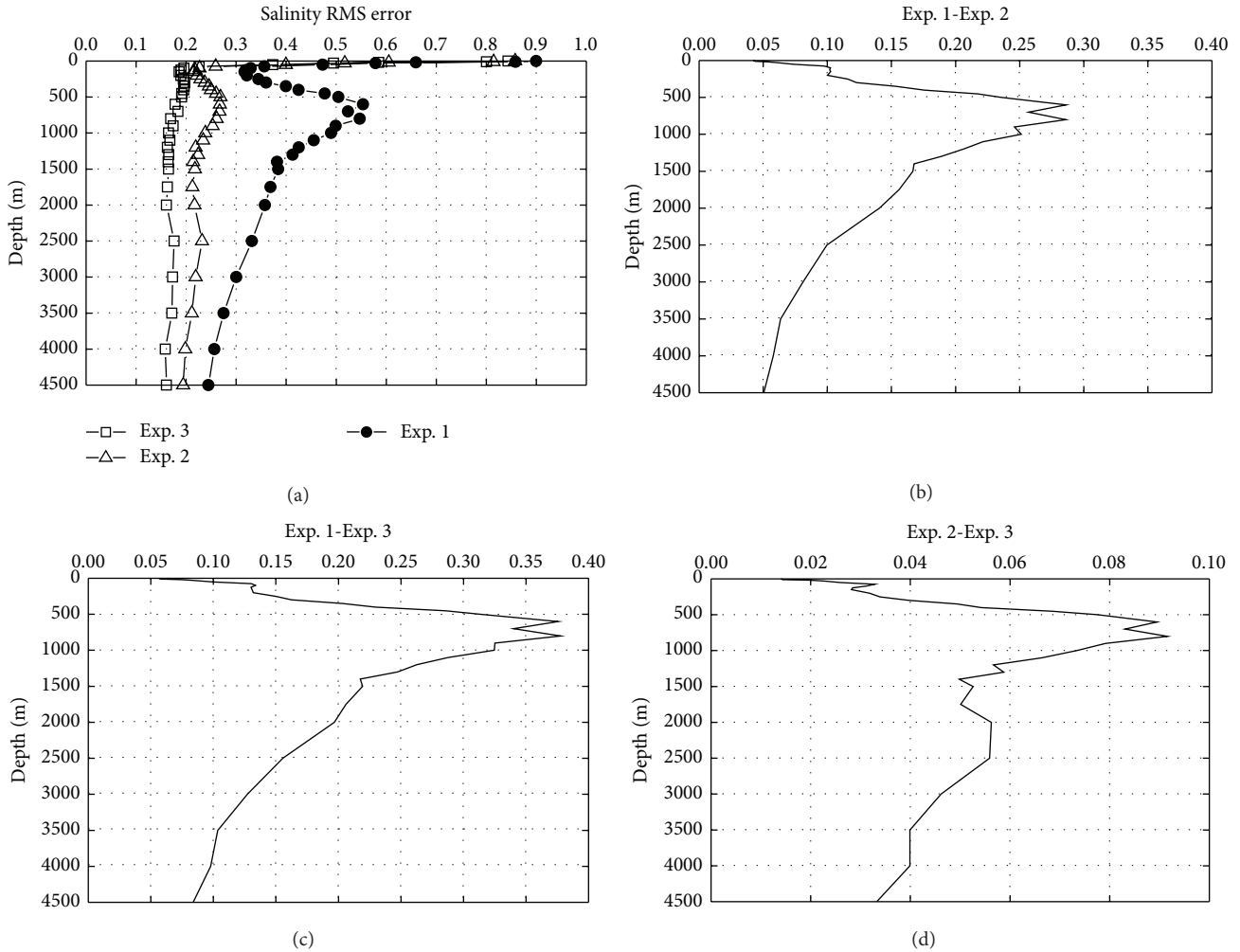


FIGURE 5: Similar to Figure 4 but for salinity. Unit: psu.

and 0.065 m/s, respectively. By assimilating “conventional observations,” V component RMSE of Experiment 2 is obviously lower than that of Experiment 1 by about 12%. By further assimilating “Argo observations,” the V component RMSE of Experiment 3 is lower than that of Experiment 2 by about 19%. Zonal flow dominates the World Ocean; however Kuroshio, the strong western boundary current, exists in this study domain, so the maximum zonal velocity and the maximum meridional velocity almost share the same value. For U component, it is found that the improvement area of Experiment 2 compared to 1 includes continental shelf area, Kuroshio, and north equator current (Figure 6(d)). Besides the above improved area, the improved area of Experiment 3 compared to 1 further includes the northwest Pacific Ocean (Figure 6(e)). The major improved area of U component by further assimilating “Argo observations” concentrates in west Pacific Ocean (Figure 6(f)). For V component, the improved area of Experiment 2 compared to 1 focuses on the strong current area (Figure 6(j)), which is different from that of U component. The major improved area of V component by further assimilating “Argo observations” concentrates in west Pacific Ocean (Figure 6(l)), which is

similar to that of U component. From Figures 7 and 8, the main improvements locate above the 2000 m level and beneath 2500 m level. In Experiment 2, between 2000 m and 2500 m, there is almost no improvement for V component and somewhat degeneration for U component. However, in Experiment 3 with “Argo observation” assimilated, U and V components for all levels are improved, and relative to Experiment 2 the main improvement concentrates in the upper 1500 m levels. The horizontal scale of the study domain is large and current velocity of most area in this study domain is small; therefore, except shallow sea, such as coastal water, geostrophic or quasigeostrophic approximation is a reasonable way for estimating current field. And under this approximation, distribution of velocity field to the first order can be determined by density field on large scale. Since the density is determined by temperature and salinity, the obvious improvement on temperature and salinity may result in the improvement on density and may sequentially result in the improvement of velocity field.

It is worth noting that although Argo profiles are mainly distributed in Pacific Ocean to the east of Ryukyu Island in this study domain, Argo data assimilation obviously

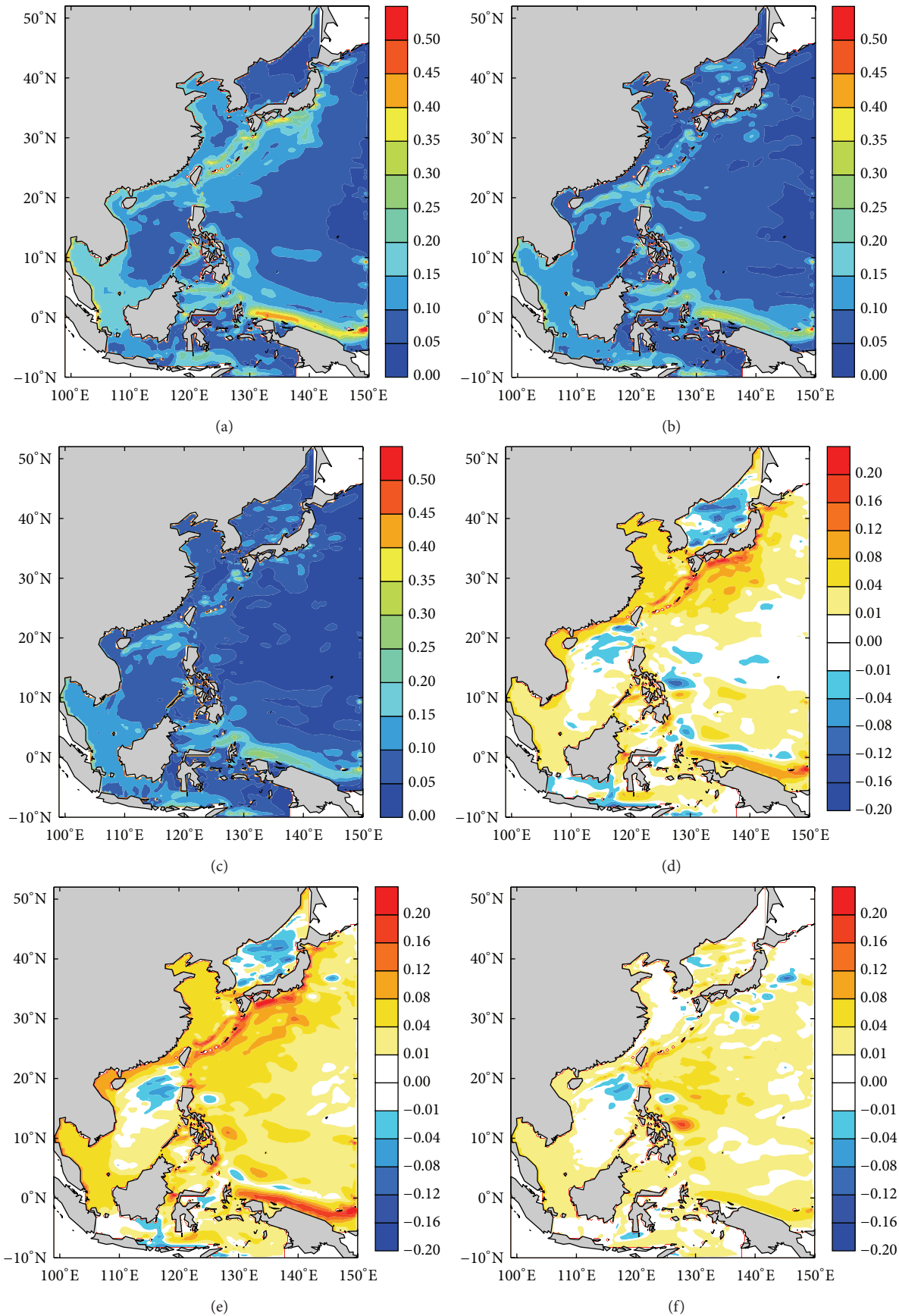


FIGURE 6: Continued.

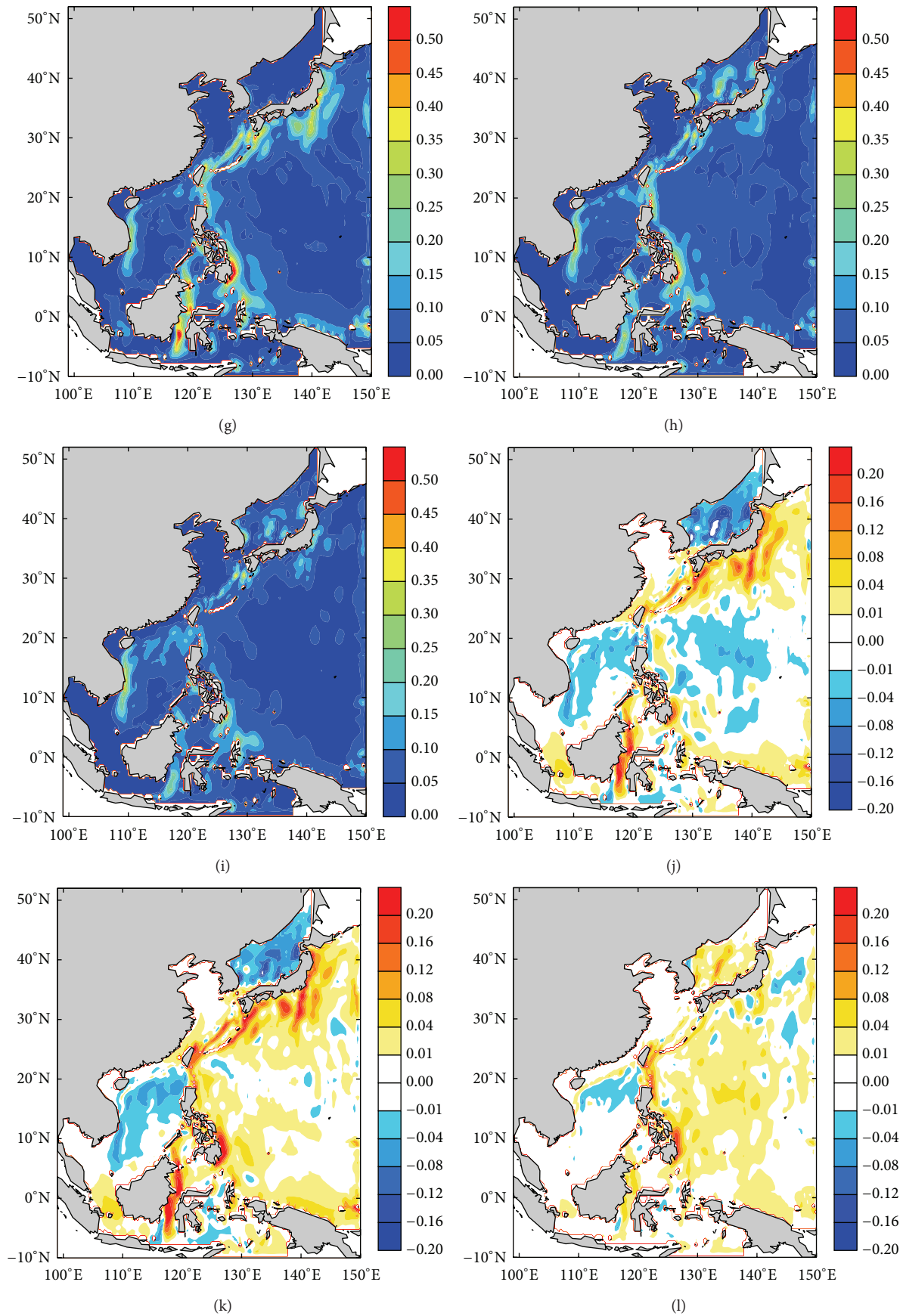


FIGURE 6: (a)–(f) are similar to Figure 3 but for U component and (g)–(l) are similar to Figure 3 but for V component. Unit: m/s.

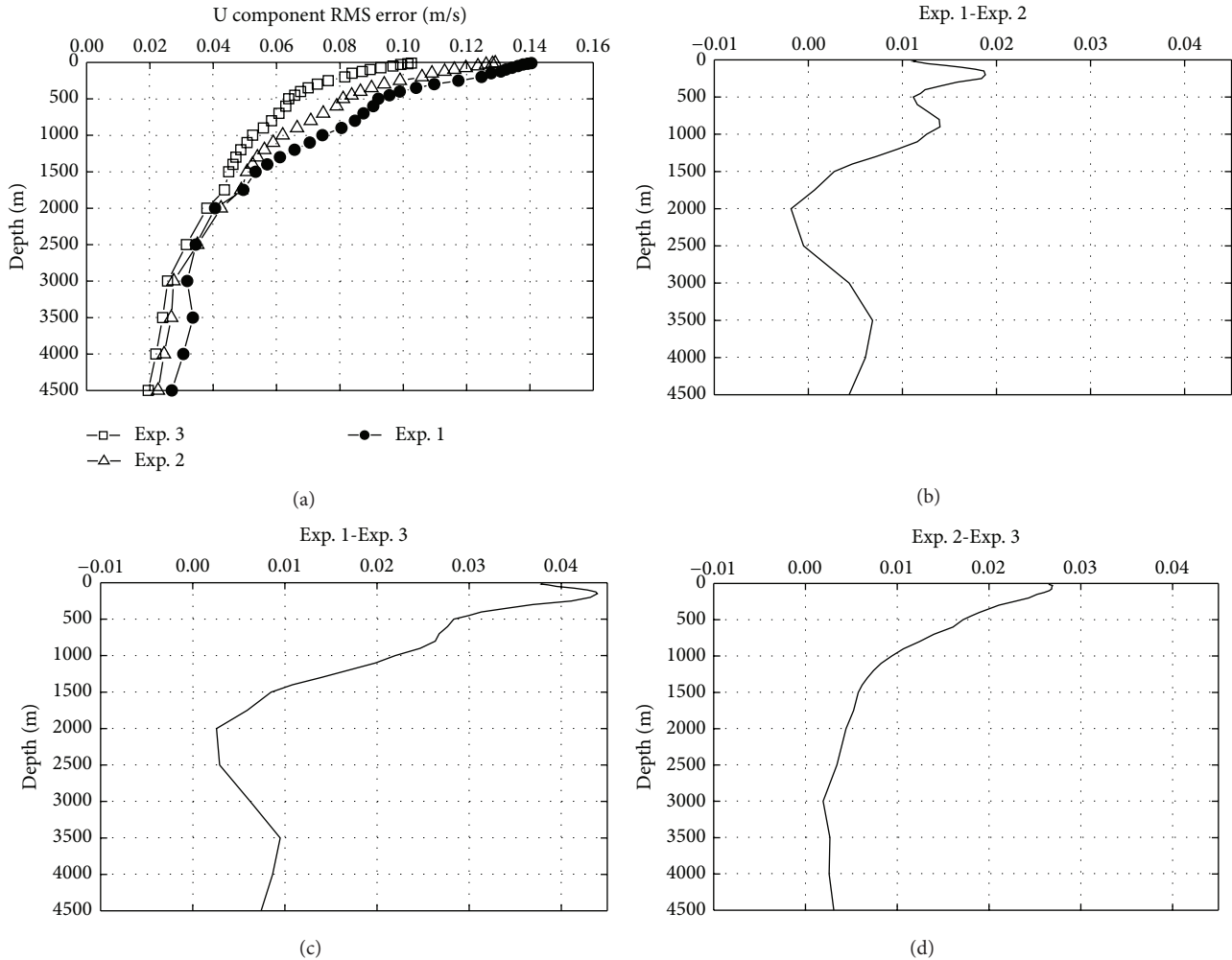


FIGURE 7: Similar to Figure 4 but for U component.

improved the Kuroshio transport of East China Sea to the west of Ryukyu Island. Figure 9 gives the time series of the differences of the Kuroshio transport at PN section of East China Sea between these three twin experiments and the truth. The PN line is an important section which is about from (124.5°E, 30°N) to (128.23°E, 27.45°N), and oceanographic data obtained along this section are the most significant in the investigation of Kuroshio in East China Sea [32]. Diagnosed from temperature and salinity observation at PN section, the average of observed PN relative geostrophic volume transport is about 25.8 Sv, with a mean seasonal maximum of 27.0 Sv in summer and minimum of 23.9 Sv in autumn [32]. In our true field, the averaged PN transport is about 26.5 Sv, and in 2007 the maximum is 29.7 Sv occurring in summer and the minimum is 23.3 Sv occurring in autumn, which is basically consistent with the observation. Due to the bad initial condition which may significantly deteriorate the Kuroshio analysis and simulation, the RMSE of Kuroshio transport in Experiment 1 is 15.1 Sv, while that in Experiment 2 with conventional observations data assimilated reduced to 4.4 Sv and that in Experiment 3 with all observations data assimilated further reduced to 2.9 Sv. Compared with

Experiment 2, further assimilation of Argo profile may improve the reanalysis accuracy of Kuroshio transport by about 1.5 Sv and speed up the current simulation toward the true field. The reason may be that since Argo data assimilation can improve the current field of Pacific Ocean to the east of Ryukyu Island which is the open boundary condition of marginal sea current field, the improvement in Pacific Ocean circulation may successively improve the marginal sea current field including the western boundary current such as Kuroshio due to the continuity of fluid. Argo profiles are widely distributed in World Ocean, so the ocean circulation field can be significantly improved by assimilating Argo.

4. Conclusion

In this paper, based on the CORA system, three twin experiments are used to evaluate the impact of Argo data on temperature, salinity, and current reanalysis results. The main conclusions can be drawn as follows.

- (1) As a necessary kind of supplement to conventional temperature and salinity observations, Argo data

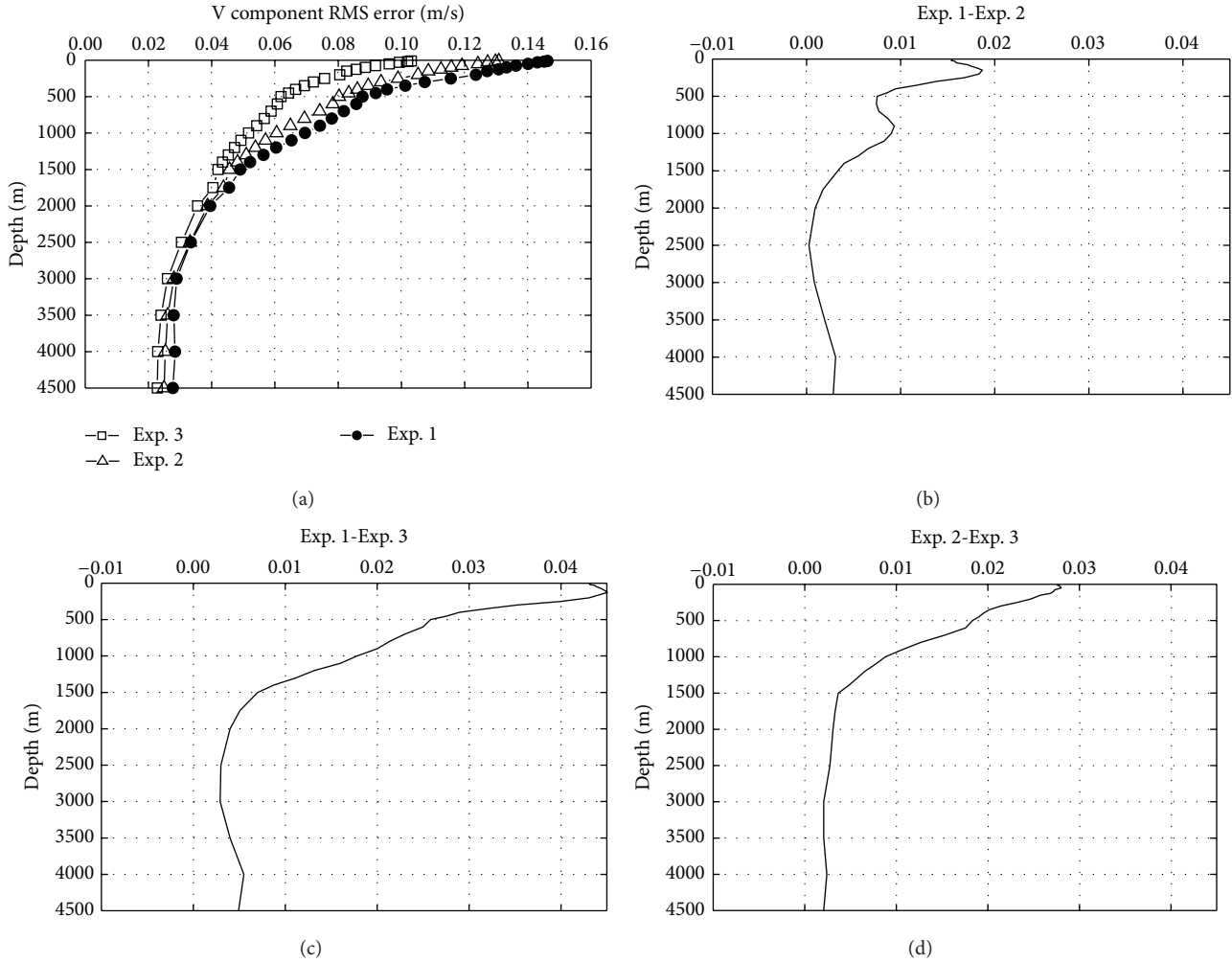


FIGURE 8: Similar to Figure 4 but for V component.

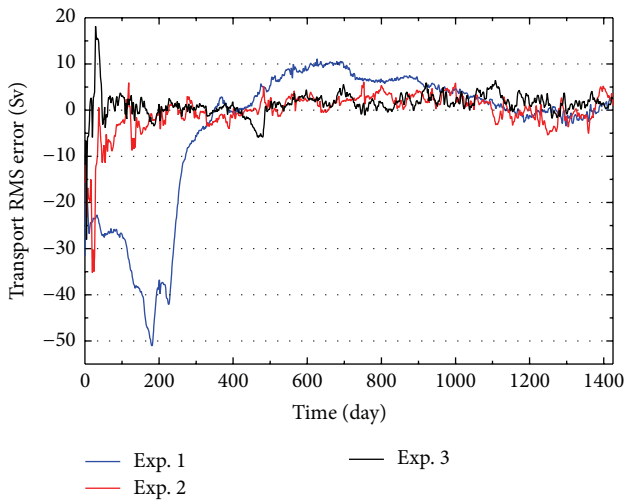


FIGURE 9: Time series of the differences of the Kuroshio transport at PN section of East China Sea between the three twin experiments and the truth obtained from the control run. Blue line is for Experiment 1 minus the truth, red line is for Experiment 2 minus the truth, and black line is for Experiment 3 minus the truth.

assimilation can further improve the reanalysis accuracy of temperature and salinity which have been improved by assimilating only conventional observations and further enlarge the improved area. With Argo profiles assimilated, the RMSEs of temperature and salinity reanalysis can be further reduced by about 10% in our study domain. Consistent with the unique feature of Argo observations, the temperature is improved in all levels and the largest improvement of salinity happens in the deep ocean.

- (2) Velocity field can be determined by density field in large scale to the first order under geostrophic or quasigeostrophic approximation; therefore, as long as temperature and salinity can be improved by data assimilation, density structure and the corresponding velocity field can be improved. Argo profiles are widely distributed in World Ocean, so the ocean circulation field can be significantly improved by assimilating Argo. With Argo profiles assimilated, the RMS errors of current reanalysis can be further reduced by about 18% in our study domain.

Conflict of Interests

The authors declare that there is no conflict of interests regarding the publication of this paper.

Acknowledgments

The authors would like to express their gratitude to two reviewers for their helpful comments and suggestions, which contributed to great improvement of the original paper. This research was jointly supported by grants of National Basic Research Program (2013CB430304), National Natural Science Foundation (41176003, 41206178, 41376013, 41376015, and 41306006), National High-Tech R&D Program (2013AA09A505), and Global Change and Air-Sea Interaction (GASI-01-01-12) of China.

References

- [1] D. Roemmich and Argo Science Team, "Argo: the global array of profiling floats," in *Observing the Oceans in the 21st Century*, C. J. Koblynsky and N. R. Smith, Eds., pp. 248–257, GODAE Project Office/Bureau of Meteorology, Melbourne, Australia, 2001.
- [2] J. A. Carton and B. S. Giese, "A reanalysis of ocean climate using Simple Ocean Data Assimilation (SODA)," *Monthly Weather Review*, vol. 136, no. 8, pp. 2999–3017, 2008.
- [3] M. A. Balmaseda, A. Vidard, and D. L. T. Anderson, "The ECMWF ocean analysis system: ORA-S3," *Monthly Weather Review*, vol. 136, no. 8, pp. 3018–3034, 2008.
- [4] E. J. Metzger, O. M. Smedstad, P. G. Thoppil et al., "US Navy operational global ocean and Arctic ice prediction systems," *Oceanography*, vol. 27, no. 3, pp. 32–43, 2014.
- [5] G. J. Han, W. Li, X. F. Zhang et al., "A regional ocean reanalysis system for coastal waters of China and adjacent seas," *Advances in Atmospheric Sciences*, vol. 28, no. 3, pp. 682–690, 2011.
- [6] A. Vidard, D. L. T. Anderson, and M. Balmaseda, "Impact of ocean observation systems on ocean analysis and seasonal forecasts," *Monthly Weather Review*, vol. 135, no. 2, pp. 409–429, 2007.
- [7] M. Balmaseda, D. Anderson, and A. Vidard, "Impact of Argo on analyses of the global ocean," *Geophysical Research Letters*, vol. 34, no. 16, Article ID L16605, 2007.
- [8] P. R. Oke and A. Schiller, "Impact of Argo, SST, and altimeter data on an eddy-resolving ocean reanalysis," *Geophysical Research Letters*, vol. 34, no. 19, Article ID L19601, 2007.
- [9] C. X. Yan, J. Zhu, and G. Q. Zhou, "Impacts of XBT, TAO, altimetry and ARGO observations on the tropical Pacific Ocean data assimilation," *Advances in Atmospheric Sciences*, vol. 24, no. 3, pp. 383–398, 2007.
- [10] B. Huang, Y. Xue, and D. W. Behringer, "Impacts of Argo salinity in NCEP global ocean data assimilation system: the tropical Indian Ocean," *Journal of Geophysical Research C: Oceans*, vol. 113, no. 8, Article ID C08002, 2008.
- [11] A. Schiller, S. E. Wijffels, and G. A. Meyers, "Design requirements for an argo float array in the indian ocean inferred from observing system simulation experiments," *Journal of Atmospheric and Oceanic Technology*, vol. 21, no. 10, pp. 1598–1620, 2004.
- [12] A. Griffa, A. Molcard, F. Raicich, and V. Rupolo, "Assessment of the impact of TS assimilation from ARGO floats in the Mediterranean Sea," *Ocean Science*, vol. 2, no. 2, pp. 237–248, 2006.
- [13] F. Raicich, "The assessment of temperature and salinity sampling strategies in the Mediterranean Sea: idealized and real cases," *Ocean Science*, vol. 2, no. 2, pp. 97–112, 2006.
- [14] S. Zhang, M. J. Harrison, A. Rosati, and A. T. Wittenberg, "System design and evaluation of coupled ensemble data assimilation for global oceanic climate studies," *Monthly Weather Review*, vol. 135, no. 10, pp. 3541–3564, 2007.
- [15] N. J. Dunstone and D. M. Smith, "Impact of atmosphere and sub-surface ocean data on decadal climate prediction," *Geophysical Research Letters*, vol. 37, no. 2, Article ID L02709, 2010.
- [16] G. J. Han, W. Li, X. F. Zhang et al., "A new version of regional ocean reanalysis for coastal waters of China and adjacent seas," *Advances in Atmospheric Sciences*, vol. 30, no. 4, pp. 974–982, 2013.
- [17] S. Zhang, M. J. Harrison, A. T. Wittenberg, A. Rosati, J. L. Anderson, and V. Balaji, "Initialization of an ENSO forecast system using a parallelized ensemble filter," *Monthly Weather Review*, vol. 133, no. 11, pp. 3176–3201, 2005.
- [18] G. L. Mellor, S. Hakkinen, T. Ezer, and R. Patchen, "A generalization of a sigma coordinate ocean model and an intercomparison of model vertical grids," in *Ocean Forecasting: Conceptual Basis and Applications*, N. Pinard and J. Woods, Eds., pp. 55–72, Springer, Berlin, Germany, 2002.
- [19] T. Ezer and G. L. Mellor, "A generalized coordinate ocean model and a comparison of the bottom boundary layer dynamics in terrain-following and in z-level grids," *Ocean Modelling*, vol. 6, no. 3–4, pp. 379–403, 2004.
- [20] M. Zavattarielli and G. L. Mellor, "A numerical study of the Mediterranean Sea circulation," *Journal of Physical Oceanography*, vol. 25, no. 6, pp. 1384–1414, 1995.
- [21] T. Ezer and G. L. Mellor, "Simulations of the Atlantic Ocean with a free surface sigma coordinate ocean model," *Journal of Geophysical Research C: Oceans*, vol. 102, no. 7, pp. 15647–15657, 1997.
- [22] X. F. Zhang, G. J. Han, D. X. Wang, W. Li, and Z. J. He, "Effect of surface wave breaking on the surface boundary layer of temperature in the Yellow Sea in summer," *Ocean Modelling*, vol. 38, no. 3–4, pp. 267–279, 2011.
- [23] X. F. Zhang, G. J. Han, D. X. Wang, Z. A. Deng, and W. Li, "Summer surface layer thermal response to surface gravity waves in the Yellow Sea," *Ocean Dynamics*, vol. 62, no. 7, pp. 983–1000, 2012.
- [24] G. Mellor and A. Blumberg, "Wave breaking and ocean surface layer thermal response," *Journal of Physical Oceanography*, vol. 34, no. 3, pp. 693–698, 2004.
- [25] Y. F. Xie, S. E. Koch, J. A. McGinley, S. Albers, and N. Wang, "A sequential variational analysis approach for mesoscale data assimilation," in *Proceedings of the 21st Conference on Weather Analysis and Forecasting/17th Conference on Numerical Weather Prediction*, 15B.7, American Meteorological Society, Washington, DC, USA, August 2005, <http://ams.confex.com/ams/pdfpapers/93468.pdf>.
- [26] W. Li, Y. F. Xie, Z. J. He et al., "Application of the multi-grid data assimilation scheme to the China seas' temperature forecast," *Journal of Atmospheric and Oceanic Technology*, vol. 25, no. 11, pp. 2106–2116, 2008.
- [27] W. Li, Y. F. Xie, S.-M. Deng, and Q. Wang, "Application of the multigrid method to the two-dimensional Doppler radar radial

- velocity data assimilation,” *Journal of Atmospheric and Oceanic Technology*, vol. 27, no. 2, pp. 319–332, 2010.
- [28] Y. F. Xie, S. E. Koch, J. A. McGinley et al., “A space-time multiscale analysis system: a sequential variational analysis approach,” *Monthly Weather Review*, vol. 139, no. 4, pp. 1224–1240, 2011.
- [29] W. Li and Y. F. Xie, “Multi-grid analysis of the three-dimensional doppler radar radial velocity: idealized cases study,” in *Proceedings of the 5th International Joint Conference on Computational Sciences and Optimization (CSO '12)*, pp. 813–816, June 2012.
- [30] W. Li, Y. Xie, and G. Han, “A theoretical study of the multigrid three-dimensional variational data assimilation scheme using a simple bilinear interpolation algorithm,” *Acta Oceanologica Sinica*, vol. 32, no. 3, pp. 80–87, 2013.
- [31] A. Troccoli, M. A. Balmaseda, J. Segschneider et al., “Salinity adjustments in the presence of temperature data assimilation,” *Monthly Weather Review*, vol. 130, no. 1, pp. 89–102, 2002.
- [32] H. Ichikawa and R. C. Beardsley, “The current system in the Yellow and East China Seas,” *Journal of Oceanography*, vol. 58, no. 1, pp. 77–92, 2002.

Research Article

Upper Ocean Thermal Responses to Sea Spray Mediated Turbulent Fluxes during Typhoon Passage

Lianxin Zhang,^{1,2} Changlong Guan,³ Chunjian Sun,¹ Siyu Gao,¹ and Shaomei Yu⁴

¹Key Laboratory of State Oceanic Administration for Marine Environmental Information Technology, National Marine Data and Information Service, State Oceanic Administration, Tianjin 300171, China

²College of Physical and Environmental Oceanography, Ocean University of China, Qingdao 266100, China

³Physical Oceanography Laboratory, Ocean University of China, Qingdao 266100, China

⁴Ocean Dynamical Laboratory, Third Institute of State Oceanic Administration, Xiamen 361005, China

Correspondence should be addressed to Lianxin Zhang; lxz.nmdis@163.com

Received 16 December 2014; Revised 30 January 2015; Accepted 18 February 2015

Academic Editor: Shaoqing Zhang

Copyright © 2015 Lianxin Zhang et al. This is an open access article distributed under the Creative Commons Attribution License, which permits unrestricted use, distribution, and reproduction in any medium, provided the original work is properly cited.

A one-dimensional turbulent model is used to investigate the effect of sea spray mediated turbulent fluxes on upper ocean temperature during the passage of typhoon Yagi over the Kuroshio Extension area in 2006. Both a macroscopical sea spray momentum flux algorithm and a microphysical heat and moisture flux algorithm are included in this turbulent model. Numerical results show that the model can well reproduce the upper ocean temperature, which is consistent with the data from the Kuroshio Extension Observatory. Besides, the sea surface temperature is decreased by about 0.5°C during the typhoon passage, which also agrees with the sea surface temperature dataset derived from Advanced Microwave Scanning Radiometer for the Earth Observing and Reynolds. Diagnostic analysis indicates that sea spray acts as an additional source of the air-sea turbulent fluxes and plays a key role in increasing the turbulent kinetic energy in the upper ocean, which enhances the temperature diffusion there. Therefore, sea spray is also an important factor in determining the upper mixed layer depth during the typhoon passage.

1. Introduction

When the wind speed reaches a certain level, surface wave breaking produces large numbers of sea spray droplets in the air-sea interface. Wave breaking and sea spray significantly affect the turbulent mixing [1, 2] and turbulent fluxes [3], respectively, which play a key role in the upper ocean in the high wind speed condition (>25 m/s) [4] (e.g., typhoon). So the research method of sea spray has been concerned for several decades. Riehl (1954) [5] was the first to point that the sea spray evaporation provided a significant amount of heat. After twenty years, the sea spray problem caught high attention again [6–11]. Wu (1974) [10] observed sea spray's concentration in the wind-wave tank and computed the evaporation of sea spray. Bortkovskii (1973) [9] simply evaluated the energy and evaporation of the sea spray droplet and claimed that it is a primary source for enhancing the sea-air interfacial transfer in the high wind speeds. In addition, Ling and Kao (1976) [11] introduced sea spray evaporation into

the equation of heat transfer and found that sea spray is also the important humidity source. In recent years, much research has focused on the effect of sea spray by developing theories [12–16]. Anthes (1982) [12] proposed that the evaporation of sea spray droplets would enhance the sensible heat transfer. Zhang and Lou [13] and Lou and Zhang [14] analyzed the physical processes of the individual sea spray droplet to get the expressions of spray heat flux and water vapor flux. Hasse (1992) [15] simply estimated the spray's impact by using three distinct arguments: the total surface area of sea spray droplet, an energy constraint, and the evaporation implied by the sea-salt aerosol. In recent years, much research has focused on the sea spray by the developing theories. Andreas [17–19] adapted Pruppacher and Klett's [20] cloud microphysical equations to study the thermal and moisture evolution of sea spray droplets. Fairall et al. [21] predigested Andreas's [17, 19] time scale and first incorporated a reasonable spray-based parameterization scheme into a simple model of the tropical cyclone boundary layer. So far, on

the basis of the above studies, it is possible to calculate the sea spray induced heat flux using the actual observed data. At the same time, the sea spray heat algorithm presented by Fairall et al. [21] is basically valid for the high wind condition, since the sea spray generation function depends on wind speed and the whitecap areal fraction. In this study, the sea spray mediated heat flux is calculated following Fairall's sea spray algorithm in the typhoon passage. However, the feedback mechanism between the sea spray and the atmosphere is not considered in Fairall's sea spray algorithm. Therefore, the study will introduce the feedback mechanism into the air-sea heat flux algorithm, which is feasible for us to calculate reasonable sea-air heat fluxes under the typhoon conditions.

Both theoretical researches [22] and field observations [23, 24] reveal that the drag coefficient leveled off or even decreased in the high wind speed. Powell et al. [23] hypothesized that sea spray could significantly influence the transfer of momentum for the wind speed above about 34 m/s. On the basis of field observations [23], Makin [25] suggested that a thin air boundary layer adjacent to the surface goes into a regime of limited saturation by suspended sea spray droplets, and the thin layer restrains the momentum transfer from the wind to the ocean. In the meantime, Makin [25] revised the wind speed logarithmic profile by the sea spray influence and derived the sea surface dynamic roughness length including the effect of sea spray at high winds. Based on the above research results, it is expected to investigate the momentum effect of sea spray during the typhoon passage through the spray induced sea surface dynamic roughness length.

Although the effect of the spray induced heat flux on air-sea interface under high winds was demonstrated by numerical simulations over a decade [26–30], the momentum effect of sea spray is hardly considered. In addition, little attention has been paid to both heat and momentum conjunct effects of sea spray on the upper ocean temperature in the period of typhoon by the numerical simulations. The goal of the present study is to investigate the impact of sea spray mediated turbulent fluxes on the upper ocean over the midlatitude oceans during a typhoon passage, using the General Ocean Turbulent Model (GOTM) that contains comprehensive turbulent mixing parameterizations. The effects of sea spray are presented from two kinds of physics processes. On the heat aspect, the impact of sea spray is considered in the form of modifying air-sea surface heat fluxes by microcosmic way, based on the sea spray microcosmic physical model from Fairall et al. [21]. On the momentum aspect, the effect of sea spray is introduced by the sea surface aerodynamic roughness length to investigate its impact on the air-sea momentum flux. As a pilot study, we present a case study of typhoon cyclone and explore the effects of sea spray in the numerical simulations.

The remainder of this study is organized as follows: model description and the spray turbulent flux algorithms are presented in Section 2. The experimental design of the numerical simulations is described in Section 3. Section 4 discusses numerical results and analyzes related mechanisms according to the model results, followed by the conclusions in Section 5.

2. Model Description

2.1. The GOTM Model. To clearly address the issue raised from the last section and avoid the complexity of a general circulation model, a one-dimensional ocean numerical model, namely, General Ocean Turbulence Model (denoted by GOTM) [31], which has a potential capability to simulate the vertical mixing processes near the upper ocean, is employed in this study. General Ocean Turbulent Model (GOTM) is a one-dimensional water column model (see <http://www.gotm.net/>), which solves the transport equations of heat, salt, and momentum. The governing equations of GOTM are formulated as

$$\frac{\partial \theta}{\partial t} - \frac{\partial}{\partial z} \left(v' \frac{\partial \theta}{\partial z} \right) - \frac{\partial}{\partial z} \left(K_h \frac{\partial \theta}{\partial z} \right) = \frac{1}{\rho_0 C_p} \frac{\partial I}{\partial z}, \quad (1)$$

$$\frac{\partial S}{\partial t} - \frac{\partial}{\partial z} \left(v'' \frac{\partial S}{\partial z} \right) - \frac{\partial}{\partial z} \left(K_q \frac{\partial S}{\partial z} \right) = 0, \quad (2)$$

where θ and S represent the mean potential temperature and salinity, respectively. v' and v'' denote the molecular diffusivities of heat and salt, respectively. C_p is the heat capacity of seawater. ρ_0 is a constant reference density resulting from the Boussinesq approximation. The source term of temperature in the right-hand side of (1) is the vertical divergence of solar radiation (I). K_q and K_h denote temperature and salinity diffusion coefficient. In the current version of GOTM, we set K_q equal to K_h for simplicity.

We will use the k - ε second turbulence closure model to simulate turbulence parameters [32]. Within the framework, K_h is equal to $c'_\mu k^{1/2} l$. The nondimensional quantity c'_μ is the function of nondimension stability parameter that describes the influence of stratification on turbulent mixing. k is the turbulent kinetic energy and $l \propto k^{3/2} \varepsilon^{-1}$ is the integral length scale, computed here from the dissipation rate ε . The transport equation for the turbulent kinetic energy k follows immediately from the contraction of the Reynolds-stress tensor. The equation of k can be written as

$$\frac{\partial k}{\partial t} = D_k + P + G - \varepsilon, \quad (3)$$

where P and G are the turbulent production of k by shear production and buoyancy generation, respectively, and ε is the dissipation term of turbulent kinetic energy. D_k represents vertical diffusion terms. In k - ε model, the rate of dissipation is balanced according to

$$\frac{\partial \varepsilon}{\partial t} = D_\varepsilon + \frac{\varepsilon}{k} (c_{\varepsilon 1} P + c_{\varepsilon 3} G - c_{\varepsilon 2} \varepsilon), \quad (4)$$

where D_ε represents the sum of the viscous and turbulent transport terms. The model constants $c_{\varepsilon 1}$, $c_{\varepsilon 2}$, and $c_{\varepsilon 3}$ are 1.44, 1.92, and 1.44, respectively.

2.2. Air-Sea Flux Parameterizations

2.2.1. COARE Model. To provide the external forcing for the GOTM, the surface fluxes in the air-sea interface are

calculated from the mean model parameters using Monin-Obukhov Similarity Theory. The COARE version 2.6 bulk model turbulent fluxes of momentum τ , latent heat H_L , and sensible heat H_S are

$$\begin{aligned}\tau &= \rho_a C_d U_{z_l}^2, \\ H_S &= \rho_a c_{pa} C_h U_{z_l} (\theta_0 - \theta_{z_l}), \\ H_L &= \rho_a L_v C_k U_{z_l} (q_0 - q_{z_l}),\end{aligned}\quad (5)$$

where ρ_a is the air density; c_{pa} is the specific heat of air at constant pressure; L_v is the latent heat of vaporization of water; θ is the potential temperature and q is the specific humidity. U is the mean horizontal wind speed and the subscript z_l denotes the lowest model level, while 0 refers to the water surface. C_d , C_h , and C_k are the drag coefficient, the transfer coefficient for the sensible heat, and the latent heat, respectively:

$$C_{dn} = \frac{\kappa^2}{\ln^2(z_l/z_0)}, \quad (6a)$$

$$C_{hn} = \frac{\kappa^2}{\ln(z_l/z_0) \ln(z_l/z_{0t})}, \quad (6b)$$

$$C_{kn} = \frac{\kappa^2}{\ln(z_l/z_0) \ln(z_l/z_{0q})}. \quad (6c)$$

Here κ is the von Karman constant, while z_0 , z_{0t} , and z_{0q} are the roughness lengths for the velocity, temperature, and humidity, respectively. From laboratory studies it has proven convenient to characterize the surface and the flow regime by the roughness Reynolds number:

$$R_r = \frac{u_* z_0}{\nu}, \quad (7)$$

where ν is the kinematic viscosity of air,

$$z_{0t} = \frac{R_t \nu}{u_*}, \quad (8a)$$

$$z_{0q} = \frac{R_q \nu}{u_*}, \quad (8b)$$

where R_t and R_q , as the functions of R_r , are roughness Reynolds number for temperature and moisture.

Based on the COARE model, the next section introduces the parameterization of sea spray. The key feature of sea spray parameterization is that the heat and momentum effects of sea spray are recognized by the microcosmic and macroscopical aspects, respectively. On the macroscopical aspect, the sea surface aerodynamic roughness length with the effect of sea spray is used to investigate the impact of the sea spray on the drag coefficient and air-sea momentum flux. On the microcosmic aspect, the effects of heat fluxes induced by sea spray are introduced by the Fairall et al. [21] spray heat algorithm (henceforth FA94). Hence, the model includes the parameterizations for both the interfacial and the sea spray fluxes.

2.2.2. Sea Spray Affected Sea Surface Dynamic Roughness. In the original COARE version 2.6 bulk model, the Charnock relation is used to calculate the sea surface dynamic roughness length,

$$z_0 = \frac{\alpha_c u_*^2}{g}, \quad (9)$$

where α_c is Charnock constant and is set to 0.011 [33]. g represents the acceleration due to gravity. Fairall et al. [33] pointed that the Charnock relation has been proven to work well for the low-moderate wind, and it is theoretically based and accurately for the interfacial turbulent fluxes for wind up to 10 m/s. When the wind speed reaches 11–13 m/s, the contribution of sea spray to the heat fluxes becomes significant. In other words, the Charnock relation does not contain sea spray droplets effect. Hence, the Charnock relation is still accurate for the interfacial turbulent fluxes when extrapolated to higher wind speeds.

For the high wind speed, the transfer coefficient for momentum flux decreases with the increasing of the wind, which is validated by the current field observations in the marine boundary layer [23, 24]. Based on the field measures [23], Makin [25] introduces the effect of sea spray into the wind speed logarithmic profile and further gives the sea surface dynamic roughness length z_0 including the effect of sea spray for high wind speed:

$$z_0 = \frac{c_l^{1-1/\omega} \alpha_c^{1/\omega} u_*^2}{g}, \quad (10a)$$

$$\omega = \min\left(1, \frac{a_{cr}}{\kappa u_*}\right), \quad (10b)$$

$$c_l = \frac{g h_l}{u_*^2}, \quad (10c)$$

where ω represents the correction parameterization indicating the effect of sea spray on the logarithm wind speed. The value of the terminal velocity a_{cr} is estimated about 0.64 m/s corresponding to a sea spray droplet radius of about 80 μ m [25]. h_l is the height of the suspension layer in the regime of limiting saturation, which is proportional to and larger than the height of the breaking waves but smaller than the significant wave height H by assuming that most of the spray at high wind speeds is produced by mechanical tearing by the wind from steep short waves. Hence, the height of the suspension layer in the regime of limiting saturation h_l is about 1/10 of the significant wave height [25, 34]. In (10c), c_l represents the nondimensionalized quantity of the height of the suspension layer in the regime of limiting saturation:

$$c_l = \frac{1}{10} \frac{gH}{u_*^2}. \quad (11)$$

It is found that the effects of sea spray are implied in the parameters ω and c_l according to (10a), (10b), (10c), and (11).

For the low-to-moderate wind conditions (<25 m/s), z_0 depends on both the wave states and wind speeds [35–39]. Donelan [40, 41] argued that laboratory experiments could

not represent field conditions for the same wave ages, so observations of the laboratory experiments and the field conditions should be discussed separately. To simulate the real open ocean, z_0 is derived from the real open ocean condition and Donelan [40] can represent most results of the foregoing researcher for the moderate wind speed:

$$\frac{z_0 g}{u_*^2} = 0.42 \left(\frac{c_p}{u_*} \right)^{-1.03}, \quad (12)$$

where c_p is peak wave phase velocity.

For the full wind speeds condition, the z_0 including the effect of sea spray is calculated by combining the z_0 for moderate wind (12) and for high wind ((10a), (10b), and (10c)), using the 3/2 power law [42] and the relation between significant wave period and peak wave period:

$$\frac{z_0 g}{u_*^2} = 0.0847^{(1-1/\omega)} 0.42^{1/\omega} \beta_*^{(3/2-253/100\omega)}, \quad (13)$$

where β_* is the wave age. When the impact of the sea spray droplets on the dynamics of the airflow at this regime is still small, ω should be equal to 1, and fully wind conditional roughness length (13) degrades the low wind conditional roughness length (12). However, the impact of the sea spray on the sea surface roughness is large enough ($\omega < 1$), which leads to the decrease of the roughness length and the drag coefficient.

2.2.3. Spray Heat Flux Algorithm. The parameterization scheme for the sea spray heat fluxes used in this study follows FA94. This parameterization builds on earlier work on droplet microphysics and the associated timescales by Andreas [17, 19]. Thus, the spray droplet mediated sensible heat flux is proportional to the mass flux of all relevant spray droplets and the air-sea temperature difference:

$$Q_s = S_v W(u) \gamma(u_{10}) \rho_w c_{pw} (T_s - T_a). \quad (14)$$

Here ρ_w and c_{pw} are the density and specific heat of liquid water. $W(u)$ is the whitecap areal fraction that is used to compute the sea spray droplet source number density spectrum. FA94 used the following form with the strong wind speed dependence:

$$W(u) = 3.8 \times 10^{-6} u^{3.4} \quad (15)$$

from Monahan and Muirheartaigh [43]. S_v is all the relevant whitecap normalized droplet volume flux:

$$S_v = \int_0^\infty \frac{4\pi}{3} r^3 f_n(r) dr, \quad (16)$$

where $f_n(r)$ is the source spectrum per unit area of whitecap. Evaluation of S_v is straightforward from three different data sources [44–46], whose value is equal to 5.0×10^{-6} m/s, which is independent of meteorological conditions.

Using the above approach, the spray droplet mediated latent heat flux is expressed as

$$Q_l = S_a h W \gamma(u_{10}) \beta(T_a) \rho_a L_e [q_s(T_a) - q]. \quad (17)$$

Here $q_s(T_a)$ is the saturation mixing ratio and spray droplets evaporate at their evaporating temperature T_{ev} , which can be regarded as a wet-bulb temperature modified for the effects of salinity and curvature, and not at the air temperature. Thus Q_l would be expected to be proportional to $q_s(T_{ev}) - q$, rather than $q_s(T_a) - q$ as given. The term

$$\beta(T_a) = \left[1 + \frac{0.622 L_e^2}{R c_{pa} T_a^2} q_s(T_a) \right]^{-1}, \quad (18)$$

where R is the gas constant of dry air. The 10 m wind speed adjusted term

$$\gamma(u_{10}) = 1 - 0.087 \ln \left(\frac{10}{h} \right). \quad (19)$$

Based on the Andreas [19] sea spray heat fluxes model, S_a is set to 0.125 s^{-1} (given by FA94). The evaporation zone scale height h is crudely defined as the height above the mean surface below which 67% of the total droplet evaporation takes place. h is the evaporation zone scale height. Both measurements [47–49] and modeling studies [11, 50] confirm that the proper scaling height for the droplet evaporation zone is the mean wave height. For simplicity, FA94 considered mean wave height as the evaporation zone scale height.

FA94 argued that Q_l and Q_s represent upper limits and that the actual spray-dependent fluxes will be reduced by a factor due to the fact that mean profiles of q and T in the droplet zone do not remain logarithmic but are modified by the presence of the spray. Based on the numerical simulations [16, 51], the limited constant is about 0.5 (given by FA94). The equations for the spray sensible heat and latent heat flux are

$$Q_s = 0.5 S_v W \gamma(u_{10}) \rho_w c_{pw} (T_s - T_a), \quad (20a)$$

$$Q_l = 0.5 S_a h W \gamma(u_{10}) \beta(T_a) \rho_a L_e [q_s(T_a) - q]. \quad (20b)$$

We note that Q_l and Q_s are the spray droplet mediated fluxes that would occur if the sea spray does not alter the normal logarithmic profile of mean q and T in the droplet evaporation zone.

2.2.4. Combined Turbulent Fluxes. The physical effects of sea spray between the air-sea interfaces are introduced from both the macroscopical and microcosmic ways. Concretely, the momentum (heat) effect of spray is introduced by the macroscopical (microcosmic) way.

Firstly, based on COARE 2.6 bulk model, the total air-sea momentum τ_{tot} (including sea spray effect) is calculated by the sea surface dynamical roughness length with the sea spray effect at the full wind speeds (13); the interfacial air-sea momentum τ_{int} (excluding sea spray effect) is computed by the Charnock relation (9). Hence the sea spray induced momentum flux is

$$\tau_s = \tau_{\text{tot}} - \tau_{\text{int}}. \quad (21)$$

Secondly, the combined spray and interfacial fluxes constitute the boundary conditions. Andreas and DeCosmo [52] give the total sensible ($H_{S,T}$) and latent ($H_{L,T}$) heat fluxes as

$$H_{L,T} = H_l + \alpha Q_l, \quad (22a)$$

$$H_{S,T} = H_s + \beta Q_s - (\alpha - \gamma) Q_l. \quad (22b)$$

Here, H_l and H_s are the interfacial latent and sensible heat fluxes that are computed by the COARE version 2.6 algorithms and described in Section 2.2.1. In (23a), αQ_l term models the latent heat flux (or moisture flux) coming out the top of the spray droplet evaporation layer that spray has contributed. However, FA94 pointed out that because the atmosphere must supply all the heat to evaporate the droplets, these droplets are a sink for sensible heat. Hence, to conserve energy, this αQ_l term in (23a) must appear with the opposite sign in the sensible heat equation (23b). The βQ_s term in (23b) models the sensible heat that spray droplets give up in cooling from the ocean surface temperature T_s to the temperature they have on returning to the sea surface. Thus, the γQ_l term in (23b) adds more sensible heat to the layer because of the increased air-sea temperature different that results from the spray's evaporative cooling of the layer.

Andreas [53] used the FA94 spray generation function to compute the spray heat fluxes and evaluate that the values of α , β , and γ are 3.3, 5.7, and 2.8 based on the HEXOS heat and moisture flux dataset. Hence coming by the above physics processes, the net sea spray contribution to the total sensible and latent heat fluxes can be estimated:

$$Q_{L,sp} = \alpha Q_l, \quad (23a)$$

$$Q_{S,sp} = \beta Q_s - \alpha Q_l + \gamma Q_l. \quad (23b)$$

Hereafter, $Q_{L,sp}$ and $Q_{S,sp}$ are called sea spray induced sensible heat flux and latent heat flux, respectively.

3. Experimental Design

Two experiments are designed to investigate the influence of sea spray in the upper ocean during the passage of typhoon Yagi. According to the descriptions in Section 2, the air-sea turbulent fluxes without the effect of sea spray are computed in Test 1. On the basis of Test 1, Test 2 introduces the effect of sea spray into the air-sea turbulent fluxes. Based on the GOTM model and KEO observations, the 1D GOTM is configured to the position of the KEO station with a 400 m depth and 1200 vertical layers with intervals of 0.33 m. To use the typhoon data, the simulation period is extended from September 17 to 29, 2006. Note that the ocean was initialized with the same temperature and salinity profiles from the KEO station in two cases. The numerical output such as air-sea momentum flux fields, heat fluxes fields, and sea temperature will be presented for sequent comparative analysis.

The Kuroshio Extension Observatory (KEO) is used in the GOTM model to simulate the typhoon Yagi, which is located at 32.4°N, 144.6°E and was first deployed in mid-June 2004. The measurements of KEO include 3 m air temperature, 3 m relative humidity, 3 m wind speed and direction, solar and

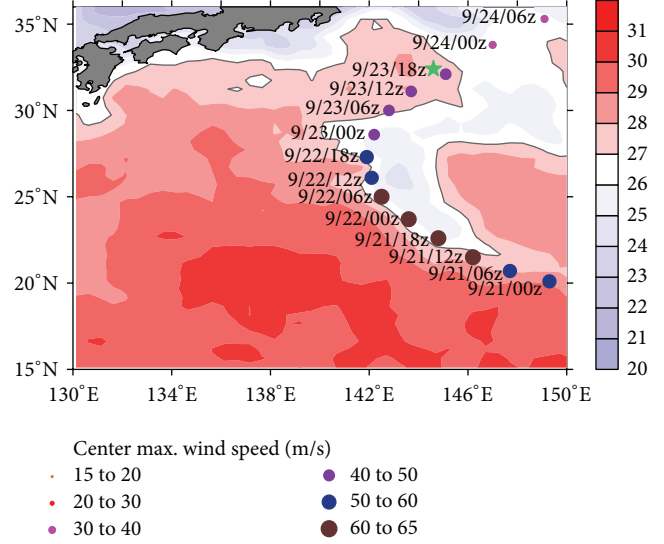


FIGURE 1: Daily averaged sea surface temperature (SST) (color fill, in °C) derived from the Reynolds SST dataset on September 23. Green pentacle represents the location of the Kuroshio Extension Observatory (KEO) mooring. Color dots indicate the center location of Yagi on September 21–24 (every 6 h). Thin black curves indicate the 27°C contour.

long-wave radiation, rain rate, sea temperature profile, and sea salinity profile. The temporal resolution of all variables is 10 min, except for the radiations being 2 minutes. The observed layers of salinity and temperature are 1, 10, 15, 50, 75, and 400 m and 1, 10, 15, 25, 50, 75, 100, 150, 200, 300, 400, 450, and 500 m, respectively. The period of KEO variables used in the simulation is from September 17 to 29, 2006.

4. Numerical Results

Figure 1 shows the track of typhoon Yagi on September 21–24 (color dots) and the distribution of sea surface temperature on September 23 (shade) in the study area (15–40°N, 130–150°E). As shown in Figure 1, the typhoon Yagi upgraded to a super typhoon on September 22. Subsequently, Yagi moved towards northeast and passed KEO station on September 23, where a broad area of low temperature can be seen distinctly around the right of Yagi [54]. On September 24, Yagi left the sea region, and the low temperature lasted until September 27 (not shown).

4.1. The Momentum Fluxes. The 10 m drag coefficient C_d according to (6a), (6b), and (6c) is shown in Figure 2. When the effect of sea spray is considered, a significant dependence of C_d on the wind speed and the wave age can be seen from the black dot lines in Figure 2. C_d (z_0 derived from (13)) increases with the wind speed until the wind speed reaches 33 m/s for different wave age. In the meantime, C_d decreases with the increasing of the wave age when the wind speed remains constant. However, when the effect of sea spray is ignored, C_d (z_0 derived from (9)) increases continually

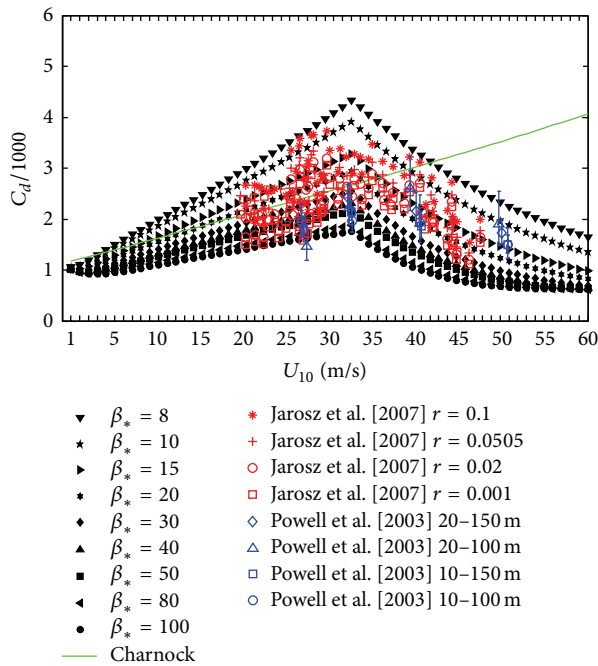


FIGURE 2: The change of drag coefficient with the 10 m wind speed on the different wave ages (8, 10, 15, 20, 30, 40, 50, 80, and 100). The black dot lines represent the drag coefficient affected by the sea spray, which are calculated by (13). The drag coefficient without the effect of sea spray is indicated by the green line and calculated by the Charnock relation (9). The observations of Jarosz et al. (2007) based on different resistance coefficients (0.1, 0.0505, 0.02, and 0.001 cm/s) are plotted by the red dots. The blue dots represent the drag coefficient observed by Powell et al. (2003).

with wind speed and remains invariable with the wave age (green line). Further, the distribution of C_d affected by the sea spray is in agreement with the counterpart obtained from the observations (Powell et al. [23] (blue markers) and Jarosz et al. [24] (red markers)). Therefore, the sea spray has positive impacts on C_d . It is important to figure out the physical process how sea spray affects C_d , which is described as follows: at very high wind speeds, a deep part of the marine atmospheric surface layer is filled with spray droplets, which forms the so-called suspension layer. In the suspension layer, the heaviest particles remain closer to the surface, so the spray droplets over the ocean form a very stable boundary layer close to the surface. As wind speeds exceed 33 m/s, the suspension layer in the regime of limiting saturation is formed, and the sea spray droplets influence the airflow dynamics, which can restrain the momentum transport from the wind to the sea surface [25].

Figure 3 depicts time series of surface momentum flux with and without sea spray at the fixed location of the KEO. As shown in Figure 3, prior to the passage of Yagi (September 20–22), sea spray has almost no effect on the momentum flux. When Yagi passed the KEO station, the momentum flux is significantly enhanced by the sea spray. The maximum total momentum fluxes (with the effect of sea spray) increase to

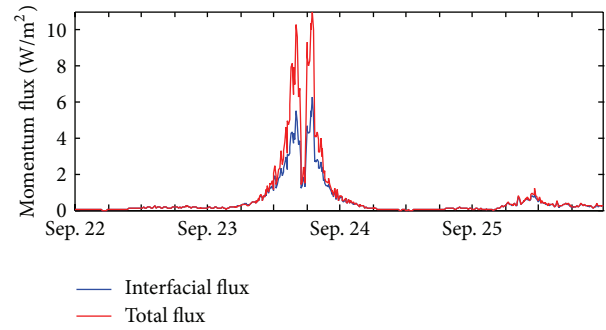


FIGURE 3: Time series of momentum flux at the KEO station where the simulated typhoon passed by at 18:00 September 23. Blue line and red line represent interfacial flux (without sea spray effect) and total flux (with sea spray effect), respectively.

10.29 N/m² and 11.38 N/m² at the peak winds on either side of the typhoon eye (Figure 3 red line). The increments of 4.79 N/m² and 5.13 N/m² are comparable with the interfacial momentum flux (without the effect of sea spray). When Yagi was far from the station gradually (September 24–29), the effect of sea spray on the momentum flux quickly decays.

4.2. The Heat Fluxes. Figure 4 shows time series of the total and interfacial heat flux, given by (22a)-(22b). As shown in Figure 4, the total heat flux (red line in Figure 4) is generally greater than the interfacial heat flux (blue line in Figure 4) during the typhoon Yagi period. The eye of typhoon Yagi passed the KEO station at 18:00 September 23 (Figure 1). The wind speed was nearly symmetric with the eye, and the maximum of the wind speed was 32.7 m/s and 34 m/s, respectively (not shown). Hence, there are double peaks of the heat flux symmetric with the typhoon eye (Figure 4). When the typhoon Yagi passed the KEO station on September 23, the maximal interfacial latent heat flux is 533.8 W/m² (blue line in Figure 4(b)), and the maximal total latent heat flux is 738.2 W/m² (red line in Figure 4(b)). The latent heat flux is maximally increased by 204.4 W/m² (spray mediated latent heat flux $Q_{L,sp}$) at the peak winds on the right side of the typhoon eyes. In the meantime, the total maximum sensible flux is 298.2 W/m² (red line in Figure 4(a)), which is an increment of 106.5 W/m² compared with the interfacial maximum sensible heat flux (blue line in Figure 4(a)).

4.3. Sea Temperature. In this section, the daily SST simulated by the GOTM during the passages of typhoon Yagi is compared with the AMSR-E and Reynolds satellite data. Figure 5 shows the variation of daily SST simulated by Test 1 (blue curves) and Test 2 (red curves) during the passage of Yagi. For comparison, the AMSR-E (black pentacle line) and Reynolds (black star line) SST are also plotted. Results of two tests are consistent with the observed SST before the typhoon Yagi passed the KEO station (on September 18–19). After Yagi left the KEO station (i.e., September 23–26.), the significant decreasing trend of the SST can be seen from variation of

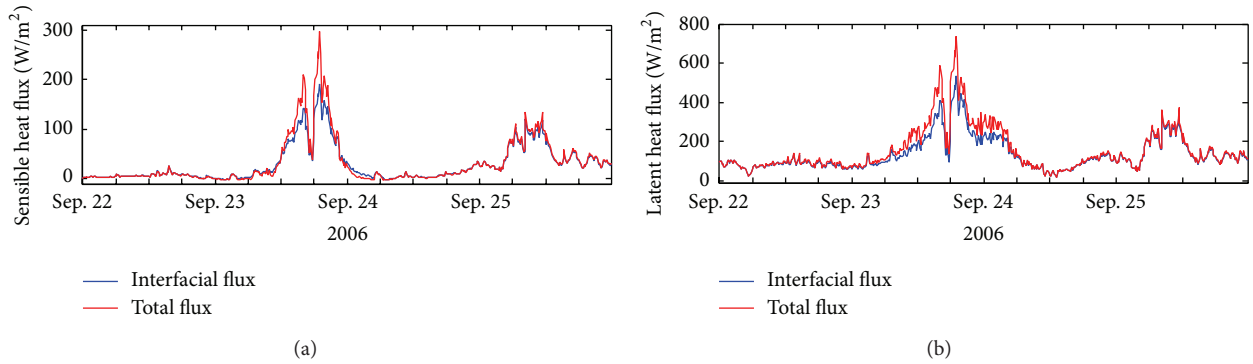


FIGURE 4: Time series of (a) sensible heat flux and (b) latent heat flux at the KEO station where the simulated typhoon passed by at 18:00 September 23. Blue line and red line represent interfacial heat flux and total heat flux, respectively.

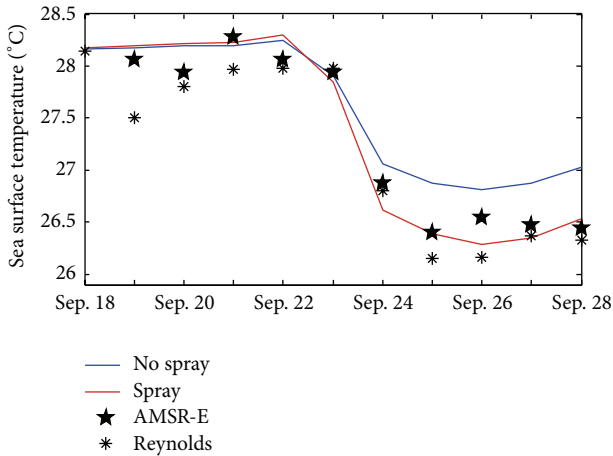


FIGURE 5: Variation of daily averaged SST during the passage of typhoon Yagi. Red and blue curves represent results of test including spray effect (Test 1) and excluding spray effect (Test 2), respectively. Black pentacle line and black star line represent AMSR-E and Reynolds SST, respectively.

daily averaged SST. On September 25, the SST of AMSR-E and Reynolds reaches 26.4°C and 26.15°C, respectively. Compared with SST simulated by Test 1 (26.88°C), the SST of Test 2 decreases to 26.39°C, which is closer to the observations from the AMSR-E and Reynolds. The difference in the two experiments indicates that the sufficient cooling of the SST can be reproduced if the effect of sea spray is considered.

Figure 6 shows time series of the mixed layer depth (MLD) for the two tests with and without the sea spray effect, where the MLD is derived from the turbulent kinetic energy threshold. When the sea spray fluxes algorithms are included in GOTM, the maximal MLD is 52.49 m for the no spray case (Test 1) and 68.87 m for the with spray case (Test 2) on September 24. The MLD difference in two tests illuminates that sea spray can deepen the MLD during the typhoon passage in the GOTM simulation.

Figure 7 shows the influence of sea spray in the upper 100 m profiles of temperature at 12:00 September 21–26

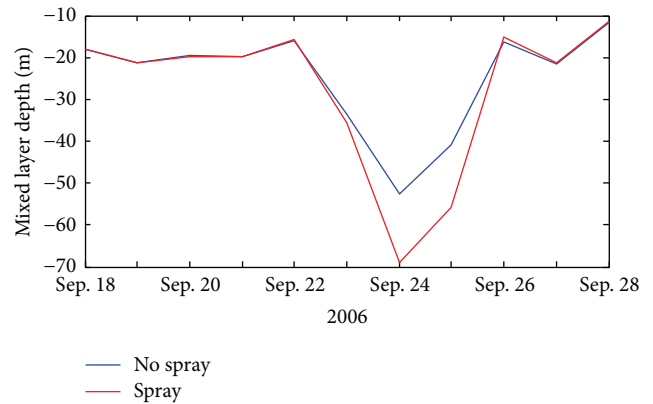


FIGURE 6: Time series (daily) of the mixed layer depth from simulations with (Test 2) and without (Test 1) sea spray effect at the fixed station. The red (blue) line is the mixed layer depth with (without) sea spray effect.

((a)–(f)). Results show that Test 2 can capture the trend of temperature reduction in the upper ocean layer after Yagi left the KEO station. The upper layer temperature profiles of Test 2 (red lines) are more similar to the KEO observations (gray asterisks) than those of Test 1 (blue lines) during the Typhoon passage. The simulated temperature profile of Test 2 especially cooled significantly after the typhoon’s passage (September 24–26). The temperature simulated by Test 2 is cooler by 0.5°C than that simulated by Test 1. Hence, the effect of sea spray can yield additional cooling during the typhoon Yagi simulation.

5. Discussion

5.1. *The Effect of Sea Spray on Momentum Fluxes.* When the sea spray droplets are ejected into the air, they are accelerated by the air drag. At one time, the sea spray droplets extract the momentum from the airflow. When sea spray droplets crash back into the sea surface, they transfer their momentum to the ocean. Momentum transfer is carried out from the air to the ocean by the sea sprays. So the effect of sea spray on

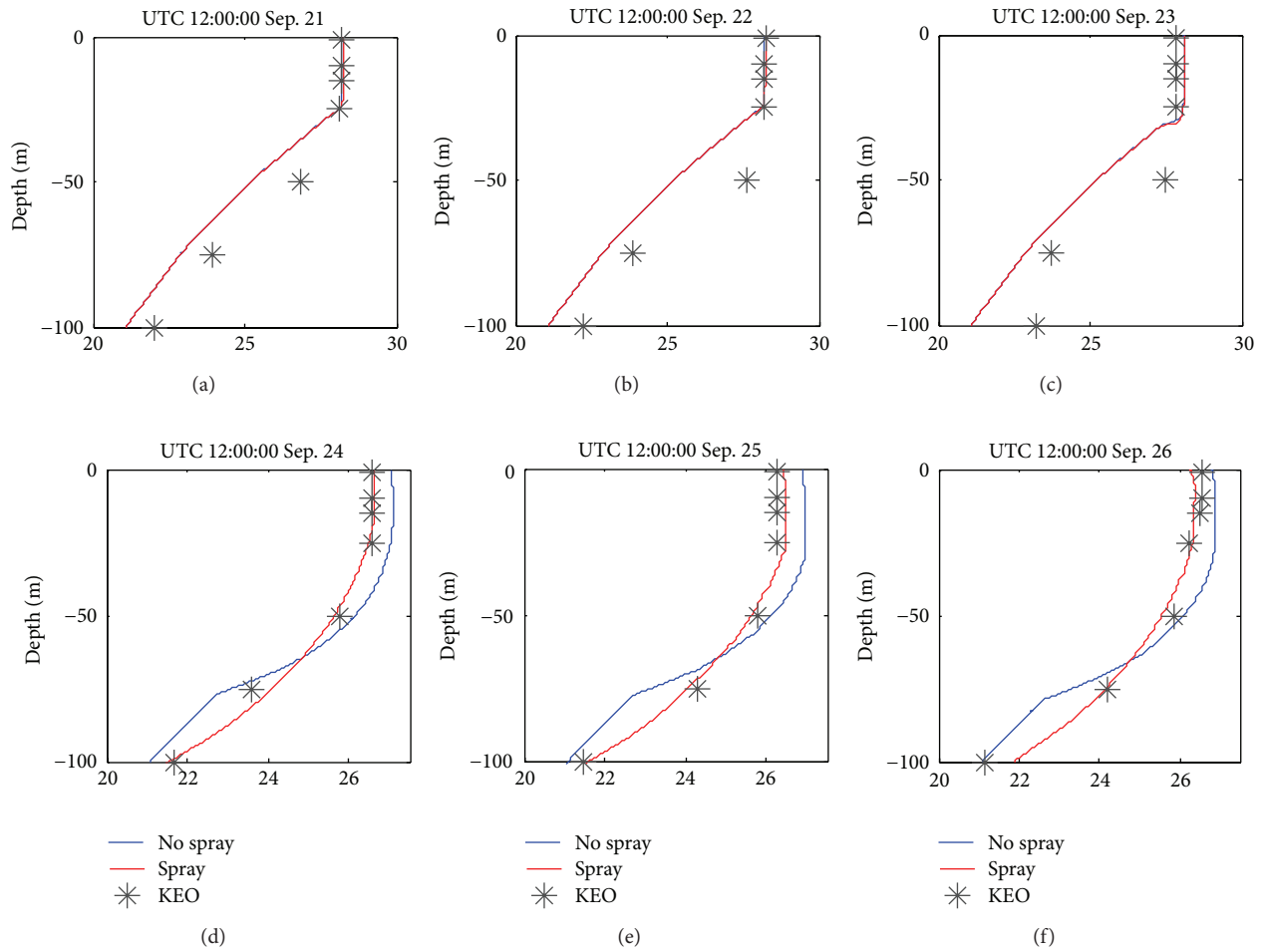


FIGURE 7: Upper 100 m temperature profiles simulated by Test 1 (no spray, blue curves) and Test 2 (spray, red curves) at ((a)–(f)) 12:00 September 21–26, 2006. Gray asterisks indicate the KEO observed temperature.

momentum exchange should be evaluated in the real typhoon period. To clearly analyze the distribution characteristic of the momentum fluxes, the trends of momentum fluxes as a function of wind speed are shown in Figure 8. For the wind speed less than 20 m/s, the spray mediated momentum flux (red dot line in Figure 8(a)) is about two orders of magnitude less than the interfacial momentum flux (blue dot line in Figure 8(a)), which is in agreement with the depiction in Andreas and Emanuel [55]. The growth rate of spray momentum flux is far less than that of interfacial momentum flux, whereas, for wind speeds over 20 m/s, the growth rate of spray momentum flux with wind increasing is much greater than the rate of interfacial momentum flux. When wind speed reaches 31 m/s, both the spray momentum flux (red dot line in Figure 8(b)) and the interfacial momentum flux (blue dot line in Figure 8(b)) are almost equal. This conclusion can be corroborated by the result of previous studies about spray momentum flux. For example, Andreas and Emanuel [55] evaluated the spray momentum flux using the spray generation functions of Andreas [19]. If the spray momentum grows using prevailing growth rates,

the interfacial momentum and the spray momentum are equal at about $u_* = 2$ m/s (Figure 8 in Andreas and Emanuel [55]); this u_* corresponds to a surface-level wind speed of about 32 m/s. Hence it indicated that result is considerably reasonable in this study. It is worth noting that, for the wind speed greater than 33 m/s, the growth of spray momentum flux does not continuously increase as the interfacial momentum flux does. The growth rate of the total momentum flux decreases due to the influence of the sea spray. Because of wind speeds exceeding 33 m/s, regime of limiting saturation suspension layer is formed by the spray in air-sea interface surface layer, which can influence the airflow dynamics. Hence, with the effect of sea spray, the growth rate of total momentum flux reduces in the high wind condition.

5.2. The Effect of Sea Spray on Heat Fluxes. Based on the results, the sea spray plays an important role in the air-sea transfer of sensible heat and latent heat. To clearly analyze the characteristic of the sea spray fluxes, the trends of sea spray mediated sensible heat flux $Q_{s,sp}$ and latent heat flux $Q_{L,sp}$ as a function of wind speed are shown in Figure 9. From

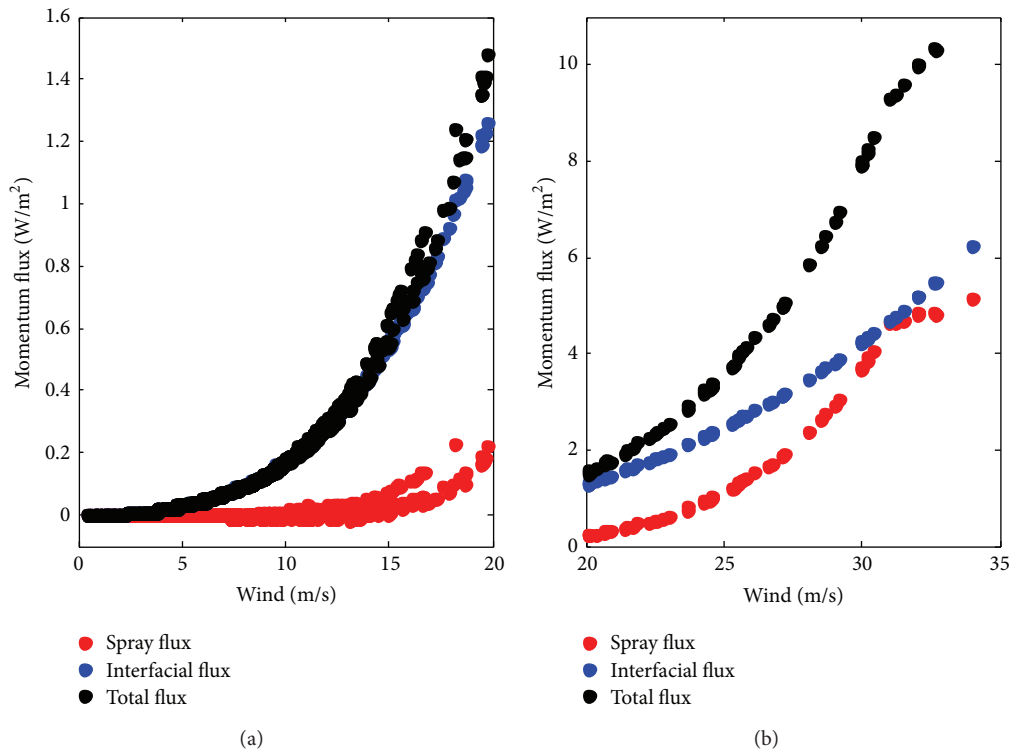


FIGURE 8: Magnitude of the momentum flux as a function of wind speed for the wind speeds from (a) 0 to 20 m/s; (b) 20 to 35 m/s. (Black dot line, blue dot line, and red dot line represent total momentum flux, interfacial momentum flux, and sea spray momentum flux, resp.).

Figure 9, one can see that the effect of sea spray on the air-sea heat fluxes is restricted by the sea surface wind speed condition. When the wind speed is greater than 10 m/s, sea spray begins to modulate the heat and moisture transfer in the air-sea interface. For wind speed greater than 20 m/s, sea spray significantly affects the air-sea sensible and latent heat flux. In addition, sea spray enhances latent heat transfer from the sea to the air for all the wind speed condition. For the sensible heat flux, sea spray sometimes enhances sensible transfer from the sea to the air and sometimes enhances sensible transfer from the air to the sea, which indicates there are complicated physical processes between the spray droplet evaporation layer and the air-sea interface in the heat exchange. In other words, the sign (positive or negative sign) of the sea spray induced sensible heat flux $Q_{s,sp}$ is decided by the sea spray giving up sensible heat term (βQ_s), the sea spray's evaporation absorbing sensible heat term ($-\alpha Q_l$), and adding more sensible heat term (γQ_l) due to the sea spray's feedback mechanism, according to (23b). For example, sea spray's evaporation absorbing sensible heat term $-\alpha Q_l$ is increased to -204.4 W/m^2 , which reduces the turbulent enthalpy flux from the ocean to the air. The maximum of βQ_s is 137.4 W/m^2 (blue line in Figure 10(b)), and γQ_l is 173.4 W/m^2 (orange line in Figure 10(a)). Hence, combining the above physics processes, the maximal spray mediated sensible heat flux $Q_{s,sp}$ increases to 106.5 W/m^2 (red line in Figure 10(b)).

5.3. *Diagnostic Analysis of Sea Temperature.* Sea spray acts as an additional source of the air-sea turbulent fluxes and can improve the magnitudes of the turbulent kinetic energy k and temperature diffusion coefficient K_h in the upper ocean, which affect the upper layer sea temperature during the typhoon passage. So k equation (3) of the model is diagnosed to investigate the effect of sea spray. Figures 11 and 12 show the shear production term P and the dissipation term ϵ of the total tke in the upper ocean (<100 m), respectively. Terms of the vertical diffusion term D_k and buoyancy generation term G are not shown because their magnitude are much smaller. The shear production term P (Figure 11) is balanced by the dissipation term ϵ (Figure 12). The most significant increment in Figure 11 is due to the high dissipation because strong shear happens there induced by strong turbulent fluxes of sea spray near the sea surface, when the typhoon Yagi passes the KEO station (on September 23). On September 24–26, the increasing trend of P spreads downward to 100 m. In a word, sea spray mediated turbulent fluxes primarily enhance the shear production term P of the total tke in the upper ocean during the typhoon Yagi passage. Hence, when the effect of sea spray is considered, the total tke is enhanced greatly in the upper ocean (see Figure 13). On the sea surface, the total tke increases from $0.0044 \text{ m}^2/\text{s}^2$ without the sea spray effect (blue line in Figure 13) to $0.0077 \text{ m}^2/\text{s}^2$ with the sea spray effect (red line in Figure 13). When the typhoon left the KEO station for 2-3 days (i.e., September 24–26), the increasing trend of

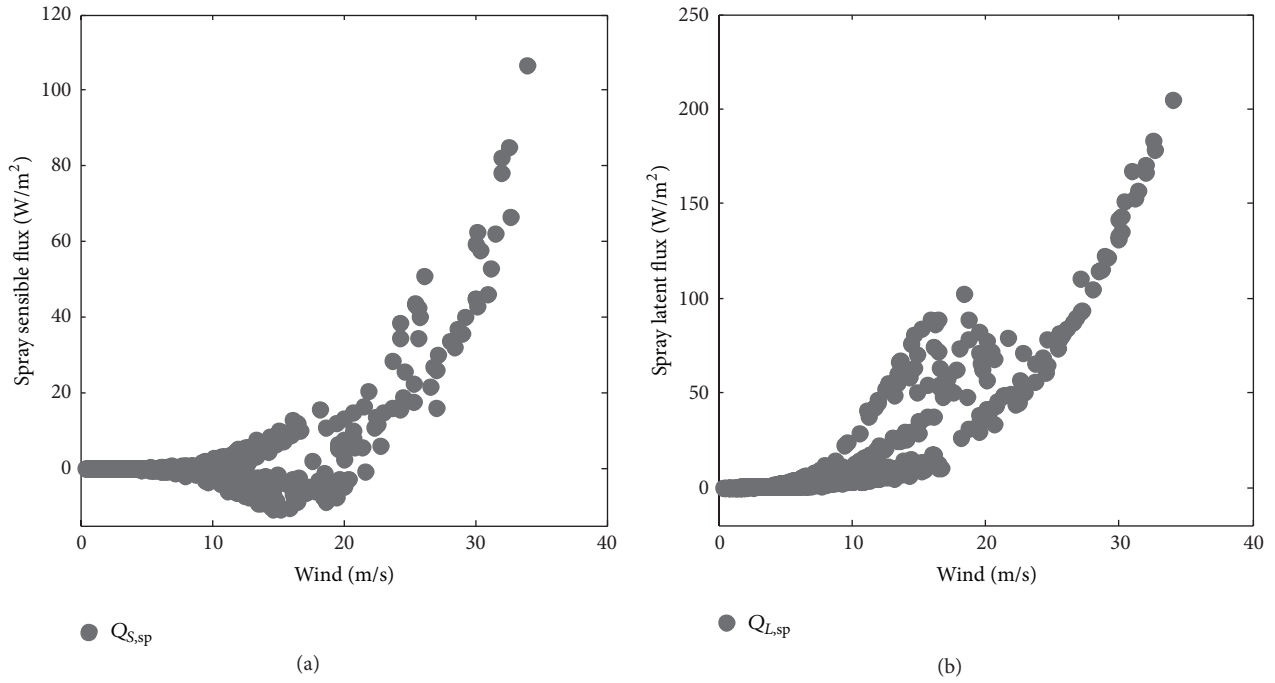


FIGURE 9: Sea spray induced heat fluxes. (a) Spray sensible flux $Q_{S,sp}$. (b) Spray latent flux $Q_{L,sp}$ as a function of wind speed.

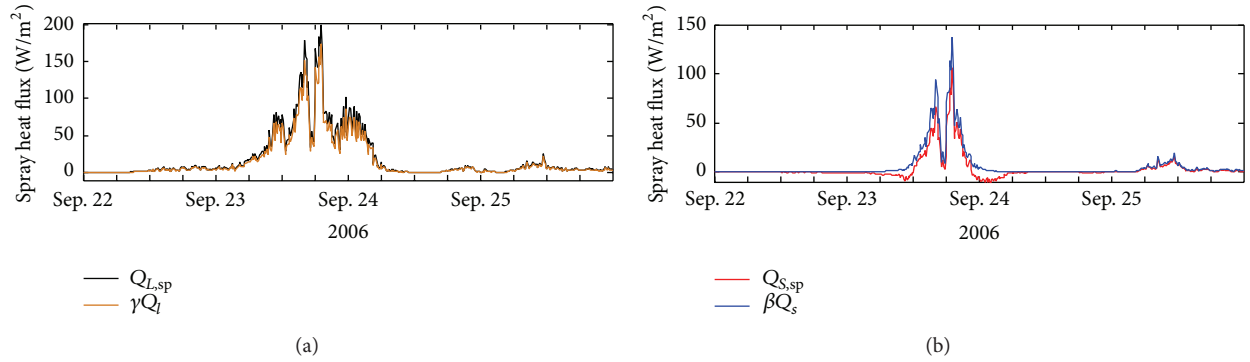


FIGURE 10: Time series of spray heat flux at the KEO station. Black line and orange line represent the sea spray mediated latent $Q_{L,sp}$ and added heat flux of spray increased air-sea temperature different rQ_i in Figure 10(a), respectively. Red line and blue line indicate sea spray mediated sensible heat $Q_{S,sp}$ flux and spray sensible heat βQ_s in Figure 10(b), respectively.

the total tke spreads downward to 100 m. The enhanced turbulent kinetic energy derived from the sea spray’s turbulent fluxes mixes the water column and makes it more homogeneous.

K_h from the surface to about 70 m depth has an increment owing to the enhancement of the turbulent kinetic energy by sea spray induced turbulent fluxes on September 23 (Figure 14(a)). K_h of Test 2 (red line in Figure 14(b)) is increased by approximately three times at the sea surface compared to that of Test 1 (blue line in Figure 14(b)). After the typhoon Yagi left the KEO station (September 24–26), the enhancing K_h spreads downwards (red line in Figures 14(c)–14(e)) cooling the temperature of the upper ocean and

increasing the depth of the ocean mixed layer. Combining the turbulent kinetic energy ε and the temperature diffusion coefficient K_h , the effect of sea spray significantly cools the temperature of the upper ocean. This cooling is maintained for 2-3 days, which is consistent with the observations in situ.

6. Conclusion

In the high wind speed condition (e.g., typhoon), breaking waves in the air-sea interface can produce large amount of sea spray droplets, which significantly affect the dynamic and the thermodynamic processes between the ocean and the atmosphere. To investigate the effects of sea spray on the sea

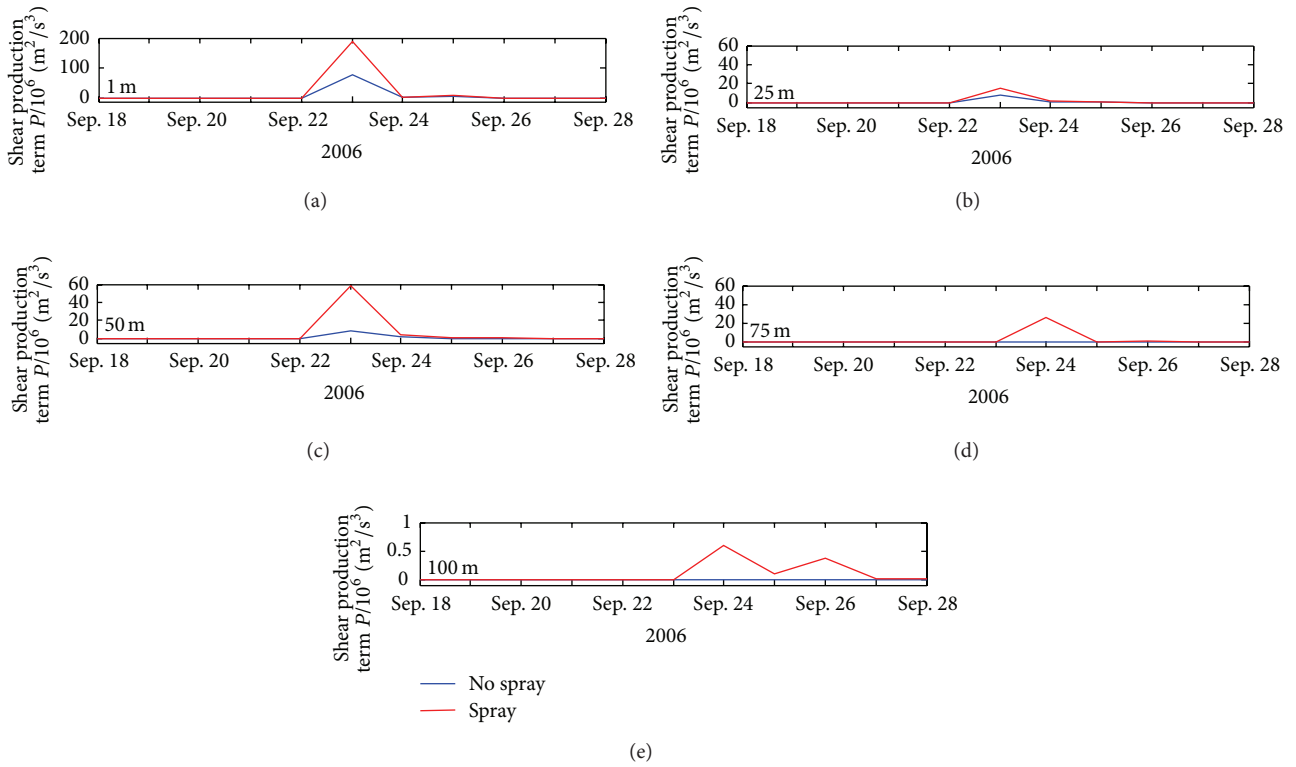


FIGURE 11: Time series (daily) of the shear production term P from simulations with (red curves) and without sea spray (blue curves) at the KEO station in (a) 1 m, (b) 25 m, (c) 50 m, (d) 75 m, and (e) 100 m depth.

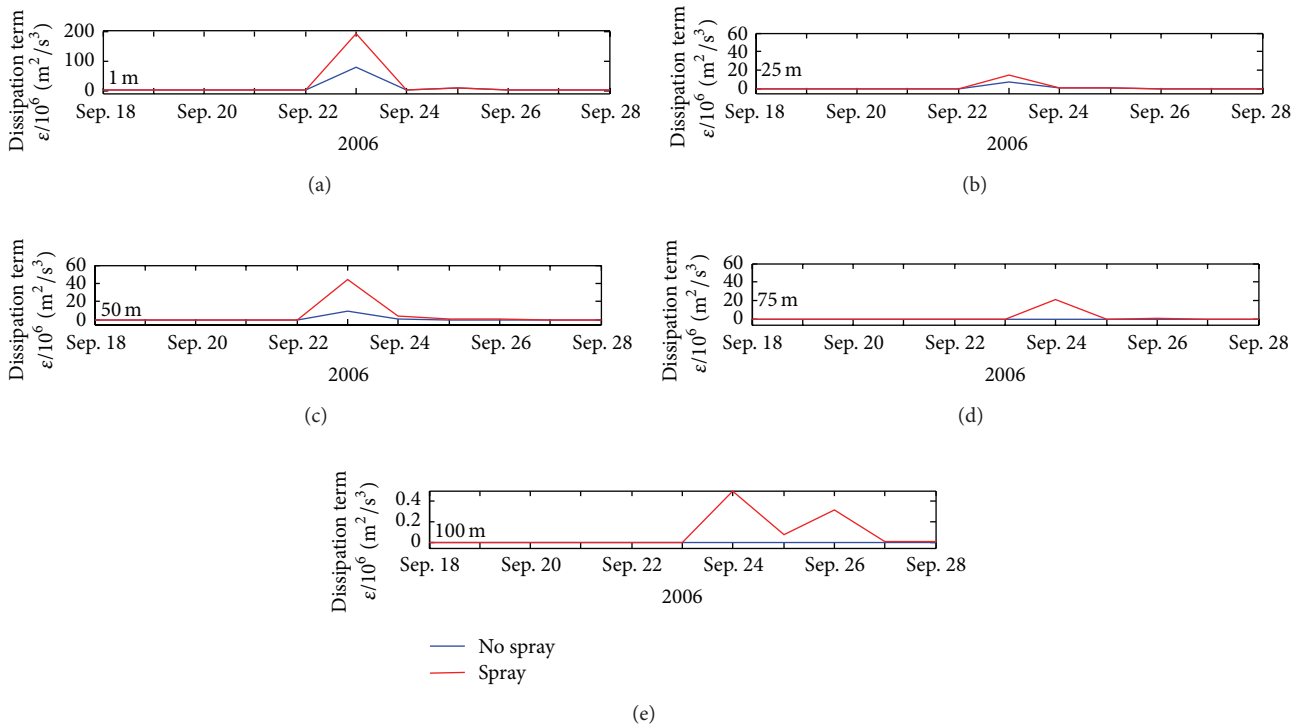


FIGURE 12: The same as Figure 11, but for the dissipation term ϵ .

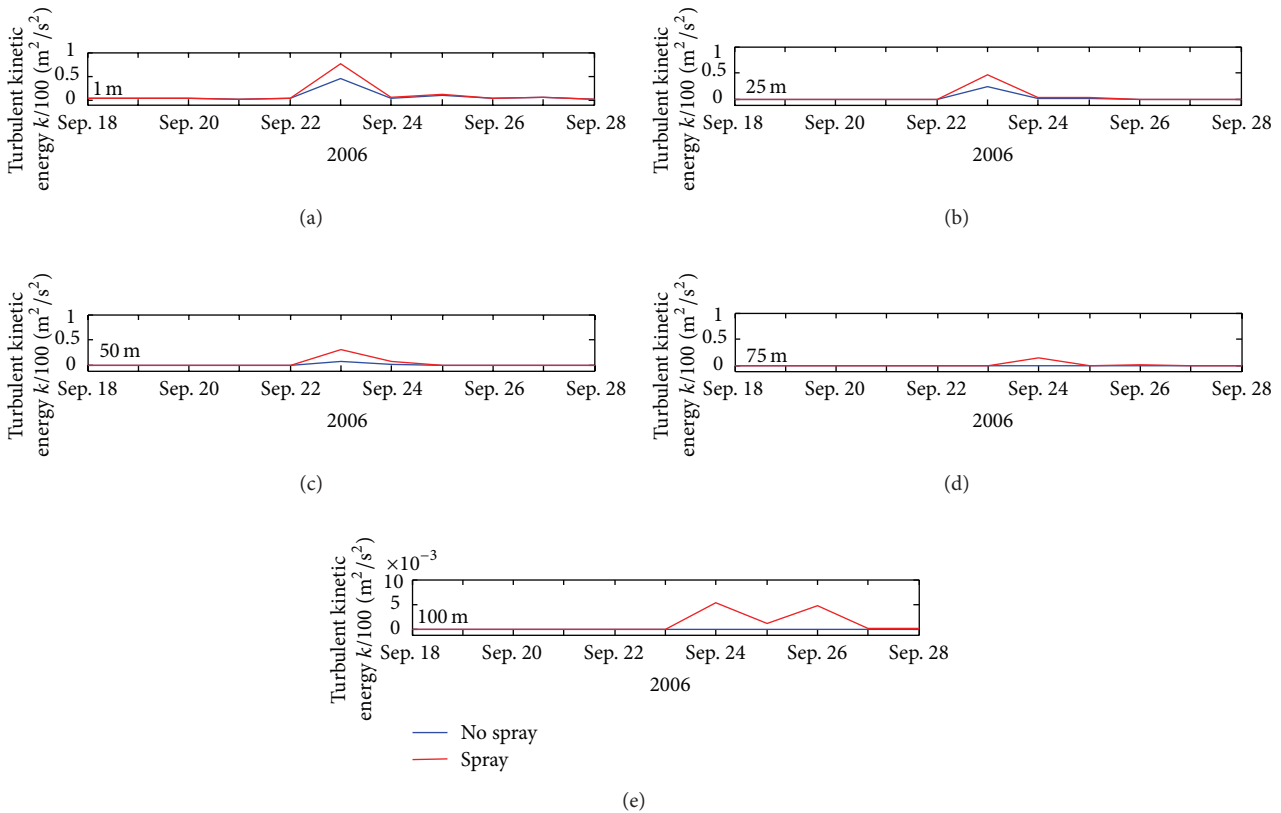


FIGURE 13: The same as Figure 11, but for the total turbulent kinetic energy k .

surface boundary layer during typhoon passage, the General Ocean Turbulent Model is used to simulate the characteristics of the upper layer sea temperature and the turbulent mixing on real typhoon Yagi in 2006. Different from early studies, the effect of sea spray on the air-sea turbulent fluxes is parameterized by the following two comprehensive ways. On the momentum aspect, the macroscopical effect of sea spray is introduced into the parameterization of sea surface roughness for the full wind speed conditions. On the heat and moisture aspect, the effect of sea spray is simulated by the FA94 microcosmic sea spray flux algorithm. In addition, the study introduces the feedback mechanism of sea spray into the air-sea heat flux algorithm. The effect of sea spray is completely introduced into the COARE model and GOTM. Numerical results show that the air-sea turbulent fluxes are significantly enhanced by introducing the impact of sea spray in the GOTM during the typhoon Yagi passage. Sea spray mediated turbulent fluxes nonlinearly increase with the wind speed increasing. When wind speed exceeds 20 m/s, sea spray begins to significantly affect the air-sea turbulent fluxes, whereas, for wind speeds over 30 m/s, the sea spray mediated momentum flux is comparable with the interfacial momentum flux. Combining the complex feedback processes of the sea spray, the maximal net contribution of the sea spray to the total latent heat and sensible heat flux is 204.40 and 106.46 W/m^2 , respectively.

In addition, the effect of sea spray on the upper ocean is analyzed by the diagnostic equation of turbulent kinetic energy and temperature diffusion coefficient. Diagnostic results show that the turbulent kinetic energy and the temperature diffusion coefficient have an increment due to considering the effect of sea spray from the surface to about 50 m depth. With the typhoon leaving the KEO station, this increasing trend spreads downward to 100 m. The enhanced turbulent kinetic energy derived from the sea spray's turbulent fluxes intensively mixes the water column and cools the temperature of the upper ocean for 2-3 days. Hence, with the effect of sea spray included, the ocean upper temperature is decreased by about 0.5°C , which is in agreement with the observations of KEO, AMSR-E, and Reynolds during the typhoon passage.

In conclusion, sea spray acts as an additional source of the air-sea turbulent fluxes and can improve the magnitudes of the turbulent kinetic energy and temperature diffusion coefficient in the upper ocean. Therefore, we suspect that sea spray is an indispensable factor in modulating the mixed layer temperature during the typhoon passage. However, there are still some discrepancies between the observation and the simulation due to the limitation of GOTM, which ignores the horizontal advection and other associated physical processes. Further, three-dimensional general ocean model or air-sea

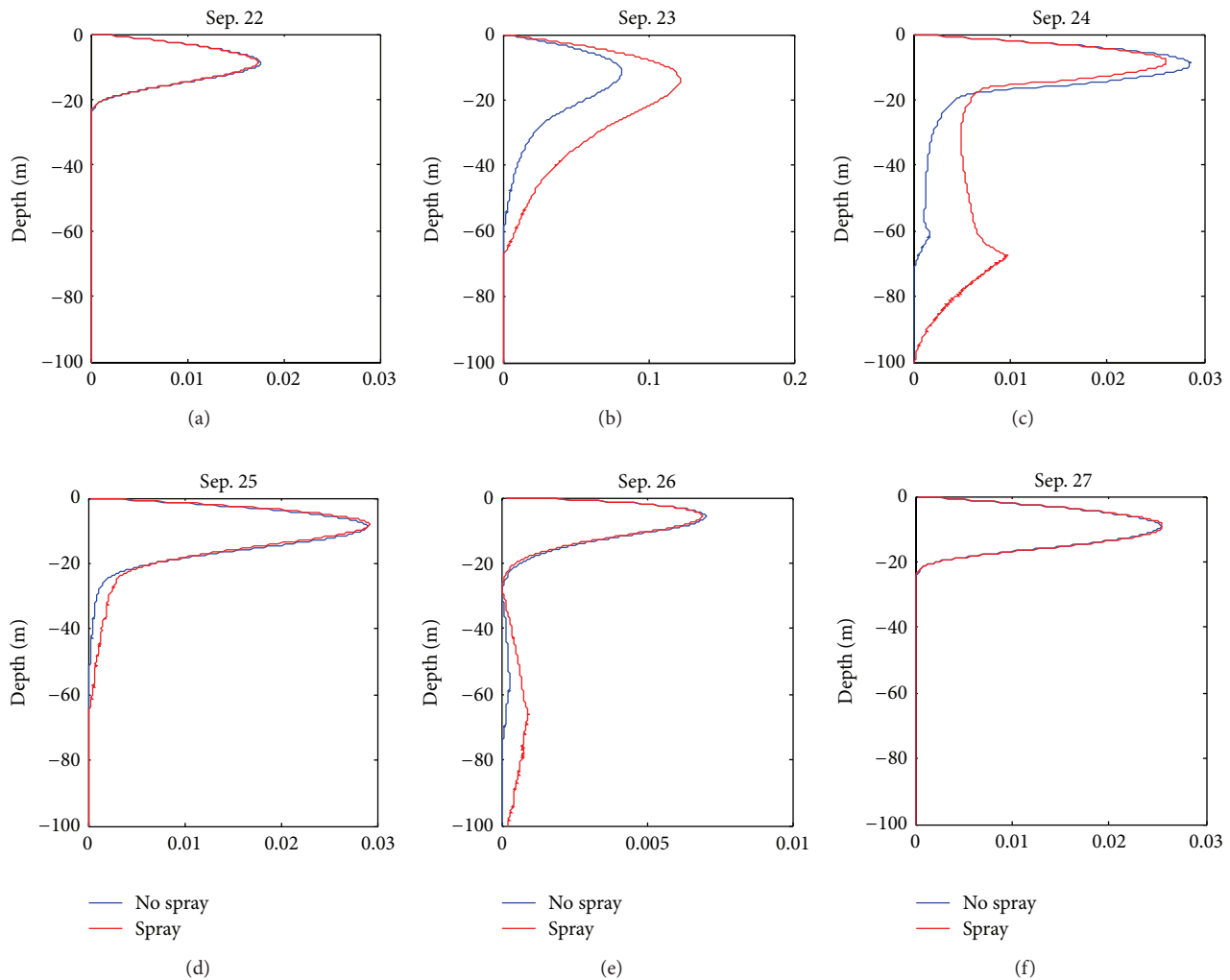


FIGURE 14: Upper 100 m K_n daily profiles simulated by Test 1 (no spray, blue curves) and Test 2 (spray, red curves) on September 22–27 ((a)–(f)), 2006.

coupled model should be used to understand the feedback process between sea spray and air-sea interface.

Conflict of Interests

The authors declare that there is no conflict of interests regarding the publication of this paper.

Acknowledgments

The authors would like to express their gratitude to two reviewers for their helpful comments and suggestions, which contributed to greatly improving the original paper. This work was supported by the National Basic Research Program of China (no. 2013CB430304), National High-Tech R&D Program of China (no. 2013AA09A505), and National Natural Science Foundation of China (nos. 41206178, 41376015, 41376013, and 41306006).

References

- [1] Z. Xuefeng, H. Guijun, W. Dongxiao, L. Wei, and H. Zhongjie, “Effect of surface wave breaking on the surface boundary layer of temperature in the Yellow Sea in summer,” *Ocean Modelling*, vol. 38, no. 3-4, pp. 267–279, 2011.
- [2] X. F. Zhang, G. J. Han, D. X. Wang, Z. Deng, and W. Li, “Summer surface layer thermal response to surface gravity waves in the Yellow Sea,” *Ocean Dynamics*, vol. 62, no. 7, pp. 983–1000, 2012.
- [3] L. X. Zhang, G. J. Han, W. Li et al., “The effects of sea spray on the air-sea turbulent fluxes during the typhoon passage,” *Acta Oceanologica Sinica*, vol. 36, no. 11, pp. 46–56, 2014 (Chinese).
- [4] L. X. Zhang, X. F. Zhang, G. J. Han et al., “Impact of sea spray on upper ocean temperature during typhoon passage: simulation with a 1-D turbulent model,” *Chinese Journal of Oceanology and Limnology*, 2015.
- [5] H. Riehl, *Tropical Meteorology*, McGraw-Hill, New York, NY, USA, 1954.

- [6] P. A. Mangarella, A. J. Chambers, R. L. Street, and E. Y. Hsu, "Laboratory studies of evaporation and energy transfer through a wavy air-water interface," *Journal of Physical Oceanography*, vol. 3, no. 1, pp. 93–101, 1973.
- [7] R. J. Lai and E. J. Plate, "Evaporation from small wind waves," Tech. Rep. CER68-69JRL35, Department of Civil Engineering, Colorado State University, 1969.
- [8] C. C. Easterbrook, "A study of spray and its contributions to total evaporation," Tech. Rep. CAL RM-2865-P-L, Cornell Teah. Lab., Inc., Buffalo, NY, USA, 1970.
- [9] R. S. Bortkovskii, "On the mechanism of interaction between the ocean and the atmosphere during a storm," *Fluid Mechanics-Soviet Research*, vol. 2, no. 2, pp. 87–94, 1973.
- [10] J. Wu, "Evaporation due to spray," *Journal of Geophysical Research*, vol. 79, no. 27, pp. 4107–4109, 1974.
- [11] S. C. Ling and T. W. Kao, "Parameterization of the moisture and heat transfer process over the ocean under whitecap sea states," *Journal of Physical Oceanography*, vol. 11, pp. 324–336, 1976.
- [12] R. A. Anthes, *Tropical Cyclones: Their Evolution, Structure and Effects*, vol. 41 of *Meteorological Monographs*, American Meteorological Society, 1982.
- [13] H. Zhang and S. L. Lou, "Effects of spray on the momentum, heat and vapor transfers over the sea I. Equations and initial values," *Journal of Ocean University of Qingdao*, vol. 25, no. 2, pp. 131–138, 1995.
- [14] S. L. Lou and H. Zhang, "Effects of spray on the momentum, heat and vapor transfers over the sea II. Numerical calculations and comparison of results," *Journal of Ocean University of Qingdao*, vol. 25, no. 2, pp. 139–145, 1995 (Chinese).
- [15] L. Hasse, "On the contribution of spray droplets to evaporation," *Boundary-Layer Meteorology*, vol. 61, no. 3, pp. 309–313, 1992.
- [16] M. P. Rouault, P. G. Mestayer, and R. Schiestel, "A model of evaporating spray droplet dispersion," *Journal of Geophysical Research*, vol. 96, no. 4, pp. 7181–7200, 1991.
- [17] E. L. Andreas, "Thermal and size evolution of sea spray droplets," CRREL Report 89-11, U.S. Army Cold Regions Research and Engineering Laboratory, Hanover, NH, USA, 1989.
- [18] E. L. Andreas, "Time constants for the evolution of sea spray droplets," *Tellus, Series B*, vol. 42, no. 5, pp. 481–497, 1990.
- [19] E. L. Andreas, "Sea spray and the turbulent air-sea heat fluxes," *Journal of Geophysical Research*, vol. 97, pp. 11429–11441, 1992.
- [20] H. R. Pruppacher and J. D. Klett, *Microphysics of Clouds and Precipitation*, D. Reidel, Norwell, Mass, USA, 1978.
- [21] C. W. Fairall, J. D. Kepert, and G. J. Holland, "The effect of sea spray on surface energy transports over the ocean," *The Global Atmosphere-Ocean System*, vol. 2, pp. 121–142, 1994.
- [22] K. A. Emanuel, "Sensitivity of tropical cyclones to surface exchange coefficients and revised steady-state model incorporating eye dynamics," *Journal of the Atmospheric Sciences*, vol. 52, no. 22, pp. 3969–3976, 1995.
- [23] M. D. Powell, P. J. Vickery, and T. A. Reinhold, "Reduced drag coefficient for high wind speeds in tropical cyclones," *Nature*, vol. 422, no. 6929, pp. 279–283, 2003.
- [24] E. Jarosz, D. A. Mitchell, D. W. Wang, and W. J. Teague, "Bottom-up determination of air-sea momentum exchange under a major tropical cyclone," *Science*, vol. 315, no. 5819, pp. 1707–1709, 2007.
- [25] V. K. Makin, "A note on the drag of the sea surface at hurricane winds," *Boundary-Layer Meteorology*, vol. 115, no. 1, pp. 169–176, 2005.
- [26] J.-W. Bao, J. M. Wilczak, J.-K. Choi, and L. H. Kantha, "Numerical simulations of air-sea interaction under high wind conditions using a coupled model: a study of Hurricane development," *Monthly Weather Review*, vol. 128, no. 7, pp. 2190–2210, 2000.
- [27] J. F. Meirink and V. K. Makin, "The impact of sea spray evaporation in a numerical weather prediction model," *Journal of the Atmospheric Sciences*, vol. 58, no. 23, pp. 3626–3638, 2001.
- [28] J. S. Gall, W. M. Frank, and Y. Kwon, "Effects of sea spray on tropical cyclones simulated under idealized conditions," *Monthly Weather Review*, vol. 136, no. 5, pp. 1686–1705, 2008.
- [29] C. L. Uang, "Impact of sea spray and oceanic on the development of tropical cyclones," in *Proceedings of the 23rd Conference on Hurricanes and Tropical Meteorology*, pp. 30–31, American Meteorological Society, Dallas, Tex, USA, 1999.
- [30] Y. M. Wang, J. D. Kepert, and G. J. Holland, "The effect of sea spray evaporation on tropical cyclone boundary layer structure and intensity," *Monthly Weather Review*, vol. 129, no. 10, pp. 2481–2500, 2001.
- [31] H. Burchard, K. Bolding, W. Kühn, A. Meister, T. Neumann, and L. Umlauf, "Description of a flexible and extendable physical-biogeochemical model system for the water column," *Journal of Marine Systems*, vol. 61, no. 3-4, pp. 180–211, 2006.
- [32] L. Umlauf and H. Burchard, "Second-order turbulence closure models for geophysical boundary layers. A review of recent work," *Continental Shelf Research*, vol. 25, no. 7-8, pp. 795–827, 2005.
- [33] C. W. Fairall, E. F. Bradley, D. P. Rogers, J. B. Edson, and G. S. Young, "Bulk parameterization of air-sea fluxes for tropical ocean/global atmosphere coupled-ocean atmosphere response experiment," *Journal of Geophysical Research C: Oceans*, vol. 101, no. 2, pp. 3747–3764, 1996.
- [34] B. Liu, C. Guan, and L. Xie, "The wave state and sea spray related parameterization of wind stress applicable from low to extreme winds," *Journal of Geophysical Research C: Oceans*, vol. 117, pp. 1–10, 2012.
- [35] A. Masuda and T. Kusaba, "On the local equilibrium of winds and wind-waves in relation to surface drag," *Journal of the Oceanographical Society of Japan*, vol. 43, no. 1, pp. 28–36, 1987.
- [36] N. Maat, C. Kraan, and W. A. Oost, "The roughness of wind waves," *Boundary-Layer Meteorology*, vol. 54, no. 1-2, pp. 89–103, 1991.
- [37] J. Monbaliu, "On the use of the Donelan wave spectral parameter as a measure for the roughness of wind waves," *Boundary-Layer Meteorology*, vol. 67, no. 3, pp. 277–291, 1994.
- [38] D. Vickers and L. Mahrt, "Fetch limited drag coefficients," *Boundary-Layer Meteorology*, vol. 85, no. 1, pp. 53–79, 1997.
- [39] H. K. Johnson, J. Højstrup, H. J. Vested, and S. E. Larsen, "On the dependence of sea surface roughness on wind waves," *Journal of Physical Oceanography*, vol. 28, no. 9, pp. 1702–1716, 1998.
- [40] M. A. Donelan, "Air-sea interaction," in *The Sea*, B. LeMehaute and D. M. Hanes, Eds., pp. 239–292, Wiley Interscience, New York, NY, USA, 1990.
- [41] M. A. Donelan, F. W. Dobson, S. D. Smith, and R. J. Anderson, "On the dependence of sea surface roughness on wave development," *Journal of Physical Oceanography*, vol. 23, no. 9, pp. 2143–2149, 1993.
- [42] Y. Toba, "Local balance in the air-sea boundary processes. I. On the growth process of wind waves," *Journal of the Oceanographical Society of Japan*, vol. 28, no. 3, pp. 109–120, 1972.

- [43] E. C. Monahan and I. O. Muircheartaigh, "Optimal power-law description of oceanic whitecap coverage dependence on wind speed," *Journal of Physical Oceanography*, vol. 10, no. 12, pp. 2094–2099, 1980.
- [44] J. B. Edson, *Lagrangian model simulation of the turbulent transport of evaporating jet droplets [Ph.D. thesis]*, Pennsylvania State University, State College, Pa, USA, 1989.
- [45] M. A. Miller and C. W. Fairall, "A new parameterisation of aerosol generation in the marine planetary boundary layer," in *Proceedings of the 7th Conference on Ocean-Atmosphere Interaction*, American Meteorological Society, Anaheim, Calif, USA, January 1988.
- [46] D. K. Woolf, P. A. Bowyer, and E. C. Monahan, "Discriminating between the film drops and jet drops produced by a simulated whitecap," *Journal of Geophysical Research: Oceans*, vol. 92, no. C5, pp. 5142–5150, 1987.
- [47] G. de Leeuw, "Vertical profiles of giant particles close above the sea surface," *Tellus*, vol. 38, no. 1, pp. 51–61, 1986.
- [48] G. de Leeuw, "Near-surface particle size distribution profiles over the North Sea," *Journal of Geophysical Research*, vol. 92, no. 13, pp. 14631–14635, 1987.
- [49] G. de Leeuw, "Profiling of aerosol concentrations, particle size distributions and relative humidity in the atmospheric surface layer over the North Sea," *Tellus*, vol. 42B, no. 4, pp. 342–354, 1990.
- [50] J. B. Edson, "Simulating droplet motion above a moving surface," in *Modeling the Fate and Influence of Marine Spray*, P. Mestayer, E. C. Monahan, and P. A. Beetham, Eds., Whitecap Report 7, pp. 84–94, University of Connecticut, Marine Sciences Institute, Groton, Conn, USA, 1990.
- [51] M. P. Rouault and S. E. Larsen, "Spray droplet under turbulent conditions," Tech. Rep. RISO-M-2845, Department of Meteorology and Wind Energy, Risø National Laboratory, Roskilde, Denmark, 1990.
- [52] E. L. Andreas and J. DeCosmo, "Sea spray production and influence on air-sea heat and moisture fluxes over the open ocean," in *Air-Sea Exchange: Physics, Chemistry and Dynamics*, G. L. Geernaert, Ed., pp. 327–362, Kluwer Academic, 1999.
- [53] E. L. Andreas, "An algorithm to predict the turbulent air-sea fluxes in high-wind," in *Proceedings of the 12th Conference on Interactions of the Sea and Atmosphere*, Amer Meteor Soc, Long Beach, Calif, USA, 2003, CD-ROM 3.4:7.
- [54] Z. H. Liu, J. P. Xu, B. K. Zhu, C. H. Sun, and L. F. Zhang, "Upper ocean to tropical cyclones in northwestern Pacific during 2001–2004 by Argo data," *Journal of Tropical Oceanography*, vol. 25, pp. 1–8, 2006 (Chinese).
- [55] E. L. Andreas and K. A. Emanuel, "Effects of sea spray on tropical cyclone intensity," *Journal of the Atmospheric Sciences*, vol. 58, no. 24, pp. 3741–3751, 2001.